Smart Sensors, Measurement and Instrumentation 11

Alex Mason
Subhas Chandra Mukhopadhyay
Krishanthi Padmarani Jayasundera
Editors

Sensing Technology: Current Status and Future Trends III

Springer

Smart Sensors, Measurement and Instrumentation

Volume 11

Series editor

Subhas Chandra Mukhopadhyay
School of Engineering and Advanced Technology (SEAT)
Massey University (Manawatu)
Palmerston North
New Zealand
E-mail: S.C.Mukhopadhyay@massey.ac.nz

More information about this series at http://www.springer.com/series/10617

Alex Mason · Subhas Chandra Mukhopadhyay
Krishanthi Padmarani Jayasundera
Editors

Sensing Technology: Current Status and Future Trends III

Springer

Editors
Alex Mason
Liverpool John Moores University
Liverpool, United Kingdom

Krishanthi Padmarani Jayasundera
Massey University (Manawatu Campus)
Palmerston North, New Zealand

Subhas Chandra Mukhopadhyay
Massey University (Manawatu)
Palmerston North, New Zealand

ISSN 2194-8402 ISSN 2194-8410 (electronic)
ISBN 978-3-319-10947-3 ISBN 978-3-319-10948-0 (eBook)
DOI 10.1007/978-3-319-10948-0

Library of Congress Control Number: 2013953628

Springer Cham Heidelberg New York Dordrecht London

Printed on acid-free paper

Springer is part of Springer Science+Business Media (www.springer.com)

Guest Editorial

The applications of Sensing Technology include gas sensing, medical diagnostics, industrial manufacturing, defense, national security, prevention of natural disaster and terrorism. The proper detection and reporting of events by high performance sensor systems delivers huge cross-sector benefits through increasing use of continuous real-time systems for improved automation and control. The continuing development of sensors, and the systems which support them, will undoubtedly continue to bring great value, and will assist in tackling global issues such as water quality monitoring, ageing populations and natural disasters. The cross-cutting nature of sensor systems demands interaction between researchers and industry from technologically advanced and developing countries in order to drive toward the sensors of the future. ICST 2013, as in previous years, brings together such people, and so we hope that it can provide a useful platform for interaction.

This book contains a collection of selected works stemming from the 2013 International Conference on Sensing Technology (ICST), which was held in Wellington, New Zealand. This was the seventh time the conference had been held, and over the years it has become an incredibly successful event – in 2013 it attracted over 220 participants and provided a forum for interaction between researchers across technologically advanced and developing countries working on design, fabrication and development of different sensors.

The conference was organized by the School of Engineering and Advanced Technology, Massey University, and we thank the department's management for extending their continued support for the conference. We would also like to thank all of the authors as they are main ingredient for any conference to succeed. In addition, the Technical Programme Committee has done a tremendous and wonderful job. We are very much indebted to everybody in the Technical Programme Committee for accepting the invitation to lend their help, support, time and effort to make ICST a great success. We would also like to extend our special thanks to the keynote and invited speakers for their time and support during the event.

The purpose of these books is to distill the highlights of the conference, and therefore track the latest developments in sensing technologies. The book contents

are quite broad, since sensors can be applied in many areas as was made apparent previously.

Chapters 1 through 5 of this volume present work on the progression of light or optical based sensor systems. Chapter 1 begins this discussing the use of fiber optic sensors in underground structures such as tunnels and car parks for the monitoring of air quality in an effort to reduce the advent of fires triggered by combustible gas build-ups. Chapter 2 describes evanescent wave absorption based fiber optic sensors, while Chapter 3 moves to the topic of using optical systems for the virtual reconstruction of complex objects, which has particular relevance in the field of quality control. In Chapter 4, an application of light based sensors is presented for determining the type of street lighting used in urban areas in order to minimize losses associated with inefficient luminaires. Chapter 5 presents a laser based system for monitoring Cesium, which it is hoped can be used in the future for monitoring a wider variety of radioactive materials in an environmental context.

Chapters 7-10 relate specifically to the growing area of Wireless Sensor Networks, presenting a variety of important aspects including medium access (Chapter 7), energy efficiency (Chapter 8), data compression (Chapter 9) and network attacks (Chapter 10).

Chapter 11 presents an interesting application sensing technology, looking at how multi-sensor use could assist in educational environments. This is quite a topical issue at present, particularly with the advent of smart/intelligent buildings and wider consideration of smart cities.

In Chapter 12, progression of work in the area of electronic noses is presented, specifically considering the application of the technology for detection micro-organisms in food and water. With standards across Europe, and the world, rising for both water and food quality, the drive for such tools is becoming ever greater.

Chapter 13 discusses the rather unique area of understanding pain, and how to sense it, in animals – work which could help considerably in help improve the effectiveness of pain control drugs administered to animals.

Chapter 14 presents work from a research team in New Zealand, well known for their work in the use of microwave-based dielectric measurement techniques, to determine the moisture content of wet sand which could have huge importance in improving the quality and consistency of, for example, building materials.

An organic molecule based sensor is presented in Chapter 15, which is specifically developed for the detection of aldehydes, which are used across a broad spectrum of industries, and represent a significant threat to humans if present in large quantities.

Chapter 16 describes the development of laser-ultrasound based system which generates and detects surface acoustic waves from steel cylindrical objects with requiring any contact. Chapters 17 and 18 present models for electrostatic capacitive sensors and muscle actuators respectively. Chapter 19 presents a method for measuring systems fabricated using micro-technological processes. Finally, Chapter 20 investigates the giant magneto-impedance properties of Iron Cobalt microwires.

This book is written for academic and industry professionals working in the field of sensing, instrumentation and related fields, and is positioned to give a snapshot

of the current state of the art in sensing technology, particularly from the applied perspective. The book is intended to give broad overview of the latest developments, in addition to discussing the process through which researchers go through in order to develop sensors, or related systems, which will become more widespread in the future.

We would like to express our appreciation to our distinguished authors of the chapters whose expertise and professionalism has certainly contributed significantly to this book.

Alex Mason, Guest Editor
Built Environment and Sustainable Technologies Research Institute,
School of Built Environment,
Liverpool John Moores University
Liverpool, United Kingdom
e-mail: A.Mason1@ljmu.ac.uk

Subhas Chandra Mukhopadhyay, Guest Editor
School of Engineering and Advanced Technology (SEAT),
Massey University (Manawatu Campus)
Palmerston North, New Zealand
e-mail: S.C.Mukhopadhyay@massey.ac.nz

Krishanthi Padmarani Jayasundera, Guest Editor
Institute of Fundamental Sciences,
Massey University (Manawatu Campus)
Palmerston North, New Zealand
e-mail: K.P.Jayasundera@massey.ac.nz

Dr. Alex Mason graduated from the University of Liverpool, UK, with a first class honors degree in Computer and Multimedia Systems, after which he went on to complete a PhD in Wireless Sensor Networks and their Industrial Applications at Liverpool John Moores University (LJMU), UK. Upon completing his PhD in 2008, he concentrated for 2 years solely on research, working on aspects of non-invasive and non-destructive sensing for the healthcare, automotive and defense sectors.

Dr. Mason currently holds the position of Reader in Smart Technologies within the School of Built Environment at LJMU, after holding a Senior Lecture post prior to this since 2010. He has continued research in healthcare and defense, in addition to new areas such as water quality monitoring. Since becoming more involved in Built Environment issues, he has also developed an interest in Structural Health Monitoring and is currently working closely with the UK Defense Science and Technology Laboratories in this field.

Dr. Mason is responsible for supervising a number of PhD students in the areas of sensing and renewable energy technologies, has coauthored over 130 publications (including 4 patents), has helped to organize national and international conferences, and gave a number of invited talks on his work. He is also an active member of the IET in the UK, and has achieved Chartered Engineer status with them.

Dr. Subhas Chandra Mukhopadhyay graduated from the Department of Electrical Engineering, Jadavpur University, Calcutta, India in 1987 with a Gold medal and received the Master of Electrical Engineering degree from Indian Institute of Science, Bangalore, India in 1989. He obtained the PhD (Eng.) degree from Jadavpur University, India in 1994 and Doctor of Engineering degree from Kanazawa University, Japan in 2000.

Currently, he is working as a Professor of Sensing Technology with the School of Engineering and Advanced Technology, Massey University, Palmerston North, New Zealand. His fields of interest include Smart Sensors and Sensing Technology, Wireless Sensors Network, Electromagnetics, control, electrical machines and numerical field calculation etc.

He has authored/co-authored over 300 papers in different international journals and conferences, edited eleven conference proceedings. He has also edited ten special issues of international journals and twenty books with Springer-Verlag as guest editor. He is currently the Series editor for the Smart Sensing, Measurements and Instrumentation of Springer-Verlag.

He is a Fellow of IEEE, a Fellow of IET (UK), a Topical editor of IEEE Sensors journal. He is also an Associate Editor for IEEE Transactions on Instrumentation and Measurements and a Technical Editor of IEEE Transactions on Mechatronics. He was a Distinguished Lecturer of IEEE Sensors council. He is Chair of the Technical Committee 18, Environmental Measurements of the IEEE Instrumentation and Measurements Society. He is in the editorial board of many international journals. He has organized many international conferences either as a General Chair or Technical Programme Chair.

Dr. Krishanthi P. Jayasundera graduated from University of Peradeniya, Sri Lanka with honors degree in Chemistry. She obtained her both Master and PhD in Organic Chemistry from Kanazawa University, Japan. After completing PhD she worked as researcher nearly 14 years in New Zealand involving various projects related to organic synthesis. Currently, she is working as a Post-doctoral researcher with the Institute of Fundamental Sciences, Massey University, New Zealand. She has published over 30 papers in different international journals and conference proceedings. She has also edited a few conference proceedings and books.

Contents

Review of the Use of the Optical Fibers for Safety Applications in Tunnels and Car Parks: Pollution Monitoring, Fire and Explosive Gas Detection

M. Debliquy[1], D. Lahem[2], A. Bueno-Martinez[3], G. Ravet[3], J.-M. Renoirt[1,3], and C. Caucheteur[3]

[1] Service de Science des Matériaux, Faculté Polytechnique, Université de Mons Mons, Belgium
[2] Materia Nova, Materials R&D Centre Mons, Belgium
[3] Service d'Electromagnétisme et de Télécommunications, Faculté Polytechnique, Université de Mons, Mons, Belgium
marc.debliquy@umons.ac.be

Abstract. Optical fiber sensors bring to measurement systems all the advantages offered by the optical fiber technology. The potential applications for these sensors are numerous and can spread from medical diagnosis to pipe line monitoring passing through geological measurements. This chapter will focus on the applications in road tunnels and undercroft car parks monitoring. It will detail the existing optical fiber sensor methods, commercially available or under development in the field of air quality monitoring, in particular NO_2 that is representative of toxic automotive pollution, flaming fire detection and combustible gas leak detection (in particular methane and hydrogen).

Keywords: optical fibers, gas sensors, pollution, fire detection.

1 Introduction

An optical fiber is a 125 μm thick cylindrical waveguide made of two concentric layers of silica (the core surrounded by the cladding) that guides light thanks to a refractive index difference between them. It is an excellent support for miniaturized sensors, allowing remote operation in very small volumes. In potentially explosive atmospheres, sensors based on optical fibers offer a set of advantages without equivalent for well-established technologies such as electrochemical sensors, semiconductor sensors or pellistors [1]. Optical fibers are indeed immune to electromagnetic interferences and present a good resistance to high temperatures and to chemical corrosion. They are also durable in high radiation environments. Their small dimensions combined with their light weight

A. Mason et al. (eds.), *Sensing Technology: Current Status and Future Trends III*, Smart Sensors, Measurement and Instrumentation 11, DOI: 10.1007/978-3-319-10948-0_1

and flexibility allow to embed them directly in the structures to monitor without affecting their mechanical resistance. Last but not least, depending on the interrogation technique that is set up, optical fibers yield distributed (the parameter is sensed all along the fiber length) or quasi-distributed (the parameter is sensed at different points cascaded along the fiber length) measurements that can be remotely addressed. This particularity is not intrinsically possible to achieve with any other sensing methods.

In this chapter, we will focus on applications in road tunnels and undercroft car parks monitoring. These closed and generally wide spaces present issues in terms of air quality control (CO and NO_x), fire detection and combustible gas leak detection. Those elements are not independent as a combustible gas leak can lead to a fire. A fire leads to the production of toxic gases such as CO or NO_x and some fire detectors are based on the detection of these tracer gases. Classically, to insure the safety level in these places, a sufficient number of point sensors/detectors is installed to cover the entire area. These solutions are generally expensive because of the costs for the installation of the detectors, the cabling and data transfer. Optical fibers bring an elegant solution as the fiber itself can ensure all functions: signal and data transfer, addressing and distributed or quasi-distributed detection at the same time.

After a review of the most often encountered optical fiber sensing technologies, this chapter will focus on the main optical fiber sensors developed in the field of air quality monitoring, in particular NO_2, flaming fire detection and combustible gas leak detection (in particular methane and hydrogen).

2 Optical Fiber Sensing Technologies

Different sensing modalities can be exploited to realize physical and chemical sensors. Physical perturbations such as temperature changes and axial strain variations induce geometrical and morphological changes that in turn impact light propagation in the fiber core. As it will be summarized hereafter, such changes can be measured through the use of interferometers, fiber gratings, polarimetry or by exploitation of back-scattering. Another transduction mechanism is often exploited for gas and chemical sensing, i.e. the measurement of surrounding refractive index change. An optical fiber is not intrinsically sensitive to surrounding refractive index changes since light is confined into the core and is therefore blind to changes occurring in the medium surrounding the cladding. To modify the optical fiber into a refractometer, the core-guided light has to be brought into contact with the surrounding medium. It is possible simply by exploitation of the Fresnel reflection at the fiber tip or along the fiber propagation axis by exposing the evanescent wave of the core guided light to the surrounding medium. This second option is obtained by polishing or etching the fiber or by using radiating gratings.

2.1 Optical Fiber Interferometric Sensors [2]

The operating principle of such sensors is based on the interference between two coherent (or partially coherent) light beams that overlap. The useful signal is then the intensity of the beating signal. Different configurations are encountered. We focus herewith on those that have been used for gas and chemical sensing.

The basic configuration of a Mach-Zehnder interferometer is depicted in Figure 1. A sensing optical fiber and a reference optical fiber are used between two couplers. Considering that the coupling ratios are equal to 0.5 and that there is no optical loss, the detected intensity at the output is given by:

$$I = I_0 \cos^2\left[\frac{\pi}{\lambda}(n_s L_s - n_r L_r)\right] \quad (1)$$

where n_s and n_r stand for the refractive indices of the sensitive and reference fibers, respectively. L_s and L_r are their length and is the wavelength of light in vacuum. In practice, both n_s and L_s change in response to external perturbations, such as mechanical strain and temperature. Hence, the information about these stimuli is known from the measured intensity. For strain sensing, L_r is periodically modulated to minimize the temperature influence and to improve the sensing performances.

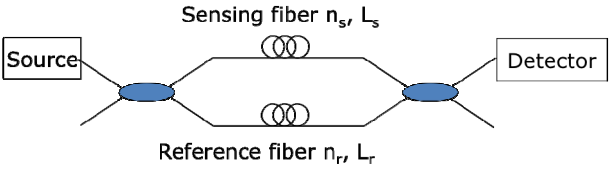

Fig. 1 Sketch of a Mach-Zehnder interferometer

A Michelson interferometer is sketched in Figure 2. It makes use of a coupler and two mirrors. It presents a similar response to a Mach-Zehnder interferometer but the light passes twice into the sensing and reference fibers, which doubles the phase shift per unit of length, and in turn increase the sensitivity of the technique. In practice, this type of interferometer requires an isolator to protect the source from light reflections.

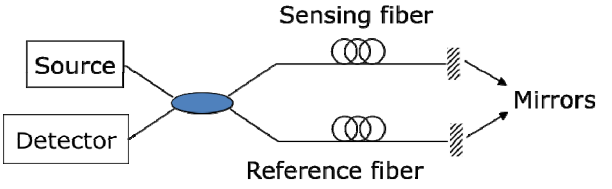

Fig. 2 Sketch of a Michelson interferometer

Contrary to Mach-Zehnder and Michelson interferometers that exploit the interferences between two waves, Fabry-Perot interferometers realize multiple interferences, thanks to the use of two mirrors that form a cavity, as sketched in Figure 3. Considering that the mirror reflectivities are smaller than 1 and identical (R_1=R_2=R), the global reflectivity and transmissivity are respectively given by:

$$R_{FP} = \frac{P_r}{P_i} \cong 2R(1+\cos\phi)$$
$$T_{FP} = \frac{P_t}{P_i} \cong 1-2R(1+\cos\phi) \quad (2)$$

where the phase shift in the cavity is expressed by:

$$\phi = \frac{4\pi nL}{\lambda} \quad (3)$$

for which n is the refractive index of the optical fiber inside the cavity.

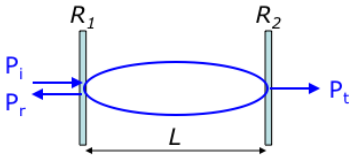

Fig. 3 Sketch of a Fabry-Perot interferometer

Hence, Fabry-Perot interferometers are sensitive to changes of the optical path between the mirrors. The distance between the mirrors can be only a few millimeters so that such sensors are considered, contrary to other interferometers that require several meters of optical fiber at least. They are often encountered for temperature, mechanical strain and pressure sensing. Their standard sensitivity is 0.1 °C for temperature and 1 µe for axial strain. They can be extrinsic or intrinsic, depending on the nature of the cavity. Intrinsic sensors are purely made in optical fiber. In this case, mirrors can be Bragg gratings (see section 2.4).

2.2 Optical Fiber Sensors Based on Backscattering

Light diffusion appears essentially due to the presence of inhomogeneity in the fiber core. Elastic diffusion occurs when the frequency (or wavelength) of the diffused light is identical to the one of the incident light. Otherwise, it is inelastic. An inelastic diffusion can be spontaneous (it results from the intrinsic properties of the medium) or stimulated, i.e. mainly due to the incident wave. Three processes are present in optical fibers:

- Rayleigh backscattering arising from reflections due to the inhomogeneity in the refractive index of the fiber core resulting from the manufacturing process [3];

- Raman backscattering resulting from interactions with the molecular vibrations of the glass matrix [4];
- Brillouin backscattering resulting from interactions with inhomogeneity generated by acoustic waves in the optical fiber (acoustic phonons) [5].

These different diffusion sources are characterized by well-defined absorption bands, as depicted in Figure 4. The Rayleigh component appears at the same wavelength as the incident wave. It is a linear diffusion. Raman and Brillouin backscattering result from nonlinear effects when the launched optical power is above a given threshold. Two Raman components appear at each side of the incident wavelength, with a frequency spacing of ~13 THz. The same occurs for the Brillouin diffusion but the frequency spacing is here close to 11 GHz. The components located above (below) the incident wavelength are called "Stokes ("anti-Stokes").

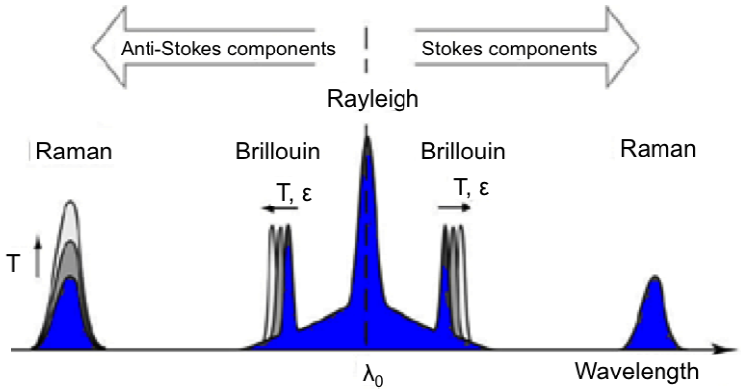

Fig. 4 Illustration of the three backscattering mechanisms in an optical fiber

The Raman backscattering is used to measure temperature from the ratio between the anti-Stokes and Stokes components. The power of the anti-Stokes component is strongly dependent on temperature. It has been demonstrated that for fiber lengths shorter than 15 km, graded-index multimode optical fibers should be privileged as they allow to obtain a superior anti-Stokes power [6]. The optimal wavelength has been estimated equal to 1320 nm. For this kind of fibers, contrary to single-mode optical fibers, the stimulated Brillouin scattering does not significantly deplete the incident wave. Sensors exploiting the Raman scattering are not sensitive to mechanical strains. They are thus used in practice for temperature profiling in applications such as pipelines monitoring or fire detection.

In the Brillouin scattering, the spectrum is sensitive to both temperature and mechanical strain. The sensing parameter is the Brillouin frequency shift, whose sensitivity is ~1MHz/°C and ~0.05 MHZ/με for temperature and strain, respectively. Commercially available Brillouin sensors offer a spatial resolution of

~10 centimeters over several (tens of) kilometers. Their main application remains axial strain sensing [7].

2.3 Evanescent Wave Sensors and Fiber Tip Sensors

These configurations bring light into contact with the surrounding medium. In this case, there is no exclusive sensitivity to a gas or chemical compound so that a specific sensitive layer is required in addition to the optical fiber probe. In all cases, the sensitive layer has to respect some practical requirements to obtain an efficient and robust sensor. In particular, it is intended to yield a fast response (of the order of several seconds or even better) and to be specific to the gas specie to detect, i.e. to be inert to other gases.

In an evanescent wave fiber optic sensor, the cladding of the optical fiber is often partially removed to place the core in direct contact with a sensitive material [8]. Ideally, this material absorbs the wavelengths carried by the fiber and modifies the absorption as a function of the gas concentration to be detected. In turn, this mechanism drains energy from the fiber core and the output power at the detector is modified as a function of the light absorption.

End coated optical fiber sensors exploit the Fresnel reflection occurring at the interface between the cleaved fiber end and the surrounding medium [9]. Here, a sensitive material deposited on the cleaved fiber end is expected to modify its refractive index as a function of the gas concentration to monitor. As a result, this modifies the reflection conditions at the interface and the reflected power varies with respect to the gas concentration.

2.4 Optical Fiber Grating Sensors

A fiber Bragg grating (FBG) is a periodic and permanent modification of the core refractive index value along the optical fiber axis [10, 11]. This modification is usually obtained by transversally exposing the core of a photosensitive optical fiber to an intense interference pattern of ultraviolet light at a wavelength around 240 nm. Indeed, due to the presence of Germanium oxide dopants inside the core, an optical fiber is photosensitive (i.e. it benefits from the property to permanently change its refractive index when exposed to light) in a wavelength band centered around 240 nm. For this reason, continuous-wave frequency-doubled Argon-ion laser emitting at 244 nm or pulsed excimer laser emitting at 248 nm are most often used to manufacture FBGs. To create an interference pattern, two writing techniques are privileged: the interferometric method (also called transverse holographic method) and the phase mask technique.

An FBG is defined by several physical parameters. The grating length L is the optical fiber length along which the refractive index modulation is realized. The periodicity and the amplitude of the refractive index modulation are labeled Λ and δn, respectively.

The order of magnitude of these parameters typically varies between 200 nm to 1000 nm for Λ, from a few mm to a few tens of cm for L and from 10^{-5} to 10^{-3} for δn. Such a perturbation induces light coupling between two counter-propagating core modes. This mode coupling occurs for some wavelengths around the Bragg wavelength defined by:

$$\lambda_{Bragg} = 2n_{eff}\Lambda \tag{4}$$

where n_{eff} is the effective refractive index of the core mode at the Bragg wavelength.

A uniform FBG acts as a selective mirror in wavelength around the Bragg wavelength to yield a pass-band reflected amplitude spectrum, as depicted in Figure 5 for a 1 cm long FBG. In fact, at each refractive index discontinuity along the fiber axis, a weak Fresnel reflection is generated. They add in phase at the Bragg wavelength, yielding an important reflection.

In practice, the effective refractive index of the core and the spatial periodicity of the grating are both affected by changes in strain and temperature. The order of magnitude of the temperature sensitivity of the Bragg wavelength is ~10 pm/°C around 1550 nm. The axial strain sensitivity of the Bragg wavelength is ~1.2 pm/με around 1550 nm. In addition to their intrinsic sensitivity to temperature and strain changes, the association of FBGs with sensitive materials opens the way to other sensing applications such as gas leak monitoring or chemical species profiling.

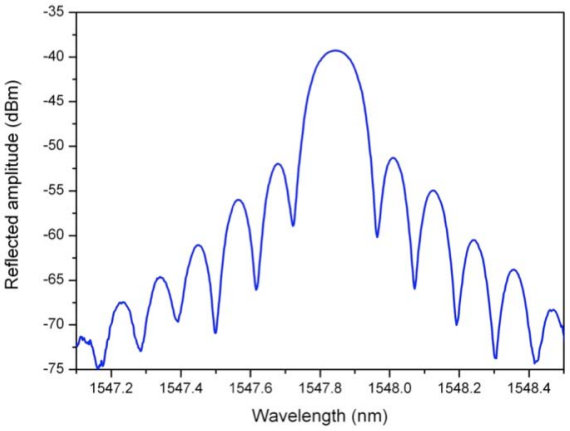

Fig. 5 Amplitude reflected spectrum of a 1 cm long FBG

Other types of fiber gratings such as tilted fiber Bragg gratings (TFBGs) and long period fiber gratings (LPFGs) couple light from the fiber to the cladding [12, 13]. TFBGs are short period gratings that present a refractive index modulation angled by a few degrees with respect to the perpendicular to the optical fiber

propagation axis. They present an amplitude transmitted spectrum composed of several tens of narrowband cladding mode resonances that present their own sensitivity to surrounding refractive index changes. The presence of the Bragg wavelength in the amplitude spectrum offers convenient temperature self-compensation, as it is not sensitive to the surrounding medium. LPFGs present a refractive index modulation period about 1000 times higher than short period-gratings. They are diffractive gratings that present an amplitude spectrum composed of several broadband cladding mode resonances. These modes can be again used for refractometry purposes. Hence, such gratings can be associated to sensitive layers that change their refractive index in response to the measurand to open up the sensing modalities (gas, chemical species in liquids, etc …).

2.5 Surface Plasmon Optical Fiber Sensors

Surface plasmon wave sensors exploit a nanometric sheath of noble metal (most often gold or silver) deposited on the cladding surface that, under particular conditions of excitation, leads to the generation of surface plasmon waves [14]. These waves propagate at the interface between the metal and the dielectric (surrounding medium). They have to be excited by an evanescent wave coming from the optical fiber. Geometries associated to the excitation of surface plasmons are therefore etched or side-polished optical fibers and radiating fiber gratings (TFBGs and LPFGs). Surface plasmon waves are strongly sensitive to a change of the surrounding refractive index. Hence, by depositing on the metal sheath a sensitive material that modifies its refractive index in the presence of the gas to detect, one obtains an efficient and very sensitive gas sensor.

In the following sections, we present some applications of optical fibers for air quality monitoring and gas leak detection.

3 Air Quality Monitoring

In this section, we will focus on the detection of CO and NO_2 which are the most important polluting gases for undercroft car parks and tunnels. Let us mention that the TLV (Threshold Limit Value) is equal to 25 ppm (29 mg/m^3) for CO and 5 ppm (9 mg/m^3) for NO_2 (recommended by American Conference of Governmental & Industrial Hygienists ACGIH). [15]

3.1 Current Technologies for NO_2 and CO Measuring Systems

The continuous monitoring of CO or NO_2 relies on different technologies depending on the concentration range, the desired accuracy and the application (interfering gases, temperature, available volume, cost). There are mainly 3 classical systems for CO and NO_2 detection: analyzers using optical methods (chemiluminescence or IR absorption), electrochemical cells and semiconductors.

Analyzers Based on Chemiluminescence [16]

Chemiluminescence is widely used for monitoring NO and NO_2 at low concentrations (<10 ppm). The working principle is based on the fact that NO is a reactive gas that can easily be oxidized resulting in the production of NO_2 in excited state. The desexcitation leads to the production of 1 photon. With ozone, this reaction is rapid and complete (equation 5).

$$NO + O_3 \rightarrow NO_2 + O_2 + h\nu \quad (5)$$

If the ozone is in excess, the intensity of the emitted light is proportional to the NO concentration. So, by injecting the gases with careful sampling and volume control in a chamber fitted with a light detector (photomultiplier tube or solid state device, the NO concentration can be accurately measured (Figure 6).

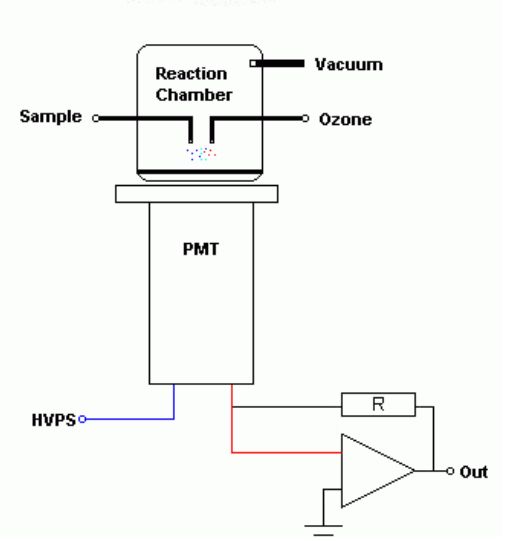

Fig. 6 Scheme of the working principle of a NO analyser

In order to measure NO_2, the gas sample is flown in a catalytic furnace to convert NO_2 to NO. Indeed at high temperature (>500 °C), NO is the stable form and NO_2 follows reaction (6)

$$NO_2 \rightarrow NO + {}^1/_2\, O_2 \quad (6)$$

The produced NO is then measured the same way as described before.

Analysers for NO and NO_2 work in 2 steps:

1 the air sample is measured passing directly to the reaction chamber giving then the NO concentration

2 the air sample is diverted in the conversion oven before entering the reaction chamber giving then the total NO_x concentration ($NO+NO_2$)

The NO_2 concentration is calculated by difference.

This system allows accurate determinations of low NO_x concentration levels (in the ppb range). As can be understood, this type of analysers is quite complicated, cumbersome, power consuming and expensive. They are usually used for environmental monitoring.

Analysers Based on Infra Red Absorption [17, 18]

For CO, the most common detection principle is based on the fact that Carbon Monoxide (CO) has a characteristic infrared absorption near 4.6 µm. The absorption of infrared radiation by CO molecules can be used to measure CO concentrations in the presence of other background gases. The non-dispersive infrared (NDIR) technique is based on this principle (Figure 7). The CO NDIR technique is generally accepted as being the most reliable continuous method for measurement of CO in ambient air and also source emissions.

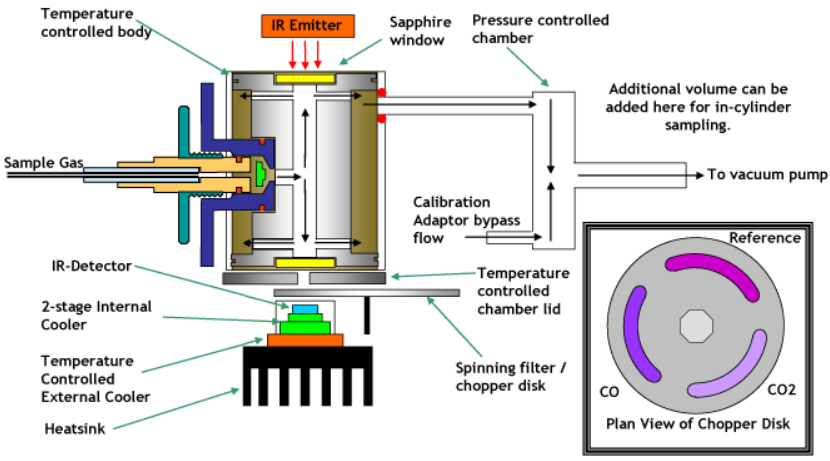

Fig. 7 NDIR technique for CO detection. Source Cambustion

In order to avoid the interferences with CO_2, a spinning filter is used.

For low CO levels for which interfering gases become a problem, the Gas Filter Correlation is implemented. Without entering in too much detail, the idea is to use pure CO as a filter to take profit of the detailed structure of the adsorption bands.

With the improved rejection of interferences afforded by the GFC technique, it is now feasible to increase the sensitivity of the analyzer. This is achieved by the multiple pass optics used in the sample cell. The IR beam traverses the cell several times (typically 20), yielding a 20- fold increase in sensitivity over conventional systems using a single pass. This allows full-scale range sensitivity down to 0-1 ppm to be used.

Again, this type of analyser is expensive and cumbersome. It is used for exhaust gas monitoring or environmental monitoring (with GFC).

Electrochemical Cells [19, 21]

Electrochemical sensors are the largest and oldest types of chemical gas sensors. Such sensors can be subdivided according to their working principle: potentiometric [22] or amperometric.

For the usual applications in safety and control, most sensors and detectors are based on liquid electrolyte cells working on an amperometric principle.

These sensors are based on the measurement of the diffusion limit current during the oxidation or the reduction of a dissolved gas in an appropriate electrolyte.

The sensor consists in 3 electrodes in contact with a liquid electrolyte (Figure 8): a sensing electrode, a counter electrode and the reference electrode setting the potential of the sensing electrode. The system is closed by a membrane permeable to the gas.

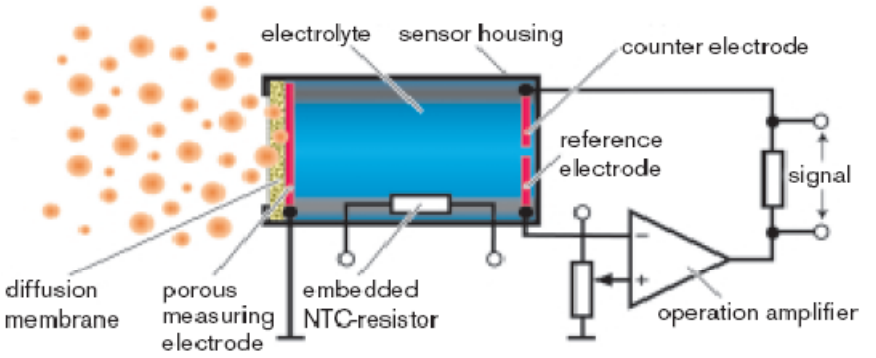

Fig. 8 Amperometric gas sensor. (doc Draeger). [23]

Let us take the example of a reducing gas like CO.

The gas diffuses through the membrane and dissolves in the electrolyte. A voltage is applied to the sensing electrode to oxidize the dissolved gas (equation 7).

$$R + 2\,OH \rightarrow RO + H_2O + 2\,e^- \quad (7)$$

If the voltage on the sensing electrode is high enough, the electrolysis current is limited by the mass transfer and there is a plateau in the i-V characteristic. At this stage, the limit current is proportional to the partial pressure of the gas outside which is in turn proportional to the outside gas concentration. Measuring the limit current is then a measure of the gas concentration.

The main advantages of these sensors are a fairly good sensitivity for the gas concentrations in the TLV range and a good selectivity. The drawbacks are a short life time (typically less than 2 years). A regular recalibration is necessary. Also, as the electrolyte needs to remain liquid, the operating temperature range is limited (usually -5 °C-50 °C). These electrochemical sensors are currently the reference

technology in the industry and the technology is mature. The main gases are: O_2, CO, H_2, Cl_2, NH_3, SO_2, ClO_2, NO, NO_2, O_3.

For NO, NO_2 and O_3 the concentrations that can be measured are superior to 1 ppm and these sensors cannot be used for environmental monitoring only for safety. The normal concentrations are in the range 0 à 200 ppb. This technology is used nowadays for the pollution monitoring of CO and NO_x produced by engines.

Semiconductor Gas Sensors [21, 24]

Chemical sensors based on semiconductors metal oxides convert a chemical reaction (ex: adsorption/desorption) into an electrical signal. During the detection process, the gas molecules adsorb on the surface of semiconductor metal oxide and if the interaction between the adsorbed gases and the semiconductor is sufficiently strong, there may be electron transfer between the adsorbed gas and the sensitive material. This induces a change in the conductivity of the latter. This change in conductivity is related to the concentration of the detected gas.

Semiconductor gas sensors consist in an insulating substrate (alumina or silicon wafer) fitted with interdigitated electrodes and a heater. The sensitive layer is deposited on the substrate as shown on Figure 9.

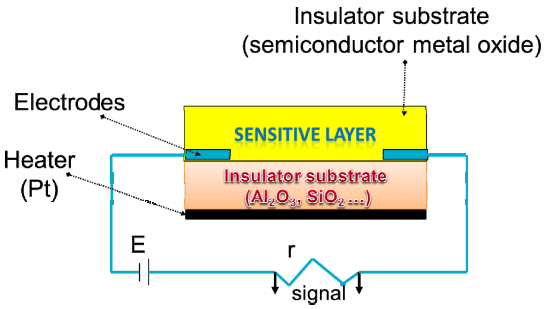

Fig. 9 General scheme of the sensors

The electrodes ensure the electrical conductivity measurements of the sensitive material, while the heater insures the control of the temperature of the sensors. It is necessary to maintain the sensitive layer at high temperature (typically from 200 to 500 ° C) because the adsorption and desorption are activated by the temperature.

Figure 10 and 11 show some commercial practical commercial sensors [25, 26]. In Figure 10 (older version), the substrate is a ceramic tube. Figure 11 presents a miniaturized version: the substrate is a thin membrane (~1µm) of a multilayer of SiO_2/Si_3N_4 and the active zone is less than 800 µm x 800 µm. This design drastically reduces the power for the heating.

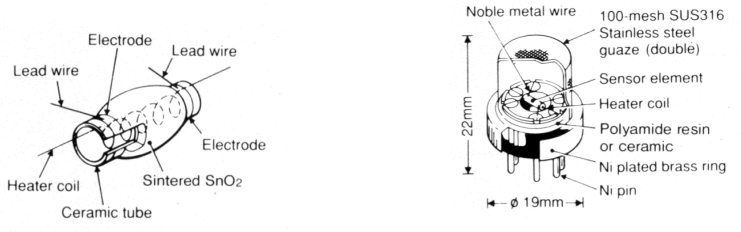

Fig. 10 Commercial design of semiconductor gas sensor (ceramic substrate). Figaro TGS.

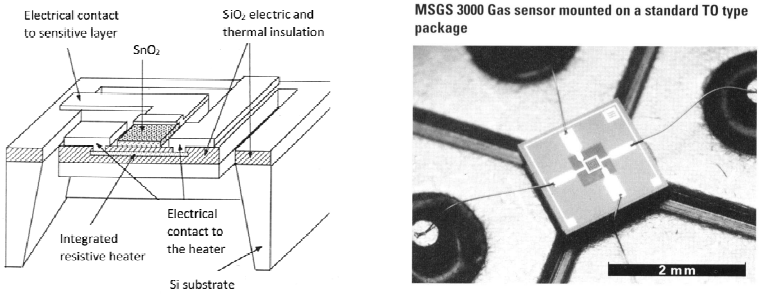

Fig. 11 Commercial design of semiconductor gas sensor (MEMS substrate). (sensor SnO_2 Microsens). [26]

As the working principle is fundamentally simple, many semiconductor materials can be exploited. For this purpose, organic and inorganic semiconductors were studied but only semiconductors based on metal oxides had a commercial success because of their better performances in terms of reliability and life time.

For example, SnO_2 is n-type semiconductor which is largely studied for gas detection, the detection in air is based on the variation of the chemisorbed oxygen species on its surface The oxygen species trap the electrons from the conducting band of SnO_2 resulting in an electrons depletion region on the surface of the sensor material. The nature of the formed oxygen species on the surface depend on the temperature (O_2^-, O^- or O^{2-}). It is admitted [20] that the O_2^- are primarily formed at working temperature superior to 250°C.

Thus, any phenomenon tending to modify the amount of adsorbed oxygen on the surface of the sensitive material of the sensor will cause a change in resistance. Therefore, a decrease in the amount of adsorbed oxygen by reducing the oxygen content in the atmosphere at the sensor surfaces, or by consumption of oxygen by heterogeneous reaction on the surface results in an increase in conductivity. Therefore, gas sensors for detection of combustible gases like CO are based on this last principle.

Generally, for n-type semiconductors, the oxidizing gases (NO_2, Cl_2, O_3,...) decrease the conductivity and the reducing gases (CO, H_2, CH_4,…) increase the

later. For p-type semiconductors, the gases have the opposite effect. However, other phenomena may render ambiguous the variation of conductivity.

The main advantages of these sensors are: high sensitivity, simple signal (variable resistance), easy insertion in electronic boards, low cost (can be produced in high volumes with standard techniques) and long life time. The main drawback of these sensors is the selectivity which limits its use as accurate instruments.

However, there are different ways to achieve greater selectivity. As discussed above, the temperature play an important role to enhance the selectivity, the surface modification of the oxides by metal catalyst [27] and selective filters can be used as alternative solutions.

The aim of the utilization of the selective filter consists on the elimination of certain gases before their reactions with the sensitive material, the filter acts as a barrier and block certain interfering gases [28-30].

The most used oxides are: SnO_2 (usually doped with catalytic metals) for CH_4, CO, hydrocarbons [31], WO_3 undoped for NO_2 [32, 33], doped with catalytic metal for hydrogen [34, 35] or Ga_2O_3 for CO in gas burners and exhaust pipes [36].

3.2 NO_2 Detection on Optical Fibers

NO_2 monitoring is generally carried out by point detectors but for wide places, distributed measurements with optical are more appropriate.

Several studies are reported in the literature concerning the use of optical fibers for NO_2 detection. Most of them are based on the change of absorption spectrum of a dye in the UV-Visible range [37, 38] or fluorescence spectrum [39]. Reference [37] presents a sensor which is in fact a dosimeter as they use a Saltzmann salt dispersed in a silica matrix. The salt reacts with NO_2 causing a change in color and the evolution rate of the absorbance (initial slope) is proportional to the NO_2 concentration. This reaction is not reversible. Reference [38] reported a point sensor using $TiPc_2$ in a SiO_2 matrix working in the range 0-100 ppm. The reversibility is very slow.

In [39], the sensitive layer made of a ruthenium complex ($Ru(bpy)_3Cl_2$) in a SiO_2 matrix is deposited at the tip of a fiber and the fluorescence spectrum at 530nm is measured. This system is not suitable for multiple interrogation on the same fiber.

Historically, optical fibers were developed for the long distance transmission of data. A whole technology was then developed to produce sources, detectors, spectrum analyzers etc… in the wavelength range [1400-1700 nm] corresponding to the minimum of losses of silica fibers which are the preferred ones as they possess the lowest attenuation. Therefore, it is interesting to exploit sensitive layers that can show an important sensitivity in this spectral range. The potential benefits lie in the use of standard equipment saving then cost and the possibility of using Tilted Fiber Bragg Gratings or Long Period Fiber Gratings as they allow measuring refractive index changes of a sensitive layer recovering them leading to

the possibility of interrogation several sensors on the same fiber in a quasi-distributed way.

Among the possible materials, lanthanide bisphthalocyanines (Figure 12 left) are good candidates. Indeed, these molecules present an absorption spectrum in the desired wavelength range and can be easily oxidized or reduced resulting in a strong spectrum change (Figure 12 right) [40].

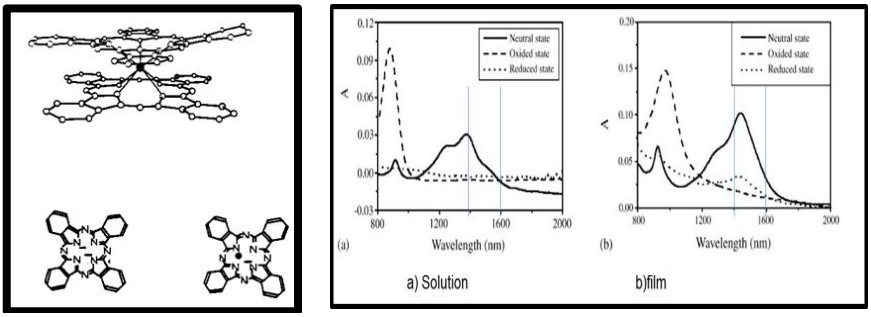

Fig. 12 Left) $LuPc_2$ molecule. Lu atom bridges the 2 planes. Right) Optical absorption spectra for $LuPc_2$ molecules in neutral, oxidized or reduced state (in solution a) or in solid film b))

The interest of using these molecules was shown in reference [41] on an optical fiber although the response time was terribly long.

NO_2 can be reversibly bound with Lutetium bisphthalocyanine ($LuPc_2$) resulting in the oxidation of the molecule which can be detected trough a change of the absorption spectrum in NIR (Figure 13). The diffusion of NO_2 in $LuPc_2$ is very slow leading to a very long response time if the grain size or the thickness of the layer is important. To avoid this effect, $LuPc_2$ was dispersed in the pores of a porous matrix in such a way that the grain size remains small leading to short response times.

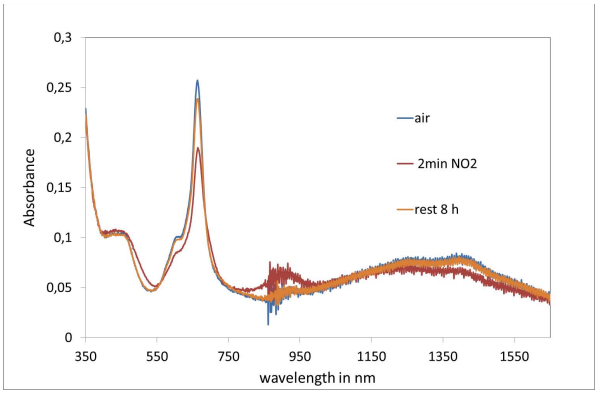

Fig. 13 Spectrum of $LuPc_2$ incorporated in the silica matrix on glass substrates after exposure to NO_2 at 10 ppm

This sensitive layer deposited on the tip of a fiber gives sensitive and reversible responses (Figure 14) [42]. The sensitivity is compatible with the applications in car parks or tunnel monitoring.

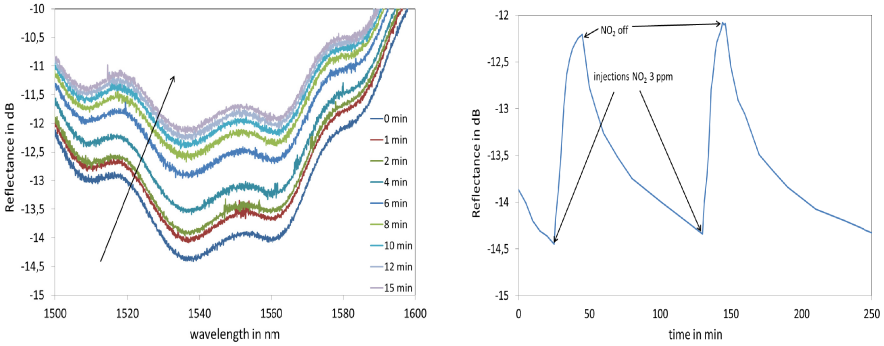

Fig. 14 Response of the fiber sensor after exposure to NO_2 at 3 ppm in air. Left) Reflectance spectrum. Right) Response to successive injections.

4 Flaming Fire Detection

All fire detection systems rely on the monitoring of physical phenomena taking place during a combustion: release of heat, release of gases (CO_2, CO, NO_x, etc) and release of particles [43-45]. Different strategies can be imagined but an important item is the cost of the installation. For the industry, the protection of the installations is essential and the investment for the fire protection can be moderate compared the total value. For domestic detectors, on the contrary, the challenge remains the cost and a tradeoff must be found.

Usually, the fires are distinguished between smouldering and flaming fires. For the flaming fires, an important amount of heat is released and is directly destructive. In that case, the detection needs to be very fast. Moreover, the quantity of particles can be very low for clean fires (burning of solvents for instance).

For smouldering fires, on the contrary, the generated heat is small but the quantity of gases and particles is important. The detection of these fires is based on the detection of particles or gases or a combination. The danger of these fires is double: they can suddenly evolve to a flaming fire and they release large quantities of toxic gases like CO and HCN. If not detected on time, humans die from suffocation.

Currently, commercial detectors, called smoke detectors are point detectors (small boxes monitoring the immediate proximity) essentially based on the optical detection of particles by following the light scattering of the particles in a chamber. As such, the flaming fires cannot be detected in all cases and a temperature sensor is added. Concerning the temperature, 2 strategies exist: the use of temperature threshold (alarm when the temperature is raised above a critical level) or the use of a temperature rise rate threshold (alarm if the temperature rise is too fast) or both. The latter strategy allows a faster detection.

More recently, in order to increase the sensitivity and reduce the false alarm rate, developments were conducted with detectors including gas sensors, in particular CO and NO_2. Currently, the commercial detectors use specially designed electrochemical cells for CO with long life time (> 5 years) [46].

For flaming fires, the monitoring of the temperature on the detector is a problem because it means that the detection happens when the fire is already well developed. This point is essential in wide places like car parks or tunnels or even in open places (oil platforms, chemical plants, etc). Therefore, flame detectors were developed to monitor the radiation emitted by the flames (UV between 120 and 260 nm to avoid ambient light or IR centered around 4.3 µm which corresponds to the emission band of CO_2). In that case, the detection can be faster [47, 48]. The commercial flame detectors are usually cumbersome and expensive.

For the monitoring of fires in tunnels or car parks and wide spaces in general, the usual strategy is the use of a network of point detectors following "good practice rules" imposed by standards. One can imagine that the installation costs rapidly increase for wide places. One strategy is the use of video [49].

Elegant solutions were proposed taking profit of the optical fibers as they are able to carry out distributed or quasi-distributed monitoring of the temperature on long distances using Bragg gratings [50] or Raman scattering [51,52]. Commercial solutions exist taking profit of the Raman scattering described above [53].

Although the interrogation system is more complex than the classical ones. The cost of the system is reduced by the fact that numerous detection points are interrogated together. The price/detection point is then favorable for optical fiber systems.

These systems however monitor the temperature rise of the fiber and therefore of the same precocity problem mentioned before.

An infrared detector for flame detection was proposed exploiting Fiber Bragg Gratings used as bolometers [54-56].

The working principle is to use a pair of Bragg gratings, one is covered with an absorbing material for IR and the other one is protected by a reflector. In the absence of radiation, both gratings follow the same temperature fluctuations in the ambient and move in parallel. In presence of IR radiation, the unprotected grating will shift due to the temperature rise while not the other. This shift is of course proportional to the intensity of the incident radiation.

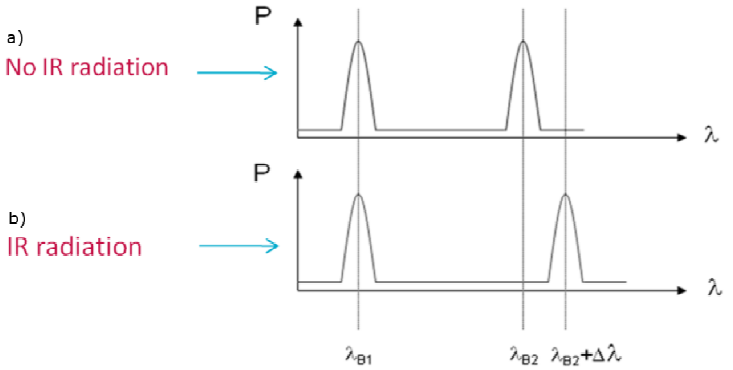

Fig. 15 Sketched optical reflected spectra of the pair of gratings – a) unexposed exposed to IR radiation and b) exposed to IR radiation

In order to increase the sensitivity, the coated grating is put in a thin glass tube exploiting then a greenhouse effect. Using a reflecting packaging (aluminum tube), the radiation may be concentrated on the coated grating and the sensitivity is further enhanced (Figure 16).

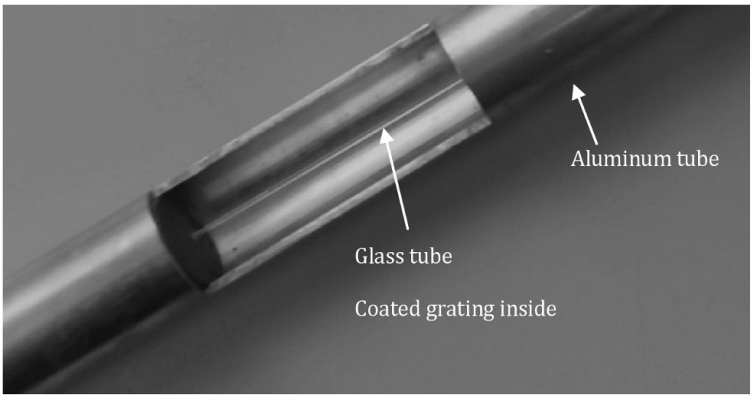

Fig. 16 Packaging made of an aluminum tube and the coated FBG inside the capillary

A sensitivity of 0.1 pm/W/m^2 was reported for this kind of device. As usual optical analyzers can detect 1 pm variations, the detection limit is about a few W/m^2.

5 Combustible Gas Leak Detection

In this part, we will review the main optical fiber sensing configurations reported for methane and hydrogen sensing and present their performances. Let us mention that the conventional detection systems are based on electrochemical cells and semiconductors as described before.

5.1 Methane Sensing

It is well known that alkanes and specifically methane, even at low concentrations, are very dangerous for human safety and environment. Efficient chemical sensors are therefore needed to monitor methane leakages.

The first report dates back to 1987 and makes use of evanescent waves at the wavelength of 3.392 µm (produced by a He-Ne laser) to detect methane, as this wavelength coincides with an absorption band of methane [57]. The fiber used in this work was very thin, rendering it very fragile. A similar spectroscopic process was then employed at 1.68 µm using a tunable DFB (distributed feedback) laser diode. A hand-held and low power sensor was demonstrated based on direct absorption spectroscopy. The achievable detection limit was reported lower than 5 ppm [58]. A hollow-core photonic band gap fiber has also been used for methane detection at the wavelength of 1670 nm [59]. The limit of detection has been reported equal to 10 ppm with this method. A transparent polymer overlay whose refractive index is modified by methane absorption has also been reported [60]. It relies again on an evanescent wave sensor. The wavelength is here 670 nm. Cryptophane molecules (A and E) were used in the polymer matrix as sensitive reagents. It was demonstrated that when alkane concentrations (methane, ethane and butane) are less than 8 %, only methane leads to an optical response. The limit of detection was computed equal to 2 % with cryptophane A and 6 % with cryptophane E. Cryptophane A has also been used in conjunction with LPFGs inside a styrene-acrylonitrile nanofilm surrounding the gratings [61]. The fiber integrity is preserved in this case and a limit of detection of 0.2 % was reported with this configuration. The better sensitivity is attributed to the transduction mechanism, based on a wavelength shift instead of a power variation, as exploited in evanescent wave sensors.

5.2 Hydrogen Sensing

Hydrogen participates to a wide range of chemical processes and also appears during energy production and transport. It is widely used in aerospace applications where it acts as fuel for rockets. Nowadays, hydrogen is considered as an alternative source of energy for automotive applications. With its high diffusivity, hydrogen is an extremely flammable gas. In air, it can burn at concentrations from about 4 % with a flame velocity almost ten times higher than that of natural gas. For security reasons, it is therefore required to manufacture efficient hydrogen

leak detectors. Spectroscopic analysis via infrared absorption or Raman scattering has been used for hydrogen sensing [62]. More robust sensors can be used thanks to the use of a sensitive layer. Combined with optical fiber sensors and more specifically FBGs sensors, two sensitive coatings have been extensively used for hydrogen sensing.

Palladium (Pd) is known for its ability to absorb hydrogen and to expand as hydrogen absorption converts Pd into hydrides PdH_x, which has a lower density and a larger specific volume [63]. When a Pd coating deposited on a FBG absorbs hydrogen, the mechanical expansion occurring in the Pd layer stretches the optical fiber and causes the grating period to expand and the effective refractive index to change via the elasto-optic effect. As the stress induced by the formation of the hydride phase is directly related to the hydrogen concentration, the shift of the Bragg wavelength can be straightforwardly linked to this concentration. Following this principle, hydrogen sensors in nitrogen environment can be achieved. Pd coatings have been associated to Mach-Zehnder interferometers, FBGs and LPFGs for hydrogen detection in the 1550 nm wavelength range [64-66]. The response time exceeds several minutes so that such sensors suffer from a hysteresis effect between increasing and decreasing hydrogen concentrations. To overcome this limitation, a very thin taper has been reported with a response time of ~10 s [67].

The use of Platinum doped tungsten trioxide nanolamellae as sensitive layer generates an exothermic reaction in the presence of hydrogen in air, as demonstrated in [68]. The reaction heat of hydrogen combustion in normal conditions is 57.8 kcal/mol. So, when exposed to hydrogen in air environment, the temperature around the FBG increases, which results in a shift of its Bragg wavelength. As detailed in [69], different environmental parameters such as ambient temperature and relative humidity level influence the reaction. Two other parameters are of great influence: the efficiency of the catalyst on the one hand and the light coupling from the fiber core to the sensitive layer on the other hand. Such light coupling can be obtained through the use of a radiating fiber gratings (LPFGs or TFBGs) that couple the core mode into cladding modes. It provides an activation energy that can stimulate the reaction. The latter indeed requires activation energy equal to 0.15 eV. In this case, a limit of detection of 0.5 % has been obtained, whatever the relative humidity level and ambient temperature.

6 Conclusions

Sensors are continuously developed for pollution monitoring, fire detection and explosive gas monitoring. In this wide range of applications, optical fiber sensors constitute a growing sector for which pioneer researches date back to only three decades. Their numerous and unique advantages bring them to the forefront for safety applications in gas production and transport sites, wide tunnels and car parks. The key parameter there is the ability of optical fiber sensors to provide numerous sensing points shared by one single interrogation device, yielding a relatively easy installation and an affordable price for the complete solution. One

can think that future developments will contribute to further improve their performances, in particular in terms of selectivity and robustness. And so, they will certainly become more widespread. This chapter has presented a review of the main state-of-the-art solutions in the field of air quality monitoring, in particular NO_2 that is representative of toxic automotive pollution, flaming fire detection and combustible gas leak detection (methane and hydrogen).

Acknowledgements. C. Caucheteur is supported by the Belgian F.R.S.-FNRS. Marc Debliquy, Antonio Bueno and Diss Lahem thank the Walloon Region of Belgium for funding the NOSens project.

References

[1] Yu, F.T.S., Yin, S., Yu, Y.T.S.: Fiber Optic Sensors. Marcel Dekker Inc., USA (2002)
[2] Jones, J.D.C.: Handbook of Optical Fiber Sensing Technology – Chapitre 12: Interferometry and polarimetry for optical sensing. John Wiley & Sons (2002)
[3] Wuilpart, M., Thévenaz, L.: Advanced Fiber Optics - Chapitre 8: Rayleigh scattering in optical fibers and applications to distributed measurements. CRC Press (2011)
[4] Frazao, O., Correia, C., Rocco Giraldi, M.T.M., Marques, M.B., Salgado, H.M., Martinez, M.A.G., Cosata, J.C.W.A., Barbero, A.P., Baptista, J.M.: Stimulated Raman scattering and its applications in optical communications and optical sensors. The Open Optics Journal 3, 1–11 (2009)
[5] Thevenaz, L.: Brillouin distributed time-domain sensing in optical fibers: State of the art and perspectives. Frontiers of Optoelectronics in China 3, 13–21 (2010)
[6] Farahani, M.A., Gogolla, T.: Spontaneous Raman scattering in optical fibers with modulated probe light for distributed temperature Raman remote sensing. Journal of Lightwave Technology 17, 1379–1391 (2009)
[7] Grattan, L.S., Meggitt, N.T.: Optical fiber sensor technology: Advanced, applications – Bragg gratings and distributed sensors. Kluwer Academic Publishers, Boston (2000)
[8] Sekimoto, S., Nakagawa, H., Okazaki, S., Fukuda, K., Asakura, S., Shigemori, T., Takahashi, S.A.: Fiber-optic evanescent-wave hydrogen gas sensor using palladium-supported tungsten oxide. Sensors and Actuators B: Chemical 66, 142–145 (2000)
[9] Arregui, F.J., Matias, I.R., Claus, R.O.: Optical fiber gas sensors based on hydrophobic alumina thin films formed by the electrostatic self-assembly monolayer process. IEEE Sensors Journal 3, 56–61 (2003)
[10] Kashyap, R.: Fiber Bragg gratings. Academic Press (1999)
[11] Othonos, A., Kalli, K.: Fiber Bragg gratings: fundamentals and applications in telecommunications and sensing. Artech House, Norwood (1999)
[12] Albert, J., Shao, L.Y., Caucheteur, C.: Tilted fiber Bragg grating sensors. Laser and Photonics Reviews 7, 83–108 (2013)
[13] Vengsarkar, A.M., Lemaire, P.J., Judkins, J.B., Bhatia, V., Erdogan, T., Sipe, J.E.: Long-period fiber gratings as band-rejection filters. Journal of Lightwave Technology 14, 58–65 (1996)
[14] Homola, J.: Surface plasmon resonance based sensors. Springer, Berlin (2006)

[15] American Conference of Governmental Industrial Hygienists (ACGIH). Documentation of the threshold limit values and biological exposure indices, 7th edn., Cincinnati, vol. 1-5
[16] Grosjean, D., Harrison, J.: Response of chemiluminescence NOx analyzers and ultraviolet ozone analyzers to organic air pollutants. Environ. Sci. Technol. 19(9), 862–865 (1985)
[17] Khandpur, R.S.: Handbook of Analytical Instruments. McGraw-Hill professional (2006)
[18] Chaney, L.W., McClenny, W.A.: Unique Ambient Carbon Monoxide Monitor Based on Gas Filter Correlation: Performance and Application. Environmental Science & Technology 11(13) (December 1977)
[19] Jaffrezic-Renault, N., Martelet, C., Clechet, P.: Capteurs chimiques et biochimiques, Techniques de l'Ingénieur, PE 360 - R 420
[20] Asch, R.: Les capteurs en instrumentation industrielle, pp. 779–807. Dunod (1991)
[21] Moseley, P.T., Norris, J., Williams, D.E.: Techniques and Mechanisms in Gas Sensing. Adam Hilger (1991)
[22] Zhuiykov, S., Ono, T., Yamazoe, N., Miura, N.: High-temperature NOx sensors using zirconia solid electrolyte and zinc-family oxide sensing electrode. Solid State Ionics 152– 153, 801–807 (2002)
[23] Draeger: Technical documentation
[24] Yamazoe, N.: Chemical Sensor Technology, vol. 3. Kodansha LTD. Elsevie (1991)
[25] Figaro company: data sheets
[26] Microsens SA: Technical documentation
[27] Yamaura, H., Tamaki, J., Moriya, K., Miura, N., Yamazoe, N.: Electrochem. Soc. 144(6) (1997)
[28] Kitsukawa, S., Nakagawa, H., Fukuda, K., Asakura, S., Takahashi, S., Shigemori, T.: Sensors and Actuators B: Chemical 65, 120–121 (2000)
[29] Fleischer, M., Seth, M., Kohl, C.-D., Meixner, H.: A selective H2 sensor implemented using Ga2O3 thin-films which are covered with a gas-filtering SiO2 layer. Sensors and Actuators B 36, 297–302 (1996)
[30] Zhang, C., Boudiba, A., Navio, C., Olivier, M.-G., Snyders, R., Debliquy, M.: Study of selectivity of NO2 sensors composed of WO3 and MnO2 thin films grown by radio frequency sputtering. Sensors & Actuators B 161, 914–922 (2012)
[31] Matsuura, Y., Takahuta, K., Matsuura, S.: Denki Kagaku 12, 1154 (1990)
[32] Boudiba, A., Zhang, C., Bittencourt, C., Umek, P., Olivier, M.-G., Snyders, R., Debliquy, M.: Hydrothermal Synthesis of Two Dimensional WO3 Nanostructures for NO2 Detection in the ppb-level. Procedia Engineering 47, 228–231 (2012)
[33] Teoh, L.G., Hung, I.M., Shieh, J., Lai, W.H., Hon, M.H.: High Sensitivity Semiconductor NO2 Gas Sensor Based on Mesoporous WO3 Thin Film. Electrochemical and Solid-State Letters 6(8), G108–G111 (2003)
[34] Samerjai, T., Tamaekong, N., Liewhiran, C., Wisitsoraat, A., Tuantranont, A., Phanichphant, S.: Selectivity towards H2 gas by flame-made Pt-loaded WO3 sensing films. Sensors and Actuators B 157, 290–297 (2011)
[35] Zhang, C., Boudiba, A., Navio, C., Olivier, M.-G., Snyders, R., Debliquy, M.: Sensing properties of Pt/Pd activated tungsten oxide films grown by simultaneous radio-frequency sputtering to reducing gases. Sensors & Actuators: B 175, 53–59 (2012)

[36] Schwebel, T., Fleischer, M., Meixner, H., Kohl, C.-D.: CO-Sensor for domestic use based on high temperature stable Ga2O3 thin films. Sensors and Actuators B 49, 46–51 (1998)
[37] Baldini, F., et al.: Sensors and Actuators B. 51, 176–180 (1998)
[38] Grant, S.A., et al.: Sensors and Actuators B. 69, 132–137 (2000)
[39] Mechery, S.J., Singh, J.P.: Fiber optic based gas sensor with nanoporous structure for the selective detection of NO2 in air samples. Analytica Chimica Acta 557, 123–129 (2006)
[40] Zhang, J., Lu, F., Huang, H., Wang, J., Yu, H., Jiang, J., Yan, D., Wang, Z.: Near infrared electrochromism of lutetium phthalocyanine. Synthetic Metals 148, 123–126 (2005)
[41] Bariain, C., Matias, I.R., Fernandez-Valdivielso, C., Arregui, F.J., Rodriguez-Mendez, M.L., de Saja, J.A.: Optical fiber sensor based on lutetium bisphthalocyanine for the detection of gases using standardtelecommunication wavelengths. Sensors and Actuators B 93, 153–158 (2003)
[42] Debliquy, M., Lahem, D., Bueno, A., Caucheteur, C., Bouvet, M., Olivier, M.-G.: Nitrogen dioxide sensor based on optical fiber coated with a porous silica matrix incorporating lutetium bisphthalocyanine. In: Proc. ICST 2013, pp. 659–663 (2013)
[43] Briers, E.: Sensibilité et performances des détecteurs de fumée. Association Nationale pour la Protection contre l'Incendie et l'Intrusion (1989)
[44] Aralt, T.T., Nilsen, A.R.: Automatic fire detection in road traffic tunnels. Tunnelling and Underground Space Technology 24, 75–83 (2009)
[45] NFPA 72 – National Fire Alarm and Signaling Code – 2010 Edition. National Fire Alarm Association (2010)
[46] Chen, S.-J., Hovde, D.C., Peterson, K.A., Marshall, A.W.: Fire detection using smoke and gas sensors. Fire Safety Journal 42, 507–515 (2007)
[47] Middletown, J.F.: Developments in Flame Detectors. Fire Safety Journal 6, 175–182 (1983)
[48] Han, D., Lee, B.: Flame and smoke detection method for early real-time detection of a tunnel fire. Fire Safety Journal 44, 951–996 (2009)
[49] Verstockt, S., Van Hoecke, S., Beji, T., Merci, B., Gouverneur, B., Enis Cetin, A., De Potter, P., Van de Walle, R.: A multi-modal video analysis approach for car park fire detection. Fire Safety Journal 57, 44–57 (2013)
[50] Lönnermark, A., Hedekvist, P.O., Ingason, H.: Gas temperature measurements using fibre Bragg grating during fire experiments in a tunnel. Fire Safety Journal 43, 119–126 (2008)
[51] Bolognini, G., Hartog, A.: Raman-based fibre sensors: Trends and applications. Optical Fiber Technology 19(6), Part B, 678–688 (2013)
[52] Ishii, H., Kawamura, K., Ono, T., Megumi, H., Kikkawa, A.: A fire detection system using optical fibres for utility tunnels. Fire Safety Journal 29, 87–98 (1997)
[53] Siemens documentation in, https://www.siemens.be/cmc/../sbt/Fibrolaser_en.pdf
[54] Renoirt, J.-M., Caucheteur, C., Olivier, M., Mégret, P., Debliquy, M.: Infrared Radiation detection using fibre Bragg grating. In: Morozhenko, V. (ed.) Infrared Radiation. InTECH Book (2012) ISBN 978-953-51-0060-7
[55] Caucheteur, C., Renoirt, J.-M., Debliquy, M., Mégret, P.: Infrared radiation detection with matched fiber Bragg gratings. IEEE Photonics Technology Letters 22, 1732–1734 (2010)

[56] Yüksel, K., Caucheteur, C., Renoirt, J.-M., Debliquy, M., Mégret, P., Wuilpart, M.: Infrared radiation detector interrogated by optical frequency-domain reflectometer. Optics and Lasers in Engineering 50, 308–311 (2012)
[57] Tai, H., Tanaka, H., Yoshino, T.: Fiber-optic evanescent-wave methane-gas sensor using optical absorption for the 3.392 μm line of a He-Ne laser. Optics Letters 12, 437–439 (1987)
[58] Hennig, O., Strzoda, R., Magori, E., Chemisky, E., Tump, C., Fleischer, M., Meixner, H., Eisele, I.: Hand-held unit for simultaneous detection of methane and ethane based on NIR-absorption spectroscopy. Sensors and Actuators B 95, 151–156 (2003)
[59] Cubillas, A.M., Silva-Lopez, M., Lazaro, J.M., Conde, O.M., Petrovich, M.N., Lopez-Higuera, J.M.: Methane detection at 1670-nm band using a hollow-core photonic bandgap fiber and a multiline algorithm. Optics Express 15, 1570–1576 (2007)
[60] Benounis, M., Jaffrezic-Renault, N., Dutasta, J.P., Cherif, K., Abdelghani, A.: Study of a new evanescent wave optical fibre sensor for methane detection based on cryptophane molecules. Sensors and Actuators B 107, 32–39 (2005)
[61] Yang, J., Tao, C., Li, X., Zhu, G., Chen, W.: Long-period fiber grating sensor with a styrene-acrylonitrile nano-film incorportating cryptophane A for methane detection. Optics Express 19, 14696–14706 (2011)
[62] Alder-Golden, M.S., Goldstein, N., Bien, F., Matthew, M.W., Gersh, M.E., Cheng, W.K., Adams, F.W.: Laser Raman sensor for measurement of trace-hydrogen gas. Applied Optics 31, 831–835 (1992)
[63] Lewis, F.A.: The Palladium Hydrogen system. Academic Press, London (1967)
[64] Butler, M.A.: Optical fiber hydrogen sensor. Applied Physics Letters 45, 1007–1008 (1984)
[65] Trouillet, A., Marin, E., Veillas, C.: Fibre gratings for hydrogen sensing. Measurement Science and Technology 17, 1124–1128 (2006)
[66] Buric, M., Chen, K.P., Bhattarai, M., Swinehart, P.R., Maklad, M.: Active fiber Bragg grating hydrogen sensors for all-temperature operation. IEEE Photonics Technology Letters 19, 255–257 (2007)
[67] Villatoro, J., Monzon-Hernandez, D.: Fast detection of hydrogen with nano fiber tapers coated with ultra thin palladium layers. Optics Express 13, 5087–5092 (2005)
[68] Caucheteur, C., Debliquy, M., Lahem, D., Mégret, P.: Catalytic fiber Bragg grating sensor for hydrogen leak detection in air. IEEE Photonics Technology Letters 20, 96–98 (2008)
[69] Caucheteur, C., Debliquy, M., Lahem, D., Mégret, P.: Hybrid fiber gratings coated with a catalytic sensitive layer for hydrogen sensing in air. Optics Express 13, 16854–16859 (2008)

Evanescent Wave Absorption Based Fiber-Optic Sensor - Cascading of Bend and Tapered Geometry for Enhanced Sensitivity

N. Punjabi[1], J. Satija[2], and S. Mukherji[1,*]

[1] Department of Biosciences and Bioengineering,
Indian Institute of Technology Bombay, Mumbai, Maharashtra, 400076, India
[2] School of Biosciences and Technology, VIT University,
Vellore, Tamilnadu 632014, India
mukherji@iitb.ac.in

Abstract. Evanescent wave absorption (EWA) based fiber-optic sensors have found widespread applications ranging from environmental sensing to biosensing. In these sensors, optical and geometrical characteristics such as optical fiber type (single-mode or multi-mode), fiber core diameter, fiber probe geometry, fiber probe length, *etc.*, are very important. These parameters affect the penetration depth and fractional power by modulating the ray propagating in the fiber probe that ultimately influences the sensitivity of the EWA sensors. Various geometries of fiber probe designs, like bent, tapered, coiled, *etc.*, have been explored for improving the sensitivity. This chapter describes the design, development and fabrication of a novel bent-tapered fiber-optic sensor. A combination of bending and tapering acts as a mode converter, which results in high penetration depth of the evanescent field. In addition, tapered region of the probe increases the coupling efficiency at the detector end by V-number matching and thus improves the signal-to-noise ratio. EWA sensitivity of the sensor was compared for different taper ratios. Finally, the optimized geometrical design was used to demonstrate biosensing application.

Keywords: fiber-optic sensor, evanescent wave, bent-tapered probe, biosensor, taper ratio, fiber geometry.

1 Introduction

In the last couple of decades, fiber-optic sensors have become one of the most important types of sensors for on-field and point-of-care sensing applications. These have entered into the domain of structural health monitoring [1], chemical sensing [2], environmental sensing [3], physical sensing [4], security [5], remote

* Corresponding author.

A. Mason et al. (eds.), *Sensing Technology: Current Status and Future Trends III*,
Smart Sensors, Measurement and Instrumentation 11, DOI: 10.1007/978-3-319-10948-0_2

sensing [6] , biosensors [7], *etc.* This prominent interest in fiber-optic sensors is due to its inherent advantages such as reduced electromagnetic interference, capability of multiplexing (by using different sensing phenomena together or multiple wavelength interrogation), fast response, ability to withstand harsh conditions, small size and high sensitivity, to list a few.

Typically, a fiber-optic sensor consists of an optical source, fiber-optic probe, modulator, modulant/analyte under study, detector and processing electronics. Various sensing phenomena like Evanescent Wave Absorption (EWA) [8, 9], Surface Plasmon Resonance (SPR) [10, 11], Localized Surface Plasmon Resonance (LSPR) [12, 13], *etc.* along with various structures like Photonic Crystal fiber (PCF) [14, 15], Optical Fiber Gratings (OFG) [16, 17], have been used with fiber-optic sensor for biosensing application. Among the above sensing schemes, evanescent wave absorption based fiber-optic biosensors have been used widely due to their simplicity of design and fabrication, robustness and field portability. Most of the research is focused on multimode optical fiber based EWA sensor because of their ease of fabrication and simple coupling mechanism due to large size and thereby high tolerance towards errors in fabrication dimension.

This chapter provides details about design and fabrication of EWA based fiber-optic sensors for biosensing applications, beginning with the theoretical background of EWA based fiber-optic sensor. A discussion about various geometries implemented to enhance the sensitivities of EWA based fiber-optic sensor is also included. A proposed setup for fabricating a bent-tapered probe, along with its bio-functionalization protocol, will also be presented. In the end, details of the experimental setup and results leading to validation of the probe design will be discussed.

2 Theory of Evanescent Wave Absorption Based Fiber-Optic Sensor

Evanescent wave absorption based sensing phenomenon is dictated by the leakage/loss of electromagnetic energy at the interface of core and cladding medium during a total internal reflection (TIR) event. This section will discuss the physics involved and parameters that govern the functioning of such sensors.

2.1 Important Parameters in Optical Fiber

Optical signals are guided through waveguides/fibers by total internal reflection. As a result the amount of light guided is modulated by the refractive indices of the various media (i.e. core and cladding) and may be expressed in terms of critical angle (θ_c) and numerical aperture (*NA*) (Eq. (1) and (2))

$$\theta_c = \sin^{-1}\left(\frac{n_{clad}}{n_{core}}\right) \tag{1}$$

$$NA = \sqrt{{n_{core}}^2 - {n_{clad}}^2} \tag{2}$$

The number of modes supported (M) depends on the *NA*, radius of fiber (r) and wavelength of the light signal (λ). The relation may be given as:

$$M = \frac{4V^2}{\pi^2} \approx \frac{V^2}{2.5}, \quad \text{where} \quad V = \frac{2\pi r}{\lambda} NA \tag{3}$$

V is referred to as the V-number for the fiber, which helps in determining the operations of the fiber i.e. single mode or multimode.

2.2 *Evanescent Wave (EW)*

Usually, the ray tracing approach is used to explain TIR in multimode optical fibers. This approach may be used if the dimensions of a fiber is large compared to the wavelength of light. It is useful for explaining the concepts such as numerical aperture and visualizing the laws of refraction. When the incident angle (θ_i) of a propagating ray is greater than the critical angle (θ_c), the ray reflects back from the core-cladding interface due to TIR. At each TIR event, a small portion of the energy of the guided wave penetrates the cladding medium and generates an electromagnetic field which is referred to as "evanescent wave" (Fig. 1).

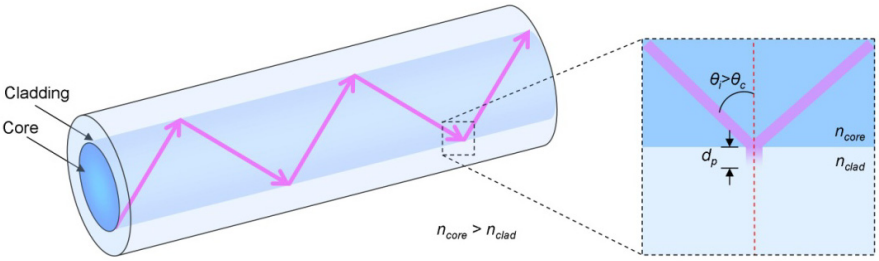

Fig. 1 A schematic representation of evanescent wave phenomenon in optical fiber using ray tracing approach

Wave theory provides an in depth understanding of the phase shifts and evanescent field that accompany the phenomenon of TIR. A detailed derivation may be found in ref. [18]. According to wave theory, the energy outside the core in case of $\theta_i > \theta_c$ (Fig. 2) is important for EWA based biosensor application. The transmitted wave equation may be given by:

$$E_T = \tau \hat{x} E_0 e^{-k_0 n_{clad} \sqrt{\left(n_{core}^2 / n_{clad}^2\right) \sin^2 \theta_i - 1}\, z} \; e^{j k_0 n_{core} \sin \theta_i y} \tag{4}$$

From the Eq. (4), it is clear that the amplitude of evanescent wave decays exponentially as the wave moves away from interface in the z-direction. It can also be seen, that the evanescent wave is very sensitive to change in RI at the core-cladding interface. These facts have been exploited to develop evanescent wave absorption based sensors.

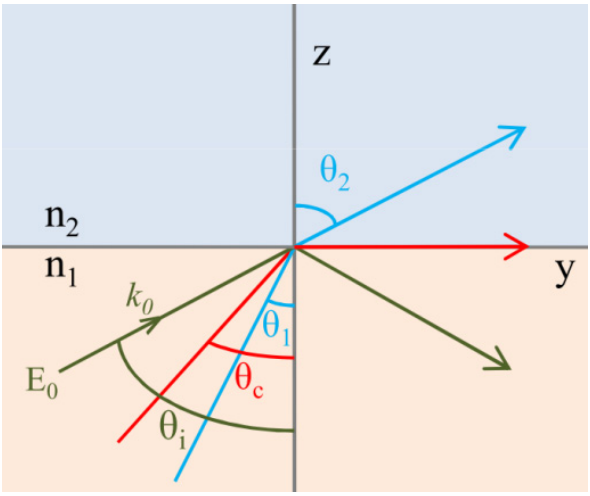

Fig. 2 A schematic representation of refraction loss and TIR phenomena

2.2.1 Evanescent Wave Parameters

Various physical, optical and geometrical parameters of both optical fiber affect the evanescent wave. Penetration depth and evanescent power (or fractional power in cladding) are the two important parameters in evaluating the application of EWA based sensors.

- **Penetration depth *(d_p)***
  The penetration depth *(d_p)* of the evanescent field i.e. the distance at which the electric field amplitude falls to 1/e of its value at the interface, increases with a decrease in the refractive index contrast at the core-cladding interface. It is also a function of the wavelength of the light and the angle of incidence (Eq. 5).

$$d_p = \frac{\lambda}{2\pi n_{core}^2 \sqrt{(\sin^2\theta_i - \sin^2\theta_c)}} = \frac{\lambda}{2\pi \sqrt{(n_{core}^2 \sin^2\theta_i - n_{clad}^2)}} \tag{5}$$

  Theoretically the evanescent wave can interact with all molecules upto an infinite distance, albeit with a reducing level of interaction. From the point of view of experimental practice, d_p is the distance upto where molecules may have a discernible effect.

- **Evanescent power (Fractional power in cladding)**
  Evanescent power can be approximated by calculating the amount of fractional power present in the cladding of a multimode fiber and given as [19]:

$$\frac{P_{clad}}{P} = \frac{4}{3\sqrt{M}} = \frac{4\sqrt{2}}{3V} \tag{6}$$

From Eq. (5),

$$\frac{P_{clad}}{P} = \frac{4\sqrt{2}}{3} \frac{\lambda}{2\pi r\sqrt{n_{core}{}^2 - n_{clad}{}^2}} \tag{7}$$

where, P_{clad} = optical power in cladding, P = total optical power in core and cladding together.

From Eq. (6), it is observed that increase in V-number will reduce fractional power in the cladding [20]. So, selection of V-number is very important in determining evanescent power of the fiber-optic sensor.

2.2.2 Evanescent Wave Absorbance

In a decladded optical fiber, evanescent wave at the surface of the core is available to interact with the surrounding medium, but limited by its penetration depth. If any absorbing molecule is present within the interaction depth of the evanescent field, it will absorb the evanescent field and results in attenuation in the amplitude of the propagating wave (guided in the fiber core). The transmitted power at the end of the decladded region is given by:

$$P_L = P_0 \times e^{-\gamma L} \tag{8}$$

where, P_L = optical power transmitted across length (L), P_0 = initial optical power launched in optical fiber, γ = evanescent wave absorption coefficient of the molecule and L = length of decladded fiber probe.

Evanescent wave absorption coefficient is proportional to fractional power in cladding (or medium surrounding the fiber core in case of decladded fiber), concentration (C) and absorption coefficient (α) of the molecule. (Eq. (9))

$$\gamma = \frac{P_{clad}}{P} \alpha C \tag{9}$$

From Eq. (8) and (9), we get the equation for evanescent wave absorbance, given by pseudo Beer-Lambert Law [21]:

$$A = \frac{P_{clad}}{P} \frac{\alpha CL}{2.303} \tag{10}$$

Combining both Eq. (7) and (10), we get the equation for evanescent wave absorbance.

$$A = 4\frac{\sqrt{2}}{3}\frac{\lambda}{2\pi r\sqrt{n_{core}{}^2 - n_{clad}{}^2}}\frac{\alpha CL}{2.303} \tag{11}$$

Thus, evanescent wave absorbance is inversely proportional to the RI contrast (between core and cladding) and radius of the optical fiber. It is directly proportional to absorption coefficient, concentration of the molecule, wavelength of the light, and length of the decladded fiber. These factors are very important to develop sensors based on evanescent wave absorption (or attenuated total reflection sensors).

2.3 Loss Due to V-Number Mismatch

When the light propagates from one fiber to another having different V-numbers (due to differences in cladding/core material or core radius), it results in loss of signal (Fig. 3). Due to low V-number in the receiving fiber, the higher-order modes of the transmitting fiber are not supported by the receiving fiber and the signal carried by the higher order modes is lost.

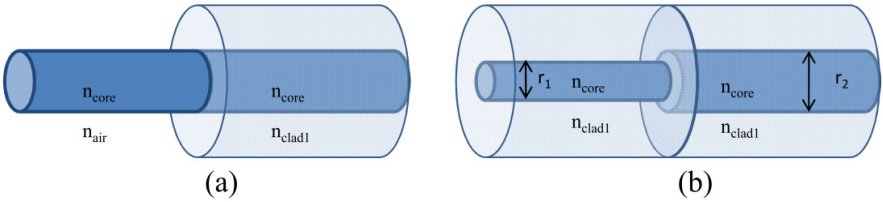

Fig. 3 Schematic representation of V-number mismatching (a). due to different cladding material (NA mismatch) and (b). differences in core radius ($r_1 < r_2$).

2.3.1 NA Mismatch

When the light propagates from a high numerical aperture fiber (NA_1) to a fiber having low numerical aperture (NA_2), it results in loss of rays (Fig. 3(a)). This loss (P_L) due to NA mismatch can be calculated using [22]:

$$P_L = -10\log\left(\frac{NA_2}{NA_1}\right)^2 \tag{12}$$

2.4 Working of EWA Based Fiber-Optic Sensor

In designing a fiber-optic sensor, all the parameters and losses mentioned in the previous sections i.e. Sec. 2.2 and 2.3 have to be considered. In Sec 2.2, we learnt

that the penetration depth of the evanescent wave is very small and it will only affect the weak cladding modes of the fiber while the core modes will remain unaffected. To improve the sensitivity, the sensing region of the fiber is typically decladded, so that the evanescent field of the core modes can interact directly with the analyte medium.

2.4.1 Refractive Loss

In a decladded fiber-optic probe, an increase in RI in the surrounding of a decladded region (i.e. sensing region) decreases the local numerical aperture and results in attenuation of light due to refraction loss. Fig. 4 explains the refractive loss in the fiber-optic sensor. When the decladded fiber is kept in RI medium (n_2), some rays (R_1 and R_2) are guided depending on the critical angle. If the surrounding RI is changed from n_2 to n_3 (n_3>n_2), it causes an increase in the critical angle. This new critical angle (θ_c') is greater than the existing angle of incidence for ray R_1, resulting in ray R_1 to get refracted and eventually lost (Fig. 4(b)). Depending upon the Fresnel reflection coefficient, some percentage of the incident light will be reflected into the fiber and will continue to propagate with reduction in power at each interaction with the core surface.

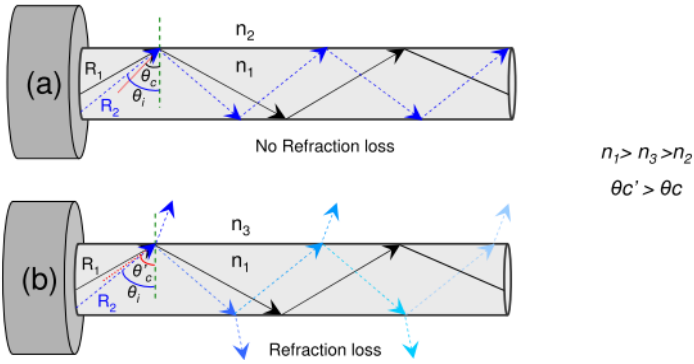

Fig. 4 Schematic representation of refraction loss in optical fiber sensor due to change in surrounding RI; (a). No refraction loss occurs because θ_i>θ_c for both the rays; (b). Change in RI from n_2 to n_3 (n_3>n_2) increases the critical angle to (θ_c') and causes the refractive loss of ray R_1. A decrease in color intensity of ray R_1 represents the decreased power of the refracted ray [23].

Refractive loss is due to increase in effective refractive index in the sensing region, and it can be calculated from Eq. (12). In the case of a sensor, the equations for refractive loss can be modified as:

$$P_{RL} = -10\log\left(\frac{NA_a}{NA_r}\right)^2 \tag{13}$$

where, P_{RL} is the refractive loss (dB), NA_a is the numerical aperture of the sensing region in the presence of the analyte, NA_r is the numerical aperture of the sensing region in presence of reference medium. This refractive loss is an instantaneous response of the fiber due to change in bulk RI.

2.4.2 EWA

As the analyte molecule comes closer to the surface (due to its affinity to surface groups or due to physical adsorption), they enter the interaction region of the evanescent field and may even get bound to the receptors on the surface of the fiber. Each molecule interacts with the evanescent wave depending on its size and optical parameters like refractive index (n) and extinction coefficient (k). Relationship between absorption coefficient and extinction coefficient is given by:

$$\alpha = \frac{4\pi k}{\lambda} \tag{14}$$

The evanescent wave absorbance given by Eq. (11) may be modified to:

$$A = 4\frac{\sqrt{2}}{3}\frac{\lambda}{2\pi r\sqrt{{n_{core}}^2 - {n_{analyte}}^2}}\frac{\alpha CL}{2.303} \tag{15}$$

This absorbance can be directly related to concentration of the analyte, if other parameters are known.

At very low concentrations, refractive loss will be negligible due to a very slight difference of RI between the analyte solution and the reference solution. So, at lower concentration EWA dominates the sensor response. On the other hand, at high concentration, first there will be refractive loss due to significant difference in bulk RI compared to reference medium. But, when the molecule start binding on the surface, it contributes to EWA and we see a first order binding curve. However, due to binding of large number of molecules, the effective RI of cladding changes significantly, which further adds to refractive loss. So the resulting sensor response is a combined effect of both refractive loss and EWA, which varies with the analyte concentration and/or its density (after binding) on sensor surface.

2.4.3 V-Number Mismatch

Typically, in an EWA sensor, decladded sensing region is followed by cladded optical fiber. It causes mismatch in the V-number between the sensing region and the receiving portion (Fig. 3(a)). This results in loss of signal, when transitioning from sensing region back to passive cladded fiber end, due to loss of higher order modes which cannot be coupled. This reduces the signal-to-noise ratio. One of the possible solutions is to reduce the fiber core radius at the output end so as to match the V-number. The criteria to reduce V-number mismatch is given by [24]:

$$r_a \leq r_{clad}\left(\frac{n_{core}^2 - n_{clad}^2}{n_{core}^2 - n_{analyte}^2}\right)^{\frac{1}{2}} \tag{16}$$

where, r_a is the radius of the core at the end of the sensing region, r_{clad} is the radius of the cladding, n_{core} is the RI of the core, n_{clad} is the RI of the cladding and $n_{analyte}$ is the effective RI due to presence of analyte in sensing region.

Thus, the sensor response of an evanescent wave absorbance based fiber-optic sensor is a combined effect of refractive loss, evanescent wave absorbance and loss due to V-number mismatch. In the next section, we will see different parameters which have been explored to improve the sensitivity of the EWA based fiber-optic sensors.

3 Sensitivity Enhancement of EWA Based Fiber-Optic Sensor

Sensitivity of an EWA-fiber-optic sensor is limited by the penetration depth and fractional power. As we observed, both of these parameters are dependent on various factors. Following is the list of factors that can be modified for improving sensitivity:

3.1 Incident Angle

From Eq. (5), it is clear that penetration depth is dependent on incident angle. Closer the incident angle to critical angle, the more will be the penetration depth (Fig. 5). Some groups have tried to modify the launch angle, so that incident angle is close to critical angle of the fiber-optic sensor probe, thereby increasing the sensitivity of the sensor [25]. It requires a complex setup for aligning source with the fiber-optic probe.

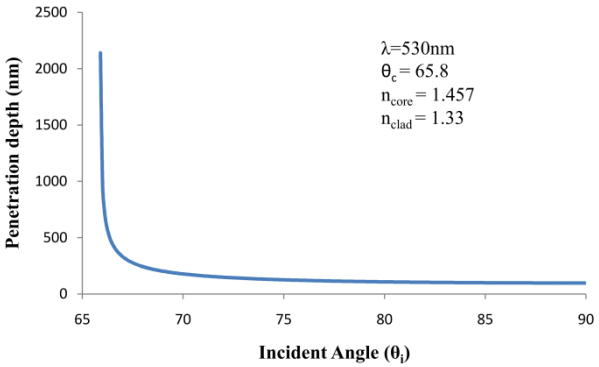

Fig. 5 Relationship between penetration depth (nm) and incident angle (θ_i)

3.2 Input Wavelength

Evanescent wave parameters are directly proportional to wavelength of the incident light. Higher the wavelength more is the penetration depth. IR wavelengths will thus have higher penetration depths. The problem here is that biological molecules are usually transparent in IR, so there are no absorption peaks. Also there is a strong absorption peak of water in IR, which may interfere with the measurement.

3.3 Geometry

Geometry of a fiber-optic probe critically affects the performance of the sensor. For biosensor applications, optical fibers are generally employed in two configurations. In the first case, analyte is detected at the distal end of the bioreceptor immobilized fiber probe (Fig. 6(a)). In distal end configurations, absorption/reflection of light input or luminescence resulting from biomolecular interactions is monitored [26]. In the second case, sensing is done on bioreceptor immobilized core of the fiber. The earliest and the most common design is the decladded straight probe as shown in Fig. 6(b). The major problem with the straight probe design is low penetration depth and thereby mediocre sensitivity. It is evident from Eq. (15) that sensitivity can be increased by increasing the length of the sensing region and decreasing the effective NA contrast and fiber radius. If the length of the decladded portion is increased, the system will become more fragile and will be difficult to handle. Also, by decreasing the fiber core diameter, complex coupling schemes will have to be implemented along with an increase in fragility and cost of the overall sensor.

By taking the above constraints into consideration, researchers have developed several geometrical designs to enhance the sensitivity of these fiber-optic sensors. These different designs have shown improved fractional power (P_{clad}/P) and penetration depth (d_p) due to mode conversion phenomenon and by increasing the number of TIR events in a shorter length [27]. Some of the typical geometrical designs are tapered fiber [28, 29], biconical fiber [30, 31] and bent fiber [32] (Fig. 6(c), 6(d) and 6(e)). These probes have been utilized for various chemical and biochemical sensing applications [33–41].

Among the different geometrical designs, bent and tapered probes have shown immense potential for biosensing applications because of high penetration depth, conversion of lower order modes into higher order and its effect on sensor performance. We will see in detail the advantages of both these designs on sensitivity enhancement of evanescent wave absorption based fiber-optic senor.

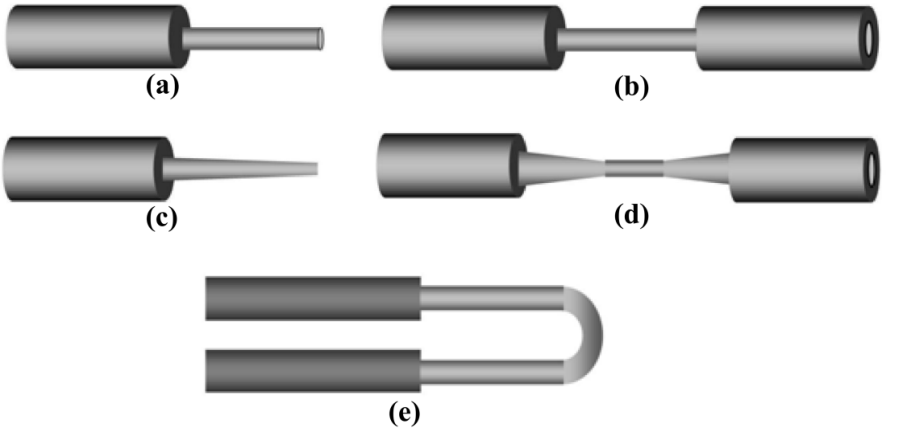

Fig. 6 Different types of fiber probe designs: (a). Tip probe; (b). Straight probe; (c). Tapered probe; (d). Biconical probe; (e). U-bent probe

3.3.1 Tapered Probes

Tapered geometry has been shown to increase the sensitivity of EWA based sensors by increasing the power in the cladding/evanescent power in the tapered region. In case of tapered probes, the high sensitivity can be achieved by adiabatic tapering that helps in maintaining all the power in the guided modes and thereby increases the power in the cladding region (Fig. 7(a)). (In adiabatic tapering, taper angle is small (i.e. taper transition is slow) enough to avoid mode coupling to higher order modes which cannot be supported in the structure).

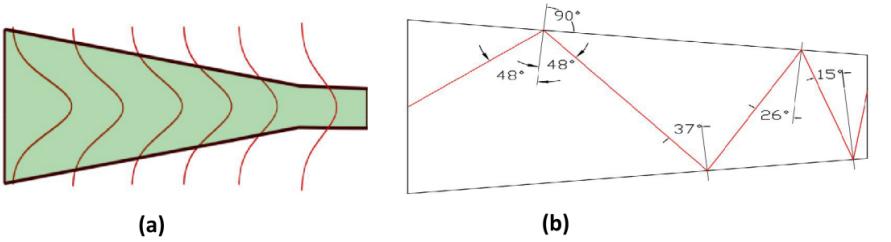

Fig. 7 (a). Propagation of the evanescent field in adiabatically tapered fiber; (b). Propagation of a ray in linearly tapered structure.

If we do the analysis using ray theory, the number of TIR events increases due to reduction in the taper width, leading to more evanescent power compared to a straight probe (Fig. 7(b)). Also, due to adiabatic taper profile, there is continuous change in the angle of propagation of the ray of light causing conversion of lower order modes to higher order modes, thereby increasing the fractional power in the cladding. Another important advantage of taper geometry is that it reduces

V-number mismatch, thereby helping in increasing the efficiency of excitation and coupling back of light from fluorescent molecules (in such cases where fluorescent markers are used) into the fiber probe.

3.3.2 U-Bent

Similar to tapered probes, U-shaped geometry has been shown to increase the sensitivity of the EWA based sensor by increasing both the evanescent wave absorption and refractive loss in the bend region. Basically, the U-bent structures cause the fiber mode to shift away from the center. An analogy can be given of a car turning at the curvature. Depending on the dimension of the bend radius and fiber width, some of the modes are lost, while others are shifted in the outward direction. This shift in outward direction causes the evanescent power and penetration depth to increase (Fig. 8(a)). The shift is because the modes see an equivalent graded refractive index profile in the bend region, causing it to shift towards higher refractive index (Fig. 8(b)).

If we see the analysis from point of view of ray theory, the number of TIR events increases, leading to more evanescent power compared to a straight probe (Fig. 8(c)). Also, due to the bending, there is a constant change in the angle of propagation of the light inside the bend region causing conversion of lower order modes to higher order modes, thereby increasing the power in the cladding. Along with high sensitivity of U-bent probe, it also leads to an ergonomic design by having both source and detector on the same side compared to tapered probes. This has helped to use the U-bent probe in a point sensor configuration and also increases ease of handling compared to a tapered probe.

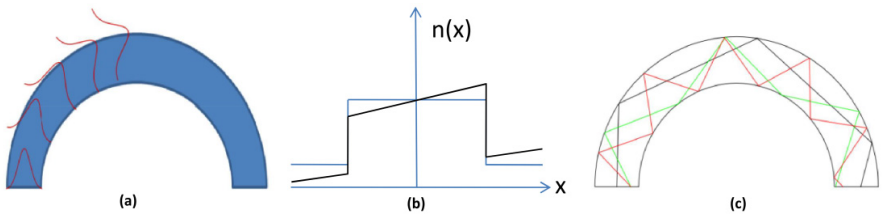

Fig. 8 (a). Mode displacement/offset in the bend; (b). Equivalent index profile (black) in the bend region. (Adapted from Ladouceur and Labeye, 1995) [42]; (c). Ray analysis of the bend region of the fiber-optic probe. (Each color represents different ray, following different path in the bend region).

Both types of fiber-optic probe design have been used for sensing of various chemicals and biochemical [43]. To further enhance the sensitivity of EWA based fiber-optic probes, we have developed a novel design by combining both bent and tapered geometry. In the next section, we will cover the details of the fabrication and sensitivity evaluation of the U-tapered probes and their application to fiber-optic biosensors.

4 Bent-Tapered Probe

As we saw in Sec. 2 and 3, there is a significant effect on fractional power in the cladding or evanescent power due to change in geometry like using bends or tapers. So, to further enhance the sensitivity as well as combine their individual inherent advantages, both geometries were cascaded in one probe. In this section, we will be dealing with the fabrication, sensitivity evaluation and analysis, and biosensing application of the bent-tapered probe.

4.1 Fabrication Setup

The bent-tapered fiber-optic probes were fabricated in three steps which involved, i) decladding of optical fibers, ii) bending of the decladded region of the optical fibers and iii) tapering of bent fiber-optic probes [44].

4.1.1 Fabrication of U-Bent Probes

Polymer cladded silicate optical fiber probe of 400 µm core diameter (CeramOptec®) was cut from a fiber spool into small pieces of ~12 cm length. Both the ends of the probe were polished using emery papers to ensure proper coupling. The buffer and cladding layers from a 2cm length in the middle of each fiber probe were carefully removed using a surgical blade. The decladded portion was heated over a butane flame and bent to get a bend diameter of 2 ± 0.2 mm [35].

4.1.2 Tapering of U-Bent Probes

The bent probes were tapered by chemical etching method using hydrofluoric acid (HF). The reaction for etching is:

$$SiO_2 + 6HF \longrightarrow H_2SiF_6 + 2H_2O$$

The set-up used for etching of bent probes is shown in Fig. 9(a). One leg of the bent probe was gently pushed in the micropipette tip in such a way that the center of the bend region is positioned very close to the rim of the micropipette tip. The diameter of micropipette tip opening fitted perfectly with the buffered fiber probe, thereby avoiding seeping out of HF. This setup was clamped vertically (in a fume hood) to keep the level of HF horizontal. Then, 60 µL of HF (49%) was poured into the micropipette tip. The height of the pipette was selected such that the decladded portion remains 2 mm above the HF level. Following standard diffusion laws, coupled with confinement of vapors in the micropipette, there is a negative gradient of HF vapor concentration from the surface of the HF liquid to the open end of the pipette. This results in a HF vapor concentration dependent etching rate leading to a tapered profile on one leg of the decladded bent probe (in the micropipette tip) (Fig. 9(b)).

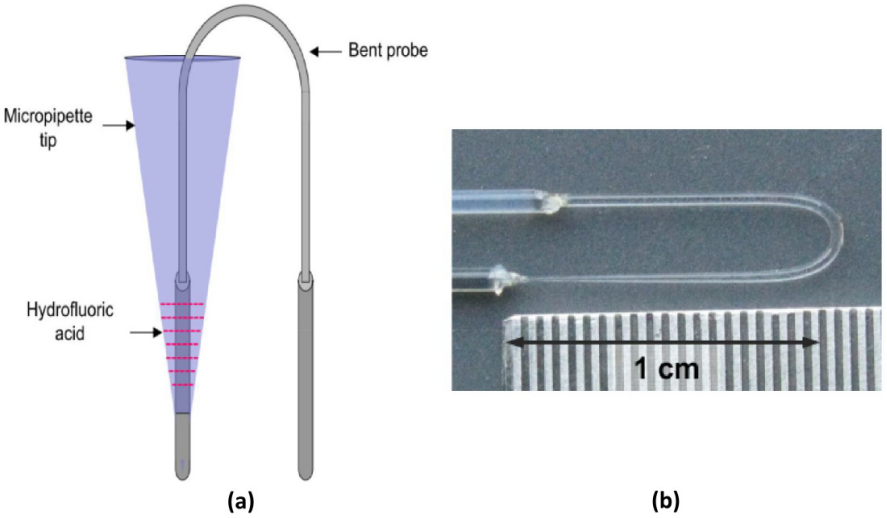

Fig. 9 (a). Schematic representation of set-up used for etching of bent fiber-optic probes; (b). Digital photograph of tapered U-bent fiber-optic probe showing both tapered and un-tapered arm [44].

By varying the time of exposure, bent-tapered probes of different taper ratios (TR) (defined as the ratio of diameter of fiber-optic probe at the output end to the diameter of the fiber-optic probe at the input end) ranging from 0.17 to 1 were fabricated. Here, TR 1 denotes probes which were not subjected to the HF treatment. Later, these fiber probes were washed thoroughly with DI water and dried with nitrogen. The dimensions of the probes were measured using optical microscope (Axioskop 2 MAT), with AxioVision software.

4.2 Functionalization

For evaluating the sensitivity of the bent-tapered fiber-optic probes based on evanescent wave absorbance, an analyte molecule should have the property to absorb light. Therefore, a fluorescent dye, i.e. fluorescein isothiocyanate (FITC) dye which has extinction maxima at 495 nm, was used in this study. Since FITC is known to have strong affinity towards amine groups, all the fiber probes were functionalized with amine terminated poly(amido amine) dendrimer (fourth generation with 64 primary amine groups) as explained earlier [45].

4.2.1 Cleaning of Fiber-Optic Probes

All the fiber probes were cleaned using a sequence of alkali and acid treatment [46]. The probes were incubated in NaOH solution (1 M) for 2 h and followed by washing with DI water. After that, the probes were dipped in mixture of methanol:HCl (1:1 v/v) for 2 h and followed by thorough washing with DI water.

In the next step, the probes were exposed to concentrated H_2SO_4 for 2 h and then extensively washed with DI water. Thereafter, cleaned probes were treated with sulphochromic acid (10 mg/ml of $K_2Cr_2O_7$ prepared in concentrated H_2SO_4) to generate –OH groups on the fiber probe surface. After 10 min, the probes were thoroughly washed with DI water and dried in hot air oven for 60 min at 110°C.

4.2.2 Dendrimerization

Dendrimers are three dimensional, hyper branched, polymeric architectures with a very high density of peripheral functional groups [47]. Most of the properties of the dendrimers are dominated by peripheral functional groups, although the internal functionality of dendrimeric crevices and central core are also of great significance [48]. Advantages of using dendrimers over other conventional linkers is in terms of better loading efficiency, uniform surface coverage and improved Limit of Detection(LOD) [49]. Since FITC has affinity towards amine groups, we functionalized the fiber probes with amine terminated fourth generation (64 primary amine groups) of poly(amido amine) (PAMAM) dendrimer

Cleaned and dried bent-tapered probes were dipped in 1,1'-carbonyldiimidazole (CDI) solution (80 mM prepared in DMSO solvent) for 24 h. Thereafter, probes were thoroughly washed with DMSO and followed by incubation in aqueous solution of PAMAM dendrimer (conc. = 20 µM) for 24 h. After that, the probes were washed thrice with DI water [45]. These dendrimer immobilized probes were used for EWA sensitivity evaluation using FITC as an analyte. For biosensing application, further treatment was carried out on dendrimer coated probes to immobilize antibodies.

4.2.3 Glutaraldehyde Activation

Dendrimer functionalized probes were incubated in 1.5%(v/v) glutaraldehyde solution for 60 min. Later, the probes were washed thrice with DI water to remove unbound or physically adsorbed glutaraldehyde molecules.

4.2.4 Antibody Immobilization

The glutaraldehyde activated probes were incubated in human immunoglobulin G (HIgG) antibody solution (conc. = 100 µg/mL, prepared in 10 mM PBS buffer, pH 7.4) for 4 h. Later, the probes were washed thrice with PBS buffer.

4.2.5 BSA Treatment

To avoid any non-specific binding of analyte to the free reactive aldehyde sites on the sensor surface, the probes were incubated in bovine serum albumin (BSA) solution (conc. = 2 mg/mL, prepared in 10 mM PBS buffer, pH 7.4) for 30 min. Thereafter, the probes were washed with PBS and then used for immunoassay experiments.

4.3 Experimental Setup

The optical set-up used for sensitivity evaluation is shown in Fig. 10.

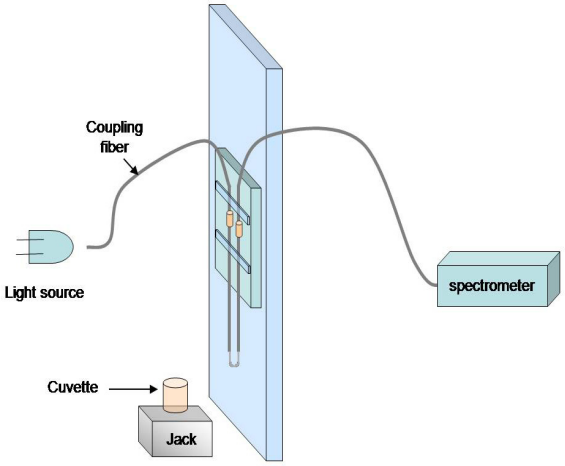

Fig. 10 Optical set-up used for evanescent wave absorption based experiment [44]

First, the bent-tapered probe was firmly fitted on the grooved fiber chuck. Then both the ends of the fiber probes were separately coupled with 20 cm long optical fiber (core diameter = 400 μm) using customized coupler. The un-tapered side of the fiber probe was coupled with the light source, i.e. white LED (Edison, 1 W), while the other end, having the tapered profile in the decladded region, was connected to the spectrophotometer (USB 4000, Ocean Optics). The measurement cuvette was kept on a vertically movable jack underneath the sensing region of the fiber probe.

For EWA sensitivity evaluation, FITC solution (0.5 mL of 50 μM, prepared in borate buffer, pH 8.3) was introduced into the cuvette and absorbance spectrum was monitored in real-time. Borate buffer solution was taken as reference.

4.4 Results and Analysis

Fig. 11(a) shows the absorbance spectra obtained after binding of FITC on bent-tapered fiber-optic probes of different TR. Fig. 11(b) depicts the comparative performance of all bent-tapered probes. It is evident from Fig. 11(b) that as the taper diameter decreased from 400 μm to 148 μm, the sensitivity of the probe is found to increase. All bent-tapered probes showed higher sensitivity compared to untapered bent probe. This is attributed to greater fractional power in the sensing region of bent-tapered due to combination of bending and tapering. Among the different taper ratio, TR 0.37 showed 2.4-fold higher sensitivity compared to

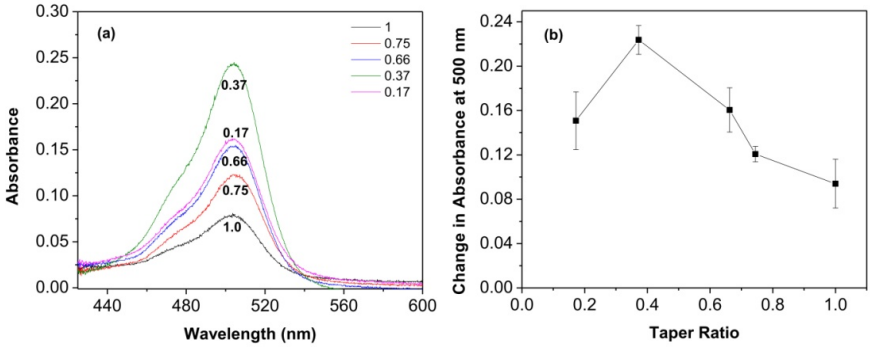

Fig. 11 (a) Absorbance spectra obtained from the binding of FITC dye on dendrimer functionalized bent-tapered fiber probes of different taper ratios. (Numbers below the peak of each spectra indicates the TR. Only for TR 0.17 the number is above the peak.); (b). Effect of taper ratio on the sensitivity of bent-tapered optical fiber sensors (n = 4 for each TR) [44].

untapered probe. This high sensitivity is in-spite of the significant reduction in the surface area (~31% in the taper region) for probe with TR 0.37 compared to untapered bent probe. Statistical data analysis also revealed the significant enhancement in the sensitivity of various taper ratios (P value < 0.02). This high sensitivity makes it suitable for application where large biomolecules are to be sensed using evanescent wave absorbance phenomenon. A further decrease in tapered diameter showed reduction in sensitivity. This is probably due to insufficient taper length of the probe, which could not satisfy the adiabatic condition, thereby causing loss of propagating modes and resulting in reduced evanescent interaction with the analyte. This is in concurrence with the previous studies of tapered probes where it can be inferred that for a fixed length, reduction in TR reduces the evanescent power [25, 50].

4.5 Biosensing Application

Based on the results of EWA sensitivity, bent-tapered probe of TR 0.37 was used for immunoassay application. Dendrimer functionalized probes were immobilized with HIgG by following the protocol as detailed in Sec 4.2. For immunoassay, FITC-tagged goat anti human immunoglobulin G (FITC-GaHIgG) was used as an analyte while PBS buffer was taken as reference solution. FITC-GaHIgG solution was prepared in PBS buffer in the concentration range from 0.01 µg/mL to 10 µg/mL. The experimental setup was same as used for EWA sensitivity measurement. Each concentration of FITC-GaHIgG was introduced into the flow cell and the response was monitored at 500 nm for 30 min for each concentration. After 30 min, sequentially higher concentration was introduced and same procedure was repeated. At the end of the experiment, the probe was washed with PBS buffer.

Fig. 12 depicts the dose-response curve for immunoassay on bent-tapered probe of TR 0.37. LOD was found to be 0.01µg/mL for 400 µm optical fiber, which is better compared to similar bare probe of 200 µm diameter [49]. Thus the bent-tapered design has better sensitivity than other reported multimode fiber-optic sensor designs along with the added advantage of sturdy nature of 400 µm diameter fiber compared to its 200 µm diameter fiber.

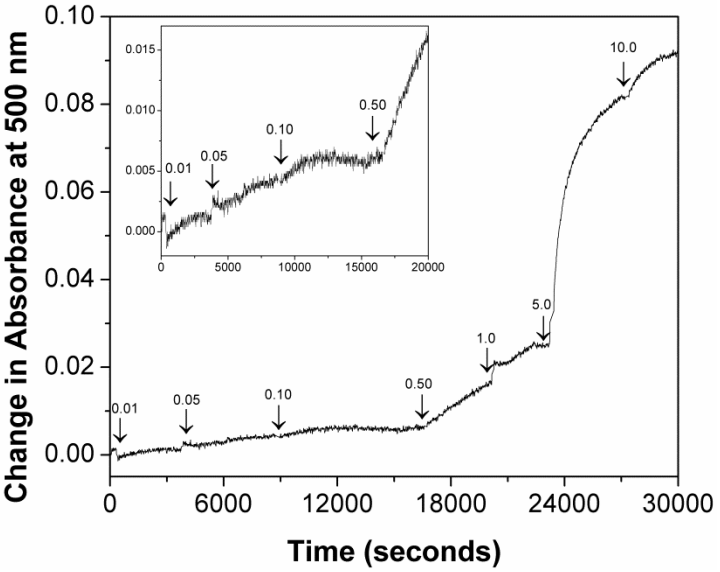

Fig. 12 Dose-response curve for binding of FITC-GaHIgG on bent-tapered fiber for TR 0.37

5 Conclusion

The potential of EWA based fiber-optic sensors for monitoring various analytes with high sensitivity along with its simple but elegant sensing phenomena, has led to continuation of research for further improving design and deployment for various applications. This chapter has provided details of the fabrication, design and sensitivity evaluation of a novel cascade of bent and tapered geometries for enhancing the sensitivity of EWA based fiber-optic sensors. Also, the basic theory underlying the working of EWA based fiber-optic sensors was discussed. The relative advantages of bent and taper geometry for evanescent wave absorption based fiber-optic sensor were discussed. The bent-tapered probes were fabricated using a HF vapor etching scheme. The EWA sensitivity was found to be 2.4 times higher than the bent probe for TR 0.37. Biosensing application was demonstrated using FITC-GaHIgG and HIgG as analyte and bioreceptor respectively. This new design achieved LOD of 0.01µg/mL. Also, this bent-tapered design allows for

V-number matching that enables light to couple back into the fiber from fluorescent molecules (if present on the surface). Other dimensions of the probes like taper length and bend diameter have to be optimized to further improve the sensitivity. Further, merging of this geometry with other sensing schemes can be explored to evaluate its potential in improving sensitivity of other fiber based sensing schemes like LSPR, *etc*.

References

[1] Lopez-Higuera, J.M., Cobo, L.R., Incera, A.Q., Cobo, A.: Fiber optic sensors in structural health monitoring. Journal of Lightwave Technology 29, 587–608 (2011)

[2] Wren, S.P., Nguyen, T.H., Gascoine, P., Lacey, R., Sun, T., Grattan, K.T.V.: Preparation of novel optical fibre-based Cocaine sensors using a molecular imprinted polymer approach. Sensors and Actuators B: Chemical 193, 35–41 (2014)

[3] Chu, C.-S., Lin, C.-A.: Optical fiber sensor for dual sensing of temperature and oxygen based on PtTFPP/CF embedded in sol–gel matrix. Sensors and Actuators B: Chemical 195, 259–265 (2014)

[4] Karimi, M., Fabian, M., Jaroszewicz, L.R., Schuster, K., Mergo, P., Sun, T., Grattan, K.T.V.: Lateral force sensing system based on different photonic crystal fibres. Sensors and Actuators A: Physical 205, 86–91 (2014)

[5] Li, X., Li, Q., Zhou, H., Hao, H., Wang, T., Zhao, S., Lu, Y., Huang, G.: Rapid, on-site identification of explosives in nanoliter droplets using a UV reflected fiber optic sensor. Analytica Chimica Acta 751, 112–118 (2012)

[6] Fernandez-Vallejo, M., Lopez-Amo, M.: Optical fiber networks for remote fiber optic sensors. Sensors (Basel) 12(4), 3251–3929 (2012)

[7] Bharadwaj, R., Sai, V.V.R., Thakare, K., Dhawangale, A., Kundu, T., Titus, S., Verma, P.K., Mukherji, S.: Evanescent wave absorbance based fiber optic biosensor for label-free detection of E. coli at 280 nm wavelength. Biosensors and Bioelectronics 26(7), 3367–3370 (2011)

[8] John, M.S., Kishen, A., Sing, L.C., Asundi, A.: Determination of bacterial activity by use of an evanescent-wave fiber-optic sensor. Appied Optics 41(34), 7334–7338 (2002)

[9] Sai, V.V.R., Kundu, T., Deshmukh, C., Titus, S., Kumar, P., Mukherji, S.: Label-free fiber optic biosensor based on evanescent wave absorbance at 280nm. Sensors and Actuators B: Chemical 143(2), 724–730 (2010)

[10] Shevchenko, Y., Camci-Unal, G., Cuttica, D.F., Dokmeci, M.R., Albert, J., Khademhosseini, A.: Surface plasmon resonance fiber sensor for real-time and label-free monitoring of cellular behavior. Biosensors and Bioelectronics 56, 359–367 (2014)

[11] Verma, R., Srivastava, S.K., Gupta, B.D.: Surface-plasmon-resonance-based fiber-optic sensor for the detection of low-density lipoprotein. IEEE Sensors Journal 12(12), 3460–3466 (2012)

[12] Sciacca, B., Monro, T.M.: Dip biosensor based on localized surface plasmon resonance at the tip of an optical fiber. Langmuir 30(3), 946–954 (2014)

[13] Jeong, H.H., Erdene, N., Park, J.H., Jeong, D.H., Lee, H.Y., Lee, S.K.: Real-time label-free immunoassay of interferon-gamma and prostate-specific antigen using a fiber-optic localized surface plasmon resonance sensor. Biosensors and Bioelectronics 39(1), 346–351 (2013)

[14] Khetani, A., Riordon, J., Tiwari, V.: Hollow core photonic crystal fiber as a reusable Raman biosensor. Optics Express 21(10), 12340–12350 (2013)
[15] Dinish, U.S., Balasundaram, G., Chang, Y.T., Olivo, M.: Actively targeted in vivo multiplex detection of intrinsic cancer biomarkers using biocompatible SERS nanotags. Scientific Reports, 4(4075), 1–7 (2014)
[16] Candiani, A., Bertucci, A., Giannetti, S., Konstantaki, M., Manicardi, A., Pissadakis, S., Cucinotta, A., Corradini, R., Selleri, S.: Label-free DNA biosensor based on a peptide nucleic acid-functionalized microstructured optical fiber-Bragg grating. Journal of Biomedical Optics 18(5), 057004-1-057004-7 (2013)
[17] Ryu, G., Dagenais, M., Member, S., Hurley, M.T., Deshong, P.: High specificity binding of lectins to carbohydrate-functionalized fiber bragg gratings: A new model for biosensing applications. IEEE Journal of Selected Topics in Quantum Electronics 16(3), 647–653 (2010)
[18] Pollock, C.R.: Fundamental of optoelectronics, pp. 36–38. Irwin publishers (1995)
[19] Gloge, D.: Weakly guiding fibers. Applied Optics 10(10), 2252–2258 (1971)
[20] Powers, J.: Introduction to fiber optic systems. Irwin publishers (1997)
[21] Tai, H., Tanaka, H., Yoshino, T.: Fiber-optic evanescent-wave methane-gas sensor using optical absorption for the 3.392-microm line of a He-Ne laser. Optics Letters 12(6), 437–439 (1987)
[22] Palais, J.: Fiber optic communications. Prentice-Hall (1998)
[23] Satija, J., Punjabi, N.S., Sai, V.V.R., Mukherji, S.: Optimal design for U-bent fiber-optic LSPR sensor probes. Plasmonics 9(2), 251–260 (2013)
[24] Ligler, F.S., Taitt, C.: Optical biosensors: Today and tomorrow. Elsevier (2011)
[25] Ahmad, M., Hench, L.L.: Effect of taper geometries and launch angle on evanescent wave penetration depth in optical fibers. Biosensors and Bioelectronics 20(7), 1312–1319 (2005)
[26] Kuswandi, B., Andres, R., Narayanaswamy, R.: Optical fibre biosensors based on immobilised enzymes. Analyst 126(8), 1469–1491 (2001)
[27] Ruddy, V., MacCraith, B.D., Murphy, J.A.: Evanescent wave absorption spectroscopy using multimode fibers. Journal of Applied Physics 67(10), 6070–6074 (1990)
[28] Love, J.D., Henry, W.M., Stewart, W.J., Black, R.J., Lacroix, S., Gonthier, F.: Tapered single-mode fibres and devices. Part 1: Adiabaticity criteria. IEE Proceedings -Journal of Optoelectronics 138(5), 343–354 (1991)
[29] Black, R.J., Lacroix, S., Gonthier, F., Love, J.D.: Tapered single-mode fibres and devices Part 2: Experimental and theoretical quantification. IEE Proceedings-Journal of Optoelectronics 138(5), 355–364 (1991)
[30] Littlejohn, D., Lucas, D., Han, L.: Bent silica fiber evanescent absorption sensors for near-infrared spectroscopy. Applied Spectroscopy 53(7), 845–849 (1999)
[31] DeGrandpre, M.D., Burgess, L.W.: Long path fiber-optic sensor for evanescent field absorbance measurements. Analytical Chemistry 60(23), 2582–2586 (1988)
[32] Gupta, B.D., Dodeja, H., Tomar, A.K.: Fibre-optic evanescent field absorption sensor based on a U-shaped probe. Optical and Quantum Electronics 28(11), 1629–1639 (1996)
[33] Gupta, B.D., Sharma, N.K.: Fabrication and characterization of U-shaped fiber-optic pH probes. Sensors and Actuators B: Chemical 82(1), 89–93 (2002)
[34] Khijwania, S.K., Srinivasan, K.L., Singh, J.P.: An evanescent-wave optical fiber relative humidity sensor with enhanced sensitivity. Sensors and Actuators B: Chemical 104(2), 217–222 (2005)

[35] Sai, V.V.R., Kundu, T., Mukherji, S.: Novel U-bent fiber optic probe for localized surface plasmon resonance based biosensor. Biosensors and Bioelectronics 24(9), 2804–2809 (2009)
[36] Thompson, V.S., Maragos, C.M.: Fiber-optic immunosensor for the detection of fumonisin B1. Journal of Agricultural and Food Chemistry 44(4), 1041–1046 (1996)
[37] Pilevar, S., Davis, C.C., Portugal, F.: Tapered optical fiber sensor using near-infrared fluorophores to assay hybridization. Analytical Chemistry 70(10), 2031–2037 (1998)
[38] Leung, A., Shankar, P.M., Mutharasan, R.: Label-free detection of DNA hybridization using gold-coated tapered fiber optic biosensors (TFOBS) in a flow cell at 1310nm and 1550nm. Sensors and Actuators B: Chemical 131(2), 640–645 (2008)
[39] Rijal, K., Leung, A., Shankar, P.M., Mutharasan, R.: Detection of pathogen Escherichia coli O157:H7 at 70 cells/mL using antibody-immobilized biconical tapered fiber sensors. Biosensors and Bioelectronics 21(6), 871–880 (2005)
[40] Zibaii, M.I., Latifi, H., Arabsorkhi, M., Kazemi, A., Gholami, M., Karimi Azar, M., Hosseini, S.M.: Biconical tapered optical fiber biosensor for real-time monitoring of bovine serum albumin at femtogram/mL levels on antibody-immobilized tapered fibers. Proccedings of SPIE 7653, 765322 (2010)
[41] Hale, Z., Payne, F., Marks, R., Lowe, C., Levine, M.: The single mode tapered optical fibre loop immunosensor. Biosensors and Bioelectronics 11(1–2), 137–148 (1996)
[42] Ladouceur, F., Labeye, E.: A new general approach to optical waveguide path design. Journal of Lightwave Technology 13(3), 481–492 (1995)
[43] Leung, A., Shankar, P.M., Mutharasan, R.: A review of fiber-optic biosensors. Sensors and Actuators B: Chemical 125(2), 688–703 (2007)
[44] Punjabi, N., Satija, J., Mukherji, S.: Novel bent-tapered mode converting multimode optical fiber sensor based on Evanescent Wave Absorption. In: Seventh International Conference on Sensing Technology (ICST), pp. 545–548 (2013)
[45] Satija, J., Mukherji, S.: Dendrimeric nano-glue material for localized surface plasmon resonance-based fiber-optic sensors. Applied Nanoscience 2(3), 293–297 (2012)
[46] Cras, J., Rowe-Taitt, C., Nivens, D., Ligler, F.: Comparison of chemical cleaning methods of glass in preparation for silanization. Biosensors and Bioelectronics 14(8–9), 683–688 (1999)
[47] Tomalia, D.A., Baker, H., Dewald, J., Hall, M., Kallos, G., Martin, S., Roeck, J., Ryder, J., Smith, P.: A new class of polymers: Starburst-dendritic macromolecules. Polymer Journal 17(1), 117–132 (1985)
[48] Astruc, D., Boisselier, E., Ornelas, C.: Dendrimers designed for functions: from physical, photophysical, and supramolecular properties to applications in sensing, catalysis, molecular electronics, photonics, and nanomedicine. Chemical Review 110(4), 1857–1959 (2010)
[49] Satija, J., Karunakaran, B., Mukherji, S.: A dendrimer matrix for performance enhancement of evanescent wave absorption-based fiber-optic biosensors. RSC Advances 4(31), 15841–15848 (2014)
[50] Yuan, Y., Ding, L.: Theoretical investigation for excitation light and fluorescence signal of fiber optical sensor using tapered fiber tip. Optics Express 19(22), 21515–21523 (2011)

Design of High-Resolution Optical Systems for Fast and Accurate Surface Reconstruction

R. Marani*, M. Nitti, G. Cicirelli, T. D'Orazio, and E. Stella

Institute of Intelligent Systems for Automation (ISSIA), National Research Council (CNR), via Amendola 122 D/O, 70126, Bari, Italy
marani@ba.issia.cnr.it

Abstract. In the last few decades, virtual reconstruction of objects has grown interest in the field of quality control. As known, smart manufactures need automatic systems for the real-time investigation of production yields, i.e. techniques, methods and technologies devoted to the analysis of quality. In particular, high-resolution systems are required for the measurement of surface profiles aimed to the detection and characterization of small defects, with sizes reaching the limit of few microns. This book Chapter describes the procedure for the design of high-resolution and high-accuracy laser scanning probes based on triangulation techniques for the exhaustive reconstruction of objects. Drawbacks and limitations will be discussed, with particular focus on occlusion problems due to possible undercut surfaces within the testing objects. A complete description of novel techniques will be thus provided together with a demonstration of a resulting optical probe. Challenging metal objects, namely drilling tools, will be then investigated, proving measurement resolutions close to the physical diffraction limit.

Keywords: 3D laser triangulation scanners, high resolution surface reconstruction, surface defects, quality control, tool inspection.

1 Introduction

The analysis of three dimensional data has gained increasing interest in the last years, since it founds its applicability in many fields of science, ranging from electronics and mechanics to environmental monitoring and hazard prevention, but also including cultural heritage and plastic surgery, just to mention a few [1-8].

As a matter of fact, manufacturing constitutes one of the most important industrial engines in Europe in terms of capability of creating employment and efforts in active research and development. This aspect has led to increasing private interests in the in-line management of the process quality, which constitutes the enabling key for the actual improvement of production processes,

* Corresponding author.

A. Mason et al. (eds.), *Sensing Technology: Current Status and Future Trends III*,
Smart Sensors, Measurement and Instrumentation 11, DOI: 10.1007/978-3-319-10948-0_3

enhancing the industrial competitiveness. In other words the automatic inspection of manufactured goods can dramatically improve the production processes, in terms of both precision and time consumption. Moreover, the growing demand of more and more miniaturized products has brought Research to the design of increasingly complex systems, that often do not meet initial requirements.

In the context of the detection of small surface defects, high resolution techniques are required for surface profile measurement and 3D modeling, with accuracies of few microns. Currently, the task of inspection of complex assemblies in mechanical industries (automotive, aerospace, etc.) is often carried out by the Coordinate Measurement Machines (CMMs) [9-13]. Such systems can be represented as made of three simple blocks: a handling system for three-dimensional (3D) motion, a touching probe, and a data collector/processor. Although achievable resolutions have been downed to the range between 2 and 10 μm, touching probes are implicitly sources of limitations for the inspection of delicate objects that could be damaged by an improper pressure. At the same time, touching probes can lead to ambiguous measurements when the probe itself is deflected by the target. Moreover, touching measurements require huge time consumption to get a consistent sampling of the target surface, suitable for the following data processing.

On the contrary, Researchers agree that fast measurements of surfaces, overcoming these problems, can be achieved exploiting contactless optical probes [14-19]. In general, the reasons of the success of optical probes, e.g. 3D laser scanners, can be found in the enabling property of being not invasive, providing at the same time high precisions and fast measurements.

This Chapter aims at the description of the design procedures that allow the robust extraction of target samples, without the presence of holes due to sensor occlusions. The first idea resides in the development of a laser triangulation scanner able to achieve high-resolution measurements in the whole testing volume with an expected sample rate of 25 kHz. Such results are achievable only defining accurate calibration steps of the whole system and high-speed techniques for the extraction of laser peaks. Furthermore, the negative contribution of sharp edges on the target, speckle noise contributions on the camera and second order reflections, typical of high-curvature surfaces, have to be mitigated for the development of a reliable instrument.

Although the problem of 3D reconstruction spans over many fields of application, the specific framework of the inspection of drilling tools will be used as reference within these lines. As suggested by the recent introduction of mechanical standards [20,21], the problem of assessing the conditions of the tools is of industrial relevance: before testing the final product, it is mandatory to assess the conditions of the tools used for its manipulation/manufacturing. As a consequence, actual necessities regard the development of robust strategies and procedures for the deep inspection of tools commonly used in the present industrial production chains, with a close focus on measurements of inner regions that are not measurable with current available imaging techniques. In fact, although present systems are very fast in measuring, available outputs regard only

the tool length and diameter [22-24]. Therefore, Researchers have preferred derive the control of micro tool properties by monitoring different signals out of the machine, e.g. sound emissions, cutting strength and power, and correlating them with the residual tool life [25-29].

However, the tool wear is an inherently 3D phenomenon and thus requires the use of 3D reconstruction techniques. Moreover, since surface defects are orders of magnitude lower in size than macro characteristics, such as height and diameter, the crucial specification regards the system resolution. Quantitatively, resolution has to be downed to 15 μm, i.e. lower than the one achievable with defocusing techniques [30]. Thus, laser scanning measurement becomes mandatory for the fulfillment of such specifications.

The characterization of drilling tools can be effectively used as a reference model for the definition of design processes, since it has many challenging aspects, starting from the constitutive medium of the targets, typically metal or ceramic. Also the presence of sharp edges constitutes a constrain in the laser measurement, since it carries to the possible formation of several spots in the image plane, where the camera can saturate. Furthermore, the fast repetitions of concave and convex regions induces second-order reflections of the laser line to the camera, thus bringing ambiguities that can alter the overall accuracy of the measurements.

Above all, drilling tools have undercut surfaces whose measurement is impossible, at a glance, without exploiting path-planning techniques [31-33]. On the contrary, the use of translational shifts of the system coordinates of the laser source will overcome this issue without path-planning approaches. In this case, the generated light beam is able to reach all the convex surfaces of the complex target. On the other hand, analytical procedures for the dataset registration on a unique reference system will include distance transformations to compensate for the origin shift. It is clear that, knowing the analytical formulation that enables the dataset registration, the time required by the whole measurement will be reduced, since post-processing steps are no longer required.

After the definition of the processing steps, the fundamental calibration task will be described in order to provide the ways to guarantee the system reliability against noise and decalibrations. The optical setup will be further characterized through the analysis of a calibration specimens, whose properties are completely known. The comparison of estimated parameters and nominal counterparts will be used as a test for the overall accuracy. The last part of this Chapter will be devoted to the discussion of results out of the triangulation scanner developed in cooperation with Speroni SpA [34], manufacturer of tool presetting centers.

2 Methodology

2.1 General Formulation

This Chapter describes how to design an accurate optical sensor for surface inspection. As state previously, the fast and accurate measurement of complex

metal targets, such as drilling tools, can be achieved through the use of a triangulation-based laser scanner. Fig. 1 reports a sketch of the presented setup.

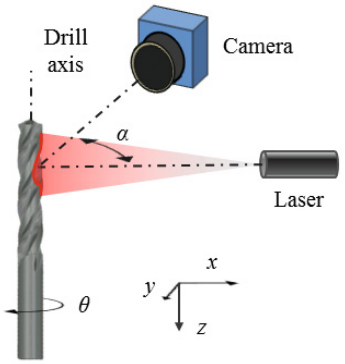

Fig. 1 Schematic view of a triangulation-based laser scanner

Following the principles of triangulation, a laser line impinging of a curved surface is bent in accordance with the target shape. Exploiting the cylindrical symmetry of mechanical tools, the main idea consists of rotating the target around its characteristic axis, and recover the shape exploiting the information brought by a rotary encoder. With reference to the sketch in Fig. 2, at a specific value of rotation angle θ, the laser line is captured by the camera and displayed in the image plane. In this case, the camera axes are labeled to form the couple (I, J). The I-axis has the same direction of the z-axis, whereas the J-axis shows opposite direction with reference to the x-axis. From now on, the pixel distance value Δp between the position of the drill axis in the camera reference system and a generic point extracted from the laser line will be named as *disparity*.

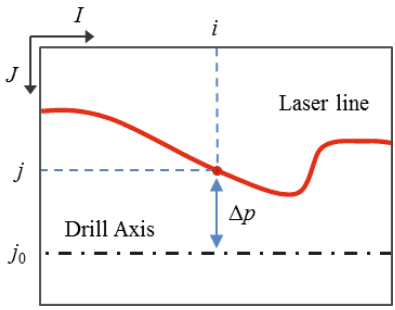

Fig. 2 Image plane with the laser line sampling the profile of the tool

Keeping the main requirement of high resolution, telecentric lenses are the best candidate to assist the laser line projection and its following capture, since they avoid perspective deformations of the profile of the laser line. Moreover, this

optical component can also guarantee the uniformity of the linewidth in the allowed depth of field. Under these hypotheses, the problem of translating disparity in metric units can be solved using the following simple formulation:

$$r = \frac{\Delta p \cdot s_{pxl}}{M \cdot \sin(\alpha)} \tag{1}$$

where r is the radial distance of the laser spot corresponding to the point (i, j) (see Fig. 2), α is the triangulation angle between the laser and camera axes, and s_{pxl} is the pixel pitch of the camera. It is worth noticing that the lens set on the camera permits the formation of an orthographic representation of the target, scaled by the magnification M.

Finally, knowing the radial component r, the corresponding metric coordinates (x, y, z) can be easily expressed as:

$$\begin{aligned} x &= r\cos(\theta) = \frac{\Delta p \cdot s_{pxl}}{M \cdot \sin(\alpha)}\cos(\theta) \\ y &= r\sin(\theta) = \frac{\Delta p \cdot s_{pxl}}{M \cdot \sin(\alpha)}\sin(\theta) \\ z &= \frac{i \cdot s_{pxl}}{M} \end{aligned} \tag{2}$$

Although triangulation laws are very simple, in practice many issues are hidden. The following paragraphs will face these aspects.

2.2 Preservation of System Resolution

The first issue regards the degradation of resolution due to the finite extension of the laser and the camera depths of field. As stated previously, the use of telecentric lenses ensures high resolution, since the laser line is sent and revealed following the principle of the orthographic projection. This guarantees the lack of perspective deformations, but at the same time it dramatically limits the depth of field of the optical device. For instance, commonly available laser sources [35] have maximum depth of field which is nominally close to few hundreds of microns. In other words, the laser line is focused if the maximum range of distances to be evaluated is lower than the nominal depth of field, in practice lower than the 80% of this value.

The shrinkage of the measuring volume has consequences on the exploitable lines of the image plane in a single-shot acquisition. Following Eqn. (1), knowing the maximum range of depths Δr_{max} where the spread of the line does not alter the system resolution, it is possible to derive the maximum disparity value Δp_{max} that can be displayed on the image plane:

$$\Delta p_{max} = \frac{M \cdot \sin(\alpha)}{s_{pxl}} \Delta r_{max} \tag{3}$$

Therefore the laser line has to fall within a bounded range, namely a region of interest, equal to $\left[p_0 - \frac{\Delta p_{max}}{2}, p_0 + \frac{\Delta p_{max}}{2} \right]$, where p_0 express the J-coordinate where the line shows its minimum width, and thus the laser beam is perfectly focused on the target.

Under these conditions, it is easy to observe that the optical probe should follow the profile of the target surface, in order to be always comprised between the image bounds. Then an analytical registration should compensate for the probe shift, thus referring the point dataset to a unique system of coordinates.

This aspect induces the need of an encoded handling of the optical probe along the direction of the x-axis, which corresponds to the J-axis in the image plane. For convenience, it is also useful to settle the origin of the encoder axis on the drill axis, which in turns is displayed in the image plane in the j_0 position: when the laser line is focused on the drill axis, the encoder returns the zero value, whereas the position of the line in the image plane is j_0.

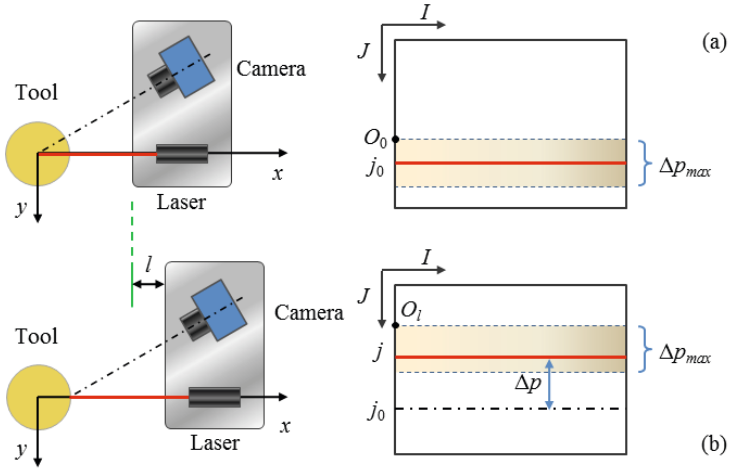

Fig. 3 Scheme for the evaluation of the reference system with a finite-sized region of interest flowing through the image plane

With reference to Fig. 3, for the sake of simplicity, it is possible to consider a single image plane with a scrolling region of interest flowing through it. The position of the region of interest, whose height is equal to Δp_{max}, is described by the coordinate O of its northwest corner.

When the optical probe is arranged to focus the light on the drill axis (Fig. 3.a), the revealed line lies on the j_0 line, which corresponds to the vertical coordinate $O_0 + \frac{\Delta p_{max}}{2}$. Since the origin of the region of interest is determined by reading the encoder output, whose value is equal to zero, the coordinate j_0 can be finally expressed as:

$$j_0 = \frac{\Delta p_{max}}{2} = \frac{M \cdot \sin(\alpha)}{2 s_{pxl}} \Delta r_{max} \tag{4}$$

On the other hand, when the target surface has to be scanned, the optical probe should be consequently shifted back by l (Fig. 3.b), enabling the observation of the laser line within the bounds of the region of interest. Here the line is detected at a generic vertical coordinate j in the system of reference defined by O_l. The shift between the two reference systems can be derived easily following Eqn. (1):

$$O_l - O_0 = \frac{M \cdot \sin(\alpha)}{s_{pxl}} \cdot l \tag{5}$$

and consequently:

$$\Delta p = (O_0 + j_0) - (O_l + j) = \frac{M \cdot \sin(\alpha)}{s_{pxl}} \left(\frac{\Delta r_{max}}{2} - l \right) - j \tag{6}$$

In this way the expression of Δp is linked to the term j by means of a transformation mediated by the value l, output of the micrometric encoder that assists the probe handling.

A complete acquisition of the target under analysis can be obtained in several rounds of the tool, but changing the optical probe position: the probe has to approach the target from the outer regions to the inner ones, by steps defined by the depth of field of the optical components.

It is worth noting that all formulations start from the assumption that it is possible to place the origin of the encoder reference onto the drill axis. This condition can be achieved using a calibrated target with known shape. When the laser line is focused on the target surface, and thus revealed in the center of the region of interest, it is possible to extract the position of the probe by reading the encoder. Then the position of the drill axis can be extracted by subtracting the radius of the target from the value returned by the encoder.

2.3 Occlusion Recovery

As already observed in the previous Paragraphs, when the laser light is not able to reach the target surface, or equivalently the field of view of the camera is occluded by an obstacle, measurements are not available. This condition constitutes a drawback in many cases, but is always present when drilling tools are scanned.

Problems belonging to the family of occlusions can be avoided by changing the position of the optical probe, getting new data and registering those points on the previous reference system. If rigid translations of the laser scanner are superimposed and the target is scanned following straight trajectories, registering is a fairly simple problem. In this case, the pose of the novel system coordinates and the transformation laws describing the target movement can be directly inverted, without any further consideration.

In the case of rotating targets, the problem is more complex. With reference to Fig. 4, a generic point P is occluded to the laser and thus would never be reached without changing the reference system of the optical probe. Here, a rigid translation t of the probe along the y-axis allows the laser for the achievement of the same point, now P', at a different angle θ.

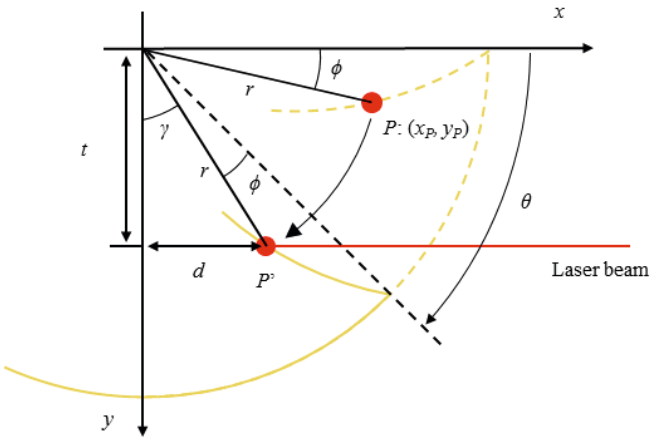

Fig. 4 Schematic view of a tool section (gold contours) in the xy-plane. The laser is shifted by t along the y-axis in order to reach self-occluded regions.

It is clear that the result of the measurement is the distance d, computed between the laser spot on the target surface and the y-axis. This result is not directly linked to the actual coordinates (x_P, y_P) in the world system of reference centered in the origin of the x and y axes.

The link between the two points P and P' is mediated by the radial distance r, whose value is constant and equal to:

$$r = \frac{d}{\sin(\gamma)} \tag{7}$$

where the angle γ is easily:

$$\gamma = \arctan\left(\frac{d}{t}\right) \tag{8}$$

Knowing the entity of the shift t and the value of the angle ϕ, equal to $\frac{\pi}{2} - \theta - \gamma$, the coordinates of the point P are:

$$\begin{aligned} x_P &= \frac{\sin(\gamma+\theta)}{\sin(\gamma)} d \\ y_P &= \frac{\cos(\gamma+\theta)}{\sin(\gamma)} d \end{aligned} \tag{9}$$

being d derived by means of Eqn. (1), where d replaces r, and Eqn. (6).

As seen for the l value, the choice of the shift term t is derived by the shape and the size of the tool under testing. In principles, only two values of t, roughly $t_0 = 0$ and $t_1 \approx r_{tool}/2$, where r_{tool} is the tool radius, are enough to overcome self-occlusions. Nevertheless, more observations of the object can to be performed at intermediate values of t in order to get more data in the point cloud.

2.4 *Laser Point Extraction*

The next issue in the design of the measuring system regards the choice of the algorithm for the extraction of points from the laser line. As mentioned before, when the line is revealed on the image plane, it is mandatory to extract the position of its maxima with sub-pixel precision. In this way it is possible to increase the resolution, since the line processing is able to reduce the physical pitch of the pixels of the camera by reconstructing mathematically the profile of the laser. Equivalently, by looking at Fig. 5, it appears clear how reconstruct the laser profile can improve the resolution. Without any *a priori* consideration, disparity is deduced exploiting the integer pixel position corresponding to the maximum intensity revealed on the image. On the contrary, when the profile of the laser beam is recovered, it is possible to get those decimals that allow the perfect extraction of the laser peak, as it is impinging on a continuum of infinitesimal-sized pixels.

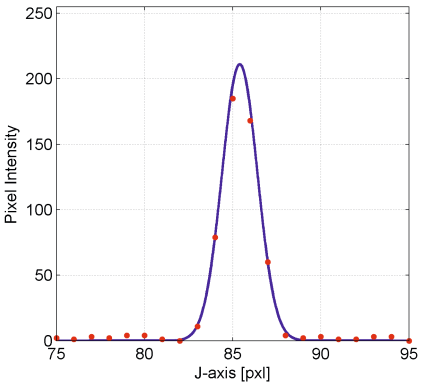

Fig. 5 Example of laser profile reconstructed to increase the resolution of the system

Many extractors have been presented so far [36]. The simplest peak detector is the Center of Mass of order n (CoM_n). If n values of the line are detected scanning the image plane columnwise, thus giving the couples (x_i, p_i), with $i = 1, \ldots, n$, the peak is estimated at position j:

$$j = \frac{\sum_{i=1}^{n} p_i x_i}{\sum_{i=1}^{n} p_i} \tag{10}$$

At the same time, parabolic extractors can be implemented. In this case, the peak is identified in $j = x_m + \delta$, where δ is the decimal part of the subpixel position of the peak and $x_m = \max\{x_i\}$. Appling the Taylor series, the term δ can be defined as:

$$\delta = -\frac{f'(x)}{f''(x)} \tag{11}$$

where $f'(x)$ and $f''(x)$ represent the first and second discrete derivatives of the input function made by the couples (x_i, p_i).

Eqns. (10) and (11) are two examples of peak detectors suitable to achieve good results when information on the profile of the projected laser line are not available. On the contrary, when the optical probe implements a laser source aided by telecentric lenses, the generated pattern follows a Gaussian profile, similar to that one reported in Fig. 5. In this case it is more appropriate to select a problem-driven extractor, namely the Gaussian approximator.

Exploiting the knowledge of the physical shape of the emitted laser line, the Gaussian approximator names the peak position as the expected value E[x] of the Gaussian distribution that fits the laser profile in the least squares (LS) sense. The problem can be linearized in order to get an efficient solution: first the laser intensities are converted in logarithms through the use of a look-up table, and then the Vandermonde matrix is constructed to obtain the LS solution of the overdetermined linear system. The linearization of the problem preserves the time efficiency of the extractor, which can work real-time during the same acquisition.

This method gives clear advantages against the noise contributions in comparison with the previous ones, as it does not make use of the exact pixel intensities, but takes into account the overall information carried by them. Furthermore, the standard deviation σ of the reconstructed Gaussian distributions can be used as a quality index of the estimation. For instance, this value can be limited by a threshold, with the aim of deleting those peaks whose corresponding widths are higher than an expected value. By this way, ambiguous estimations are completely removed preventing the increase of the measurement uncertainty.

3 Experimental Understanding

The formulations brought in the previous Section are useful to understand the mathematics that governs the measurement processes. However, this information is not sufficient to develop the actual experimental setups. The main issues of bridging theory into practice will be faced and solved in the following Paragraphs.

3.1 Choice of the Optical Components

The optical probe is made of three elements: the laser source, the high-resolution camera and its lens.

Following the principles described before, the laser source affects the system performance, specifically the lower its width, the higher the resolution, since small depth differences can be solved as small disparity changes. On the other hand, the projected line should have a Gaussian profile able to cover more than three pixels along the *J*-axis in order to enable the peak estimation. These two conditions fix the specification for the laser choice.

For example, the Lasiris TMFL-55 telecentric laser emitter [35] is one of the best candidate to play this role. It shows a constant thickness of the generated line equal to 9 μm ($1/e^2$ estimation) at its working distance of 55 *mm*, over a length of 10 *mm*. Moreover it shows an operative wavelength of 660 *nm*, whereas its depth of field, equal to 200 μm, determines the maximum height of the region of interest extracted from the camera plane (see Δr_{max} in Eqn. (3)), where the nominal resolution is preserved.

On the other hand, the system performances are determined by the optical receiver made by the set of camera and lens. This block defines the pixel pitch and the magnification, whose ratio directly affects the minimum detectable change of disparity that can be resolved on the image plane. It follows that this ratio has to be kept as low as possible, so as best conditions for the measurement resolution can be achieved. Consequently, the camera has to guarantee:

- high resolution: the sensor size has to be close to 5 Megapixels to acquire the laser line on its whole length;
- small pixel pitch: approximately of few microns, better close to 2 μm to guarantee a consistent sampling of the laser line;
- fast frame rate: requirements set the maximum frame rate to at least 15 *fps*, which leads to more than 50 *fps* in the acquisition of the region of interest;
- simple transmission interface: it is more convenient to use one of the standard of transmission developed for industrial camera (GigE Vision, Camera Link, USB, etc.).

With regards to the choice of the lens, it has to ensure:

- high magnification: the lens has to magnify (or reduce) the laser line to fit on the horizontal size of the camera plane;
- suitable depth of field: this parameter has to be higher than the one of the laser, so that the extension of the region of interest is merely defined by the optical emitter and not altered by the receiver;
- image format: the lens has to be selected with reference to the sensor size of the corresponding camera.

As an example, the set of components for the optical receiver can fall on the IDS-uEye camera (Model name: USB3-UI-3480CP-M [37]) and the Lensation TC5M-10-110i telecentric lens [38].

The last parameter to be set for completing the actual design of the experimental setup is the triangulation angle α, comprised between the laser and camera optical axes (see Fig. 1). As the triangulation angle impacts the resolution following Eqn. (1), it is clear that its sine has to be as high as possible. However, the increase of this angle has effects on the raising of severe occlusions, since small changes of depth can hide the laser spot to the camera. A good balance can be obtained by setting the angle close to $\pi/4$, which returns an overall transformation coefficient from disparity to metric units of about 3.5 μm, for the proposed devices.

3.2 Calibration Steps

Systematic errors represent the first source of degradation for any measurement. All devices have to be calibrated before their use in order to derive the measurement parameters that can transduce the subject of inspection into meaningful correlated entities. Furthermore, the mechanical consistency of the setup has to be kept in mind as a mandatory condition to be preserved.

In the case of 3D reconstruction of small objects, the validation and calibration steps are the basis for a successful inspection. An example of experimental setup, with micrometric handlings supporting the optical probe, is reported in Fig. 6.

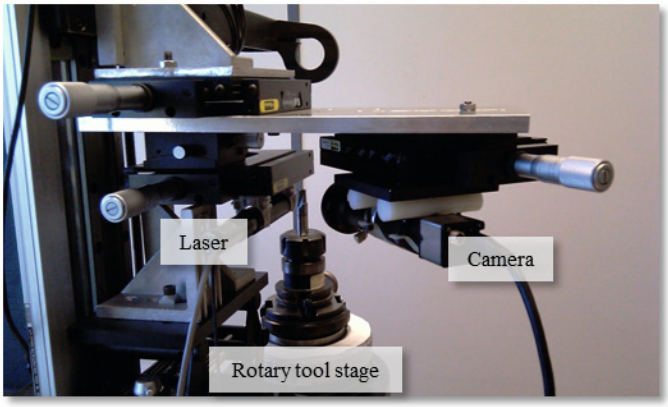

Fig. 6 Picture of an experimental setup for 3D reconstruction of tools. Slits and goniometers allow the calibration phase before the actual acquisition of the target. All handlings of the probe are numerically managed via an external controller.

The whole set of translational and rotational stages, together with the use of a calibrated specimen, namely a cylindrical tool with known radius r_c, is enough to guarantee the reliability of the laser scanner when the following steps are checked:

i. Camera orientation: Switching the laser off and increasing the time exposure of the camera, the optical receiver is oriented until the detected edge of the calibration tool is perfectly horizontal, parallel to the *I*-axis of the camera plane;
ii. Laser position: The laser is roughly pointed on the tool surface and fed with a suitable current. Decreasing the camera exposure time, the emitter is oriented until the revealed line is displayed parallel to the *I*-axis. Then the laser is shifted along the *y*-axis in the world coordinates in order to be aligned with the tool axis. This task can be achieved by looking at the horizontal position of the line (along the *J*-axis), until it reaches its maximum value;
iii. Focusing of laser and camera: Both devices are shifted along the direction defined by their characteristic axes with the aim of reaching the minimum laser linewidth, close to its nominal value;
iv. Choice of the injection current: The laser is fed with different levels of injection current, finding the condition that allows the reduction of light scattering from the tool surface and the preservation of image saturation;
v. Estimation of the triangulation angle α: Exploiting the relationship in Eqn. (1), the value of α can be determined by means of a simple inverse fit of parameters, exploiting the encoded handling of the probe. Collecting data from the encoder and estimating the line position in the image plane, an overdetermined linear system can be solved in the LS sense to find the expression of $\sin(\alpha)$.

All these processes, in conjunction with the calibration of the position of the drill axis, permit the unique definition of a stable setup, able to minimize systematic errors.

4 Results

Once triangulation laws are deeply understood and calibration steps are followed for the definition of reliable setups, it is possible to verify results through the inspection of known targets and generic tools. The next subsections will deal with the analysis of results, thus giving the assessment of system performances.

4.1 Setup Validation

The first test consists of validating the measurement system through the analysis of a calibrated specimen with known sizes. For this purpose, a standard ceramic probe sphere, with diameter equal to 18 *mm*, has been used. It is worth noting that a robust validation needs a proper location of the calibration sphere within its seat. The alignment of the center of the sphere around the rotation axis can be obtained by using a high-precision mechanical comparator, able to reduce the maximum

error to about 2 μm. Fig. 7 highlights the results of the measurement, reporting both the point cloud data and the corresponding surface mesh, made of triangular elementary surfaces. In this case, results are related to the analysis of a ring extracted from the spherical specimen, whose height is equal to 6 *mm*. This region corresponds to the maximum field of view reachable along the *z*-direction, in a single scan of the ceramic sphere.

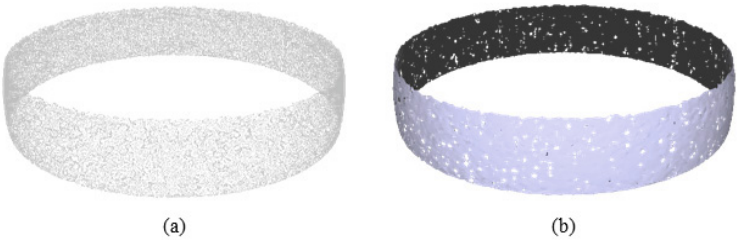

Fig. 7 (a) Point cloud (79669 vertices) and (b) reconstructed surfaces (156135 elementary triangles) of the calibration sphere

The inspection of the point cloud proves the agreement of results in comparison with the nominal value of the radius. In particular, the estimated radius of the ceramic sphere is equal to 8.994 *mm*, with a consequent absolute error in depth estimation of 6 μm.

4.2 Tool Inspection

The proposed acquisition scheme can be set to measure any tool. The first case of study regards the analysis of a defective thread mill with radius equal to 5 *mm*. With reference to Fig. 8(a), the tool has a defective lip, which downs its quality and thus precludes its use in any manufacturing process. As a matter of fact, the identification and characterization of the surface defect represents the most important requirement in the context of quality control. In this case, the qualitative insight of Fig. 8(b) clearly attests the capability of the system to get back dense datasets that allow the efficient and complete evaluation of the tool wear.

From a quantitative point of view, results have been collected on a simple surface model in order to derive the amplitude of the ~99% confidence interval. As a consequence, the estimated mean noise value has been found equal to 8.976 μm.

Fig. 9 reports the case of study of a twist drilling bit covered by a film of titanium nitride, where regions highlighted in red are the reconstructed undercut surfaces. The inspection of the tool has been performed spanning the t value of the y-shift of the optical probe in the range between 0 and 2 *mm*, by steps of 1 *mm*. On the other hand, longitudinal shifts l are made between 0 and 3 *mm* by steps of 175 μm, i.e. the effective exploitable depth of field of the telecentric laser.

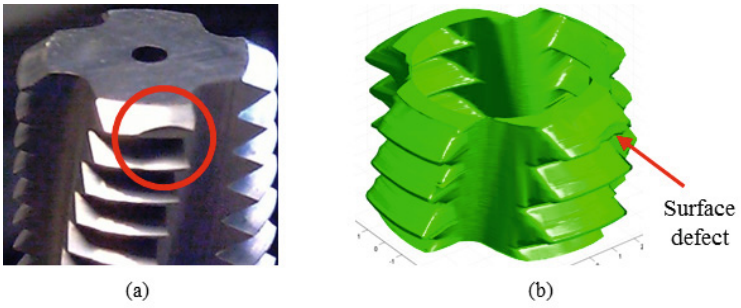

Fig. 8 (a) Picture of a generic defective tool and (b) corresponding reconstructed surface made of 691042 elementary triangles

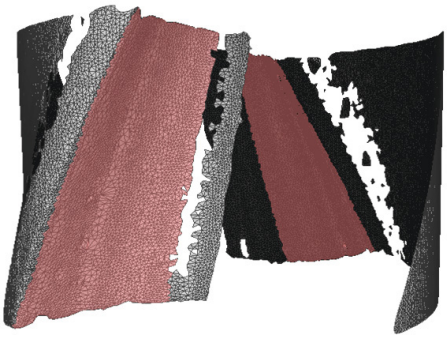

Fig. 9 Example of occluded surfaces out of the inspection of a twist drilling bit

In this case, the total number of revolutions needed to complete the acquisition of the tool under analysis is equal to 51 (17 spans of l by 3 values of t), and consequently the overall measurement time is close to 600 s. This result comes out by the camera frame rate, which is equal to 30 *fps*, and the angular resolution, assumed equal to 1 degree by specification. This leads to a measurement time for a single revolution of the tool of about 12 s, and thus to the overall time defined previously.

It is important to underline that image processing, i.e. the extraction of the laser peaks from the revealed line, does not delay in the inspection of the tool. In other words, the time requirement can be downed significantly by means of faster cameras with higher frame rate, which is the only term that limits the measurement efficiency.

Finally, further examples of different-shaped tools are reported in Fig. 10, with the aim of showing the capability of the developed laser scanner to inspect both the tips and the inner occluded regions of complex targets, with multiple constitutive media, including High Speed Steel (HSS) and cobalt steel alloys. Furthermore, all datasets have size higher than 10^6 vertices.

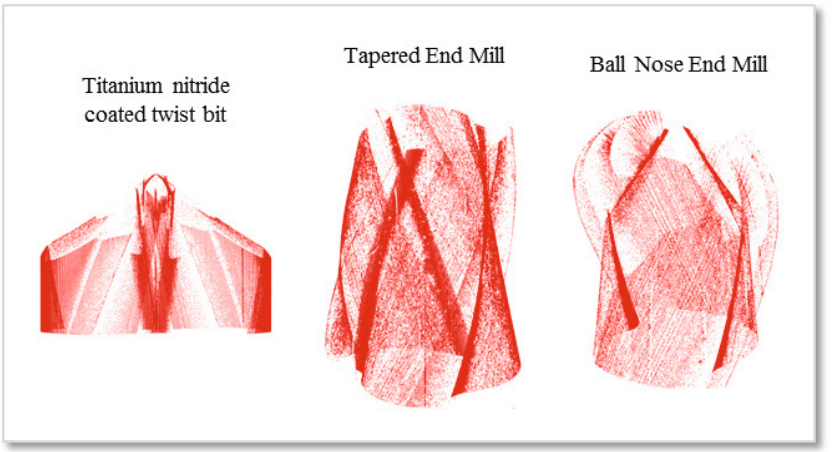

Fig. 10 Further examples of datasets extracted from several tools with different shapes

5 Conclusions

This Chapter has described the steps for the correct design of a triangulation-based laser scanner, able to reconstruct three-dimensionally the shape of complex objects.

Starting from the description of triangulation laws, this Chapter has faced problems regarding the finite extension of the depth of field of the optical components, the presence of unavoidable occlusions of undercut regions, and the efficient extraction of intensity peaks from the detected laser line. The problem has been focused on the deep inspection of drilling tools, whose shape makes challenging the exhaustive reconstruction of the constitutive surfaces. Optical components have been chosen in accordance to the initial specification of system resolution, here set to 15 μm, i.e. close to the diffraction limit at the laser wavelength. Finally, calibration steps have been briefly described with the aim of ensuring the system reliability against noise contributions and setup decalibrations.

Experiments have been run for the analysis of a calibrated specimen, namely a ceramic probe sphere, with results proving the accuracy of the proposed setup in finding its radius, which is equal to 9 mm. Specifically, the estimated radius differs by 6 μm from the nominal value. Further experiments on common drilling tools have shed light on the possibility of reconstructing undercut surfaces with the proposed optical probe. Additionally, the analysis of outcomes has proved the reduction of the measurement time below the limit of few minutes, preserving the resolution and the size of the datasets, made of more than 10^6 vertices.

Acknowledgements. This work is within the ISSIA-CNR Project "CAR-SLIDE: Sistema di Monitoraggio e Mappatura di Eventi Franosi" (Ref. Miur PON 01_00536). A great contribution for the mechanical implementation of the system had been done by the industrial partner Speroni SpA - Via Po, 2 - 27010 Spessa (PV) Italy. The Authors would thank Giuseppe Roselli for his role in the development of the system, and Professor Giovanni Moroni and Assistant Professor Stefano Petrò (Department of Mechanical Engineering - Polytechnic of Milano). Finally, the Authors would like to thank Mr. Michele Attolico and Mr. Arturo Argentieri for their technical support in the preparation of the experimental setup.

References

[1] Milroy, M.J., Weir, D.J., Bradley, C., Vickers, G.W.: Reverse engineering employing a 3D laser scanner: A case study. The International Journal of Advanced Manufacturing Technology 12(2), 111–121 (1996)

[2] Son, S., Park, H., Lee, K.H.: Automated laser scanning system for reverse engineering and inspection. International Journal of Machine Tools & Manufacture 42, 889–897 (2002)

[3] Aung, S.C., Ngim, R.C.K., Lee, S.T.: Evaluation of the laser scanner as a surface measuring tool and its accuracy compared with direct facial anthropometric measurements. British Journal of Plastic Surgery 48(8), 551–558 (1995)

[4] Kau, C.H., Richmond, S., Zhurovc, A.I., Knox, J., Chestnutt, I., Hartles, F., Playle, R.: Reliability of measuring facial morphology with a 3-dimensional laser scanning system. American Journal of Orthodontics and Dentofacial Orthopedics 128(4), 424–430 (2005)

[5] Marino, F., De Ruvo, P., De Ruvo, G., Nitti, M., Stella, E.: HiPER 3-D: An Omnidirectional Sensor for High Precision Environmental 3-D Reconstruction. IEEE Transaction on Industrial Electronics 59(1), 579–591 (2012)

[6] Levoy, M., Pulli, K., Curless, B., Rusinkiewicz, S., Koller, D., Pereira, L., Ginzton, M., Anderson, S., Davis, J., Ginsberg, J., Shade, J., Fulk, D.: The Digital Michelangelo Project: 3D Scanning of Large Statues. In: Proceedings of the 27th Annual Conference on Computer Graphics and Interactive Techniques, pp. 131–144 (2000)

[7] Kampel, M., Sablatnig, R.: Rule based system for archaeological pottery classification. Pattern Recognition Letters 28(6), 740–747 (2007)

[8] Sansoni, G., Trebeschi, M., Docchio, F.: State-of-The-Art and Applications of 3D Imaging Sensors in Industry, Cultural Heritage, Medicine, and Criminal Investigation. Sensors 9, 568–601 (2009)

[9] Zhang, G., Veale, R., Charlton, T., Borchardt, B., Hocken, R.: Error Compensation of Coordinate Measuring Machines. CIRP Annals - Manufacturing Technology 34(1), 445–448 (1985)

[10] Donmez, M.A., Blomquist, D.S., Hocken, R.J., Liu, C.R., Barash, M.M.: A general methodology for machine tool accuracy enhancement by error compensation. Precision Engineering 8(4), 187–196 (1986)

[11] Teeuwsen, J.W.M.C., Soons, J.A., Schellekens, P.H.J., van der Wolf, A.C.H.: A General Method for Error Description of CMMs Using Polynomial Fitting Procedures. CIRP Annals - Manufacturing Technology 38(1), 505–510 (1989)

[12] Cheng, W.L., Menq, C.H.: Integrated laser/CMM system for the dimensional inspection of objects made of soft material. The International Journal of Advanced Manufacturing Technology 10(1), 36–45 (1995)
[13] Schwenke, H., Wäldele, F., Weiskirch, C., Kunzmann, H.: Opto-tactile Sensor for 2D and 3D Measurement of Small Structures on Coordinate Measuring Machines. CIRP Annals - Manufacturing Technology 50(1), 361–364 (2001)
[14] Lopez-Escogido, D., De Luca, A.: 2-D High Precision Laser for Detecting Small Defects in PCBs. In: 9th International Conference on Electrical Engineering, Computing Science and Automatic Control (CCE), pp. 1–6 (2012)
[15] Ke, X., Chaolin, Y.: On-Line Defect Detection Algorithms for Surface Inspection of Hot Rolled Strips. In: International Conference on Mechanic Automation and Control Engineering (MACE), pp. 2350–2353 (2010)
[16] Qun, Z., Wenbo, H., Chenghao, J., Yutong, J., Jinhua, Y.: Studies on Portable 3D Laser Scanner for Surface Flaws. In: Second International Conference on Instrumentation & Measurement, Computer, Communication and Control, pp. 1297–1299 (2012)
[17] Zhang, L., Zhao, M., Zou, Y., Gao, S.: A New Surface Inspection Method of TWBS Based on Active Laser-triangulation. In: Proceedings of the 7th World Congress on Intelligent Control and Automation, pp. 1174–1179 (2008)
[18] Zhou, A., Guo, J., Shao, W.: Automated Detection of Surface Defects on Sphere Parts Using Laser and CDD Measurements. In: IECON 2011 - 37th Annual Conference on IEEE Industrial Electronics Society, pp. 2666–2671 (2011)
[19] Kowal, J., Sioma, A.: Surface defects detection using a 3D vision system. In: 13th International Carpathian Control Conference (ICCC), pp. 382–387 (2012)
[20] International Organization for Standardization, ISO 3685 Tool-life testing with single-point turning tools (1993)
[21] UNI, UNI ISO 8688-1/2 (1998)
[22] Dutta, S., Pal, S.K., Mukhopadhyay, S., Sen, R.: Application of digital image processing in tool condition monitoring: A review. CIRP Journal of Manufacturing Science and Technology 6(3), 212–232 (2013)
[23] Su, J., Huang, C., Tarng, Y.: An automated flank wear measurement of microdrills using machine vision. Journal of Materials Processing Technology 180, 328–335 (2006)
[24] Duan, G., Chen, Y.-W., Sukegawa, T.: Automatic optical flank wear measurement of microdrills using level set for cutting plane segmentation. Machine Vision and Applications 21, 667–676 (2010)
[25] Malekian, M., Park, S.S., Jun, M.B.: Tool wear monitoring of micro-milling operations. Journal of Materials Processing Technology 209(10), 4903–4914 (2009)
[26] Tansel, I., Arkan, T., Bao, W., Mahendrakar, N., Shisler, B., Smith, D., McCool, M.: Tool wear estimation in micro-machining: Part I. International Journal of Machine Tools and Manufacture 40, 599–608 (2000)
[27] Tansel, I., Arkan, T., Bao, W., Mahendrakar, N., Shisler, B., Smith, D., McCool, M.: Tool wear estimation in micro-machining: Part II. International Journal of Machine Tools and Manufacture 40, 609–620 (2000)
[28] Jemielniak, K., Arrazola, P.J.: Application of AE and cutting force signals in tool condition monitoring in micro-milling. CIRP Journal of Manufacturing Science and Technology 1, 97–102 (2008)

[29] Zhu, K., Wong, Y.S., Hong, G.S.: Multi-category micro-milling tool wear monitoring with continuous hidden markov models. Mechanical Systems and Signal Processing 23(2), 547–560 (2009)
[30] Ng, W., Moon, K.S., et al.: Measurement of 3-d tool wear based on focus error and micro-coordinate measuring system. In: Proceedings of 16th Annual Meeting of American Society for Precision Engineering (ASPE), Virginia, USA (2001)
[31] Xi, F., Shu, C.: CAD-based path planning for 3-D line laser scanning. Computer-Aided Design 31(7), 473–479 (1999)
[32] Mahmud, M., Joannic, D., Roy, M., Isheil, A., Fontaine, J.F.: 3D part inspection path planning of a laser scanner with control on the uncertainty. Computer-Aided Design 43, 345–355 (2011)
[33] Zhao, H., Kruth, J.P., Van Gestel, N., Boeckmans, B.: Philip Bleys, Automated dimensional inspection planning using the combination of laser scanner and tactile probe. Measurement 45(5), 1057–1066 (2012)
[34] http://www.speronispa.com
[35] http://www.coherent.com/downloads/TMFL_DS_0410.pdf
[36] Naidu, D.K., Fisher, R.B.: A Comparative Analysis of Algorithms for Determining the Peak Position of a Stripe to Sub-pixel Accuracy. In: British Machine Vision Association Conference (BMVC), pp. 217–225 (1991)
[37] http://en.ids-imaging.com/IDS/spec_pdf.php?sku=AB00043
[38] http://www.lensation.de/downloads/LS_CAT_2013.pdf

On the Use of Light Sensors and Pattern Recognition Techniques for Automated Detection of Street Lighting Lamps

G.M. Soares[1], A.G.B. Almeida[1], R.M. Mendes[1], E.C. Teixeira[1], H.A.C. Braga[1,*], M.N. Machado[2], R.S. Broetto[2], M.V.H.B. Castro[2], H.O. Gomes Filho[2], F.M. Varejão[2], J.G. Pereira Filho[2], A.B. Candeia[3], and R.A.A. Sousa[3]

[1] Modern Lighting Research Group (NIMO), Universidade Federal de Juiz de Fora, Juiz de Fora, Brazil
[2] Universidade Federal do Espírito Santo, Vitória – ES, Brazil
[3] EDP (Escelsa and Bandeirante), Vitória – ES; Mogi das Cruzes – SP, Brazil
henrique.braga@ufjf.edu.br

Abstract. The misinformation between the actual public lighting equipment and those reported by municipalities to the electricity companies may result in a kind of loss mainly referred as commercial loss. The usual adopted procedure to minimize this problem is sending technician teams to the field to do a low effective inspection of the lighting points. This scenario motivated the development of the methodology described in this chapter. The approach comprises both hardware and software elements, and were developed to give electricity companies more precise information about the actual luminaries and bulbs installed on the lighting poles, with a high degree of automation. The hardware is composed mainly by a set of light sensors, managed by a digital signal processor. The selection of the sensors and the overall hardware architecture are described, as well as the issues associated to the communication between the data acquisition module and an external CPU unit with data storage and user interface attributes. In sequence, the data mining techniques and pattern recognition strategies are discussed. In order to establish the elements for the required training and validation procedures, a laboratory environment was developed to reproduce some on-the-field configurations. The results of the laboratory experiments and field tests are analyzed and discussed. These results conducted to the development of the software components that integrate the system.

Keywords: public lighting, commercial losses, light sensors, pattern recognition, data acquisition system, classifier.

* Corresponding author.

A. Mason et al. (eds.), *Sensing Technology: Current Status and Future Trends III*,
Smart Sensors, Measurement and Instrumentation 11, DOI: 10.1007/978-3-319-10948-0_4

1 Introduction

Public and street lighting are essential services for modern life, being directly related to people safety, emblazonment of urban areas, enhancement of public spaces, increment of trading activities and incentive to night tourism, among other benefits.

Until very recently, public lighting fixtures installation and maintenance were of responsibility of electricity companies in Brazil. However, due to current government regulations, those tasks are being delegated to municipalities, although the energy billing process is still issued by electricity distribution companies. Under this scenario, it is not rare to see the municipalities installing new lighting circuits or making changes in old ones without properly reporting it to the energy companies. This misinformation may result in a kind of loss mainly referred as commercial loss, being of major concern to regulatory agencies and electricity companies, which may face serious economic, technical and efficiency impairments [1], [2].

To minimize this problem, companies carry out inspection services by sending technician teams to the field to see if there is a need to perform updates to their public lighting database. Hence, the inspection team visits the public areas and streets to identify the existence of new lighting points as well as their main characteristics, such as the global positioning, adopted lighting technology and power wattage of bulbs. Since this task is not of trivial execution, it is necessary in most cases that the personnel climbs the pole (with the aid of appropriate stairs or by means of bucked boom trucks) and visually retrieve the required information. It is a slow and expensive service, with a doubtful effectiveness. Moreover, depending on the qualifications of the inspection team (staff or outsourced), the service cannot be trusted. In very common cases it can be observed that the technicians avoid the *in loco* inspection (for being a delicate and time-consuming procedure) and prefer to inform an approximate condition that result in mistaken data, leaving out new lighting points (e. g. network extensions).

Currently, public lighting in Brazil employs about nine different models of lamps. The two most common employed technologies are mercury vapor and high-pressure sodium, which can be found in over 30% and 60% of locations of the country, respectively (see Table 1). It is also observed that several lighting patterns can co-exist, combining the design of the luminaires, the different lamp rated powers and the various types of public roads, making the job of automatic identification of a given installation even more complex.

The conditions described here motivated the development of a computational methodology (incorporating elements of software and hardware) to determine, with a high degree of automation, the type and power of the lamps installed in the lighting poles. Assuming objective and reliable approaches it could be expected a fast update of the energy company public lighting registers, allowing the estimation of the losses caused by the lack of consumption information. It is interesting to observe that the proposal of an electronic equipment to minimize commercial losses was the object of previous studies, such as the one published in [3].

Therefore, this chapter describes the developed methodology and its main features. Besides this Introduction, the text is organized as follows: Section 2 presents the system architecture principles and the hardware overview. A brief description on spectrum signature detection is presented in Section 3. Section 4 discusses the pattern recognition techniques employed to identify the luminaires. A laboratory apparatus, built in order to do the first experiments, is described in Section 5. Section 6 details several experimental results, either from laboratory tests or from actual street incursions. In Section 7, the developed software systems are described. Finally, the main conclusions are presented in Section 8.

Part of this work was recently published in [4].

2 System Architecture

The hardware that composes the system can be described as an electronic equipment that could be installed over a vehicle and is capable of acquiring lighting information of the environment (Fig. 1). All the electronics are embedded into a case, which is designed to provide the proper accommodation for all the electronic modules. The case offers the necessary mechanical strength, protection against ambient humidity or dust and, specially, avoids the influence of other (neighbor) light sources, i.e., those who are not under evaluation at that time.

Table 1 Distribution of Lamp Technologies, as Employed by the Brazilian Public Lighting Systems (Base Year: 2008)

Lamp Type	Percentage Use
Sodium (HPS)	62.93%
Mercury Vapor (MV)	31.84%
Mixed (Mercury-Tungsten)	2.22%
Incandescent	1.42%
Fluorescent	0.81%
Metal Halide (MH)	0.73%
Other	0.03%

The vehicle should be positioned right below the luminaire under study, with the aid of the vehicle driver, which is helped by a number of light sensors arranged in order to provide the information about the best positioning of the equipment.

The lamp location is given immediately by a GPS device that integrates the system. Due to the nature of acquired data and processing procedures, the system does not provide immediate information about lamp type and power. However, the amount of data is stored in a bulky memory and is processed offline later. Those post-processing routines are able to deduce, finally, the lamp type and power. Associated with the GPS data and a picture of the luminaire (taken by a digital

camera that compose the equipment), the information about the poles of the evaluated area are given by the system with good reliability.

2.1 Data Acquisition Equipment Overview

The hardware that constitutes the overall system consists of electronic sensors, which are capable of gathering different information about the illumination equipment under evaluation. Fig. 2 depicts the main equipment architecture, which was devised to constitute the main database as required to feed the computational system.

The main data acquisition devices are a set of low cost, off-the-shelf, analog and digital light sensors, with different spectral responses. Besides those main light sensors, other transducers have been adopted, such as the positioning sensors (light sensors that inform the operator if the car is right below the luminaire), an accelerometer (that computes the slope of the ground) and a global positioning system (GPS) device that gives the pole geographical localization.

All sensors are managed by a digital signal processor (DSP), which collects their information and sends them via Bluetooth protocol to an external data storage system allocated inside the vehicle, such as a tablet computer. A digital camera,

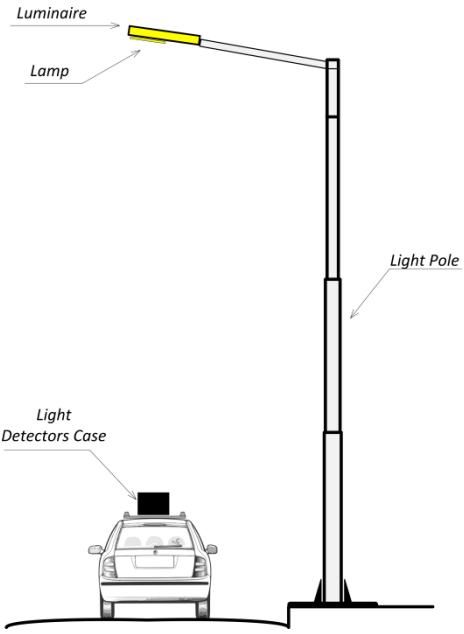

Fig. 1 Vertical cut view of a typical acquisition scene including transportation vehicle, device case and street lighting equipment

which is currently used to provide additional positioning information, completes the system. The camera is placed inside the system case as well as the main board.

A picture of the main printed circuit board is shown in Fig. 3 (top and bottom view). The top face just houses the light sensors and second layer tracks. The bottom of the board holds the DSP device, the GPS unit and the Bluetooth chip, as well as the analog conditioning circuits. The design of the board and case was conceived in order to prevent undesired reflections of the incident luminous radiation over the sensors.

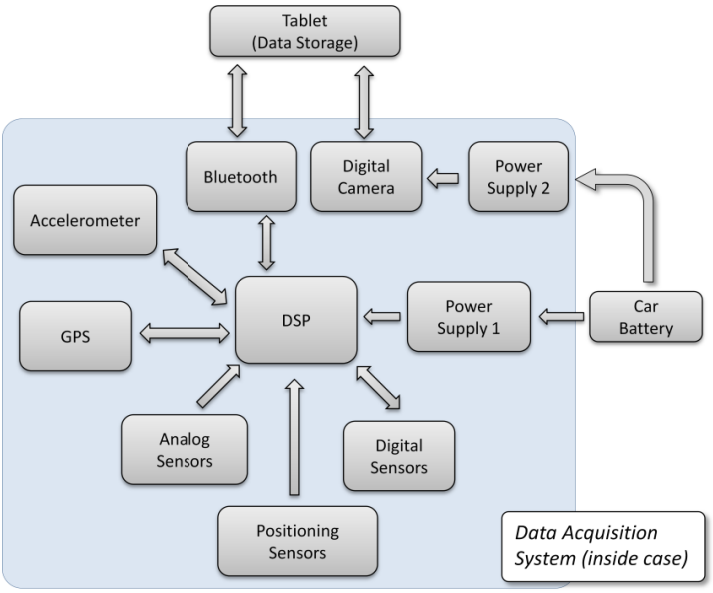

Fig. 2 Data acquisition equipment architecture

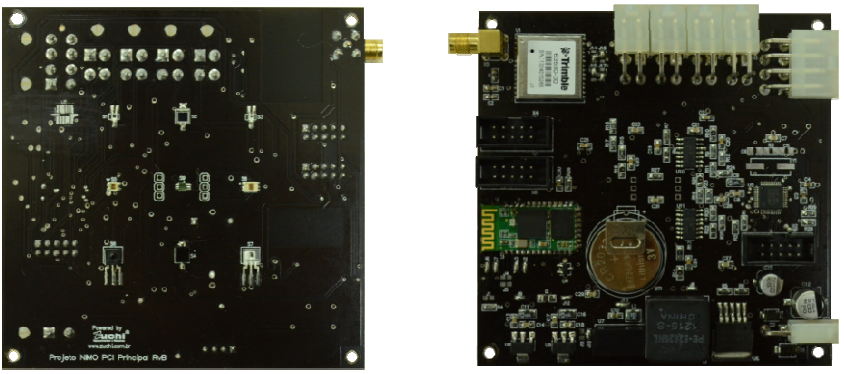

(a) (b)

Fig. 3 A picture of the implemented electronic board: (a) Top face: light sensors; (b) Bottom layer: main modules and analog conditioning circuits

3 Spectrum Signature Detection

In association to the electricity company that supported this study, EDP – Energias de Portugal, it was decided to focus the study on three main lamp technologies being used at the cities under its management: mercury vapor (MV), high-pressure sodium (HPS) and metal halide (MH).

In order to analyze the spectrum of the radiation emitted by these lamps, radiometric measurements were done in an integrating sphere. The results of this evaluation are shown in Fig. 4. Note that the radiation emitted by each lamp is composed by different spectral lines, yielding a spectrum signature, which depends on its chemical composition [5].

Therefore, it is possible to determine the lamp type by analyzing the spectral content of each lamp. In order to perform this task, a set of radiometric sensors were used. The choice of each sensor was based on the emission characteristics of the lamps.

Fig. 4 also shows the relative spectral sensitivity of two sensors that were used in the mentioned set.

The optical sensors are transducers that convert the sensitizing radiation (weighted by its sensitivity curve) in electrical current (also called photocurrent). Hence, the optic sensor output can be defined as

$$M = K\int_{0}^{\infty} J(\lambda)S(\lambda)d\lambda\,. \tag{1}$$

Where K is a constant of proportionality, $J(\lambda)$ is the spectral distribution of the lamp and $S(\lambda)$ is the spectral sensitivity of the sensor.

Since each lamp has its own spectral signature and the chosen sensors have different sensitivity features, the lamp type can be deduced by analyzing the sensors output. From Fig. 4, it is possible to see that sensor A has the sensitivity peak around 550 nm and sensor B has the maximum sensitivity at 800 nm. This ascertainment means that sensor A is more sensitive for blue and green radiations and sensor B is more sensitive for red and infrared radiations. Therefore, sensor A is more sensitized for MV and MH lamps while sensor B is more sensitive for HPS lamp radiation. Therefore, these sensors carry information that can be used to identify the lamp type.

As mentioned, sensors A and B are part of a group of devices used to gather information of the lamps. The choice of the other sensors was done so that the maximum sensibility of each device is in a different wavelength. This strategy increased the detection capability of the proposed system.

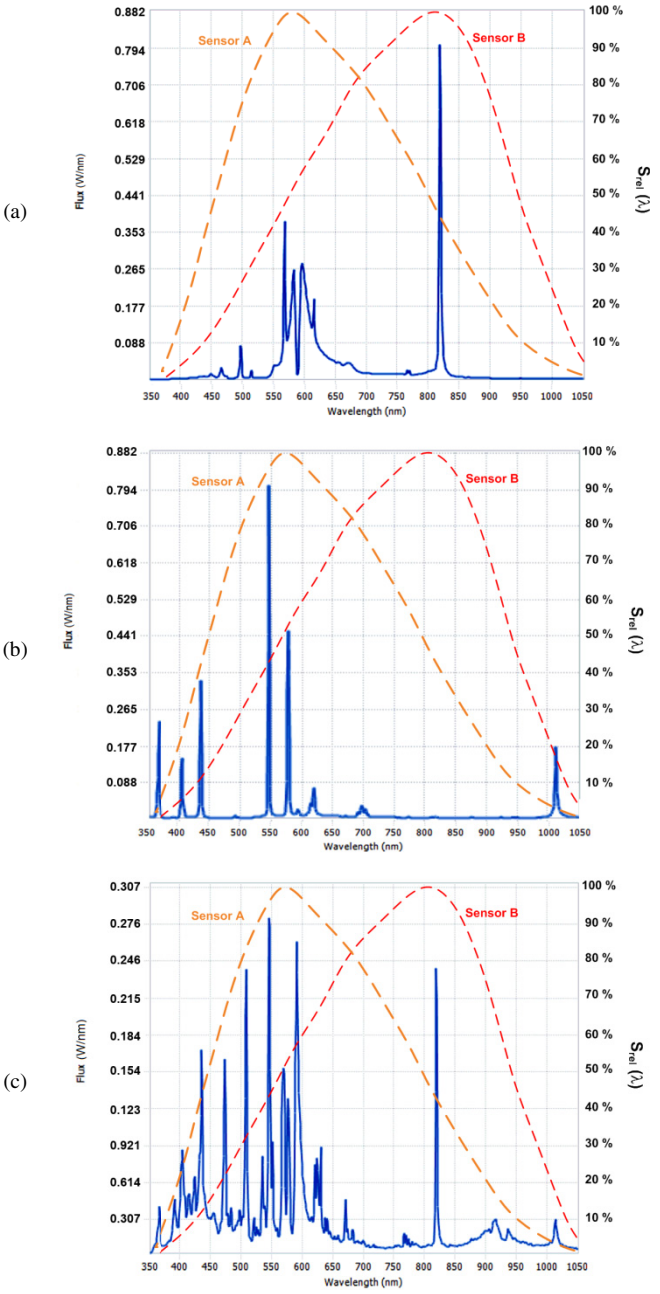

Fig. 4 Radiometric response (spectral flux, in W/nm, against wavelength, in nm) of several three light lamp technologies and relative spectral sensitivity of two radiometric sensors (called Sensor A and Sensor B): (a) mercury vapor (125 W); (b) high pressure sodium (70 W); and (c) metal halide (70 W)

Other important feature that influences the sensors response is the magnitude of the spectral lines, which carry the lamp power information. However, this magnitude depends on other variables, such as the pole height and the boom angle. Due to this behavior, the task of power lamp recognition is much more complicated. Furthermore, the theoretical forecast of the influence of each parameter aforementioned is a hard task, since all of these variables are correlated. Fortunately, pattern recognition techniques could be used to deal with this intricate problem in order to infer the most probable condition concerning a practical situation.

4 Pattern Recognition Techniques

The process of recognition of lamp power and type by radiometric information can be modeled as a pattern recognition problem, and some well-known techniques can be used. This means that each lamp should be treated as a class, having attributes provided by the optical sensors. So, if a lamp has a unique set of attributes, it can be identified by a classification algorithm. It is important to highlight that this algorithm must have the capability to deal with the sources of error, which are originated from the non-measured variables, such as the environment temperature, lamp lifetime and variations in the lamp supply voltage.

Some pattern recognition techniques were selected for learning and evaluating classification algorithms [6]. Classifiers were built using three different supervised learning techniques: induction of decision trees, nearest neighbors, and neural networks. Feature selection was employed to eventually improve the system accuracy. Stratified cross-validation and leave-one-out strategies were utilized for evaluating the system performance. An open source software called Weka [7], which provides a collection of algorithms for data mining, was used for performing these tasks.

4.1 Classification Algorithms

A mathematical function that maps input data to a category is known as a classifier. Classification learning algorithms implement classifiers by analyzing a set of data input instances whose category membership is known [8].

This work uses the J48, IBK and Multilayer Perceptron classification learning algorithms. J48 is the Weka implementation of the C4.5 algorithm developed by Ross Quinlan [9]. Its learning model utilizes a decision tree and is an extension of Quinlan's earlier ID3 algorithm [10]. C4.5 finds high precision hypotheses through a specific and characteristic method, seeking pruning rules obtained from the decision tree constructed during the training phase. Since the aforementioned technique uses the concept of information entropy, it is often referred as a statistical classifier [11].

IBK is the Weka implementation of the k-Nearest Neighbors algorithm (k-NN) [12], a non-parametric method for classifying objects based on the closest training examples in the feature space. It is a type of instance-based learning (IBL), and it is amongst the simplest of all machine-learning algorithms [13]. In this method, an instance is classified by a majority vote of its neighbors, with the object being assigned to the most common class amongst its k nearest neighbors (k is a positive integer, typically small). The most used way for identifying the closest neighbors is by computing the Euclidean distance between the object to be classified and its neighbors, though it can be used any form of metrics, such as the Mahalanobis distance [14]. Fig. 5 illustrates an example of k-NN classification. For k = 1 or k = 3, the point is classified as a triangle. Otherwise, for k = 5 the point is classified as a square. In this work it was always used k = 1, thus reducing k-NN to the nearest neighbor (NN) method.

The Multilayer Perceptron (MLP) [15] is a kind of feedforward artificial neural network. Typically, a neural network consists of a set of sensor units (source nodes) comprising the input layer, one or more hidden layers and an output layer of computational nodes. The input signal propagates through the network in a forward direction on a layer-by-layer basis. Fig. 6 shows the architecture of an MLP network with an input layer, two hidden layers and an output layer.

Each of these three methods (J48, IBK and MLP) demands setting configuration parameters. In order to simplify the experiments, it was decided to use the default values for Weka parameters. The most important parameters of each method and their default values are: (i) for J48, the pruning confidence was 0.25; (ii) for IBK, the number of neighbors, k was 1 and for MLP, the learning rate, momentum rate and number of epochs were 0.3, 0.2 and 500, respectively. The default values for the number of hidden layers and number of nodes of the hidden layers are, respectively, 1 and *(number of attributes + number of classes) / 2*.

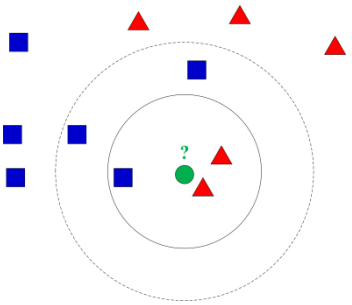

Fig. 5 Example of the k-NN classification

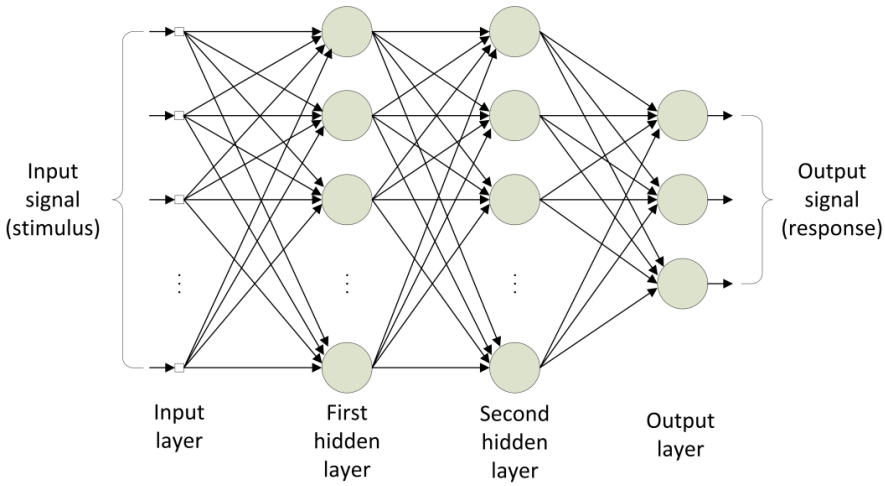

Fig. 6 Architecture of an MLP neural network with two hidden layers

4.2 Feature Selection

Feature selection is the process of choosing a subset of relevant features for use in classifiers construction [16]. The central assumption when using a feature selection technique is that the data often contains many redundant, irrelevant and noisy features. Redundant features are those that provide no more information than the currently selected features. On the other hand, irrelevant features provide useless information in any context, while noisy features generally decrease the classifiers performance. Therefore, beyond allowing shorter learning times, feature selection also enhances classification performance and generalization by reducing overfitting.

A feature selection algorithm is basically composed of a selection criterion and a search strategy. The selection criterion scores the different feature subsets. The search strategy proposes new feature subsets.

The two main categories of selection criteria are the filter and the wrapper approaches. The filter approach uses different criteria than classification performance to judge a feature subset. Common measures are Pearson correlation coefficient, mutual information and the scores of significance tests for each class-features combination. The wrapper approach consists of taking the estimated performance (typically accuracy) of a classifier as the proper feature selection criterion. Therefore, each feature subset is used for constructing a classifier, which is tested for estimating its performance. The feature subset that achieves the best performance is chosen. As wrapper methods build a new classifier for each subset, they are very computationally intensive, but usually provide the best performing feature set for that particular type of classifier. In this work, the wrapper approach was adopted.

There are also many different search strategies for proposing the feature subsets. The simplest algorithm is to test each possible subset of features finding the one which maximizes the accuracy. This is an exhaustive search of the space, and is computationally intractable for all but the smallest of feature sets. Since an exhaustive search is computationally unfeasible, sub-optimal search strategies are often chosen. This work employs the most common search strategy – the Sequential Forward Selection (SFS) [17]. It starts with an empty set and then tests each candidate together with the already selected features. The feature that performed best is included in the already selected set. The algorithm stops when no single feature expansion to the current subset results in a higher merit score.

4.3 Training and Validation Methodologies

It is common to measure a classifier's performance in terms of accuracy. The classifier predicts the class of each instance. The accuracy is the proportion of correctly classified instances over the whole set of instances.

In general, building classifiers and evaluating its accuracy can be divided in two steps: training and validation. The training step is done in order to define the parameters of the classifier algorithm based on a labeled database, which has both the inputs (i.e., sensors data) and the outputs (i.e., lamps) known a priori. The validation step uses an unlabeled database, which has only the inputs known. In this case, the classifier algorithm must infer the output based on the provided data using the parameters found in the training step.

Frequently, the way the data is split to evaluate the performance leads to overoptimistic results [18]. The training database and the validation database must be different from each other in order to become possible the quantification of the classifier generalization capability. A simple unique division of the available database into a x% training data set and 100 – x% validation data set potentially introduces a considerable bias for the estimated performance.

A good compromise between statistical significance and computational complexity is to use the stratified k-fold cross validation (CV) where the data set is divided into k subsets, each subset is used once for test and $k - 1$ times for training. When the training time of the classifier is not excessive, the leave-one-out (LOO) cross validation can be used. LOO gives a more reliable estimate than simple train-validation data division, since almost every example is used for training and validation whilst keeping these sets disjoint. LOO is a special case of k-fold cross validation where the total data set has k patterns. Once feature selection is computationally intensive, the experiments used stratified 10-fold CV for selecting the features [19]. LOO was used for comparing the classifiers accuracy.

5 Experimental Setup

In order to create the required database for the training and validation procedures, a "quasi-controlled" laboratory environment equipped with a height adjustable 6 m pole, as well as a boom angle adjustment system, was built (Fig. 7). Using this environment, a huge number of semi-controlled experiments have been conducted and had their respective information registered, including different lamp bulbs (of many wattages and technologies), different kinds of luminaires (open, enclosed and from different manufacturers) and several booming angles. Moreover, the methodology has considered spreading the acquisition events over a wide range of temperature and climate conditions (that, obviously, cannot be controlled). Therefore, from this environment it was possible to emulate the field conditions.

Prior to the algorithms evaluation, the built structure was of great importance during the development of the electronic system, since the first experiments let the proper adjust of the sensors gain.

Using the information provided by the electricity company, it was possible to define a number n of classes that should be studied, which reflected over 97% of actual street lighting conditions of the cities attended by the company.

Table 2 shows the instances (i.e., combinations of lamp type and power, luminaire, pole height and the boom angle) gathered from the quasi-controlled environment. In this table, luminaire names A to F are concerned to most typical commercial models as indicated by the electricity company.

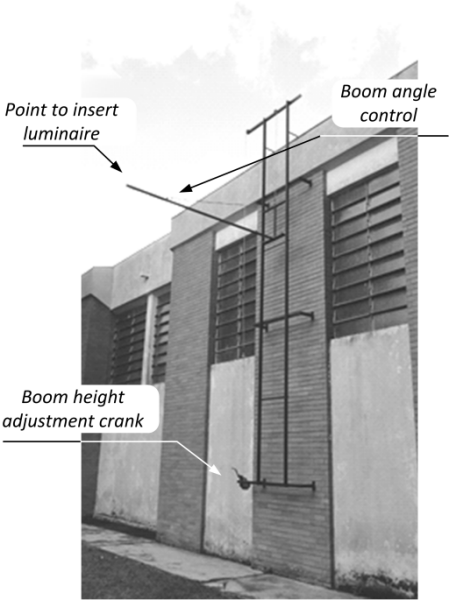

Fig. 7 Quasi-controlled laboratory environment used to create the required database

Table 2 Description of evaluated instances

Lamp Type	Wattage (W)	Luminaire	Pole height (m)	Boom angle
Mercury Vapor (MV)	125	A, B and C	4.0 - 4.8 - 5.6	0º- 10º - 20º
	250	D, E and F	4.0 - 4.8 - 5.6	0º- 10º - 20º
	400	D, E and F	4.0 - 4.8 - 5.6	0º- 10º - 20º
Sodium (HPS)	70	A, B and C	4.0 - 4.8 - 5.6	0º- 10º - 20º
	100	D, E and F	4.0 - 4.8 - 5.6	0º- 10º - 20º
	150	D, E and F	4.0 - 4.8 - 5.6	0º- 10º - 20º
	250	D, E and F	4.0 - 4.8 - 5.6	0º- 10º - 20º
	400	D, E and F	4.0 - 4.8 - 5.6	0º- 10º - 20º
Metal Halide (MH)	70	A, B and C	4.0 - 4.8 - 5.6	0º- 10º - 20º
	150	A, B and C	4.0 - 4.8 - 5.6	0º- 10º - 20º
	250	D, E and F	4.0 - 4.8 - 5.6	0º- 10º - 20º
	400	D, E and F	4.0 - 4.8 - 5.6	0º- 10º - 20º
Total number of instances				324

5.1 Algorithms Evaluation

Two approaches were employed to perform the classification process of the collected data from the structure. The first evaluated method consisted in dividing the classification task in two parts: the classification of the lamp type and classification of its power, i.e., a compound classifier. First, the data are submitted to the lamp type classifier (LTC), which splits into three sets MV, HPS and MH and thereafter the output of the first classifier is submitted to a lamp power classifier (LPC). Therefore, using this methodology, four classifiers were required and each one was evaluated using the aforementioned algorithms. Diagram of Fig. 8 illustrates the method applied to the evaluated instances.

The other tested methodology used a unique classifier to determine both type and power of the evaluated lamp instance.

In order to observe the performance of the classifiers, two experiments have been accomplished for each one of the aforementioned approaches. In the first experiment, only the data provided by the sensors set were used in the algorithms training step. On the other hand, the second experiment used the optical sensors information as well as the pole height as an input data for the algorithms training.

6 Experimental Results

This section presents the main experimental results obtained with laboratory and field tests. In each case, the two approaches mentioned in Section 5 were applied, for comparison purposes.

6.1 Laboratory Results

For the 324 instances related in Table 2, the validation process for the compound classifier architecture yielded the results shown in Table 3 for lamp type classifier (LTC), without and with the pole height information. For the LTC, it can be seen that the pole height information did not affect significantly the results. In addition, it is shown that the MLP algorithm achieved the best performance for lamp type classification, reaching about 97.5% of success rate.

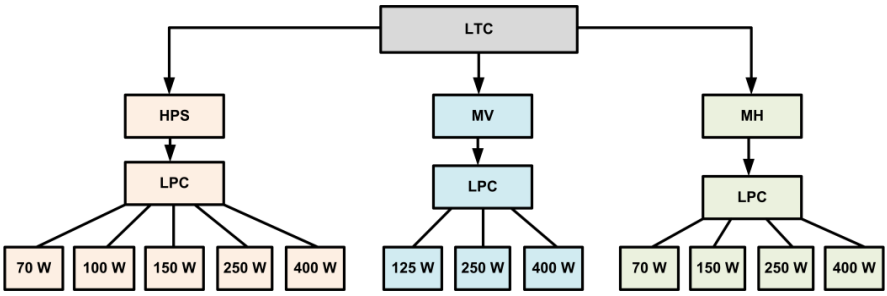

Fig. 8 Method of the compound classifier (1 LTC + 3 LPCs)

The success rate of the LPCs for HPS, MV and MH lamp types are shown in Table 4, Table 5 and Table 6, respectively. For all cases, when the pole height is an input parameter, the average algorithm performance is improved. Interestingly, some relatively poor hit rates obtained without height information were substantially improved when this parameter was considered, as occurred for the HPS 100 W lamps (Table 4).

Since the intensity of the radiation that sensitizes the sensors is dependent on the pole height, an improvement in the hit rates is expected when this information is known. This assumption can be confirmed with the results obtained from the classification process for the data acquired in the quasi-controlled laboratory environment. Furthermore, the results show that, as observed for LTC, the MLP algorithm was also the best classifier for the LPC.

The unique classifier method was applied to the laboratory instances, yielding the success rates shown in Table 7 and Table 8, without and with pole height information, respectively.

Table 3 Results of the Lamp Type Classifier for laboratory experiments

Without the pole height information				
Classifier	**Lamp Types**			***Weighted***
	MV	**HPS**	**MH**	***Average***
J48	88.9%	93.3%	86.1%	89.8%
IBK	80.2%	97.0%	93.5%	91.7%
MLP	96.3%	100%	95.4%	97.5%
With the pole height information				
Classifier	**Lamp Types**			***Weighted***
	MV	**HPS**	**MH**	***Average***
J48	87.7%	93.3%	87.0%	89.8%
IBK	86.4%	96.3%	91.7%	92.3%
MLP	98.8%	97.0%	97.2%	97.5%

Table 4 Results of the lamp power classifier for HPS lamps for laboratory experiments

Without the pole height information						
Classifier	**Lamp Wattages**					***Weighted***
	70 W	**100 W**	**150 W**	**250 W**	**400 W**	***Average***
J48	92,6%	33,3%	70,4%	70,4%	96,3%	72,6%
IBK	88,9%	48,1%	63,0%	77,8%	81,5%	71,9%
MLP	96,3%	66,7%	63,0%	88,9%	96,3%	82,2%
With the pole height information						
Classifier	**Lamp Wattages**					***Weighted***
	70 W	**100 W**	**150 W**	**250 W**	**400 W**	***Average***
J48	92,6%	70,4%	70,4%	85,2%	88,9%	81,5%
IBK	100%	81,5%	81,5%	85,2%	92,6%	88,1%
MLP	100%	81,5%	85,2%	88,9%	96,6%	89,6%

Table 5 Results of the lamp power classifier for MV lamps for laboratory experiments

Without the pole height information				
Classifier	**Lamp Wattages**			***Weighted***
	125 W	**250 W**	**400 W**	***Average***
J48	96,2%	70,4%	85,2%	83,8%
IBK	92,3%	92,6%	92,6%	92,5%
MLP	96,2%	100%	100%	98,8%
With the pole height information				
Classifier	**Lamp Wattages**			***Weighted***
	125 W	**250 W**	**400 W**	***Average***
J48	96,2%	96,3%	88,9%	93,8%
IBK	96,2%	100%	96,3%	97,5%
MLP	96,2%	100%	100%	98,8%

Table 6 Results of the lamp power classifier for MH lamps for laboratory experiments

Without the pole height information					
Classifier	**Lamp Wattages**				***Weighted Average***
	70 W	**150 W**	**250 W**	**400 W**	
J48	100%	85,2%	51,9%	81,5%	78,9%
IBK	100%	85,2%	51,9%	81,5%	78,9%
MLP	100%	88,9%	66,7%	92,6%	86,2%
With the pole height information					
Classifier	**Lamp Wattages**				***Weighted Average***
	70 W	**150 W**	**250 W**	**400 W**	
J48	92,6%	92,6%	55,6%	92,6%	82,6%
IBK	100%	100%	74,1%	85,2%	89,0%
MLP	100%	100%	74,1%	85,2%	89,0%

Table 7 Results of the unique classifier for laboratory experiments (without pole height information)

Lamp Class		**Classifier**		
		J48	**IBK**	**MLP**
HPS	70 W	85.2%	85.7%	86.7%
	100 W	43.8%	56.0%	64.0%
	150 W	43.9%	67.9%	71.4%
	250 W	69.2%	72.4%	92.0%
	400 W	88.5%	88.5%	92.9%
MV	125 W	92.3%	95.7%	89.3%
	250 W	67.9%	67.9%	71.4%
	400 W	84.6%	87.5%	82.1%
MH	70 W	86.2%	78.1%	88.0%
	150 W	91.7%	80.8%	92.9%
	250 W	66.7%	48.1%	79.2%
	400 W	74.2%	71.4%	85.2%
Weighted Average		74.5%	74.7%	82.9%

Table 8 Results of the unique classifier for laboratory experiments (with pole height information)

Lamp		Classifier		
Class		J48	IBK	MLP
HPS	70 W	91.6%	100.0%	100.0%
	100 W	62.1%	70.0%	80.0%
	150 W	65.4%	66.7%	84.6%
	250 W	77.8%	76.9%	92.6%
	400 W	85.2%	85.2%	96.3%
MV	125 W	92.0%	92.0%	88.9%
	250 W	81.5%	96.2%	92.6%
	400 W	85.7%	89.7%	100.0%
MH	70 W	86.2%	89.3%	100.0%
	150 W	88.9%	100.0%	96.3%
	250 W	68.2%	61.5%	81.5%
	400 W	73.3%	65.4%	92.6%
Weighted Average		79.9%	82.7%	92.3%

6.2 Field Results

The lamp classification task based on the acquisitions obtained in field (actual streets) is quite harder than that performed using the data from experimental laboratory setup. Some practical difficulties, which are related to the field acquisition procedure, could be the non-predicted inclination of the poles and luminaries, difficulties to find a representative quantity of instances for a lamp class in the prospected region and even traffic impairments. The later could also impose the technical team to do the measurements at late night, especially when a specific lamp type or power is located at busy avenues and streets.

Moreover, an effective method for measuring the pole height in the field is still missing. Therefore, the height information was not used in the classifier during the field experiments. It seems that the missing of this information was not that bad because the majority of the measured lamps, considering the particular city related to this study, were installed at almost the same pole height.

In spite of the impairments cited in the previous paragraph, field experiments produced results close to those obtained in laboratory. The field measurements were taken in a city with the public lighting network managed by EDP. An amount of 276 instances was evaluated, comprising 167 instances of HPS lamps (rated at 70, 100, 150, 250 and 400 Watts) and 109 instances of MH (150, 250 and 400 Watts). In the related location, MV lamps are not used for street lighting. Therefore, lamps of this technology were not considered.

The employed classification methodology were the same used for laboratory tests. For the compound classifier, the obtained results are shown in Table 9 for the LTC and in Table 10 and Table 11 for LPC, without selection of features.

The field results obtained using the unique classifier architecture are shown in Table 12. In this case, all the sensors data were employed for classification. By applying the feature selection, the results are shown in Table 13.

Table 9 Field Results of the LTC (276 instances)

Classifier	Lamp Type		Weighted Average
	HPS	MH	
J48	97,60%	99,10%	98,20%
IBK	100,00%	100,00%	100,00%
MLP	100,00%	100,00%	100,00%

Table 10 Field Results of the LPC for HPS lamps (167 instances)

Classifier	Lamps Wattages					Weighted Average
	70W	100W	150W	250W	400W	
J48	66,70%	70,40%	65,90%	55,00%	77,50%	67,30%
IBK	77,80%	88,90%	76,90%	64,30%	75,70%	76,60%
MLP	81,30%	80,00%	78,00%	81,50%	83,80%	80,90%

Table 11 Field Results of the LPC for MH lamps (109 instances)

Classifier	Lamps Wattages			Weighted Average
	150W	250W	400W	
J48	100,00%	76,40%	79,40%	82,40%
IBK	91,30%	79,60%	75,70%	80,70%
MLP	91,30%	90,20%	97,10%	92,80%

Table 12 Field Results of the Unique Classifier (without feature selection)

Lamp Class		Classifier		
		J48	IBK	MLP
HPS	70 W	80.0%	93.3%	83.3%
	100 W	59.4%	75.0%	81.3%
	150 W	77.1%	82.9%	94.3%
	250 W	33.3%	54.5%	63.6%
	400 W	81.1%	78.4%	78.4%
MH	150 W	87.0%	91.3%	87.0%
	250 W	79.6%	81.6%	87.8%
	400 W	75.7%	78.4%	81.1%
Weighted Average		71.7%	79.0%	82.3%

Table 13 Field Results of the Unique Classifier (with feature selection)

Lamp Class		Classifier		
		J48	**IBK**	**MLP**
HPS	70 W	80.0%	93.3%	80.0%
	100 W	59.4%	81.3%	78.1%
	150 W	85.7%	88.6%	88.6%
	250 W	30.3%	63.6%	69.7%
	400 W	86.5%	78.4%	86.5%
MH	150 W	87.0%	91.3%	87.0%
	250 W	81.6%	85.7%	81.6%
	400 W	67.6%	78.4%	91.9%
Weighted Average		72.5%	82.3%	83.0%

As discussed in Section 4, it can be verified that the averaged results for the classification with selection of attributes are, in general, better than those obtained for the classification with the totality of sensors data, due to the elimination of redundant and irrelevant information.

For both approaches (without and with selection), the field results confirmed that, among the three algorithms tested, MLP was the classifier with best hit rates, as occurred for the laboratory experiments. In addition, the field experiments results suggest that the unique classifier architecture with feature selection obtains the better results.

Due to an almost plane relief profile of the city where the field experiments were accomplished, the accelerometer information was not used as an input data for the classifiers. In addition, it was not used for the laboratory tests. However, the accelerometer could enhance the efficiency of the classifiers, when applied to a lighting network installed over a city with a rugged relief.

Moreover, it can be noted that, although the pole height was not considered for running the classifier in field results, the hit rates remained in most cases superior to 70% (the exceptions occurred with the J48 algorithm for some lamp classes). This can be justified by the regular pole height profile of the city chosen for tests, as mentioned. However, this is not the actual scenario in numerous cities in Brazil, where a diversity of luminaires heights would impair the achieving of acceptable success rate indices, if the pole height is not taken into account as an input data.

7 Software Overview

The goal of this Section is to describe the software systems developed to deal with the entire data processing path, starting from the control of the electronic setup for gathering data from the lighting poles to finally bringing to Electricity Company the real status about its lighting park. The computational platform is composed by two main subsystems, which are called in this work *Data Acquisition Interface* (DAI) and *Information System* (IS).

While DAI manages the electronic setup installed over the vehicle during the measurements, generating the readout request signals and storing data from the electronic system, the IS counterpart employs offline processing. It must be noted that DAI is installed on a mobile computer system (e.g. a tablet device) and operates in real-time, while IS is usually installed on a desktop or workstation and is fed by data previously acquired and stored by DAI. Fig. 9 depicts the interaction between both subsystems.

7.1 Data Acquisition Interface

DAI is the software responsible for gathering information from the different data sources handled by the system: lamps, digital camera and GPS. The interface was designed with the purpose of simplifying the process of collecting street lighting lamps data, allowing, therefore, this task to be performed in a short interval of time by an operator. For the version reported in this work, the interface was implemented on a tablet device running an Android operating system.

The implemented software can be divided into four main modules: (i) Data Acquisition for Training; (ii) Data Acquisition for Classification; (iii) Data Acquisition for Auditing; and (iv) Data Transfer. These are the main functions available to the operator.

Fig. 9 Interaction between the subsystems

DAI interacts with the DSP, which concentrates all the information given by the board sensors and GPS, via *Bluetooth* connection. A USB cable connection is used to establish the communication between the tablet and the digital camera. The lamp image and radiometric data start to be gathered by clicking on the "Measure" button in the interface screen, shown in Fig. 10. The user should observe when the color of the icons representing the positioning sensors changes to green and, at the same time, the image provided by the digital camera moves to the center of the screen, denoting that the equipment is ready (in a proper position) for starting the acquisition process.

The *training* option should be selected by the user when data with purpose of creating a database for training a classifier is going to be collected. In this case, the type and wattage of the lamps are known beforehand. Then, the classifier can learn how to differentiate the types and wattages based on data just collected.

The *auditing* option allows user to verify how successful the classifier algorithms (implemented in the Information System) are, i.e., it is used to check their hit rates. As in the training option, the type and wattage of the lamps are known in advance.

With the *data transfer* option, users can transfer to the Information System specific database all the data stored in each one of the tablets used in the data acquisition operation. Therefore, this option establishes a communication link between the mobile device that contains the collected data and the computer where the Information System is installed. Once the download operation is complete, the user can see the status of the transfer in the tablet screen. In the case a communication failures, a new transfer can be restarted by following the instructions on the screen.

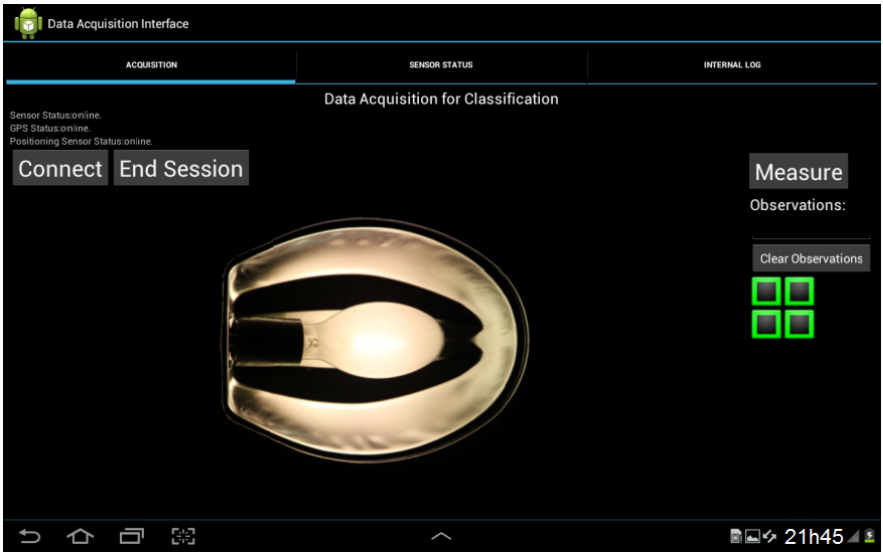

Fig. 10 Data Acquisition Interface screen – Classification option. The picture shows the system ready to start acquisition.

It should be mentioned that the camera set used in the prototype had no programming libraries for the Android operating system. Therefore, it was necessary to develop a communication protocol between the camera and the tablet in order to access essential system functions, such as viewing real-time images of the lamps, retrieving useful image parameters and capturing high-resolution photos directly from the camera to the tablet.

7.2 The Information System

The Information System (IS) has been developed to manage the huge mass of radiometric and image data acquired from the street lighting points and update the corporative lighting lamps database. Based on the data provided by the set of sensors and digital camera stored by the DAI system, and making use of previously known data from company's lighting lamps, the IS applies the pattern recognition techniques discussed in the previous section in order to infer the lamp technology and wattage. The IS also provides other important functions, such as classifier training, auditing and update of the company database.

The IS is divided into four main components or modules: (i) Import Module; (ii) Training Module; (iii) Classifier Module and (iv) Update Module. The main system interface is shown in Fig. 11.

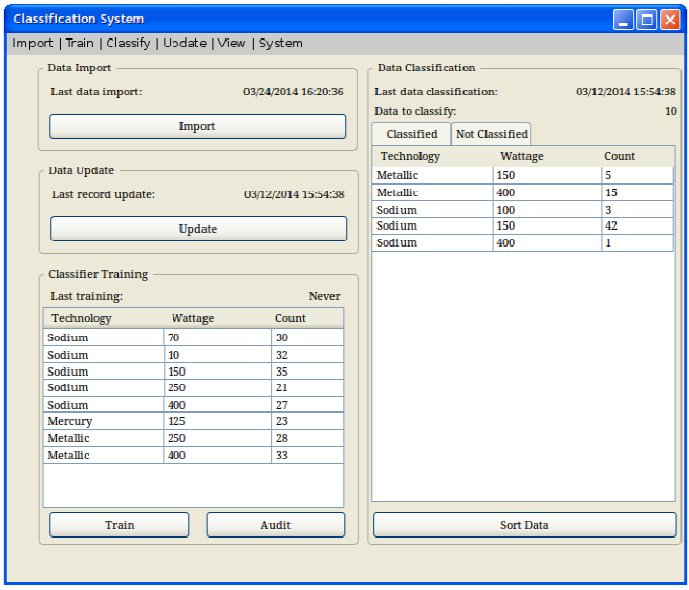

Fig. 11 View of Information System interface

A. Import Module

This component is responsible for populating the local database with the lighting lamps radiometric data, acquired by a tablet device, which holds the DAI. The imported data can be used for either training or classification, depending on user purposes. The Import Module was designed to provide simplicity of operation. It also aims to ensure high recoverability through failures.

B. Training Module

As the process of lamps recognition is as a pattern recognition problem, the Training Module is responsible for implementing the learning phase of this process, i.e., training the classification algorithms to recognize lamps wattage and type based on data provided by a set of street lighting lamps whose electric power and type features are known a priori. The module feeds the classifier learning algorithms with radiometric attributes recorded by the embedded analog and digital light sensors that compose the hardware. Since the Multilayer Perceptron (MLP) technique systematically achieved the better results on the performed experiments, it is the only learning method included on the training module.

C. Classifier Module

The Classifier is the component responsible for the assignment of a label (type and wattage) to each street lighting point exposed to system classification. After importing the radiometric sensor data from the DAI, the classifier module uses the current trained MLP classifier to analyze and classify the data from each pole lamp.

D. Update Module

After finishing the lamp classification process, the system is ready to update the corporative database, what is done by the Update Module. The updating process requires a procedure to set up the correspondence between the lighting lamps evaluated in the streets and the corporative database. This is necessary because the system needs to recognize what records have to be updated or if a new register has to be created as a result of the matching procedure.

Fig. 12 Visualization of geographical data (from *Google Earth* website)

The Update Module uses GPS information and graph isomorphism algorithms to find out if two lighting points are close enough to be considered as the same element, or if a selected light point has to be considered a new one. In this case, the correspondent data need to be inserted into the corporative database. For the sake of better visualization, the Update Module also generates two files in *.kml* format, to facilitate the visualization in Google Earth, as displayed in Fig. 12. The elements shown in the map can be identified by color. Red elements, for example, indicate points that are not found in any company database registers.

8 Conclusions

This chapter described a methodology intended to collect and process street lighting lamps information, in order to find out the lamps type and power. The strategy uses hardware and software components. The hardware system, composed by an optical sensors set, is responsible to gather the lamp spectral signature. A digital camera and a GPS system complement the information about the pole position and geographical localization of the investigated lighting points.

It was shown that the lamp spectral lines position carries the lamp type information, while the lamp wattage information is associated to the spectral lines magnitude, which depends upon other variables, such as the pole height and the boom angle. Due to this feature, a theoretical forecast about the complete lamp information based on the spectral signature and the optical sensor sensitivity curve is a complex task.

Aware of these difficulties, the original problem was modeled as a pattern recognition problem, allowing the use of intelligent algorithms. The performance of J48, IBK and MLP algorithms was tested.

With the purpose of validating the proposed methodology, a quasi-controlled laboratory environment that simulates a street lighting pole was built. A huge number of measurements were done with the sensors set, varying the lamp type and power, the pole height and the boom angle. Thereafter, the data collected in these experiments were analyzed using the aforementioned algorithms.

Although the field measurements face some practical drawbacks as mentioned in the text, the street collected data ratified the laboratory results, with acceptable success rates. The feature selection strategy could even improve the results, since redundant, irrelevant and noisy information can be eliminated.

Two approaches were applied both for the laboratory experiments and for the field tests. The first one adopted a compound classifier, where a first classifier was employed to find out the lamp type (MV, MH or HPS). In sequence, new classifiers were applied to the subsets, finding out the lamp wattages. It is interesting to note that the hit rates obtained for the lamp type classifier are quite superior to those obtained for the lamp power classifiers. It is an expected result, since the spectrum content of the radiation emitted by the different lamp types are well distinguishable, and relatively independent of their wattages. On the other hand, it was noted that many factors could affect the classification of lamp power.

The second method consisted of adopting a unique classifier, capable of discriminate both type and power of the evaluated lamps. In general, this technique led to better results. However, results for both approaches are shown, for comparison purposes.

Apart from the method of classification and other considerations, as the choice of the use or not of the pole height information of applying feature selection, it is possible to note that the best results were achieved when the MLP classifier was employed. Therefore, from the three investigated classifiers, MLP was the only one built in the Information System (IS), the software system developed to concentrate data from different measurement runs, and to perform the training and classification procedures in order to update the Company database. The IS is fed by data temporarily stored in a mobile computer, where is installed a software called Data Acquisition Interface (DAI). DAI works online, and is the interface between operators and the Electronic System allocated on the rooftop of company vehicle.

The system is still being developed, in order to improve the classification results. Some issues have to be considered for this purpose. The most important are: (i) the need to extend the database, which tends to improve the system capability of generalization; (ii) a faster and more accurate online measurement of pole height; (iii) the use of image attributes, taken by the digital camera.

It is believed that the present study can be used to help municipalities and electricity companies to obtain a more reliable and realistic public lighting database. This is even more useful in a transition legislative scenario that allows many entities to interfere and share the responsibility to try meeting people demands.

References

[1] National Agency of Electrical Energy (ANEEL), Technical Note nº 271/2010 – Methodology of regulatory treatment for non-technical electricity losses, Brasília (2010) (in Portuguese)

[2] Comassetto, L., Bernardon, D.P., Canha, L.N., Abaide, A.R.: Technical and commercial losses of electrical energy in distribution systems. In: VII Conferência Brasileira sobre Qualidade de Energia Elétrica, Santos (August 2007) (in Portuguese)

[3] Evaldt, M.C., Canto dos Santos, J.V., Figueiredo, R.M., da Silva, L.T., Stracke, M.R.: Payback analysis in identification and monitoring of commercial losses in distribution networks. In: International Conference on European Energy Market (EEM 2012), pp. 1–6 (2012)

[4] Soares, G.M., Almeida, A.G.B., Mendes, R.M., et al.: Detection of street lighting bulbs information to minimize commercial losses. In: 2013 IEEE Seventh International Conference on Sensing Technology, ICST 2013, Wellington, New Zealand (December 2013)

[5] Keeffe, W.M.: Recent progress in metal halide discharge-lamp research. In: IEE Proceedings A Physical Science, Measurement and Instrumentation, Management and Education - Reviews, vol. 127, pp. 181–189 (1980)

[6] Devijver, P.A., Kittler, J.: Pattern Recognition: A Statistical Approach. Prentice Hall (1982)
[7] Witten, I.H., Frank, E., Hall, M.A.: Data Mining: Practical Machine Learning Tools and Techniques. Morgan Kaufmann Publishers (2011)
[8] Kotsiantis, S.B.: Supervised Machine Learning: A Review of Classification Techniques (2007)
[9] Quinlan, J.R.: C4.5: Programs for Machine Learning. Morgan Kaufmann Publishers (1993)
[10] Quinlan, J.R.: Induction of Decision Trees. Machine Learning 1(1), 81–106 (1986)
[11] Vijayarani, S., Divya, M.: An efficient algorithm for generating classification rules. International Journal of Computer Science and Technology, vol 2(4) (2011)
[12] Cover, T., Hart, P.: Nearest neighbor pattern classification. IEEE Trans. on Information Theory 13(1), 21–27 (1967)
[13] Aha, D.W., Kibler, D., Albert, M.K.: Instance-Based Learning Algorithms. Kluwer Academic Publishers, Boston (1991)
[14] Gu, F., Liu, D., Wang, X.: Semi-supervised weighted distance metric learning for kNN classification. In: International Conference on Computer, Mechatronics, Control and Electronic Engineering (CMCE), vol. 6, pp. 406–409 (2010)
[15] Haykin, S.: Neural Networks: A Comprehensive Foundation, (2). Prentice Hall (1998)
[16] Kudo, M., Sklansky, J.: Comparison of algorithms that select features for pattern classifiers. Pattern Recognition 33, 25–41 (2000)
[17] Guyon, I., Elisseeff, A.: An introduction to variable and feature selection. J. Mach. Learn. Res. 3, 1157–1182 (2003)
[18] Japkowicz, N., Shah, M.: Evaluating Learning Algorithms: A Classification Perspective. Cambridge University Press (2011)
[19] Geisser, S.: Predictive Inference: An Introduction. Chapman&Hall (1993)

Cesium Environmental Monitoring System for Assaying Temporal Changes in Atomic Disintegration Products Using Laser-Induced Breakdown Spectroscopy

S. Ikezawa* and T. Ueda

Graduate School of Information Production and Systems, Waseda University,
2-7 Hibikino, Wakamatsu, Kitakyushu, Fukuoka, 808-0135, Japan
ikezawa@y.fuji.waseda.jp

Abstract. In this work, a new method for real-time in-situ environmental monitoring of measured radioactive elements is presented. Currently, germanium semiconductor detectors are used for the analysis of radioactive materials. Germanium semiconductor detectors exhibit sensitivities much higher than those exhibited by other analytical instrumentation techniques. However, the equipment is lab-based and cannot address the need for on-site monitoring. Moving radioactive samples is strictly legally prohibited for safety reasons. The frequency of use is limited by the facility installation space, workforce supply considerations regarding safety, legal considerations for carrying and storing radioactive samples, and waste disposal methods. The presented method using laser-induced breakdown spectroscopy (LIBS) offers an affordable sensing system that can be applied at point-of-use for environmental analyses to provide an indication of impending problems. The applicable range of conventional LIBS, which has been used only to determine the elemental composition, is expanded to obtain an estimate of the isotope ratio by measuring the variation due to temporal changes in the atomic disintegration products. This method takes full advantage of LIBS, such that no pretreatment of the measured sample is required. In this work, a confirmation test for the LIBS measurement of cesium and barium based on the results of the disintegration of cesium is demonstrated as part of a preliminary survey for developing a monitoring system for actual radioactive materials.

Keywords: environmental monitoring, *in situ* analysis, optical methods, laser-induced breakdown spectrometry, laser-induced plasma, radioactive measurement, time-resolved spectroscopy.

* Corresponding author.

A. Mason et al. (eds.), *Sensing Technology: Current Status and Future Trends III*,
Smart Sensors, Measurement and Instrumentation 11, DOI: 10.1007/978-3-319-10948-0_5

1 Introduction

There has been growing concern about radioactive element dispersion, such as that of cesium 137, into the atmosphere, water, and soil since the nuclear accident in March 2011 in Japan. Even 28 months since the accident, there are still problems with the storage methods and conditions of radioactive cooling water, which is used to cool the reactor, because the damaged reactors require a large amount of one-way cooling water, even under cold shutdown conditions. According to an announcement made by the Tokyo Electric Power Company (TEPCO) on July 26, 2013, 750,000,000 Bq/L from cesium 134 (Cs-134) and 1,600,000,000 Bq/L from cesium 137 (Cs-137) were observed in underground trench water near a well. This well was recently established between the turbine building housing reactor 2 and the sea in July 2013 at the Fukushima nuclear plant site for monitoring purposes. This radioactivity level is the highest ever since observation began. This indicates the ongoing problem of underground water contamination. The technique that is currently in use for the measurement of radioactive materials is typified by germanium detectors located at dedicated facilities. Despite the current method having an advantage with respect to radioactivity detection sensitivity, the frequency of its use is limited by the facility installation space, workforce supply considerations regarding safety, legal considerations for carrying and storing radioactive samples, and waste disposal methods. These issues are caused by the measurement method, which requires retrieving and sending the sample to a laboratory. For this reason, the development of a simplified real-time and on-site monitoring system is necessary to enable the construction of a sensing network for multipoint detection on a regional scale. In contrast, the presented elemental detection system using laser-induced breakdown spectroscopy (LIBS) has the advantages of noncontact sensing, remote sensing without any intervention, and applicability to a stand-alone power system because of its low energy consumption, as demonstrated recently with a robotic rover named Curiosity on NASA's Mars Science Laboratory mission [1-5]. In addition, the in-situ measurement using LIBS alleviates the problems of storage and disposal of radioactive waste. Previous research studies reported that some of the suspicious elements containing radioactive isotopes derived from nuclear plants, such as uranium [6-14], cesium [15-17], strontium [18-20] and barium [21-23], are suitable for LIBS measurement because of their low limit of detection (LOD). The main objective of this project study is Real-time monitoring of nuclear contamination of water through sensor fusion. The role of the presented LIBS system in fusion sensors is detection and precise elemental identification in the early stage of the measurement process. Information regarding the elemental components and temporal variation of disintegrated elements obtained through LIBS measurement over mid-term and long-term periods will be applied to other sensor units in the future.

2 Importance of Cesium and Barium Measurement

From the fission of uranium (U-235), iodine (I-129, I-131, I-135), samarium (Sm-149), promethium (Pm-147), strontium (Sr-90), technetium (Tc-99), cesium

(Cs-133, Cs-134, Cs-137), zirconium (Zr-93), and others are produced. Cesium and iodine, in particular, are considered dangerous because their low boiling points and high volatility allow them to be easily disseminated. The boiling points of cesium and iodine are 944 K and 457 K, respectively. The half-lives of iodine are 15.7 Myr (I-129), 8.02 d (I-131), and 6.57 h (I-135). The half-life of Cs-137 is 30.17 yr, and Cs-133 is stable. Cs-137 remains a persistent threat to human life. Figure 1 (a) illustrates one of the U-235 nuclear fissions and the beta disintegration of Cs-137. Cs-137 is a radioactive isotope of cesium, which is one of the more common fission products obtained by nuclear fission of U-235 and other fissionable isotopes in nuclear reactors. Figure 1 (b) illustrates the beta disintegration scheme of Cs-137. Cs-137 decays as a result of neutron-to-proton conversion with the transformation of a down quark to an up quark, emitting an antielectron neutrino and a high-energy electron. Furthermore, Cs-137 changes to Ba-137 directly or by way of a metastable nuclear isomer, Ba-137m, with the emission of gamma rays.

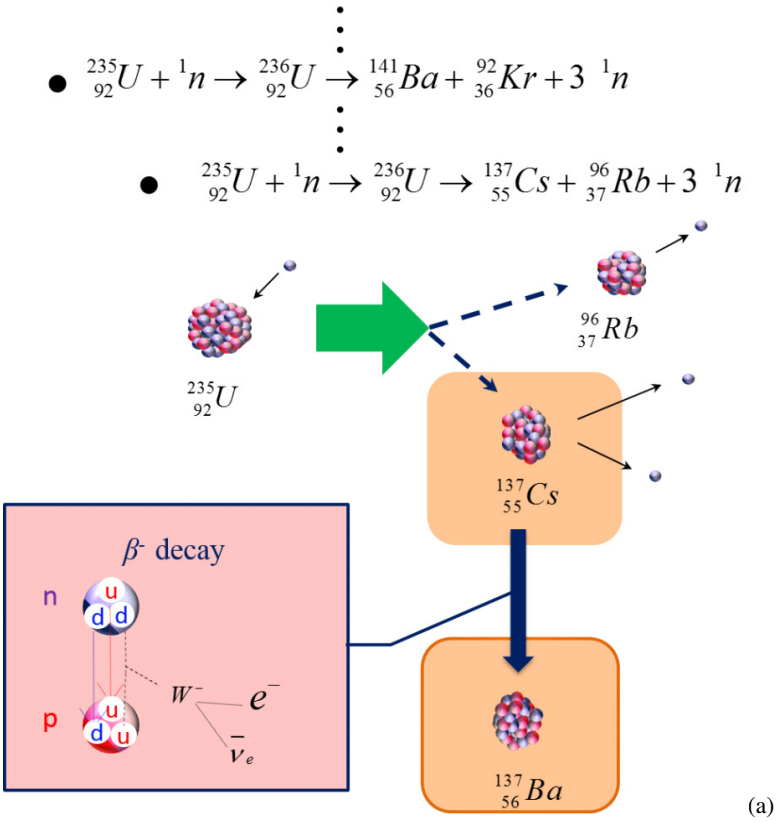

Fig. 1 Schematic of nuclear fission: (a) Uranium-235 fission, (b) Beta ray disintegration scheme of cesium-137

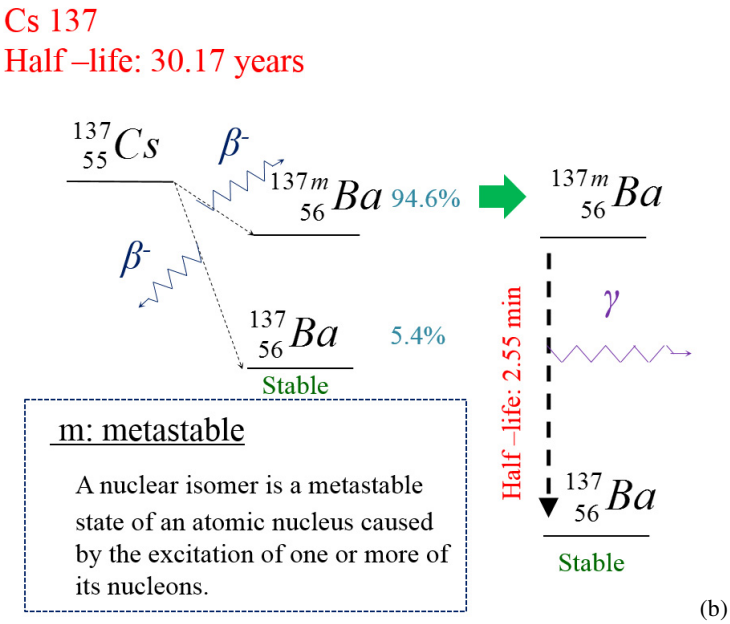

Fig. 1 (*continued*)

As described above, noncontact in-situ elemental analysis of cesium and barium is an effective method for monitoring purposes because cesium can be more easily disseminated than the other fission products, in addition to being quite chemically reactive and therefore difficult to handle.

3 Elemental Detection of Cesium and Barium in Sea Sand Soil

Sea sand was used as basement soil for measurement with the assumption that measurement in underground water close to sea is conducted at a practical phase. To use the LIBS system at a practical phase to estimate the isotope ratio by measuring the variation due to long-term temporal changes in the atomic disintegration products, a small enclosed bottle (see Figure 2) is used and the LIBS measurement is performed directly inside the bottle.

Fig. 2 Photograph of the sealed bottle for long-term LIBS in-situ measurement to detect the increased ratio of disintegration materials

For the confirmative performance test of the presented LIBS system in the laboratory, sea sand is used as basement soil.

3.1 Configuration of the LIBS System

Figure 3 shows the configuration of the LIBS system. The laser is controlled with a delay pulse generator. The trigger signal is input into the laser. To generate plasma with the sample, the laser pulse is focused with a lens. The sample materials are vaporized using the focused laser beam to generate plasma on the surface. Emissions from the laser-produced plasma are collected using three lenses and are guided to a spectrograph; the spectral signal is temporally processed using a streak camera. Finally, a charge-coupled device (CCD) camera is used to measure the streak pattern, which is displayed on a computer monitor.

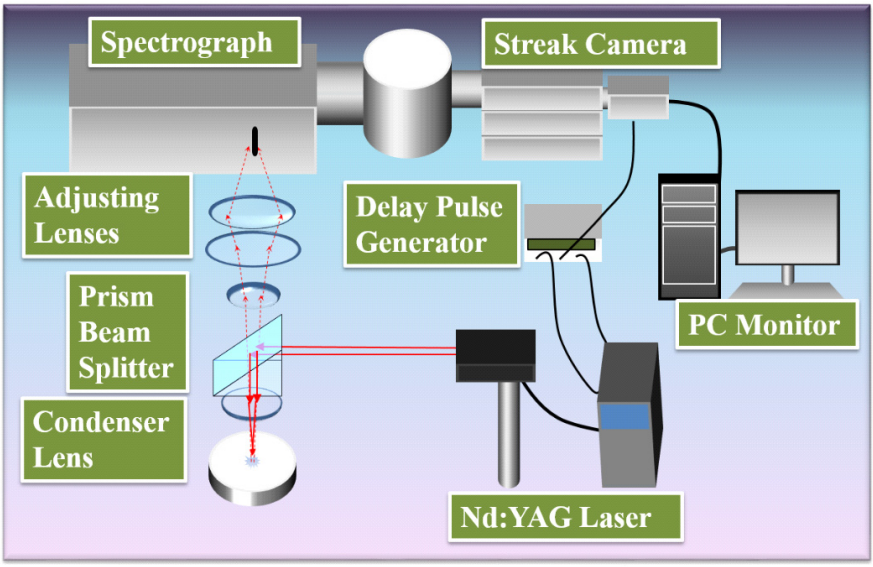

Fig. 3 Schematic of the LIBS configuration

3.2 Experimental Setup for the LIBS Configuration Equipment

- Delay Pulse Generator: The trigger signal is input to the laser. The delay pulse generator provides the first delay signal (185–285 μs) to the Q-switch control and the second delay signal (179–199 μs) to the streak camera, which passes the delay signal to the shutter control. These temporal setting values correspond to the inclusive delays due to, inter alia, the flash lamp and cable length.
- Laser: A Nd:YAG laser is operated at 1064 nm to generate a 50-mJ pulse with a width of 8 ns at full width at half maximum (FWHM). The laser pulse is focused with a lens with a focal length of 50 mm, thereby yielding a power density of terawatts per square centimeter.
- Spectrograph: The imaging monochromator spectrograph has a focal length F = 250 mm and an aperture ratio f/4. A diffraction grating with a groove density of 1200 lines/mm is used in the experiment.
- Streak Camera: The streak camera has a time resolution of 5 ps or greater and is operated by directing the light onto a photocathode. The photons produce electrons via the photoelectric effect. The electrons are accelerated in a cathode ray tube and passed through an electric field produced by a pair of sweep electrode plates, which deflect the electrons laterally. By modulating the electric potential between the plates, the electric field is quickly changed to induce time-varying deflection of the electrons, sweeping the electrons, amplified by a microchannel plate (MCP), across a phosphor screen at the end of the tube. In this experiment, the temporal gate width is set to 20 μs and the temporal resolution is set to 40 ns.

3.3 Sample Setting

Figure 4 shows a photograph of the laser-induced plasma of the sample on the sea sand. This photograph was recorded using a high-speed camera operating at 240 fps. A plastic wrap covers the petri dish to avoid sample splashing. The pulsed laser is operated at 100 shots for signal-averaging integration.

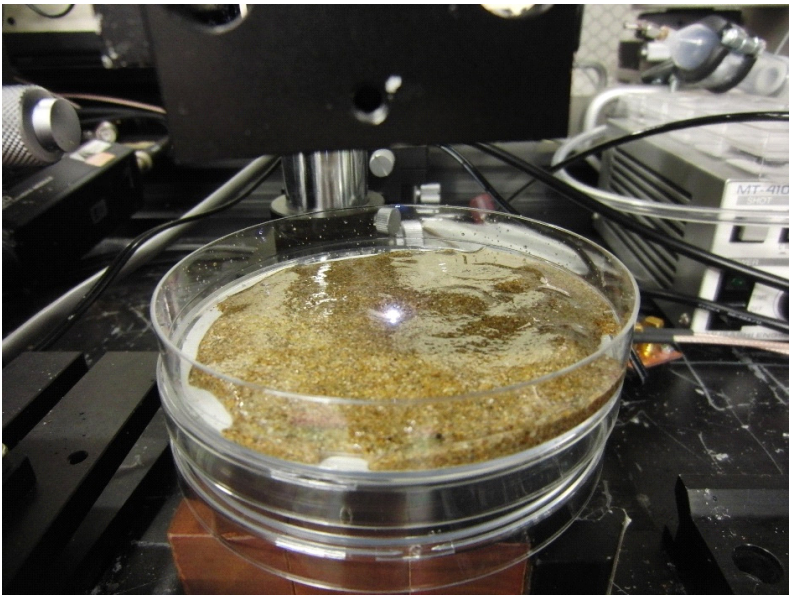

Fig. 4 Photograph of laser-induced plasma on the sea sand sample

According to the time-resolved analysis using the LIBS system, numerous photons are produced during plasma generation by bremsstrahlung radiation after a few hundred nano-seconds of laser pulse irradiation; the elemental spectra are observed for a few tens of microseconds following the bremsstrahlung radiation.

4 Experimental Results

4.1 LIBS Measurements in Sea Sand

Figures 5 and 6 show the experimental data for the barium spectrum obtained from the sea sand sample with added barium sulfate ($BaSO_{4)}$ powder. These

measurements were carried out in the wavelength range of 487–499 nm, and the obtained barium spectrum was observed at a wavelength of 493.408 nm. The intensity of the signal is based on the average data obtained for 100 laser pulse shots operating at 2 Hz within 1 min in ambient air. Signals obtained from the sea sand with added $BaSO_4$ powder and the background signal obtained without the $BaSO_4$ powder are presented in Figure 5. As shown in Figure 6, the signals are calculated by subtracting the background signal from the signal obtained from the $BaSO_4$-powder-containing sample.

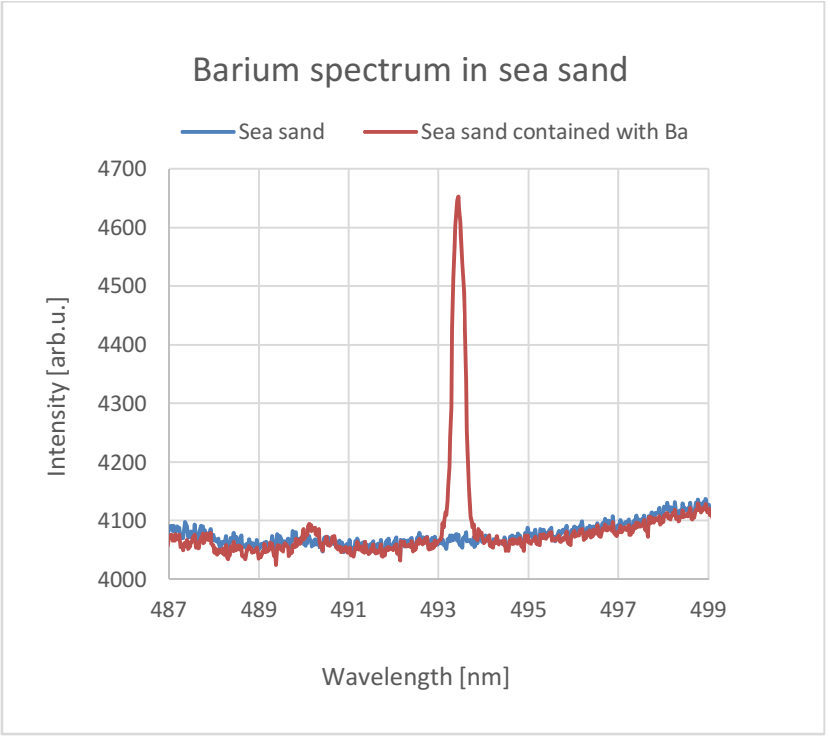

Fig. 5 Barium spectrum and background signal obtained from sea sand

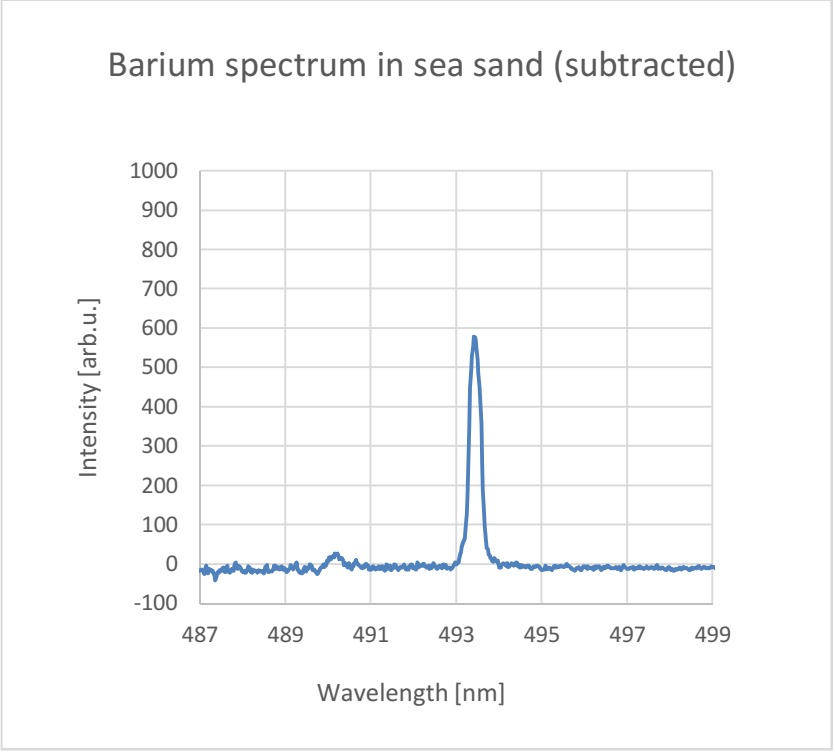

Fig. 6 Barium spectrum after subtracting the background signal

Figures 7 and 8 show the experimental data for the cesium spectrum obtained from the sea sand sample with an additional cesium-containing mineral [$(Cs,Na)(AlSi_2)O_6.nH_2O$]. These measurements were carried out in the wavelength range of 667–679 nm, and the obtained cesium spectrum was observed at a wavelength of 672.447 nm. The intensity of the signal is based on the average data obtained for 100 laser pulse shots operating at 2 Hz within 1 min in ambient air. Signals obtained from the sea sand with added cesium and the background signal obtained without cesium are presented in Figure 7. As shown in Figure 8, the signals are calculated by subtracting the background signal from the signal obtained from the cesium-containing sea sand.

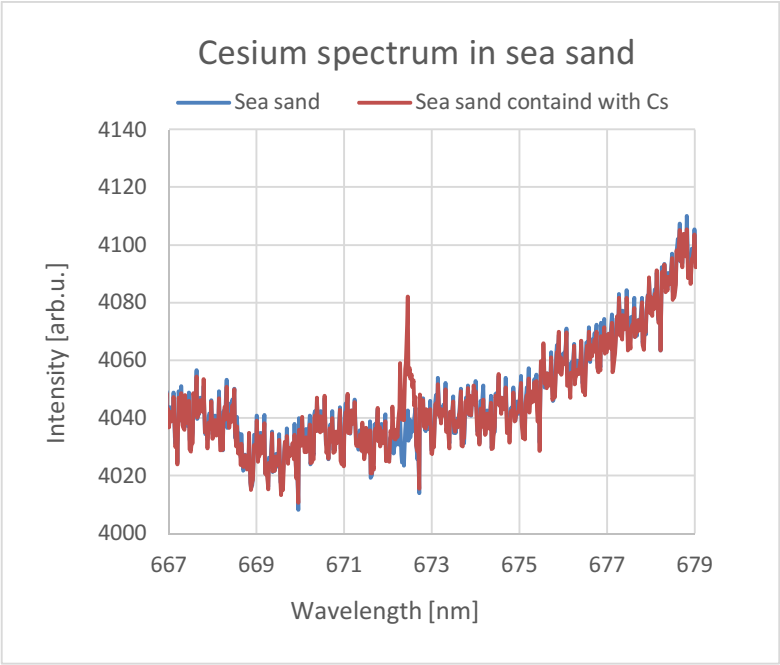

Fig. 7 Cesium spectrum and background signal obtained from sea sand

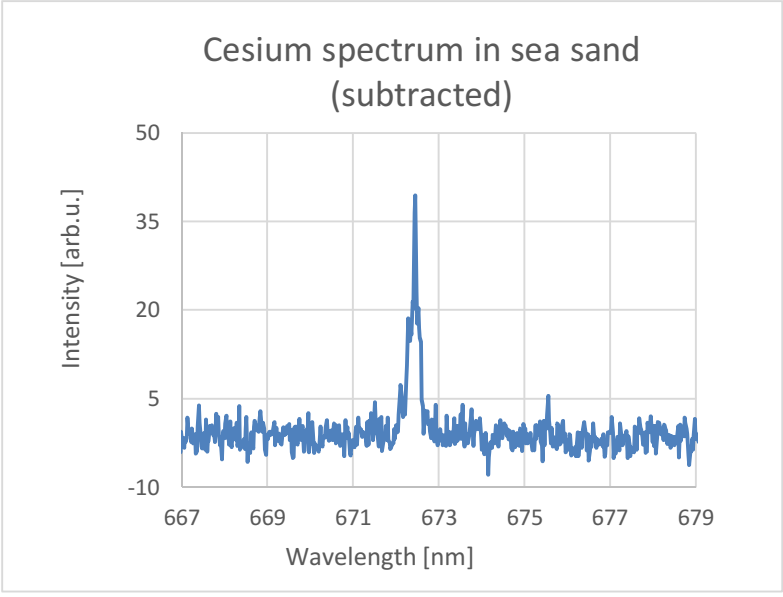

Fig. 8 Cesium spectrum after subtracting the background signal

4.2 Sensitivity Comparison between Cesium and Barium

The wavelengths of barium and cesium in the figures above exhibit the highest intensities observed in the experiments carried out in the wavelength range of 240–1100 nm using the LIBS system. Thus, spectra at wavelengths of 493.408 nm for barium and 672.447 nm for cesium are defined as the detection wavelengths in this study. Figure 9 shows an intensity comparison between barium, sodium, and cesium.

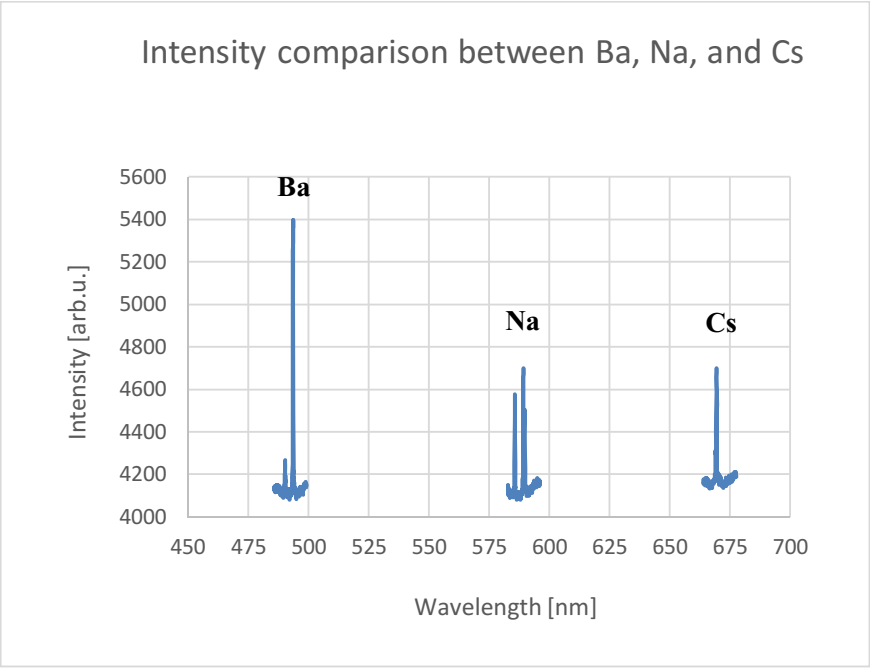

Fig. 9 Intensity comparison between barium, sodium, and cesium using the LIBS system with 100 laser shots under the same conditions

The intensity values in Figure 9 correspond to the different preliminary experimental results obtained from different samples. To obtain the ratios of the elements contained in the samples, SEM-EDX analysis was carried out. According to the SEM-EDX analysis, the atomic percentages of Ba, Na, and Cs were estimated to be 16.7%, 1.6%, and 3.2%, respectively. Table 1 summarizes the relative intensities of Ba, Na, and Cs estimated with the LIBS system and NIST database for reference. To fit the quantitative calibration curve of intensity versus the elemental density of sodium, the intensity values are normalized on the basis of the sodium content. The relative intensity ratio estimated from the experimental results using the LIBS system is adopted in this study.

Table 1 Estimated values of the relative intensities of barium, sodium, and cesium

Element (spectral line)	Background-subtracted intensities [arb.u.], as shown in Fig. 9	Relative intensity estimated by elemental ratio correction	Ratio of relative intensity to that of Na	Relative intensity (NIST[1])	Ratio of relative intensity to that of Na (NIST[1])
Ba (λ = 493.408 nm)	1277.7	7651.2	0.21	6900	0.09
Na (λ = 588.995 nm)	580.9	36303.8	1.0	80000	1.0
Cs (λ=672.447 nm)	530.0	0.46	0.46	960000	12.0

Referring to a previous work [24] for the quantitative analysis of a sodium chloride solution and intensity dose conversion factor summarized in Table 1, the densities of barium in sea sand (Figure 6) and cesium in sea sand (Figure 8) are concluded from the demonstrated experiments to be 1.049 mol/L (Ba) and 0.0346 mol/L (Cs). Table 2 summarizes the estimated detection limits (LOD) for Ba, Na, and Cs using the LIBS system by applying the relative intensity ratio of sodium obtained from our previous work database.

Table 2 Estimated detection limits for barium, sodium, and cesium with the LIBS system

Element (spectral line)	100 laser shot measurements	1000 laser shot measurements
Ba (λ = 493.408 nm)	0.02276 [mol/L]	0.00657 [mol/L]
Na (λ = 588.995 nm)	0.00478 [mol/L]	0.00138 [mol/L]
Cs (λ=672.447 nm)	0.01039 [mol/L]	0.003 [mol/L]

With the assumption that the measurement element is cesium 137, 1.37×10^9 atoms are required for 1 Bq emission. Thus, the LODs estimated using 100 and 1000 laser shot measurements with the LIBS system for Cs-137 are 4.57 TBq/L and 1.32 TBq/L, respectively, without the concentration treatment. In the case where some of the sensitivity enhancement techniques are applied for 0.1-ppb measurement [25], the LOD using LIBS for Cs-137 is estimated to be 0.16 MBq/L (using the relative intensity database of NIST, as summarized in Table 1).

5 Discussion

The estimation of the existence ratio of Cs-134 to Cs-137 (Cs-134/Cs-137) is very important for identifying the origin of cesium in a nuclear reactor. According to

[1] National Institute of Standards and Technology (NIST), Physical Meas. Laboratory.

previous reports [26, 27], the radioactivity ratio of Cs-134 to Cs-137 (Ecs134/Ecs137) was close to 1.0 immediately following the accident at the Fukushima nuclear plant. In the other cases, for example, the Chernobyl nuclear reactor accident in 1986, the radioactivity ratio immediately following the accident was reported to be 0.5–0.6, and that in the case of a nuclear-weapons test was reported as 0 because less Cs-134 was produced [26, 29]. These differences are known to be influenced by the nuclear reactor type and the fuel rod usage history. The radioactive decay graph across the ages, represented by equation (1), is shown in Figure 11. The initial concentration is given as 1 MBq/L.

$$N = N_0 \cdot (1/2)^{t/T} \tag{1}$$

In equation (1), N is the radioactivity, N_0 is the initial value of radioactivity, and T is the half-life period. The existence ratio of cesium (Cs-134/Cs-137) with time is estimated from the radioactive decay graph. To generate the existence ratio graphs of Cs-134, Cs-137, and their disintegration products, the corresponding number-concentration of atoms (parts/L), radioactivity ratio (Ecs134/Ecs137 = 1.0), and calculated value of the ratio of emissive photon energy (Table 3) are used. The ratio of emissive photon energy of Cs-134 to Cs-137 [(134)/(137)] is calculated to be 2.76, as listed in Table 3. The total emission ratio of Cs-134 is greater than 100% because of two-(multi-)photon production. As for Cs-137, the other photon energy emissions are not taken into account from the database because of the low photon energy or low emission ratio values. According to the dose conversion datasheet produced by IAEA [30], measured in unit-base [Sv/h], the ratio of radioactivity of Cs-134 to Cs-137 is calculated to be 2.6. The above calculation is in close agreement with the reported value.

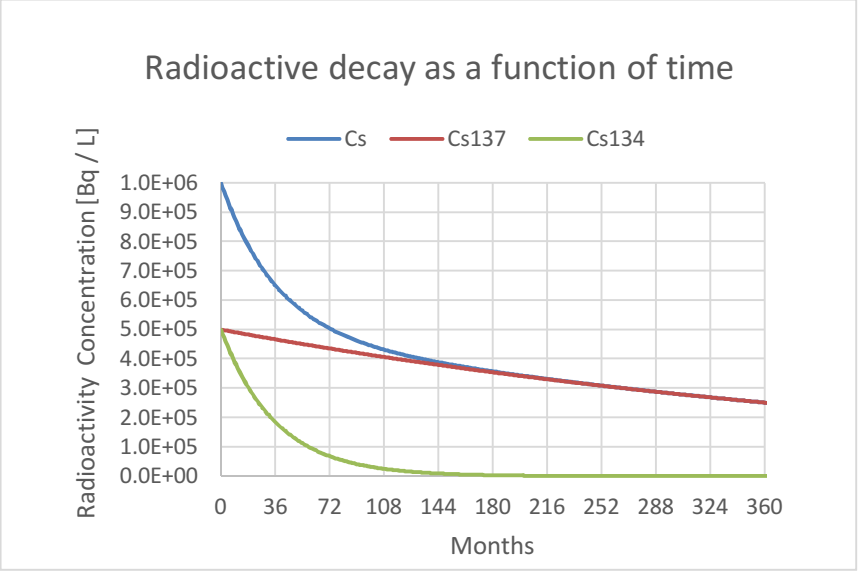

Fig. 10 Radioactive decay as a function of time

Table 3 Emission ratio corresponding to photon energy[2]

Cs isotope	Photon energy ε n [keV]	Emission ratio Pn [%]	Photon energy per decay $\bar{\varepsilon}$ = Σ(εn×Pn/100) [keV]	Ratio of photon energy of Cs-134 to Cs-137 $\bar{\varepsilon}(134) / \bar{\varepsilon}(137)$
Cs-134	242.738	0.027	1554.8	2.76
	326.589	0.0162		
	475.365	1.486		
	563.246	8.35		
	569.331	15.38		
	604.721	97.62		
	795.864	85.53		
	801.953	8.69		
	1038.61	0.988		
	1167.968	1.789		
	1365.185	3.014		
Cs-137	661.657	85.1	563.07	

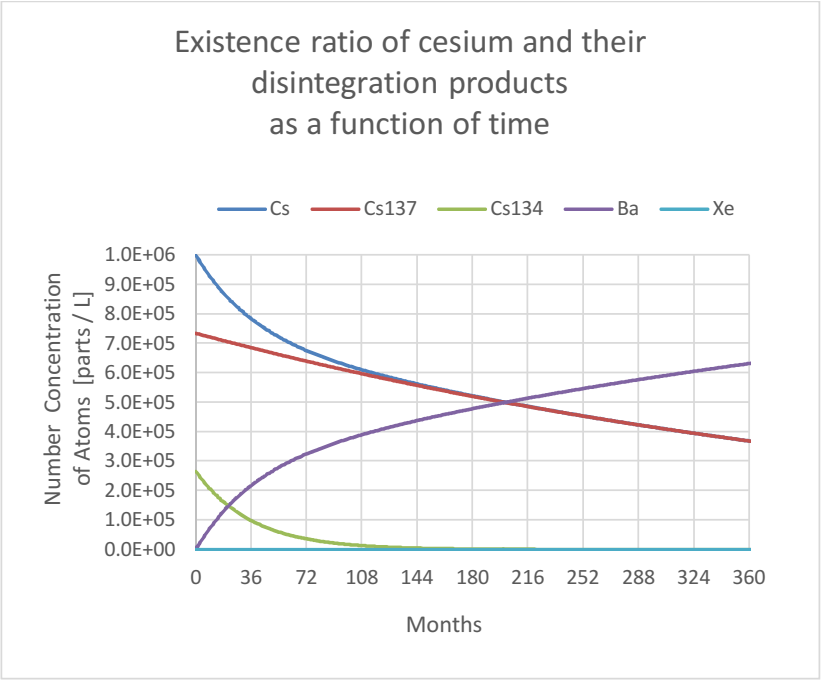

Fig. 11 Variation in the existence ratio of cesium (Cs-134, Cs-137) and their disintegration products as a function of time

[2] The database of photon energy and emission ratio is provided by the Japan Chemical Analysis Center (JCAC). (`http://www.jcac.or.jp/series.html`)

The initial existence ratio of cesium (Cs-134/Cs-137) is calculated to be 0.36 from the abovementioned radioactivity ratio (Ecs134 / Ecs137 = 1.0) and ratio of emissive photon energy [(134) / (137) = 2.76]. Figure 11 shows the existence ratio graphs of Cs-134, Cs-137, and their disintegration products corresponding to the number-concentration of atoms across the ages. This graph is generated with the assumption that the initial cesium number-concentration is 1 million per liter and the major components of cesium (Cs) are Cs-134 and Cs-137, where Cs-137 produces Ba-134 (Ba), and Cs-134 produces 99.9997% Ba-134 (Ba) and 0.0003% Xe-134 (Xe).

6 Conclusion

LIBS measurement of cesium and barium in sea sand is demonstrated under actual measurement conditions. When comparing the detection limits between the presented LIBS and the currently used germanium semiconductor detector, the germanium semiconductor exhibits sensitivity (LOD: 1 Bq/L) much higher than that exhibited by LIBS (LOD: 100 ng/L). However, a spectrum without self-emission cannot be obtained by the semiconductor detector because a stable isotope does not self-emit gamma rays. As shown in Figure 11, the amount of the stable element Ba-134 increases year by year. This implies that, while the gamma-ray level decreases with long-term monitoring, the amount of disintegrated elements increases; thus, the role of elemental analysis under sealed conditions is important. To realize a system combining all the advantages of the techniques discussed above, the expansion of the detection wavelength using LIBS in the gamma-ray region is one of the keys. In addition to the development of a high-sensitivity LIBS system, some additional techniques such as a high-power laser using a temporal double-pulse firing system, orthogonal beam crossing, and an optical layout with 45° observation are required. Although problems with in-situ measurement still exist, portable and real-time radiological assessment techniques have emerged for laboratory-based equipment through this study.

Acknowledgements. We would like to acknowledge the support by the DAIWA Anglo-Japanese Foundation Project, grant number: 9050/9942, for providing a grant. We are deeply grateful to the Japan Atomic Energy Agency (JAEA) for visiting the related facilities in Takasaki city and for the discussion. This work was also financially supported in part by a Waseda University Grant for Special Research Projects (2013B-198).

References

[1] Fabre, C., Maurice, S., Cousin, A., Wiens, R.C., Forni, O., Sautter, V., Guillaume, D.: Onboard calibration igneous targets for the Mars Science Laboratory Curiosity rover and the Chemistry Camera laser induced breakdown spectroscopy instrument. Spectrochimica Acta Part B 66(3-4), 280–289 (2011)

[2] Maruyama, Y., Blacksberg, J., Charbon, E.: A 1024×8 700ps time-gated SPAD line sensor for laser Raman spectroscopy and LIBS in space and rover-based planetary exploration. In: 2013 IEEE International Solid-State Circuits Conference (ISSCC 2013), pp. 110–112 (2013)
[3] Sobron, P., Wang, A., Sobron, F.: Extraction of compositional and hydration information of sulfates from laser-induced plasma spectra recorded under Mars tmospheric conditions — Implications for ChemCam investigations on Curiosity rover. Spectrochimica Acta Part B 68(1-16) (2012)
[4] McCanta, M.C., Dobosh, P.A., Dyar, M.D., Newsom, H.E.: Testing the veracity of LIBS analyses on Mars using the LIBSSIM program. Planetary and Space Science 81(48-54) (2013)
[5] Roger, R.C., et al.: The ChemCam instrument suite on the Mars Science Laboratory (MSL) rover: Body unit and combined system tests. Space Science Reviews 170(1-4), 167–227 (2012)
[6] Cremers, D.A., Beddingfield, A., Smithwick, R., Chinni, R.C., Jones, C.R., Beardsley, B., Karch, L.: Monitoring Uranium, Hydrogen, and Lithium and Their Isotopes Using a Compact Laser-Induced Breakdown Spectroscopy (LIBS) Probe and High-Resolution Spectrometer. Applied Spectroscopy 66(3), 250–261 (2012)
[7] Chinni, R.C., Cremers, D.A., Radziemski, L.J., Bostian, M., Northrup, C.N.: Detection of Uranium Using Laser-Induced Breakdown Spectroscopy. Applied Spectroscopy 63(11), 1238–1250 (2009)
[8] Fichet, P., Mauchien, P., Moulin, C.: Determination of Impurities in Uranium and Plutonium Dioxides by Laser-Induced Breakdown Spectroscopy. Appl. Spectrosc. 53, 1111 (1999)
[9] Young, J., Botheroyd, I.M., Whitehouse, A.I.: Remote Analysis of Steels and Other Solid Materials Using Laser-Induced Breakdown Spectroscopy (LIBS). In: Conference on Lasers and Electro-Optics Europe, CLEO 1998, p. 201 (September 1998)
[10] Penin, S.T., Chistyakova, L.K.: Uranium detection in aerosol particles on emission spectra of a laser plasma. J. Aerosol Sci. (27 Suppl.1), 333–334 (1996)
[11] Shen, X.K., Lu, Y.F.: Detection of uranium in solids by using laser-induced breakdown spectroscopy combined with laser-induced fluorescence. Applied Optics 47(11), 1810–1815 (2008)
[12] Wachter, J.R., Cremers, D.A.: Determination of Uranium in Solution Using Laser-Induced Breakdown Spectroscopy. Applied Spectroscopy 41(6), 1042–1048 (1987)
[13] Sarkar, A., Alamelu, D., Aggarwal, S.K.: Determination of thorium and uranium in solution by laser-induced breakdown spectrometry. Applied Optics 47(31), G58–G64 (2008)
[14] Emmert, L.A., Chinni, R.C., Cremers, D.A., Jones, C.R., Rudolph, W.: Comparative study of femtosecond and nanosecond laser-induced breakdown spectroscopy of depleted uranium. Applied Optics 50(3), 313–317 (2011)
[15] Frey, L., Kubodera, S., Wisoff, P.J., Sauerbrey, R.: Spectroscopy and kinetics of the ionic cesium fluoride excimer excited by a laser-produced plasma. JOSA B 6(8), 1529–1535 (1989)
[16] Ikezawa, S., Wakamatsu, M., Ueda, T.: Detection of Cesium from Pollucite Using Laser-Induced Breakdown Spectroscopy. Solid State Phenomena 199, 285–290 (2013)
[17] Cremers, D.A., Radziemski, L.J., Loree, T.R.: Spectrochemical Analysis of Liquids Using the Laser Spark. Applied Spectroscopy 38(5), 721–729 (1984)

[18] Vadillo, J.M., Vadillo, I., Carrasco, F., Laserna, J.J.: Spatial distribution profiles of magnesium and strontium in speleothems using laser-induced breakdown spectrometry. Fresenius J. Anal. Chem. 361(2), 119–123 (1998)
[19] Yamamoto, K.Y., Cremers, D.A., Ferris, M.J., Foster, L.E.: Detection of Metals in the Environment Using a Portable Laser-Induced Breakdown Spectroscopy Instrument. Applied Spectroscopy 50(2), 222–233 (1996)
[20] Mao, X., Bol'shakov, A.A., Choi, I., McKay, C.P., Perry, D.L., Sorkhabi, O., Russo, R.E.: Laser Ablation Molecular Isotopic Spectrometry: Strontium and its isotopes. Spectrochimica Acta Part B: Atomic Spectroscopy 66(11–12), 767–775 (2011)
[21] Cremers, D.A., Barefield II, J.E., Koskelo, A.C.: Remote elemental analysis by laser-induced breakdown spectroscopy using a fiber-optic cable. Applied Spectroscopy 49(6), 857–860 (1995)
[22] Multari, R.A., Foster, L.E., Cremers, D.A., Ferris, M.J.: Effect of sampling geometry on elemental emissions in laser-induced breakdown spectroscopy. Applied Spectroscopy 50(12), 1483–1499 (1996)
[23] Eppler, A.S., Cremers, D.A., Hickmott, D.D., Ferris, M.J., Koskelo, A.C.: Matrix Effects in the Detection of Pb and Ba in Soils Using Laser-Induced Breakdown Spectroscopy. Applied Spectroscopy 50(9), 1175–1181 (1996)
[24] Ikezawa, S., Wakamatsu, M., Pawlat, J., Ueda, T.: Sensing system for multiple measurements of trace elements using laser-induced breakdown spectroscopy. IEEJ Transactions on Sensors and Micromachines 129(4), 115–119 (2009)
[25] Kuwako, A., Uchida, Y., Maeda, K.: Supersensitive detection of sodium in water with use of dual-pulse laser-induced breakdown spectroscopy. Applied Optics 42(30), 6052–6056 (2003)
[26] Kawada, Y., Yamada, T.: Isotope News, vol. 697, pp. 16–20 (2012)
[27] Hino, Y.: Isotope News, vol. 690, pp. 20–24 (2011)
[28] Aoyama, M.: Radioisotopes, vol. 55, pp. 429–438 (2006)
[29] IAEA-TECDOC-1162, Generic procedures for assessment and response during a radiological emergency, p. 99

Energy-Efficient WSN Systems

R.S. Semente*, F.D.M. Oliveira, A.S. Lock, T.A.C. Melo,
S.N. Junior, and A.O. Salazar

Laboratório de Automação e Medição de Petróleo (LAMP),
Universidade Federal do Rio Grande do Norte, Salgado Filho Avenue, Natal, Brazil
rsemente@yahoo.com.br

Abstract. Due to increasing number of controllers, sensors and actuators in conventional instrumentation systems, cabling connection complexity has also grown, increasing time and maintenance cost. As a result, the use of IEEE 802.15.4 standard in Wireless Sensors Networks (WSN) have also increased, allowing faster maintenance time, as well as layout changes. In some applications, where there are no reliable sources of energy, the aspect of energy consumption is very important, as in environmental monitoring, mobile applications, agricultural industry and automation of oil wells. This book chapter presents the mainly practices to reduce energy consumption in wireless sensor networks and new techniques. A few of the new power-saving techniques are the Dynamic Scaling Voltage that is a real time reduction of the supply voltage, the Dynamic Modulation Schedule that allows channel characteristics changes according to the need for energy economy, Rational Time Sampling that change the duty cycle of the device dynamically, and the most used and most economical network protocols. A design of an energy-efficient system is presented, show the hardware and software detail of subsystem and communications aspects, emphasizing the control subsystem of charge and discharge, for uses with a solar panels, as well as software optimized for task of network controlling and sensing, both characteristics that leads a reduced consumption of energy. This chapter also presents a consumption estimation method to be used in WSN designs projects that allows the engineer to define the network characteristics as a set of performance requirements and suggests further developments in this area.

Keywords: Wireless Sensor Network, IEEE 802.15.4, Energy Efficiency, Power Management.

1 Introduction

Due to increasing number of controllers, sensors and actuators in conventional instrumentation systems, cabling connection complexity has also grown, increasing time and maintenance cost. As a result, the use of wireless networks has

* Corresponding author.

A. Mason et al. (eds.), *Sensing Technology: Current Status and Future Trends III*,
Smart Sensors, Measurement and Instrumentation 11, DOI: 10.1007/978-3-319-10948-0_6

also increased, allowing faster maintenance time as well layout modifications, among others [1-2]. In these networks information reliability and time response are important characteristics, found in cabling networks i.e. Fieldbus protocol [3]. However, wireless networks can barely satisfy Fieldbus protocol. In this sense, a number of international standards have modified gradually this scenario [4-5], by means of new technologies and protocols [3].

In power limited environments these problems are increased, since limited data retransmissions and signal power level decrease the reliability of the network.

A wireless sensor network must provide four key requirements that need to be satisfied for a credible deployment of WSNs in industrial environments [6-7]:

Scalability: the number of deployed sensor nodes may be very high, especially when large geographical areas need to be monitored;

Reliability: percentage of data packets correctly delivered to the network coordinator;

Timeliness: data packets delivered to the network coordinator within a predefined deadline;

Energy efficiency: extremely important as sensor nodes are typically powered by batteries with limited energy.

This book chapter presents the main techniques to save energy in WSN system based on IEEE 802.15.4, ensuring the four key requirements, especially energy efficiency requirement. A simple prototype WSN system is used and the techniques of rational sampling time, and a new efficient battery charger circuit, using solar panels present in the sensor nodes are implemented and tested. The network routing protocols are studied, presenting his energy consumption aspects through a simulation in NS2 with a scenery of large number of nodes. Experimental results have demonstrated the good performance of presented system.

1.1 Related Works

It is possible to save battery lifetime in energy scarce environments by means of many energy efficiency techniques, there are approaches based on energy saving techniques, data compression (Compressive Distribute), improvements in the routing algorithms [8] [9], and in sensor node hibernating scheme [10].

Regarding energy saving techniques, the most notable and recently used techniques are discussed in [11] as: Dynamic Voltage Scaling (DSV), Dynamic Modulation Scaling (DMS), Rational Time communication sampling and data compression.

[12] Presents a Harvesting Aware Speed Selection (HASS) system with two modes, centralized and distributed versions that use DMS and DSV techniques to control network consummation under dynamic performance changes, and tests by system simulating in TOSSIM Simulator. The results are compared with a system with no adaptive technique, show that HASS can reduce consummation in the tested environment.

[13] Presents a technique for DMS applications for long distance by using heuristics and testing in an simulation platform.

[14] Presents a distributive data compression scheme for large networks to reduce the amount of packets sent. It`s showed that central nodes spent more energy at compression, so its developed a algorithm that reduce data compression at these nodes. A MATLAB simulation compares the efficiency trough rise of number of nodes, proving the efficiency o the technique.

[15] Presents a hybrid system (centralized and distributed) to reduce the rate of sent packets, allowing a semi perpetual network, proving its feasibility through laboratory tests, and using a simulated rechargeable model based on values of solar panel power source obtained in practical tests. Unlike these articles, the system shown here is implemented and tested in real devices, and optimized according to the needs of a real plant to be controlled.

The recently works presents high efficient circuits using DMS and DSV, achieving a energy consuming of 375 nAh, to performs two measures and send information on 17.5 ms [16]. To achieve this efficiency its necessary uses low power microprocessor, several recent motes uses the MSP430, that 0.42 mA to 1.5 mA in wake mode and 0.6 uA to 2.6 uA in sleep mode [15-18].

IEEE 802.15.4 standard includes a power management mechanism [5], based on duty cycle, to minimize the activity of sensor nodes. However, this management mechanism provides very low reliability in terms of the percentage of data packets correctly delivered to the coordinator node [19].

2 System Overview

Transceivers (transmitters/receivers) based on IEEE 802.15.4 can operate in Industrial Scientific Medical (ISM) band, at 2,4 GHz frequency.

As this work is based on IEEE 802.15.4 it works with two types of nodes: Full Function Device (FFD) and Reduced Function Device (RFD). FFD nodes can work as a coordinator and as a final node. Coordinator is responsible for initiate, location addressing, network maintenance and nodes acknowledge, among others. FFDs can work also as intermediate routing without coordinator [20]. RFDs work as a final nodes, and transmit sensor signals and receiving commands to the actuators devices.

IEEE 802.15.4 normally supports star and cluster tree topologies. Mesh topology was introduced by Zigbee protocol [21]. Star topology allows that every final node (RFD) transmit information directly to network coordinator FFD, which can also route information among RFDs. However, RFDs cannot communicate each other. Star topology is more adequate for this work, since it possess only a few sensing nodes, at short distance. In addition, this topology is more adequate for energy efficiency, since it does not need to keep routing tables [20].

2.1 System Architecture

WSN system are organized in subsystems according to [22]:

1) Power supply subsystem: consisted in a solar panel, a battery pack and a battery charger, which is responsible for RFDs power feeding.

2) Sensing and actuators subsystem: perform sensor data acquiring and valves controlling in RFDs, as can be seeing at Fig. 1(b). It communicates with computing subsystem.

3) Computing subsystem: it is consisted of a flash memory and a PIC microcontroller. It is part of RFD and FFD nodes. In FFDs computing subsystem, the Programmable Logic Controller (PLC) is controls the plant. Also performs a modbus communication, which allows integration with higher-level services, including access devices for a supervisory system [23]. These supervisory can be accessed by internet, thus forming part of a large system, called "Internet of Things" (IOT), in a similar system detailed in [24].

4) Communication subsystem: it is basically an UHF radio composed by a few radio-frequency (RF) modules, according to IEEE 802.15.4. It is part of RFD and FFD nodes.

Subsystem communication RF modules are XBEE OEM RF Serie 2 (RFDs) and XBEE-PRO OEM RF Serie 2 (FFD coordinator). Both of them have a 32 KByte flash memory according to IEEE 802.15.4.

As communication interface between RFD and FFD nodes, PIC18F14K50 microcontroller is used. PIC microcontroller is chosen also because it is cheap and easy to access in national market. Microcontroller has the following functions: A/D conversion of pressure sensors, battery voltage verification, actuators command; digital input verification for piston sensors; communication with FFD coordinator, last data sensors storing; and USB communication (error communication verification) among others.

Figure 1 shows a block diagram of RFD (a) and FFD (b) nodes. Fig. 2 shows a RFD mounting according to subsystems set up considered [22]. It is placed in an industrial plant similar to the used in this work. In addition, as it can be observed in the Fig. 2, an explosion proof box is provided. This is due to high risk explosion environment. Thus, in a worst case, WSN network could help to evaluate damages.

2.2 Firmware

Figure 3(a) shows a flow diagram of a FFD coordinator. As it is shown in this figure, FFD is always waiting for an event: in transceivers, PLC, or USB. In addition, FFD firmware is verifying continuously for a change in the actuators commanded by PLC. If this information is received (that is represented by 'Yes' message at flow diagram), it responses accordingly: store the change in a register, actualize PLC registers, actualize USB registers, or command the actuators, respectively.

RFD devices present a sequence algorithm shown in Fig. 3(b). At start, a sleeping state of 5 s is introduced, for synchronization purposes. After that, microcontroller and transceivers wakes up. Microcontroller activates sensors and actuators, and then it sends data collected information to FFD by transceivers. All this must be performed in a 1.8 ms time period. After microcontroller sends its data, it introduces a 5 s sleep state. Thus, the entire cycle is beginning again.

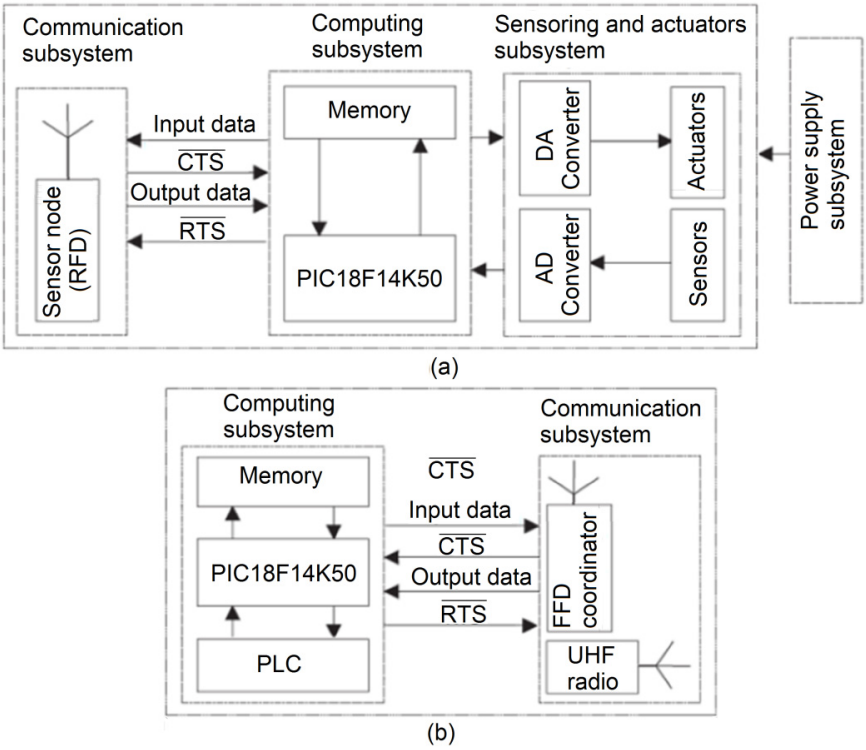

Fig. 1 (a) RFD block diagram. (b) FFD block diagram

Fig. 2 RFD sensor node Setup with solar panel

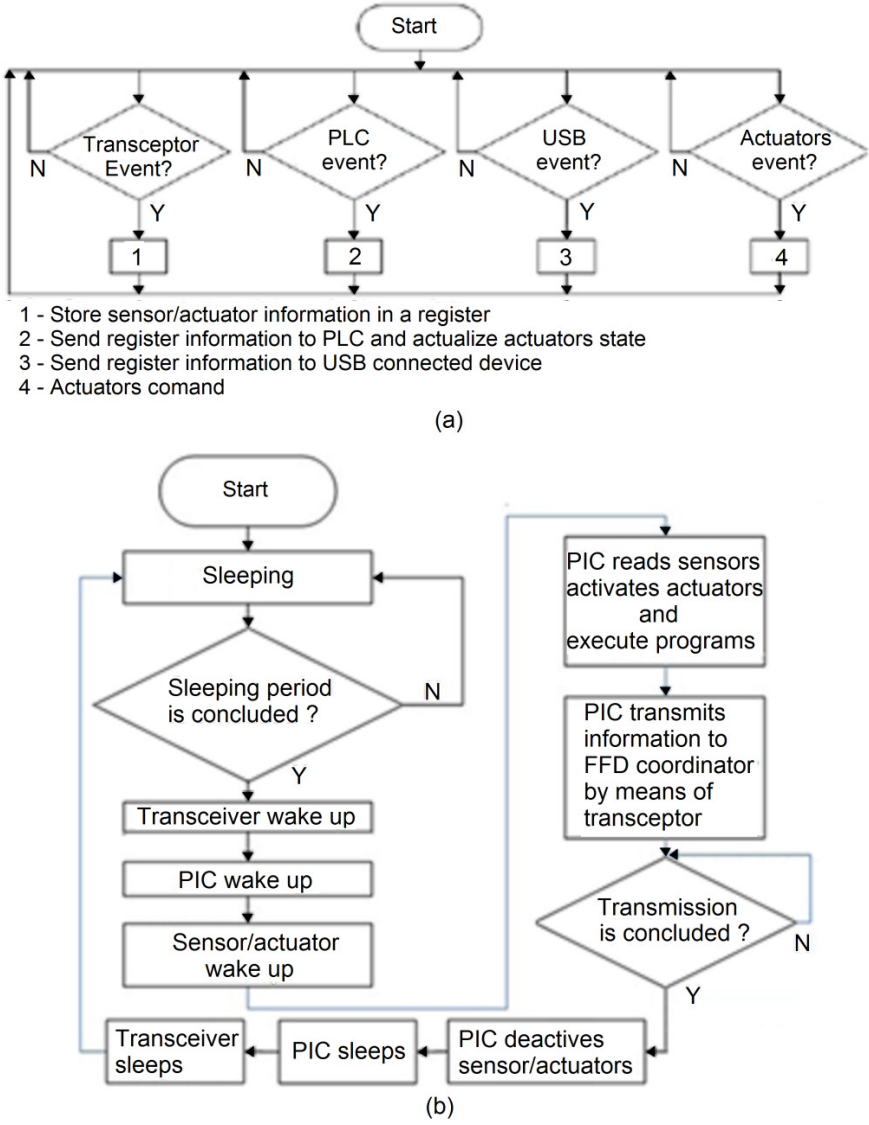

Fig. 3 Network logical diagrams a) Flow diagram of a FFD coordinator. b) RFD firmware, flow diagram

A RFD time diagram is shown in Fig. 4, for simplification purposes, it is considered two sensors and an actuator only. At first, sensor (S1) measures a physical variable (Mx) and transmits the data (Tx) to FFD coordinator (C). In this ideal case, FFD receives (Rx) the right data, with no communications error, and then it begins to sleep for 5 s. When sensor (S1) sleeps, sensor (S2) is sleeping also, waking up in a fixed time Δt, which is generated by microcontroller. After

wake up, sensor (S2) perform the same procedure that sensor (S1). After sensor (S2) sleeps, actuator (A) wake up, and waits for control data valves from coordinator (C).

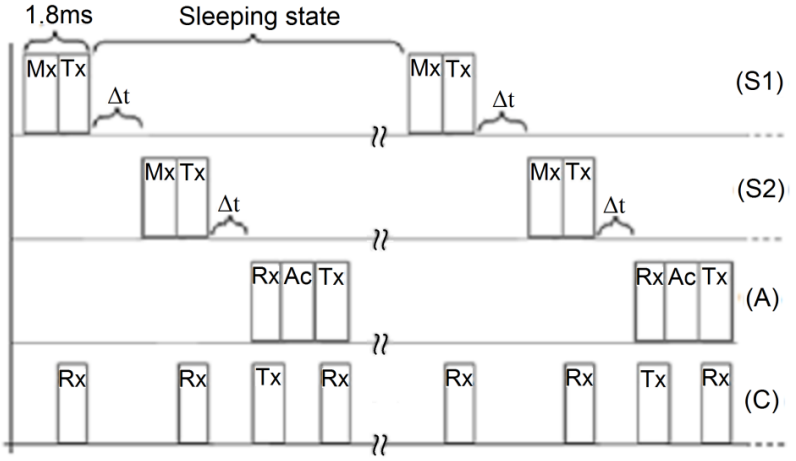

Fig. 4 RFD time diagram for two sensors and an actuator

After actuator (A) receives control data from coordinator (C),a control action is executed. Then actuator (A) sends a message to coordinator (C), communicating that its function was accomplished. After that, actuator (A) begins to sleep by 5 s. Thus, in a general way, RFD devices wake up in its respective cycle; do its function, and then sleeps again. It could be important to notice that a PLC acquisition time of 1.8 ms in a total period of 5000 ms guarantees perfectly also, impossibility of data collision.

3 Battery Charger Configuration

Many energy efficiency systems are proposed for scarce energy resource systems to extend battery lifetime [11]. However, in places where there is plenty of solar energy, these techniques can also be used. Battery discharges supplying sensors, actuators and microcontrollers when solar energy is missing (during night and foggy days). When solar energy is present, battery chargers supply energy to batteries and electronic equipment, using solar panels. The Fig. 5 show the battery charge topology configuration, presenting a consuming modeling of sensor is sleep resistan1ce R_{teN}, load resistance R_{LN} and the Key S_N.

In Fig. 5, battery chargers are CC converters in a Buck (reducer) configuration [7]. Switches Sk (k = 1, 2... n) symbolizes load charge when it is turned on/off. Load charge is turned on in a cyclic way. Solar Modules SM1, SM2, SMn are Solar Modules.

These modules feed battery chargers 1,2...n. Battery chargers energize battery pack E_1,E_2...E_n, constant load R_{te1},R_{te2}...R_{ten} and load charger R_{L1},R_{L2}…R_{Ln}.

3.1 Batery Charger Experimental Results

Experimental results are given in Fig. 6(b) for a battery charger type Buck converter. L = 1 mH, C = 2200 uF. The battery charger circuit is presented in Fig. 6(a), and it`s equivalent to any of battery chargers shown in Fig. 4. It is a closed loop, Pulse Width Modulation (PWM) controlled system, carrier frequency of 10 KHz. A MOSFET switch is chosen at the input converter, due to its low price, easy to access in market, and by its high input resistance, which allows simple firing circuits.

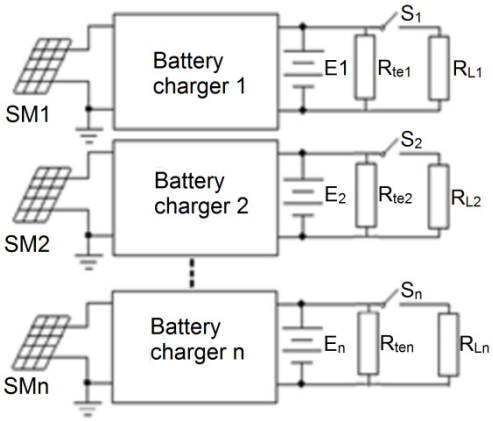

Fig. 5 Battery chargers topology for a battery pack

Solar radiation is assumed to change faster in order to induce V_{in}, output voltage solar-module, as a triangular wave with a period of 10 s. This is done to test battery charger dynamic performance. Since in real case, solar radiation can change slowly. Note that battery is represented only by a capacitor C to verify battery charger performance in harder conditions. Switch S is on/off synchronized to V_{in} to illustrated capacitor voltage behavior, which does not change against different values of Vin, when S is on/off, see Fig. 6(a). In addition, it can be noted that inductor current (i1) presents a discontinuous behavior and Drain-Source voltage of power MOSFET (v1) is relatively low (normally 1.5 V) peak voltage is also 1.5 V due to low voltages involved, see Fig. 6(b).

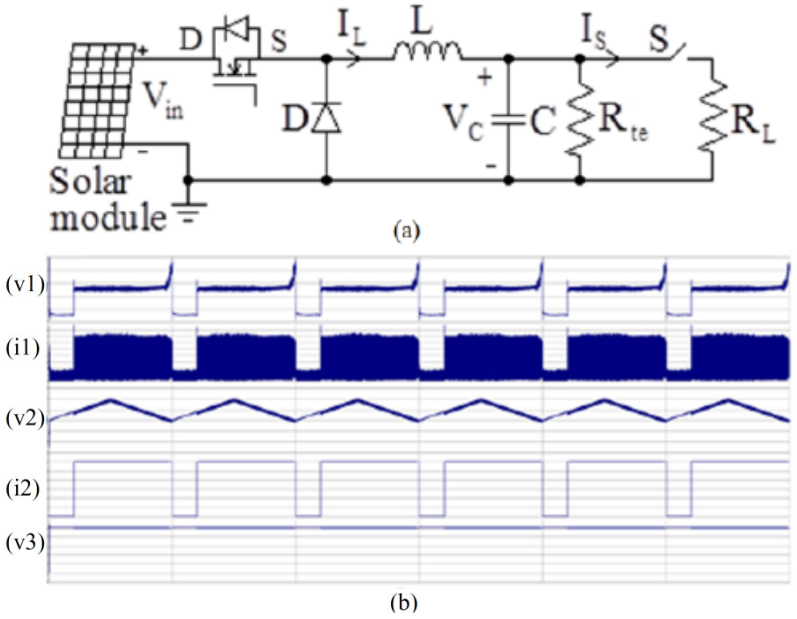

Fig. 6 a) Battery charger based on a Buck CC/CC converter. (b) Experimental result. (v1) Drain-Source voltage V_{DS} (0.5V/div). (i1) Inductor current I_L (0.2 V/div). (v2) Solar module voltage Vin (5 V/div). (i2) Switch current I_S (0.1 A/div). (v3) Output voltage V_C (2 V/div). Time: 5 s/div. R_{te2} R_{L2} E_2 S_2

Outdoor test parameters, performed in industrial environment, are the following:

- Communication time: 24 days.
- Total number of sent packets for a RDF node: 6965.
- Total number received packets for a FFD coordinator: 6274.
- Distance among RFD and FFD nodes: 5 meters.
- Max Distance among RFD nodes: 2 meters.

4 Routing Techniques

Routing in WSNs can be more demanding than in other wireless networks, such as mobile ad-hoc networks or cellular networks, for the following reasons [25]:

- WSN nodes usually are stationary nodes after their installation, which results in predictable and infrequent topological changes;
- Sensor nodes demand a careful management of resources because of their severe restrictions on energy, processing, and storage;
- The project requirements of a WSN depend on the application because WSNs are designated to a specific kind of application;

- Almost all the applications of WSNs requires flow of sensing data from several sources to a particular base station;
- The data collection is, under normal conditions, based on location, therefore, the correct position of sensor nodes is important. The position is detected by using methods based on triangulation, for instance by the transceiver power and for some known points. Thus, it is possible to use a hardware equipped with Global Positioning System (GPS) for this purpose. However, it is desirable to have independent solutions of GPS for the problem of location in sensor networks because the use of GPS generates additional energy consumption.

Due to these factors, several new routing mechanisms have been developed and proposed to solve the problem of routing in WSNs. These mechanisms have considered inherent characteristics of WSNs along with application and architecture requirements. A scheme of efficient routing will offer significant reductions of energy costs and improve the longevity of the network. Finding and maintaining routes in WSNs are important issues to worry about because restrictions on energy and unexpected changes on the node status (for example, inefficiency or failure) can give rise to frequent and unexpected topological changes. Routing techniques proposed in the literature for WSNs use some tactics of routing that are known and appropriated for WSNs in order to minimize their energy consumption [26].

The routing protocols can be classified as flat (reactive or proactive), hierarchical, location-based, and hybrid [27].

In reactive routing protocols, the network nodes only start the processes of route discovery at the point that there is any information to be transmitted. An advantage of this strategy is that the routes are adaptable to an environment that can constantly change in a WSN (by inserting and removing nodes, for example), once that every node may update its routing table when it happens a change of topology and then, determining new routes. This, however, implies constant recalculation during the data transmission and then, resulting in highest latency of network and increasing energy consumption [27]. Some examples of traditional reactive protocols are DSR [28] and AODV [29].

Proactive routing protocols try to keep on the consistency by updating the routing information from every node to all the other nodes from the network. The use of proactive protocols, therefore, is not recommended to all of the applications because a significant part of network bandwidth is exclusively consumed for maintenance of routing tables of network nodes [30]. Examples of traditional proactive protocols are OLSR [31] and DSDV [21].

Normally, when a wireless network grows up (beyond a certain limit), the flat routing protocols become unfeasible due to the link and data processed overhead. A way to solve this problem consists in hierarchical routing. The wireless hierarchical routing is based on the idea of organizing nodes in groups by assigning different characteristics in and out of the group. Both the size of the routing table as the update package size is reduced by inserting the nodes in a

single portion of network instead of in it all. Thus the overload of data becomes low. The most common way to implement the hierarchy is by grouping nodes geographically close to each other to form a group (cluster). Every node in the cluster has a leader (cluster head) that communicates itself with the other nodes in the cluster [26]. CGSR [32] and LEACH [33] are examples of traditional hierarchical protocols.

The routing protocols based on geographical location use information about the position of nodes to determine the best route. The position of the node in the network is determined by the GPS (Global Position System). Such protocols can behave as simple or hierarchical if techniques and devices of geolocation had been inserted. The location-based protocols can represent, therefore, a limiting factor to the use in WSNs due to hardware constraints and, specially, the additional energy consumption in sensor nodes [26]. Due to these factors, such protocols are not used in simulations in this work. Examples of protocols based on location that are worried about the economy of energy: GEAR [34] and GPSR-TPC [35].

Hybrid routing protocols can merge characteristics of flat and hierarchical protocols by using or not geolocation techniques. These protocols were designed to improve the scalability allowing that close nodes work together to form a kind of group and then, reducing the overload of network from the route discovery. It is usually performed by the proactive maintenance of routes among the neighboring nodes and determining routes of distant nodes through the technique of route discovery [26]. Some hybrid routing protocols are DDR [36] and ZRP. ZRP is used by ZIGBEE communication protocol [37].

4.1 Fault-Tolerant Routing Protocols Oriented by Energy Conservation

The characteristics of the environment where wireless sensor nodes typically operate, in addition to severe limitations of resources and energy, turn the routing into a challenging problem. The route selection must be done by considering maximized the network lifetime [38].

There are some techniques that can help in developing routing protocols oriented by energy conservation. A simple strategy is avoiding that routes that do not guarantee reliability affect the performance of WSNs as a whole. Link failures and packet losses provide several retransmissions which results in high-energy consumption [39]. Thus, a careful selection of links is desirable to increase the performance of a fault-tolerant routing protocol. The nodes can also use adaptive mechanisms of resources based on their levels of energy. If the node is in critical level of energy, it can reduce its participation in routing operations by reducing or eliminating certain activities completely, such as data or control packet forwarding which are not addressed to it [38].

Another technique consists in minimizing the energy consumption by avoiding linkages with high cost of communication, thus making the congestion control to be vital [40]. The routing protocol must also guarantee that the network

connectivity is maintained for as long as possible. A good method that guarantees the availability is the uniform load distribution through the network instead of avoiding that part of the route is diverted due to shortage of energy of the nodes from that region [41].

The approach of power adjustment allows the nodes varying their transmission power to reduce their energy consumed in transmission. Instead of transmitting in high power of transmission, the nodes work collaboratively to adjust and find the transmission power appropriated to form a network connected [42]. The approach of power mode is the technique that explores the resource of the operation mode available on the network interface of sensor nodes to obtain energy saving. There are four modes of operation for nodes: sleep, idle, transmit, and receive. In order to transmit or receive packets, the nodes must transit to idle mode. However, the ongoing listening of packets received that are not addressed to idle nodes can contribute to the dissipation of high energy that is very significant if it is compared with the ones on sleep mode. It suggests that the redundant nodes that are on idle mode can be changed to the mode of energy saving, that is, to sleep mode. This resource has been used in topology control to optimize energy and to prolong the network lifetime without sacrificing its capacity and connectivity [43].

Another technique that guarantees energy saving is data aggregation. The data collected by several sensor nodes of same kind and in proximity has higher probability to be similar, which allows their data being aggregated, and so eliminating redundancy and decreasing the network transmissions [44].

Partitioning the network into clusters also results in higher energy conservation. In WSNs that use this technique, each grouping (cluster) is managed by a node, called by the name of clusterhead, and its responsibility is coordinating activities within the grouping and forwarding data among the clusters [38]. Routing protocols that use this technique are called hierarchical, as described above, and they can reduce the energy consumption for a variety of reasons: a node can communicate with its clusterhead instead of communicating directly with the central node, and so it reduces the cost of routing and, consequently, transmissions through the network. Furthermore, within a cluster, the sensing data can maintain data patterns similar to their neighboring nodes, which allows using the technique of data aggregation, the one that was seen previously [45]. The advantage of clustering is that a particular task can be restricted to a set of nodes called by the name of clusterheads, and they can be assigned to the collecting, processing, and forwarding of packets of non-clusterheads nodes. This mechanism provides an efficient organization of the network. Other benefits of clustering approaches include load-balancing and data aggregation or data compression to prolong the network lifetime. In some clustering approaches, the selection of clusterheads remains fixed. Thus, clusterheads usually experience the energy depletion more rapidly because they are overloaded with several tasks. This problem is overcome by randomizing of the selection of clusterheads and, consequently, distributing the load fairly among the network nodes [42][46].

The hybrid approach is a technique of topology control that uses some way of clustering combined with other techniques such as, power adjustment or mode of energy to reach the additional energy saving [42]. This approach will be seen in practice through simulation and testing of the proposed system.

Therefore, fault-tolerant routing protocols and oriented by energy conservation developed for WSNs represent an additional challenge because they cannot be computationally complex but efficient, guaranteeing the continuity of the network when failures that can arise.

4.2 Simulation Parameters and Metrics

All simulations were performed on NS-2, using XBeePro (TM) parameters, based on IEEE 802.15.4 standard, operating on 2.4G hz frequency, whose outdoor communication has a reach of up to 1,600 m. The data rate is assumed to be 250 kbps and the power of transmission is set to 60mW. The simulation scenario was consisted by 80 sensor nodes that was distributed in grid 300m distant from each other, and one sink, positioned in the upper left corner of the scenario. The entire message size is assumed to be 70 Bytes. The energy required to perform a communication is 40mA (Tx) and 38mA (Rx). The power consumption in sleep mode is 3.5 μA. The initial energy of each node was estimated at 10 Joules. Transmission time is set up to 41ms and, in sleep mode communications, sleep time is assumed to be 5s. To improve the accuracy of the tests, 10 rounds of 1000s were performed for both always-on and sleep communication modes.

The metrics considered for the simulations are based on [47].

The Routing protocols used in the simulations are AODVJr (reactive flat), LEACH and HTR (these last ones are hierarchical). The AODVJr and HTR are the protocols used by ZIGBEE communication protocol [37].

4.3 Remaining Power of Sensor Nodes in Data Transmission

The remaining power of a sensor node in data transmission is considered as the metric to analyze the performance of the protocols in terms of power. In the graphs generated, two situations are observed: critical condition, where it is considered that 51% of the nodes start to get dangerously out of energy to perform the operations of data transmission (value set at 5 J) and; node failure, when the remaining power reaches a value equal to or less than 2 J.

Figure 7 illustrates the behavior of the three routing protocols analyzed in continuous transmission (always-on mode). The AODVjr and the LEACH started their communication on very close times (T = ±180 s), while the HTR started at time T = ± 50.2 s.

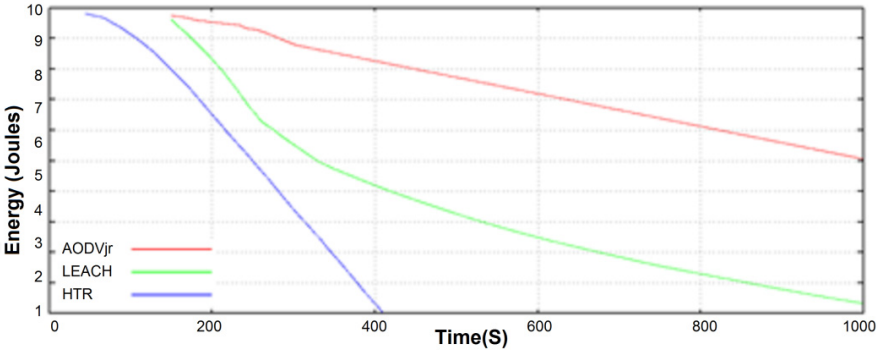

Fig. 7 Average Remaining Power of Sensor Nodes x10 rounds in Data Transmissions at Always-on Scheme. Comparative between AODVjr, LEACH and HTR.

In always-on mode it is observed that the AODVjr had the best performance compared to the other two protocols analyzed, even entering in critical condition during the simulation time. Despite a delay to start the transmission, due the allocation of tables into the nodes and into the sink, once recognized all network nodes, such tables do not need more to be rebuilded, since this scenario has no mobile node and no node enters or leaves the network. This situation is not observed with LEACH , passing to the critical state at T = 329.84 s and crashing at T = 680.53 s. The worst performance was recorded by HTR because at T = 250.95 s the nodes entering on a critical state, failing at T = 345.74 s. The poor performance of hierarchical networks in always-on mode is due to the necessity of the existence of clusters coordinator nodes, tending to an increase in energy consumption , if compared to AODVjr that, being flat, requires only a single coordinator (sink).

Best situation for the hierarchical protocols can be seen in Fig. 8, whose simulated communication scheme was the sleep mode. The AODVjr entered in critical condition at T = 450.73 s, no longer transmitting data to the sink at T = 895.73 s. The reason for this poor performance is the constant reboot of the routing tables at each restart of the transmission cycle, representing a considerable increase in energy consumption of the nodes. The HTR and LEACH protocols had an excellent performance, even entering in critical condition during the simulation time where the HTR got small advantage. How hierarchical protocols do not need to reset the routing tables at each restart of the communication cycle, the energy consumption in all cycles is much lower than that registered by the plans protocols, such as AODVjr. So, in terms of energy consumption, hierarchical protocols, at sleep mode have the best performance in topologies similar to that used in this simulation scenario.

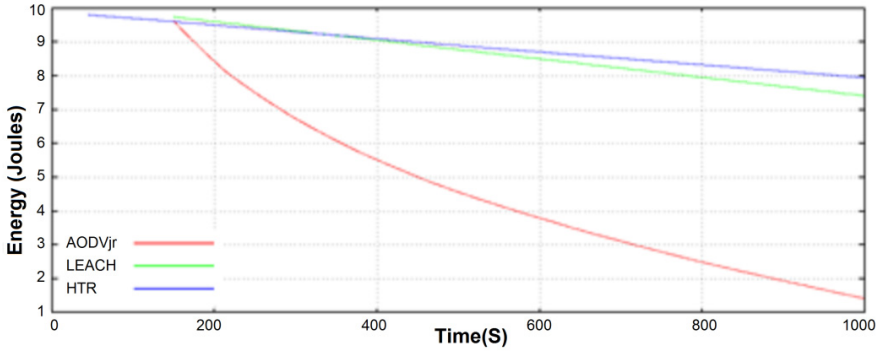

Fig. 8 Average Remaining Power of Sensor Nodes x10 rounds in Data Transmissions at Sleep Mode Scheme. Comparative between AODVjr, LEACH and HTR.

4.4 Throughput

The throughput metric measures how well the network can constantly provide data to the sink. Throughput is the number of packet arriving at the sink per second.

Figure 9 shows average throughput of existing studied protocols. In this chart, is noted that the AODVjr maintained a higher throughput in always-on mode (555 B/s) compared to the LEACH (392.3 B/s). The HTR had the lowest throughput (61.9 B/s), since this protocol fails prior to the simulation end, thus sending no data to the sink. Thus AODVjr is the most suitable routing protocol in scenarios similar to the one used in this simulation, when energy saving is not a factor impacting the application.

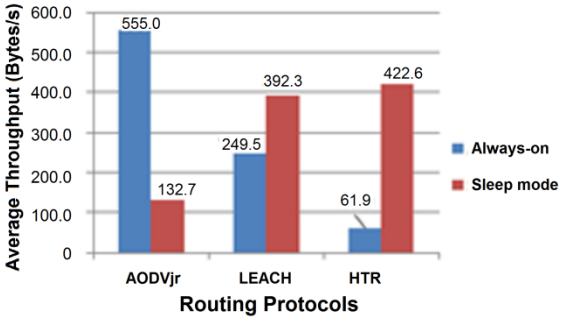

Fig. 9 Average throughput x10 rounds in always-on and sleep communication scheme. Comparative between AODVjr, LEACH and HTR.

When the sleep mode is implemented, there is a significant improvement of throughput in hierarchical protocols if it is compared to AODVjr (132.7 B/s). The LEACH and the HTR had the highest throughput rates (392.3 B/s and 422.6 B/s, respectively). Those protocols have maintained their energy performance during

the simulation time, transmitting more packets to the sink, while the AODVjr failed before the end of the simulation. Therefore, for WSN applications that require greater energy savings, hierarchical protocols (notably the HTR, which achieved better results) were more suitable for schemes that require hibernate the transmitter sensor node.

4.5 Packet Loss

One of the most important metrics in real-time remote sensing networks is packet loss and reflects the number of data packets that are not successfully sent to the destination during the transmission. In Fig. 10 LEACH and HTR presented higher packet losses in always on scheme (75.24% and 94.72%, respectively). This corroborates the fact that the hierarchical protocols have a greater energy consumption during the communication process due to maintenance sub-coordinators, that are responsible for each cluster, thus precluding their use in networks similar to the topology used in this work . The AODVjr got the lowest packet loss registered in continuous communication (16.45%), which confirms the fact of maintaining routing tables during the simulation time and the existence of a single coordinator for management of the entire network, spending less total energy, consequently.

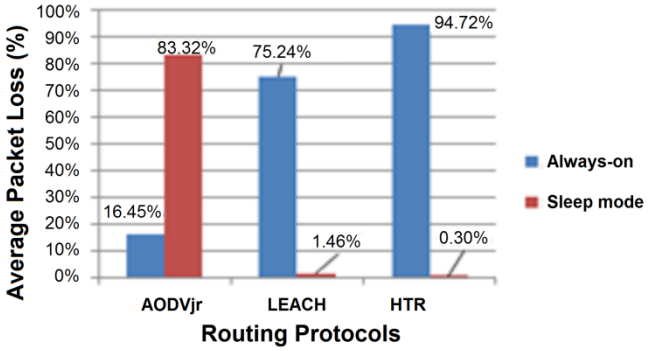

Fig. 10 Average packet loss x10 rounds in always-on and sleep communication scheme. Comparative between AODVjr, LEACH and HTR.

Significant improvements in packet loss can be perceived in sleep mode communications, except for AODVjr, gbgbafgvwhich registered a loss of 83.32%, indicating the rebuilding of routing tables with each new round of activation of the sensor node, taking considerable time, extrapolating the communication limit and increasing the power consumption. Both LEACH and HTR maintained an acceptable percentage of losses (1.46% and 0.30% respectively), below the desirable margin of 5% for this application, showing its viability in hierarchical networks configuration.

5 Lifetime Estimation

To calculate the expected lifetime of a sensor node it can be useful define the duty cycle (δ), given by (1).

$$\delta = tc / T \tag{1}$$

Where t_C is time when load charge is on (electronic equipment) and T is sample time. T can take a number of values according to process. For petroleum and chemistry process T is considered a few seconds. The others parameters used in equations of this section are presented in Table 1.

Table 1 Parameters used in the equations for estimating the lifetime

Parameter	Description
δ	Duty cycle
t_C	Time when load charge is on
T	Sample time
T_m	Sampling process times
Ta	Autonomy Time
C_B	Maximum current that battery can supply
I_B	Battery consuming current
Ite	Consuming current energy circuits
I_L	Consuming current microcontroller and communications system

However, for system synchronization T must be the minimum sample time. Thus, if T_1, T_2...T_m are sampling process times, T must be

$$T = \min\{T_1, T_2 \ldots T_n\} \tag{2}$$

Considering a slow system with T is 5 s, corresponding to slow process, and t_C corresponds to a Programmable Logical Computer (PLC) acquisition time (1.8 ms). Other useful concepts are battery capacity C_B (Ah) and autonomy time T_a (h). C_B is maximum current that battery can supply in an hour. Autonomy time T_a is time that battery can work before it needs to be substituted. Thus, for a battery consuming I_B (A) constantly, its autonomy time (in hours) is

$$T_a = C_B / I_B \tag{3}$$

Analogously, for a battery consuming I_{te} (A) constantly and a current I_L when in active mode only δ (%) of time, its Autonomy Time Ta is

$$T_a = C_B /(I_{te} + \delta I_L) \tag{4}$$

This is what energy efficiency techniques usually do. Instead of consuming a constant current I_{te} (load circuits) plus a load current I_L (microcontroller and communications system) all the time, electronic equipment is energized only part

of the time (δ%) increasing autonomy time. For instance, consider Cb = 2000 mAh, Ite = 10 mA and I_L = 20 mA. In this case Ta = 67 hours. If now load current duty cycle is considered, i.e. δ = 0.01, then Ta = 196 hours (almost three times).

However, for rechargeable battery technologies, this time can be extended. In present work, battery set up is formed by ten AA battery pack (Li-ion) of 1.2 V, Cb = 1100 mAh and dimensions of 44 mm x 10 mm.

Equation (4) was used to calculate autonomy time. Time and current consumption parameters measured in an oscilloscope are presented ate Table 2.

Table 2 Parameters used in estimating the lifetime of the developed system

Parameter	Description	Value
T_{rx}	Receiving time	0.6 ms
T_{tx}	Transmission time	1 ms
T_{ma}	Measure/Actuating time, for measuring a variable or turn on/off an actuator	1.8 ms
T_{slp}	Optical scattering (fluorescence)	5 s
I_{rx}	Current consumed when data is received	38.4 mA
I_{tx}	Current consumed when data is transmitted	43.2 mA
I_{ma}	Current consumed when a variable is measured	63.2 mA
I_{slp}	Current consumed in sleeping state	0.018 mA

The I_{ma} parameter has two cases, when a variable is measured (5 mA) or when an actuator is turned on/off (20 mA) plus 43.2 mA consumed by computing subsystem. This is 48.2 mA for a measured variable (sensor node) or 63.2 mA for an actuator as can be seeing at Fig. 11.

As a consequence, I_{ma} can be considered as 63.2 mA. So, this is the larger current, then it's considered to be present during a duty cycle δ = 0.00036.

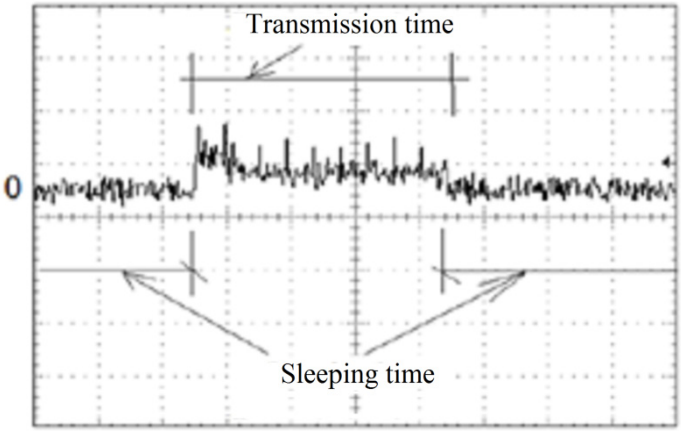

Fig. 11 Current consumption for a sensor RFD node (Vert.: 100mA/div, Hor.: 0.25ms/div)

With no sleeping state considered, Autonomy Time, WSN system is 17.4 h which is not acceptable.

However, with sleeping state $\delta = 0.00036$, $I_L = I_{ma} = 63.2$ mA and $I_{te} = I_{slp} = 0.018$ mA in (4). Thus, Autonomy Time, T_a, is 26992 h or 1124.689 days (3.08 years).

A qualitative analysis of (4) can be realized by simulations as it is shown in Fig. 12. In this figure, Autonomy Time vs. duty cycle is presented as a function of load current I_L. An Autonomy Time T_{al} of 6 months (4320 h) is used as a reference. It can be observed that an increasing in load current leads to a diminution in duty cycle, to achieve the same Autonomy Time.

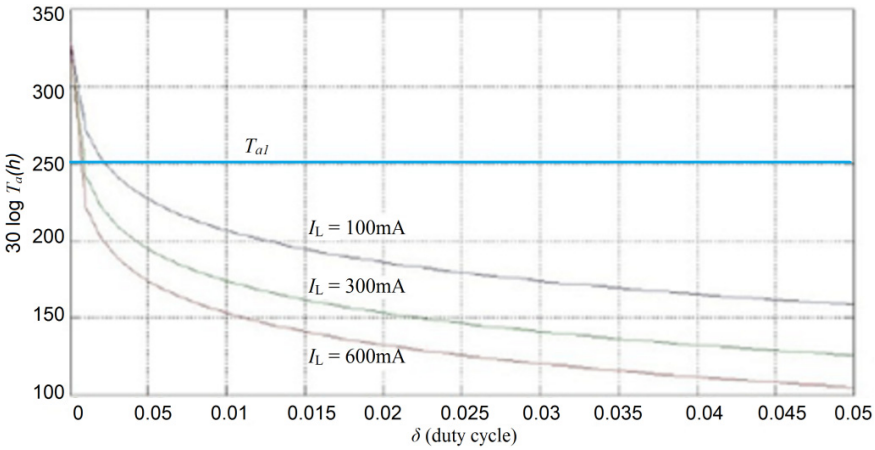

Fig. 12 Battery Autonomy Time in hours T_a (30log) vs. duty cycle δ, as a function of load current, I_L. $T_{al} = 4320$ h or 6 months (30log) is used as a reference

6 Conclusion

This book chapter presents a WSN network system, mainly ensuring the key requirement of energy efficiency, through the study and implementation of a battery charger mechanism, present in the sensor nodes, by use of a rational time sampling technique, and a network simulation to test the routing protocols.

As shown at the experimental results, WSNs based on IEEE 802.15.4 standard can easily increasing the sensor lifetime, due to a energy harvest system, like solar panels, and a rational hibernating system.

Using energy harvest system, the battery lifetime can be improved by three times of the original time. Moreover, using both resources: the energy harvest and the rational sampling, the lifetime can be improved in years, representing almost a perpetual system.

Experimental results are also present to illustrate battery charger dynamic and static behavior. Particularly, it is useful to observe battery charger response against

solar panel input voltage. This is, since solar energy variation is slow, the solar modules can randomly capture that energy.

At network layer, a simulation scenario was created under a large number of sensor nodes, comparing three routing protocols (AODVjr, LEACH and HTR), showing that AODVjr is the most suitable for networks that use the always-on technique and showing that HTR is the most efficient protocol at networks that use the sleep mode technique.

The physical energy efficiency scheme based on solar panel battery charger, that was developed at this work, could also be used with other topologies or approaches, since this is a hardware level implementation.

An estimation lifetime method was also presented, that has main simplicity characteristics and low input parameters. It was used to calculate the expected lifetime of the presented system, giving 3.08 years of energy to operate.

References

[1] Gungor, V.C., Hancke, G.P.: Industrial Wirelless Sensor Networks: Challenges, Design Principles, and Technical Approaches. IEEE Trans. Industrial Electronics 56, 4258–4265 (2009)

[2] Petersen, S., Doyle, P., Vatland, S., Aasland, C.S., Andersen, T.M., Sjong, D.: Requirements, drivers and analysis of wireless sensor network solutions for the Oil & Gas industry. In: 2007 Proc. ETFA Conf., 25-28, pp. 25–28 (2007)

[3] Willig, A., Matheus, K., Wolisz, A.: Wireless Technology in Industrial Networks. Proc. of the IEEE, 1130–1151 (2005)

[4] IEEE 802.11a-1999: Highspeed Physical Layer in the 5 GHz Band. IEEE Standard (1999)

[5] IEEE 802.15.4-2006: Wireless Medium Access Control (MAC) and Physical Layer (PHY) Specifications for Low-Rate Wireless Personal Area Networks (LR_WPANs). IEEE Standard (2006)

[6] Willig, A.: Recent and emerging topics in wireless industrial communications: A selection. IEEE Trans. Industrial Informatics 4(2), 102–124 (2008)

[7] Zurawski, R.: Networked embedded systems: An overview. In: 2009 Proc. Networked Embedded Systems, pp. 1.11–1.16 (2009)

[8] Heo, J.-Y., Hong, J.-M., Cho, Y.-K.: EARQ: Energy aware routing for real-time and reliable communication in wireless industrial sensor networks. IEEE Trans. Industrial Informatics 5(1), 3–11 (2009)

[9] LoBello, L., Toscano, E.: An Adaptive Approach to Topology Management in Large and Dense Real-Time Wireless Sensor Networks. IEEE Trans. Industrial Informatics 5(3), 314–324 (2009)

[10] Anastasi, G., Conti, M., Francesco, M.D.: Extending the lifetime of wireless sensor networks through adaptive sleep. IEEE Trans. Industrial Informatics 5(3), 351–365 (2009)

[11] Anastasi, G., Conti, M., Francesco, M.D., Passarella, A.: Energy conservation in wireless sensor networks: A survey. Ad Hoc Networks 7, 537–568 (2009)

[12] Bo Zhang, R., Simon, H.: Aydin,: Harvesting-Aware Energy Management for Time-Critical Wireless Sensor Networks With Joint Voltage and Modulation Scaling. IEEE Trans. Industrial Informatics 9(1), 514–526 (2013)
[13] Zhang, W.X., Ru, Y.D., Ma, Y.H., Guo, J.K.: The Study on Communication Energy Saving Algorithm of Wireless Sensor Network. Key Engineering Materials 500, 500–556 (2012)
[14] Caione, C., Brunelli, D., Benini, L.: Distributed Compressive Sampling for Lifetime Optimization in Dense Wireless Sensor Networks. IEEE Trans. Industrial Informatics 8(1), 30–40 (2012)
[15] Liu, R.-S., Fan, K.-W., Zheng, Z., Sinha, P.: Perpetual and Fair Data Collection for Environmental Energy Harvesting Sensor Networks. IEEE/ACM Trans. Networking 19(4), 947–960 (2011)
[16] Nanda, K., Babu, H., Selvakumar, D., Dwarakanath, T., Nayak, K., Venkatesh: Smartmote - An innovative autonomous Wireless Sensor Node architecture. In: 2014 IEEE International Conference on Electronics, Computing and Communication Technologies (IEEE CONECCT), January 6-7, pp. 1–6 (2014)
[17] Ivoghlian, A., Wang, K.I.-K., Salcic, Z.: AWSAM-3: A low power miniaturised wireless sensor mote. In: 2013 Seventh International Conference on Sensing Technology (ICST), December 3-5, pp. 103–108 (2013)
[18] Watteyne, T.: eZWSN: Experimenting with Wireless Sensor Networks using the eZ430-RF2500. tutorial. University of California, Berkeley (2012)
[19] Anastasi, G., Conti, M., Francesco, M.D.: A Comprehensive Analysis of the MAC Unreliability Problem in IEEE 802.15.4 Wireless Sensor Networks. IEEE Trans. Industrial Informatics 7(1), 52–65 (2011)
[20] Karl, H., Willig, A.: Protocols and Architectures for Wireless Sensor Networks. Wiley, New York (2005)
[21] ZigBee Alliance, ZigBee specification standard (October 2007)
[22] Vieira, M.A.M., Coelho Jr., C.N., Silva Jr, D.C., Mata, J.M.: Survey on wireless sensor network devices. In: 2003 Prof. IEEE-ETFA Conf., pp. 537–544 (2003)
[23] Maitelli, A.L., Salazar, A.O., Novaes, F., Xavier, D., Cortez, E.: Simulador do Método de Elevação Artificial Plunger Lift. In: 2012 Proc. Rio Oil & Gas Expo Conf., pp. 1–10 (2012)
[24] Kyusakov, R., Eliasson, J., Delsing, J., van Deventer, J., Gustafsson, J.: Integration of Wireless Sensor and Actuator Nodes With IT Infrastructure Using Service-Oriented Architecture. IEEE Trans. Industrial Informatics 9(1), 43–51 (2013)
[25] Savvides, A., Han, C., Srivastava, M.: Dynamic Fine-Grained Localization in Ad-Hoc Networks of Sensors. In: Proc. 7th ACM Annual International Conference on Mobile Computing and Networking (MobiCom), Italy, pp. 166–179 (2001)
[26] Junhai, L., Liu, X., Danxia, Y.: Research on Multicast Routing Protocols for Mobile ad-hoc Networks. Computer Networks 52(5), 988–997 (2008)
[27] Perkins, C.E.: Ad-hoc on-demand distance vector routing. In: Mobile Computing Systems and Applications, pp. 90–100 (1999)
[28] Perkins, C.E., Watson, T.J., Bhagwat, P.: Highly dynamic destination-sequenced distance-vector routing (DSDV) for mobile computers. In: SIGCOMM 1994 Proceedings of the Conference on Communications Architectures, Protocols and Applications, pp. 234–244 (1994)
[29] Chiang, C.-C.: Routing in clustered multihop, mobile wireless networks with fading channel. In: IEEE SICON 1997, pp. 197–211 (1997)

[30] Clausen, T., Jacquet, P.: Optimized link state routing protocol (OLSR). Project Hipercom, INRIA, pp. 1–56 (2003)
[31] Heinzelman, W., Chandrakasan, A., Balakrishnan, H.: Energy-efficient communication protocol for wireless microsensor networks. In: Proceedings of the 33rd International Conference on System Sciences (HICSS 2000), pp. 1–10 (2000)
[32] Vakulya, G., Simon, G.: Energy-efficient and reliable round-robin TDMA for wireless sensor networks. In: Instrumentation and Measurement Technology Conference (I2MTC), pp. 1179–1183 (2012)
[33] Vieira, M.A.M., Coelho Jr., C.N., Silva Jr, D.C., Mata, J.M.: Survey on wireless sensor network devices. In: 2003 Prof. IEEE-ETFA Conf., pp. 537–544 (2003)
[34] Yu, Y., Govindan, R., Estrin, D.: Geographical and Energy Aware Routing: A recursive data dissemination protocol for wireless sensor networks. In: UCLA, pp. 2–11 (2001)
[35] Macedo, D.F., Macedo, P.F., Correia, L.H.A., Santos, A.L., Loureiro, A.A.F., Nogueira, J.M.S.: Um protocolo de roteamento para redes ad hoc com qos baseado no controle da potência de transmissão. In: Simpósio Brasileiro de Redes de Computadores, vol. 24, pp. 605–620 (2006)
[36] Nikaein, N., Labiod, H., Bonnet, C.: DDR – Distributed dynamic routing algorithm for mobile ad hoc networks. In: MobiHOC 2000 First Annual Workshop on Mobile and Ad Hoc IEEE Networking and Computing, pp. 19–27 (2000)
[37] ZigBee Alliance, ZigBee specification standard (October 2007)
[38] Sohraby, K., Minoli, D., Znati, T.: Wireless sensor networks: Technology, protocols, and applications. Wiley (2007)
[39] Weise, M.: Energy Efficient Initialization of Wireless Sensor Networks. Dissertação (Mestrado). Swiss Federal Institute of Technology, Zurich (2007)
[40] Yangfan, Z.: Energy Efficient Initialization of Wireless Sensor Networks. Dissertação (Mestrado). Chinese University of Hong Kong (2006)
[41] Chou, P.H., Park, C.: Energy-efficient platform designs for real-world wireless sensing application. In: Proc. 2005 IEE/ACM International Conf. Computer-aided Design, San Jose (2005)
[42] Aziz, A.A., Sekercioglu, Y.A., Fitzpatrick, P., Ivanovich, M.: A Survey on Distributed Topology Control Techniques for Extending the Lifetime of Battery Powered Wireless Sensor Networks. IEEE Communications Surveys & Tutorials 15(1), 121–144 (2013)
[43] Feeney, L.M., Nilsson, M.: Investigating the energy consumption of a wireless network interface in an ad hoc networking environment. In: IEEE INFOCOM, vol. 3, pp. 1548–1557. Citeseer (2001)
[44] Youen, K., Li, B., Liang, B.: Distributed Minimum Energy Data Gathering and Aggregation in Sensor Networks. In: Proc. 2006 IEE International Conf. Communication, Istanbul, Turquia (2006)
[45] Guo, C., Guo., H.R., Pawelczak, P.: Analysis and Optimization of Energy Efficient Cluster Forming for Wireless Sensor Networks. In: IEEE Int. Conf. Vehicular Technology, Baltimore, USA (2007)
[46] Pantazis, N.A., Nikolidakis, S.A., Vergados, D.D.: Energy-Efficient Routing Protocols in Wireless Sensor Networks: A Survey. IEEE Communications Surveys & Tutorials 15(2), 551–591 (2013)
[47] Rahman, A., Islam, S., Talevski, A.: Performance Measurement of various Routing Protocol in Ad-Hoc Network. In: IMECS, vol. 1, pp. 321–323 (March 2009)

Simple Autonomous Active Period Selection Technique for Cluster-Based IEEE 802.15.4 Wireless Sensor Networks with Dynamic Network Changes

K. Mori*

Division of Electrical and Electronic Engineering,
Graduate School of Engineering, Mie University,
1577 Kurima-machiya, Tsu, Mie, 514-8507, Japan
kmori@elec.mie-u.ac.jp

Abstract. This chapter aims to provide discussions of active period selection technique for the cluster-tree type wireless sensor networks (WSNs) employing traffic adaptive IEEE 802.15.4 beacon enabled mode under dynamic network changes, and proposes an autonomous distributed superframe duration (SD) selection scheme to reduce beacon collisions by using simple control mechanism. The dynamic network changes, including network topology changes and frame structure changes, cause severe beacon collisions in the cluster-tree type WSNs and greatly degrade their system performance. To overcome this problem, the proposed scheme autonomously selects an active SD by using beacon reception power monitoring with distributed fashion and also introduces a beacon status notice from sensor nodes (SNs) to their parent cluster heads (CHs) in order to prevent unnecessary SD selection at CHs. To enhance the system performance, this chapter also applies the traffic adaptive distributed backoff mechanism, previously proposed in our recent work, to the autonomous distributed SD selection scheme and investigates an effect of the distributed backoff to the system performance. The results evaluated by computer simulation show that the proposed scheme can improve the transmission performance while keeping the better power consumption performance in cluster-tree type WSNs under cluster mobility environments.

Keywords: wireless sensor networks, IEEE802.15.4, cluster topology, beacon collision, active period selection, backoff, distributed control, autonomous control, cluster mobility, network change.

1 Introduction

Recent intensive researches and developments on wireless sensor networks (WSNs) accelerate their application to various practical systems such as

* Corresponding author.

A. Mason et al. (eds.), *Sensing Technology: Current Status and Future Trends III*,
Smart Sensors, Measurement and Instrumentation 11, DOI: 10.1007/978-3-319-10948-0_7

environmental surveillance, home automation (HA), process automation (PA), and factory automation (FA). In WSNs, sensor nodes (SNs) normally operate with limited battery and less computational (processing) capability due to limitation of their operating environment and cost, and thus, higher power consumption efficiency and simpler processing mechanism (algorithm) are absolutely required for WSNs to achieve long-time network operation with limited network resources, such as battery power and CPU processing resources [1, 2]. Duty cycle operation, where sensor nodes (SNs) repeat active and inactive states alternately, and a cluster-tree type network structure, where several neighboring SNs form a cluster and each SN transmits the measured data to its cluster head (CH) and then the CH sends the aggregated data to the sink node, are the promising candidates for achieving high power consumption efficiency in WSNs.

The beacon enabled mode of IEEE802.15.4 medium access control (MAC) [3], which is one of typical practical examples of MAC mechanisms for WSNs, offers power saving mechanism by using duty cycle operation. The smaller duty cycle rate, which is a time ratio of the active to inactive periods, achieves lower power operation, however, the duty cycle rate also affects data collection performance, such as throughput and transmission delay. Thus, the appropriate duty cycle rate should be selected after careful consideration of both power consumption efficiency and data collection performances. This means that under traffic fluctuating environments, traffic adaptation control should be required for achieving appropriate duty cycle operation. Then, several works [4-8] have proposed the traffic adaptive duty cycle operation to achieve power efficient WSNs with better data collection performance.

In the cluster-tree type WSNs, on the other hand, multi-hop transmissions reduce power consumption at the SNs due to lower required transmission power and lower packet collision probability. In addition the cluster topology also improves data collection performance due to decentralization of network traffic to each cluster. To enhance system performance further, a combination of the duty cycle and cluster tree topology have been investigated [7, 8]. These works have proposed an adaptive active period control mechanism based on cluster traffic load for IEEE 802.15.4 beacon-enabled mode, which provides better system performance under various traffic fluctuations.

However, the cluster-tree type WSNs with IEEE 802.15.4 beacon enabled mode fundamentally have a beacon collision problem, and it is critical how to allocate superframe duration (SD), which corresponds to active period for duty cycle operation in IEEE 802.15.4 beacon enabled mode, to the clusters under less, hopefully no interference between clusters (inter-cluster interference). Against this issue several works [9-14] have been performed to avoid the beacon collision and then achieved better data collection performance and less power consumption. The IEEE 802.15.4 beacon enabled mode originally has an ability of avoiding the beacon collision by allocating SDs in different time part on the superframe to different clusters with the adequate parameter settings of *BeaconOrder* (BO) and *SuperframeOrder* (SO). These existing mechanisms adopt this ability and achieve the better system performance.

Under practical applications, in addition to traffic fluctuations, the WSNs suffer from various network variations, for example topology changes due to cluster mobility, under which a whole of the cluster, a CH and its subordinate SNs, move together with the same direction and velocity. Under such situations, however, the existing mechanisms may cause some difficulties in applicability to cluster mobility and feasibility under limited power and computational resources, and so on. In addition, existing mechanisms do not take into account traffic adaptation at all, and this leads to another problem under traffic fluctuating environments. Thus, it is generally difficult for them to always provide better system performance under various operational environments.

Moreover, the cluster-tree type WSNs with IEEE 802.15.4 beacon enabled mode also cause channel access congestion at the beginning part of the SD. Employing the duty cycle operation, due to existence of the inactive period where SNs cannot transmit their date, many SNs concurrently access the channel at the beginning of the next SD, and this situation accelerates the access congestion at the beginning part of the SD. Then, some works [15-18] have investigated for the mitigation of the channel access congestion during the SD in IEEE 802.15.4 MAC. However, these mechanisms cannot provide proper transmission performance under various network fluctuations including traffic fluctuation and topology changes.

The objective of this chapter is to provide power-efficient and high-performance active period allocation mechanism with simple processing algorithm for cluster-tree type WSNs employing IEEE 802.15.4 beacon enabled mode, even under dynamic network changes. To achieve this objective, this chapter proposes simple active period selection scheme which can provide better network performance with limited node resources under topology changes and traffic fluctuations due to cluster mobility [19]. The proposed scheme autonomously and distributively selects the active SD, in which the CH and its subordinate SNs put into active state, at each CH by just utilizing communication related function, such as monitored reception status of beacons transmitted from other CHs. The advantage of the proposed scheme is to reduce beacon collision and thus inter-cluster interference even when the number of SDs allocable to clusters is less than that of the existing clusters, leading to an improvement in network performance. In addition, to reduce packet collision at the beginning part of the active SD, the proposed scheme also adopts the traffic adaptive distributed backoff mechanism [20]. The proposed scheme is expected to obtain the improvement of the system performance due to less packet collision provided by the distributed backoff mechanism. The performance for the proposed scheme is evaluated through computer simulation and its effectiveness is demonstrated.

2 IEEE 802.15.4 Beacon Enabled MAC and Its Problem

IEEE 802.15.4 MAC [3] provides a beacon enable mode, in which the duty cycle operation is performed by using superframe structure. In the beacon enabled

WSNs, coordinators periodically broadcast beacons and their subordinated SNs receive the beacons to synchronize to the superframe defined by the coordinator.

In cluster-tree type WSNs, one center node becomes a PAN coordinator (PANC) and communicates with cluster heads (CHs). The CH is also categorized into a coordinator and broadcasts the beacon to the subordinated SNs.

2.1 Superframe Structure in IEEE 802.15.4 Beacon Enabled Mode

The superframe consists of active and inactive parts, as illustrated in Fig. 1. The active part is divided into two parts: contention access period (CAP) and contention free period (CFP). In the CAP, the subordinated nodes access the channel with slotted carrier sense multiple access with collision avoidance (slotted CSMA/CA). The length of the superframe (so-called beacon interval: BI) and its active part length (so-called superframe duration: SD) are determined by beacon order *BO* and superframe order *SO*, which are broadcast by a coordinator via a beacon to all subordinated nodes.

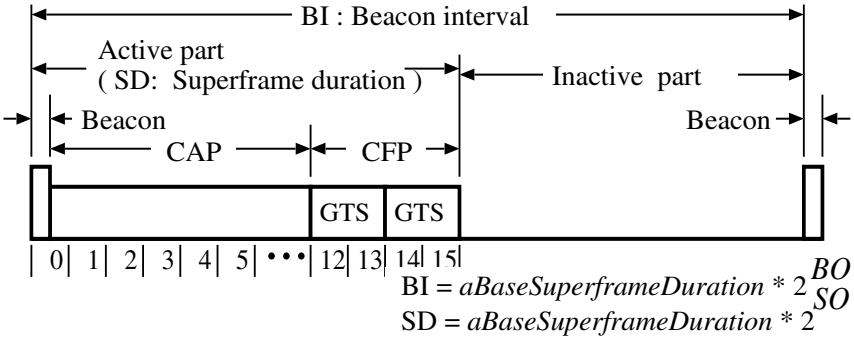

Fig. 1 Superframe structure in IEEE 802.15.4 beacon enabled mode

The PANC determines superframe structure, specifically *BO* and *SO*, and broadcasts them to subordinated CHs and then the CHs also broadcast to the subordinated SNs. In a given WSN, each of *BO* and *SO* is common for all network elements and the all belonging to the same WSN synchronize to the superframe with the same structure.

2.2 Problem with SD Allocation

In cluster-tree type WSNs, not only the PANC but also the CHs transmit the beacon to their SNs. Therefore, each cluster should use different SD on different time position in the superframe to avoid beacon collision and inter-cluster interference.

The allocation of the different SD to the different cluster is easy to achieve when the number of SDs allocable to clusters is more than that of the existing clusters. However, the SD allocation with no beacon collision and no inter-cluster interference is quite difficult to achieve under the situation that the number of clusters exceeds that of allocable SDs. This situation likely occurs when employing traffic adaptation, where the parameters *BO* and *SO* are controlled by the traffic conditions. For example, under the same *BO*, small *SO* can acceptable for the light traffic load, where the number of allocable SDs is large enough for that of clusters, whereas the heavy traffic load forces large *SO*, where each cluster cannot obtain the different SD and the beacon collision and sever inter-cluster interference occur.

In addition, under the conditions with heavy traffic and/or many clusters, network variations, for example topology changes due to cluster mobility, affect the SD allocation largely and then lead to the degradation in the system performance. With topology changes, the SD allocation appropriate to the network in a given time point is not always suitable for any other time points, and the SD allocation should be adjusted according to the topology changes. Thus, we should develop a countermeasure against this problem in consideration of the network variations including the traffic adaptation and the topology changes.

2.3 Problem with Slotted CSMA/CA in CAP

In the slotted CSAM/CA used during the CAP, the backoff slots, whose duration is referred as 'unit backoff period (UBP)', are aligned with the start of the beacon transmission. Every SN, wishing to transmit packets during the CAP, locates its backoff starting time on the boundary of the next backoff slot and then waits for a random number of UBPs.

Due to the duty cycle operation mentioned above, SNs cannot transmit packets during the inactive part in the superframe. Therefore, the SNs storing packets should be transmitted access the channel concurrently at the beginning of the next active part (CAP), and thus, the channel access congestion occurs at the beginning part of the CAP. This leads to the degradation in the transmission performance of the WSNs employing IEEE 802.15.4 MAC. The degree of this congestion depends on the traffic loaded into the cluster in the cluster-tree type WSNs: severe congestion appears for heavy traffic load, and light congestion for light one. Thus, we should also develop a countermeasure against this problem in consideration of the amount of the cluster traffic.

3 Related Work

The beacon collision and channel access congestion are one of most critical problems arising in WSNs employing IEEE 802.15.4 beacon mode. Therefore, several approaches have been proposed to avoid these problems in such WSNs.

3.1 Existing Approaches against Beacon Collision Problem

The time shift grouping access [10] and the time division beacon scheduling (TDBS) [11] have been proposed to allocate the SD without beacon collision in centralized control fashion. The centralized approach, however, is not suitable for the WSNs with the cluster mobility due to continuous and dynamic network topology change. This is because a central node, such as a PANC, needs to recognize the current network topology immediately upon the cluster movement, which may be impossible for WSNs with limited network resources.

The group-mobility predictive location-based beacon scheduling (GLBS) [14] has been investigated for IEEE802.15.4/ZigBee WSNs, which also employs centralized control fashion. In this mechanism, each CH needs to get its exact location through some localization mechanisms, for example global positioning system (GPS), and to predict its future location, and a central node also needs to collect the location information regarding all CHs in entire WSN. However, CHs cannot always obtain their locations from the GPS system due to impossible situation of receiving GPS signals under the indoor applications such as FA, and the location prediction and its notice to a central node consume large amounts of computational and power resources. Because less power operation with limited resources is a key requirement for WSNs, the GLBS is not suitable for WSNs under practical environments.

3.2 Existing Approaches for Mitigating Access Congestion in CAP

Some works [15-18] have investigated for mitigation of the channel access congestion during the CAP in IEEE 802.15.4 MAC. Most of them belong to the backoff window control, in which a backoff exponent (BE) is controlled to enhance system performance. The BE is related to how many UBPs a SN shall wait before attempting to assess a channel and is initialized to the value of *macMinBE* in IEEE 802.15.4 MAC.

The adaptive backoff control method [15] has been proposed for the traffic adaptive 2-level active period control in cluster-tree type IEEE 802.15.4 WSNs. In this method, each SN autonomously controls the initial value of BE corresponding to the current CAP length of its cluster, which reflects the cluster traffic load and is informed from the CH of the cluster. This method greatly improves the throughput performance, whereas degrades delay performance severely in heavy traffic load regions. Therefore, we cannot obtain proper transmission performance under the temporal and spatial traffic fluctuations.

4 System Model

In this chapter, a cluster-tree type WSN with one PANC and N_{ch} CHs subordinating N_{sn} SNs (the total number of SNs: N_{ch} x N_{sn}) is assumed as illustrated in Fig. 2. Each cluster belongs to either of two categories: location-fixed cluster with no mobility, and moving one with the cluster mobility.

The number of fixed and moving clusters is defined by $N_{\text{ch\_f}}$ and $N_{\text{ch\_m}}$, respectively. The fixed clusters are on a regular hexagonal grid whose distance between CHs is d_1 [m], as illustrated in Fig. 3. Each SN is distributed randomly within a radius of d_2 [m] and d_3 [m] from its parent CH, for the fixed and moving clusters, respectively, and any CHs are also located within the communication range of the PANC.

The WSN employs the beacon enabled mode of the IEEE 802.15.4 MAC. Each CH and its SNs perform the duty cycle operation based on the common superframe structure for entire network, and thus, all the network elements operate following the same BI and SD, which are determined by *BO* and *SO*. The CH is active during one of SDs on the superframe, and transmits a beacon frame at the beginning of the active SD, as illustrated in Fig. 4. The SNs are also active during the SD, in which they receive the beacon frame transmitted from their parent CH, and transmit data packets in the CAP following the received beacon.

One carrier frequency channel is used across the network, and thus, the maximum number of SDs $N_{\text{SD}}^{\max}$ allocable to CHs is defined by $N_{\text{SD}}^{\max} = 2^{BO-SO}$. The active SD for the fixed clusters are fixed and selected so as to cause no inter-cluster interference with each other, and that for the moving clusters are selected from current available SDs by using some kind of SD selection mechanisms. To avoid the beacon collision, the different SD from those allocated to other clusters (CHs) in the interfering area should be allocated to each cluster (CH), as illustrated in Fig. 4.

The traffic adaptation mechanism proposed in [7] is also adopted to handle the traffic fluctuations. In this traffic adaptation, the superframe structure is adjusted by only changing *SO* value, while the *BO* value remains to be fixed. Therefore, the $N_{\text{SD}}^{\max}$ is varying with current traffic situations: large and small $N_{\text{SD}}^{\max}$ for light and heavy traffic loads, respectively. Under heavy traffic loads, the beacon collision likely occurs due to the shortage in the $N_{\text{SD}}^{\max}$ when it is less than the number of the existing clusters, leading to degradation in system performance. From this aspect, traffic adaptation control greatly impacts the performance of the SD allocation control, and therefore, the SD allocation mechanism should be designed under consideration of the traffic adaptation mechanism.

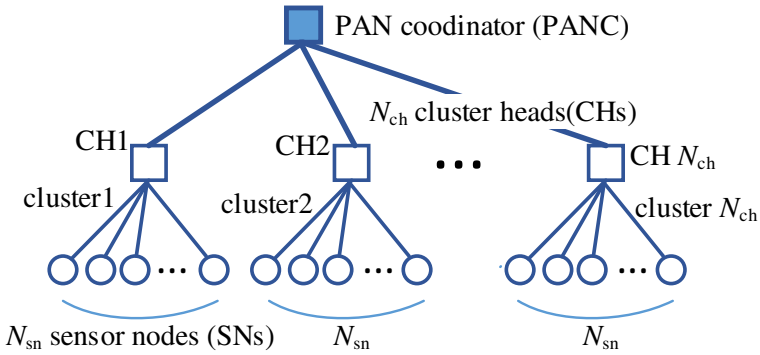

Fig. 2 Network topology

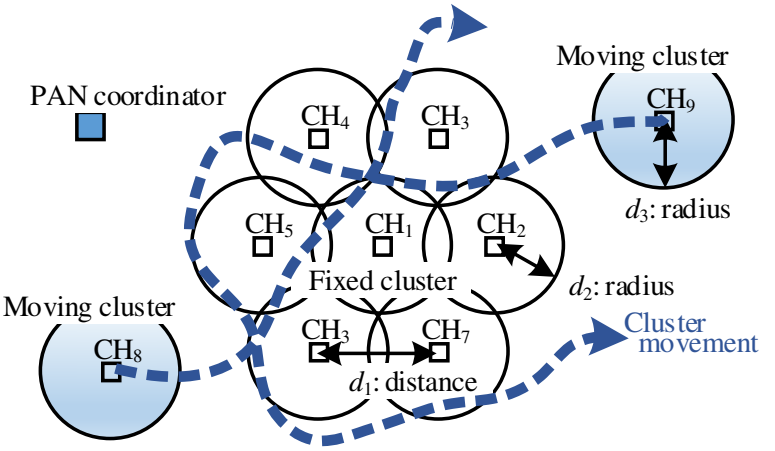

Fig. 3 Cluster configuration

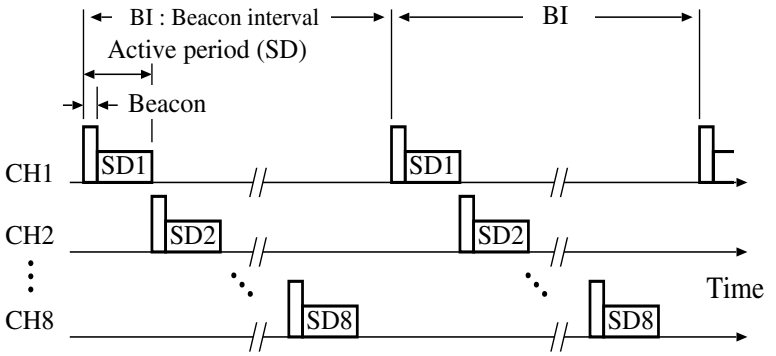

Fig. 4 Active SD allocation in the case of $N_{ch} = 8$

5 Simple Autonomous Distributed Active Period Selection

To overcome the above-mentioned drawbacks of the conventional approaches, this section discusses the simple autonomous distributed active period selection mechanism [19], aiming to enhance the network performance for IEEE 802.15.4 beacon enabled cluster-tree type WSNs.

5.1 Requirements for Active Period Selection

Considering frequent changes in network topology and superframe structure caused from the cluster mobility and traffic adaptation control under practical

environments such as PA and FA applications, the followings are required for the active period selection to achieve our goal:

- Autonomous distributed control fashion, and
- Simple control algorithm.

Regarding the control fashion, the centralized control is not suitable to handle frequent topology changes because frequent exchange of control messages is required between network elements in the centralized control. This leads to large signaling overhead and then negatively affects the network performance. Therefore, autonomous distributed control fashion should be introduced to the active period selection.

In addition, simple control algorithm without any complicate control mechanisms is essential to achieve our goal. It is more preferable to use no any other functions such as GPS rather than communication related ones such as reception power monitoring. Therefore, the control algorithm should be simple and power-efficient in the active period selection.

5.2 SD Selection Based on Beacon Reception Power Monitoring

As active period selection scheme which satisfies the above requirements, this section discusses a SD selection scheme based on beacon reception power monitoring. This SD selection scheme utilizes only the monitoring result of the beacon signals transmitted from neighboring CHs with autonomous and distributed control fashion and uses no other additional functions rather than communication related ones.

In the SD selection scheme, each CH monitors the reception power level of the beacons hearing from the other CHs, as illustrated in Fig. 5. Every predefined selection interval T_{int}, based on the monitoring result, it autonomously selects the SD under the following conditions as its active SD:

(1) With the smaller beacon reception power than a predefined threshold θ_{rxpb},
(2) With the smallest beacon reception power if any SDs do not satisfy the condition (1),
(3) With rearguard position closet to the current active SD on the superframe, if multiple SDs satisfying the condition (1) or (2) are detected.

The first and second conditions ensure the least inter-cluster interference and lead to reduction in the possibility of beacon collision. The third condition reduces the number of beacon searches at SNs after the CH changes its active SD, and contributes reduction in power consumption at SNs.

Note that the CHs cannot monitor the reception power level transmitted from other CHs in the current active SD because the CHs themselves transmit their beacon in the active SD. Therefore, the current active SD is outside the scope of the SD selection procedure.

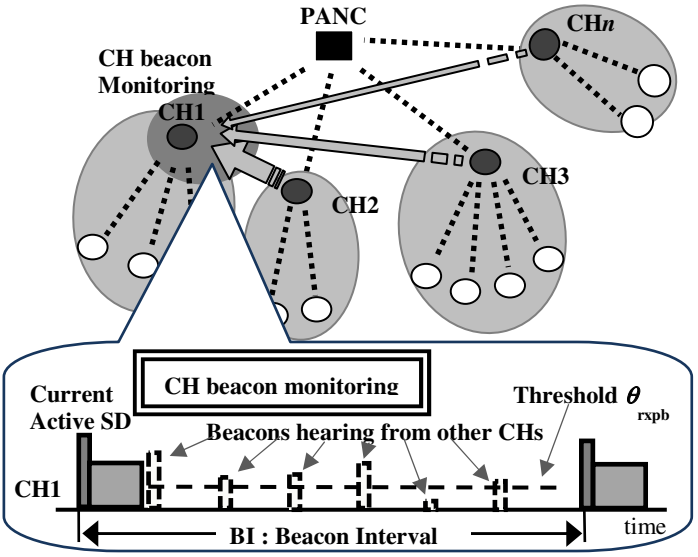

Fig. 5 SD selection based on beacon reception power monitoring

5.3 Beacon Status Notice from SNs

Using the SD selection, the active SD changes every selection interval T_{int} because the active SD during the next interval is selected from the SDs other than the current active one. This causes unnecessary change of the active SD when the current active SD is good enough for continuous use due to less inter-cluster interference. The unnecessary active SD change may result in increase in the inter-cluster interference and also the beacon searches at SNs, leading to degradation in the network performance.

To prevent this problem, the SD selection scheme introduces beacon status notice from the SNs to their parent CH. On the beacon status notice, the SNs monitor the reception status, specifically signal to interference and noise ratio (SINR) in this chapter, of the beacon signals transmitted from their CH, as illustrated in Fig. 6. Then, they inform the monitored SINR value to their CH by inserting it in their transmitting data packet at data transmission phase. After then, the CHs having the informed SINR value regarding their beacon judge whether they need to change the current active SD or not. If one of SINR values informed from subordinate SNs is less than a predefined threshold θ_{SINRb}, the CHs execute the SD selection procedure described in Sec. 5.2 at the next control point, otherwise they skip the SD selection.

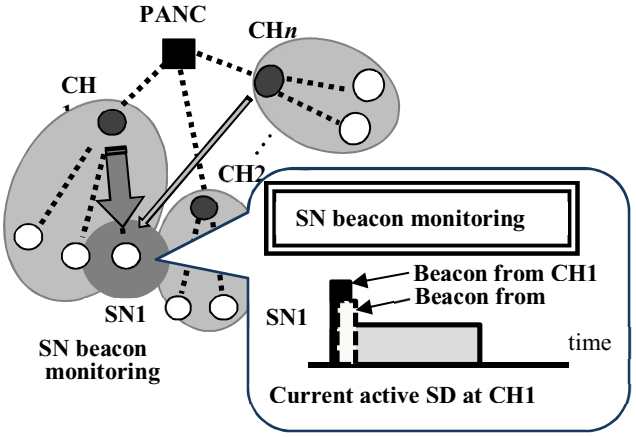

Fig. 6 Beacon monitoring at SNs in beacon status notice

With the beacon status notice, it is expected that the CHs avoid the unnecessary SD selection and their subordinate SNs reduce the beacon search, leading to improvement in the network performance. Note that the beacon status notice requires no additional control massage (packet) from SNs to their CH because the beacon status information can be piggybacked onto a data packet with small modification on its packet format. Therefore, this control increases tiny bits of control overhead and gives less impact to the network performance.

6 Distributed Backoff Mechanism

To overcome the above-mentioned drawbacks of the conventional backoff control mechanisms for IEEE 802.15.4 MAC, this section discusses the distributed backoff mechanism [20], aiming to reduce the performance degradation with the conventional method.

6.1 Concept of Distributed Backoff

The channel access congestion arises at the beginning part of the CAP due to the nature of the slotted CSMA/CA under the duty cycle operation, as illustrated in Fig. 7 (a). Even employing a random backoff technique, the severe access congestion arises and leads to packet collisions, resulting in the degradation in the transmission performance even under the light traffic conditions due to the duty cycle operation. The conventional method described in Sec. 3.2 mitigates the packet collisions by adjusting the initial BE based on the cluster traffic load and obtains some throughput improvement. However, since this conventional method just enlarges the backoff window size to reduce the packet collisions, it cannot resolve the access congestion itself at all, and therefore, the drastic degradation in

delay performance, resulting from longer backoff window, appears as a cost of the throughput improvement, especially under heavy traffic load conditions.

From the viewpoint of this consideration regarding to the conventional method, we need to mitigate the access congestion itself to reduce the delay degradation while keeping the throughout improvement. In this chapter, then, we consider distributing simultaneous channel accesses at the beginning of the CAP to the whole region of the CAP, as illustrated in Fig. 7 (b). Note that, unlike the

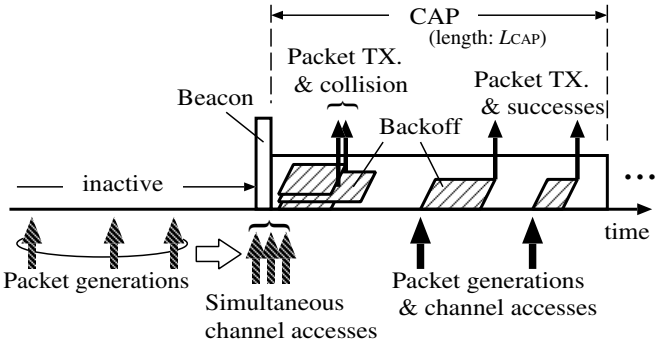

(a) Channel access in IEEE 802.15.4 MAC based system.

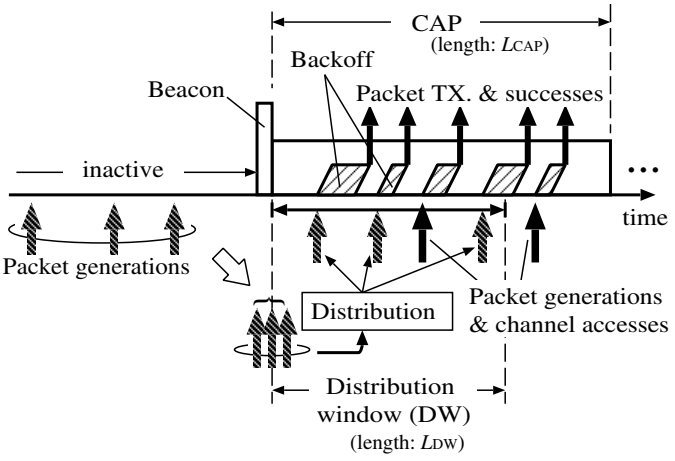

(b) Distributed channel access in proposed mechanism.

Fig. 7 Channel access procedure during CAP (a) IEEE 802.15.4 based systems (conventional method). (b) Distributed backoff mechanism.

conventional method, this mechanism employs a constant initial BE regardless of the traffic load, which is initialized to the value of *macMinBE* and is most always shorter than that for the conventional method. By using this approach, since the starting time of the backoff process for each SN is distributed to the wide range within the CAP, the packet collisions would be reduced even with the shorter backoff window size than the conventional method. As a result, the delay degradation would be mitigated while keeping the better throughput performance.

The distributed backoff mechanism is premised on being used together with the traffic adaptive 2-level active period control [7], which controls the length of the CAP based on the current cluster traffic load. Therefore, the CAP length at a given time point can be utilized as an indicator of the traffic load at that time point in the distributed backoff mechanism.

6.2 Distribution of the Backoff Starting Time

In the distributed backoff mechanism, the SNs, wishing to transmit their packet, autonomously adjust the backoff starting time for their packet transmission at the head of the CAP in the IEEE 802.15.4 superframe. The backoff starting time is randomly selected from a given pre-defined range, hereafter called 'distribution window (DW)'. This DW should be determined according to traffic loads since the degree of the access congestion depends on the traffic loads. Specifically, the DW should be set to large (long) size for heavy traffic conditions because of high access congestion, while small size for light traffic conditions. Therefore, the size of the DW is determined according to the current CAP length, which is determined by the CH and is informed to every SN via the beacon.

Each SN storing the packet should be transmitted determines the backoff starting time T_{sboff} at:

$$T_{\mathrm{sboff}} = T_{\mathrm{SCAP}} + rand(0, L_{\mathrm{DW}}) \tag{1}$$

where T_{SCAP} is the starting time of its CAP for the cluster (this time is an original starting time), L_{DW} is the length of the distribution window, which is determined following Sec. 6.3, and *rand* (*x*, *y*) is the function which gives a random number from *x* to *y* following a uniform distribution.

Note that this control is applied only for the SNs which already have stored the packets at the beginning of the CAP. The SNs, which will have new packets during the CAP, access the channel with normal backoff procedure because new packet generations during the CAP are uniformly distributed and then never cause additional access congestion.

6.3 Setting of Distribution Window Size LDW

The DW size L_{DW} is a key parameter of the distributed backoff mechanism because it greatly affects the transmission performance for the WSNs. For a given

traffic load, too short L_{DW}leads to incomplete avoidance of the access congestion, resulting in poor throughput performance, while too long L_{DW} leads to long waiting time for the channel access and then poor delay performance. Therefore, the L_{DW} should be set an adequate value corresponding to the current traffic loaded into the cluster. The distributed backoff mechanism introduces the adaptive distribution window (ADW), which is given by using the current CAP length L_{CAP}, which reflects the current cluster traffic.

The L_{DW} for the ADW is determined in proportion to the L_{CAP}, however, the proportionality factor F_{ADW} ($0 < F_{\mathrm{ADW}} \leq 1.0$) is variable according to the L_{CAP}. The F_{ADW} should be controlled so as to be a smaller value for the short L_{CAP} and a larger value for the long L_{CAP}. To satisfy this requirement, the distributed backoff mechanism employs the proportionality factor F_{ADW} of $L_{\mathrm{CAP}}/L_{\mathrm{CAP}}^{\max}$, where $L_{\mathrm{CAP}}^{\max}$ is a maximum length of the CAP which is a predefined system parameter with a constant value. Then, the L_{DW} in the ADW is given by:

$$L_{\mathrm{DW}} = F_{\mathrm{ADW}} \cdot L_{\mathrm{CAP}} = L_{\mathrm{CAP}}/L_{\mathrm{CAP}}^{\max} \cdot L_{\mathrm{CAP}} = (L_{\mathrm{CAP}})^2/L_{\mathrm{CAP}}^{\max} \quad (2)$$

Applying above-mentioned control, the backoff starting time around the head of the CAP would be distributed, and then, the access congestion at the beginning of the CAP can be mitigated. Moreover the distribution range is controlled by the amount of traffic load in the cluster. Due to this feature the distributed backoff mechanism would improve the transmission performance: both throughput and delay for the cluster-tree type WSNs.

7 Performance Evaluation

The performance for the proposed scheme described in Sec. 5 and 6 is evaluated through computer simulation by using the original purposely-built simulator constructed by the C language with the following assumptions.

7.1 Radio Channel Model

The radio channel includes distance attenuation with a coefficient α and independent Rayleigh fading, which is constant during the duration of a packet. It also includes the shadowing fluctuations with a standard deviation σ_{sh} [dB] only in the propagation channels between different clusters.

The CHs can receive the packets only if their received power and SINR are both greater than the required levels P_{dem} and $SINR_{\mathrm{dem}}$. For the channel sensing, a channel busy state can be detected only if the sufficient power level P_{cs} in the frequency channel can be detected.

7.2 Traffic Model

The packets are continuously generated at each SN following Poisson distribution with an average traffic load of G/N_{sn}, where G [packets/superframe] is an average traffic load per cluster. The length of the packets is constant of L_{pkt}[UBPs]. Then, the network traffic load λ is given by $N_{\mathrm{ch}} \cdot G \cdot L_{\mathrm{pkt}}/(T_{\mathrm{aBSD}} \cdot 2^{BO})$, where T_{aBSD} [UBPs] is *aBaseSuperframeDuration* defined in the IEEE 802.15.4 standard.

The packets are re-transmitted after transmission failures.

7.3 Mobility Model

For the cluster mobility, the moving cluster conforms to the Random Waypoint model [21] with an average pause time of T_{ps}[s] and an average velocity of v_{mv} [m/s], which follow an exponential distribution.

The CHs moves within the circumscribed rectangle covering the area of $N_{\mathrm{ch\_f}}$ fixed clusters.

7.4 Power Consumption Model

The power consumption at each node is calculated based on the same model as that used in [7, 8], assuming the 2.4GHz IEEE 802.15.4/ZigBee-ready RF transceiver of TI CC2420 [22].

7.5 Parameter Settings

Using the parameter settings listed in Table 1, we collect the statistics for the communication from SNs to CHs.

8 Evaluation Results

The average throughput S [kbps] and transmission delay D [BIs] are evaluated over the whole network. The standard deviation σ_{pdr} for the packet delivery rates of N_{ch} clusters is also evaluated to show the performance uniformity between clusters. In addition, for the power consumption performance we evaluate a packet cost C_{pkt}, which is defined as consumed power per successful packet transmission at the SNs.

The performances for the proposed schemes with/without the distributed backoff ("Prop.SDsel. w DB" / "Prop.SDsel. w/o DB" in Figs.) are compared with those for a random SD selection scheme ("Rdm.SDsel."), which selects the active SD randomly from the current available SDs.

Table 1 Simulation parameters

	Symbol	Value	
Number of clusters	N_{ch_f} , N_{ch_m}	7, 1 to	
Number of sensor nodes	N_{sn}	9	[/cluster]
Cluster distance	d_1	15	[m]
Cluster radius	d_2, d_3	35	[m]
Transmission rate	R_{rate}	5	[kbps]
Distance coefficient	α	250	
Standard deviation of shadowing	σ_{sh}	2	[dB]
Transmission power	P_{tx}	3.0	[dBm]
Required power for demodulation	P_{dem}	-50	[dBm]
Required SINR for demodulation	$SINR_{dem}$	-70	[dB]
Required power for carrier sensing	P_{cs}	6.0	[dBm]
Duration of *aUnitBackoffPeriod*	UBP(T_{UBP})	-70	[ms]
aBaseSuperframeDuration	T_{aBSD}	0.32	[UBPs]
Beacon order	*BO*	48	
Superframe order	*SO*	8	
Beacon interval (Superframe length)	*BI*	2 to 5	[s]
Beacon frame length	L_{bcn}	3.9	[UBPs]
Data packet length	L_{pkt}	5	[UBPs]
ACK packet length	L_{ack}	12	[UBPs]
SD selection interval	T_{int}	2	[s]
Threshold for beacon reception power	θ_{rxpb}	6.7	[dBm]
Threshold for beacon SINR	θ_{SINRb}	-70	[dB]
Average pause time for mobility	T_{ps}	9.0	[s]
Average velocity for mobility	v_{mv}	10	[m/s]
		1.5	

8.1 Throughput Performance

Figure 8 shows the average throughput *S* for the proposed schemes with and without the distributed backoff and that for the random SD selection.

The proposed schemes achieve better throughput than the random SD selection for all traffic load conditions, and the proposed simple autonomous active period selection control is effective for improving the throughput performance.

Applying the proposed distributed backoff mechanism, the proposed scheme enhances the throughput further, and therefore, the distributed backoff is quite effective for throughput improvement in the proposed scheme. This is considered to come from the fact that the distributed backoff mechanism reduces the packet collisions at the beginning part of the SDs overlap-assigned to multiple clusters.

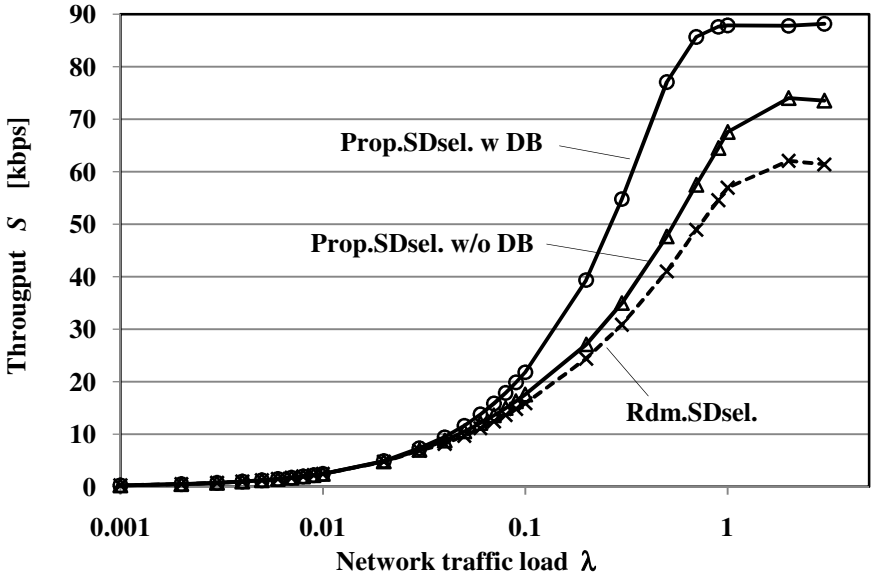

Fig. 8 Throughput performance for $N_{ch} = 10$ (N_{ch_f}, $N_{ch\_m} = 7, 3$)

8.2 Transmission Delay Performance

Figure 9 shows the transmission delay D for the proposed schemes and the other scheme.

The proposed schemes improve the delay performance in the light and middle traffic load conditions, compared with the random SD selection scheme. This shows the proposed simple autonomous active period selection control is also effective for improving the delay performance in the light and middle traffic conditions.

The delay for the proposed scheme with the distributed backoff achieves the same delay performance as that without the distributed backoff under the condition up to around $\lambda = 0.1$. This means the distributed backoff mechanism gives no impact to the delay under such traffic conditions. For high traffic conditions, however, the delay performance gradually degrades when applying the distributed backoff mechanism to the proposed scheme. In this region, the proposed scheme with the distributed backoff gets throughput improvement at a cost of the delay degradation.

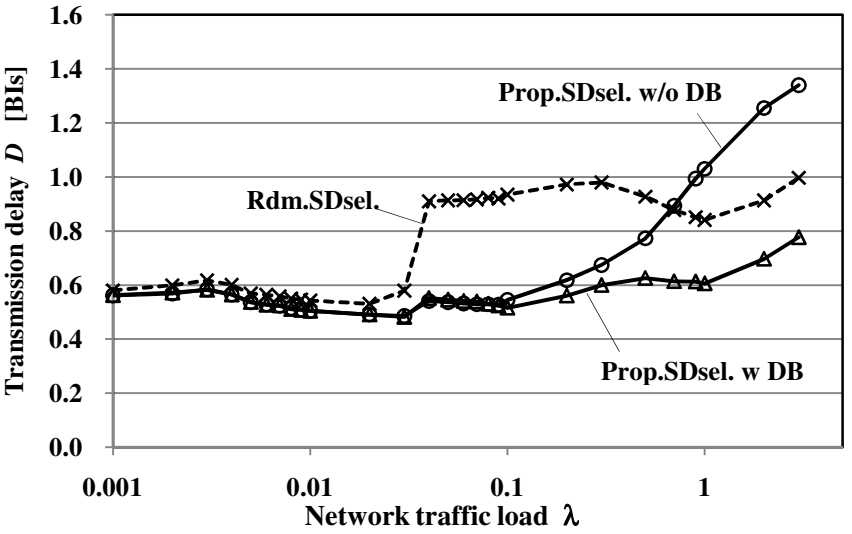

Fig. 9 Transmission delay performance for N_{ch} = 10 (N_{ch_f}, N_{ch_m} = 7, 3)

8.3 Performance Uniformity

Figure 10 shows the standard deviation σ_{pdr} of the packet delivery rate for three schemes. The small σ_{pdr} value means uniform condition for the packet transmission performance in each cluster.

The proposed scheme without the distributed backoff achieves the improvement in the σ_{pdr} performance for all traffic load conditions, especially in the middle traffic conditions, and therefore, the proposed scheme can mitigate the performance non-uniformity in such traffic load regions.

The proposed scheme with the distributed backoff shows a little bit worse σ_{pdr} compared with that without the distributed backoff up to around λ = 0.05. However, compared with the random selection scheme, the proposed scheme achieves smeller σ_{pdr} in such traffic load regions, and therefore, the proposed scheme also improves the performance uniformity between clusters, compared with the random selection scheme.

8.4 Power Consumption Performance

Figure 11 shows the packet cost C_{pkt} for three schemes.

The packet cost C_{pkt} also can be reduced by applying the proposed simple autonomous active period selection control, and further reduced by applying the distributed backoff mechanism.

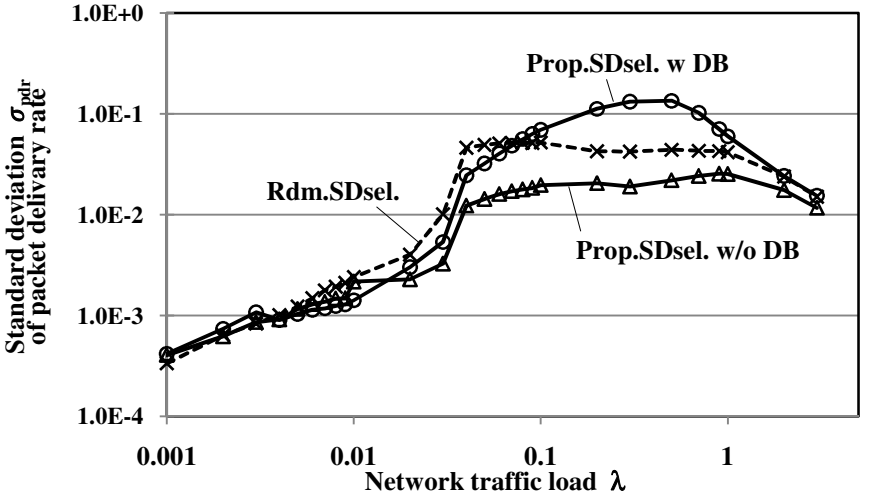

Fig. 10 Performance uniformity in packet delivary rate between clusters for $N_{ch} = 10$ (N_{ch_f}, $N_{ch\_m} = 7, 3$)

The packet cost greatly improves with the distributed backoff for the middle and high traffic load conditions, over $\lambda = 0.02$. For the region over $\lambda = 0.02$, the maximum number of SDs available for the assignment to CHs gets smaller than that of existing clusters. Therefore, the distributed backoff is effective for reducing the power consumption under the situations where larger inter-cluster interference exists.

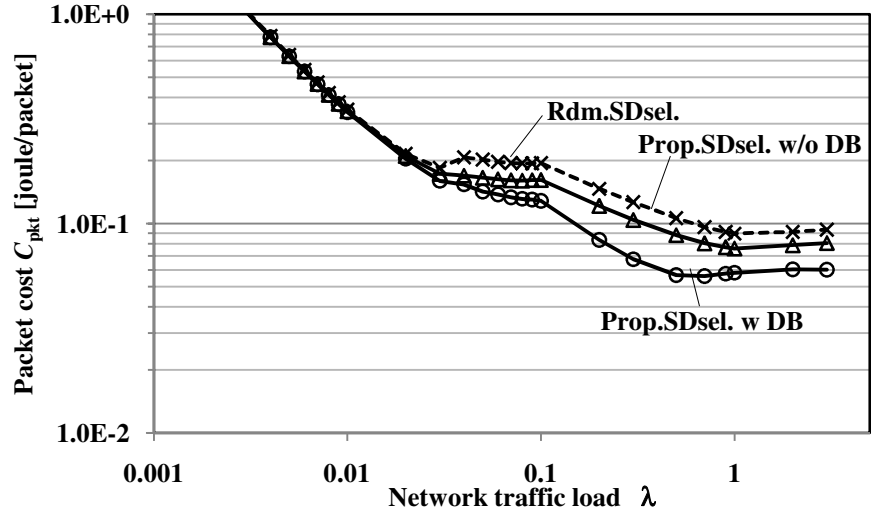

Fig. 11 Packet cost performance at SNs for $N_{ch} = 10$ (N_{ch_f}, $N_{ch\_m} = 7, 3$)

8.5 *Performances under Varying the Number of Moving Clusters N_{ch_m}*

Figures 12-14 show the system performance under varying the number of moving clusters N_{ch_m} from 1 to 9 with N_{ch_f} of 7 (total number of CHs N_{ch} of 8 to16) at the traffic load $\lambda = 0.06$.

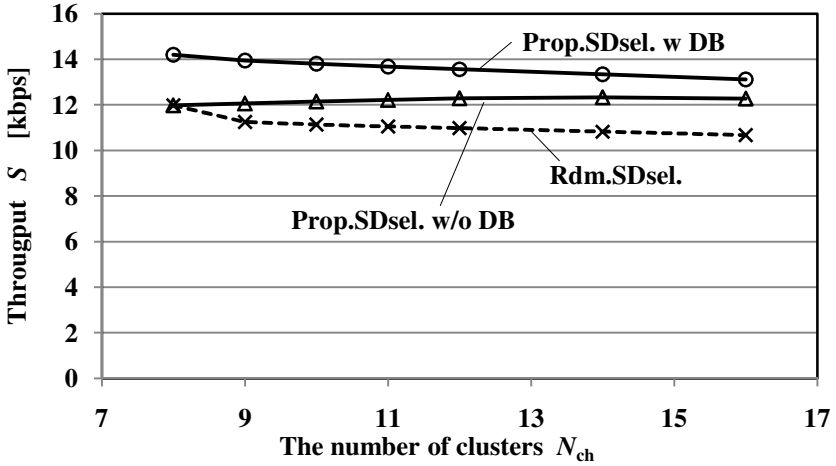

Fig. 12 Throughput performance with varying N_{ch} (N_{ch_f}, N_{ch_m} = 7, variable)

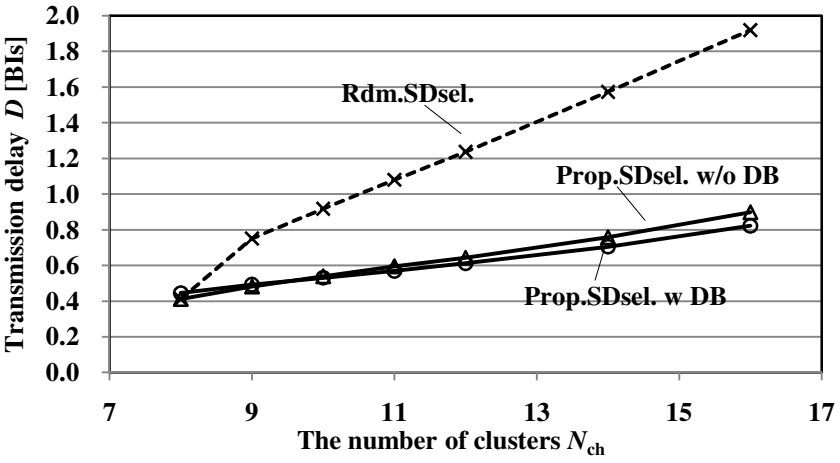

Fig. 13 Transmission delay performance with varying N_{ch} (N_{ch_f}, N_{c_-m} = 7, variable)

All performances improve with applying the distributed backoff, and the improvement rate from the random selection scheme tends to increase with the number of N_{ch_m}. This result indicates the proposed scheme can work well even for the network with many moving clusters.

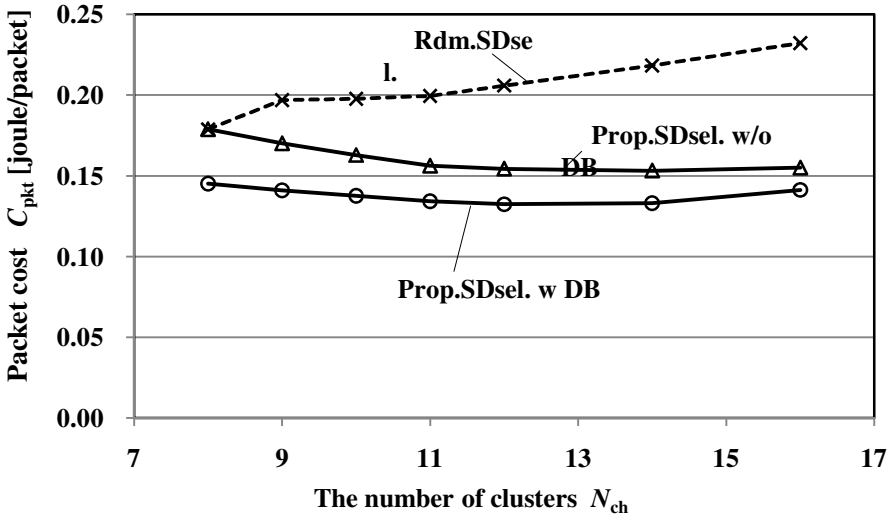

Fig. 14 Packet cost performance with varying N_{ch} (N_{ch_f}, N_{c_-m} = 7, variable)

9 Conclusions

This chapter have discussed the simple autonomous active period selection control scheme with the distributed backoff mechanism and evaluated its system performance for the cluster-tree type traffic adaptive IEEE 802.15.4 WSNs with cluster mobility. The throughput, transmission delay, performance uniformity and power consumption for the proposed scheme have been evaluated though computer simulation.

From these evaluation results, the simple autonomous active period selection control and the distributed backoff mechanism greatly improve the throughput and power efficiency performances for such WSN with cluster mobility.

Accordingly, the proposed scheme is quite effective for cluster-tree type WSNs with cluster mobility, employing traffic adaptive IEEE 802.15.4 beacon enabled mode.

Acknowledgements. This work is partly supported by Japan Society for the Promotion of Science (JSPS), Grant-in-Aid for Scientific Research (c) 25420366, 2013-2015.

References

[1] Akyildiz, I.F., Su, W., Sankarasubramaniam, Y., Cayirci, E.: Wireless sensornetworks: A survey. Comput. Netw. 38(4), 393–422 (2002)
[2] Tilak, S., Abu-Ghazaleh, N., Heinzelman, W.: A taxonomy of wirelessmicro-sensor network models. Mobile Computing and Communication Review 6(2), 28–36 (2002)
[3] IEEE 802.15.4, Part 15.4: Wireless MAC and PHY Specifications forLow-rate WPANs (September 2006)
[4] Lin, P., Qiao, C., Wang, X.: Medium access control with a dynamic duty cycle forsensor networks. In: IEEE WCNC 2004, vol. 3, pp. 1534–1539 (March 2004)
[5] Neugebauer, M., Ploennigs, J., Kabitzsch, K.: Duty cycle adaptation with respect to traffic. In: IEEE ETFA 2005 (September 2005)
[6] Kwon, Y., Chae, Y.: Traffic adaptive IEEE 802.15.4 MAC for wireless sensor networks. In: Sha, E., Han, S.-K., Xu, C.-Z., Kim, M.-H., Yang, L.T., Xiao, B. (eds.) EUC 2006. LNCS, vol. 4096, pp. 864–873. Springer, Heidelberg (2006)
[7] Arzamendia, M., Mori, K., Naito, K., Kobayashi, H.: Traffic adaptive MAC mechanism forIEEE802.15.4 cluster based wireless sensor networks with various trafficnon-uniformities. IEICE Trans. Commun. E93-B(11), 3035–3047 (2010)
[8] Kubo, K., Mori, K., Naito, K., Kobayashi, H.: Enhanced 2-Level Traffic Adaptive Active PeriodControl for IEEE802.15.4 Cluster-Based Wireless Sensor Networks. IEICE Trans. Commun. E94-B(9), 2521–2531 (2011)
[9] Koubaa, A., Nieuwenhuyse, A.V., Attia, M., Alves, M.: Collision-Free Beacon Scheduling Mechanismfor IEEE 802.15.4/ZigBee Cluster-Tree Wireless Sensor Networks. In: ASWN 2007 (May 2007)
[10] Yamaoand, Y., Takagishi, S.: Time Shift Grouping Access in IEEE 802.15.4 MACBeacon Mode for Layerd-Tree Networks. In: IEEE CCNC 2008 (January 2008)
[11] Koubaa, A., Cunha, A., Alves, M., Tovar, E.: TDBS: A time division beacon scheduling mechanismfor ZigBee cluster-tree wireless sensor networks. Int. Journal Real-Time Systems 40(3), 321–354 (2008)
[12] Casilari, E., Hurtado-duenas, J., Cano-garcia, J.M.: A Study of Policies for Beacon Scheduling in802.15.4 Cluster-Tree Networks. In: WSEAS ACS 2008 (October 2009)
[13] Cho, J., An, S.: An Adaptive Beacon Scheduling Mechanism Using PowerControl in Cluster-tree WPANs. Int. Journal Wireless Pers. Commun. 50(2), 143–160 (2009)
[14] Haoru, S., Nam, H., An, S.: Group-mobility Predictive Location-based BeaconScheduling in ZigBee Cluster-tree Networks. In: ICMIC 2011, pp. 87–90 (September 2011)
[15] Mori, K., Naito, K., Kobayashi, H.: Adaptive Backoff Control Method for Traffic Adaptive Active Period Control in Cluster-based IEEE 802.15.4 WSNs. In: Proc. of IEEE VTC2009-fall (September 2009)
[16] Ko, J., Cho, Y., Kim, H.: Performance evaluation of IEEE 802.15.4 MACwith different backoff ranges in wireless sensor networks. In: Proc. of IEEE ICCS 2006 (October 2006)
[17] Rao, V.P., Marandin, D.: Adaptive backoff exponent algorithm for Zigbee(IEEE 802.15.4). In: Koucheryavy, Y., Harju, J., Iversen, V.B. (eds.) NEW2AN 2006. LNCS, vol. 4003, pp. 501–516. Springer, Heidelberg (2006)

[18] Koubaa, A., Alves, M., Nefzi, B., Song, Y.: Improving the IEEE 802.15.4slotted CSMA/CA MAC for time-critical events in wireless sensor networks. In: Proc. of RTN 2006, p. 35–44 (July 2006)
[19] Mori, K., Naito, K., Kobayashi, H.: Simple Active Period Selection Scheme for Cluster-basedIEEE 802.15.4 WSNs with Dynamic Network Changes. In: IEEE VTC 2013-Spring (June 2013)
[20] Mori, K., Naito, K., Kobayashi, H.: Traffic Adaptive Distributed Backoff Control Mechanism for Cluster-Based IEEE802.15.4 WSNs with Traffic Fluctuations. IEICE Trans. Commun. E95-B(5), 1702–1710 (2012)
[21] Johnsonand, D.B., Maltz, D.A.: Dynamic source routing in ad hoc wirelessnetworks. In: Mobile Computing, vol. 353, ch. 5, pp. 153–181. KluwerAcademic Publishers (1996)
[22] Texas Instrument, 2.4GHz IEEE802.15.4 / ZigBee-ready RF transceiver CC24230 Data Sheet Rev.C (March 2013)

Exploring Energy Efficiency of Hardware-Architectures for IMU Based Orientation Estimation

H.-P. Brückner, C. Spindeldreier, and H. Blume*

Institute of Microelectronic Systems, Architectures and Systems Group,
Leibniz Universität Hannover, Appelstraße 4, Hannover, 30167, Germany
blume@ims.uni-hannover.de

Abstract. Various applications demand mobile, accurate and reliable motion capturing. Wireless inertial measurement units provide non-reactive and undisturbed real-time tracking of human movements. The use of customized sensor fusion methods is crucial for achieving the highest orientation accuracy. Due to the high dependency of movement data on orientation estimation accuracy based on inertial measurement data a comparison of the various algorithms presented in literature is hampered. Furthermore, the execution time and energy efficiency of the algorithms on programmable, heterogeneous and ASIC platforms is an important design space parameter. Therefore, this chapter compares the orientation estimation accuracy of inertial sensor fusion algorithms based on a single data set using a highly accurate optical motion capturing system as reference. The data set comprises of RAW data of from a commercial and from a custom developed wireless measurement unit. The provided energy consumption, execution time and achievable accuracy analysis of eleven different sensor fusion algorithms enables the selection of the optimal orientation estimation algorithm with regard to application demands and processing architecture. Furthermore, a customized processor core with the presented Kalman filter based orientation estimation hardware accelerator demonstrates techniques for increasing energy efficiency in respect of achievable throughput rate.

Keywords: inertial sensor fusion, orientation estimation, design space exploration, wireless inertial measurement unit.

1 Introduction

Fully mobile and wireless motion capturing is a mandatory requirement for undisturbed and non-reactive analysis of human movements. Therefore, inertial measurement units (IMU) are used in applications that analysis sports or

* Corresponding author.

A. Mason et al. (eds.), *Sensing Technology: Current Status and Future Trends III*,
Smart Sensors, Measurement and Instrumentation 11, DOI: 10.1007/978-3-319-10948-0_8

rehabilitation training sessions [1]. In contrast to camera based systems IMUs do not suffer from line-of-sight issues. The variety of commercial and custom hardware platforms require a systematic design space exploration for choosing an optimal processing platform regarding the application requirements. Important design space parameters for platform independent efficient inertial sensor fusion are energy consumption, execution time and hardware costs. Energy efficiency plays an important role due to the limited battery capacity of the small-sized IMUs. Furthermore, an open and deterministic communication protocol of the IMU enables platform independent usability.

Besides execution time the main differentiator of sensor fusion algorithms is the achievable orientation estimation accuracy. In general, the comparison of sensor fusion algorithms from literature is hampered due to the different data-sets used within the accuracy evaluation. Therefore, eleven sensor fusion algorithms, including several Kalman filters (KF), are compared based on a single data set recorded while performing an unconstrained real-world movement. In addition to the common Euler angle error measure a quaternion based error measure is proposed and applied to overcome the limitations due to singularities of Euler angles. The presented accuracy and corresponding execution time evaluation allows the selection of an optimal sensor fusion algorithm for a wide range of application specific requirements.

Furthermore, a Kalman filter modification is proposed. Due to the known and time invariant sensor noise characteristics some KF parameters are computed offline and set to fixed values. Thereby the number of operations per filter iteration and thus the execution time is highly reduced. A comparison of accuracy and execution time against the original filter is provided.

Generally, hardware platforms without a dedicated floating-point unit, like many microcontrolllers, feature a significant lower execution time of algorithmic operations when using a fixed-point number representation compared to floating-point based computation. In advance of creating a fixed-point KF hardware accelerator for sensor fusion the bit-width dependent orientation estimation accuracy is analyzed. Furthermore, the execution time of the fixed-point KF implementation is evaluated on multiple hardware platforms including microcontrollers and RISC processors. In addition, a dedicated hardware accelerator module for KF based sensor fusion is developed and evaluated. The presented hardware accelerator features scalability by enabling the parallelization of sub-tasks and the instantiation of multiple modules.

Finally, the results of KF execution time and energy efficiency of various programmable, customized and FPGA-based hardware are evaluated.

The chapter is organized as follows: Section 2 presents a review for various IMU RAW data based orientation estimation methods. Section 3 illustrates a technique for orientation estimation execution time reduction utilizing KFs. The applied method for objective orientation estimation accuracy estimation assessment is introduced in Section 4. Section 5 briefly presents the wireless custom inertial measurement unit development platform. The results of the objective orientation estimation accuracy and execution time analysis are given in

Section 6. The bit-width dependent orientation estimation accuracy of KF based sensor fusion is analyzed in Section 7. The dedicated hardware accelerator architecture and implementation results are given in Section 8. Section 9 reports the results of the comprehensive design space exploration. Conclusions are drawn in Section 10.

2 Algorithms for Orientation Estimation Based on IMU RAW Data

Common classes of algorithms for inertial sensor data fusion are **integration**, **vector observation**, **complementary filtering** and **Kalman filtering**. Integration estimates orientation based only on gyroscope data. Vector observation algorithms depend on the accelerometer and magnetometer measurements for orientation estimation. Compared to gyroscope integration a drift free fusion of the two measurement vectors is achieved as no error accumulation occurs. Complementary and Kalman filters enable the fusion of gyroscope, accelerometer and magnetometer data for orientation estimation. In contrast to vector observation algorithms the sensor noise characteristics are modeled. A mathematical description of each algorithm won't be provided here, as this section merely provides an overview.

In general, Euler angles, orientation matrices and quaternion are commonly used for orientation representation. Due to the singularity free and compact nature of quaternions this representation is best for most applications.

2.1 Gyroscope Rate Integration

Integration algorithms estimate the orientation based only on gyroscope data. The data from the three orthogonal mounted gyroscopes is integrated in time, in order to get orientation estimation, represented as direction cosine matrix or quaternion. In the later evaluation section a first order integration algorithm and a third order integration [2] are analyzed in terms of computational cost and orientation error. Both integration algorithms utilize the Quaternion orientation representation.

2.2 Vector Selector Method

Vector observation algorithms use least square minimization techniques, which provide optimized estimations for a given set of measurements. In inertial sensor data fusion, these algorithms provide orientation estimation based on accelerometer and magnetometer data. This method is therefore not vulnerable to drifts caused by integration of biased data, but is dependent on reliable magnetometer and accelerometer measurements. As there are no correction steps for external acceleration, these methods are only accurate while tracking moving

objects with slight acceleration variance. Also magnetic disturbance influences the orientation estimation.

A common algorithm is the QUEST algorithm [3], which is based on the TRIAD [4] algorithm. Further developments are the FQA [5], FOAM [6] or the O2OQ algorithms [7]. For example, the QUEST algorithm computes elevation, roll and azimuth quaternions based on tri-axial accelerometer and magnetometer data.

2.3 Complementary Filter

In orientation estimation the goal of complementary filter algorithms is to combine the static accuracy of the accelerometer and magnetometer and the short term accuracy of the gyroscope within dynamic movements. Recently an adaptive algorithm with movement situation-dependent switching of the gain factor has been proposed [8]. Another implementation is proposed in [9].

2.4 Kalman Filter

Kalman filters are optimal estimators with respect to the minimization of the error covariance [10]. In literature, there are various proposals to use Kalman filters in inertial sensor fusion [11], [12]. The approaches basically differ in the state vector size and measurement preprocessing steps. In general there are cyclic prediction and correction steps according to Fig. 1. Detailed introduction into the Kalman filter theory are presented in [10], [13] and [14].

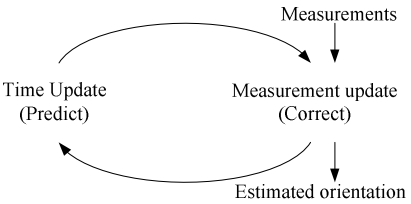

Fig. 1 Kalman filter operation

3 Exploration of Orientation Estimation Accuracy and Execution Time of Inertial Measurement Unit Sensor Fusion Algorithms

A major issue in evaluating inertial sensor fusion algorithms is the generation of suitable reference data. Camera-based optical tracking systems provide highest accuracy in the tracking of unconstrained movements in 3D-space. This method has been applied in [15], [16].

The accuracy of most algorithms is highly dependent on the characteristics of the movement. A comparison of different algorithms is only feasible when using the same data set. Therefore, a comparison between different proposed algorithms based on the provided data is hampered. Hence, the results presented in Section 5 rely on processing an equal data set for all algorithms comprising rotations around each coordinate axis.

3.1 Reference Data Generation

In order to generate reliable reference data Vicon Nexus software and eight Vicon T-Series cameras [17] are used. In general, the level of accuracy achievable is highly dependent on the movement and the quality of the motion capturing of the optical reference system. Specifically the occlusion of multiple markers may result in inaccurate reference data. Therefore, multiple markers are used, but maintain a sufficient distance from the individual markers to avoid the situation where multiple markers are used to compute a single marker position due to the camera perspective.

The wooden measurement object used for robust tracking of an Xsens MTx IMU [18] and the proposed (IM)²SU is shown in Fig. 2. Fourteen reflective markers and both IMUs are attached to the rigid wooden board. Initial orientation offsets of both IMUs where corrected in a preprocessing step, before evaluating the orientation estimation accuracy.

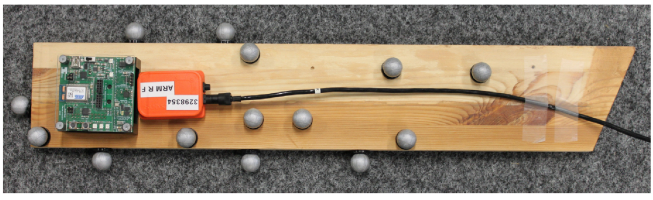

Fig. 2 IMUs and reflective markers attached to rigid measurement object

3.2 Quaternion-Based Error Measure

Computing a root mean square value (RMS) by computing the difference between the orientation estimated by the IMUs and the optical reference using Euler angles is the common way of measuring the accuracy of motion capturing. Exemplarily this method is applied in [19], [20], and [15]. To overcome the lack quality of the Euler angle measure, a quaternion based error measure is proposed here. In contrast to the Euler angle representation the quaternion orientation representation does not suffer form singularity issues. To compute the error measure based on quaternions first the distance between the IMU quaternion and the optical system quaternion in 3D space is computed according to equation (1). Finally, the RMS

value of the quaternion distance, dependent on the number of captured samples N of the dataset, is computed according to equation (2).

$$w_{3D} = 2 * \text{acos}\left(\left|quat_{IMU} * quat_{Optical}\right|\right) \quad (1)$$

$$RMS_{Quat} = \sqrt{\frac{1}{N}\sum_{k=0}^{N} |w_{3D}|} \quad (2)$$

The following showcase highlights the reliability of the quaternion orientation error measure. A movement is performed using two IMUs with a constant displacement of approximately 20° on the yaw axis. During the captured movement the displaced sensors are rotated along the pitch axis for approximately 90° and back to the starting position. The Euler angle representation of both IMUs is shown in Fig. 3. After a period in an initial position a rotation around the pitch axis is performed. Finally, the IMUs are rotated back to the initial position.

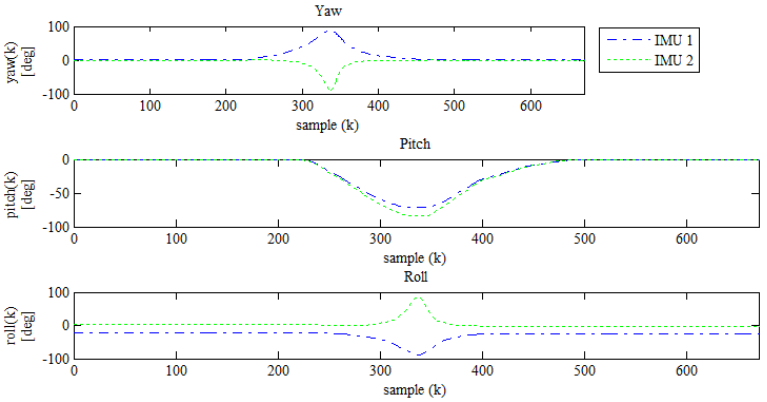

Fig. 3 Euler trace of the two IMUs movement

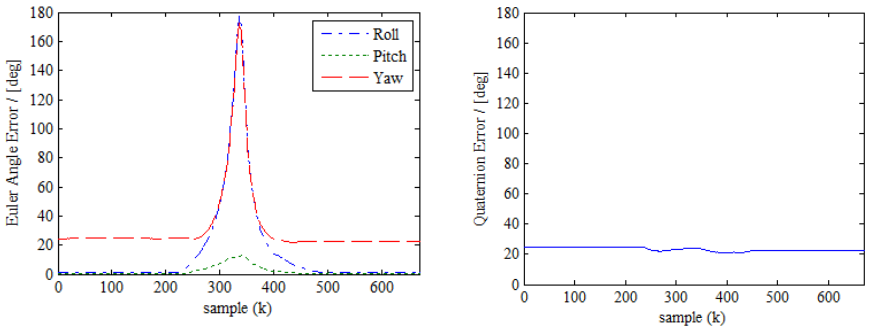

Fig. 4 (a) Euler angle error representation of the performed movement, (b) evaluation of the movement using Quaternion RMS error measure

In general, due to the fixed displacement of both IMUs the expected error value is the displacement itself, e.g. approximately 20°. In the initial orientation in Fig. 4 Euler angle representation and quaternion measure both show a displacement of 20°. During the movement only the quaternion measure fulfills expectations and maintains a constant difference between both fixed IMUs. In contrast, the Euler angle measure shows a non static behavior during the captured movement. Therefore, in contrast to the commonly used Euler angle measure the quaternion measure is more suitable for the evaluation of multi-axis movements.

4 Low-Cost, Wireless IMU Prototyping Platform

State-of-the-art small sized commercial inertial sensors [18] either lack the availability of an open, platform independent protocol, wireless connectivity or extension interfaces for additional sensors. Therefore, a extensible, wireless inertial sensor unit called Institute of Microelectronic Systems Inertial Measurement Unit $(IM)^2SU$, featuring onboard inertial sensor fusion, for use in home based stroke rehabilitation is proposed [21]. To evaluate orientation estimation accuracy an optical system is used as golden reference.

To overcome the deficiencies of commercial platforms, the presented wireless, low power sensor platform provides a platform independent protocol. The following aspects are the main development targets:

- low power RF module and MCU
- full access via platform independent interfaces
- real-time onboard orientation estimation

The system architecture of the Institute of Microelectronic Systems Inertial Measurement Unit (IM)²SU is separated into hardware and software. Both aspects are detailed in the next sections. A comprehensive description of the IMU architecture and performance characteristics like overall latency and orientation estimation accuracy are provided in [21].

4.1 Hardware Architecture

Comparable to state-of-the-art inertial sensors the (IM)²SU comprises tri-axial accelerometers, magnetometers and gyroscopes. In order to ease the system's design, the following sensor packages integrating aligned tri-axial sensors, analog amplifiers and AD converters, and digital interfaces for sample read-out, are chosen:

- InvenSesne ITG-3200 (gyroscope)
- STMicroelectronics LIS3DH (accelerometer)
- Xensor Integration XEN-1210 (magnetometer)

The Atmel ATZB-24-A2 samples the onboard sensors and communicates wirelessly with other (IM)²SU units. Two chip antennas, the IEEE 802.15.4 compliant transceiver, and an Atmel ATmega1281V MCU are integrated. The accelerometer and gyroscope are connected via I²C bus, and the magnetometer via SPI to the ATZB-24-A2. The (IM)²SU is programmable over an USB interface connected to the virtual COM port IC FT323R from FTDI. The board is powered by a lithium ion battery with a maximum charge of 650 mAh.

The (IM)²SU prototype is shown in Fig. 5. For debug and development purposes, JTAG and ISP interfaces are provided. Custom expansion headers could be used in future for the connection of force sensors for grasping task assessment. The PCB dimensions are 60 mm by 60 mm (a), the area optimized PCB dimensions are 23 mm by 31 mm (b).

4.2 Software Architecture

Motion capturing applications require movement data to be acquired from predefined positions on the observed body. To process this measurement data, exact timing relations from the incoming samples must be known. The software of the (IM)²SU is designed to guarantee synchronous motion capturing from up to 10 wireless devices, deterministic latency behavior and robust communication performance while exposing low latency.

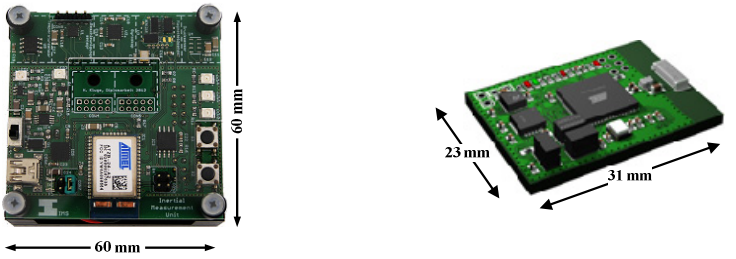

Fig. 5 (IM)²SU prototype (a) and area optimized (IM)²SU unit preview (b)

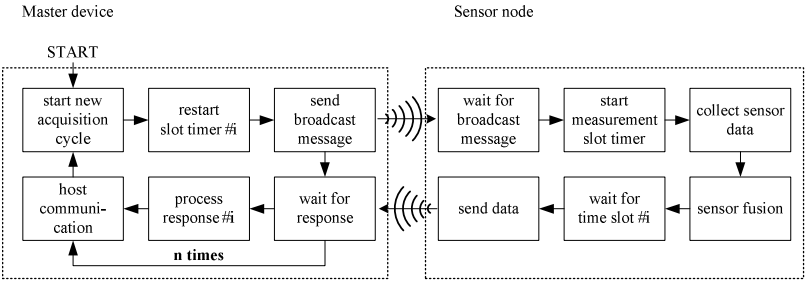

Fig. 6 Communication and processing steps of the (IM)²SU system

A deterministic communication is achieved by implementing a TDMA protocol on a pre-configured 802.15.4 channel. The master and each slave start a slot timer after sending or receiving the broadcast message, respectively. Each slave associates it's network address with distinct time slot #i. During the corresponding time slot the quaternion data is transmitted. The master associates the incoming packet with the appropriate IMU and passes the data to the host system. Because of the centralized master and decoupled slot timers, the overall system behaves robustly in cases of packet loss or failing of single IMUs. The software processing steps of the (IM)²SU devices are shown in Fig. 6.

5 Design Space Exploration of Algorithmic Approaches for Orientation Estimation Regarding Accuracy and Execution Time

Based on the methodology introduced in Section 4.1 and Section 4.2 a variety of orientation estimation algorithms are evaluated. The analysis is performed on notebook comprising an Intel Core i7-4500U processor at 1.8 GHz and 8 GB RAM.

Evaluation objectives are execution time and achievable orientation estimation accuracy based on the RAW data of the proposed (IM)²SU and an Xsens MTx IMU [18]. Both IMUs comprise tri-axial gyroscopes, accelerometers and magnetometers. Dependent on the algorithm a subset of the available sensors is used for orientation estimation.

Table 1 lists the algorithms considered within the evaluation presented in this Section. Besides gyroscope data integration, vector selector algorithms, Complementary filters and Kalman filters with different orders are evaluated.

Table 1 Algorithms considered in the evaluation

Algorithm	Abbreviation	Reference
Integration (1st order)	Integ1	[12]
Integration (3rd order)	Integ3	[22]
Factored Quaternion Algorithm	FQA	[5]
Optimal two-observation Quaternion estimation method	O2OQ	[7]
Complementary filter according to Calusdian	CompCal	[8]
Complementary filter according to Madgwick	CompMadg	[9]
4th order Kalman filter	KFLee	[11]
7th order Kalman filter	KFYun	[12]
9th order Kalman filter	KFRoet	[23]
9th order Kalman filter	KFSuh	[22]
Xsens Kalman filter	XKF	[18]

The orientation estimation accuracy utilizing both IMUs RAW data and execution time on the reference platform are presented in Table 2 and Table 3 respectively. In general, the tri-axial gyroscope is suffering from sensor specific bias. The evaluation results of the integration based methods show a significant degradation due to the gyroscope bias, observable as long-term drift. The goal of the complementary Filter and KF methods is to estimate gyroscope bias and perform adaptive drift compensation. In comparison to the plain integration methods an enhancement is observable, but the CompMadg, KFRoet and KFSuh methods are still inapplicable for accurate human motion capturing. In general, the larger gyroscope bias of the (IM)²SU compared to the Xsens MTx IMU results in an lower accuracy of these methods utilizing the (IM)²SU unit. Considering the orientation estimation accuracy based on both IMUs RAW data the KFLee methods perform best. Furthermore, the execution time of these methods is quite optimal within the overall methods evaluation.

Table 2 Orientation estimation accuracy and execution time of Kalman filter versions performed on an Intel Core i7-4500U processor utilizing Xsens MTx IMU Raw data

Algorithm	Orientation estimation accuracy / [° RMS]				Execution time / [µs]
	Quaternion error measure	Euler angle error measure (roll, pitch, yaw))			
Integ1*	30.0	22.4	18.7	14.3	0.01
Integ3*	19.0	14.2	11.2	9.9	4.96
FQA	22.2	3.4	6.0	21.5	4.53
O2OQ	7.7	3.2	2.3	6.7	3.48
CompCal	3.2	2.0	2.0	2.1	4.53
CompMadg*	2.9	1.8	1.7	1.9	2.90
KFLee	2.9	1.8	1.7	2.0	10.16
KFYun	7.4	3.3	2.0	6.6	25.39
KFRoet*	14.2	9.0	6.4	9.0	25.15
KFSuh*	19.9	16.4	9.5	10.0	85.03
XKF	5.8	1.8	1.9	5.3	-

Table 3 Orientation estimation accuracy and execution time of Kalman filter versions performed on an Intel Core i7-4500U processor utilizing (IM)²SU IMU Raw data

Algorithm	Orientation estimation accuracy / [° RMS]				Execution time / [µs]
	Quaternion error measure	Euler angle error measure (roll, pitch, yaw))			
Integ1*	55.86	55.28	11.36	11.91	0.01
Integ3*	50.05	49.10	11.88	10.53	4.96
FQA	17.69	3.94	4.06	16.94	4.53
O2OQ	9.59	3.64	2.67	8.52	3.48
CompCal	6.03	3.15	2.77	4.56	4.53
CompMadg*	15.52	6.26	8.68	10.13	2.90

Table 3 (*continued*)

KFLee	4.90	3.26	2.16	3.39	10.16
KFYun	8.54	3.64	2.43	7.93	25.39
KFRoet*	34.44	30.93	9.54	12.63	25.15
KFSuh*	48.11	46.31	14.08	8.14	85.03

* Long term drift observable due to gyroscope bias in respect of inadequate compensation or estimation

6 Kalman Filter Modification

The results presented in section 5 demonstrate that the KFLee [11] operates accurately with a moderate execution time. Therefore, algorithmic modifications are implemented and evaluated to reduce the number of operations required for the computation of a Kalman filter update. Applying predefined values for several matrices is possible due to prior knowledge of constant sensor and process noise characteristics.

A simplified Kalman filter algorithm is proposed in [19] using pre-computed a priori and a posteriori error covariance matrices. This reduces computational demand by about 25 %. However, the authors do not consider the usage of an additional magnetometer and the evaluation of multi axis movements. In [20] a two stage Kalman filter with reduced computational complexity is presented. The preprocessing relies on the QUEST / FQA algorithm, which shows a less accurate result compared with the O2OQ algorithm used in this work. A custom ASIP was designed to speed up computations and allow real-time operation at a 1 kHz sampling rate. The paper focuses on ASIP design and lacks an orientation estimation accuracy and fixed-point analysis.

6.1 Algorithmic Modification

Using pre-computed covariance matrices and a pre-computed Kalman gain matrix results in less required operations. The Kalman gain matrix also becomes independent from the actual filter step and can be computed offline due to the constant a priori and a posteriori error covariance matrices. The pre-computation of the Kalman gain matrix achieves a high reduction of computational demands, as it eliminates the computation of a 4x4 matrix inverse in each filter step.

This concept is applied to the Kalman filter according to Lee and Park [11] enabled by knowledge about constant sensor noise characteristics. The influence on the filter structure is analyzed in [24], highlighting the reduction of required computation steps. The values for the error covariance matrices and the Kalman gain matrix then have to be computed in advance.

The difference in the orientation estimation compared to the original algorithm is 0.08 °RMS, 0.01 °RMS and 0.19 °RMS (roll, pitch, and yaw) [24]. Further orientation estimation accuracy results and a comparison to other algorithms will be provided in Section 6.

6.2 Evaluation of the Modification

A comparison of floating-point operations required for a single Kalman filter step of the modified Kalman filter compared to the initial version is given in Table 4. The modification significantly reduces the number of operations. The predefined a priori and a posteriori error covariance matrices and the Kalman gain matrix were established by tracing the matrices on a PC based implementation using captured (IM)²SU (wireless IMU proposed in Section 4) and Xsens MTx IMU RAW data.

Table 4 Comparison of operations per filter step of the Kalman filter versions

Algorithm	Number of operations			
	'ADD', 'SUB'	'MUL'	'DIV'	'$\cos^{-1}$'
O2OQ	147	197	31	1
Original KF	579	524	46	0
Modified KF	60	37	20	0

Utilizing $(IM)^2SU$ RAW data the accuracy is 3.4 ° RMS (quaternion error measure), respectively 2.9 ° RMS for orientation estimation based on MTx RAW data. In general, these values are comparable to the accuracy of the original filter algorithm.

7 Kalman Filter Based on Fixed-Point Data Representation

A variety of state-of-the-art low-power processor cores and System-on-Chips (SoC) are insufficient for computation of floating-point intensive algorithms due to the absence of a floating-point unit (FPU). Therefore, a fixed-point version of the Kalman filter algorithm is developed.

Fixed-point computations are especially suitable for real-time orientation estimation based on customized processor cores or dedicated hardware accelerators. Using a fixed-point data representation enables the throughput requirements demanded by applications like monitoring training sessions in sports or medical rehabilitation to be achieved [25], [26].

7.1 Fixed-Point Bit-Width Evaluation Method

To determine required minimal total bit-width and the number of integer and fraction bits for each Kalman filter variable, a template based C++ framework, described and applied in [27], is used. The framework enables code re-usage at data-type level by abstracting the data-type.

For analysis using this framework the floating-point data type (e.g. float or double) has to be replaced by the frameworks template based data type. Setting the template data-type to float or double results in a floating-point reference

implementation. For fixed-point analysis the template data-type has to be replaced by a hybrid floating-point or integer type (e.g. int32_t, int64_t) and parameters specifying total bit-width and fixed-point position. An additional data-type implemented in the framework allows accuracy assessment, comparison to floating-point results and overflow detection at bit-level.

7.2 Fixed-Point Kalman Filter Evaluation

A fixed-point version of the Kalman filter according to [11] is established due to the high orientation estimation accuracy at moderate computational costs according to the analysis presented in section 5. The results of the bit-width dependent orientation estimation error analysis based on the RAW data of the Xsens MTx and the (IM)²SU IMU shown in Fig. 7. The analysis starts with an internal representation using 64 bits for each element within the data-flow reducing to 20 bits. The orientation estimation shows a reliable behavior down to a bit-width for the overall data-flow of 32 bits. At that bit-width estimation error increases and the orientation estimation becomes unusable.

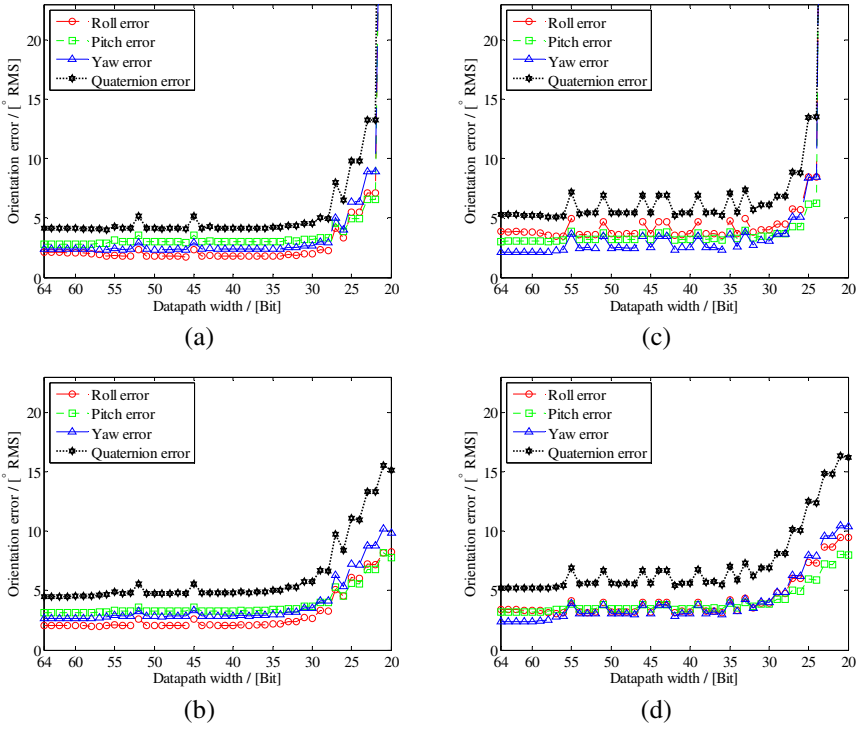

Fig. 7 Bit-width dependent orientation estimation error of the KFLee (a) and modified KFLee (b) utilizing MTx RAW data respectively the results utilizing (IM)²SU IMU RAW data (c), (d)

8 Dedicated Kalman Filter Module

Arising heterogeneous architectures like the Xilinx All Programmable SoCs or Altera SoC FPGAs enable the flexible customization of basic hardware architectures. Both SoCs comprise of a programmable processor core (Cortex A9 dual core) and a FPGA fabric. The FPGA fabric allows the flexible integration of dedicated hardware accelerators. This Section presents the architecture and performance characteristics in terms of execution time and energy consumption of a dedicated module for inertial sensor fusion by Kalman filtering [25], [26].

8.1 Hardware Architecture

The hardware accelerator can either be used in a final ASIC design or as an accelerator on FPGA based platforms. In general the application demands of human motion capturing are that each IMU is sampled at up to 100 Hz, while up to ten IMUs are used to capture complex full body movements. The Kalman filter module is designed to operate at a clock frequency of 100 MHz on Xilinx Series 7 FPGA architectures. Therefore, a maximum processing time of 19,531 clock cycles (10 IMUs at 512 Hz) is targeted. Due to the large number of clock cycles resource optimization is focused.

As shown in Fig. 8 the hardware accelerator comprises of six sub-modules, forming the dataflow of the Kalman filter. Furthermore, four arithmetic modules enable sharing of resource intensive operations to reduce hardware costs. In addition to increased throughput requirements a pipelined design can be established by introducing pipeline stages between the dataflow sub-modules.

Required Kalman filter parameters like noise covariance matrices, Kalman gain matrices, state vector and others reside in a 36 Kbit dual port Block-RAM. One port is connected to a BUS- Interface (e.g. AXI-BUS), while the other is used by the sub-modules to load and store parameters. The interface to the IMUs is realized as a separate hardware-module.

A finite state machine controls the global dataflow using handshake signals. Due to the separation of arithmetic operations into sub-modules the state machine further controls the allocation of the arithmetic sub-modules. A detailed description of the data-flow is presented in [26].

8.2 Kalman Filter Module Execution Time and Hardware Costs

The designed hardware module is applicable in two main categories. Firstly, the module can be used as an accelerator in FPGA based architectures. Secondly, the module can be used to increase throughput or energy efficiency in heterogeneous SoC designs. Therefore, this section presents the hardware costs and execution time of the module for FPGA based architectures and the ASIC synthesis results based on a 40 nm TSMC LP library.

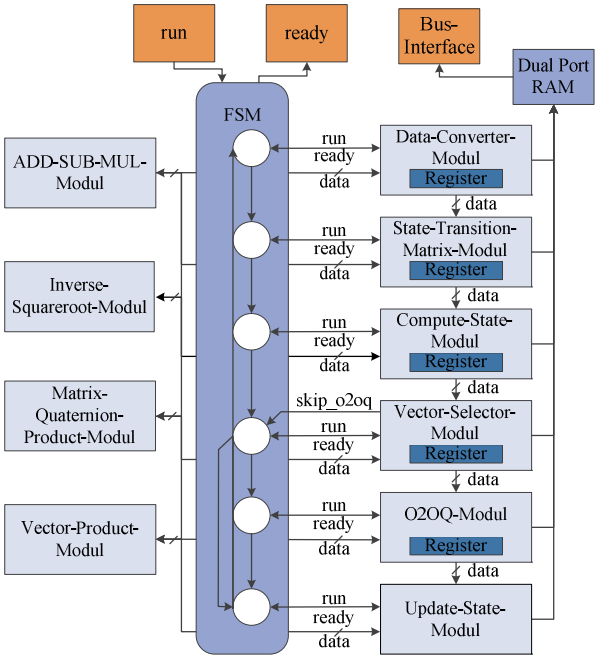

Fig. 8 Hardware architecture of the Kalman filter module

In [26] the hardware costs and execution time of the custom designed Kalman filter module and the results of arising High Level Synthesis (HLS) tools are presented. As input description for the HLS tools the bit-true software reference of the fixed-point Kalman filter algorithm has been used. Kalman filter modules are created using Mentor Graphics Catapult C (version 2010.a.104) and Xilinx Vivado HLS (version 14.6). Table 5 shows the hardware resources of the HLS generated modules and a custom resource consumption optimized module utilizing the Xlinx Zynq 7020 FPGA fabric.

Although HLS tools allow short development times for hardware accelerators, the presented results show the current inapplicability of these tools in generating highly efficient accelerators. Furthermore, performing a fixed point analysis using external tools is still required, subsequently increasing the overall development time.

Table 5 Comparison of FPGA resource consumption and execution time at 100 MHz of the Kalman filter module versions

Kalman filter module	FPGA Hardware resources				Execution time / [clock cycles]
	Registers	LUTs	DSP slices	RAMB36	
Catapult C	10,532	14,550	38	0	829
Vivado HLS	12,663	20,104	227	3	1,344
Custom module	4,395	7,035	1	1	1,623

The maximum achievable clock frequency of the Kalman filter module performing an ASIC synthesis based on a 40 nm TSMC LP library is 176 MHz. The silicon area consumption is 0.15 mm^2 and the energy consumption per iteration is 27.8 nJ. In general, the throughput can be increased if desired by using the output registers of each algorithmic module as pipeline registers and by increasing the number of algorithmic modules.

9 Design Space Exploration Results

Common design exploration objectives are energy consumption and execution time of the Kalman filter for orientation estimation within motion capturing sessions on various processing architectures. Besides commercial and customized programmable architectures, heterogeneous and dedicated architectures are analyzed. This Section presents the execution time and energy consumption results using the Kalman filter algorithms according to [11] and the modified version on programmable architectures presented in section 6.

9.1 Programmable Architectures

In [24] the optimal number representation (e.g. floating- or fixed-point) achieving lowest latency for each platform is analyzed. In general, the processors data-width, the presence of a floating-point unit, and the performance of the floating-point operations emulation affect the optimal number representation.

The Hardware platforms considered within the evaluation are listed in Table 6 cover a wide range available platforms ranging form flexible general purpose processors to low power microcontrollers. The architecture features given in the table highlight the specific details.

Table 6 Hardware platforms considered in the evaluation

Processor	Clock frequency	Features
ATmega1281	8 MHz	8-bit low cost MCU
AT32UC3A0128	64 MHz	32-bit MCU
Nios II (fast core)	50 MHz	Altera soft-core processor with FPU
ARM 1176	700 MHz	32-bit RISC core with coprocessor FPU
ARM Cortex A8	1.0 GHz	32-bit RISC core with fixed-point and floating-point SIMD unit
Core i7 4500U	1.8 GHz	64-bit general purpose processor with floating point SIMD units enabling vector operations

Table 7 shows the execution time per filter iteration of the original and modified Kalman filter according to [11] utilizing the optimal number representation for each processing architecture (fixed- or floating-point). The

bit-width of the fixed-point version is set to the appropriate multiples of the processors data-width. Based on the results presented in Section 7 a word length of 32 bits is chosen. According to [24] the fixed-point KF versions are used for computations utilizing the ARM Cortex A8, AT32UC3A, and Nios II processor. All further processor cores use the floating-point version of the KF, due to the faster execution time on that architecture.

Table 7 Execution time of Kalman filter based orientation estimation utilizing various programmable hardware architectures and the respective power dissipation

Processor	Execution time / [µs]		Power dissipation / [mW]
	Original	Modified	
ATmega1281	24,061.50	9,430.25	70 [2]
AT32UC3A0128	464.08	140.47	120 [2]
Nios II (fast core)[1]	2,189.00	682.00	780
ARM 1176	22.43	8.66	202 [2]
ARM Cortex A8	31.46	8.41	6,000 [3]
Core i7 4500U	10.16	5.68	≈ 8,500 [4]

[1] Nios II mapped on an Altera Cyclone II 2C35 FPGA, power dissipation estimated by Altera PowerPlay software.
[2] Estimated based on typical electrical characteristics values provided in the datasheet.
[3] According to Texas Instruments C6 Integra C6A816x power estimation spreadsheet.
[4] Measured power consumption utilizing power meter (Sony Vaio SVP1322C5E notebook, Windows 7).

The results presented in Table 7 clarify the benefit in execution time on all processor architectures due to the filter modification. Furthermore, the absolute execution time and power dissipation of each processor is highly architecture dependent. The design space exploration in Section 9.3 will focus on the properties execution time and energy consumption for performing a single filter iteration considering all presented processing architectures.

9.2 Heterogeneous FPGA Fabric / RISC Architecture (SoC FPGA)

A design objective for utilizing hardware accelerator based orientation estimation is increased energy efficiency. Arising platforms like the heterogeneous FPGA fabric / RISC Xilinx Zynq enable increased design flexibility by incorporating configurable logic into a high-level programmable SoC. From the system designers perspective optimization goal could either be increasing throughput or enhancing energy efficiency.

The analysis results presented in this Section focus on increasing energy efficiency due to the system requirements stated in Section 8.1. Increasing the

throughput rate could be achieved by introducing pipeline stages within the accelerator module or the instantiation of multiple modules [26]. The analysis evaluates the execution time and energy consumption of the modified Kalman filter proposed in Section 3.

The results presented in Table 8 show the execution time and energy consumption of the custom Kalman filter hardware accelerator module synthesized for a Xilinx Series 7 FPGA in comparison to a single filter iteration computed based on an ARM Cortex A9 RISC core. For the analysis the Xilinx Zynq 7020 SoC is used. The results demonstrate the enhanced energy efficiency of the custom module in comparison in to execution on the RISC core. Furthermore, the integrated FGA fabric enables throughput scalability regarding future application demands.

Table 8 Execution time and energy consumption evaluation exploring the Xilinx Zynq 7020 heterogeneous SoC partitioning abilities

Hardware accelerator module	**Execution time / [µs] (clock cycles)**	**Energy consumption / [nJ]**
ARM Cortex A9	4.11	2,922
Custom module	16.23 (1.623)	2,550

9.3 Dedicated Architectures

This Section compares the execution time and energy consumption of dedicated architectures for KF based orientation estimation. The energy consumption is estimated based on a power dissipation simulation utilizing Modelsim respectively the Tensilica design suite.

First, an Application Specific Instruction Set Processor (ASIP), based on the Tensilica Xtensa LX4 processor template [25] is optimized for fixed-point KF computation. The processor core is extended by custom instructions for square root and reciprocal computation to reduce execution time and enhance energy efficiency. The area consumption of the optimized processor core (without memory area) is based on a 40 nm LP process is 0.29 mm^2, with a maximum clock frequency of 350 MHz.

Furthermore, the result of an ASIC synthesis of the custom accelerator module presented in section 8 for a target operation frequency of 100 MHz is reported. ASIC synthesis based on a TSMC 40 nm LP library results in an area consumption of 0.15 mm2.

Table 9 shows the energy consumption advantages of the custom hardware accelerator module in comparison to the LX4 processor core. Furthermore, the module provides enhanced scalability by parallel instantiation and pipelining in contrast to the LX4 processor core. The analysis is based on the modified KF algorithm presented in section 3.

Table 9 Comparison of execution time and energy consumption of the ASIC architectures

Processing architecture	Execution time / [µs] (clock cycles)	Energy consumption / [nJ]
Tensilica LX4 ASIP	23.13 (8,096)	472.8
Custom module	16.23 (1.623)[2]	27.8

9.4 Overall Evaluation Energy, Accuracy, Execution Time

This section focuses on exploring the design space properties execution time and energy consumption at architecture level. While energy consumption is a major issue for mobile processing platforms, the execution time limits the maximum sampling frequency of the IMUs. The results enable an application requirement driven trade-off between the properties for selection of the optimal processing architecture. In general, the distance from the origin for an optimal solution is small.

The summarized results comprising programmable, heterogeneous and dedicated architectures presented in Fig. 9 clearly mark the Core i7 processor as the fastest architecture for KF based orientation estimation among the evaluated architectures. In contrast, the custom hardware accelerator module achieves highest energy efficiency. Moving along the Pareto-front the ARM Cortex A9 and the ARM 1176 processor are corner points. The microcontroller-based architectures and the Nios II softcore processor show a clearly non-optimal behavior with regard to analysis properties.

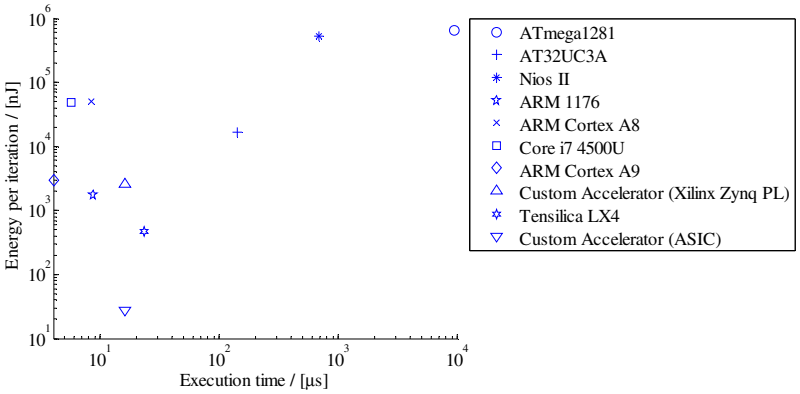

Fig. 9 Design space exploration of processing architectures for modified KF based orientation estimation considering execution time and energy consumption

10 Conclusions

The presented results tackle multiple issues in choosing an appropriate algorithm for IMU based orientation estimation and the selection of a processing architecture.

The presented algorithms for orientation estimation in section 2 highlight the various algorithmic solutions. In general, major concerns regarding the algorithms are execution time and orientation estimation accuracy. For accuracy assessment an objective error measure is mandatory. Therefore, a quaternion based error measure is proposed in section 4. A showcase highlights the advantages of this measure compared to traditional Euler angle based accuracy assessment. In contrast to the Euler angle measurement the quaternion based measurement results in a constant error value while performing a movement utilizing two IMUs with a constant displacement.

Results of the evaluation of orientation estimation accuracy and execution time of various algorithms for IMU sensor fusion are presented in section 6. The results enable the selection of the optimal sensor fusion algorithm regarding the applications throughput and accuracy demands. In general, there is a non homogenous distribution regarding both objectives among the different algorithms. Although the Kalman Filter according to Lee and Park 2009 achieves highest accuracy, there are KF based approaches showing a non reliable orientation estimation performance. Furthermore, the reduced computational complexity Kalman filter proposed in section 3 enables orientation estimation featuring high accuracy and low execution time.

Based on the results in section 6 an analysis of the orientation estimation accuracy dependency from the datapath word length is analyzed in section 7. The results clarify a minimum datapath word length of 32 bits for orientation estimation without any accuracy degradation. Further word length reduction results in increasing orientation errors.

Section 8 presents a hardware accelerator module utilizing a 32 bit datapath based on the modified Kalman filter presented in section 3. The accelerator enables highly energy efficient sensor fusion and flexible scalability according to various application throughput requirements. The module is applicable as accelerator in heterogeneous RISC / FPGA SoCs or custom ASICs. Furthermore, based on a fixed-point C / C++ description of the modified KF algorithm hardware accelerators are developed utilizing state-of-the-art HLS tools. The hardware costs evaluation presented in Section 8 highlights the advantages of a custom design compared to using HLS tools.

The design space exploration in section 9 analyzes the execution time and energy consumption of KF based orientation estimation among various processing architectures. Besides programmable architectures, arising heterogeneous RISC / FPGA architectures, as well as customized processor cores and the custom hardware accelerator, are considered. In general, the custom hardware accelerator achieves highest energy efficiency, but requires the design of an ASIC or the

usage of a heterogeneous architecture. Arising platforms like the Xilinx Zynq SoC will provide further design flexibility with regard to the flexible usage of hardware accelerators and enhanced design partitioning aspects.

References

[1] Zhou, H., Hu, H., Tao, Y.: Inertial measurements of upper limb motion. Med. Biol. Eng. Comut. 44, 479–487 (2006)
[2] Jekeli, C.: Inertial Navigation Systems with Deodetic Applications. de Gruyter (2001)
[3] Shuster, M., Oh, S.: Three-axis attitude determination for vector observations. Journal of Guidance and Control 4(1), 70–77 (1981)
[4] Black, H.: A passive system for determining the attitude of a satellite. AIAA Journal 2(7), 1350–1351 (1964)
[5] Yun, X., Bachmann, E.R., McGhee, R.B.: A Simplified Quaternion-Based Algorithm for Orientation Estimation From Earth Gravity and Magnetic Field Measurements. IEEE Transactions on Instrumentation and Measurement 57, 638–650 (2008)
[6] Markley, F.: Attitude determination from vector observations: A fast optimal matrix algorithm. Journal of Astronautical Sciences 41(2), 261–280 (1993)
[7] Markley, F.: Fast quaternion attitude estimation from two vector measurements. AIAA J. Guidance, Control, and Dynamics 25(2), 411–414 (2002)
[8] Calusdian, J., Yun, X., Bachmann, E.: Adaptive-gain complementary filter of inertial and magnetic data for orientation estimation. In: IEEE International Conference on Obotics and Automation (ICRA), pp. 1916–1922 (2011)
[9] Madgwick, S.: An efficient orientation filter for inertial and inertial/magnetic sensor arrays. Report x-io, University of Bristol, UK (2010)
[10] Welch, G., Bishop, G.: An introduction to the kalman filter. In: International Conference on Computer Graphics and Interactive Techniques (2001)
[11] Lee, J.K., Park, E.: A minimum-order kalman filter for ambulatory real-time human body orientation tracking. In: IEEE International Conference on Robotics and Automation, ICRA 2009, pp. 3565–3570 (2009)
[12] Yun, X., Bachmann, E.: Design, Implementation, and Experimental Results of a Quaternion-Based Kalman Filter for Human Body Motion Tracking. IEEE Transactions on Robotics 22, 1216–1227 (2006)
[13] Simon, D.: Kalman filtering. Embedded Systems Programming 14, 72–79 (2001)
[14] Faragher, R.: Understanding the Basis of the Kalman Filter Via a Simple and Intuitive Derivation (Lecture Notes). IEEE Signal Processing Magazine 29(5), 128–132 (2012)
[15] Young, A.: Comparison of Orientation Filter Algorithms for Realtime Wireless Inertial Posture Tracking. In: Sixth International Workshop on Wearable and Implantable Body Sensor Networks, BSN 2009, pp. 59–64 (2009)
[16] Brückner, H.-P., Spindeldreier, C., Blume, H., Schoonderwaldt, E., Altenmüller, E.: Evaluation of Inertial Sensor Fusion Algorithms in Grasping Tasks Using Real Input Data. In: 2012 Ninth International Conference on Wearable and Implantable Body Sensor Networks (BSN), pp. 189–194 (2012)
[17] Vicon Motion Systems, `http://www.vicon.com/products/nexus.html`
[18] Xsens Technologies BV, `http://www.xsens.com`

[19] Sabatelli, S., Sechi, F., Fanucci, L., Rocchi, A.: A sensor fusion algorithm for an integrated angular position estimation with inertial measurement units. In: Design, Automation Test in Europe Conference Exhibition, DATE (2011)
[20] Sabatelli, S., Galgani, M., Fanucci, L., Rocchi, A.: A double stage Kalman filter for sensor fusion and orientation tracking in 9D IMU. In: 2012 IEEE Sensors Applications Symposium, SAS (2012)
[21] Brückner, H.-P., Nowosielski, R., Kluge, H., Blume, H.: Mobile and wireless inertial sensor platform for motion capturing in stroke rehabilitation sessions. In: 2013 5th IEEE International Workshop on Advances in Sensors and Interfaces, pp. 14–19 (2013)
[22] Suh, Y.S.: Orientation Estimation Using a Quaternion-Based Indirect Kalman Filter With Adaptive Estimation of External Acceleration. IEEE Transactions on Instrumentation and Measurement, 1–10 (2010)
[23] Roetenberg, D., Luinge, H., Baten, C., Veltink, P.: Compensation of magnetic disturbances improves inertial and magnetic sensing of human body segment orientation. IEEE Transactions on Neural Systems and Rehabilitation Engineering 13, 395–405 (2005)
[24] Brückner, H.-P., Spindeldreier, C., Blume, H.: Modification and fixed-point analysis of a Kalman filter for orientation estimation based on 9D inertial measurement unit data. In: 2013 35th Annual International Conference of the IEEE Engineering in Medicine and Biology Society (EMBC), pp. 3953–3956 (2013)
[25] Brückner, H.-P., Spindeldreier, C., Blume, H.: Design and Evaluation of a Hardware-Accelerator for Energy Efficient Inertial Sensor Fusion on Heterogeneous SoC Architectures. In: The 15th International Conference on Biomedical Engineering. IFMBE Proceedings, vol. 43, pp. 227–230. Springer International Publishing (2014)
[26] Brückner, H.-P., Spindeldreier, C., Blume, H.: Energy-efficient inertial sensor fusion on heterogeneous FPGA-fabric/RISC System on Chip. In: 2013 Seventh International Conference on Sensing Technology (ICST), pp. 506–511 (2013)
[27] Pfitzner, M., Cholewa, F., Pirsch, P., Blume, H.: Close-to-hardware error analysis for real-time wavenumber domain processing. In: 7th International Conference on Radar RADAR (2012)

The Integrated versus Standalone Operation Mode for Second and Subsequent Fragments Headers Compression Scheme in 6LoWPAN

S.A.B. Awwad[1,*], C.K. Ng[2], N.K. Noordin[1], B.M. Ali[1], F. Hashim[1], and N.H.A. Ismail[1]

[1] Department of Computer and Communication Systems, Faculty of Engineering
[2] Institute of Gerontology, Universiti Putra Malaysia, UPM Serdang, 43400 Selangor, Malaysia
samer_awwad80@yahoo.com

Abstract. In 6LoWPAN, IPv6 is capable to provide identity and wireless embedded internet aims for efficiently providing IP global connectivity for wireless, small size, low power, low rate, limited memory and limited computation capabilities embedded smart objects. However, the relatively huge header size of upper layer protocols (e.g. TCP, UDP and IPv6) will deplete the frame payload to approximately 33 bytes. Some schemes had been designed to compress the headers to provide more space for the data payload. Recently, a standalone operation mode for Second and Subsequent Fragments Headers Compression (S&SFHC) scheme for header compression in 6LoWPAN has been proposed. This scheme exploits the correlation between the first and the subsequent fragments' headers to avoid carrying the redundant headers of second and subsequent fragments. In this paper, an extended version of S&SFHC for 6LoWPAN is proposed. This new scheme is introduced by integrating S&SFHC with other existing scheme like LOWPAN_IPHC. When the proposed new scheme incorporates with another scheme, the existed scheme is used to compress the header for the first fragment only. The second and subsequent fragments will be compressed by using S&SFHC scheme. The integration between S&SFHC and LOWPAN_IPHC schemes can achieve up to 30% and 10% higher packet delivery ratio, 30% and 10% higher throughput, 18% and 6% lower average delay, 24% and 4% lower average energy consumption compared to LOWPAN_IPHC and S&SFHC standalone mode respectively when the packet size is 600 bytes.

Keywords: 6LoWPAN, header compression, IPv6, IEEE802.15.4, fragmentation and reassembly.

* Corresponding author.

A. Mason et al. (eds.), *Sensing Technology: Current Status and Future Trends III*,
Smart Sensors, Measurement and Instrumentation 11, DOI: 10.1007/978-3-319-10948-0_9

1 Introduction

Internet of Things (IoT) is the internet that connects not only computers and hand held devices but also other physical objects [1, 2]. In the future revolution of IoT, physical objects (humans, animals, machines, devices, buildings, etc.) are identified, connected and controlled through the internet. When you want to communicate, control and search for specific things, the best to enquiry is the IoT. You can enquire about everything and anything anytime and anywhere. IoT is really smart and hence, it is also called as the internet of smart objects. Things or objects need to be smart in order to be part of the IoT. Based on the characteristic of smart objects [3–6], and the characteristic of IoT, Smart objects in IoT need to have the following specific characteristics:

- global unique identity.
- ability to communicate effectively with the internet.
- ability to keep its data.
- ability to share information about its characteristics, features and needs through its lifecycle.
- ability to senses, survey and control its environment.
- ability to make a decision or participating in decisions making.

6LoWPAN is the part of IoT that concerns with providing global unique identity and internet connectivity to smart objects in wireless personal area network (WPAN). However, providing these characteristics for wireless, small size, low power, low rate, limited memory and limited computation capabilities embedded smart objects is challenging for 6LoWPAN. It needs to enable the transmission of IPv6 packets over LoWPANs IEEE 802.15.4 frames. The relatively huge header size of IPv6 packets will deplete the IEEE 802.15.4 frame payload leaving few bytes for actual data. In order to overcome this problem, several header compression schemes had been introduced to compress packet's headers. As an example, 6LoWPAN header compression scheme for Datagram Transport Layer Security (DTLS) had been proposed in [7]. This scheme reduces the additional security bits of heavyweight DTLS header. Hence, end-to-end security for IoT is achieved while conserving security bits for actual data transmission.

LOWPAN_HC1 [8] was the first IPv6 header compression scheme for 6LoWPAN. This scheme can compress only IPv6 link local addresses where source and destination addresses are stateless configured link-local addresses. This scheme cannot compress the global IPv6 addresses. LoWPAN_HC1g [9] is an extension of LoWPAN_HC1. It is designed to compress IPv6 global addresses. However, this scheme assumes that 6LoWPAN network is assigned a default, single, compressible and global address prefix. When source or destination addresses' prefixes match the default one, they can be compressed. Otherwise the global address prefix remains uncompressed.

LOWPAN_IPHC [10] can compress link-local and global unicast addresses. This specification expects that a conceptual context is shared between the node

that compresses the packet and the node(s) that need(s) to expand it. However, how the contexts are shared and maintained, and what information is contained within the context information was not determined by the scheme. The capabilities of this encoding scheme had been extended and complemented by IPsec header compression mechanism [11]. In this compression scheme, the next header compression scheme defined in [10] is used to compress both the IPsec Authentication Header (AH) and Encapsulated Security Payload (ESP).

The performance of LOWPAN_HC1 and LOWPAN_IPHC header compression schemes had been evaluated in term of throughput, energy consumption, memory usage and round trip time in [12]. However, the performance of the schemes is evaluated based on increasing payload size. This paper, in addition to compare the performance of the schemes among each other, shows the compression capabilities of each of them under different scenarios. Hence, it shows a detailed evaluation for each scheme in order to overcome their drawbacks.

Second and Subsequent Fragments Headers Compression (S&SFHC) Scheme for IPv6 Header in 6LoWPAN Network had been proposed to compress IPv6 packet header [13]. The scheme exploits the correlation between the first and the subsequent fragments' headers. Hence, the redundant headers that are transmitted within the first fragment will not be carried again within the second and the subsequent fragments. The S&SFHC can either work as a standalone technique or be integrated with other compassion techniques. However, the standalone mode of the scheme has been examined in [13]. In this paper, we propose and assess the integrated operation mode of the scheme. In this integrated mode, the first fragment is compressed using other existed compression scheme and the second and subsequent fragments are compressed using S&SFHC. The integrated versus the standalone mode of operation has been examined in this paper as well.

The rest of this paper is organized as follows: header compression in communication technology is presented in section 2. The IPv6 header compression schemes in 6LoWPAN are discussed in section 3. The proposed Second and Subsequent Fragments' Headers Compression scheme for IPv6 packet's headers in 6LoWPAN network (S&SFHC) is introduced in section 4. The performance of S&SFHC scheme in both standalone and integrated modes is evaluated is section 5. Finally, the paper is concluded in section 6.

2 Header Compression in Communication Technology

Header compression is widely used in communication technology. It aims to increase actual transmitted data intensity. Hence, a portion of the packet that is allocated for header is conserved and then is used for transmitting actual data. In the following subsections, we touch briefly the header compression in three communication technology: UMTS, WiMAX and LTE.

2.1 UMTS

Header compression had been proposed in most communication technology. It aims to efficiently use the expensive and valuable bandwidth and radio resources

[14–18]. In Universal Mobile Telecommunications System (UMTS), RObust Header Compression (ROHC) [19–26] had been used to compress IPv4, IPv6, UDP, RTP and ESP headers [27]. The performance of ROHC in UMTS had been implemented, investigated and analyzed [27, 28].

2.2 WiMAX

In WiMAX, header suppression and header compression had been used to remove redundant data in the headers and hence, efficiently use the radio resources [29]. As in UMTS, ROHC had been introduced to achieve higher compression efficiency in wireless environments [24]. It is used in mobile WiMAX and WiMAX femto cells in order to enhance the efficiency of the radio link utilization [30, 31]. In addition, Header compression scheme over hybrid satellite-WiMAX network called Hybrid-ROHC had been proposed [32]. The scheme enables the saving of bandwidth resources over the hybrid network.

2.3 LTE

Long Term Evolution (LTE) is the 4th generation mobile wireless communication standards for cellular networks. It is a major step forward for communication industry that provides super fast data transfer for mobile phones and data terminals. It is extremely fast, efficient and intelligent [33]. It has been defined and developed by 3rd Generation Partnership Project (3GPP) [34]. Unlike earlier circuit-switching cellular communications networks generations, LTE is fully packet-switching IP-Based architecture [35, 36]. Hence, the transport is taking place using either IPv4 or IPv6. Several operators had initially sat up their services using IPv4. However, the exhausted IPv4 shows inability to support this new technology [37]. On the other hand, IPv6 proves its scalability to support large address space. However, when the operators consider and deploy their services using IPv6, the large header size of IPv6 leaves impacts on the network since IPv6 has 20 extra header bytes compared to IPv4. This necessitates the existence of header compression techniques in LTE. The migrating impacts from IPv4 to IPv6 have been explored and analyzed, and the performance of ROHC with IPv4 and IPv6 packets has been evaluated empirically [37]. The ROHC implementation, on a per hop basis, for IP headers including IP/UDP/RTP in LTE had been discussed [38]. Based on this implementation, ROHC can achieve high compression ratio and hence, increasing link bandwidth while decreasing packet processing for downstream devices.

3 IPv6 Header Compression Schemes in 6LoWPAN

Header compression is the process of minimizing the header size of the packet before the packet is being transmitted and decompressing the received header to

its origin in the receiver side [39]. Many header compression schemes had been introduced. Some of these schemes were introduced to compress TCP/IP packet overhead [14] while others to compress UDP packet overhead [15]. The ROHC is a standard that had been introduced to compress the IP, UDP, RTP, and TCP headers of internet packets [19].

Although header compression is needed to improve the performance in different networks, it is an urgent need in 6LoWPAN because of the relatively huge headers' sizes that depletes the packet payload in this network. Based on the protocol stack, 6LoWPAN header compression involves the following headers compression:

- Application layer header compression.
- Transport layer header compression (TCP, UDP and ICMP).
- Network layer header compression (IPv6 unicast and multicast, routing and other extension headers).
- Adaptation layer header compression (fragmentation, compression, mesh routing and IP routing headers).

In the following subsections, we examine the existed IPv6 header compression schemes in 6LoWPAN network.

3.1 IPv6 Header Compression in LOWPAN_HC1

LOWPAN_HC1 is the first IPv6 header compression scheme for 6LoWPAN [8]. It specifies the compression format for IPv6 header. Based on the mechanism, IPv6 header's fields can be compressed as shown in table 1.

Table 1 IPv6 Header Compression in LOWPAN_HC1

IPv6 Field	**Original Field Size (bits)**	**Comp. Field Size (bits)**	**Compression manner**
IP Version	4	0	The value is 6 for all packets.
Traffic Class	8	0,8	The value is assumed to be zero.
Flow Label	20	0, 20	The value is assumed to be zero.
Payload Length	16	0	Can be inferred from layer 2 or datagram size of the fragmented packet.
Next Header	8	0,8	It has three possibilities (UDP/TCP/ICMP).
Hop Limit	8	8	Uncompressed.
Source Address & Destination Address	128	0,64	They are link local addresses; the prefixes can be inferred from link local prefix while the interface identifier can be inferred from layer 2 addresses.
		128	Uncompressed link local or global addresses.

As we can observe from table 1, the header can be compressed to 8 bits (1 byte). The LOWPAN_HC1 encoding needs 1 byte and the dispatch value bit pattern for LOWPAN_HC1 needs 1 byte. Hence, IPv6 header can be compressed to 3 bytes. However, this scheme can compress only IPv6 link local addresses where source and destination addresses are stateless configured link-local addresses. This scheme cannot compress the global IPv6 addresses. This means that when a global address is involved in the packet, the address remains uncompressed.

In addition to LOWPAN_HC1, LOWPAN_HC2 had been proposed for compressing selected IPv6 extension header like UDP header [8]. Hence, when UDP data packet is transmitted, the frame will carry UDP encoded header, as a next header, after the IPv6 encoded header. Fig. 1 shows the structure of both IPv6 and UDP encoded headers using LOWPAN_HC1 and LOWPAN_HC2 encoding schemes respectively.

As can be depicted from the figure, the maximum and the minimum headers' sizes of LOWPAN_HC1 and LOWPAN_HC2 can be calculated by considering the maximum and the minimum sizes of each field in both headers respectively. Hence, the maximum header's size can be calculated as:

Maximum header size = LOWPAN_HC1 Dispatch Size+ LOWPAN_HC1 encoding + LOWPAN_HC1 max.header size + LOWPAN_HC2 Encoding + LOWPAN_HC2 max. header size.

$$= 1 + 1 + \sum_{i=1}^{n} HC1\_F_{i-max} \; + \; 1 \; + \sum_{j=1}^{m} HC2\_F_{j-max} \qquad (1)$$

and hence,

Maximum header size = 1+ 1 + (1+8+8+8+8+1+2.5+1) + 1 + (2+ 2+ 2+2)
= 2 + 37.5 + 1 + 8
= **48.5 bytes**

On the other hand, the minimum header's size can be calculated as:

Minimum header size = LOWPAN_HC1 Dispatch Size + LOWPAN_HC1 encoding + LOWPAN_HC1 min. header size + LOWPAN_HC2 Encoding + LOWPAN_HC2 min. header size.

$$= 1 + 1 + \sum_{i=1}^{n} HC1\_F_{i-min} \; + \; 1 \; + \sum_{j=1}^{m} HC2\_F_{j-min} \qquad (2)$$

and hence,

Minimum header size = 1+ 1 + (1+0+0+0+0+0+0+0) + 1 + (0.5+ 0.5+ 0+2)
= 2 + 1 + 1 + 3
= **7 bytes**

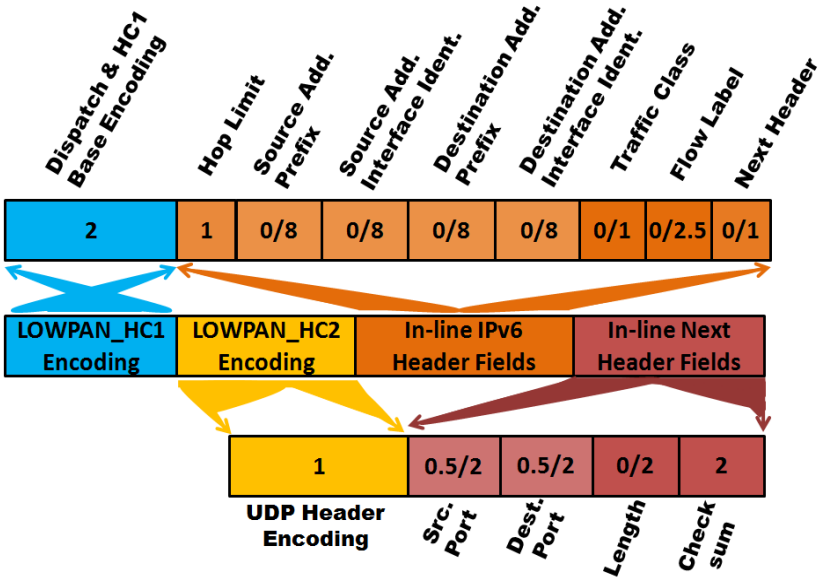

Fig. 1 LOWPAN_HC1/ LOWPAN_HC2 encoded headers

Where:

HC1_Fi-max is the maximum possible size of field (i) in LWOPAN_HC1 Header.
HC1_Fi-min is the minimum possible size of field (i) in LOWPAN_HC1 Header.
n is the number of the fields in the LOWPAN_HC1 header (excluding encoding byte).
HC2_Fj-max is the maximum possible size of field (j) in LOWPAN_HC2 Header.
HC2_Fj-min is the minimum possible size of field (j) in LWOPAN_HC2 Header.
m is the number of the fields in the LOWPAN_HC2 header (excluding encoding byte).

3.2 IPv6 Header Compression in LOWPAN_HC1g

LoWPAN_HC1g [9] is an extension of LoWPAN_HC1. It is designed to compress IPv6 global addresses. However, this scheme assumes that 6LoWPAN network is assigned a default, single and compressible global address prefix. When source or destination addresses' prefixes match the default one, it can be compressed. Otherwise, the global addresses' prefixes remain uncompressed.

3.3 IPv6 Header Compression in LOWPAN_IPHC

LOWPAN_IPHC [10] expands the capabilities of LOWPAN_HC1. It can compress both link-local and global unicast addresses. In addition, LOWPAN_IPHC applies some changes to LOWPAN_HC1. Based on LOWPAN_IPHC mechanism, IPv6 header's fields can be compressed as shown in table 2. The table shows the IPv6 fields and the possible sizes of each field based on the compression manner.

Table 2 IPv6 header compression in LOWPAN_IPHC

IPv6 Field	**Original Field Size (bits)**	**Comp. Field Size (bits)**	**Compression manner**
IP Version	4	0	The value is 6 for all packets.
Traffic Class& Flow Label	28	0,8,24,32	These fields can be completely carried inline or partially compressed.
Payload Length	16	0	Can be inferred from layer 2 or datagram size of the fragmented packet.
Next Header	8	0,8	This field can be compressed and processed by LOWPAN_NHC.
Hop Limit	8	0,8	This field can be compressed based on predefined values.
Source Address & Destination Address	128	0	They are link local addresses; the prefixes can be inferred from link local prefix while the interface identifier can be inferred from layer 2 addresses
		16, 64	Partially compressed link local or global addresses.
		128	Uncompressed link local or global address.

As we can observe from table 2, the header can be compressed completely. The LOWPAN_IPHC encoding needs 1 byte and the dispatch value bit pattern for LOWPAN_IPHC needs 1 byte. Hence, IPv6 header can be compressed to 2 bytes. However, even this scheme can compress both link local and global addresses, the compression ratio depends on the way that the addresses had been configured. In some cases, the address remains uncompressed.

In addition to LOWPAN_IPHC, LOWPAN_NHC had been proposed for compressing selected IPv6 extension header like UDP header [10]. Hence, when UDP data packet is transmitted, the frame will carry UDP encoded header, as a

next header, after the IPv6 encoded header. Fig. 2 shows the structure of both IPv6 and UDP encoded headers using LOWPAN_IPHC and UDP LOWPAN_NHC encoding schemes respectively.

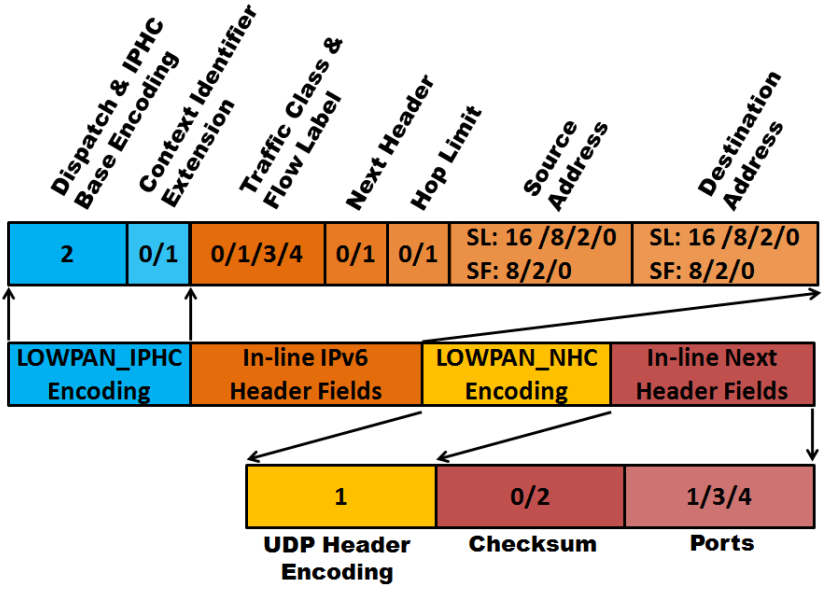

Fig. 2 LOWPAN_IPHC/ LOWPAN_NHC encoded headers

As explain earlier, the maximum and the minimum headers' sizes for LOWPAN_IPHC and LOWPAN_NHC can be calculated as:

Maximum header size = LOWPAN_IPHC Dispatch Size+ LOWPAN_IPHC encoding + Context Identifier Extension + LOWPAN_IPHC max. header size + LOWPAN_NHC Encoding + LOWPAN_NHC max. header size.

$$= 1 + 1 + 1 + \sum_{i=1}^{n} IPHC\_F_{i-max} \; + \; 1 \; + \sum_{j=1}^{m} NHC\_F_{j-max} \qquad (3)$$

and hence,

Maximum header size = 1 + 1+ 1 + (4+1+1+16+16) + 1 + (2+4)
= 3 + 38 + 1 + 6
= **48 bytes**

Minimum header size = LOWPAN_IPHC Dispatch Size+ LOWPAN_IPHC encoding + Context Identifier Extension + LOWPAN_IPHC min. header size + LOWPAN_NHC Encoding + LOWPAN_NHC min. header size

$$= 1 + 1 + 0 + \sum_{i=1}^{n} IPHC\_F_{i-min} \; + \; 1 \; + \sum_{j=1}^{m} NHC\_F_{j-min} \qquad (4)$$

and hence,

$$\begin{aligned} \text{Minimum header size} &= 1+ 1 + 0 + (0 + 0 + 0 + 0 + 0) + 1 + (1 + 0 + 1) \\ &= 2 + 0 + 1 + 2 \\ &= \mathbf{5\ bytes} \end{aligned}$$

Where:

IPHC_Fi-max is the maximum possible size of field (i) in LOWPAN_IPHC Header.
IPHC_Fi-min is the minimum possible size of field (i) in LWOPAN_IPHC Header.
n is the number of the fields in the LOWPAN_IPHC header (excluding encoding byte and context identifier extension).
NHC_Fj-max is the maximum possible size of field (j) in LOWPAN_NHC Header.
NHC_Fj-min is the minimum possible size of field (j) in LOWPAN_NHC Header.
m is the number of the fields in the LOWPAN_NHC header (excluding encoding byte).

4 Second and Subsequent Fragments Headers Compression Scheme

6LoWPAN is not only about header compression but also involves fragmentation and reassembly. When IPv6 packet is transmitted over 6LoWPAN, the packet will be predominantly fragmented. The IPv6 large packet is hard to be fitted into a single IEEE 802.15.4 frame. Hence, the intermediate node in IPv6 cannot perform fragmentation; the fragmentation is performed by the introduced adaptation layer.

In [13], we designed a header compression scheme to compress 6LoWPAN packet's header for fragmented IPv6 packet. The technique is used to compress the header of the second and subsequent fragments belong to the same IPv6 packet. Hence, we called this compression scheme as Second and Subsequent Fragments' Headers Compression (S&SFHC). The technique utilizes the correlation between the first and subsequent fragments' headers as shown in Fig. 3. The correlated headers are compressed and, mainly, only the header of the first fragment will be sent. The compressed headers will be inferred from the first fragment's header at the receiver side.

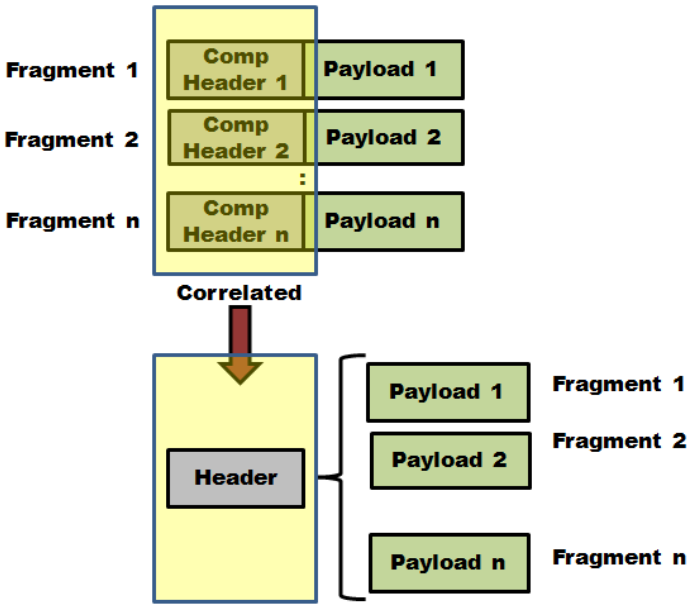

Fig. 3 Correlation between first and subsequent fragments' headers in S&SFHC scheme

The source node, before transmitting the IPv6 packet over the 6LoWPAN link, checks the size of the packet. When the packet needs to be fragmented, the node checks whether there are header compression techniques should be applied to the headers or not. If there is header compression techniques involved, the header compression techniques are applied and a compressed header will be added to the first fragment. Otherwise, the original uncompressed headers will be added to the fragment. After that, the first fragment will be prepared with compressed, uncompressed or partially compressed header, and then the first fragment will be sent to the receiver.

In S&SFHC scheme, the receiver keeps the following components:

- Header Dictionary: it is a dictionary that keeps a copy of a header (compressed, uncompressed or partially compressed) that is being received in the first fragment.
- Link Unique Identifier (LUI): it is an 8-bits identifier. This identifier is issued by the receiver after receiving the first fragment. It identifies the subsequent fragments belong to the same packet of a specific source. This identifier will be mapped to the source address and the header in the header dictionary.
- Free Unique Identifier List (FUIList): it is a list that includes all un-used identifiers. The receiver will assign one of these identifiers to the header.

In the receiver side, after receiving the first fragment, the receiver determine whether this fragment is the first fragment or not. If it is the first fragment, the receiver performs the following tasks:

- Adding the header to the header dictionary.
- Assigning LUI to the sender and map it to the header.
- Removing the assigned LUI from FUIList.
- Book a free buffer for the packet's fragments. The datagram size field informs the receiver about the total buffer size that is needed to save all the packet's fragments. The datagram size field is carried in the first fragment only.

The receiver sends the assigned LUI back to the transmitter. After the transmitter receives the LUI, it will use it to replace the IPv6 header in the second and subsequent fragments. In the destination side, these headers can be inferred from the first fragments' headers which had been kept in the header dictionary. In this case, the headers of the subsequent fragments will be compressed regardless the header of the first fragment is being compressed or not. In addition, this header will be compressed regardless of the compression technique used to compress first fragment's header (in case the first fragment is compressed using other compression scheme).

In order to avoid searching process for unused unique identifier, the FUIList is designed as stack. When the destination node assigns LUI, that identifier will be popped out of the FUIList. On the other hand, when the identifier is freed by the destination, the identifier will be pushed back into the FUIList.

Our scheme uses hop-by-hop transmission. It uses stop and wait Automatic repeat request flow control mechanism. After the transmitter sends the fragment n it stop and wait for acknowledgment for fragment n+1. When the transmitter receives an acknowledgment for fragment n+1, it then transmits it. This will avoid carrying the fragmentation and reassembly header since the packet will arrive in sequence. However, this will increase the delay slightly. If the fragment gets loss, the fragment is retransmitted for a maximum retransmission time that is specified by the MAC layer. If the acknowledgment for that fragment is not received, the fragment is considered loss. IPv6 fragment hold time has been set to 60 seconds. If the fragment hold time for a specific fragment is expired, the receiver drops all the fragments belong to the same packets from the buffer and the whole packet is considered lost. This will avoid a buffer overflow that may happen if fragments are kept in the buffer for long period of time.

4.1 S&SFHC Scheme Operation Modes

The S&SFHC scheme had been introduced to work in either one of two modes; standalone or integrated with others existed schemes. When the scheme works as a standalone, the first fragment is sent without being compressed. The second and the subsequent fragments are compressed using S&SFHC scheme. On the other hand, in the integrated Mode, when the scheme incorporates with other existed schemes, the existed schemes are used to compress the header for the first fragment only. The second and the subsequent fragments are not compressed

using the existed schemes that were used to compress the first fragment. Instead, those fragments (the second and the subsequent fragments) are compressed using our introduced S&SFHC scheme. Fig. 4 shows the S&SFHC in both modes, when it is used as a standalone and integrated with other schemes.

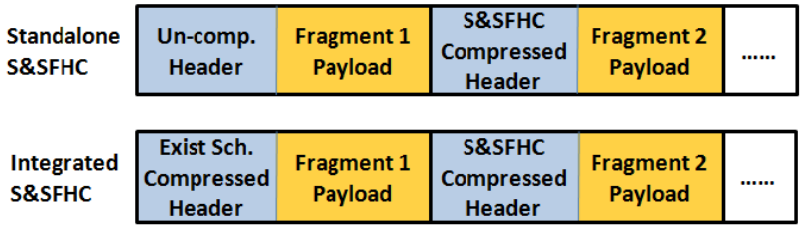

Fig. 4 S&SFHC Scheme in both standalone and Integrated Modes

In the integrated mode, the S&SFHC scheme, can integrate with any other compression schemes like LOWPAN_HC1/ LOWPAN_HC2 or LOWPAN_IPHC/ LOWPAN_NHC schemes. When S&SFHC scheme is integrated with LOWPAN_HC1/ LOWPAN_HC2, the IPv6 header of the first fragment is compressed using LOWPAN_HC1 and the UDP header (next header) in the first fragment is compressed using LOWPAN_HC2. The IPv6 and UDP headers in the second and subsequent fragments are compressed using S&SFHC scheme. Similarly, when S&SFHC scheme is integrated with LOWPAN_IPHC/ LOWPAN_NHC, the IPv6 header of the first fragment is compressed using LOWPAN_IPHC and the UDP header (next header) in the first fragment is compressed using LOWPAN_NHC. The IPv6 and UDP headers in the second and subsequent fragments are compressed using S&SFHC scheme.

Fig. 5 shows the integrated modes of S&SFHC scheme with both existed schemes: LOWPAN_HC1/ LOWPAN_HC2 in part (a) and LOWPAN_IPHC/LOWPAN_NHC in part (b).

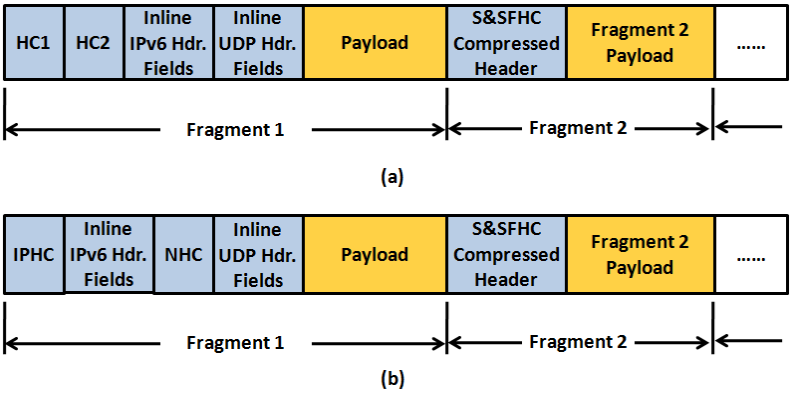

Fig. 5 (a) S&SFHC Integrated with LOWPAN_HC1/ LOWPAN_HC2, (b) S&SFHC Integrated with LOWPAN_IPHC/ LOWPAN_NHC

Even when routing header is involved, the header is compressed using S&SFHC. In this paper, we examine the standalone and integrated mode of S&SFHC and LOWPAN_IPHC/ LOWPAN_NHC based on the simulation.

5 Performance Evaluation of S&SFHC Schemes

The performance of S&SFHC standalone mode had been studied [13]. In this paper, we evaluate the performance of S&SFHC integrated mode in comparison with standalone mode and IPHC based on simulation. Fig. 6 shows the scenario that has been used to evaluate S&SFHC schemes. In this scenario, three hosts are generating CBR traffic. Each node generates 100 packets. The sizes of these packets are varied between 50 and 600 bytes. The scenario has been implemented using Qualnet simulator. The performance evaluation of S&SFHC schemes has been evaluated based on packet delivery ratio, throughput, average delay and average energy consumption.

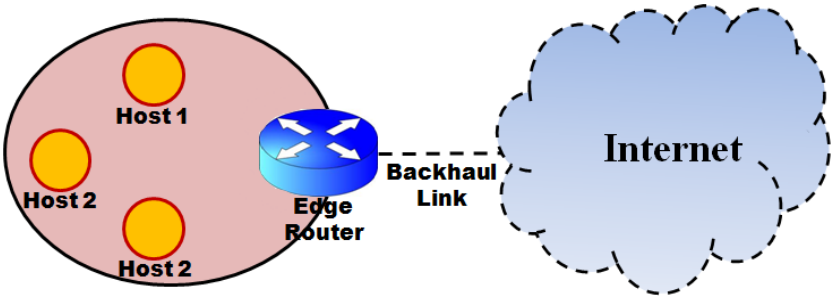

Fig. 6 6LoWPAN Scenario

5.1 Simulation Parameters and Assumptions

In order to evaluate the performance of S&SFHC integrated mode, the following layers' parameters are assumed as follows:

IP layer configuration parameters and encoded header:

- Stateless address configuration is assumed.
- No context identifier extension is used since the address is stateless.
- Traffic class is only carried inline (1 byte).
- Hop limit is carried inline (1 byte).
- IPv6 source and destination addresses are configured as follow:
  - 64 bits of the IPv6 address are carried inline. The other 64 bits are elided (link local prefix padded with zero or global prefix). (8 bytes each).

Transport layer (UDP) configuration parameters and encoded header:

- Source and destination ports use stateless compression. Each of them are compressed to 4 bits within range 0xf0b0 to 0xf0bf. (4 bits each, Total = 1 byte).
- The length is compressed; it can be computed from IPv6 header length information. The value of the UDP length field is equal to the payload length from the IPv6 header minus the length of any extension headers present between the IPv6 header and the UDP header. (0 bytes).
- The whole 16 bits UDP Checksum are carried in-line. (2 bytes).

Adaptation layer configuration parameters:

- The S&SFHC is tested in mesh under 6LoWPAN routing, the mesh under routing header should be carried inline. The originator and final destination addresses are carried inline (16 bytes).
- Fragmentation header is carried inline. (4 bytes for the first fragment and 5 bytes for the subsequent ones).
- Header compression header including Dispatch & IPHC Basic Encoding (2 bytes) and UDP header encoding (1 byte). (Total = 3 bytes).

IEEE 802.15.4 Layer Configuration parameters

- The nodes are assumed to have extended 64 bits MAC address.
- No security header is considered.

5.2 Result and Discussion

The performance of S&SFHC integrated mode has been evaluated based on four performance metrics; packet delivery ratio, throughput, average delay and average energy consumption. The packet delivery ratio depends on the number of fragments that the packet is split into and the size of each of these fragments. At the beginning, when the packet size is too small (the packet is not fragmented), the compression schemes give almost the same packet delivery ratio. A very limited difference occurs due to the different packets' sizes that happen due to different header size. When the packet's size grows and need to be fragmented, the scheme that gives less number of figments gives higher packet delivery ratio as shown in Fig. 7. As can be depicted from the figure, the transition from a lower to higher number of fragments can be noticed in the figure with the sharp drop (almost vertical) in packet delivery ratio.

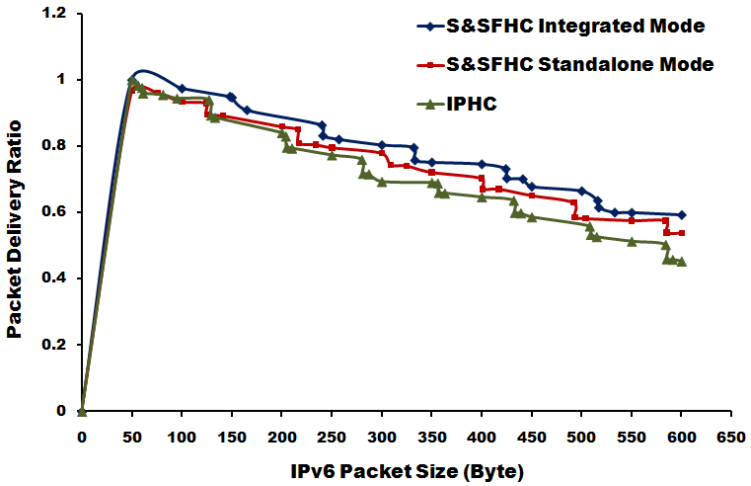

Fig. 7 Packet delivery ratio versus IPv6 packet size

When the size of the fragmented packet is increased, both S&SFHC standalone and integrated modes achieve higher packet delivery ratio compared to IPHC. The IPHC uses higher number of fragments to occupy the same size fragmented packet compare to both S&SFHC modes. As the fragmented packet size is increasing, the gap in number of fragments used is increased. Since the header size in both S&SFHC modes is smaller, the accumulative saved header bytes leads to additional fragments saving when the fragmented packet size is increased. In addition, the IPHC scheme transits to a higher number of fragments to occupy the same packet earlier compared to both S&SFHC modes. As can be depicted from the figure, standalone and integrated modes outperform IPHC in term of packet delivery ratio by 19% and 30% respectively when the fragmented packet size is 600 bytes. This percentage can even be higher when the fragmented packet size is larger.

However, S&SFHC integrated mode gives the highest packet delivery ratio. It has lower number of fragments compared to a standalone mode and hence, it can achieve 10% higher packet delivery ratio than standalone mode when packet size is 600 bytes. When both modes has the same number of fragment, the size of the last fragment in the integrated mode is less than the size of the last fragment in the standalone mode. However, the gab in the number of fragments between standalone and integrated modes is not increasing when the packet size is increased since the header of the second and subsequent fragment is similar in both modes.

Fig. 8 shows the throughput of the three schemes. When small size un-fragmented packets are transmitted, the schemes give almost similar and low throughput. When the packets' sizes grow and need to be fragmented, the schemes that send less number of fragments for the same packet achieves a higher throughput. When the scheme uses less number of fragments, the actual data

intensity becomes higher which result in a higher throughput. In addition, the header size carried by each fragment is affecting the throughput as well. A higher throughput can be achieved when the fragment's header size is small. As S&SFHC standalone and integrated modes use less fragments and the fragments' headers are smaller than the fragment's header for IPHC, they can achieve higher throughput compared to IPHC. The standalone and the integrated modes achieves 18% and 30% higher throughput respectively compared to IPHC when the fragmented packet size is 600 bytes. However, the integrated mode outperforms the standalone mode by 10% higher throughput at the same packet size.

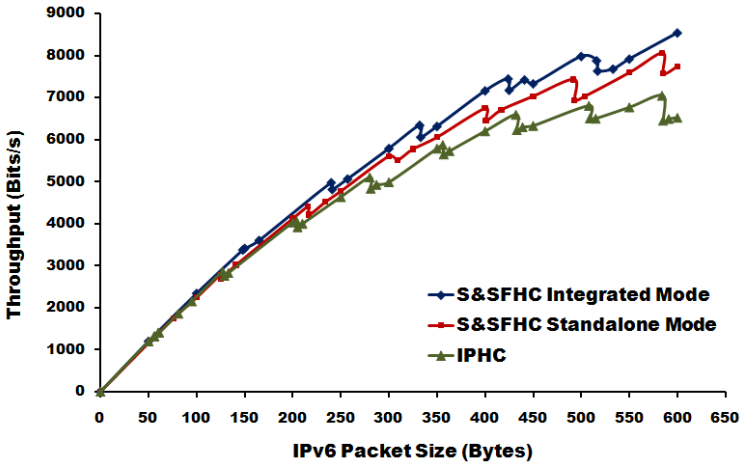

Fig. 8 Total throughput versus IPv6 packet size

Fig.9 depicts the average delay needed to deliver a single packet to its destination. The main factor that affects the average delay of the fragmented packet is the number of packet's fragments. When a fragment is received by the destination, it should be held until receiving the reset of the fragments belonged to the same packet, then the fragments are reassembled and the reassembled packet is passed to the network layer. Hence, when the packet produces higher number of fragments, each of these fragments need to wait for the rest of the fragments before being reassembled. This clarifies the higher delay when the number of fragments is higher. In addition, when the number of the fragments is high, the transmitting of the fragments take relatively longer time especially in high traffic and contention based environment. Based on the aforementioned reasons, IPHC has higher average delay compared to both S&SFHC standalone and integrated modes. As shown in the figure, when the packet size equals 600 bytes, Standalone and integrated modes achieves 13% and 18% respectively lower average delay than IPHC. On the other hand, integrated mode outperforms standalone one by 6% lower average delay at the same packet size.

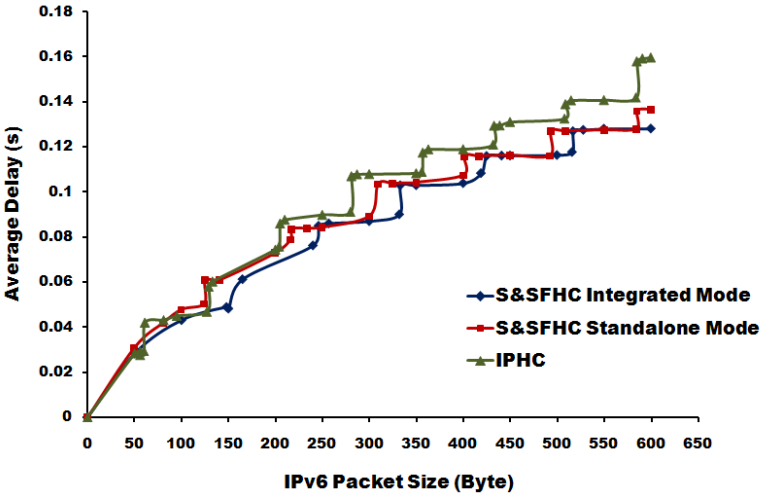

Fig. 9 Average delay versus IPv6 packet size

Fig. 10 shows the average energy consumption to deliver a single packet to its destination for the three schemes; IPHC, standalone and integrated S&SFHC. As can be depicted from the figure, when the packet size is higher, the consumed energy used to transmit the packet from the source to the destination is increased. However, the average energy consumption depends on the number of the fragments that the packet is split into and the size of these fragments. When the scheme has less number of fragments for a specific packet, it can achieve lower average energy consumption.

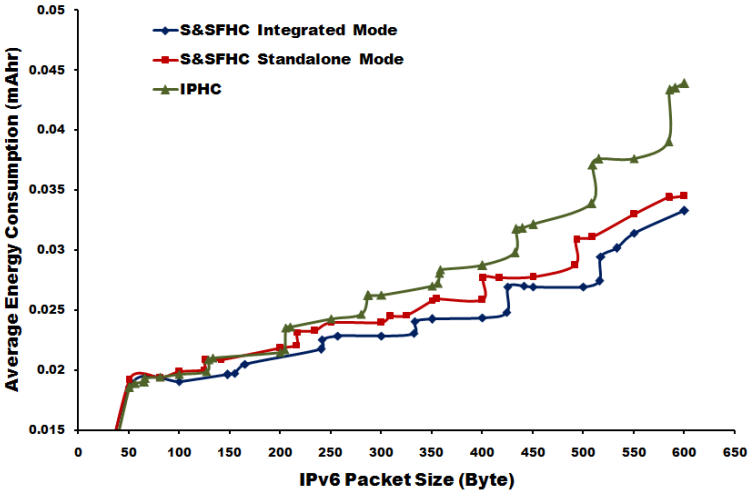

Fig. 10 Average Energy Consumption versus IPv6 Packet Size

As the figure shows, when the packet size is 600 bytes, IPHC uses higher number of fragments compared to S&SFHC modes. Hence, S&SFHC standalone and integrated modes achieve 21% and 24% respectively lower energy consumption compared to IPHC. In addition, S&SFHC integrated mode achieves 4% less energy consumption compared to standalone one at the same packet size.

6 Conclusion

Low power, low rate, limited computation and communication resources wireless smart objects are considered main components in the IoT. Providing such a limited capabilities objects with the internet connectivity is challenging due to the wide gap between these devices and the internet protocol stack. 6LoWPAN was introduced to settle the incompatibility to enable the transmission of large IPv6 packet over low power wireless personal area network. 6LoWPAN adaptation layer harmonize the tiny smart objects with the internet. One of the main issues to settle is the relatively huge headers' sizes of upper layer protocols (e.g. TCP, UDP and IPv6). These headers deplete the IEEE 802.15.4 frame and leave few bytes for the actual data. Some schemes had been designed to compress the headers to provide more space for the data payload. Recently, Second and Subsequent Fragments Headers Compression (S&SFHC) scheme had been proposed to compress these headers. This scheme exploits the correlation between the first and the subsequent fragments' headers to avoid carrying the redundant headers of second and subsequent fragments. This scheme can operate in two modes; standalone and integrated. In standalone mode, the first fragment of each packet is sent uncompressed. In this paper, an extended version of S&SFHC for 6LoWPAN is proposed. This new scheme is introduced by integrating S&SFHC with other existing schemes like LOWPAN_IPHC/ LOWPAN_NHC. When the proposed new scheme incorporates with other schemes, the existed schemes are used to compress the headers for the first fragment only. The second and subsequent fragments' headers will be compressed using S&SFHC scheme. The integration between S&SFHC and LOWPAN_IPHC/ LOWPAN_NHC schemes can enhance the performance of S&SFHC compared to both S&SFHC standalone mode and LOWPAN_IPHC/ LOWPAN_NHC in terms of packet delivery ratio, throughput, average delay and average energy consumption.

References

[1] Ashton, K.: That “Internet of Things” Thing, in the real world things matter more than ideas. RFID J. (2009)
[2] Mattern, F., Christian, F.: From the Internet of Computers to the Internet of Things. Inform. 33(2), 107–121 (2010)
[3] Eddy, B.: A Service-Based Methodology for RFID-Smart Objects Interactions in Supply Chain. Int. J. Multimed. Ubiquitous Eng. 4 (2009)

[4] Mcfarlane, D., Sarma, S., Lung, C.J., Wong, C.Y., Ashton, K.: The intelligent product in manufacturing control and management. In: 15th Trienn. World Congr. IFAC, Barcelona (2002)
[5] Eddy, B.: Ambient Services Modeling Framework for Intelligent Products. In: Smart Object Syst. Work. on UbiComp 2005 (2005)
[6] Goumopoulos, C., Kameas, A.: Smart Objects as Components of UbiComp Applications. Int. J. Multimed. Ubiquitous Eng. 4 (2009)
[7] Raza, S., Trabalza, D., Voigt, T.: 6LoWPAN Compressed DTLS for CoAP. In: IEEE Int. Conf. Distrib. Comput. Sens. Syst. (DCOSS 2012), Hangzhou, China (2012)
[8] Montenegro, G., Kushalnagar, N., Hui, J.: Transmission of IPv6 Packets over IEEE 802.15.4 Networks. RFC 4944, IETF Netw. Work. Gr. 802.15.4 Networks (2007)
[9] Hui, J., Culler, D.: Stateless IPv6 Header Compression for Globally Routable Packets in 6LoWPAN Sub-networks. 6LoWPAN WG Draft (2007)
[10] Hui, J., Thubert, P.: Compression Format for IPv6 Datagrams over IEEE 802.15.4-Based Networks. RFC 6282, IETF (2011)
[11] Raza, S., Duquennoy, S., Slander, G.: Compression of IPsec AH and ESP Headers for Constrained Environments. Internet-Draft (2013)
[12] Ludovici, A., Calveras, A., Catalan, M., Gómez, C., Paradells, J.: Implementation and evaluation of the enhanced header compression (IPHC) for 6LoWPAN. In: Oliver, M., Sallent, S. (eds.) EUNICE 2009. LNCS, vol. 5733, pp. 168–177. Springer, Heidelberg (2009)
[13] Awwad, S.A.B., Ng, C.K., Noordin, N.K., Ali, B.M., Hashim, F.: Second and Subsequent Fragments Headers Compression Scheme for IPv6 Header in 6LoWPAN Network. In: Seventh Int. Conf. Sens. Technol. (2013)
[14] Jacobson, V.: Compressing TCP/IP Headers for Low-Speed Serial Links. RFC 1144 (1990)
[15] Degermark, M., Nordgren, B., Pink, S.: Header Compression for IPv6. RFC 2507. Stand. Track (1999)
[16] Casner, S., Jacobson, V.: Compressing IP/UDP/RTP Headers for Low-Speed Serial Links. RFC 2508, Stand. Track (1999)
[17] Degermark, M., Engan, M., Nordgren, B., Pink, S.: Low-loss TCP/IP header compression for wireless networks. Wirel. Networks 3, 375–387 (1997)
[18] Giovanardi, G., Mazzini, M.R., Zorzi, M.: Improved Header Compression for TCP/IP over Wireless Links. IEEE Electron. Lett., 1958–1960 (2000)
[19] Bormann, C., et al.: RObust Header Compression (ROHC): Framework and four profiles: RTP, UDP, ESP, and uncompressed. RFC 3095, Standards Track (2001)
[20] Bormann, C.: Robust Header Compression (ROHC) over PPP. RFC3241, Stand. Track (2002)
[21] Jonsson, L.-E., Pelletier, G.: RObust Header Compression (ROHC): A Compression Profile for IP. RFC 3843, Stand. Track (2004)
[22] David, E.T., Andreas, H., Andreas, D., Gero, D.: Robust header compression (ROHC) in next generation network processors. IEEE/ACM Trans. Netw. 13 (2005)
[23] Jonsson, L.-E., Sandlund, K., Pelletier, G., Kremer, P.: Corrections and Clarifications to RFC 3095. RFC 4815, Stand. Track (2007)
[24] Sandlund, K., Pelletier, G.: RObust Header Compression Version 2 (ROHCv2): Profiles for RTP, UDP, IP, ESP and UDP-Lite. RFC 5225 (Proposed Stand. Internet Eng. Task Force (2008)
[25] Sandlund, K., Pelletier, G., Jonsson, L.-E.: The RObust Header Compression (ROHC) Framework. RFC 5795, Stand. Track (2010)

[26] Pelletier, G., Sandlund, K., Jonsson, L.-E., West, M.: RObust Header Compression (ROHC): A Profile for TCP/IP (ROHC-TCP). RFC 6846, Stand. Track (2013)
[27] Couvreur, A., Le Ny, L.-M., Minaburo, A., Rubino, G., Sericola, B., Toutain, L.: Performance Analysis of a Header Compression Protocol: The ROHC Unidirectional Mode. Springer Telecommun. Syst. 31, 85–98
[28] Nuaymi, L., Bouida, N., Lahbil, N., Godlewski, P.: Headers Overhead Estimation, Header Suppression and Header Compression in WiMAX. In: Third IEEE Int. Conf. Wirel. Mob. Comput. Netw. Commun, WiMob 2007 (2007)
[29] Wang, B., Schwefel, H.-P., Chua, K.C., Kutka, R., Schmidt, C.: On Implementation and Improvement of Robust Header Compression in UMTS. In: 13th IEEE Int. Symp. Pers. Indoor Mob. Radio Commun., vol. 3, pp. 1151–1155 (2002)
[30] Woo, H., Jooyoung, K., Lee, M., Kwon, J.: Performance analysis of Robust Header Compression over mobile WiMAX. In: 10th Int. Conf. on Adv. Commun. Technol. ICACT 2008, vol. 3, pp. 1742–1746 (2008)
[31] Fitzek, F.H.P., Schulte, G., Piri, E., Pinola, J., Katz, M.D., Huusko, J., Pentikousis, K., Seeling, P.: Robust Header Compression for WiMAX Femto Cells. In: WiMAX Evolution: Emerging Technologies and Applications, pp. 183–197 (2009)
[32] Chong, Y.-W., Mohamad, I.J., Wan, T.-C.: Header Compression Scheme over Hybrid Satellite-WiMAX Network. In: Wyld, D.C., Wozniak, M., Chaki, N., Meghanathan, N., Nagamalai, D. (eds.) NeCoM/WeST/WiMoN 2011. CCIS, vol. 197, pp. 167–176. Springer, Heidelberg (2011)
[33] Universal Mobile Telecommunications System (UMTS): LTE: Architecture and functional description (3GPP TS 36.000 series, Release 9)
[34] http://www.3gpp.org/ (available online as on January 2012)
[35] Beming, P.: Lte-sae architecture and performance. Ericsson Rev. 20(3) (2007)
[36] Nossenson, R.: Long-Term Evolution Network Architecture. In: IEEE Int. Conf. COMCAS, pp. 1–4 (2009)
[37] Venmani, D.P., Duprez, M., Ibrahim, H., Gourhant, Y., Boucheret, M.-L.: Impacts of IPv6 on Robust Header Compression in LTE Mobile Networks. In: ICNS 2012 Eighth Int. Conf. Netw. Serv. IARIA (2012)
[38] Naidu, D., Tapadiya, R.: Implementation of Header Compression in 3GPP LTE. In: Sixth Int. Conf. Inf. Technol. New Gener. TNG 2009, pp. 570–574 (2009)
[39] AB. Effnet: An Introduction to IPv6 Header Compression. white pap (2004)

Wireless Sensor Network Attacks: An Overview and Critical Analysis with Detailed Investigation on Jamming Attack Effects

A. Tayebi*, S.M. Berber, and A. Swain

Department of Electrical and Computer Engineering, University of Auckland,
38 Princes Street, Level 2, Room 240, Auckland, New Zealand
atay530@aucklanduni.ac.nz

Abstract. Wireless Sensor Networks (WSNs) are gaining a lot of attention from researchers due to their massive applications. Network security is one of the important requirements of those applications. This chapter analyses possible network attacks that are essential for researchers to understand while developing robust security countermeasure. In this study, a systematic overview of different kinds of attacks for WSNs has been carried out and a critical analysis of the existing research results is presented. In this chapter, we also observe jamming attack consequence on WNSs in depth by investigating the effect of jamming attack on performance of WSN's communication using binary spreading sequences. The binary sequences in this chapter are generated according to the IEEE 802.15.4a standard. Mathematical expressions of probability of bit error in a communication channel are derived considering the effects of noise and channel fading. Further, we investigate the effects of using interleaver and deinterleaver on bit error rate (BER) in the case of jamming. Matlab simulation results are presented to confirm the validity of the derived theoretical expressions.

Keywords: Networks security, wireless sensor networks, security attacks, Jamming attack, probability of error.

1 Introduction

Recently, due to the wide range of applications, Wireless Sensor Networks (WSN) are becoming one of the hottest research topics. One of the basic design requirements in these networks is high level of security against malicious attacks. In this chapter, the result of preliminary research in this field with a critical overview of the security vulnerability in wireless sensor networks is presented. The overview of the attack is a necessary step towards the development of the idea of efficient cross layer countermeasures. In this chapter, attacks are classified

* Corresponding author.

A. Mason et al. (eds.), *Sensing Technology: Current Status and Future Trends III*,
Smart Sensors, Measurement and Instrumentation 11, DOI: 10.1007/978-3-319-10948-0_10

based on the target of the attacker. Based on this view, attacks are grouped in three main categories: Denial of Service (DoS), Privacy and Impersonation as shown in Fig. 1. Note that, these attacks may accrue in the different OSI layer.

Traditionally, depending on some of the typical features, the various attacks of WSN are classified either as passive or active, internal or external, stealthy or non-stealthy etc [1]. In this study we propose some new categories of the WSNs attacks. In this category, attacks are sorted based on the target of the attacker. For instance, some attacks are designed for destroying the signal, some other are targeting the privacy issues. Based on this view, we group attacks in three main categories: Denial of Service (DoS), Privacy and Impersonation as shown in Fig. 1. Note that, these attacks may accrue in the different OSI layer.

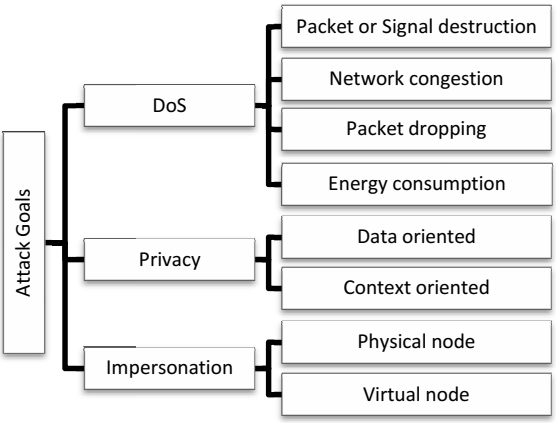

Fig. 1 Classification of attacks based on attacking goals

The first category is DoS attacks. The main target of DoS attacks is, malfunctioning the service that a WSN supposed to provide. There are four ways for denying the service in WSNs. It can be done by destroying packets or signal, congesting the network, dropping the packets or consuming the energy of network elements.

The second category is privacy attacks. Unlike the DoS attacks, in this attack, the attacker does not target the services of the networks, instead, it looks for information about the sensed and query data (Data oriented) or information related to the network specifications (Context oriented) e.g. what kind of MAC protocol the victim is using.

The last group is Impersonation attack. In this attack, the attackers want to impersonate themselves either as a physical node or a number of virtual unexciting nodes. This kind of attack might not sound very harmful for WSN, but they can be combined with DoS attacks and make them more destructive.

In this chapter, we begin with introducing the state of the art attacks based on this classification. Then, each category of attack is analyzed; and future possible

attacks for each of DoS groups are proposed. Also we demonstrate the effect of jammer on communication bit error rate.

2 Denial of Service Attacks

As mentioned earlier, there are four different ways of denying a service in the WSNs.

2.1 Packet or Signal Destruction (Jammers)

This group of attacks is called Jammers which try to destroy a signal or a packet. The term "destroying" here means reshaping a signal or changing few bits of the packet by making interferences during communication. Jammers are one the oldest and famous attacks in WSN. Jamming can happen in the networks' deferent OSI layer. Note that jamming in the each layer means targeting the specific packets related to that layer, e.g., ACK packets in layer two.

2.1.1 Physical Layer Jammers

In this attack, radio signals are jammed with a Radio Frequency (RF) transmitter. Because the communication media is shared between the nodes, the adversaries have a great chance to interfere and deny the service.

In [2], the authors introduce four techniques for physical layer jamming. An attacker can send nonstop random bits (Constant jamming) or sends continuous stream of regular packets (Deceptive jamming). Attacker can also send the jamming signal in a random periodic format to save the energy of the jamming device (Random jamming). All three techniques mentioned above are considered as active jamming, because, the jammer can be detected. However, in reactive jamming, the attackers do not jam the idle channel. They stay quiet until they sense activities on the channel. This is the most effective way of jamming.

2.1.2 Link Layer Jamming

Link layer jammers are more energy efficient and complicated than physical layer jammers. In link layer jamming, the target is data packets whereas in physical layer, the target is just any packet. Thus, this attack in link layer is harder to detect [3]. Note that, the link layer jamming might also focus on the controlling signal such as ACK message. These specific jammers are called collision makers [4].

Link layer jammer tries to jam the data packets. Since different types of MAC protocol exist, the jammer should jam based on the type of the MAC protocol in WSN. The challenge for link layer jamming is in predicting the arrival of the data packets. In [5], jamming for different MAC protocols has been proposed. Authors in [5] suggest a jamming attack by observing and clustering the probability distribution of data packet time intervals.

2.2 Network Congestion

These kinds of attacks try to make the network congested. Congestion can cause delay in delivering the data. These attacks pose a major threat to networks in which the data freshness is playing important roll. Here we review the main congestion makers.

2.2.1 Unfairness

Some MAC layer algorithms use "aMacBattLifeExt". This technique will set priority to the nodes that are depleting the energy of their battery. In other words, the nodes that are near to death, have priority to send the packets. An adversary node can take the advantage and set its "aMacBattLifeExt" to true. By setting this bit to true, the adversary node will get higher priority for sending data and make unfairness [6]. The application of this kind of attack depends on the implemented MAC layer protocol in sensor networks.

2.2.2 Wormhole

Wormhole is a low latency connection (tunneling) between two adversary nodes, geographically located in different parts of WSN. This connection can be fiber or high power wireless connection. In this attack, the adversaries forward the received packets to the other end of the tunnel. Therefore, the nodes located on the two sides of tunnel think that they are either neighbors or just have one hop distance. Therefore, this attack is dangerous for routing protocols and also MAC techniques which relay on the neighboring exchange [7].

2.2.3 Sinkhole

An adversary in the sinkhole attack redirects packets to itself or to a specific node. In other words, it makes a sink that absorbs all packets. For implementing this attack, the attacker needs to make itself or a particular node more attractive for the other nodes. For instance, it can announce false optimal route, by advertising wrong and attractive routing parameters, such as a high bandwidth or a low delay path. For making this attack more effective, the adversary can be placed near the cluster head or gateway and absorbs all WSN's packets or direct them to the busy part of the network and make it congested [8].

2.2.4 False Routing

In false routing, an adversary node tries to make and propagate false routing information. There are many ways to implement this attack. Generally, there are four ways of performing the false routing attack: Overflowing routing table with nonexistence routes, poisoning either routing table or routing cache (this way only applicable for on-demand routing protocols) and finally rushing attack.

Rushing attack is proposed in [9] for on-demand routing protocols (such as the AODV protocol [10]). In this attack, attacker sends continues ROUTE-REQUEST to its neighbors, in order to full the neighbors' processing queue. This causes huge delay for other node's ROUTE-REQUEST to be processed.

2.3 Packet Dropping

The main target of this attack is dropping or discarding the packets (packet forwarding) or cause the packets to be dropped or discarded (De-Synchronization).

2.3.1 Selective Forwarding

The target in selective forwarding attack is to forward some selected packets and dropping the rest. To perform this attack the attacker should be on the packet route. If the attacker is already on the route, it can easily perform the attack and drop or forward any packet it wants. But, if the attacker is not on the route, it needs to use another kind of attack such as sinkhole, or router poisoning in order to absorb the packet and position itself on the route [11]. Also, the attacker can drop all the packets and do not forward any of them. This specific type of selective forwarding attack is called black hole [12].

2.3.2 Synchronization Attack

Synchronization attacks can be used for layer two or layer four of OSI model. In [13], the idea of Synchronization attacks for Listen-Sleep Slotted MAC protocols has been proposed. This type of attacks tries to focus on messages which are exchanged for synchronization of sleeping and listening schedule. For example, in listen-sleep slotted MAC protocol such as Sensor-MAC (S-MAC) protocol [14], in order to decrease the latency, each node tries to synchronize its listening and sleeping schedule with its neighbors. In this attack, the adversary node tries to extend its listening slot and propagates the extended listening slot to the other nodes. When the new extended listening schedule has been received by the other nodes, they also try to propagate the new listening schedule for their neighbors. Investigation in [13] shows that this attack has two effects. 1) Sleep deprivation: the nodes listing time will be extended which makes the nodes to consume more energy. 2) Message drop: synchronizing different listening schedules will make misalignment in listening between nodes. This will cause packet drop or delay.

2.3.2.1 Local Time De-synchronization

Time synchronization protocols provide a mechanism for WSN to synchronize their local clock with the reference clock. There are three protocols for WSN local time synchronization: Reference Broadcast Synchronization (RBS), which is based on the local time deference exchange, Time-sync Protocol for Senor

Network (TPSN), which uses hieratical tree format, and Flooding Time Synchronization Protocol (FTSP) that uses tree format with dynamic root selecting algorithm.

The authors in [15] proposed synchronization attack for each protocol by sending the wrong time deference exchanges for RBS, placing itself as high level in the network's hieratical tree for TPSN and impersonating as a root for FTSP. Because of broadcasting nature of local time synchronization protocols, in this attack, an attacker can affect the entire networks.

2.4 Energy Consumption

Although all DoS attacks can make a node to consume its battery power, these attacks are specifically designed for draining the node's energy.

2.4.1 Hello and Session Flooding

Some routing protocols are using hello packets for establishing the neighborhood relationship or connection request. An adversary can constantly send a hello packet by using a high power radio transmitter. The nodes which receive the hello packet believe that the adversary node is their neighbor, even though the adversary node is located far away. Attacker also can send the session request to the victim nodes till they get exhausted or they reach their limit for maximum number of connections [16].

3 Privacy Attacks

In these attacks, the target is finding the information. The information that the attackers are interested in can be divided into two groups. Data oriented and Context oriented [17]. Data oriented information is the data collected by nodes and query posted to WSN. Also, context-oriented information is related to the network and communication techniques, protocols such as timing of traffic flows in WSN. Here are the common Privacy attacks.

3.1 Eavesdropping and Traffic Analysis

Eavesdropping and Traffic analysis [17] are two main types of attacks for privacy. In eavesdropping, the attacker listens to the packets and tries to find the sensed data or ask to be sent. For example, in health application, an attacker may try to access the patient's confidential medical information. Since, most of WSN uses encryption for data delivery; attacker needs to have the encryption key in order decrypt the packets. If the attacker does not have the encryption key, it can perform the packet analyses attack. In this attack, the attacker listens to the packets and analyses them without knowing the content of the packet. For

instance, when an attacker wants to do link layer jamming, it needs to analyze the distribution of data packet arrivals. Therefore, it performs traffic analyses attack first, and then based on the information provided by this attack it starts link layer Jamming attack.

3.2 Tempering Attacks

Tempering attacks are generally about attacking the physical component of devices. In this attack, the attacker gets direct access to the nodes hardware component such as microcontroller or EEROM. Since, WSN nodes are usually used in a field and left unattended, they are vulnerable to tempering attacks. For example, attacker might extract cryptographic secrets or change the nodes' program. In [18] the tampering attacks are well investigated and categorized into three difficulty levels called easy, medium and hard. The higher the difficulty level is, the more access and control over the victim hardware component. On the other the hand, the easier attacks need less facility.

4 Impersonation Attacks

As mentioned earlier, in impersonation attacks, the attacker tries to impersonate a legitimate node or make multiple fake nodes.

4.1 Physical Node Impersonation (Physical Layer Identification)

Physical layer identification or radio frequency fingerprinting is used to identify the wireless devices in a network. It is based on the distinctive physical layer characteristics of a single device which are mainly due to manufacturing imperfection. There are two main techniques for device identifications. Transient-based technique which is based on the unique features during the transient phase when radio is turning "ON" [19]. The other technique is Modulation based techniques in which, modulation imperfection of wireless transceivers is the focusing point [20].

The target of the attacker is to impersonate a target device by generating packets or signals that contain factors which are sensitive to the fingerprint device. Therefore, the attacker can impersonate himself as one of targeted devices.

4.2 Virtual Node Impersonation (Sybil)

In Sybil attacks, the adversary node makes multiple identities. These identities could be fabricated or stolen identities. Fabricated identities are fake identities which are randomly generated by the attacker. For example, if a node ID is represented by 32 bits, an attacker can randomly create 32 bits identities. In some

networks which new nodes are not allowed to join, the attacker can steal the identities of legitimate nodes and use them for Sybil attack [21].

In [21] different attack techniques for Sybil attack has been proposed. For example, if nodes need to vote for a task, an adversary can use its Sybil nodes to increase its vote chance. Also, Sybil attack can make unfairness in the WSN. For instance, in frame base MAC protocols such as Traffic Adaptive MAC Protocol (TRAMA) [23], which allocates time slot for each node; an adversary can occupy more time slots (one for each virtual node) and limit the resources for the other nodes. Furthermore, in misbehavior detection algorithms, an adversary can easily spread the blame between Sybil nodes and stay undetected, or if it is detected, stay in the network with different ID.

5 Jammers Effect in Communication

In this section we investigate the effect of jammers on WSNs communication quality. Here, we assume that the WSN uses code division multiple access systems (CDMA) based on the 16 binary sequences as it is defined in IEEE802.15.4 standard [22]. These sequences are presented in Table 1. Each chip has expected value equal to 0.5.

Table 1 Standard spreading sequences

Data symbol, decimal	Data symbol, Binary. b0,b1,b2,b3	Chip values (c0, c1, …, c32)
0	0000	11011001110000110101001000101110
1	1000	11101101100111000011010100100010
2	0100	00101110110110011100001101010010
3	1100	00100010111011011001110000110101
4	0010	01010010001011101101100111000011
5	1010	00110101001000101110110110011100
6	0110	11000011010100100010111011011001
7	1110	10011100001101010010001011101101
8	0001	10001100100101100000011101111011
9	1001	10111000110010010110000001110111
10	0101	01111011100011001001011000000111
11	1101	01110111011100011001001011000000
12	0011	00000111011110111000110010010110
13	1011	01100000011101111011100011001001
14	0111	10010110000001110111101110001100
15	1111	11001001011000000111011110111000

The system block-schematic is presented in Fig.2. This schematic is based on the IEEE 802.15.4a which is proposed in [22]. In this study, for sending a chip, we make M interpolation samples of each chip, also because the power of each set of sequence is equal to 0.5, for simplicity, we multiply it by $\sqrt{2}$. Also, as can be seen from Fig.2, in the modulation block, the chip sequence $m(k)$ is split into

even-indexed in-phase ($m_I(k)$) and odd-indexed quadrature sequences ($m_Q(k)$). Therefore, the outcome of the modulation block can be presented as

$$s(k) = m_I(k)\sqrt{2E_c / M} \cdot \cos\Omega_c k + m_Q(k)\sqrt{2E_c / M} \cdot \sin\Omega_c k \quad (1)$$

where E_c is the energy for each chip and Ω_c is the frequency of the carrier.

5.1 Channel Behavior

In this study we assume that white Gaussian noise and channel fading are present in the channel. For modeling the noise, we use pass-band noise. We make M repeated samples of Nosie for each chip. Thus the noise can be expressed as

$$n(k) = n_I(k)\sqrt{2E_N / M} \cdot \cos\Omega_c k - n_Q(k)\sqrt{2E_N / M} \cdot \sin\Omega_c k \quad (2)$$

where, E_N is the energy of noise per bit. This energy is equal to $M\sigma^2$. Also, $\sigma^2=BN_0$. Since we are making M repeated samples of the noise, the bandwidth (B) is $1/2M$. Thus, the average energy of the noise is $N_0/2$.

Also, based on the Fig. 2, fading effect can be included as coefficient α. Note that the fading coefficient is a random variable with Rayleigh distribution, which has a mean value $\eta_\alpha = (\pi b/4)^{1/2}$ and variance $\sigma^2{}_\alpha = b(4-\pi)/4$.

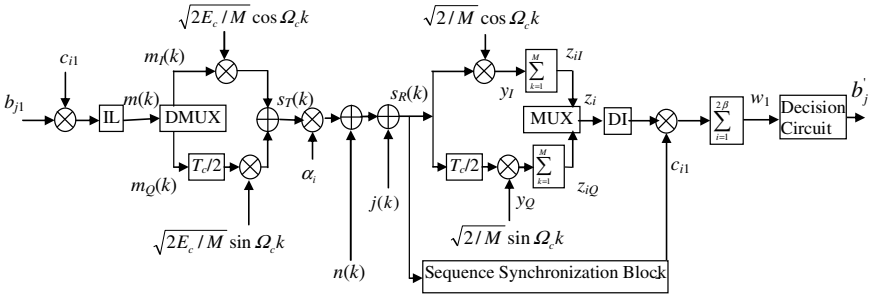

Fig. 2 Block-schematic of WSNs communication

5.1.1 Jammer

Jammers in our scenario periodically jam the communication system. In other words, they will be either in ON sate OFF state. When the jammer is in ON state, it jams the system same as a constant jammer, and when the jammer is OFF, it stays silence. This technique helps the jammer to improve its battery life and stealth.

Based on this assumption, two kinds of jammer can be defined: slow switching jammer and fast switching jammer. The ON and OFF duration in the slow switching jammer is higher than the fast switching jammer. As matter of fact, durations in slow switching jammer are higher than bit duration of the victim's communication system. Therefore, slow jammer might hit some bits in its ON

state and leave the others untouched in the OFF state; whereas, in fast jammer these durations are lower than the bit duration. Thus, the fast switching jammer hits all bits.

Jammers are using random signals to jam the system which behaves like Gaussian noise. Therefore, it can be presented as

$$j(k) = j_I(k)\sqrt{2E_j / M} \cdot \cos\Omega_c k - j_Q(k)\sqrt{2E_j / M} \cdot \sin\Omega_c k \tag{3}$$

where E_N is energy of jammer and j is the Gaussian random sequence and the average energy is $N_j/2$.

5.1.2 Interleaver and De-interleaver

Interleaver and deinterleaver are implemented in order to decrease the effect of burst errors. In direct sequence spread spectrum (DSSS) systems, every bit is represented by a sequence of chips. Because chips are sent in continuous order, we can assume that the fading effect for each chip belonging to a given bit is constant, whereas it might be different for each bit. Interleaver is mixing the chips from different bits and then sends them through the channel. By this technique the effect of the channel fading will be distributed to all bits. Therefore, it is necessary to implement interleaver and deinterleaver in order to decrease the channel fading effect.

5.1.3 The Received Signal Soft Values Calculation

In table 2, we represent the received signal soft values obtained at the output of sequence correlators based on the different channel conditions. Note that these values are imputes to the decision making circuit in Fig. 2.

Table 2 outcome signal based on the different scenarios

Channel Scenario	No jammer hit (W_{hit})	Jammer hit (W_{miss})
WGN	$\sqrt{E_c}\sum_{i=1}^{32} c_{i1}^2 + \sqrt{E_N}\sum_{i=1}^{32} n_i \cdot c_{i1}$	$\sqrt{E_c}\sum_{i=1}^{32} c_{i1}^2 + \sqrt{E_N}\sum_{i=1}^{32} n_i \cdot c_{i1}$ $+\sqrt{E_j}\sum_{i=1}^{J} j_i \cdot c_{i1}$
WGN + fading	$\sqrt{E_c}\sum_{i=1}^{32} \alpha_1 . c_{i1}^2 + \sqrt{E_N}\sum_{i=1}^{32} n_i \cdot c_{i1}$	$\sqrt{E_c}\sum_{i=1}^{32} \alpha_1 . c_{i1}^2 + \sqrt{E_N}\sum_{i=1}^{32} n_i \cdot c_{i1}$ $+\sqrt{E_j}\sum_{i=1}^{J} \alpha'_1 . j_i \cdot c_{i1}$
WGN +fading +Interleaver	$\sqrt{E_c}\sum_{i=1}^{32} \alpha_i . c_{i1}^2 + \sqrt{E_N}\sum_{i=1}^{32} n_i \cdot c_{i1}$	$\sqrt{E_c}\sum_{i=1}^{32} \alpha_i c_{i1}^2 + \sqrt{E_N}\sum_{i=1}^{32} n_i \cdot c_{i1}$ $+\sqrt{E_j}\sum_{i=1}^{2\beta} \alpha'_i \, j_i \cdot c_{i1}$

where l is the number of hit chips per bit by jammer. Node that when the interleaver is implemented all chips are a bit will be hit.

5.2 Slow Switching Jammer Effect on Bit Error Rate

For calculating the effect of the jammer on probability of error, we assume that the soft values have Gaussian distribution. Therefore the probability of error can be expressed

$$P_e(w) = \frac{1}{2} erfc\left(\frac{E[w]}{\sqrt{2 \cdot \mathrm{var}[w]}}\right), \tag{4}$$

where the random variables w are defined in Table 2. Because the switching speed is not so fast, the jamming signal hits all chips (l=32) of some bits and misses the others. Therefore, the probability of error rate can be calculated according to this expression

$$\begin{aligned} &\textit{Average probability of error} = \\ &\quad P_{hit} \,.\; P_e(\textit{jammer hit}) \\ &+ P_{miss} \cdot P_e(\textit{jammer miss}). \end{aligned} \tag{5}$$

Where the P_{hit} and P_{miss} are probability of hitting the original signal by jammer and probability of missing the original signal respectively. P_{hit} and P_{miss} depend on the jammer's switching speed. Let us assume that the jammer hit the original signal for T_h second in one ON and OFF cycle and one cycle takes T_t seconds. Also we define φ as probability of hit which is the ratio of T_h to T_t. Therefore, φ is the probability of hitting the original signal by jammer and (1- φ) is the probability missing the original signal.

To calculate average probability of error, we need to calculate the variance and mean value of the random variables W from Table 2 and used them in (4). Here, we derived the mathematical expression for WGN with jammer hit as an example following same procedure.

As mentioned earlier for calculating the probability of error we need to find the mean value as follows

$$\begin{aligned} w_{WGN-hit} &= \sqrt{E_c}\sum_{i=1}^{32} c_{i1}^2 + \sqrt{E_N}\sum_{i=1}^{32} n_i \cdot c_{i1} + \sqrt{E_j}\sum_{i=1}^{32} j_i \cdot c_{i1} \\ &= A + B + C \end{aligned} \tag{6}$$

$$\eta_{w_{WGN-hit}} = E\{w_{WGN-hit}\} = \sqrt{E_c}\sum_{i=1}^{32} E\{c_{i1}^2\} = 32E\{c_{i1}^2\}\sqrt{E_c} = 32\sqrt{E_c} \;. \tag{7}$$

Next we have to calculate the variance of $w_{WGN-hit}$

$$\begin{aligned} \sigma_{w1}^2 &= E\{w_{WGN-hit}^2\} - \eta_{WGN-hit}^2 = E\{(A+B+C)^2\} - \eta_{WGN-hit}^2 \\ &= E\{A^2\} + E\{B^2\} + E\{C^2\} - \eta_{WGN-hit}^2, \end{aligned} \tag{8}$$

$$E\{A^2\} = \left\{\left[\sqrt{E_c}\sum_{i=1}^{32} c_{i1}^2\right]^2\right\} = 32E_c[E\{c_{i1}^4\} + 31E\{c_{i1}^2\}E\{c_{j1}^2\}]. \tag{9}$$

The required mean values are

$$E\{B^2\} = E\left\{\left[\sqrt{E_N}\sum_{i=1}^{32} n_i \cdot c_{i1}\right]^2\right\} = 32E_N E\{c_{i1}^2\} \tag{10}$$

$$E\{C^2\} = E\left\{\left[\sqrt{E_j}\sum_{i=1}^{32} j_i \cdot c_{i1}\right]^2\right\} = 32E_j E\{c_{i1}^2\}. \tag{11}$$

Also, the mean squared value is equal to

$$\eta_{w_{WGN-hit}}^2 = E^2\{w_1\} = 32E_c E^2\{c_{i1}^2\} + 32\times 31E_c E\{c_{i1}^2\}E\{c_{j1}^2\}. \tag{12}$$

Therefore, the variance is equal to

$$\sigma_{w_{WGN-hit}}^2 = 32E_c[E\{c_{i1}^4\} + 31E\{c_{i1}^2\}E\{c_{j1}^2\}] + 32E_N E\{c_{i1}^2\} + 32E_j E\{c_{i1}^2\} - 32E_c E^2\{c_{i1}^2\} - 32\times 31E_c E^2\{c_{i1}^2\}E^2\{c_{j1}^2\}. \tag{13}$$

By replacing $E\{C_{i1}{}^4\} = E\{C_{i1}{}^2\} = 1$, which is valid for a binary spreading, we may have

$$\sigma_{w_{WGN-hit}}^2 = 32E_N + 32E_j. \tag{14}$$

So based on the (7) and (14), the probability of error is equal to

$$p_e(w_{WGN-hit}) = \frac{1}{2} erfc\left[\left(\frac{E_b}{N_0}\right)^{-1} + \left(\frac{E_b}{N_j}\right)^{-1}\right]^{-1/2}, \tag{15}$$

$$p_e(w_{WGN-hit}) = \frac{1}{2} erfc\left[(SNR)^{-1} + (SJR)^{-1}\right]^{-1/2} \tag{16}$$

where, SNR and SJR are abbreviation of signal to noise ratio and signal to jam ratio. Respectively, the probability of error for the WGN system when the jammer misses the original signal is

$$p_e(w_{WGN-Miss}) = \frac{1}{2} erfc\left[\left(\frac{E_b}{N_0}\right)^{-1}\right]^{-1/2}. \tag{17}$$

Finally, by using (17) and (16) in (5) the average probability of error in the case of WGN is:

$$p_{e(Average-WGN)} = \frac{\varphi}{2} erfc\left[(SNR)^{-1} + (SJR)^{-1}\right]^{-1/2} + (1-\varphi)\times erfc\left[\left[(SNR)^{-1}\right]\right]^{-1/2} \tag{18}$$

The average probability of error for the other scenarios is presented in Table 3.

5.3 Fast Jammer

When the jammer is switching fast we can assume that the jammer will hit some chips of all bits. The main difference between fast and slow jammer is that, in fast jammer all bits are hit by the jammer whereas in slow jammer some bits remain untouched. Therefore, the average probability of error can be directly calculated from (4). Therefore we have

$$\begin{aligned} w_{Fast-WGN} &= \sum_{i=1}^{32} z_i c_{i1} = \sqrt{E_c}\sum_{i=1}^{32} c_{i1}^2 + \sqrt{E_N}\sum_{i=1}^{32} n_i \cdot c_{i1} + \sqrt{E_j}\sum_{i=1}^{l} j_i \cdot c_{i1} \\ &= A + B + C \end{aligned} \tag{19}$$

where l is the number of hit chips per bit. Its mean value is equal to

$$\eta_{w_{Fast-WGN}} = E\{w_{Fast-WGN}\} = \sqrt{E_c}\sum_{i=1}^{32} E\{c_{i1}^2\} = 32E\{c_{i1}^2\}\sqrt{E_c} = 32\sqrt{E_c} \tag{20}$$

and the variance is equal to

$$\begin{aligned} &\sigma^2_{w_{Fast-WGN}} = E\{w^2_{w_{Fast-WGN}}\} - \eta^2_{w_{Fast-WGN}} = E\{(A'+B'+C')^2\} - \eta^2_{w_{Fast-WGN}} \\ &= E\{A'^2\} + E\{B'^2\} + E\{C'^2\} - \eta^2_{w_{Fast-WGN}}. \end{aligned} \tag{21}$$

the mean values for each part (A',B',C') are

$$\begin{aligned} E\{A'^2\} &= \left\{\left[\sqrt{E_c}\sum_{i=1}^{32} c_{i1}^2\right]^2\right\} \\ &= 32E_c[E\{c_{i1}^4\} + 31E\{c_{i1}^2\}E\{c_{j1}^2\}], \end{aligned} \tag{22}$$

$$E\{B'^2\} = E\left\{\left[\sqrt{E_N}\sum_{i=1}^{32} n_i \cdot c_{i1}\right]^2\right\} = 32E_N E\{c_{i1}^2\} \tag{23}$$

$$E\{C'^2\} = E\left\{\left[\sqrt{E_j}\sum_{i=1}^{l} j_i \cdot c_{i1}\right]^2\right\} = lE_j E\{c_{i1}^2\}. \tag{24}$$

Also, the mean squared value is equal to

$$\begin{aligned} \eta^2_{w_{Fast-WGN}} &= E^2\{w_1\} = 32E_c E^2\{c_{i1}^2\} \\ &+ 32\times 31E_c E\{c_{i1}^2\}E\{c_{j1}^2\}. \end{aligned} \tag{25}$$

Therefore, the variance is equal to

$$\begin{aligned} \sigma^2_{w_{Fast-WGN}} &= 32E_c[E\{c_{i1}^4\} + 31E\{c_{i1}^2\}E\{c_{j1}^2\}] \\ &+ 32E_N E\{c_{i1}^2\} + lE_j E\{c_{i1}^2\} - 32E_c E^2\{c_{i1}^2\} \\ &- 32\times 31E_c E^2\{c_{i1}^2\}E^2\{c_{j1}^2\}. \end{aligned} \tag{26}$$

By inserting $E\{C_{i1}{}^4\}= E\{C_{i1}{}^2\}=1$ in (26), we may have the variance in a simplified form

$$\sigma^2_{w_{Fast-WGN}} = 32E_N + lE_j \tag{27}$$

So, the probability of error is equal to

$$p_e(w_{Fast-WGN}) = \frac{1}{2} erfc\left[\left(\frac{E_b}{N_0}\right)^{-1} + \left(\frac{l}{32}\right)\left(\frac{E_b}{N_j}\right)^{-1}\right]^{-1/2} \tag{28}$$

$$p_e(w_{Fast-WGN}) = \frac{1}{2} erfc\left[(SNR)^{-1} + \left(\frac{l}{32}\right)(SJR)^{-1}\right]^{-1/2}. \tag{29}$$

The ratio of $\frac{l}{32}$ is equal to probability of hitting (φ). Therefore the (29) can be rewritten as:

$$p_e(w_{Fast-WGN}) = \frac{1}{2} erfc\left[(SNR)^{-1} + \varphi(SJR)^{-1}\right]^{-1/2}. \tag{30}$$

The probability of error for other scenarios are provided in the Table 3.

Table 3 Probability of error for in deferent scenarios in case of fast and slow jammers

Scenario	probability of error for fast jammer	probability of error for slow jammer
WGN	$\frac{1}{2} erfc\left[(SNR)^{-1} + \varphi(SJR)^{-1}\right]^{-1/2}$	$\frac{\varphi}{2} erfc\left[(SNR)^{-1} + (SJR)^{-1}\right]^{-1/2} + \frac{(1-\varphi)}{2} erfc\left[\left[(SNR)^{-1}\right]\right]^{-1/2}$
WGN + fading	$\frac{1}{2} erfc\left[\frac{2(4-\pi)}{\pi} + \frac{4}{\pi}(SNR)^{-1} + \frac{4}{\pi}\varphi(SJR)^{-1}\right]^{-1/2}$	$\frac{\varphi}{2} erfc\left[\frac{2(4-\pi)}{\pi} + \frac{4}{\pi}(SNR)^{-1} + \frac{4}{\pi}(SJR)^{-1}\right] + \frac{(1-\varphi)}{2} erfc\left[\frac{2(4-\pi)}{\pi} + \frac{4}{\pi}(SNR)^{-1}\right]^{-1/2}$
WGN +fading +Interleaver	$\frac{\varphi}{2} erfc\left[\frac{(4-\pi)}{16\pi} + \frac{4}{\pi}(SNR)^{-1} + \frac{4}{\pi}(SJR)^{-1}\right] + \frac{(1-\varphi)}{2} erfc\left[\frac{2(4-\pi)}{\pi} + \frac{4}{\pi}(SNR)^{-1}\right]^{-1/2}$	$\frac{\varphi}{2} erfc\left[\frac{(4-\pi)}{16\pi} + \frac{4}{\pi}(SNR)^{-1} + \frac{4}{\pi}(SJR)^{-1}\right] + \frac{(1-\varphi)}{2} erfc\left[\frac{2(4-\pi)}{\pi} + \frac{4}{\pi}(SNR)^{-1}\right]^{-1/2}$

Fig. 3 shows the effects of the fast jammer on probability of error. The black line represents the probability of error without jammer. The probability of error in the system with a jammer is presented by the dashed line. In this scenario the jammer is always hitting the original signal (l=32 and φ=1), with the SJR of 5 dB. As can be seen from the figure, the jammer has great effect on the probability of error. Fig. 3 also shows the simulation results (BER) which are presented by triangles.

For simulating the system, we used Matlab simulator developed in our research group, which simulates the transmitter, channel and receiver and sends repeated blocks of random 20 bits to calculate BER. The simulation results matches very well with theoretical expressions.

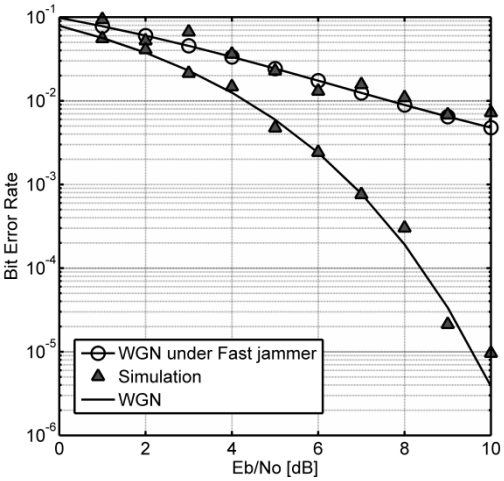

Fig. 3 Probability of error curves for the system with no-inteleaver in AWGN channel: theoretical (WGN), theoretical in case a fast jammer and bit error rate values obtained by simulation (Triangles)

Fig. 4 and Fig. 5 present probability of error rate for slow and fat jammers effect in different scenarios based on the SJR. In both figures the SJR is equal to 5 dB, but, the probability of hit (φ) in Fig. 4 is 0.25 whereas in Fig. 5 it is equal to 0.75. As can be concluded form both figures, the probability of error decreases by increasing the jammer power. However, in the scenarios with the low probability of hit (smaller φ), the fast jammer has greater impact on the error rate. Because the slow jammer can hit only a group of bits and leave some bits untouched, whereas the fast jammer hits all the bits. Therefore, by increasing the jammers power the fast jammer can affect all bits and decrease the probability of error more than the slow jammers. However, as it is presented in Fig. 5, the fast jammer and slow jammers effects are become equal by increasing the hitting probability.

Fig. 4 and Fig. 5 also show the effect of intruding the interleaver to the system. Generally Interleaver is used in this kind of communication system to protect the system against the burst error. Here, since the fast jammer hits a section of chips

in each bit, as communication points of view, its effect can be considered as a burst error. Therefore, the interleaver can decrease the high power fast jammer effect on the probability of error.

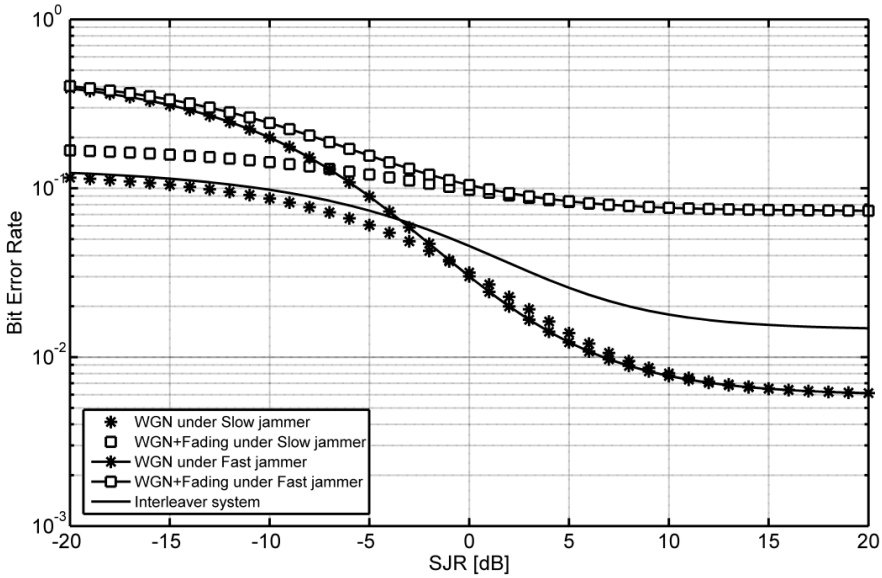

Fig. 4 BER curves for fast and slow jammer in deferent scenario with probability of hit (φ) equal to 0.25

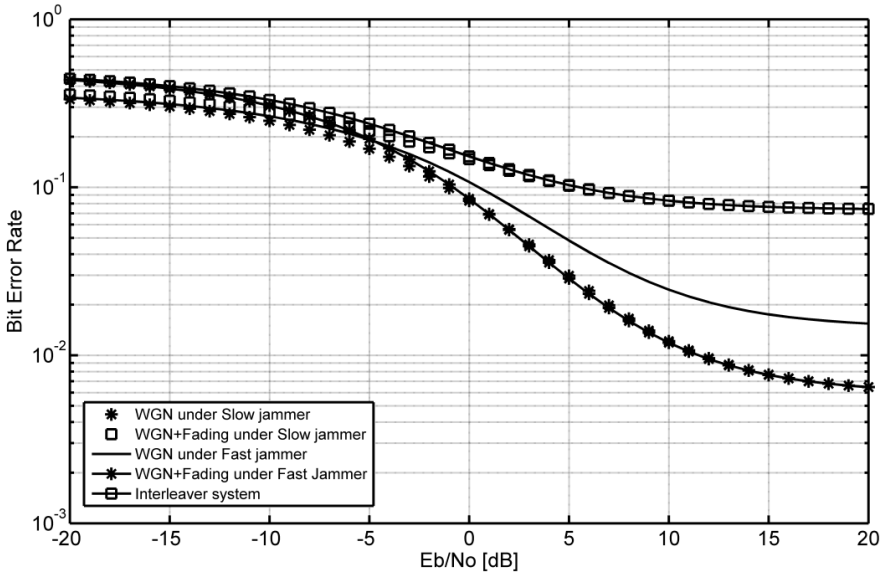

Fig. 5 BER curves for fast and slow jammer in deferent scenario with probability of hit (φ) equal to 0.75

6 Result of Analysis and Proposals

In this section we review current attacks in WSN based on the new attack's target category. Now, we summarize, analyses and propose future possibility for each group.

6.1 Packet or Signal Destruction (Jammers)

This is one of the oldest attacks in WSNs, which can have huge effects on the communication. Furthermore, this attack can be done to any networks. Because in order to jam a network, it is not necessary for attacker to be informed about network's context oriented information. However, the cover area of the attack is limited by the transmission range of the attacker. In addition, this attack is detectable due to propagation of electromagnetic signals. Note that jamming in the layer two could be stealthier than the physical layer jamming; but it is more complicated to implement. Here we propose the future possible jammers.

Hybrid jamming in physical layer: Here we suggest a hybrid jamming. The hybrid jammer is combination of the Reactive jammer and Random jammer. It jams when the channel is busy and instead of jamming constantly, it uses random jamming. It can stay longer in the field and be hidden from monitoring and intrusion detection devices.

Higher layer jamming: Until now, the jammers are mainly focusing on layer two and layer one. Here we suggest higher layer jamming as a potential attack. In higher layer jamming, the target is interfering with layer three and layer four controlling signals such as routing table updates. Jamming in higher layers can be more effective, energy efficient and harder to detect. However, as a tradeoff, it might be harder and more complicated to implement. For instance, whenever nodes are exchanging the periodic routing table update a jammer can interfere. Interfering the routing tables can make serious problem for whole network. The high layer jammer can interfere, connection establishment and periodic authentication. Because the jammer needs to know what the right time to jam is, it can only target the periodic exchanges such as periodic updates or multi-level exchanges such as multi way hand shaking messages.

6.2 Congestion Makers

Congestion makers can make huge delay in the WSNs. However, most of them except wormhole need impersonation. For instance, in false routing, attacker needs to impersonate itself in order to force other nodes to send their packets to the attacker's favorite route. Furthermore, wormhole attack needs physical implementation in the field, which might be physically detected in the field.

Unlike jammers, the congestion makers are not limited to a certain area and can fairly affect whole of the network. These attacks, especially wormhole and sinkhole, have a great supporting potential. Supporting attacks can be combined with the other attacks to enhance them. The possibilities of combining various attacking methods are discussed in the next section.

We propose distributed wormhole attack. Generally, in wormhole attack two adversary nodes are connected to each other. Here, we suggest using distributed fiber connection to connect multiple adversary nodes. The distributed wormhole attack may have more effect and can cover larger area.

6.3 Energy Consumers

These attacks are designed to consume a node's energy. Energy saving is one of the main targets in the WSN. Generally, all DoS attacks can make a node to consume energy. However, attacks such as hello and session flooding are specially designed to make the nodes busy until they finish all their batteries' power.

These attacks can affect only the attacker's neighboring nodes. Moreover, attackers sometimes are equipped with battery and are sending the constant requests, which is not energy efficient for attacker. Furthermore, some MAC layer protocols such as S-MAC are using fix sleep and listen schedule. So, constant request sending might not be very efficient.

As mentioned before, some MAC protocols are using fixed sleep and listen schedule and an attacker might use battery. Therefore, we suggest using periodic hello and session flooding. These attackers learn the other nodes schedule and try to attack on their listening period.

6.4 Packet Dropping

Packet droppers need impersonation like congestion makers. As mentioned earlier, packet forwarding and de-synchronization are main packet droppers. Packet forwarding attack can affect the packets that pass form the attacker. Therefore, the effect of this attack is highly dependent on the position of the attacker. This attack is more effective if the attacker is placed near to the cluster head or the gateway sensor. However, in de-synchronization, the attack area can be fairly distributed in the whole network. This attack can have huge effect for network's applications in which time synchronization is vital.

Here we suggest layer two selective forwarding. In the selective forwarding, the packets to the specific destination will be dropped. In this study, we propose the layer two selective forwarding attack, which drops the data packets and forwards the control packets. In this attack, the network's management functionality performs every well but the data cannot be sent. Therefore, layer two selective forwarding attack is hard to detect.

6.5 Privacy Attacks

Privacy attacks can provide key information for the attacker. Context oriented information such as the MAC layer algorithm and packet interval time, can help attacker to perform DoS attack. Some DoS attacks such as false routing and sinkhole attacks depend on the information that can be provided by eavesdropping, traffic analysis and tempering attack. However, these attacks have some limitation.

Eavesdropping and Traffic analysis are area limited which means that they can cover a limited area of a network. Also for eavesdropping the attacker needs to know the encryption key in case that the data is encrypted.

Tempering attacks can provide important information such as encryption key; however, as mentioned earlier, this requires physical access to the node and high standard lab facility.

6.6 Impersonation Attacks

Personate attacks by themselves cannot be harmful as they cannot provide information or deny a service. This is the main difference between impersonate attack with other types of attacks. However, they are very important for performing other type of attacks such as Session flooding, False routing, RBS De-synchronization and Unfairness. For instance, in De-synchronization, the attacker needs to impersonate itself to makes the other nodes change timer local time.

7 Conclusion

WSNs are vulnerable to different kinds of attacks. An adversary can attack for different purposes. Attacks are categorized based on attacking goals and different OSI layers. In this chapter, the main attacks of WSNs are identified, discussed, and presented in systematic form to allow their comparison and trace the future research activities in this field. To qualify and quantify the possible attacks in WSNs and understand their properties, we propose new attacks for WSNs. This chapter also analyzes the performance of the physical layer of WSN's against jamming attack. In this study, WSN's uses spread spectrum communications with binary sequences for spreading that are defined by the Standard for wireless sensor networks. For analyzing the system resistance against jamming, the mathematical expressions of bit error rate in case of WGN and fading presence in the channel are derived in closed form.

References

[1] López, J., Zhou, J.: Wireless Sensor Network Security, vol. 1. IOS Press Inc. (2008)
[2] Xu, W., Ma, K., Trappe, W., Zhang, Y.: Jamming sensor networks: attack and defense strategies. IEEE Network 20, 41–47 (2006)

[3] Znaidi, W., Minier, M., Babau, J.-P.: An Ontology for Attacks in Wireless Sensor Networks (2008)
[4] Yee Wei, L., Marimuthu, P., Lodewijk Van, H., Jeroen, D., Pieter, H., Paul, H.: Energy-efficient link-layer jamming attacks against wireless sensor network MAC protocols. ACM Trans. Sen. Netw. 5, 1–38 (2009)
[5] Law, Y.W., van Hoesel, L., Doumen, J., Hartel, P., Havinga, P.: Energy-efficient link-layer jamming attacks against wireless sensor network MAC protocols. Presented at the Proceedings of the 3rd ACM Workshop on Security of Ad Hoc and Sensor Networks, Alexandria, VA, USA (2005)
[6] Xiao, Y.: Security in Sensor Networks. Uerbach Publications (2006)
[7] Hu, Y.-C., Perrig, A., Johnson, D.B.: Wormhole attacks in wireless networks. IEEE Journal on Selected Areas in Communications 24, 370–380 (2006)
[8] Krontiris, I., Giannetsos, T., Dimitriou, T.: Launching a Sinkhole Attack in Wireless Sensor Networks; The Intruder Side. In: IEEE International Conference on Wireless and Mobile Computing Networking and Communications, WIMOB 2008, pp. 526–531 (2008)
[9] Kim, H., Oliveira, R., Bhargava, B., Song, J.: A Novel Robust Routing Scheme Against Rushing Attacks in Wireless Ad Hoc Networks. Wireless Personal Communications 70, 1339–1351 (2013)
[10] Jian, L., Fang-min, L.: An Improvement of AODV Protocol Based on Reliable Delivery in Mobile Ad Hoc Networks. In: Fifth International Conference on Information Assurance and Security, IAS 2009, pp. 507–510 (2009)
[11] Shila, D.M., Yu, C., Anjali, T.: Mitigating selective forwarding attacks with a channel-aware approach. IEEE Transactions on Wireless Communications, WMNS 9, 1661–1675 (2010)
[12] Tiwari, M., Arya, K.V., Choudhari, R., Choudhary, K.S.: Designing Intrusion Detection to Detect Black Hole and Selective Forwarding Attack in WSN Based on Local Information. In: Fourth International Conference on Computer Sciences and Convergence Information Technology, ICCIT 2009, pp. 824–828 (2009)
[13] Xiaoming, L., Spear, M., Levitt, K., Matloff, N.S., Wu, S.F.: A Synchronization Attack and Defense in Energy-Efficient Listen-Sleep Slotted MAC Protocols. In: Second International Conference on Emerging Security Information, Systems and Technologies, SECURWARE 2008, pp. 403–411 (2008)
[14] Sakya, G., Sharma, V., Jain, P.C.: Analysis of SMAC protocol for missioon critical applications in wireless sensor networks. In: 2013 IEEE 3rd International on Advance Computing Conference (IACC), pp. 488–492 (2013)
[15] Manzo, M., Roosta, T., Sastry, S.: Time synchronization attacks in sensor networks. Presented at the Proceedings of the 3rd ACM Workshop on Security of Ad Hoc and Sensor Networks, Alexandria, VA, USA (2005)
[16] Erdene-Ochir, O., Minier, M., Valois, F., Kountouris, A.: Resiliency of wireless sensor networks: Definitions and analyses. In: 2010 IEEE 17th International Conference on Telecommunications (ICT), pp. 828–835 (2010)
[17] Ponomarchuk, Y., Dae-Wha, S.: Intrusion detection based on traffic analysis in wireless sensor networks. In: 2010 19th Annual Wireless and Optical Communications Conference (WOCC), pp. 1–7 (2010)
[18] Skorobogatov, S.P.: Semi-invasive attacks-a new approach to hardware security analysis, Technical report, University of Cambridge, Computer Laboratory (2005)

[19] Danev, B., Capkun, S.: Transient-based identification of wireless sensor nodes. In: Proceedings of the 2009 International Conference on Information Processing in Sensor Networks, pp. 25-36 (2009)
[20] Zeng, K., Govindan, K., Mohapatra, P.: Non-cryptographic authentication and identification in wireless networks [Security and privacy in emerging wireless networks]. IEEE Wireless Communications 17, 56–62 (2010)
[21] Newsome, J., Shi, E., Song, D., Perrig, A.: The sybil attack in sensor networks: analysis & defenses. In: Proceedings of the 3rd International Symposium on Information Processing in Sensor Networks, pp. 259–268 (2004)
[22] Berber, S., Yuan, Y., Suh, B.: Modeling and Simulation of a Physical Layer for WSNs based on Binary Sequences
[23] Chih-Lin, I., Pollini, G.P.: The tree-search resource auction multiple access (TRAMA) protocol for wireless personal communications. In: 1994 IEEE 44th Vehicular Technology Conference, vol. 2, pp. 1170–1174 (1994)

Learning with Great Care: The Adoption of the Multi-sensor Technology in Education

M.C. Liu, C.H. Lai, Y.N. Su, S.H. Huang, Y.C. Chien,
Y.M. Huang, and J.P. Hwang*

Department of Engineering Science, National Cheng Kung University,
University Road, Tainan, 701, Taiwan
jan.pan.hwang@gmail.com

Abstract. Satisfying students' different needs for learning is an important issue in the education domain. However, teachers used to take an exam to understanding students' learning progress often in the past, resulting in increasing students' stress and frustration. Owing to the advent of sensor technology, it provides educators a new way to conveniently assess every student's learning status in diverse dimensions. For example, a cushion with pressure sensors can find the variety of learners' sitting postures. With the experiences in the development of sensor and educational technologies, we have seen an emerging trend in the application of multi-sensor technologies to educational environments. Therefore, this article aims to investigate the suitability of different kinds of sensors for the educational scenario, and the potential benefits of integrating multi-sensor technology in schools. It is hoped to suggest readers a further research blueprint for this topic.

Keywords: sensor technologies, learning devices, emotion, affective computing, intelligence classrooms, technology-enhanced learning.

1 Introduction

In the recent decades, with rapid advancement of multimedia, network and mobile technology, development of digital learning is flourishing. This drives academic research of integrating education with information technology (e.g. mobile learning [1-4], web learning[5-8], Ubiquitous learning[9, 10]). However, almost all of subject disciplines involve computers and digital technology, as well as learning and teaching activities [11-13]. Thus, digital learning has been deeply rooted in various fields (e.g., education, medical science, commerce, physics & chemistry, and engineering). Meanwhile, it has great impact on reformation in teaching and learning. On the other hand, the development of digital learning can promote effective integration of different disciplines and training of interdisciplinary talents.

* Corresponding author.

A. Mason et al. (eds.), *Sensing Technology: Current Status and Future Trends III*,
Smart Sensors, Measurement and Instrumentation 11, DOI: 10.1007/978-3-319-10948-0_11

Currently, digital learning development is not limited to application of information equipment and Internet, and integrates different technologies and elements, such as cognition science, community network, cloud technologies and sensing technologies [11, 14-16]. Various sensing technology-based applications and learning methods emerge in the increasingly mature environment, such as context awareness learning, argument reality, posture learning, data capture and emotion recognition [17, 18]. Many recent studies have proposed innovative thinking and change model of teaching, even paradigm shift.

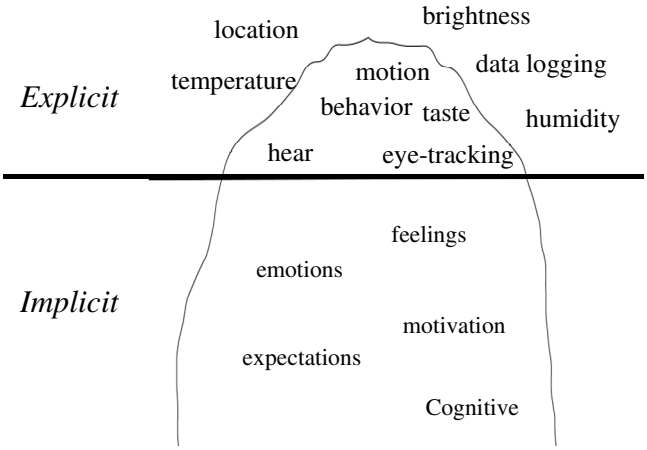

Fig. 1 Iceberg model [19]

This section uses four cases for analysis and introduced application of current sensing technologies to education. It mainly discusses impact of environmental factors (indoor/outdoor) and learning factors (implicit/explicit) on education through various sensors. The interaction between learners and sensing equipment and the use may change due to different involvement of sensing technology in teaching activities, different field domains and different purposes. Case 1: in outdoor teaching, learners used environment sensors to sense change of water quality in different points in field observation. The main purpose is to make learners combine knowledge with examples in real life by using inquiry by discovery and information collected by the sensing equipment. Case 2: in classroom environment, the three sensors including cushion with pressure sensor, video sensor and mouse with physiological signal sensor were used to sense change in learning state of learners, and effectively analyze and understand learning retention of learners. Case 3: in reading environment, video sensor and pressure sensor were used with tablet computers to understand reading behavior of learners during reading. Case 4: established one graphic identification system, and understand emotion changes of learners through facial recognition technology. The teaching field domain is online learning, and can be divided into synchronous environment and asynchronous

environment. By understanding emotion change of learners in learning portfolio, assistance can be provided for learners and teachers.

However, most information collected by the sensors is explicit learner behavior and environment events. This is only a tip of the iceberg. Like the iceberg model as proposed by psychologist Satir [19], the concept and implications can be seen in Fig. 1. The explicit behaviors and context are a tip of the iceberg, and like the information collected by the sensors. Intrinsic motives, feeling, cognition and emotions of learners cannot be understood further. More significant information related to learners is concealed below the horizontal line and has not been fully obtained and used. Thus, deep application of sensing technology to learning and teaching has a long road to go.

2 Sensor Applied in Education/Learning

Classroom is a professional field of teaching and learning. After going to classrooms, teachers have to face curriculums, each student and class management and other dimensions and needs. Besides careful management, adjustment of teaching strategies should be considered according to individual difference, and this can achieve win-win relationship between teachers and students, and create a friendly learning environment in classrooms. In order to establish win-win relationship between teachers and students, if teachers are qualified managers, improvement of teachers' professional ability is a necessary condition. Classroom observation is an important link of developing teacher's professional ability [20] in a real classroom. The main purpose of the classroom observation is to know classroom context, student's learning status, use of textbooks and other dimensions [20] and help teachers analyze teaching methods and effectiveness of strategies to improve teacher's teaching abilities[1].

In recent years, with the rise of the multiple assessment concept, implementation of classroom observation has become more possible. The trend of thought in contemporary education pays attention to learning portfolio of students. The learning portfolio can reflect not only learning results but also growth process of students [21]. Thus, many researchers and teachers are attracted to analyze and explore learning portfolios [22-25]. Analysis of learning portfolio can help teachers know the learning situations, and some teachers use multiple assessment instrument as the methods to observe the learning status of each student. Observation of implicit behaviors of students through classroom observation [26] or observation of explicit behavior of students to provide learning support is a very clear assessment context. However, acute observation of teaching context is the foremost when teachers implement classroom observations, and however this ability needs long accumulated experience in teaching. Only with this ability, teachers can explain classroom event and student behaviors [20] and further interpret implicit behaviors (cognition and emotions) and explicit behaviors (learning retention and learning behavior). In recent years, as sensing technology has become mature, intelligence classroom concept has been implemented by many researchers. For example,

analysis of implicit and explicit behaviors of students through sensing technology is one of the objects in establishment of intelligence classrooms. In addition, some studies have implemented sensing technology in discipline learning to explore and observe the physical properties of real learning environment [27, 28]. Thus, there are application examples of sensing technology in teaching scene. Meanwhile, it creates a friendly learning environment for teachers and students.

Currently, sensing technology development is diversified. Applicability of sensors used for education field is introduced through implicit and explicit concepts. Explicit sensors measure pressure, sensing distance, video signals, GPS and illumination. Most of them are used for sensing environment (e.g., water quality, soil and position), student behavior (e.g., sitting posture, move path, and strength) and facial recognition (e.g., visual attention and blink); implicit sensors sense brain waves, blood oxygen, pulse, and galvanic skin response. Most are used to measure physiological data of learners. On the other hand, researchers use multiple explicit sensors in experimental analysis, and attempted to establish correlation between explicit behavior performance and learning retention and psychological state of learners. The detailed results are described in the following cases.

The sensors used for teaching field can be divided into two types according to the functions. The first type is physical orientation, and is used to sense physical changes in the environment. Furthermore, the combination of sensors with teaching activities can achieve teaching goal and has significance. For example, sensors are used to sense temperature [29], humidity [30], oxygen content [31], intensity of illumination [32] and other physical properties in environment. Learners can further understand changes and meanings of the physical properties in the natural environment; on the other side, the physiological oriented sensors are used to measure physiological status of learners, including brain wave [33], facial recognition system [34], blood oxygen content [35] and pressure sensors [14, 36]. The collected data contribute to deduction and analysis through which relationship between learning state, emotions and cognitive development of learners [37, 38] can be understood, and relevant information can be provided for teachers, as well as suitable textbooks, teaching methods or teaching aids. This can improve learning motivation of learners and achieve self-learning development.

3 Methodology

In the Methodology, we proposed the methodology how do sensing technology implementing in the learning environment. Every sensing technology are significantly develop in different learning situation areas.

3.1 Applying "Sensing Technology" into Informal Learning Environment

Sensing technology can be applied into formal learning environment, as well as informal learning environment. This section discusses the outdoor teaching

situations, and introduces how sensing technology is applied into teaching in the outdoors and anticipate benefits of embedment of sensing technology.

As compared to teaching in tradition classrooms, the teaching in the outdoors can make students learn more and better because teaching in traditional classrooms are passive or static learning of textbooks. The kind of knowledge instruction lacks reality. Although teachers provide video material course in the classroom, this cannot replace actual experience of students in outdoor teaching [39-41]. Teaching in the outdoors can make students contact with real objects, and interact with environment and society to get direct learning experience, and they may have more affective learning [42].

Currently, teaching in the outdoors has been applied to many disciplines and acquires good learning effectiveness [43]. For example, students can be guided to rethink formation of valleys by observing rivers and lakes and valleys so as to enhance learning in areas of science. Students can join outdoor camping activities, and experience outdoor fishing, cooking in the open air, and erection of tents to increase outdoor survival skills of boy scouts. The students observe the footprint of wild animals and collect relevant information to speculate source of footprints and increase their abilities of exploring the nature. Direct experience of environment also helps us foster our attitudes, value and concepts of environment, and enhance environment education. In the outdoor, students can learn how to use compass to guide directions, estimate distance using number of steps and at last draw one map. Diversity of mathematics courses can be achieved by presenting life problems. In sum, teaching in the outdoors can make students observe, deeply understand and acquire knowledge of different fields to supplement the course contents in schools.

Due to difficulty in coordination between resources and time, how to arrange outdoor education time to maximize efficiency is one of concerns by educators. How to make learners fully interact with environment and make the most effective exploration is the key to successful outdoor learning. This topic has attracted more attention, and many studies have attempted to employ mobile technology into outdoor exploration. For example, some studies have used GPS to guide students to explore the environment in outdoor learning [44-46].

At current, most of mobile handheld devices are used to display of digital textbooks, or guide positions [41, 47], and, however, lack of support can make learners more directly interact with environment and actively explore the nature. Thus, this section describes application of sensing technology to outdoor learning and analyzes usability of sensors in outdoor learning.

In the study by Kamarainen et al.[48], the mobile devices and science environment probes were used in field observation of ecology in order to make students explore environment and connect the learned nature science knowledge with daily life environment. This study anticipated mobile devices and scientific probes, and their computing abilities can be used to display real time environment

data and graphs, and illustrate abstract concepts with concrete variables to support inquiry-based learning.

A total of 71 sixth grade USA students participate their study. The research equipment includes smart phones, Texas Instruments (TI) NSpire handheld devices and Vernier environmental probes. The probes can sense four environment variables: dissolved oxygen concentrations, turbidity, pH and water temperature. The curriculum includes preparatory course, teaching in the outdoors and post course discussion. In the preparatory course, the students mainly learn the concepts of dissolved oxygen concentrations, turbidity, pH and water temperature. Teachers provided five groups of observation stations in the classrooms, including different levels of water quality. The students were asked to record the 4 variables in the five stations, and then each group discussed the observed results. In actual outdoor exploration, the students paired up and used TI NSPIRE and water quality probes to observe pond water quality at different places. The students should record water quality data at each place and compare the water quality at different places. The students may compare the data difference with other groups. After teaching in the outdoors, in post course discussion, teachers use the data to guide students to discuss whether fish is in a healthy environment, and how these data affect survival of other species.

At last, the research results show that students in sensing technology-embedded outdoor teaching experiment can facilitate their acquirement of knowledge, and their sense of self-efficacy is also increased. Moreover, the students can control their learning pace by operating the sensors instead of passively receiving teaching contents. In other word, teaching in the outdoors with sensing technology achieves learner-centered instruction.

Fig. 2 Texas Instruments (TI) NSpire (*Source :[49]*)

Fig. 3 Vernier environmental probes (*Source :[50]*)

3.2 A Sensor-Assisted Model for Estimating the Accuracy of Learning Retention in Computer Classroom

This study proposed a sensor-assisted model (SAM) using sensor technology, in order to determine the learning retention of learners in the learning process, and further provide assistance or feedback. The identification rule of this system is constructed based on decision tree algorithm ID3 (C4.5). The system determined the learning retention according to the learners' visual attention recognition, sitting position variability, and physiological signals analysis. The purpose is to establish a feasible architecture through SAM, use data measured from multiple sensors to assist judgment of decision tree rules and establish effective standard for normal learning retention.

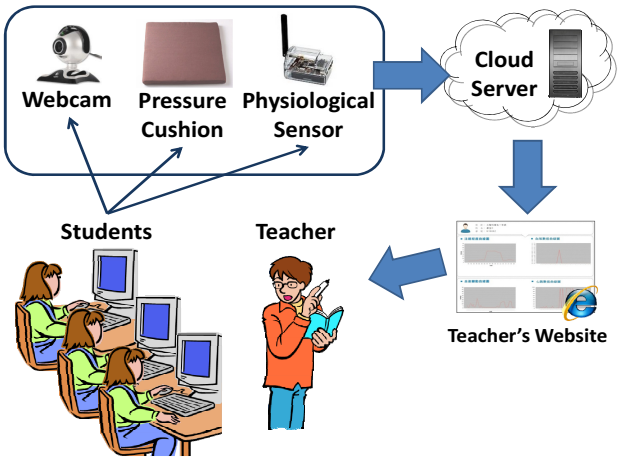

Fig. 4 System Architecture (*Source: [14]*)

The judgment rules for collected data are based on decision tree algorithm ID3. The visual attention recognition, sitting position variability and physiological signals analysis are used to judge learning retention. The system architecture is shown in Fig. 4. The system is based on e-book platform and applied to traditional classrooms.

The experimental samples in this case are the sensor data of 15 minutes e-book reading of 60 undergraduates. Three sensors were used to collect the data. Next, ID3 algorithm was used to construct decision tree model with the data. Two senior teachers and one scholar were invited to observe 40 undergraduates reading articles in the computer classroom for 15 minutes, in order to determine whether the learning retention was normal in the learning process. The results served as the training data for building the decision tree. Final, trimming the decision tree, the error rate is set as 5%, 10% and 20% to prune the decision tree in this study. When the error rate standard is 5%, the decision tree pruning prunes the noise from data set, so the error rate is close to the unpruned decision tree. When the PER is set as 10%, the decision tree pruning prunes the special cases from data set, so the error rate is about 2% different from the pruned decision tree, which is within the reasonable range. When the PER is set as 20%, the decision tree pruning may prune the original key data from data set, so the error rate is increased significantly, as compared with the unpruned decision tree. The accuracy rate of decision tree will decrease. . After the constructed decision tree was verified with the test data, the accuracy was between 86% and 90%. The results proved that the system is feasible, and the decision tree rule can identify the learning retention effectively.

Fig. 5 Pulse Mouse & Pressure Analysis Cushion. (*Source: [14-16]*)

This study combined multiple sensors with decision tree construction using ID3 algorithm to collate multiple data for judging learning retention rules and priority. In this study, the performance of extrinsic behavior is successfully connected with intrinsic learning retention.

3.3 Case 3: Application of Sensing Technology to E-book Reading Activities of Primary Schools

The case was derived from the three academic papers of symposium published in Educational Technology Research & Development, Interacting with Computers and ICST 2013 respectively [23, 49-51]. In this case, the researches integrated Tablet Personal Computer based on mobile technology with video sensors and pressure sensor to develop a series of e-book learning system for reading class in elementary schools. The case contents are described as follows [23, 49-51]:

In this case, the researchers intended to assist teachers in observation of the reading process of students and analyze the meanings of "learning retention" and "reading behavior" in reading. Reading is a complicated cognitive process, including character decoding, sentence pattern processing, and understanding of textual meaning [51]. If the teachers can know reading situations in the cognitive process, the individualized reading instruction provided for students is expected. However, traditional classrooms are limited to a class size of elementary schools and the teaching burden of teachers. Generally, reading instruction is suitable instruction provided by teachers when they find problems of students and make a proper intervention. If the teachers are busy in teaching affairs, or cannot observe the field teaching due to inadequate experience. If the students meet difficulty in reading and the teachers fails to give instructions, the teaching effect will be affected. In view of this above context, focus of the case is to assist teachers in observation of reading portfolios of students by finding suitable scheme based on the technical advantages.

The learning retention sensing technology integrates webcam of the tablet personal computers. The main function is to capture whether eyes of the students are fixed on the screen. If the eyes of the students are normal, and captured by the system, it is deemed that the students are watching the screen, and if not, they are not watching the screen. The pictures on the webcam are analyzed through learning retention sensing technology, and see the following figure.

Fig. 6 The detection technique of learning retention through webcam

R&D is conducted for reading rate analysis technology and learning retention sensing technology to integrate them with the e-book learning system. In this way, a reading activity context which can assist teachers in observation of classrooms can be achieved, and it can assist the teachers in obtaining learning retention and reading behavior of students, and find the problems of students in reading as early as possible and make proper interventions. In the traditional context, teachers are busy in teaching affairs, or cannot sharply observe the teaching field, resulting in failure of teachers to give timely instructions. Now, this situation can be improved.

After completion of the system development, in order to understand the applicability of the e-book learning system in the elementary schools, the third grade and fourth grade students were investigated, and several Chinese reading activities were designed to evaluate the system functions. The experimental results showed that the system can sense learning retention of students and reflect the reading behavior of students through the reading rate. The relevant real-time information is returned to the teachers, and can help teacher to observe the classrooms. In this way, whether the system can integrate with the real reading activities and improve reading abilities of the students still needs further verification in long-term experimental activities. The following figure shows situations of independent reading of students in experimental activities.

Fig. 7 The primary student read an e-book through the tablet PC (*Source*:[51])

The main contribution of this case is to aim at reading activities in the elementary schools, and provide an instrument of classroom observation for teachers. The reading is a complicated cognitive process, and part of the process may reflect reading rate, learning retention and other explicit behaviors. If the relevant explicit behavior of the students in reading can be obtained, they can help teachers observe reading situations of each student, and provide suitable reading instruction. This system architecture is based on the touch screen and webcam. The reading rate of students namely retention is captured through reading rate analysis and learning retention sensing. This method can assist teachers in observation of explicit behaviors of students in reading, reduce the teaching burden of the teachers, and help teachers find reading problems and assist students in reading. Due to touch screen of tablet personal computer, video camera and other sensors are popular, and this scheme is one of the choices in application of sensing technology to teaching field.

3.4 Analysis Personal Emotion with Sensors in Learning Environment

The studies on collection of learning emotions using sensing system have been conducted for many years [52]. The current emotional response can be roughly estimated through physiological response of learners [23, 53-55]. In recent years, facial emotion recognition is one of the sensing systems. This method is used to judge and analyze current facial expressions of learners [56]. The core technologies are image capture, recording and analysis in this process. The previous facial emotion recognition encountered many technical problems (e.g., difficulty of image capture, failure to real-time analysis, and facial feature extraction [57-59]). These problems can be solved with sensing technology and cloud technology [60, 61].

The case is a feasible case in which facial emotion recognition is used to know current state of learners [62]. This case can be used to illustrate how to use facial emotion recognition technology in teaching or learning environment. The application of the technology to education is described as follows.

In this case, one learning retention model was developed to analyze features of five emotions of the learners through the algorithm, such as happy, sad, surprise, angry and disgust. Besides analysis of the five emotions, the emotions result has been concluded. In this case, the developed model must contain three important parts:

1. Feature extraction and generation:
2. Feature subset selection:
3. Learning emotion recognition:

This case presents one more detailed analysis process in the second part of the feature subset selection, and combines immune memory clone feature selection algorithm (IMCFS) and support vector machine (SVM). The analysis is shown in Fig. 8.

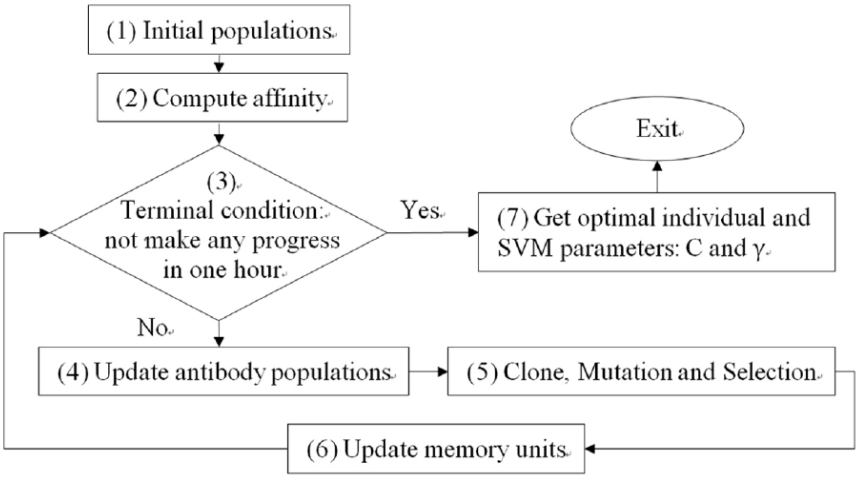

Fig. 8 Description of Feature selection algorithm (*Source*:[63])

The model must have 7 steps. In the seven steps, the subset selection can undergo optimal operation. Through the operation, accuracy of feature subset selection can be effectively increased. The model was developed based on this method, and the model is used to analyze data from open database. The accuracy of the analysis results reaches over 97%. The model has accuracy in emotion recognition.

In this case, besides the developed emotions recognition model and system, the personnel on the education scene urgently need what benefits the system can bring. In this case, the experiment design was conducted for real situation. The designed long-distance teaching system is very useful for students in distance learning. In this case, the environment is divided into synchronous environment and asynchronous environment, and it is discussed impact of the learning emotion recognition model developed from facial emotional recognition technology on learning in the synchronous and asynchronous distance-learning.

In this experiment, Face SDK 4.0 was used for facial emotional recognition. As shown in Fig. 9, the experiment environment is synchronous learning environment. Through windows of the environment, the learning picture of the learners can be observed, and further Face SDK is used to recognize the facial emotions. The recognition results can be used to understand the current learning state of the learners.

Fig. 9 Facial emotional recognition technology in synchronous learning environment (*Source*: [63])

The features can be marked through Face SDK, as shown in Fig. 10. After feature extraction, the current facial emotions can be analyzed.

Fig. 10 Feature point display from learning emotion recognition model (*Source*: [63])

This case shows image recognition has been gradually applied to learning environment besides crime investigations. The facial emotions of the learners shall be recognized and analyzed. In read situation, the application can be also extended to learners and teachers. For the learners, their self-control and self-regulating functions can be enhanced through the technology. Also, it can be applied to emotion management, and emotional self-regulation psychological guidance. Apart

from benefits for learners, teachers can master emotions of students, and this is very useful for the teaching process.

4 Result

Above of the sensing technology, one of the methodology of case, the reading behavior could be assessed with touch sensing[64]. In this case, touch screen on hardware architecture of tablet personal computer and webcam were used as sensors, and e-book learning system can be separately developed based on Microsoft Windows. The core technologies of this system are divided into reading rate analysis technology and learning retention sensing technology. The reading rate analysis technology integrates touch screen of tablet personal computers. When the fingers of students touch the screen and browse an e-book by sliding the picture, number of words read by students can be calculated and used to reckon reading rate per minute. Because reading rate can reflect reading behavior of students, this method is used to capture reading rate of students. In other words, the reading behavior of students can be detected. The teachers can know reading situations of students and properly intervene in them to provide individualized instructions. The comparison between reading rate and reading behavior is shown in the table below.

Table 1 A summary of reading rates and reading behaviors*(Source:[22, 54])*

Reading status	Reading rate (wpm)	Reading behavior
On-reading	0-1,000	
Slowing	<50	Excessively slow Inefficient reading Disfluent Labored Inexpressive Unenthusiastic rendering
Memorizing	50-100	Sustained attention In-depth reading
Learning	100-200	Oral reading Concentrated reading Annotation (highlight)
Reading	200-400	Silent reading Keyword spotting
Skimming	400-700	One-time reading Reading selectively
Scanning	700-1,000	Browsing and scanning Non-linear reading
Off-reading		
Flipping	≧ 1,000	Flip pages Glance and glimpse text

Above the summary of reading rates, it would helpful in identify elementary students' reading behavior. After identify those variable, the module of reading fluency would be easier to integrating out. This would be important in future works.

5 Conclusions

Based on the current education situations, this study analyzes the application and development of sensing technology, and uses different sensors to discuss the impact of environment factors and learning factors in education. However, the traditional teaching environment can be also extended to intelligence classroom concept, and in combination with sensors (e.g., cushion, video signal, mouse) the physiological and psychological states of learners are sensed, including implicit behavior (e.g., cognition and emotion) and explicit behaviors (e.g., learning retention and learning behavior). In addition, the technology can be embedded into the outdoor learning environment. Learners can understand the external state of the environment through observation and experience of learning. With the sensors (e.g., soil, water quality, temperature, humidity, oxygen content), they can further understand internal changes of environment.

During the learning process, physiological state and psychological state of the learners should be sensed, and some devices need to wear in part of the experiment (e.g., brainwave, earphones and mobile-bracelet). Further the experiment involves personal privacy of learners. Thus, adults or parents of teenagers need to sign a letter of intent. The experimental data are difficult to obtain, and this may result in an insufficient sample number. Thus, the learning situations cannot be observed in short time. Next, with rapid scientific development, personal information about learners and environment information can be obtained through sensors. This may also cause disputes, such as Google Glass. Through the sensors, physiological and psychological changes of the learners can be known more rapidly. However, personal private information is difficult to be obtained. This is one of the limitations in the sensor research. These sensors are mainly used to recognize the physiological state of learners, such as facial emotions recognition and retention sensing. The physiological states of learners are easily to obtain, and through the physiological change learning state of learners can be deduced. There are many factors affecting psychological states, and the psychological states of learners cannot be timely known through the senses. As a result, the learning situations cannot be deduced according to the psychological states. To date, the current sensors have difficulty in sensing changes in psychological states of learners.

In future application of sensing technology to education, learning factors (implicit/explicit) will be sensed to know states of learners, and sensors can be used for feedback of learning stages of learners (e.g., learning retention can be judged by sensing cushion pressure), and the learning states are provided for teachers to adjust teaching contents and progress. The technology can be also applied to indoor teaching, and the feasibility will be discussed. On the other hand, by combing real environment with sensing technology, learners can integrate into real context, and further understand change of the natural environment. Apart from observation of change in the natural environment, the main purpose of applying sensing technology to learners or the experiment environment is to understand the physiological and psychological change of learners, timely provide learning

feedback for learners and teachers, and improve learning effect and teaching quality.

Acknowledgements. This work is partially supported by the "International Research-Intensive Center of Excellence Program" of NTNU and National Science Council, Taiwan, R.O.C. under Grant no. NSC 103-2911-I-003-301, NSC 102-3113-P-006-019-, NSC 100-2511-S-006-014-MY3, and NSC 100-2511-S-006-015-MY3.

References

[1] Huang, Y.-M., Chiu, P.-S.: The effectiveness of a meaningful learning-based evaluation model for context-aware mobile learning. British Journal of Educational Technology n/a–n/a (2014)
[2] Jeng, Y.L., Wu, T.T., Huang, Y.M., Tan, Q., Yang, S.J.H.: The add-on impact of mobile applications in learning strategies: A review study. Educational Technology & Society 13, 3–11 (2010)
[3] Hwang, G.J., Wu, P.H., Zhuang, Y.Y., Huang, Y.M.: Effects of the inquiry-based mobile learning model on the cognitive load and learning achievement of students. Interactive Learning Environments 21, 338–354 (2013)
[4] Huang, Y.M., Lin, Y.T., Cheng, S.C.: Effectiveness of a mobile plant learning system in a science curriculum in Taiwanese elementary education. Computers & Education 54, 47–58 (2010)
[5] Huang, Y.M., Huang, Y.M., Wang, C.S., Liu, C.H., Sandnes, F.E.: Supporting self-regulated learning in web 2.0 contexts. Turkish Online Journal of Educational Technology 11, 187–195 (2012)
[6] Huang, Y.-M., Huang, Y.-M., Liu, C.-H., Tsai, C.-C.: Applying social tagging to manage cognitive load in a Web 2.0 self-learning environment. Interactive Learning Environments 21, 273–289 (2011)
[7] Lin, Y.T., Lin, Y.C., Huang, Y.M., Cheng, S.C.: A Wiki-based teaching material development environment with enhanced particle swarm optimization. Educational Technology & Society 16, 103–118 (2013)
[8] Lin, Y.C., Huang, Y.M.: A fuzzy-based prior knowledge diagnostic model with multiple attribute evaluation. Educational Technology & Society 16, 119–136 (2013)
[9] Wu, T.T., Sung, T.W., Huang, Y.M., Yang, C.S., Yang, J.T.: Ubiquitous English learning system with dynamic personalized guidance of learning portfolio. Educational Technology & Society 14, 164–180 (2011)
[10] Huang, Y.M., Wu, T.T.: A systematic approach for learner group composition utilizing u-learning portfolio. Educational Technology & Society 14, 102–117 (2011)
[11] Huang, Y.-M., Chen, H.-C., Hwang, J.-P., Huang, Y.-M.: Application of Cloud Technology, Social Networking Sites and Sensing Technology to E-Learning. In: Huang, R.-H., Kinshuk, Spector, J.M. (eds.) Reshaping Learning, pp. 343–364. Springer (2013)
[12] Huang, Y.M., Huang, S.H., Wu, T.T.: Embedding diagnostic mechanisms in a digital game for learning mathematics. Educational Technology Research and Development 62, 187–207 (2014)

[13] Hwang, G.J., Chu, H.C., Shih, J.L., Huang, S.H., Tsai, C.C.: A decision-tree-oriented guidance mechanism for conducting nature science observation activities in a context-aware ubiquitous learning environment. Educational Technology & Society 13, 53–64 (2010)
[14] Hwang, J.-P., Wu, T.-T., Lai, F.-J., Huang, Y.-M.: A sensor-assisted model for estimating the accuracy of learning retention in computer classroom. In: 2011 Fifth International Conference on Sensing Technology (ICST), pp. 650–654 (2011)
[15] Wu, T.-T., Hwang, J.-P., Huang, Y.-M., Tan, Q., Mukhopadhyay, S.: Using a Sensor-Assisted Model for Learning Retention in an e-Book Reading Environment. In: 2012 IEEE International on Instrumentation and Measurement Technology Conference (I2MTC), Graz, Austria, pp. 2553–2557 (2012)
[16] Hwang, J.-P., Wu, T.-T., Huang, Y.-M., Huang, Y.-M.: Development and Evaluation of Peer Feedback in the English Quiz Game Design in Social Network. In: 2012 IEEE 12th International Conference on Advanced Learning Technologies (ICALT), pp. 235–239 (2012)
[17] Deaney, R., Hennessy, S., Ruthven, K.: Teachers' strategies for making effective use of datalogging. School Science Review 88, 103–110 (2006)
[18] Deng, F., Chen, W., Chai, C.S., Qian, Y.: Constructivist-oriented Data-logging Activities in Chinese Chemistry Classroom: Enhancing Students' Conceptual Understanding and Their Metacognition. The Asia-Pacific Education Researcher 20, 207–221 (2011)
[19] Satir, V., Gomori, M., Gerber, J.: The Satir Model: Family Therapy and Beyond: Science and Behavior Books (1991)
[20] Chen, M.-Y.: Classroom observation I - a teachers' professional competence be omit. Educators and Professional Development 15, 48–54 (1998)
[21] Ćukušić, M., Alfirević, N., Granić, A., Garača, Ž.: e-Learning process management and the e-learning performance: Results of a European empirical study. Computers & Education 55, 554–565 (2010)
[22] Liang, T.-H., Huang, Y.-M.: An investigation of reading rate patterns and retrieval outcomes of elementary school students with E-books. Educational Technology & Society 17, 218–230 (2014)
[23] Huang, Y.M., Liang, T.H., Su, Y.N., Chen, N.S.: Empowering personalized learning with an interactive e-book learning system for elementary school students. Etr&D-Educational Technology Research and Development 60, 703–722 (2012)
[24] Zhang, W., Zhang, Y., Yang, X., Xu, W.: A class of on-line portfolio selection algorithms based on linear learning. Applied Mathematics and Computation 218, 11832–11841 (2012)
[25] Cáceres, M.J., Chamoso, J.M., Azcárate, P.: Analysis of the revisions that pre-service teachers of mathematics make of their own project included in their learning portfolio. Teaching and Teacher Education 26, 1186–1195 (2010)
[26] Smolkowski, K., Gunn, B.: Reliability and validity of the Classroom Observations of Student–Teacher Interactions (COSTI) for kindergarten reading instruction. Early Childhood Research Quarterly 27, 316–328 (2012)
[27] Takahashi, M., Ishiji, T., Kawashima, N.: Handmade oxygen and carbon dioxide sensors for monitoring the photosynthesis process as instruction material for science education. Sensors and Actuators B: Chemical 77, 237–243 (2001)

[28] Millan-Almaraz, J.R., Torres-Pacheco, I., Duarte-Galvan, C., Guevara-Gonzalez, R.G., Contreras-Medina, L.M., Romero-Troncoso, R.D.J., et al.: FPGA-based wireless smart sensor for real-time photosynthesis monitoring. Computers and Electronics in Agriculture 95, 58–69 (2013)
[29] Resnick, M., Silverman, B.: Some reflections on designing construction kits for kids. In: Proceedings of the 2005 Conference on Interaction Design and Children, pp. 117–122 (2005)
[30] Ogata, H., Yin, C., Yano, Y.: JAMIOLAS: Supporting Japanese mimicry and onomatopoeia learning with sensors. In: Fourth IEEE International Workshop on Wireless, Mobile and Ubiquitous Technology in Education, WMUTE 2006, pp. 111–115 (2006)
[31] Towndrow, P.A., Tan, A.-L., Yung, B.H., Cohen, L.: Science teachers' professional development and changes in science practical assessment practices: What are the issues? Research in Science Education 40, 117–132 (2010)
[32] Drigas, A., Karyotaki, M.: E-learning and ICTs Applications in Nutrition Science. International Journal of Recent Contributions from Engineering, Science & IT (IJES) 1, 4–10 (2013)
[33] Panksepp, J.: Affective neuroscience: The foundations of human and animal emotions. Oxford university press (1998)
[34] Tian, Y., Kanade, T., Cohn, J.F.: Facial expression recognition. In: Handbook of face Recognition, pp. 487–519. Springer (2011)
[35] Afonso, N., Silva, J., Manga, A., Tcharmtchi, M.H., Abrego-Moya, V., Thammasitboon, S., et al.: 151: Integrating Evidence-Based Learning Sciences Into Continuing Education for Pediatric Sepsis. Critical Care Medicine 41, A32 (2013)
[36] Su, Y.-N., Hsu, C.-C., Chen, H.-C., Huang, K.-K., Huang, Y.: Developing a sensor-based learning concentration detection system. Engineering Computations 31, 7–7 (2014)
[37] Jeannerod, M.: The cognitive neuroscience of action. Blackwell Publishing (1997)
[38] Huang, Y.M., Huang, Y.M., Liu, C.H., Tsai, C.C.: Applying social tagging to manage cognitive load in a Web 2.0 self-learning environment. Interactive Learning Environments 21, 273–289 (2013)
[39] Huang, Y.M., Liao, Y.W., Huang, S.H., Chen, H.C.: A jigsaw-based cooperative learning approach to improve learning outcomes for mobile situated learning. Educational Technology & Society 17, 128–140 (2014)
[40] Huang, Y.M., Huang, Y.M., Huang, S.H., Lin, Y.T.: A ubiquitous English vocabulary learning system: Evidence of active/passive attitudes vs. usefulness/ease-of-use. Computers & Education 58, 273–282 (2012)
[41] Looi, C.K., Seow, P., Zhang, B.H., So, H.J., Chen, W.L., Wong, L.H.: Leveraging mobile technology for sustainable seamless learning: A research agenda. British Journal of Educational Technology 41, 154–169 (2010)
[42] Cachelin, A., Paisley, K., Blanchard, A.: Using the significant life experience framework to inform program evaluation: The nature conservancy's Wings & Water Wetlands education program. Journal of Environmental Education 40, 2–14 (2009)
[43] Hammerman, D.R., Hammerman, W.M., Hammerman, E.L.: Teaching in the outdoors, 5th edn. Prentice-Hall (2000)
[44] Hsiao, H.S., Lin, C.C., Feng, R.T., Li, K.J.: Location based services for outdoor ecological learning system: Design and implementation. Educational Technology & Society 13, 98–111 (2010)

[45] Liu, M.-C., Wen, D., Kinshuk, Huang, Y.-M.: Learning animal concepts with semantic hierarchy-based location-aware image browsing and ecology task generator. In: 6th IEEE International Conference on Wireless, Mobile and Ubiquitous Technologies in Education (WMUTE 2010), Kaohsiung, Taiwan, pp. 42–49 (2010)
[46] Liu, M.C., Huang, Y.M., Kinshuk, Wen, D.W.: Fostering learners' metacognitive skills of keyword reformulation in image seeking by location-based hierarchical navigation. Etr&D-Educational Technology Research and Development 61, 233–254 (2013)
[47] Liu, M.-C., Huang, Y.-M.: Research on mobile and web 2.0 learning: A comparative review approach. In: 21th International Conference on Computers in Education (ICCE 2013), Denpasar Bali, Indonesia (2013)
[48] Kamarainen, A.M., Metcalf, S., Grotzer, T., Browne, A., Mazzuca, D., Tutwiler, M.S., et al.: EcoMOBILE: Integrating augmented reality and probeware with environmental education field trips. Computers & Education 68, 545–556 (2013)
[49] V. Vernier Software Technology. Texas Instruments. (2014), http://www.vernier.com/platforms/texas-instruments/navigator/ti-nspire/
[50] V. Vernier Software Technology. Vernier environmental probes (2014), http://www.vernier.com/products/sensors/dissolved-oxygen-probes/odo-bta/
[51] Lai, C.-H., Pan, L.-C., Hsu, C.-C., Su, Y.-N., Jeng, Y.-L., Liu, C.-J., et al.: Department of Engineering Science. In: 2013 Seventh International Conference on Sensing Technology (ICST), pp. 356–360. National Cheng Kung University, Tainan (2013)
[52] Huang, Y.M., Hsu, C.C., Su, Y.N., Liu, C.J.: Empowering classroom observation with an e-book reading behavior monitoring system using sensing technologies. Interacting with Computers (in press)
[53] Chen, H.C., Yang, H.M.: A study on oral reading rate in elementary school students. Bulletin of Special Education and Rehabilitation 18, 1–30 (2008)
[54] Liang, T.H.: Empowering personalized learning with e-book technology: The development of the interactive e-book learning system (IELS) for elementary school students. Doctor, Department of Engineering Science, National Cheng Kung University, Tainan (2013)
[55] Clynes, M.: Biological basis for sharing emotion-pure pulse of musical genius. Psychology Today 8, 51–55 (1974)
[56] Damasio, A.: Feelings of emotion and the self. Annals of the New York Academy of Sciences 1001, 253–261 (2003)
[57] Pantelopoulos, A., Bourbakis, N.G.: A survey on wearable sensor-based systems for health monitoring and prognosis. IEEE Transactions on Systems, Man, and Cybernetics, Part C: Applications and Reviews 40, 1–12 (2010)
[58] Picard, R.W., Vyzas, E., Healey, J.: Toward machine emotional intelligence: Analysis of affective physiological state. IEEE Transactions on Pattern Analysis and Machine Intelligence 23, 1175–1191 (2001)
[59] Haxby, J.V., Hoffman, E.A., Gobbini, M.I.: Human neural systems for face recognition and social communication. Biological Psychiatry 51, 59–67 (2002)
[60] Bartlett, M.S., Littlewort, G., Fasel, I., Movellan, J.R.: Real time face detection and facial expression recognition: development and applications to human computer interaction. In: Conference on Computer Vision and Pattern Recognition Workshop, CVPRW 2003, pp. 53–53 (2003)

[61] Michel, P., El Kaliouby, R.: Real time facial expression recognition in video using support vector machines. In: Proceedings of the 5th International Conference on Multimodal Interfaces, pp. 258–264 (2003)
[62] Anderson, K., McOwan, P.W.: A real-time automated system for the recognition of human facial expressions. IEEE Transactions on Systems, Man, and Cybernetics, Part B: Cybernetics 36, 96–105 (2006)
[63] Lin, K.C., Huang, T.-C., Hung, J.C., Yen, N.Y., Chen, S.J.: Facial emotion recognition towards affective computing-based learning. Library Hi Tech 31, 294–307 (2013)
[64] Wu, T.T., Huang, Y.M., Chao, H.C., Park, J.H.: Personlized English reading sequencing based on learning portfolio analysis. Information Sciences 257, 248–263 (2014)

Detection of Microorganism in Water and Different Food Matrix by Electronic Nose

V. Sberveglieri[1,2,*], E. Núñez Carmona[1,3], and A. Pulvirenti[1,2]

[1] Department of Life Sciences, University of Modena and Reggio Emilia, via Amendola 2, 42014, Reggio Emilia, Italy
[2] CNR-INO SENSOR Lab, via Valotti 9, 25133, Brescia, Italy
[3] CNR-IBF, via Ugo la Malfa 153, 90146 Palermo, Italy
veronica.sberveglieri@unimore.it

Abstract. Nowadays in alimentary industry exist very restrictive quality controls to assure the security of the products and the consumer health. It is assumed that features like the product technology and microbiological quality has been tested when a product arrives on the market. One of the most critical points in food industry today is to avoid microbiological contamination of the products during the different step of the food chain production. The importance of prevention of this episodes relapse not only in the safety of the consumer but also in the prevention of huge economic losses for the industry. On the other hand the presence of microorganisms in food industry is totally required since some kind of them are one of the most important food matrix processors. The current microbiological quality test or those carried out to select the most adequate strains for a determinate target, requires a substantial amount of money, specialized skills and time to reveal the results. The aim of this study was to survey the microbial development trough the Electronic Nose (EN) to be applied in food quality control laboratories. The novel EN used in this study is equipped with an array of chemical gas sensor composed by 6 MOS (Metal oxide sensor) two of this constructed using nanowire technology. This combination of sensors array allow enhancing the threshold of the instrument detecting compounds in low concentration. It also provides information of the presence of a determinate microorganisms and their development in a food matrix reducing drastically the required time for the classical microbiological analysis.

Keywords: Water, Lactic Acid Bacteria (LAB), Coliforms, Electronic Nose, Nanowire technology, Volatile Organic Compound (VOC), Volatile fingerprint, GC-MS-SPME.

* Corresponding author.

A. Mason et al. (eds.), *Sensing Technology: Current Status and Future Trends III*,
Smart Sensors, Measurement and Instrumentation 11, DOI: 10.1007/978-3-319-10948-0_12

1 Introduction

In Food Industry a very accurate surveillance of every product is done in all the stages of production ensuring that all the required quality control is performed due to guarantee the health of the consumer.

The set of microorganisms that is possible to isolate in a determinate food matrix can change in a hugely way depending on the kind of the product, the stage of the processing food chain and the storage time. The ensemble of these microorganisms is known as Food Microbiota and it is composed by bacteria, yeast and molds. This variety of microorganism opens a wide range of possible transformations of food matrix since they can carry out different type fermentations, ripening and also spoiling [1-2].

Regarding the food matrix, water can be considering the most primitive food matrix. It is essential for life and it is present in all the living organisms, in some cases is the 90% of the total weight. At the same time water is the developing environment of some organisms and the vector of transport as well.

There are a lot of kinds of microorganisms that are able to develop in water but one of the most concerning group are Coliforms. This group is used as the most common contamination indicator in water but also in other foodstuff. The most representative microorganism for this group is *Escherichia coli* that is used also as indicator of fecal contamination.

For the developing countries the water quality control is in most of times is very deficient. Is broadly documented and well known that this inadequate control carried out epidemic events that affect the most disadvantages ages ranges. In the case European Union (EU), for example, has been establish very restrictive law about the microbiological analysis to do, the acceptable levels and the periodicity of the analysis to control the potable.

Despite this controls existence, around 9500 of confirmed cases of *E. coli* toxins producing strains are reported by year where the most affected age range are children from 0 to 4 years (Fig.1) as reported in the annual epidemiological report 2013 from the European Center of Control Disease. This number has been increased since 2010 being the most common way of infection is by consuming contaminated food, such as undercooked or contaminated meat or vegetables, water but direct contamination between humans or transmission from animals can also occur. The infection may lead in the worst cases to fatal hemolytic uremic syndrome (HUS) affecting the renal system and requiring hospital care.

Conversely in other cases the presence of microorganisms is very required. Some of the most important process in food industry like fermentations and ripening are carried out by microorganisms.

Lactic Acid Bacteria (LAB), is one of the most used group in food industry. Since ancient times LAB have been used as a conservator. Their metabolisms are based in a fermentation process that finally reverts in the production of lactic acid. The acidification of the environment inhibits the growth of spoilage agents. In addition the products of their metabolic activities contribute to the organoleptic

and texture characteristic in a determinate food matrix. In general this kind of bacteria are ubiquitous, being part of the micro flora of human mucosal surface as well.

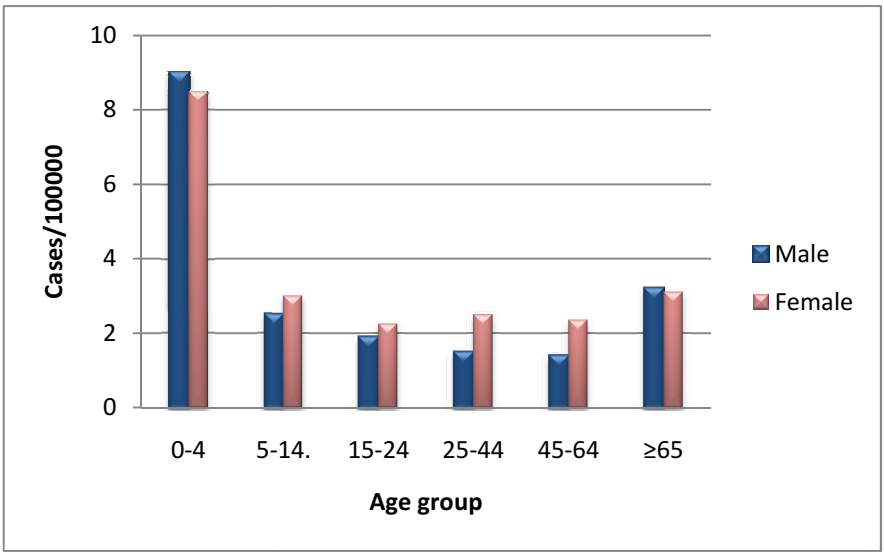

Fig. 1 Cases of *E. coli,* toxin producing strains by age and gender in in the EU in 2013

Regarding to their ubiquity, and in the context of the food industry, LAB are not always consider as a processor microorganisms. This kind of bacteria can also acts as a spoiling organism when it's found in some kind of matrix causing huge economic looses in industry [3].

It is necessary to highlight that the common characteristic of all this variety group of microorganism is that all execute a very complex metabolic pathways. Most of the metabolites produce during their metabolic activities are volatile and are known as Volatile Organic Compounds (VOCs). The set of all the VOCs create a sort of volatile fingerprint characteristic of every specie of microorganisms.

Currently the methods used for the quality control of a given matrix, or for the spoilage detection this requires in most of cases a big amount of time. This time is not always available chiefly in industry. Ordinary methodology involves conventional techniques such as classical microbiology, chemical or molecular techniques. One of the most used are the enzymatic methods. Enzymatic arrays are able to detect and determinate the concentration of a specific metabolite and provide in an indirectly way the microbial load. Nonetheless this method is expensive and requires specific skills and frequently when contamination is detected the product is widely contaminated.

The aim of this work was the establish a new fouling based the use of a novel EN supported by classical techniques, like GC-MS coupled with classical microbiology, for the detection of bacterial presence in water and other foodstuff [4-6].

2 Nanowire Technology and the EN EOS835

The EN EOS835 (SACMI IMOLA Scarl, Imola, Italy) is equipped with a thermally controlled sensor chamber of 20 ml internal volume where are placed 6 MOX gas sensors. The EN used in this work is on the market but the sensor array have been replaced in cooperation with the Sensor Lab CNR INO Brescia in Italy. Four of these sensors were prepared with the RGTO thin film technology [7], and the other two were constructed with nanowire technology [8]. The nanowire sensors manifest a very high length-to-width ratio creating a 3 dimensional network. In this way the adsorption surface is increased in a huge amount enhancing the response of the instrument and decreasing the threshold.

It was also provided with the auto-sampler headspace system HT200 (HTA srl, Brescia, Italy), supporting a 40 loading sites carousel and a shaking oven to equilibrate the sample headspace that allow to carried out a sustained analysis for 20 hours.

3 Microbiological Contaminants in Water

To acquire an adequate back ground a preliminary study was performed using microorganism perfectly characterized. According to this, three microorganisms that can be easily isolated in water matrix, *Escherichia coli, Listeria monocytogenes* and *Salmonella typhimurium* were selected for this purpose.

3.1 Materials and Methods

Liquid cultures of the three microorganisms were performed separately using Brain Heart Infusion (BHI) [9] media. Once inoculated, the cultures where incubated during 24 h at 35ºC. When the incubation time ends the turbidity of the cultures was adjusted adding BHI media until it match with the number three of the McFarland standard series. The number 3 of the McFarland standard correspond with a concentration of $9x10^8$ bacteria/ml.

It was followed the same procedure for all three microorganisms. Sterilized chromatographic vials containing 2 ml of BHI, where inoculated with 100 µl of the adjusted culture to number 3 of McFarland standard series. The analysis was carried out during 72 h in three steps. Once inoculated all the vials were cover with an aluminum crimp and a coated Teflon septum. All the samples were prepared and inoculated at 0 time but crimped just when the time to analyze. During this time all the samples where conserved in the incubator at 35ºC.

3.2 *Electronic Nose*

Regarding to the analysis of EN, the vials were placed in a randomized mode into the HT200 carousel. Each vial was incubated at 40°C for 10 min into the HT200 oven, by shaking it during all the incubation. The sample headspace (4 ml) was then extracted from the vial in static headspace path and injected into the carried flow (speed 4 ml min) through a properly modified gas chromatography injector (kept at 40°C to prevent any condensation). The sensor baseline was performed by using synthetic chromatographic air with a continuous flow rate of 10 ml/min and the recovery time was 28 min.

The data analysis was run by means of Principal Component Analysis (PCA), operated with the Nose Pattern Editor software (SACMI Imola Scarl, Imola, Italy).

In the Figure 2 it is possible to observe the evolution of the samples during the first step of analysis (first 24 h) comparing with the control and the butanol. The role of the butanol in the analysis is acting as internal standard of the instrument, In this case butanol (blue squares) form a compact cluster so the data can be consider. Regarding the rest of the samples the controls (Blue circles) as butanol forma compact cluster remaining stable during the time of analysis. Remarkable are the result that concern to the inoculated samples all three microorganisms follows a very similar pattern of position in the PCA score plot. That means that as the microorganisms grow inside the sample the set of volatile compound changes, and this changes can be perfectly monitored by the EN. This particular pattern is specular with the growth of the microorganisms.

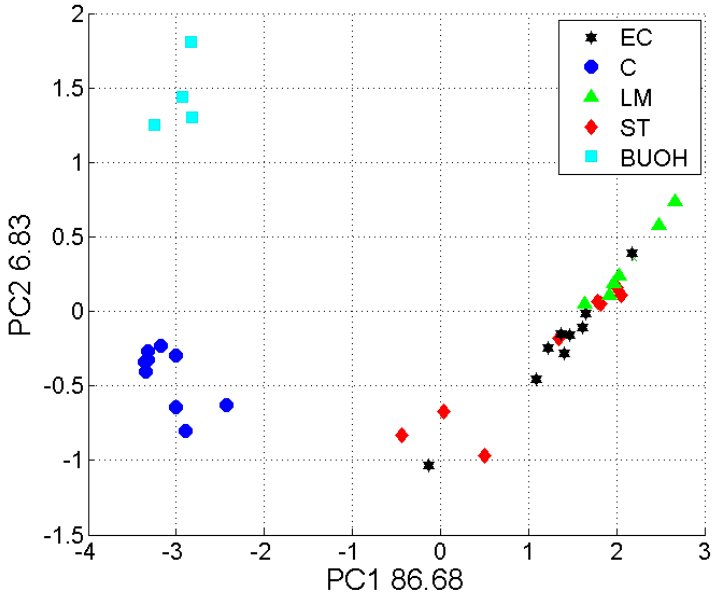

Fig. 2 PCA score plot showing the evolution of *E. coli, L. monocytogenes and S. typhimurium* during the first 24 h of analysis comparing with the control and the internal standard of the EN.

The next three figures is figures represent the evolution of the three microorganisms E. *coli* (Fig. 3), *L. monocytogenes* (Fig. 4), *and S. typhimurium* (Fig. 5), during the 72 h of analysis comparing with the control. It is possible to observe that all three cultures follow the same evolution where the control is separated from the rest of the samples forming a compact cluster remaining stable for all the analysis time. In the case of inoculated samples in all three cases the first 24 h form an independent line while the samples that belong to the rest of 48 h of analysis remain very near in the PCAs although it doesn't mix. All the microorganisms inside the sample has complete the vital cycle because of this the head space remain stable.

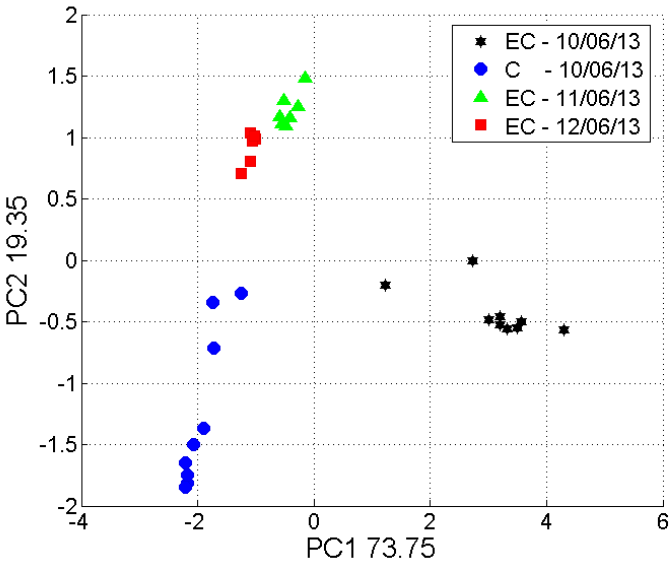

Fig. 3 PCA score plot showing the evolution of *E. coli,* during the 72 h of analysis comparing with the control

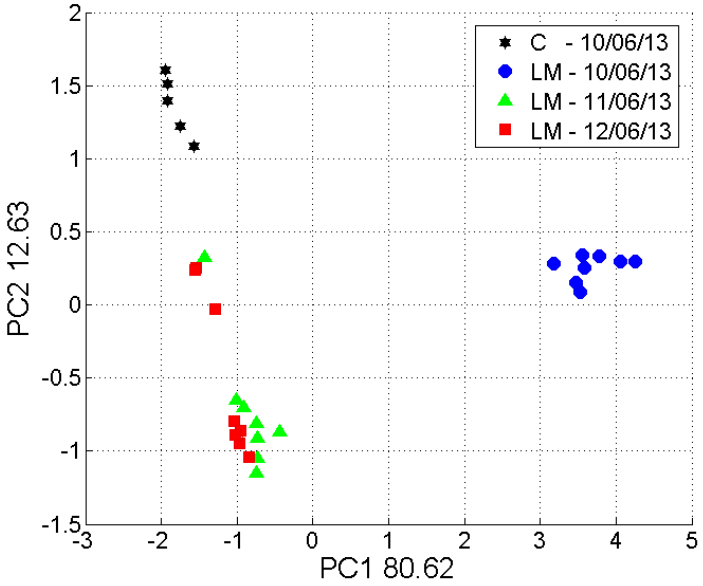

Fig. 4 PCA score plot showing the evolution of *L. monocytogenes,* during the 72 h of analysis comparing with the control

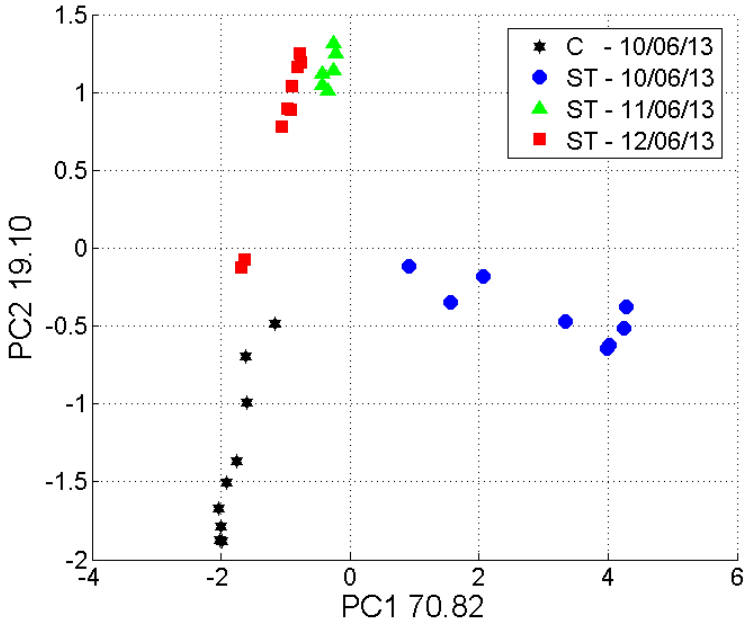

Fig. 5 PCA score plot showing the evolution of *S. typhimurium,* during the 72 h of analysis comparing with the control

4 Water Analysis

Concerning the microbiological water analysis it has been selected the group of Coliforms as a target because this group is broadly used as quality indicator in water [10]. They are universally present in the feces of warm-blooded animal in large number, in soil, seeds and vegetables. Normally they don't causes serious illness in developed countries, but their presence is used as indicator of the presence of other pathogenic organisms of fecal origin. Coliforms group is defined as Gram-negative, rod-shaped, non-spore forming bacteria which can produce acid and gas by ferment lactose when incubates at 35-37ºC in aerobic or reduced oxygen condition. It can be found in the aquatic environment, on vegetation and soil. It is important to remark that not all the Coliforms are from fecal origin a very important character from the public health point of view. This different can be easily detected changing the parameter of isolation and incubation of the samples.

4.1 Materials and Methods

In this study an aliquot of water from WC and a well was dispersed in 2 Petri dishes with Violet Red Bile Agar (VRBA) (OXOID) [11]. VRBA is a selective medium used for the detection and enumeration of Coliform bacteria in water and other food dairy products. The goal was to isolate the single colonies that were used later to inoculate liquid tubes of Brilliant Green Bile medium (OXOID) [12] to obtain pure liquid cultures. Brilliant Green Bile medium is a modification of MacConkey's liquid medium for the isolation of Enterobacteriaceae and has been formulated to obtain maximum recovery of bacteria of the coli-aerogenes group, while inhibiting most gram-positive. The second step of inoculation in Brilliant Green Bile medium ensure the isolation of microorganisms of fecal origin.

For the 2 kinds of samples the followed procedure was the same. Once the Petri dishes were inoculated, were conserve at room temperature for 2 days. Then single colonies were selected and inoculated in liquid tubes of Brilliant Green Bile media and incubated for 24 hours at the optimal growth temperature for coliforms 35ºC.

After 24 hours the turbidity of the tubes was evident, and it was adjusted (diluted, using sterile Brilliant Green Bile medium) until the turbidity was the same as the number 3 of the McFarland series standards.

To perform the samples of EN and GC-MS the used procedure was the same. Sterilized chromatographic vials containing 2 ml of Brilliant Green Bile media were inoculated with 100 µl of the number 3 of McFarland standards of the cultures prepared before. Once inoculated all the vials were cover with an

aluminum crimp and a coated Teflon septum and crimped. The controls where performed adding 100 µl of sterile Brilliant Green Bile media.

CG-MS and EN samples where prepared the first day of the analysis taking this day like 0 time (T0). Once prepared, all the samples were stored and incubate under the same conditions during all the lasting of analysis, namely 35ºC for a total of 24 hours.

The analyses were done the same day of inoculation, and second cycle of GC-MS and EN was made 24 hour later. In addition at the end of the EN analysis the samples where reanalyzed with GC-MS in order to follow the changes of the head space during the performance time. In this cases, the samples were not crimped and the ensemble was cover with aluminum foil in order to keep vial and cap joined to maintain the sterility inside and, at the same time, provide the aerobic condition for the bacterial growth this second cycle of analysis of GC-MS was perform in order to compare how changes the head space of the samples from the beginning to the end of the analysis of EN.

4.2 Electronic Nose

The same procedure as in the section 3.2 was used for the analysis of samples and data.

In the Figure 6 it can be observed the PCA score plot of the samples belonging to the control well, and WC during the first 24h of analysis. It is possible to observe that control samples form a compact cluster in the bottom of the image followed for the samples inoculated with the microorganisms isolated from the well water. Two of the samples of this group are closed to the control samples, it is due to the time that the microorganisms need to start the development inside the sample, that why in the first stages the head space of both group of samples are similar.

Remarkable results came out from the samples formed by the inoculation of the microorganisms isolated from WC water. It is possible to observe not a compact cluster but a curve of development of the head space. This curve follows the steps of the general curve of microbial growth.

Regarding the last 24 hours of the analysis the control samples still form a compact cluster remaining stable, while the WC samples and well samples form another cluster where the separation was not evident. Highlighting his result it is fear to think that the head space of the samples has been saturated. Being bacteria from the same taxonomical group the produces metabolites are similar so do are the head space created in the sample the 48 hours of analysis. Normally bacteria from this group incubated at the optimal conditions develop a whole life cycle in the first 24 hours.

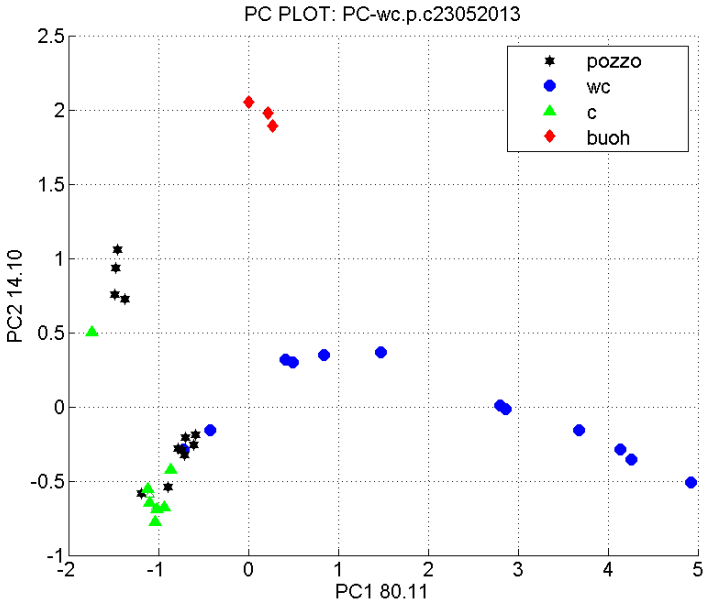

Fig. 6 PCA score plot of the samples belonging to the control (green) weel – "pozzo"(black star), and wc (blue circle) during the first 24h of analysis

4.3 Gas Chromatography – Mass Spectrometry

It was selected GC-MS with SPME technique in order to characterize the volatile profile of the microorganisms and proceed with the analysis in a similar way as EN. The vials were incubated in an oven thermostatically regulated at 40ºC for 15 minutes due to create the headspace equilibrium. In order to extract the volatile compound of the samples was used a DVB/Carboxen/PDMS stable flex (50/30 µm) (Supelco Co.Bellefonte, PA, USA) SPME fiber. To provide the adsorption of volatile compounds the SPME fiber was exposed to the headspace of the vials for 15 minutes at room temperature. For desorption of the compounds the fiber was placed in the injector of the heated GC for 6 min.

The column ramp temperature was performed in the following way: 40°C for 3.5 min to 90°C at 5 C°/min, followed by a rise from 90°C to 220°C at 12°C/min and then this temperature kept for 7 min Chromatographic analysis was accomplished using a HP 6890 series GC system, 5973 mass selective detector with a DB-WAX capillary column. The injection was verified in splitless mode at 240ºC using helium as gas carrier with a setting flow of 1.5 ml/min.

In the Figure 7 it can be observed trends followed by the most representative compound observed in the samples inoculated with the isolated microorganisms from the wc.

As a result of microbial metabolism compounds like formic acid and benzaldeide are consumed. Other compounds like acetone, 2-fluoropropen, 3-methyl 1 butanol and 4-methyl thiazole were not present in the beginning and appear in the sample then the first 24 hours of analysis. These neo-formation compounds are part of the set of VOCs that characterize the coliform group.

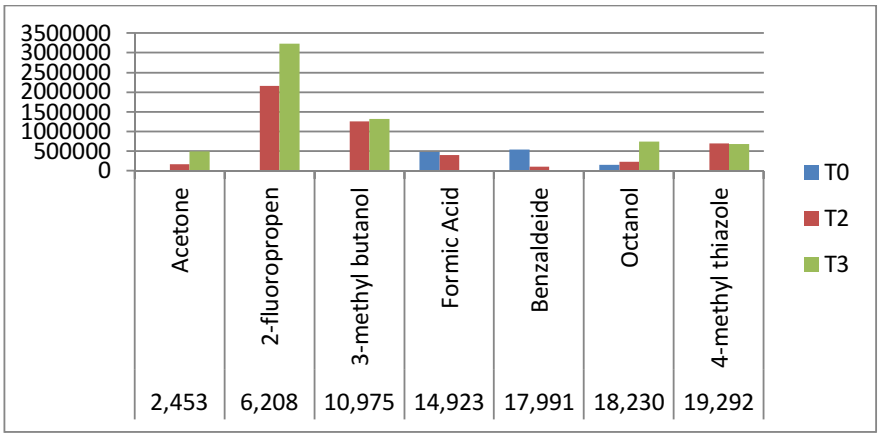

Fig. 7 Histogram showing the development of the headspace of the samples belonging to the wc during the 48 h of analysis

In this case EN is able to detect differences between samples while the GC-MS is not able to reveal a production of metabolites until 24 hours later inoculation. The differences detected by EN is owning to the consumption, by the bacteria, of some metabolites present in the medium during their grow but not for the neo-formation compounds.

5 Lactic Acid Bacteria (LAB)

Lactic Acid Bacteria (LAB) are a clade of rod or cocci shaped, Gram-positive, acid-tolerant, non-respiring and non-sporulating bacteria. To classify LAB genera are used two main hexose fermentation Pathways, Homolactic and Heterolactic bacteria. Homolactic bacteria under limited oxygen and excess of glucose catabolized it to produce lactic acid, while Heterolactic bacteria following a different pathway catabolized glucose to produce, lactic acid, ethanol and carbon dioxide [13-14].

5.1 Materials and Methods

In the case of LAB analysis the samples were performed using spoilage lactic acid micro flora isolated from the chicken meat. The followed procedure for sampling

method was conducted as described below. Under sterile conditions 10 g of chopped chicken meat were placed in a stomacher bag with 90 ml of sterile physiological solution and shacked off in Lab Blender *Stomacher 400* (Type *BA 7021 Seward*, London) for 1 min at normal speed (200 paddles/min).

It was inoculated one ml of the supernatant in Man, Rogosa and Sharpe Agar medium (MRSA) (OXOID) [15] Petri dish following the inclusion method. Once the first layer was solid, a second layer was added in order to create the micro aerobic conditions for the LAB growth. MRSA medium was designed to favor the growth of Lactobacilli. The plates, inside jar with the gas generating kit (OXOID), were incubated during 48 hours at 30ºC.

Then the 48 hours 3 random colonies were picked up and inoculated separately in a MRS liquid tube in order to obtain liquid cultures. The 3 typologies of tubes were incubated for 48 hours at 30ºC.

The samples for EN and GC-MS analysis were performed using the same procedure. Sterilized chromatographic vials (20 ml) containing 2 ml of MRSA media were inoculated separately with 100 µl of the number 3 of McFarland standards of the 3 kinds of cultures prepared before.

Once inoculated all the vials were cover with an aluminum crimp, a coated PTFE/silicon septum and crimped. The controls where performed just adding 100 µl of sterile MRSA medium to remain in the same range of volume as in the case of the inoculated one to maintain the uniformity in the preparation of the samples.

Analysis with EN and GC-MS where done at 0 time, inoculation day, and 24 hours later a second cycle of GC-MS was performed to make a control of the head space changes at the end of the EN analysis.

5.2 Electronic Nose

The same procedure as in the section 3.2 was used for the analysis of samples and data.

Regarding to Figure 8 it can be observed the PCA score plot formed by the samples that belong to Kind one during the 48 hour of the analysis. It is possible to observe that in the first 24 h (T0) samples of control (black stars) and colony one (blue circles) are missed in the PCA. It is because the metabolism of LAB is slower as for example coliforms, and the volatile profile of inoculated samples and the control is very similar. Different result came are observed regarding the last 24 hour of development of this kind of samples (green square). It is possible to distinguish the formation of an individual cluster differentiated from the control and the first 24 hours.

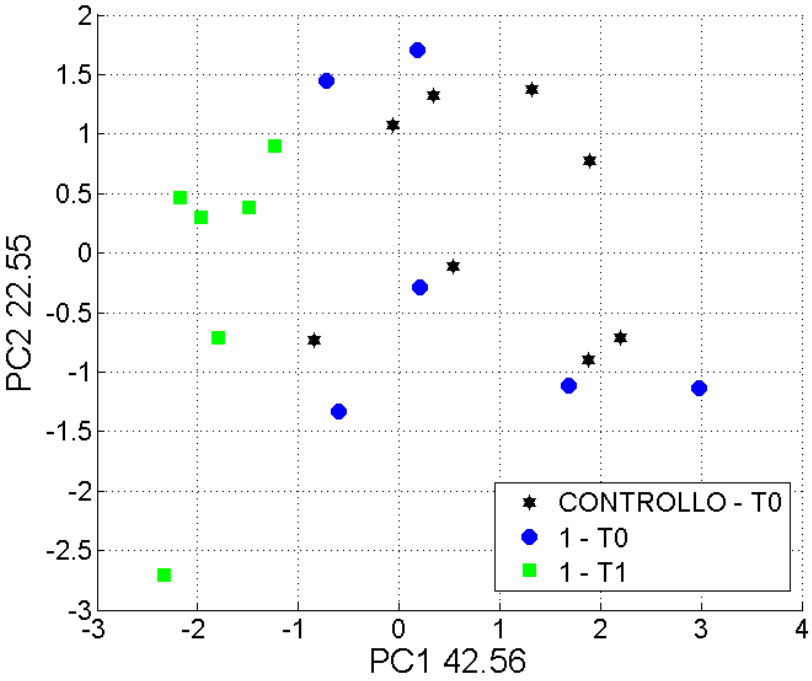

Fig. 8 PCA score plot of the samples belonging to the first isolated during the 48 h of analysis comparing with the control

In the Figure 9 are showed the result from the PCA analysis of the 3 kinds of LAB in the first 24 h comparing with the control. It can be separate 3 principal groups of clusters. One refer to the internal standard (red), second one is formed for the overlapping of the 3 typologies of LABS and the last one formed by the control samples (blue). The formation of cluster like this one can be dude to the similarity of the colonies because of the same origin of the samples, all them indigenous contaminated of the chicken meat. Regarding the Kind 1 (black), samples belonging to colony 1 it worth to think that can be a bacteria from the same group but perhaps to different species or even different strains so it will explain that some of the samples start to move away from the general cluster.

5.3 Gas Chromatography – Mass Spectrometry

The same procedure as in the section 4.3 was used for the analysis of samples and data.

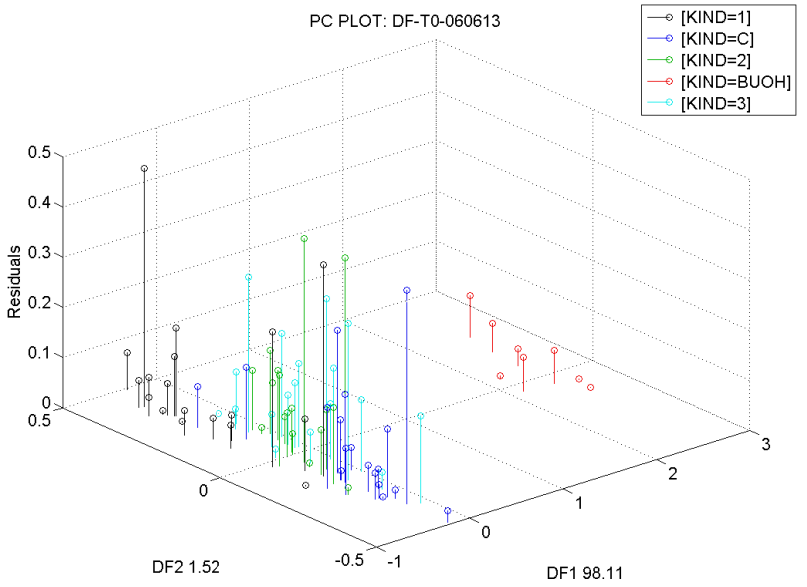

Fig. 9 PCA score plot of the evolution of the 3 kinds of LAB during the 24 h of analysis comparing with the control

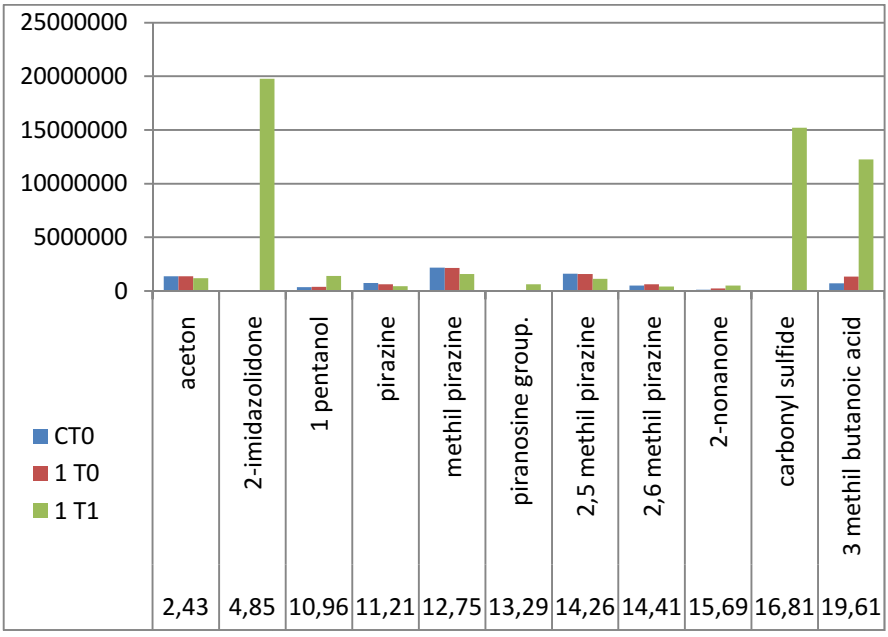

Fig. 10 Histogram showing the development of the head space of the samples belonging to the Kind 1 during the 48 h of analysis comparing with the control

In the figure 10 it is possible to observe the development of samples belonging to Kind 1 comparing with the control. One of the events that characterized the GC-MS analysis is the reduction the pirazines and methyl pirazine group, consumed by the metabolisms of the microorganisms. On the other hand it is possible to observe the neo-formation of 2-imidazolidone, piranosine and carbonyl sulfide at the end of 48 h of analysis. It is possible to say that these compounds are characteristic of the organic volatile profile of LAB.

6 Conclusion

This work exposes that the EN equipped with 4 MOX thin film gas sensors and 2 MOX nanowires gas sensors once trained, is a potential and advantageous device for the early detection of the presence of bacteria in different food matrix. Sensor tech like EN provide a speedier answer than the conventional and classical techniques. The achieved results shows the EN very effective and fast tool for monitoring, of microbiological spoilage and food quality control and strongly recommend the use of this kind of sensing technology like a quality and safety control tool in industry laboratories. The obtained results seem to be in good agreement with those obtained with the classical chemical and microbiological techniques. As future work will be interesting correlate the CFU with the answer produce by the EN to establish a threshold of the instrument always reflecting the complexity of the different alimentary matrix and the possible interaction of the characteristics VOCs.

Acknowledgements. This work was partially supported by CAFIS Project "Utilizzo di tecniche analitiche per la determinazione di indici di qualità nel caffè verde, tostato e macinato", Progetto Operativo FESR 2007-2013 – CUP G73F12000120004.

References

[1] Canhoto, O.F., Magan, N.: Electronic nose technology for the detection of microbioal and chemical contamination of potable water. Sensord and Actuators B 106, 3–6 (2005)

[2] Valerio, F., De Bellis, P., Lonigro, S., Visconti, A., Lavernicocca, P.: Use of Lactobacillus plantarum fermentation products in bread-making to prevent Bacillus subtilis ropy spoilage. International Journal of Food Microbiology 122(3), 328–332 (2008)

[3] Plessas, S., Fisher, A., Koureta, K., Psarianos, C., Nigam, P., Koutinas, A.: Application of Kluyveromyces marxianus, Lactobacillus delbrueckii ssp. Bulgaricus and L. helveticus for sourdough bread making. Food Chemistry 106(3), 985–990 (2008)

[4] Gobbi, E., Falasconi, M., Concina, I., Mantero, G., Bianchi, F., Mattarozzi, M., Musci, M., Sberveglieri, G.: Electronic Nose and Alicyclobacillus spp. spoilage of fruit juices: An emerging diagnostic tool. Food Control 21(10), 1374–1382 (2010)

[5] Falasconi, M., Concina, I., Gobbi, E., Sberveglieri, V., Pulvirenti, A., Sberveglieri, G.: Electronic Nose for Microbiological Quality Control of Food Products. International Journal of Electrochemistry 2012, 1–12 (2012)
[6] Concina, I., Falasconi, M., Sberveglieri, V.: Electronic noses as flexible tools to assess food quality and safety: Should we trust them? IEEE Sensors Journal 12(11), 3232–3232 (2012)
[7] Sberveglieri, G., Faglia, G., Groppelli, S., Nelli, P., Camanzi, A.: A new technique for growing large surface-area SnO2 thin-film (RGTO technique). Semiconductor Science and Technology 5(12), 1231–1233 (1990)
[8] Sberveglieri, G., Concina, I., Comini, E., Falasconi, M., Ferroni, M., Sberveglieri, V.: Synthesis and integration of tin oxide nanowires into an electronic nose. Vacuum 86(5), 532–535 (2012)
[9] Corry, J.E.L., Curtis, G.D.W., Baird, R.M.: de Man, Rogosa and Sharpe (MRS) agar. In: Handbook of Culture Media for Food Microbiology Progress in Industrial Microbiology, vol. 37, pp. 419–412 (2003)
[10] James, J.M., Loessner, M.J., Golden, D.A., David: Indicators of Food Microbial Quality and Safety. In: Modern Food Microbiology, 7th edn. Food Science Text Series, pp. 471–476. Springer Science + Business Media, Inc., New York (2005)
[11] Corry, J.E.L., Curtis, G.D.W., Baird, R.M.: Violet red bile (VRB) agar. Handbook of Culture Media for Food Microbiology Progress in Industrial Microbiology 37, 629–631 (2003)
[12] Corry, J.E.L., Curtis, G.D.W., Baird, R.M.: Brilliant green bile (BGB) Broth. In: Handbook of Culture Media for Food Microbiology Progress in Industrial Microbiology, vol. 37, pp. 419–412 (2003)
[13] James, J.M., Loessner, M.J., Golden, D.A.: David.: Milk, Fermentation, and Fermented and Nonfermented Diary Product. In: Modern Food Microbiology, 7th edn. Food Science Text Series, pp. 149–174. Springer Science + Business Media, Inc., New York (2005)
[14] James, J.M., Loessner, M.J., Golden, D.A., David: Non Diary Fermented Food and Product. In: Modern Food Microbiology, 7th edn. Food Science Text Series, pp. 175–196. Springer Science + Business Media, Inc., New York (2005)
[15] Corry, J.E.L., Curtis, G.D.W., Baird, R.M.: de Man, Rogosa and Sharpe (MRS) agar. In: Handbook of Culture Media For Food Microbiology. Progress in Industrial Microbiology, vol. 37, pp. 511–513 (2003)

Pain Sensing in Animals

I. Al-Bahadly*, P. Murphy, and K. Alkhumaisi

School of Engineering and Advanced Technology, Massey University,
Palmerston North, New Zealand
i.h.albahadly@massey.ac.nz

Abstract. This chapter presents a new pain sensing system in animals based on the use of stepping motor for applying force and flexi-force sensor for measuring the applied force. The purpose of the system is to apply a force to the sheep's leg via a probe. The force should slowly be increased by moving the probe into the leg of the sheep. When the animal reacts to the pain the user should be able to retract the probe and record the force which was applied and time the force was applied for. The system was intended to replace an old device which used pneumatics to apply a pressure to the animal. This device had several problems including leaks, inaccuracies, and safety issues. The system is intended for research into pain sensitivity in sheep. The research aims to measure the mechanical nociceptive threshold (MNT) in sheep. The MNT is defined as the minimum pressure that induces a pain response. This system could be used to investigate the effectiveness of pain control drugs for sheep. It could also be developed for research on other animals. For similar sized animals no modifications would be necessary. This chapter covers a background into the need for the system and other aspects involved with the development of this system. It contains a description of all technical aspects of the system and how the design was reached. It covers calibration and testing of the system and results and conclusions developed from these.

Keywords: Pain sensing, flexi-force, stepping motor, force measurement.

1 Introduction

There have been strong relationships between animals and human throughout the centuries. As we rely on them in many life aspects such as: sports and recreation, food, companionship, fertilizer, cloths and other products that support and facilitate the living of human in earth. New Zealand economy relies heavily on exporting animal products and life animals. Therefore, a good understanding of animal behaviour and problems that they encounter would guarantee a more efficient production practices [1].

* Corresponding author.

A. Mason et al. (eds.), *Sensing Technology: Current Status and Future Trends III*,
Smart Sensors, Measurement and Instrumentation 11, DOI: 10.1007/978-3-319-10948-0_13

Many problems and difficulties encounter researchers when they study animal behavior or diseases. One of these problems is to know how much an animal suffer during a certain process such as lameness episode, tail docking, ear tagging or how efficient is the analgesics on the animal.

In UK claw lameness in dairy cows is causing a major welfare problem, where the UK national incidence has announced difficulty in measuring it. Therefore, a study was carried out to develop a better understanding of the claw lameness in heifers. The study was conducted during heifer's first parturition to find out the development of claw lameness after the first parturition and to find the relationship between claw pathology, gait score and hyperalgesia, as indicated by nociceptive threshold [2].

The mechanical nociceptive was pressed against the dorsal aspect of the metatarsus until a clear leg lift was detected. By carrying these tests to a number of cows it was possible to obtain information about the nature of the sensitization. However, by applying mechanical nociceptive it is not possible to differentiate between a peripheral sensitization and spinal sensitization, but it confirms that the locomotion changes are likely to be as a result of the animal's hyperalgesic state [2].

Another example where mechanical nociceptive was applied and measured was in domestic cats. The reason behind the experiment of applying pain and measuring it was to gain better understanding of the effect of analgesia in cats, which would lead to a better control of pain in cats. The device used for the experiment was pneumatic having 3 pins within a bracelet on the forearm. The three pins are advanced simultaneously by manual bladder inflation [3].

There are many benefits behind pain measurement; these benefits can be summarized in the following points:

- Finding out at what age the species feels more pain.
- Measuring the pain intensity or level of disability in the measured part of the species.
- Assigning the appropriate treatment according to the pain measurement results. For example, if the species got very intense pain and little disability then analgesic treatment should be given first [4].
- Testing the efficiency of a treatment. This is by looking at what force would the species respond when the medication is taken and checking the effectiveness period of the medication [4].

2 Traditional System

At Massey University, research is being conducted based upon applying measurement of mechanical nociceptive thresholds (MNT) in sheep and other large farm animals. Measurement of MNTs involves applying a mechanical stimulus to the animal and measuring the force required to see a behavioral response. The device currently used to apply the mechanical stimulus and measure the pain threshold is shown in Figure 1.

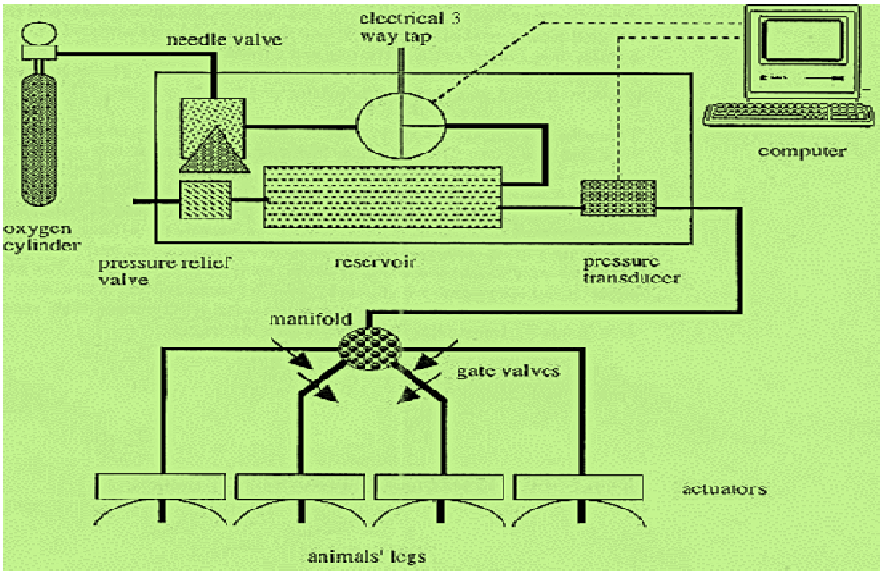

Fig. 1 Mechanical device for applying and measuring pain in sheep [5]

The device uses pressurized gas to push a blunt-ended pin onto the leg of the subject animal with constantly increasing force. The actuator itself comprises a plastic syringe barrel and modified plunger carrying the pin. As the pressure of the gas in the system increases, it pushes the plunger down the barrel of the syringe, increasing the force with which the pin is pushed onto the animal's leg.

This device is pneumatic and uses compressed oxygen from a size E cylinder to power the equipment. The oxygen passes through a micro-adjustable needle valve, which functions as a variable resistor to control the flow of the oxygen going to the device and to allow changes in the rate of force applied by the pin [5].

After the needle valve, the oxygen passes through a solenoid three way valves. When the power to the solenoid is on the oxygen flows to the reservoir then to the pressure transducer and then to the actuator at the animal end. The transducer is connected by a strain gauge amplifier to computer. When the power to the solenoid is off, the end of the device is open to the atmospheric pressure and the compressed oxygen does not flow to the actuator [5].

To reduce the likelihood of tissue damage on the sheep's leg, the MNT device was 'programmed' to limit the maximum force on the pin to 25N; the force was to be constantly increased to reach this maximum in 1 minute. To achieve this, the regulator was set to limit the gas pressure to that corresponding to 25N of force on the pin and the needle valve set so that the rate of increase in force was 25N/min.

The mechanical/pneumatic device currently used to apply the noxious stimulus and measure the force at which the subject responds (pain threshold) has several problems. These problems can be summarized in the following points:

- Friction in the system, particularly between the syringe plunger and barrel, results in inconsistent rate of force application.
- Indirect and inaccurate measurement of the force applied to the animal. As, it is the pressure of the gas at the point of the transducer that is measured, not the actual force applied through the pin to the leg of the animal.
- Leaks in the system. When the regulator is set to limit the gas pressure to 25N of force on the pin, and the needle valve is set so that the rate of increase is 25N/min. It is noticed that after 40 seconds of application, the graph shows that the force begins to level off just below 25N.
- Device is impractical and dangerous to use. This is because of the large size of the components and the unwieldy design. The existing pneumatic MNT device is impractical and can only be used in carefully controlled environments. In addition, because the actuator is not remote, the application of the device is also limited to restrained animals. The use of compressed gas to drive the pin is problematic and potentially dangerous.
- Other problems are slippage of the holder used to attach the actuator to the animal's leg. This means that the pin isn't consistently positioned over the bone of the lower leg, which could have a significant impact on the force required to elicit a withdrawal response. Moreover, frequent damage to connection between the actuator and the rest of the system limits the use of this device.
- In addition, a trembler switch used to be used to switch off the device when the animal moved its leg as a result of the pain. However, this switch was abandoned as it could not differentiate between a normal movement and a response to the stimulus.

There were two different approaches taken in account to solve the existing problems:

1) Improving the existing pneumatic/mechanical device.
2) Replacing the pneumatic device with an electrical one (Motor replaces pressure in pushing the pin on animal).

The decision on what approach should be taken was mainly based upon which approach would best minimize the existing problems. After searching and analyzing the problems it was found that most of the problems exist in the current device can be minimized. However, the electrical proposed model (motor) would have the advantage of being small, portable and the ability to put everything in small box, which could go to the top of the animal back as shown in figure 2.

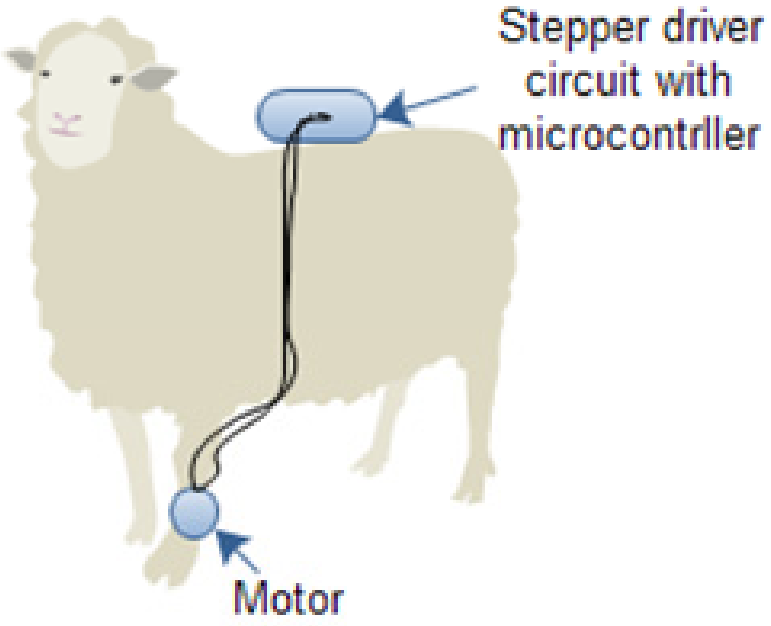

Fig. 2 Proposed model for pain measurement system

3 Proposed System

The approach taken to solve the existing problems is to replacing the pneumatic device with an electrical one (Motor replaces pressure in pushing the pin on animal) [10], [11]. A linear stepper-motor has been chosen in which a pin is fixed in the shaft of the motor.

The movement of the shaft will allow the pin to touch and apply force to the leg muscle of the animal. The motor is fixed on the leg of the animal with the help of flexible holder. Figure 3 shows a block diagram for the proposed system.

The stepper motor is driven by a standard driver. The drive signal is controlled from the applied force information. A force sensor from Flexiforce [6] has been used to measure the applied force to the animal. The force sensor is mechanically inserted between the motor and the pin which applied force on to the animal.

The force is measured with the help of an embedded microcontroller. The microcontroller has been used with the aim of extending the capability of the system such as remote controlled, fast reversing, quick release of force etc.

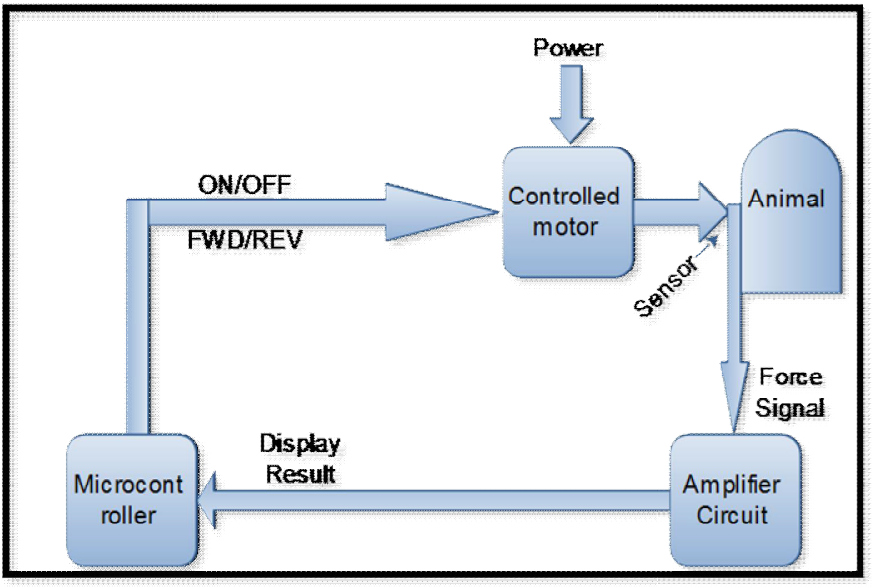

Fig. 3 Block diagram of the proposed system

4 New System Design

4.1 Circuitry

4.1.1 Stepper Motor Driver

The circuit for the stepper driver used four IRLR2703 power MOSFETs to switch the coils on and off. These were switched by signals from the microcontroller which provided the sequences for stepping. Protection diodes were supplied for each MOSFET. Sensing resisters were added at the sources of the MOSFETS to measure the current flowing through the coils of the motor. These would be used to detect if a high current was flowing so the microcontroller could take action to limit the current.

The schematic for the circuit used is shown below in Figure 4. Signals A1, A2, B1, and B2 are the stepper pulses from the microcontroller. Sen1 and sen2 are the sensing voltages for each coil. These were sent to the microcontroller as analogue signals. 1, 2, 3, 4, 5, and 6 are the wires to the stepper motor.

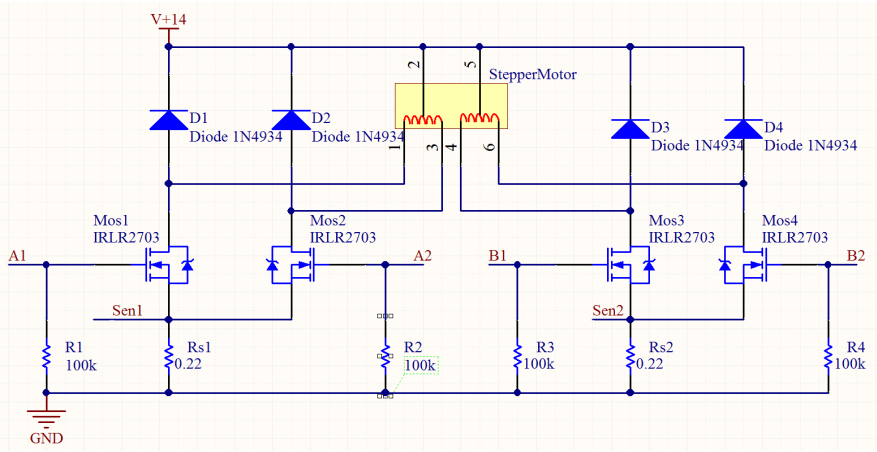

Fig. 4 Schematic of stepper motor driver

4.1.2 Force Sensing Circuitry

The force was measured using a Flexiforce A201 sensor. The flexiforce sensor is a circuit printed on thin flexible polyester film [6]. It acts as a variable resistor whose resistance decreases as a force is applied to the sensing area. The flexiforce sensor is shown in Figure 5 below.

Fig. 5 Flexiforce sensor

The resistance of the sensor changes inversely proportional to the force applied. This means it is directly proportional to the conductance of the sensor. A plot of resistance vs. force applied and a plot of conductance vs. force applied are shown in the Figure 6 below.

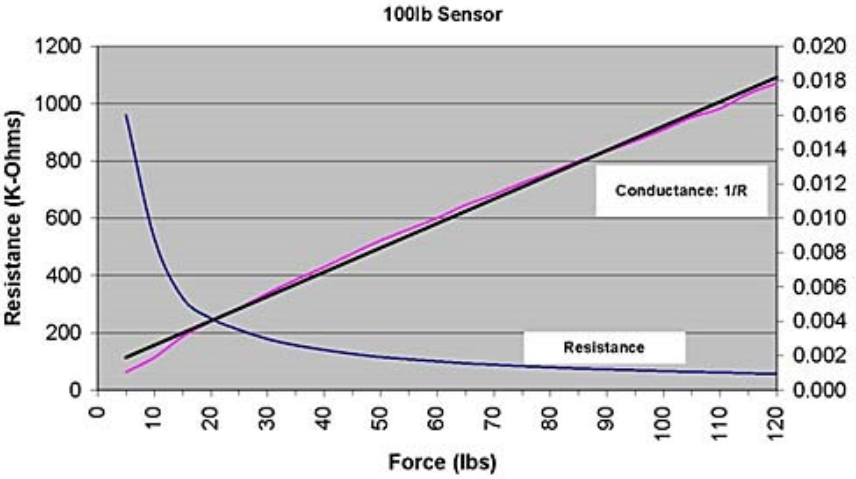

Fig. 6 Resistance and conductance vs. force

The circuit suggested by the manufacturer was used for the sensor. This circuit applied a -5V signal to one pin of the sensor. The other pin of the sensor is fed into the inverting input of an op amp. Negative feedback is applied to the op amp. The non-inverting input is grounded. This circuit provides an output signal: V_{out} = -5V *(R_f / R_s). Where R_f is the feedback resistance and R_s is the resistance of the sensor.

This makes the output voltage directly proportional to the force applied.

The circuit is shown in Figure 7 below.

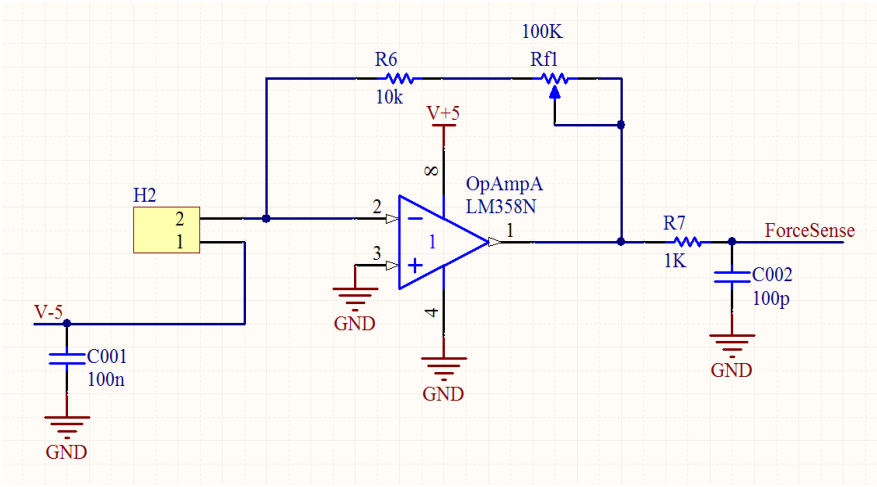

Fig. 7 Processing circuit for flexiforce sensor

The only change made to this circuit was the addition of R6 which is a fixed value resistor in the feedback path. This insures the feedback resistance is never zero.

The output of this circuit was then sent to the microcontroller as an analogue input.

A switch board was also designed to deliver the appropriate logic levels to the microcontroller for the input from each switch. A simple circuit design used pull-up resistors on the switches with the other input connected to ground. This gave a high when the switch was off and a low when the switch was on. The circuit design is shown below in Figure 8.

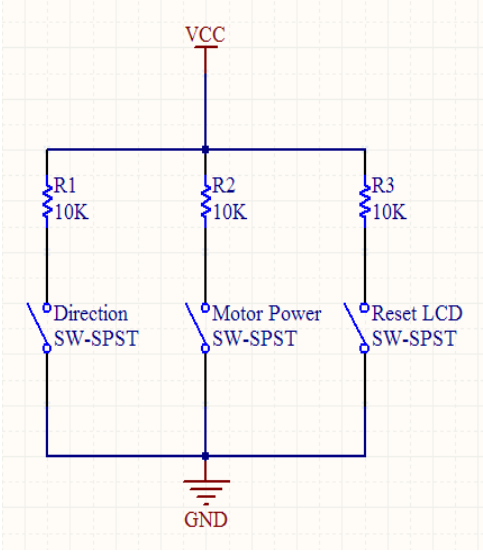

Fig. 8 Switchboard design

All the circuits were produced in a schematic sheet in Altium Designer. All the circuits were fit onto an 85mm by 93 mm board. The fully assembled board is shown in Figure 9 below.

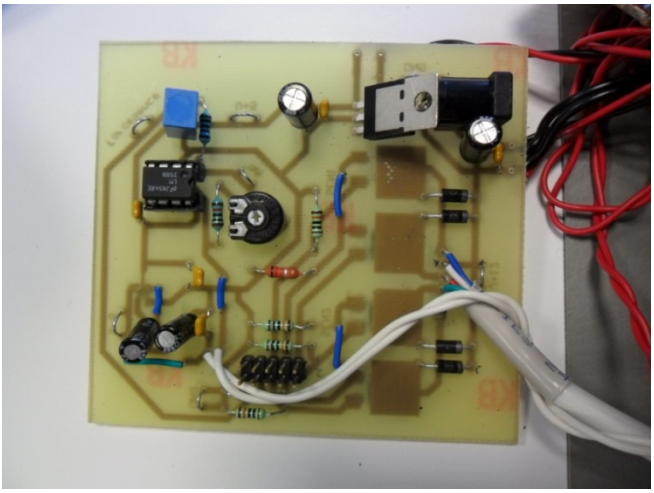

Fig. 9 Assembled PCB

A 2×10 pin header was included in the PCB to interface to the microcontroller. This port contained the 4 output signals from the microcontroller for the pulses to drive the stepper motor, the two analogue inputs to the micro from the sensing resistors, and the analogue input to the micro from the force sensor.

An RS323 socket was used to connect the PCB to the stepper motor cable. The socket is wired to the PCB directly.

4.2 Stepper Motor

Stepper motors are made up of a rotor and a stator. The rotor contains a rotating permanent magnet. The stator is made of electromagnetic coils. The rotor rotates itself to align with the magnetic field created by the stator. When a coil in the stator is activated the north pole of the rotor is pulled towards it causing a rotation of the rotor. To rotate the motor continuously the coils are switch on and off in sequence. The stepper motor used in the system is a small 4 phase uni-polar motor with a built in linear actuator. The output force of the motor is between 27 and 45 N, has a weight of 90 g, a diameter of 46 mm and a height of 56.4 mm including the linear actuator [7], [9]. These specifications were considered to be suitable for this application. The motor is shown in Figure 10.

Fig. 10 Crouzet linear stepper motor used in design

The logic for the stepper driver was implemented on the microcontroller. This logic was used to switch the MOSFETs on the PCB.

4.3 Microcontroller

The microcontroller board used was the Silicon Laboratories C8051F020 LCD board; the board is shown below in Figure 11. The microcontroller was underused in the existing device. It was only used to except the analogue signal from the force sensor and convert it to Newton units then display it on the LCD screen.

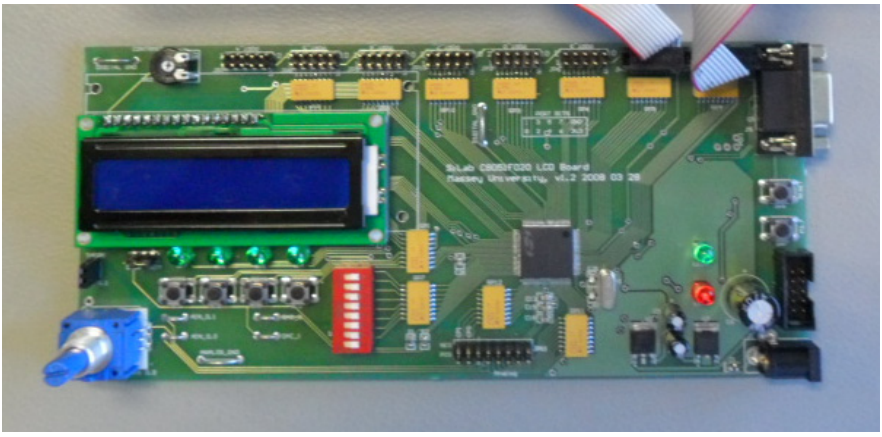

Fig. 11 Silicon Laboratories C8051F020 LCD board

This microcontroller is capable of performing many other tasks so it was decided to make more use of it and eliminate the need for other components which existed [8].

This chip offers different peripherals including:

- 8 I/O ports
- Timers/Counters
- UARTs (Universal Asynchronous Receiver Transmitters)
- SPI and SMBus serial transceivers
- ADC and DAC

It was decided to use the microcontroller to perform all the logic for the stepper driving, accept user inputs from the switch board to control the motor speed and direction, implement a timer to show the time the force was applied for and display it on the screen, and also do the force conversion and display from the existing design.

The expansion board for the micro has extra features as well. The features utilised in this project were the 2×10 headers for each I/O port, a potentiometer which can be used as an analogue input, and an LCD screen.

Two of the I/O ports were used for this project. Port 1 was used to output the four signals which control the stepper motor pulses; it was also used to input three analogue voltages which were the two current sensing signals and the signal from the force sensor. Port 2 was used to receive digital inputs from the switch board. There were three inputs; motor direction control, motor power, and the reset LCD button.

5 Power Consumption

The estimated power consumption is important to estimate the life of the battery supply. Most of the system draws a constant current except for the stepper motor.

To estimate the current in the rest of the circuit, the system was run off an exterior power supply in the lab. These power supplies show the current being drawn. The stepper motor was turned off and the current being drawn by the system was observed to be 0.088A.

To estimate the current in the motor it was run in forward and a force close to 25N was applied to the probe. This was to simulate the maximum torque which would be required by the motor. The oscilloscope was attached to the outputs of the sensing resistors and the waveform was recorded. The average voltage was also displayed on the screen. The screen captures from the oscilloscopes are shown below in Figure 12.

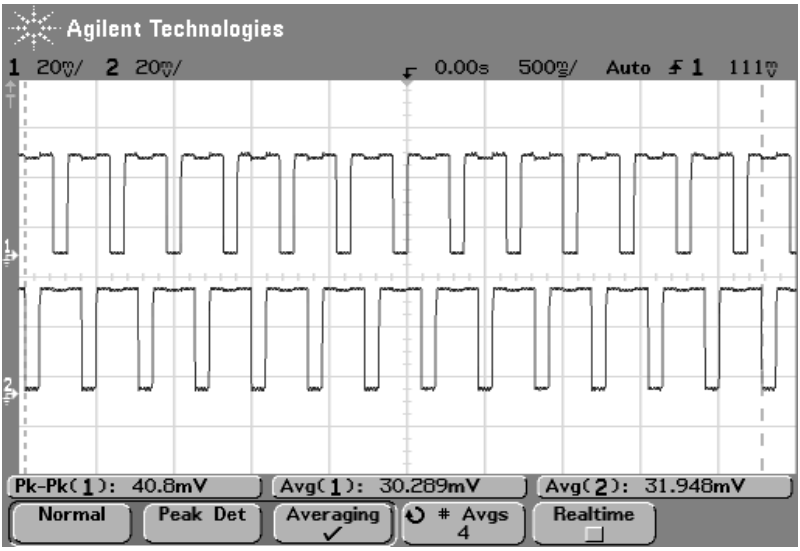

Fig. 12 Waveform at sensing resistors at full load

The sensing resistors are 0.22Ω each. Using the higher of the two voltage difference to give a conservative result and ignoring the resistance of the oscilloscope probes, this gives a current through the windings of 0.29 A. Adding this to the current dissipated through the rest of the circuit, the total current will be 0.378 A.

From this the battery life can be estimated. If the average trial lasts for two minutes, at this consumption rate the energy storage used would be 12.6 mA hours. The standard energy stores of an AA battery are around 2100 mA hours. Based on this the batteries could do 160 trials. However this would likely be less because when the voltage of the batteries falls below a certain level the motor will not be able to supply enough torque to cause a pain reaction from the animal and the batteries will require changing.

6 Sensor Calibration

After the circuitry had been designed and assembled and the analogue inputs were being displayed on the LCD screen there was a need to calibrate the sensor. At this point the number being display was simply the reading from the ADC. An equation needed to be found to calculate the force in Newton units which was being applied to the probe. Based on information from the manufacturer this would be a linear equation.

A method to calibrate the sensor was developed which held the actuator/sensor unit in place with a frame above a set of scales. The frame was then positioned so that the probe was nearly touching the scales as illustrated by Figure 13.

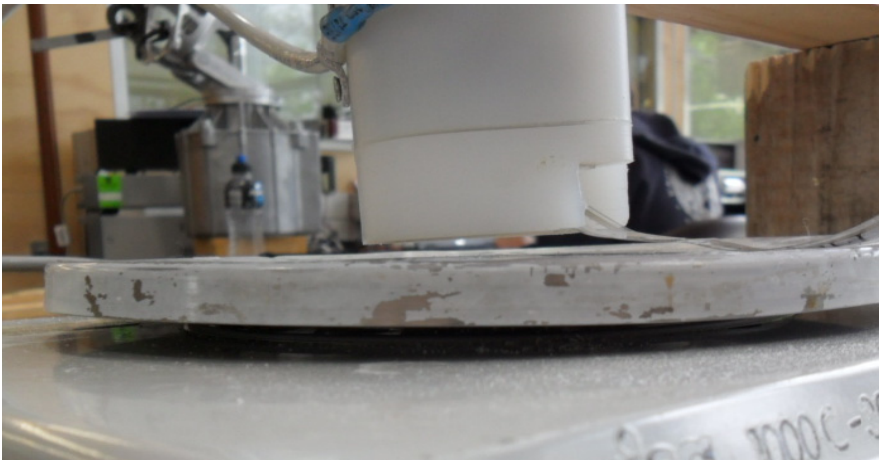

Fig. 13 Actuator/sensor unit positioned above scales

The unit was attached to the frame using brackets which fit into the design of the device without causing any damage. The full set up used is shown below in Figure 14. The frame was held in place with a quick grip clamp which allowed the set up to be moved around during the process to ensure result would be consistent under different conditions.

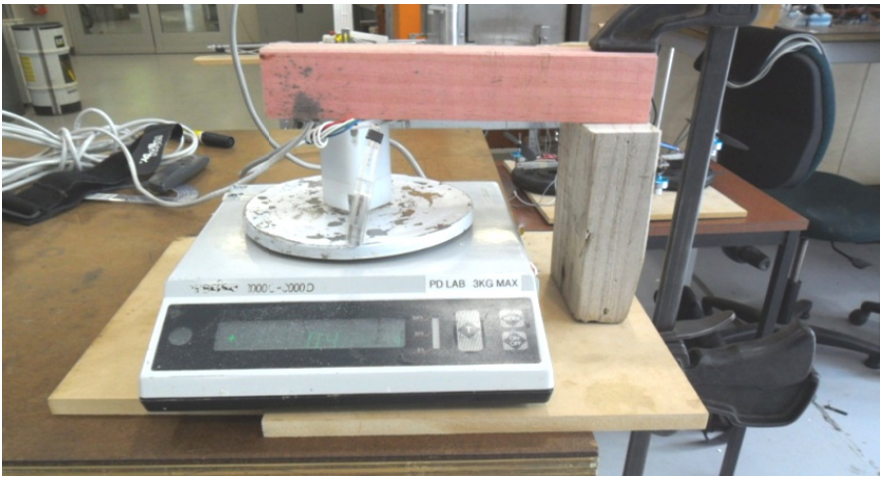

Fig. 14 Force calibration set up

To apply a force the motor was run until it was touching the scales. The motor was then run in short bursts and the reading from the sensor and the reading from the scales were recorded for each position. The process was repeated to give more

points and to check for repeatability. The readings from the scales were converted to Newton units. These values were then tabulated and a linear trend line added. The plot of the actual force vs. the ADC reading is shown below in Figure 15.

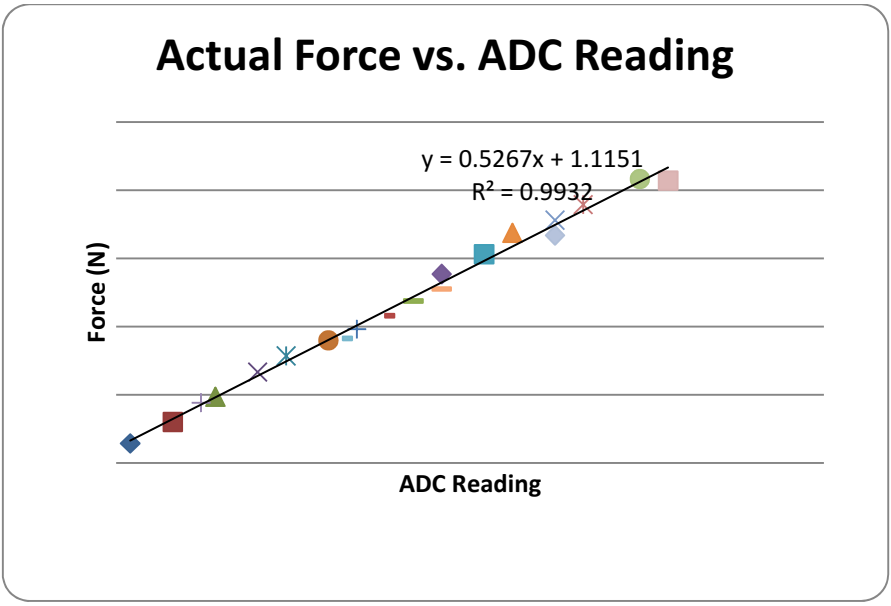

Fig. 15 Plot of actual force vs. ADC reading for sensor calibration

The R^2 value from the trend line was very close to 1, indicating a strong linear relationship between the two variables.

The equation was taken from the graph and used to generate a force reading in Newton units. This was then displayed on the LCD screen.

7 Testing and Results

These tests would be used to test the consistency of the application of the force and the force measurement system.

The testing plan was to run the system on several samples and observe the time taken to reach the maximum force of 25 N. This maximum value was set to limit the maximum force that would be applied to a live animal to ensure the welfare of the animals tested.

Six samples were chosen to run the tests on. These were:

- Wood
- Foam
- Plastic sheet over foam

- Foam over wood
- Cloth over foam
- Cloth over cardboard over foam

First the device was fixed to the sample using the strap. The motor was run in forward until the force displayed reached 25 N then the motor direction was reversed and the time taken was recorded. The LCD was then reset for the next run. For each run the probe was repositioned to a new area of the sample to ensure the run was not affected by the last. Five observations were recorded for each sample.

The results were gathered and analysed to find the average time taken to reach 25 N for each sample and the standard deviation of the time. The standard deviation was used to gauge the variation of the device on different materials. A small standard deviation would indicate the device is performing consistently. Table 1 shows the average times for each sample and the standard deviations of the samples.

Table 1 Average times taken to reach 25 N and the standard deviations of the samples

Sample	**Wood**	**Foam**	**Plastic sheet over foam**	**Foam over wood**	**Cloth over foam**	**Cloth over card-board over foam**
Average Time	NA	28.6	8.2	20.6	16.6	35.8
Standard Deviation	NA	15.6	1.6	8.9	1.7	2.2

When the device was tested on wood the force applied immediately reached the full force. This was because the wood had no give. For this reasons observations could not be gathered for the wood sample. From Table 1 it can be seen that the foam and foam over wood samples had large standard deviations. This indicated inconsistency in force application. However it was found that this was not due to inconsistent force application by the device instead it was cause by the inconsistent physical properties of the foam. It can be seen that these large standard deviations occurred only when the probe was in direct contact with the foam. The reason was that sometimes the probe would pierce the surface of the foam to different levels and other times it would not pierce it all. Figure 16 shows the foam after testing; the different depths to which the probe travelled can be seen clearly.

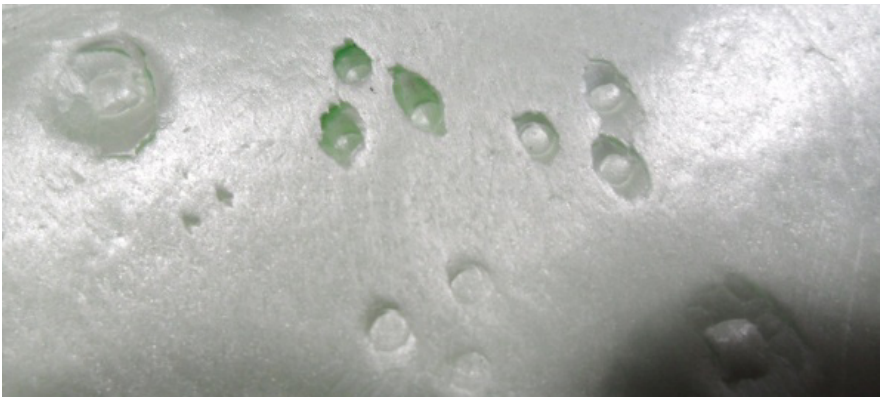

Fig. 16 Foam sample showing markings from probe

Other than these two samples the rest had small standard deviations which indicated that the device was performing consistently.

8 Conclusion

This chapter presented a new pain sensing system in animals based on the use of stepping motor for applying force and flexiforce sensor for measuring the applied force. The new pain sensitivity measurement system consists of six main parts which are: stepper motor, stepper motor driver board, motor case, motor case holder, force measurement system and microcontroller. Testing showed the upgraded device performed well and produced consistent results. The force measurement part of the system was first calibrated in the lab and the relationship between force and the microcontroller ADC output was obtained. The new sensing system was successfully built and tested.

References

[1] Bachelor of Science, Animal Science (2010), http://www.massey.ac.nz/massey/study/programme-course-and-paper-search/programme.cfm?prog_id=92411&major_code=2262

[2] Whay, H.R., Waterman, A.E., Webster, A.J.F.: Associations between locomotion, claw lesions and nociceptive threshold in dairy heifers during the peri-partum period. Veterinary Journal 154(2) (1997)

[3] Dixon, M.J., Taylor, P.M., Steagall, P.V.M., Brondani, Luna, S.P.L.: Development of a pressure nociceptive threshold testing device for evaluation of analgesics in cats. Science Direct 82(1) (2007)

[4] Usefulness of the scales measuring pain, disability and quality of life, http://www.webdelaespalda.org/english/cientifica/instrumentos/utilidad.asp
[5] Chambers, J.P.: Development of equipment to measure nociceptive thresholds in large animals. In: The Influence of Chronic Pain on the Action of Analgesic Drugs. PhD thesis, ch. 2. Bristol University (1992)
[6] FlexiForce®: Standard & Custom OEM Force Sensing Solutions. tekscan.com, http://www.tekscan.com/flexiforce/flexiforce.html
[7] Alkhumaisi, K., Al-Bahadly, I.H., Mukhopadhyay, S.C., Beausoleil, N., Johnson, C.: A smart sensing system to apply measured controlled force to animals to study pain sensitivity. In: 4th Int Conference on Sensing Technology, Italy, pp. 163–168 (2010)
[8] Chew, M.T., Sen Gupta, G.: Embedded Programming with Field-Programmable Mixed-Signal Micro Controllers (2005)
[9] Al-Bahadly, I.H., Murphy, P., Alkhumaisi, K.: Forced based pain sensing in animals using stepping motor. In: International Conference on Sensing Technology (ICST 2013), New Zealand, pp. 978–971 (December 2013) ISBN 978-1-4673-5221-5
[10] Lakshmanan, V., Yang, T.H., Reuben, R.L., Hammer, J., Else, R.W.: Assessing the quality of biological tissues using structure-property relationships: Macro-scale tests on engineered phantoms. Studies in Health Technology and Informatics 133 (2008)
[11] Frank, E.H., Jin, M., Loening, A.M., Levenston, M.E., Grodzinsky, A.J.: A versatile shear and compression apparatus for mechanical stimulation of tissue culture explants. Journal of Biomechanics 33(11), 1523–1527 (2000)

Moisture Content Estimation of Wet Sand from Free-Space Microwave Techniques

S. Richards*, A. Tan, I. Platt, and I. Woodhead

Lincoln Agritech Ltd, Christchurch, New Zealand
sean.richards@lincolnagritech.co.nz

Abstract. The book chapter presents theory and best-practice measurement techniques to extract complex permittivity and hence volumetric moisture content from moist sand. The proposed technique can also be applied to other well-mixed particulate materials. In the scenario discussed a wideband horn antenna is positioned above the sample which is backed by a metal reflector plate and S11 measurements taken in the range 1 – 6GHz.

Necessary EM theory derived from transmission line techniques is reviewed in the context of use in reflection measurements. Practical considerations such as antenna-to-sample separation distance, sample size and thickness constraints are discussed. Antenna calibration issues are investigated along with the use and impact of background subtraction for removal of system responses. Residual system responses require the use of more sophisticated techniques for removal and in the proposed technique we demonstrate the use of time-domain gating, and present the effects of zero-padding and windowing prior to transforming into the time domain and post time-gating operations. Next numerical solutions are used on the processed S11 to extract the complex permittivity of the sand.

By using range information and time-of-flight calculations we present a method to provide accurate initial values for the numerical solution to ensure rapid convergence and reliable solutions. Using integration of the time domain reflection pulse from the free-space to sample interface we propose a relationship between the energy contained in the reflection pulse and permittivity of the sample. This information is used to position the time-gate window in time and for the generation of initial values for the numerical solution.

Measured results on moist sand with thicknesses of 100-300mm and with moisture contents of ~5 – 25% show that the approach presented can extract moisture content values to within 1% accuracy.

Keywords: microwave, reflection, VNA, antenna, dielectric, permittivity.

* Corresponding author.

A. Mason et al. (eds.), *Sensing Technology: Current Status and Future Trends III*,
Smart Sensors, Measurement and Instrumentation 11, DOI: 10.1007/978-3-319-10948-0_14

1 Introduction

Knowledge of the bulk permittivity of material is a critical metric in process environments both for knowledge of the input constituents and control of process outputs. One key parameter than can be determined once bulk permittivity is known is the volumetric moisture content of a material.

Determination of bulk permittivity in particle materials and hence estimation of moisture content etc can be performed using electromagnetic theory in conjunction with microwave measurements. These measurements can be obtained [1] using reflection and/or transmission measurements, resonator methods, and resonant-perturbation methods to name the most common. For many industrial processes and other 'real world' applications only non-contact measurements are possible. This can be due to constraints in the measurement environment or the demand for 'real time' measurements.

Reflection methods can be Fresnel [2] based methods or, as covered in this book chapter short-circuited reflection methods (SCR), where the rear of a particle sample is short-circuited [3] with a metal reflector.

2 Short-Circuited Reflection (SCR) Method

2.1 Using Guided Waves

Early work on microwave measurements using a short-circuited reflection method was published by von Hippel [4, 5], using what was then a newly developed 'hollow pipe' method. Accuracy analysis and computational methods for solutions on coaxial lines or rectangular waveguides were presented by Nelson [6]. Barker-Jarvis [7] provided an extensive overview of short-circuited reflection techniques using either a Vector Network Analyzer (VNA) and transmission lines or a slotted line [8] as in von Hippel's earlier work together with correction equations and uncertainty analysis.

2.2 Extended to Free-Space

The guided wave methods mentioned above can equally be applied to free-space measurements. The use of free-space measurements has the advantage of not requiring a rigorous sample preparation and does not require corrections [7] for air-gaps etc. Ghodgaonkar [3, 9] used a lensed horn short-circuited reflection setup to measure both liquid and slab material in the 14.5-17.5GHz range.

2.3 Theory

The proposed method is based on transmission line theory for an ideal transmission line terminated in a short circuit – this is directly analogous to the free space situation.

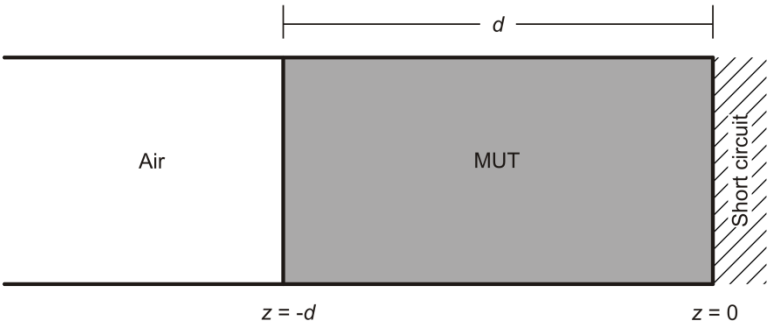

Fig. 1 Short-circuited reflection in a transmission line

(1) shows the most common derivation of the SCR solution found in the literature

$$S_{11} = \frac{jZ_n \tan \beta_n d - 1}{jZ_n \tan \beta_n d + 1}, \tag{1}$$

where Z_n is the normalised (in respect to the impedance of free-space Z_0) impedance of the transmission line section. Z_n can be derived as

$$Z_n = \frac{Z}{Z_0} = \sqrt{\frac{\mu_r}{\epsilon_r}}, \text{ as } \mu_r = 1 \rightarrow \frac{1}{\sqrt{\epsilon_r}}, \tag{2}$$

where

$$Z = \sqrt{\frac{\mu_0 \mu_r}{\epsilon_0 \epsilon_r}}, Z_0 = \sqrt{\frac{\mu_0}{\epsilon_0}}, \tag{3}$$

$$\beta = \omega\sqrt{\mu\epsilon}\left\{\frac{1}{2}\left[\sqrt{1 + \left(\frac{\sigma}{\omega\epsilon}\right)^2} + 1\right]\right\}^{\frac{1}{2}}, \text{ as } \sigma{=}0 \rightarrow \beta{=}\ \omega\sqrt{\mu\epsilon}, \text{ and} \tag{4}$$

$$\beta_n = \frac{\beta}{\sqrt{\mu_0\epsilon_0}} = \frac{\omega\sqrt{\mu_0\mu_r\epsilon_0\epsilon_r}}{\sqrt{\mu_0\epsilon_0}} = \omega\sqrt{\mu_r\epsilon_r}, \text{ as } \mu_r = 1 \rightarrow \beta_n = \omega\sqrt{\epsilon_r} \tag{5}$$

If we consider a transmission line section with characteristic impedance Z terminated in a short-circuit, the reflection coefficient Γ of this section is

$$\Gamma = \frac{Z - Z_0}{Z + Z_0}. \tag{6}$$

When (6) is normalised with respect to Z_0 this reduces to

$$\Gamma = \frac{Z_n - 1}{Z_n + 1}. \tag{7}$$

The impedance of a perfect conductor (our ideal short circuit) is approximated as

$$Z \cong (1 + j)\sqrt{\frac{\omega\mu}{2\sigma}}. \tag{8}$$

Since the conductivity of a perfect conductor is ∞ the impedance Z is 0Ω. The reflection coefficient of an ideal short-circuit is therefore -1, i.e.

$$\Gamma = \frac{0 - Z_0}{0 + Z_0} = -1. \tag{9}$$

The input impedance at the start of the section of short-circuited transmission line can be described by the ratio of the voltage and current at that point of the line.

$$Z_{in} = \frac{V(-d)}{I(-d)}, \tag{10}$$

where d is the length of the line section. The voltage of the line section at a point z is given by

$$V(z) = V_0^+\left[e^{-j\beta z} + \Gamma e^{j\beta z}\right] = V_0^+\left[e^{-j\beta z} - e^{j\beta z}\right]. \tag{11}$$

Using

$$e^{-j\beta z} + e^{j\beta z} = -2j\sin\beta z, \tag{12}$$

(11) reduces to

$$V(z) = -2jV_0^+\sin\beta z. \tag{13}$$

The current in the line section is

$$I(z) = \frac{V_0^+}{Z}\left[e^{-j\beta z} - \Gamma e^{j\beta z}\right] = \frac{V_0^+}{Z}\left[e^{-j\beta z} + e^{j\beta z}\right], \tag{14}$$

and using

$$e^{-j\beta z} + e^{j\beta z} = 2\cos\beta z, \tag{15}$$

(14) is reduced to

$$I(z) = \frac{2V_0^+}{Z}\cos\beta z\,. \tag{16}$$

This leads to an expression for the impedance at a given point z in the line section

$$\frac{V(z)}{I(z)} = \frac{-2j\sin\beta z}{\frac{2V_0^+}{Z}\cos\beta z}, \quad \text{using } \tan\beta z = \frac{\sin\beta z}{\cos\beta z} = -jZ\tan\beta z. \tag{17}$$

Substituting in normalised impedance (2) and phase constant (5) leads to an expression for the impedance of the line section at z =-d.

$$Z_{in}(-d) = j\,\mathrm{Z_n}\tan\beta_n d. \tag{18}$$

Substituting (18) in to (7) gives (1) as

$$S_{11} = \frac{jZ_n\tan\beta_n d - 1}{jZ_n\tan\beta_n d + 1}$$

3 Measurement and Signal Processing

3.1 Antenna-MUT Separation

To assume a plane wave propagating front in free-space measurements the distance d between the antenna and Material Under Test (MUT) should be at least the *Fraunhofer distance*[1]. This is calculated [10] as $2D^2/\lambda$ where D is the largest dimension of the source of the radiation. For electrically small antenna 2λ can be used instead.

[1] Distance where the spherical wave front radiated by an antenna becomes a close approximation to the ideal planar phase front of a plane wave.

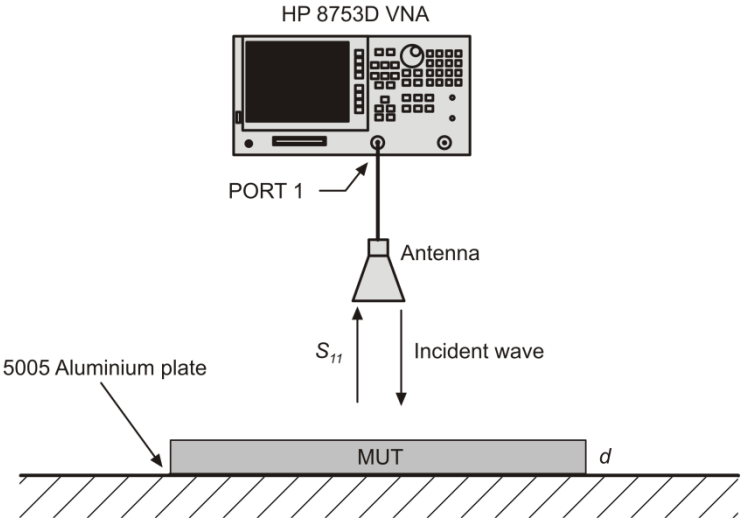

Fig. 2 Measurement setup for short-circuited reflection

3.2 MUT Size

To minimise diffraction effects and achieve accurate results the size of the sample should be greater than the wavelength of the EM wave [1]. A further constraint is that the 3dB illumination area of the antenna must be completely filled [11] by the antenna. Given the antenna beam pattern and knowing the Fraunhofer distance D_f for the lowest frequency we can calculate the minimum MUT size $a_{MUT,min}$ with

$$a_{MUT,min} = 2D_f \tan\left(\frac{\alpha_{3dB,max}}{2}\right) \tag{19}$$

3.3 Calibration

Microwave measurements are subject to three general types of error

1. **Systematic:** repeatable errors due to imperfections in components, connectors, test fixture, etc.
2. **Random:** vary unpredictably with time and cannot be removed. From noise, connector repeatability, etc.
3. **Drift:** caused by changes in system characteristics after a calibration has been performed due to temperature, humidity and other environmental variables.

The effects of systematic errors [9] can largely be removed by performing a system calibration. In general VNA calibration [12] is performed using a standard

calibration kit (SOLT or similar) and the inbuilt calibration routines of the VNA in use. This can remove any systematic errors up to the antenna connection. A 3 standard method [13] can be used for free-space calibration (Fig. 3) with the offset distance d a quarter of the operating wavelength [14].

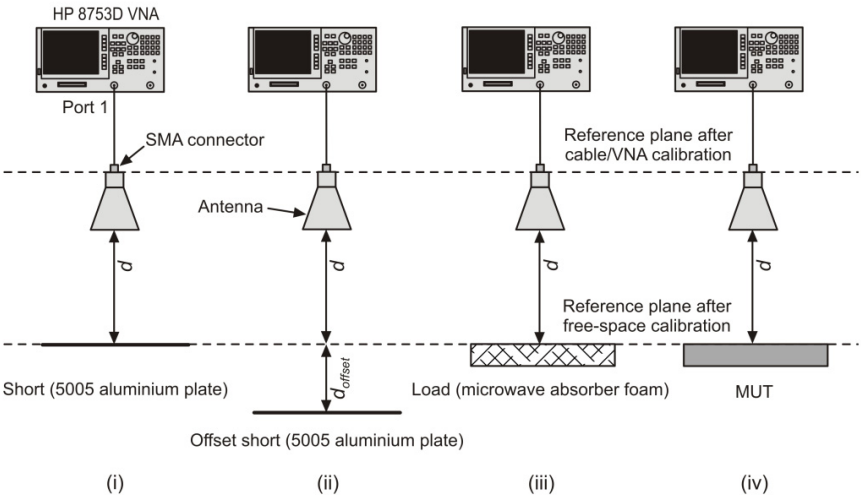

Fig. 3 Free space calibration using offset short method

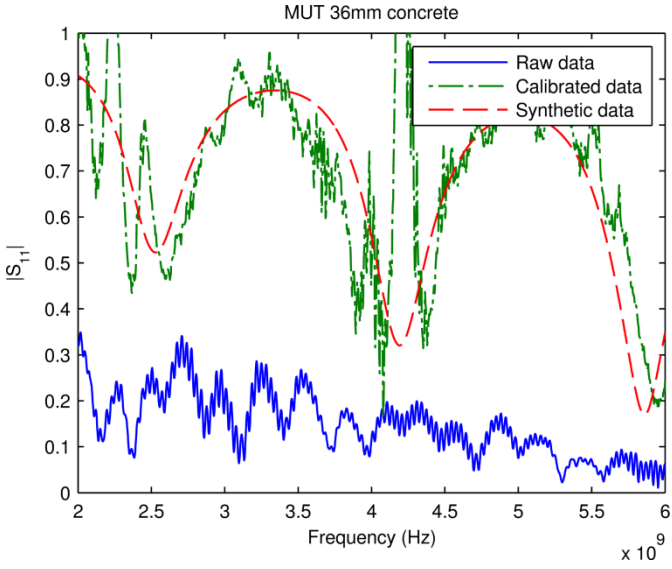

Fig. 4 Offset short calibration applied to sample data

Time variance in the reflection measurements degrades the effectiveness of the free-space antenna calibration and continuously re-calibrating the antenna in an online system is not feasible. As seen in Fig. 4 calibration is not able to reduce experimental data to the ideal case due to the use of non-ideal calibration standards, connector repeatability and time variance in the system (temperature dependence is one example) and residual errors remain in the calibrated data.

3.4 Time-gating

Free-space measurements taken in a less than ideal environment contain the response from both the environment and non-ideal components in the signal path such as cables, antenna and connectors. Time gating is a commonly used method to remove unwanted responses from the desired signal [3, 15, 16, 17]. The frequency domain signal is transformed into a Fourier domain impulse response using an Inverse Fourier Transform. The impulse is then gated over the expected signal interval using a window function then Fourier Transformed to recover the original frequency domain signal minus the unwanted components.

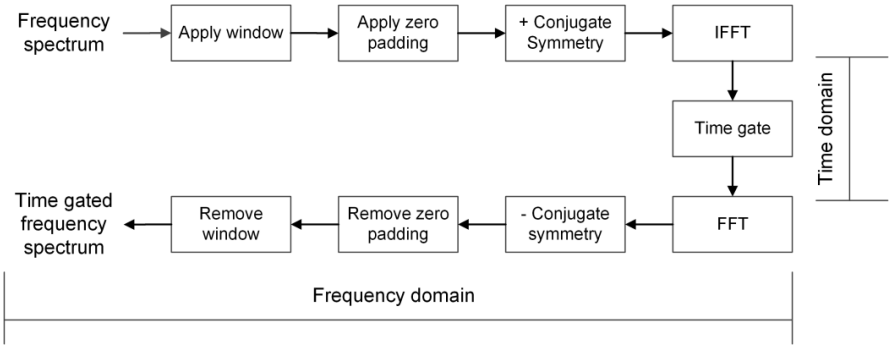

Fig. 5 Process steps for time-gating of VNA data

3.4.1 Windowing

Directly applying an IFT to the frequency domain data can introduce signal artefacts due to the *Gibbs phenomenon*[2]. To avoid the phenomenon a 'window' [18, 19], function can be applied to the spectral data. A window function is a mathematical function that is zero-valued outside of a defined interval. Applying the window function causes the signals to go to zero at the ends of the frequency spectrum. A *Kaiser-Bessel* window [18] is a commonly used function for windowing and the choice (Fig. 6) of the β parameter values [19] is a trade-off between reductions in spectral leakage caused by data truncation and limiting

[2] "The Gibbs phenomenon consists in an overshoot which can occur in a Fourier synthesis of a function containing a step discontinuity" [26].

band edge effects [16] created when applying the inverse window to the gated impulse response. Increasing the value of β also works like a smoothing kernel 'smearing' the response in time and reducing resolution.

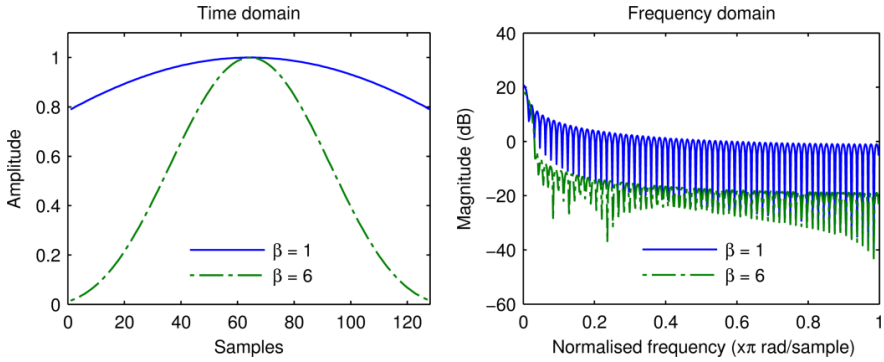

Fig. 6 Kaiser-Bessel window with β parameters of 1, 3, and 6

3.4.2 Zero-padding

When data is prepared (c.f. Fig. 7) for the IDFT the frequency spectrum is often 'zero padded' at the high frequency ends (also down to DC for time domain low pass mode [20] as used here) to avoid 'wrapping' or other aliasing issues (This is also necessary when performing convolution by FFT to avoid circular convolution).

3.4.3 Data Preparation

The Inverse Fourier Transform operates on a signal that is assumed to be periodic For the IDFT the input requirements [21] are that the signal is conjugate symmetric about N/2 (where N is the length of the input). Conjugate symmetry [22] is enforced by zero padding from the lowest frequency to DC, then taking the complex conjugate of the resulting frequency spectrum and reflecting it to the negative frequencies.

3.4.4 Gating

Time domain gating is the process of isolating a region of interest (in time) and setting the value of all data points outside this region to zero. The gate function cannot be a "brick-wall" function as this would causes truncation in the frequency domain. A rectangular window with *Hanning*[18] slopes is proposed by some authors [23, 24] while elsewhere [25] a rectangular function modified by a *Kaiser-Bessel* window is used. Of importance is ensuring that the gate is centred on the desired impulse response [25]. In this book chapter the window function used (Fig. 8) is a *Tukey* [18] window – a tapered cosine window.

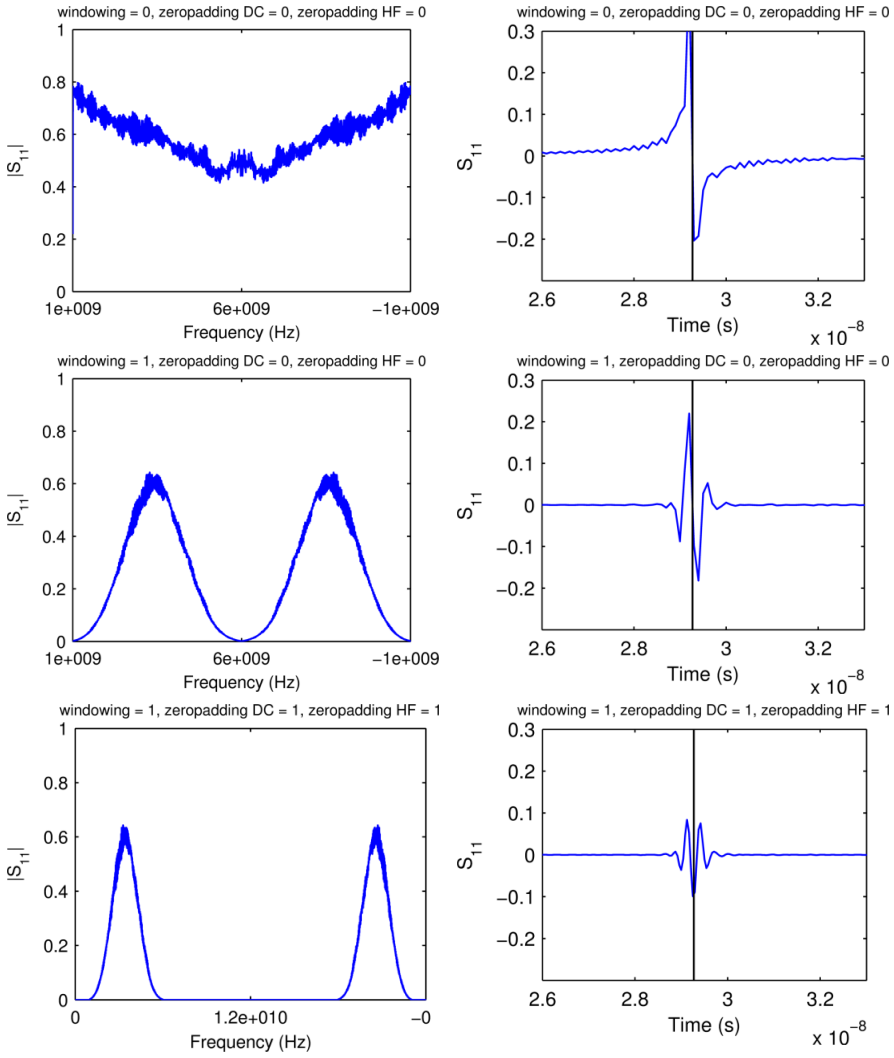

Fig. 7 Impact of windowing and zero-padding on impulse response of a short-circuited coaxial cable

An effect of the gating operation is a lowering of the endpoints of the time-gated frequency domain response. This is described in detail in Agilent application note AN 1287-12 [19], who have a proprietary solution used in their network analysers that compensates for this using a post-gate renormalization.

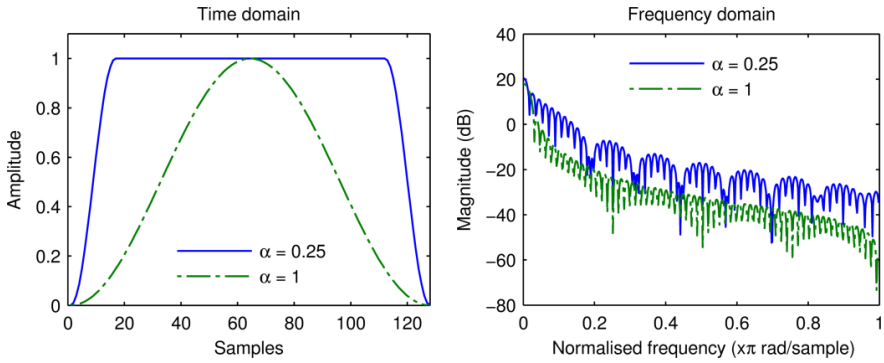

Fig. 8 Tukey window

3.4.5 Retrieving the Frequency Domain Data

Following the steps in retrieving the time gated frequency domain data is straight forward. The last step – removing the window that was applied before the IFFT needs some discussion. The original data was multiplied by this window so to remove it requires division by the same window. Remembering the shape of the window out at the ends, this will be a division of by near zero – any spectral leakage, ringing, numerical inaccuracies, etc is going to cause a 'blowup' at these ends Increasing the value of β exacerbates this phenomenon and this is a further constraint when choosing the value of β.

3.5 Post Time-Gate Normalisation

Translation of the measurement plane to the front face of the MUT can be achieved in free space by de-convolving the S_{11} measurement data with an S11 measurement of a metal reflector positioned at the front face of the MUT [15, 17, 26].

$$S_{11normalised} = \frac{FFT\{S'_{MUT}(t)\}}{FFT\{S'_{reflector}(t)\}} \tag{20}$$

3.6 Solving for Permittivity

$$S_{11} = \frac{jZ_n \tan \beta_n d - 1}{jZ_n \tan \beta_n d + 1}$$
$$Z = \frac{1}{\sqrt{\varepsilon^*}}, \qquad \beta = \frac{2\pi}{\lambda}\sqrt{\varepsilon^*} \tag{21}$$

Since ε^*cannot be expressed explicitly in terms of S_{11} and d, it needs to be solved numerically [3, 7]. In this work we have used *Muller's method* [27] a generalisation of the secant method. This used quadratic interpolation over three points and allows the solution of complex roots.

4 Experimental Work

We wish to measure moist sand in the frequency range 1 to 6GHz with moisture content as shown in Table 1 and thicknesses from 100 to 300mm in 100mm steps.

Table 1 Sand sample moisture content

sample	mean θv	std. dev.	variance
A	6.35	0.40	0.16
B	11.47	0.57	0.33
C	19.37	0.95	0.90
D	24.08	1.54	2.38

4.1 MUT Size

A ridged horn antenna (Fig. 9) [28] is used for these experiments combining the necessary wide bandwidth and a well described beam-pattern (in the frequencies of interest [29]).

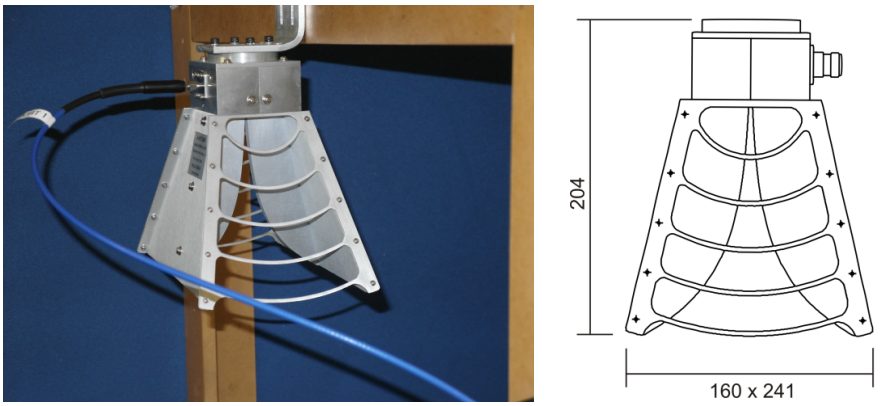

Fig. 9 A-Info LB1080 horn antenna

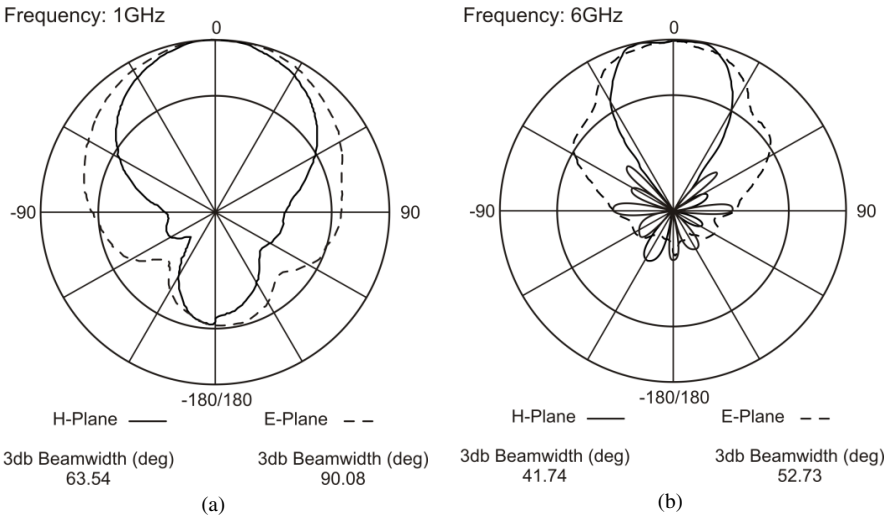

Fig. 10 Antenna patterns at 1 GHz and 6 GHz

The *Fraunhofer* distance is given by (22)

$$2D^2/\lambda = 2 * 0.240^2/0.2998 = 0.384m \tag{22}$$

the 3db beamwidth of the horn antenna is a maximum of ~90° in the frequency range 1 – 6GHz (see Fig. 10) and the minimum MUT size is calculated using (19) and is

$$2D_f \tan\left(\frac{\alpha_{3dB,max}}{2}\right) = 2 * 0.384 * \tan(45) = 0.77m \tag{23}$$

with antenna MUT separation distances of up to 0.57m due to measurement setup geometry constraints then the practical minimum MUT size is 1.2m

4.2 Time Gate Location and Initial Value Estimation

The position of the time gate needs to be determined with some accuracy and in an online system without human intervention. Using range information acquired from a ranging system (3D camera, laser scanner, etc) it is trivial to calculate the physical distance to the air-MUT interface from a reference position such as the antenna aperture. To be able to locate this position in time we need to accurately determine the position of the antenna aperture in time given knowledge of the cable length and propagation characteristics. Using a reflector plate at a known distance (Fig. 11) we can calculate the antenna-air interface with some accuracy.

1. Short-circuit @ 150mm located in time @ 3.167E-8 secs
2. Travel time for 150mm = (2 * 0.15) / C = 1.0007E-9 secs
3. Location of antenna-air interface = 3.167E-8 – 1.0007E-9 = 3.0669E-8 secs

Table 2 S11 measurements

Sample	Thickness (mm)	Actual θv (%)
A	0.1	6.35
A	0.2	6.35
A	0.3	6.35
B	0.1	11.50
B	0.2	11.50
C	0.1	19.40

S_{11} measurements were made on the sand samples with properties as shown in Table 3. The intent of the measurements was to develop a process (Fig. 12) to automate the time gate positioning and generation of initial values for the numerical solution. Using range information combined with time-of-flight calculations the approximation location in time of the front of the MUT was calculated. An inverse Fourier Transform was performed on the frequency domain data then signature analysis was used to locate the impulse response for the front interface and hence the exact position in time. For each front reflection pulse location (shown with black markers in Fig. 14) power contained in the pulse envelope was estimated by integrating over a fixed time interval around the pulse location then normalised for distance effects using the integration of the pulse from a reflector at the same distance over the same time interval. The mean (frequency dispersion effects creates a range of values of permittivity) real permittivity value was calculated for each volumetric moisture content measured and the power data (Fig. 13) fitted to an exponential model (24).

$$y = 0.06218e^{(0.154\varepsilon')} \tag{24}$$

The mean permittivity value is used as an initial point for searching for the reflection pulse from the short circuit located at the rear of the MUT. The size of the reflection pulse is determined by the distance through the MUT and the real permittivity value; hence for some larger values of permittivity (higher moisture content) the pulse will be completely attenuated. As before time-of-flight calculations were used to obtain the starting position and then the local area was searched using signature analysis to locate any existing pulse. Pulse locations are shown (Fig. 14) with white markers. The location of the reflection pulses is used to automate [30] the locating of the time-gate used for removing background reflections and residual errors post calibration.

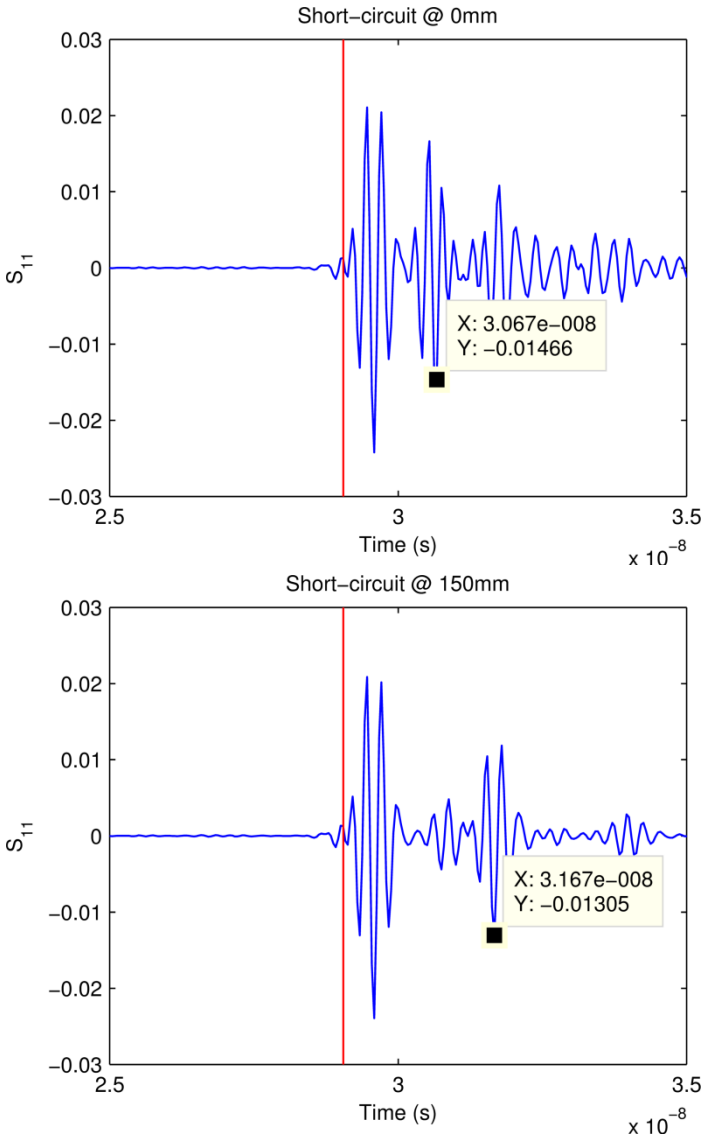

Fig. 11 Time domain response of short-circuit @ 0 and 150mm

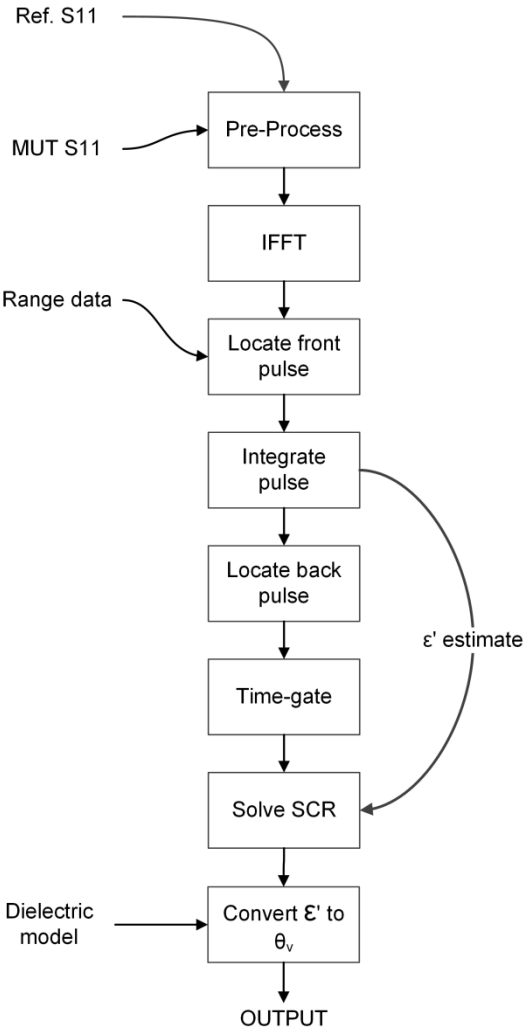

Fig. 12 Process outline

With the location of the front and rear impulse response now known then using time-of-flight calculations we can achieve a reliable estimate of the real part of permittivity for the MUT. Using a dielectric model [31] for moist sand from the real part we can calculate the corresponding imaginary part of permittivity across the frequency spectrum we have used and generate the initial values for the numerical solution.

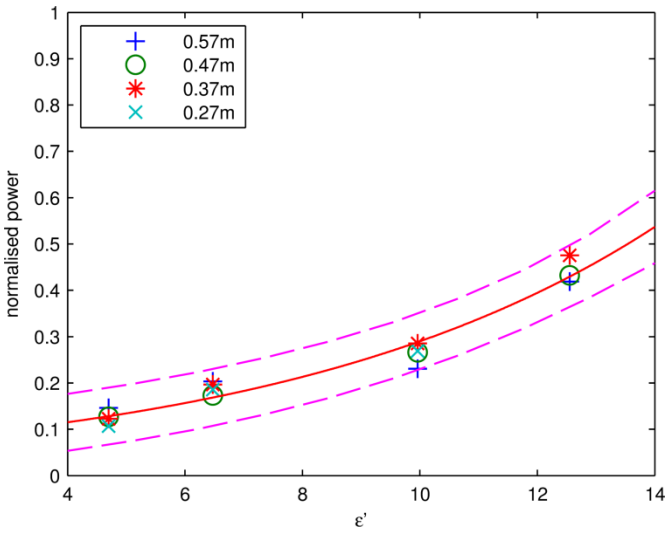

Fig. 13 Normalised power from front reflection

The proposed technique was applied to the measurement data with good results. Table 3 tabulates the measurement instances, sand samples at various thicknesses and moisture content. Three samples of sand are used: A, B and C. Sample A has a volumetric moisture content of 6.35%; Sample B 11.50%; Sample C 19.40%. The volumetric moisture content is calculated from extracted permittivity values using a dielectric model for moist sand developed by the authors [31]. This is a dielectric model for wet pure sand based on the fundamental physical properties such as the permittivity of the host material, geometry and size of the sand particles, and the frequency dependent processes that determine the permittivity of water. It assumes a non-porous host material and characterizes the permittivity based on dry host and film water which is then related to the specific surface area (SSA), in turn related to the particle size distribution (PSD). A saturation model is then used to calculate the water permittivity which is then compensated for frequency effects and combined with the host permittivity using a mixing model. Sample A is measured at three thicknesses – 100, 200, and 300mm. For all three thicknesses extracted volumetric moisture content matches that of the actual θv, with errors that are less than 0.33% Sample B is measured at two thicknesses – 100 and 200mm. The extracted volumetric moisture content matches that of the actual θv with errors less than 1%. For Sample C the sand is fully saturated and we have difficulty in achieving greater sample thickness due to physical and practical constraints in the measurement setup. Hence only 100mm thickness is measured with an error of 0.80%. From all the instances of measurement we have achieved accurate (error < 1%) moisture content extraction from moderately wet to fully saturated sand samples.

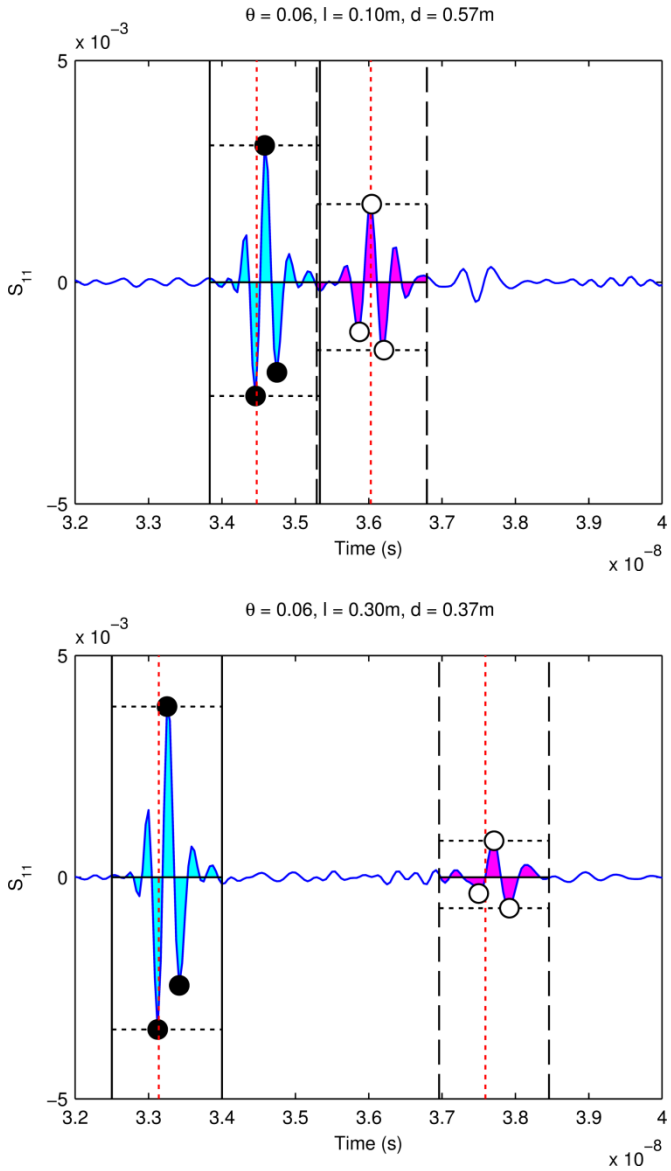

Fig. 14 Time-domain responses for 100 and 300mm sand with θv = 6.35%

Table 3 Extraction of moisture content

Sample	Thickness (mm)	Actual θv (%)	Extracted θv (%)	Error (%)
A	100	6.35	6.02	0.33
A	200	6.35	6.49	0.14
A	300	6.35	6.53	0.18
B	100	11.50	12.34	0.84
B	200	11.50	11.63	0.13
C	100	19.40	18.57	0.80

5 Conclusions

We have proposed a method for processing microwave reflection measurement data using the short-circuited reflection method in an online situation where time-gate position and initial values for the numerical solution are generated automatically. Background theory of the short-circuited reflection method has been discussed together with theory and practice of system calibration and associated data pre-processing such as windowing and time-gating. Measured data has been compared with expected results with good correlation.

References

[1] Chen, L.F., Ong, C.K., Neo, C.P., Varadan, V.V., Varadan, V.K.: Microwave Electronics: Measurement and Materials Characterization. Wiley (2004)
[2] Sagnard, F., Bentabet, F., Vignat, C.: In situ measurements of the complex permittivity of materials using reflection ellipsometry in the microwave band: theory (part I). IEEE Transactions on Instrumentation and Measurement 54(3), 1266–1273 (2005)
[3] Ghodgaonkar, D., Varadan, V., Varadan, V.: A free-space method for measurement of dielectric constants and loss tangents at microwave frequencies. IEEE Transactions on Instrumentation and Measurement 38(3), 789–793 (1989)
[4] Roberts, S., Von Hippel, A.: A New Method for Measuring Dielectric Constant and Loss in the Range of Centimeter Waves. Journal of Applied Physics 17(7), 610–616 (1946)
[5] von Hippel, A.: Dielectric Materials and Applications. MIT Press (1954)
[6] Nelson, S.O., Stetson, L.E., Schlaphoff, C.W.: A General Computer Program for Precise Calculation of Dielectric Properties from Short-Circuited Waveguide Measurements. IEEE Transactions on Instrumentation and Measurement 23(4), 455–460 (1974)
[7] Baker-Jarvis, J., et al.: Transmission/reflection and short-circuit line permittivity measurements (1990)
[8] Operating Instructions for TYPE 874-LBA SLOTTED LINE

[9] Ghodgaonkar, D., Varadan, V., Varadan, V.: Free-space measurement of complex permittivity and complex permeability of magnetic materials at microwave frequencies. IEEE Transactions on Instrumentation and Measurement 39(2), 387–394 (1990)
[10] Balanis, C.A.: Antenna Theory: Analysis and Design, 3rd edn. John Wiley & Sons (2005)
[11] Braun, H., Detlefsen, J.: Broadband free-space material measurement using the reflection coefficient only. In: The 7th Conference of ISEMA 2007 on Electromagnetic Wave Interaction with Water and Moist Substances (2007)
[12] Rytting, D.: Network analyzer error models and calibration methods (1998)
[13] Smith, F., Chambers, B., Bennett, J.: Calibration techniques for free space reflection coefficient measurements. IEE Proceedings A Science, Measurement and Technology 139(5), 247–253 (1992)
[14] Mikhnev, V., Vainikainen, P.: Microwave Imaging of Layered Structures in Civil Engineering. In: 32nd European on Microwave Conference (2002)
[15] Grosvenor, C., Johnk, R., Baker-Jarvis, J., Janezic, M., Riddle, B.: Time-Domain Free-Field Measurements of the Relative Permittivity of Building Materials. IEEE Transactions on Instrumentation and Measurement 58(7), 2275–2282 (2009)
[16] Shirai, H., Ishikawa, M.: Complex permittivity estimation from free space RCS measurement. In: 2010 Third International Conference on Communications and Electronics, ICCE (2010)
[17] Zhang, J., Huang, Y.: Extraction of dielectric properties of building materials from free-space time-domain measurement. In: High Frequency Postgraduate Student Colloquium 1999 (1999)
[18] Harris, F.: On the use of windows for harmonic analysis with the discrete Fourier transform. Proceedings of the IEEE 66(1), 51–83 (1978)
[19] Technologies, A.: Time Domain Analysis Using a Network Analyzer (2012)
[20] Dunsmore, J.P.: Handbook of Microwave Component Measurements: With Advanced VNA Techniques. John Wiley & Sons, Ltd. (2012)
[21] Smith, S.W.: The Scientist and Engineer's Guide to Digital Signal Processing. California Technical Publishing, San Diego (1997)
[22] Oppermann, I., Hamalainin, M., Iinatti, J. (eds.): UWB Theory and Applications. John Wiley & Sons, Ltd. (2004)
[23] Sjostrom, M.: Properties of smoothing with time gating. In: The 2000 IEEE International Symposium on Circuits and Systems Proceedings of the ISCAS 2000, Geneva (2000)
[24] Archambeault, B., Connor, S., Diepenbrock, J.: Time domain gating of frequency domain S-parameter data to remove connector end effects for PCB and cable applications. In: 2006 IEEE International Symposium on Electromagnetic Compatibility, EMC (2006)
[25] Dunsmore, J.: Gating effects in time domain transforms. In: ARFTG Microwave Measurement Symposium (2008)
[26] Caspers, F., Chaloupka, H.: Permittivity Determination using Time-Filtered Data from Antenna-Near-Field Measurements on Bounded Structures. In: 11th European Microwave Conference (1981)
[27] Press, W.H., Teukolsky, S.A., Vetterling, W.T., Flannery, B.P.: Numerical recipes in C: The art of scientific computing, 2nd edn. Cambridge University Press, New York (1992)
[28] Volakis, J.: Antenna Engineering Handbook, 4th edn. McGraw-Hill (2007)

[29] Bruns, C., Leuchtmann, P., Vahldieck, R.: Analysis and Simulation of a 1-18-GHz broadband double-ridged horn antenna. IEEE Transactions on Electromagnetic Compatibility 45(1), 55–60 (2003)
[30] Richards, S., Tan, A., Platt, I., Woodhead, I.: Time Domain Gating for Short Circuited Reflection Measurements. In: Proceedings of the 10th International Conference on Electromagnetic Wave Interaction with Water and Moist Substances (2013)
[31] Richards, S., Tan, A., Platt, I., Woodhead, I.: Moisture Content Estimation of Wet Sand from Free-Space Microwave Techniques. In: 2013 Seventh International Conference on Sensing Technology, ICST (2013)
[32] Champeney, D.C.: A Handbook of Fourier Theorems. Cambridge University Press (1989)

Organic Molecule Based Sensor for Aldehyde Detection

A.N. Mallya and P.C. Ramamurthy*

Department of Materials Engineering, Indian Institute of Science, Bangalore-560012, India
onegroupb203@gmail.com

Abstract. Aldehydes are used in food and beverage industries, production of resins, soap and perfume industries. When used in excess quantity or found in products in undesired quantity this is a threat to humans. Hence it becomes very important to detect these VOCs even at lower concentration. The other sources of aldehyde are polluted air and water. Exposure to aldehyde can cause gene mutation and cancer. Conductometric sensors with metal oxide semiconductors as sensing films, cataluminesence based sensors, quartz crystal microbalance sensors, analytical methods such as HPLC have been used for the detection of aldehydes. These are sophisticated techniques require skilled staff to perform the tests. Chemiresistor is a simple method of fabrication of conductometric sensor. In this method the sensing layer is a film cast between two electrodes deposited on an insulating substrate. The response of the sensor to various analytes is monitored by recording the changes taking place in the sensing element. Organic molecule based sensors are low cost and operate at room temperature. Selectivity of the sensors to a particular analyte is an issue in sensors. An analyte molecule can interact with the various binding sites on a molecule. A molecule has to be designed and synthesized to be selective to a particular analyte of interest. This can be achieved by selecting a molecule which has a functional group that interacts with the analyte molecule. The mechanism of interaction of the analyte with the sensing molecule can be understood by doing molecular simulations. Molecular modelling allows monitoring the interaction of the analyte and sensing molecule. Here an example of organic molecule based sensor for selective interaction with aldehydes is illustrated. The organic molecule o-phenylenediamine blended with carbon black as sensing element of the chemiresistor to decrease the resistance. Molecular modelling can be used to understand the interaction between aldehyde and o-phenylenediamine molecule.

Keywords: organic molecules, volatile organic compound, chemiresistor, molecular modelling, interaction energy.

* Corresponding author.

A. Mason et al. (eds.), *Sensing Technology: Current Status and Future Trends III*,
Smart Sensors, Measurement and Instrumentation 11, DOI: 10.1007/978-3-319-10948-0_15

1 Introduction

Volatile organic compounds (VOCs) are found in environment from polluted air and many of the everyday used products such as toys, furniture, carpets, adhesives, cosmetics, air fresheners, paint, etc. The vapors of these chemicals effect on human body. The health effects may be short term and long term. Short-term exposures can cause headaches, eye/throat irritations whereas long-term exposure may result in cancer and liver/kidney damage. VOCs are highly flammable chemicals. The vapors of these chemicals should be detected below low flammable limit (LFL) to avoid the fire accidents. Therefore it is necessary to detect VOC at their low concentrations. Many organizations such as Environmental Protection Agency (EPA), World Health Organization (WHO), National Institute for Occupational Safety and Health (NIOSH), Occupational and Safety Health Administration (OSHA) have set exposure limit for the concentration of VOC. Beyond this limit, harmful effects are observed.

Aldehydes are compounds of the form R-CHO, where R can be hydrogen, alkyl or aryl group. Aldehydes have carbonyl group C=O functional group. Some examples of aldehydes are given in Fig.1.

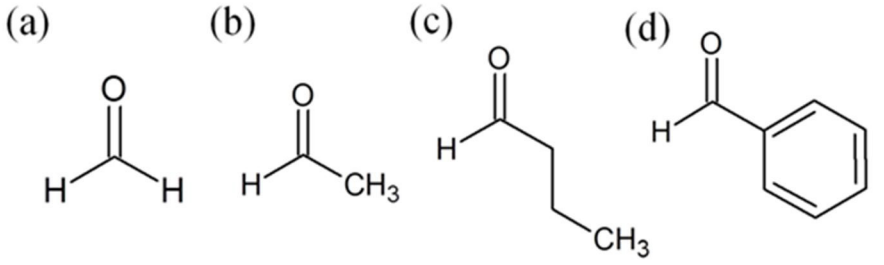

Fig. 1 Structure of aldehydes- (a) Formaldehyde, (b) Acetaldehyde, (c) Butaraldehdye, (d) Benzaldehyde

Acetaldehyde is also produced in fruits at ripening stage [1]. It is also applied on fruits to prevent post harvest rots because of its insecticide and fungicide property. High concentration of acetaldehyde application of causes fruits to lose flavour, inhibit production of ethylene and causes damages to fruits. Benzaldehyde has bitter almond smell. It is used in flavoring agents and food stuffs. Benzaldehyde is also widely used in perfume and soap industry. Benzyl alcohol is used as an antimicrobial agent. It is used as a co solvent in liquid pharmaceutical products. The oxidation of benzyl alcohol converts it to benzaldehyde. This can occur on long term storage, heat sterilization [2]. Formaldehyde is used in construction materials, synthesis of resins.

Environmental pollution caused by various sources also contains aldehyde vapors. Aldehydes are found in cigarette smoke, beverages, vehicle exhaust, sewage, solid biological wastes, open burning of gas, oil, coal,. The source of aldehyde exposure can be direct or indirect. Direct exposure could be due to inhalation of combustion of fuel in vehicle exhaust, cigarette smoke, burning of coal and fossil fuels, during alcohol fermentation. Indirect exposure is due to consumption of alcoholic beverages. These beverages contain ethanol which when consumed by humans is metabolized to acetaldehyde by alcohol dehydrogenase.

In small concentration exposure to aldehydes can cause eye/nose irritations and higher concentrations can cause dizziness and unconsciousness. Larger concentration exposure can also cause skin allergies. Prolonged exposure can cause gene mutation and cancer. The allowed level of acetaldehyde in ambient air is ~ 0.005 ppm. The permissible exposure limit by OSHA for acetaldehyde is 200 ppm. For formaldehyde, the OSHA has set a permissible exposure limit of 0.75 ppm and the World Health Organization has set exposure concentration to be < 0.05 ppm.

2 Various Sensors for Aldehyde Detection

Analytical methods for detection of acetaldehyde in air is based on the reaction of acetaldehyde with 2, 4 dinitrophenylhydrazine. The reaction produces hydrazone derivatives which are then analyzed using high performance liquid chromatography (HPLC) or gas chromatography (GC) [3]. The quantification of acetaldehyde in food products has been done using solid phase micro extraction in combination with gas chromatography/mass spectrometry-time of flight analysis [4]. These analytical instruments such as HPLC, gas chromatography and mass spectrometer are capable of accurately detect and determine the volatile organic compounds as low as parts per trillion These are bulky, high maintenance and expensive instruments. These require skilled person to operate and analyze the data. Therefore, gas sensors should have fast response to vapors of VOC, low maintenance and must be easily operated. Thus hand held VOC detectors that can be easily handled and operated are found in market. To make this available, lot of research has been carried out on the synthesis of new sensing material, fabrication of device, analysis of the data obtained. Efforts are made to make a sensor that is specific to a particular aldehyde. Studies are carried out to make a sensor that can detect low concentration of aldehyde that shows good stability of response, and has minimum cross sensitivity.

Chemiluminesence-based gas sensor uses nanosized catalysts such as $BaCO_3$, Y_2O_3, MgO, Fe_2O_3 for the detection of aldehyde [5,6]. Cataluminesence/ chemiluminesence sensors working principle is that the vapor reacts with solid

catalyst surface. The catalyst oxidises on reacting with vapor. An intermediate of organic molecule (vapor) in excited state is formed which then is de-excited to ground stare and emits radiation in visible- infrared region. Here the signals are generated from excited intermediates of the analyte during catalytic oxidation on the catalyst surface unlike other sensors where sensitive materials are used for sensing. The limit of detection of this type of sensor (nanosized Y_2O_3 [6]) for benzaldehyde is ~ 0.90 ng/mL

Colorimetric sensors are sensors that change colour of the sensitive material when exposed to the sensing gas. In colorimetric sensor for formaldehyde detection a primary amine ($R\text{-}NH_2$) containing sensing material adds to formaldehyde by nucleophilic addition to form imine (R=NH). The formation imine generates a color change [7-9]. Feng et al [10] have used pH indicator with amine functionalised polymer to detect the presence of formaldehyde. This method can detect formaldehyde concentrations as low as 50 ppb within 10 min. The colour change can be observed by eye.

In conductivity method, the conductivity of sensing material is monitored. Conductivity of sensing material changes on exposure to analyte is monitored. Metal oxide semiconductor conductivity sensor working mechanism has been explained as follows [11-13]. Oxygen species in the air are adsorbed on the semiconductor surfaces and ionized to O^{2-}, O^{-}, O^{2-} by capturing free electrons of the semiconductor. The type of oxygen ion species formed depends on the operating temperature of the metal oxide semiconductor sensor [14]. The adsorption of oxygen species on the surface creates space-charge layer. The conduction and valence band bends upwards which increases the potential barrier. When a reducing gas such as aldehyde interacts with surface, the aldehyde reacts with the adsorbed oxygen to form CO_2 and H_2O with the release of electrons. The thickness of space charge layer decreases and the potential barrier also decreases and hence the current increases. This indicates the response of the sensor to presence of an aldehyde. The sensitivity, selectivity stability of the device is dependent on many other factors. Nanostructures of ZnO, SnO_2 grown by different methods have been studied to increase the response time, stability sensitivity of the sensor to aldehydes [12-15]. Metal oxides such as SnO_2, In_2O_3, combination of oxides such as WO_3–Sb_2O_4, SnO_2–In_2O_3–CdO have been studied for formaldehyde sensing [11,16]. The combination of oxides in some have shown higher sensing property compared to individual compounds [11]. Selectivity of Zinc oxide sensor is also improved by doping it with Gallium [17].

In Quartz crystal microbalance (QCM) sensors for formaldehyde detection, QCM sensors have a quartz crystal coated with sensing layer. When the analyte interacts with the sensitive layer, the mass of the quartz crystal increases which changes the resonant frequency of the crystal. The sensing layer can be a polymer film [18,19], molecular imprinted polymer film[20], and inorganic-organic hybrid film [21,22]. The table 1 presents the aldehyde sensors using different mechanism.

Table 1 Aldehyde sensors with various detection methods

Method of detection	Analyte	Material	Reference
Colorimetric biosensor	Formaldehyde	Alcohol oxidase	[23]
Fluorescence	Aldehydes-acetaldehyde, formaldehyde, propionaldehyde	Metal–organic coordination polymers	[24]
Fluorescence	Aldehydes-acetaldehyde, formaldehyde, propionaldehyde	5-aminofluorescein	[25]
Chromogenic and fluorogenic	Formaldehyde	N-(rhodamine B)-deoxylactam-ethylenediamine.	[26]
Chromogenic / fluorogenic	Formaldehyde	Amination of 4-nitrophenol, umbelliferone and 4-methylumbelliferone gave the corresponding oxyamines	[27]
Luminescence	Aldehydes	Silance functionalized nanocrystals of Zinc oxide	[28]
Fluorogenic	Benzaldehyde		[29]
Chemiresitor	Formaldehyde	Primary amine functionalized Polyaniline	[30]
Chemiresitor	Formaldehyde	Graphene/PMMA	[31]
UV and HPLC	Benzaldehyde		[2]
Dispersive liquid–liquid micro extraction followed by GC	Benzaldehyde		[32]

Table 1 (*continued*)

Gas Chromatography	Benzaldehyde		[33]
Reversed-phase micellar liquid chromatographic method	Benzaldehyde		[34]
Photoelectrochemical detection (PED) coupled with HPLC	Benzaldehyde		[35]

3 Commercially Available Gas Sensors

Many aldehyde sensors are available to monitor indoor air in homes and workplaces. Some of sensors that are selective to formaldehyde are Synkera Technologies [36] has formaldehyde sensor that uses tin oxide as sensing element. It can detect less than 0.25 ppm of formaldehyde. The sensor has been tested for cross sensitivity for benzene, CO and water vapor. The nanostructure patterning of the tin oxide layer and incorporation of a molecular recognition sensing material into the pattern has been able to reduce the cross sensitivity to other chemical vapors. RKI instruments [37] have a colorimetric formaldehyde sensor that can detect 0.4 ppm with response time of 30 min. RAE Systems [38] formaldehyde gas sensors can detect over range of 0 to 10ppm of formaldehyde. Other sensors available use colorimeteric method [39] and MEMS metal oxide semiconductor sensing technology [40] for detecting aldehydes.

4 Conjugated Molecule Sensors

Organic electronic devices such as organic sensors, organic light emitting diodes, organic solar cells, and organic field effect transistors are emerging field of research. These devices are attractive as they are low cost, light weight, and flexible. Organic sensors operate at room temperature and consume low power. These can be used in flexible circuits. The organic devices use conjugated molecules for active layer. Conjugated molecules can be small molecules or polymers. These are also called as organic semiconductors. The solution processability of these materials is useful in printing on flexible substrates. Conjugated molecules are the organic molecules with π conjugation. The carbon atom in these molecules is sp^2 hybridized and the electron in the p_z orbital is delocalized over the molecule. The delocalization of the π electron cloud over the molecule gives the conductivity in these materials. Some of the examples of conjugated molecules are given in the following Fig. 2.

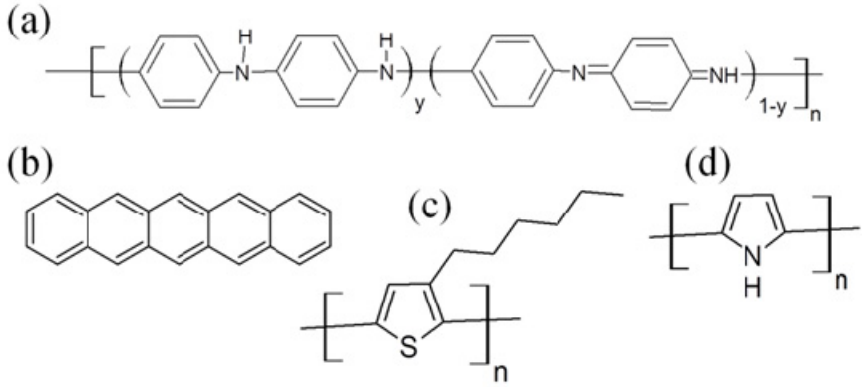

Fig. 2 Conjugated molecules – (a) polyaniline (b) pentacene, (c) poly (3-hexyl thiophene, (d) polypyrrole

Chemical vapor sensors detect the presence of volatile organic compounds (VOC) in the environment. The VOC interacts with the active layer (organic material) in the sensors. Chemical sensing response of organic molecule based sensors to various analyte can be monitored by the changes happening to the properties of the organic molecules. The properties of the materials are monitored using UV-Vis spectroscopy, fluorescence quenching, electrical conductivity etc.

Conducting polymers have been studied as sensing materials. Organic-Inorganic hybrid materials have been studied as sensing materials for volatile organic vapors [41]. The organic part being a conducting polymer and the inorganic part is metal oxide semiconductor. Here the advantages using the organic polymer are that it decreased the operating temperature of the sensor [42]. It has been found that the organic –inorganic hybrid sensor exhibited enhanced sensitivity compared to individual components [43].

Polyaniline is well studied conducting polymer. It is widely used in many applications because of the ease of synthesis and its stability in air. The conducting form of the polymer will de-dope in presence of ammonia easily and hence is used as ammonia sensor. Formaldehyde sensor with polyaniline (PANI) as active layer changes conductivity and indicates the presence of the aldehyde. The sensitivity of the sensor could be increased by blending the polymer with other organic or inorganic compounds for formaldehyde detection. PANI with fluoral-p as sensing element has been used for detection of formaldehyde gas [44]. The compound fluoral-p on reaction with formaldehyde forms a fluorescent compound and hence is used in colorimetric sensor for formaldehyde. The reaction also produces ammonia gas. PANI de-doped in presence of ammonia and hence formaldehyde gas sis detected by the change in conductivity of the sensor. The detection limit of this PANI/fluoral-p sensor is 3.7 ppm with response time of ~42s. Polyaniline and poly (o-anisidine) intercalated molybdenum oxide was investigated for sensing of aldehyde. The detection limit of this sensor is ~tens of

ppm or several ppm [45]. Itoh et al have prepared PANI/MO_x hybrid film with a different process [46]. The hybrid film by this process detects tens of ppb of aldehyde.

The good characteristics of vapor sensors are –

- specificity (selectivity to a vapor),
- sensitivity,
- repeatability,
- reproducibility,
- long term stability,
- response of the sensor should not change much with variation in temperature and humidity changes.

The selectivity of the sensor is dependent on the sensing material. Most of the sensor lack selectivity. The reason organic molecule based sensors lack selectivity is because the molecule has sites that can bind to the analyte molecule. A molecule has to be designed such that it is specific to one analyte and give no or minimal response to others (Fig. 3(a)). This can be achieved by selecting a molecule which has a functional group that interacts with the analyte molecule. Organic materials that are specific can be synthesised by a synthetic chemist.

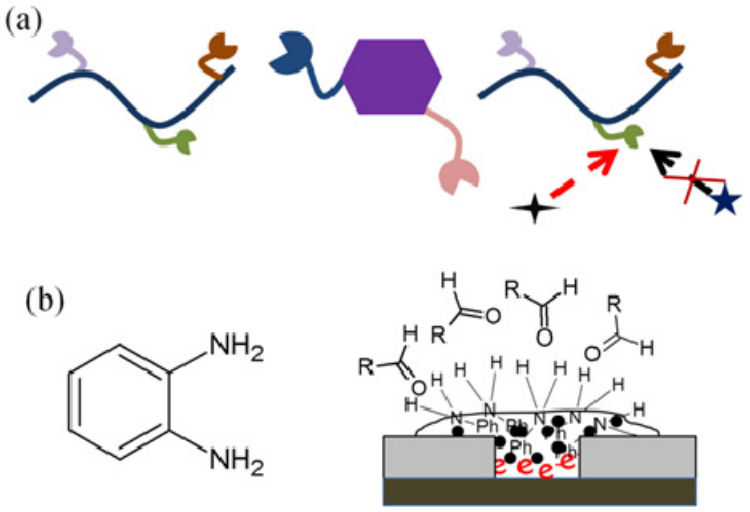

Fig. 3 (a) Selectivity in organic materials (b) Structure of o-phenylene diamine (OPD) and composite of OPD chemiresistor interaction with aldehyde functional group

It has been shown that aldehyde functional group can react with amine (-NH2) group [1,47]. An amine functional group reacts with aldehyde to form imine [7,28]. A compound with –NH2 group can selectively interact with the acetaldehyde. If the compound with amine group has conjugation, then sensing

film will be conducting. Hence the change due to vapor absorption can be monitored. Primary amine functionalised polyaniline has been used for detection of formaldehyde [30]. O-pheneylene diamine (OPD) is used in organic reactions and undergoes condensation reactions with aldehydes and ketones. OPD has two -NH2 groups and conjugation bonds are present in the phenyl ring will give the conductivity for the sensing film (Fig. 3(b)). Hence it is expected that the sensor would be more responsive to aldehydes and ketones.

5 Sensor Response Characteristics Conjugated Molecule Sensors

Conductometric sensing involves monitoring of conductivity of the sensing element. Organic semiconductor molecules such as conducting polymer and small molecules can be used as sensing elements. Conductometric sensors include the chemiresistors, chemically sensitive field effect transistors (CHEMFET) and electrochemical devices- Ion selective field effect transistor (ISFET), amperometric sensors. Organic molecule based chemiresistor has a film which is sandwiched between the two electrodes. An organic semiconductor device can be represented by an equivalent circuit. The circuit comprise of impedances arising from contact bulk, surface and the interface of the device. The bulk, surface and interface impedance are connected in parallel. This is then connected to the contact impedance is in series [48,49].

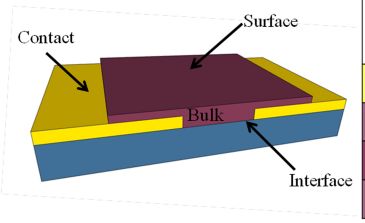

Impedance	Organic chemiresistor (direct current mode)	
	Capacitance	Resistance
Contact	×	√
Surface	×	√
Bulk	×	√
Interface	×	√

Fig. 4 An organic semiconducting device. The table presents the operating mechanism of the device.

Since the devices operate in direct current mode, the capacitance need not be taken into consideration (Fig. 4). Only the resistance of the device is taken into consideration. The contact resistance arises from the mismatch between energy levels of metal and conjugated molecule. The surface, bulk and the interface resistances are from the organic semiconductor. The interface resistance comes into picture, if there is any third layer in contact with the active layer such as dielectric-organic semiconductor interface in CHEMFET. A change in the contact/surface/bulk/interface resistance in the device results in change of overall

resistance of the device. The response of the organic sensor to chemical vapors is mainly due to modulation of the bulk resistance. Thus change in resistance of the bulk of the organic semiconductor is the most important than surface resistance in case of organic chemical vapor sensors. Chemiresistor is a simple method of fabrication of conductometric sensor (Fig. 5). The use of dc resistance measurement technique makes it a low power operating device [50,51].

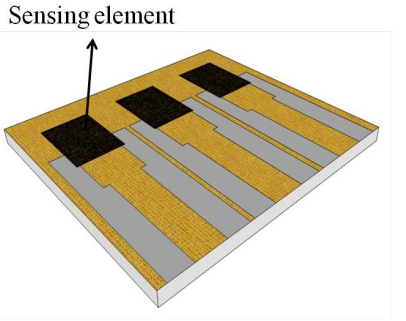

Fig. 5 Schematic of a simple chemiresistor with sensing element

$$\text{Resistance is given as } R = \rho\,(l/A) \tag{1}$$

where ρ is resistivity, l is length and A is area of cross section.

$$\text{The conductivity } (\sigma) \text{ is inversely related to resistivity. } \rho = 1/\sigma \tag{2}$$

The conductivity of a conducting polymer [52] is given by

$$1/\sigma = 1/\sigma_{\text{intramolecular}} + 1/\sigma_{\text{intermolecular}} + 1/\sigma_{\text{ionic}} \tag{3}$$

where σ is conductivity of the polymer, $\sigma_{\text{intramolecular}}$ is the intramolecular conductivity, $\sigma_{\text{intermolecular}}$ is the intermolecular conductivity and σ_{ionic} is the ionic conductivity, respectively.

When the polymer film is exposed to an analyte the conductivity of the polymer will change. The change in conductivity occurs depending on the nature of the analyte-polymer interaction. The intramolecular conductivity changes due to the change in the electron density on the main chain. For example, when the analyte is a reducing/oxidising agent for the polymer then, intramolecular conductivity will change because of the change in doping levels of conducting molecule [53].

Most of the polymer sensors operation mechanism is explained by the solubility parameter [54-58]. The sorption of analyte vapor will induce swelling of the polymer and this affects the electron density on the polymer chain [59]. It also changes the intermolecular spacing between the polymer chains. Polymers swell in good solvents. This is because solubility parameter of the polymer and solvent are almost equal. The strength of interaction depends in the solubility parameter of the polymer. Thus the resistance change of the sensor device that occurs due to

presence of VOC can be correlated with the solubility parameter. The interchain conductivity may also change because of the change in crystallinity of the polymer due to vapor-polymer interaction.

The ionic conductivity changes usually in the polymer containing ions [51]. This type of polymers is especially used in humidity sensors. The conductivity of ionic polymer changes rapidly in presence of water vapor [55, 60]. The analyte interaction increases the mobility of ions in the polymer [61,62]. The increase in mobility of the ions may be because of various reasons. The analyte may act as plasticiser in the polymer matrix and reduces the viscosity of the polymer matrix. This will increase the mobility of the ion in polymer matrix. The increase of mobility of ions can also be due to improved solvation of the ionic charge carriers, or dielectric screening of the charged polymer backbone by the analyte molecules.

The sensing material used in organic chemical sensor may be a non-conducting [63,64, 65] or conducting type [59]. Insulating polymer - carbon black composites are usually used in the chemiresistor. Arrays of these sensors with various polymers that have affinity to different analytes are prepared and their response is recorded and analysed. Conductive fillers such as carbon black [54], carbon nanotubes [55], conducting polymer [56], conducting polymer grafted to carbon black [65,66] can be distributed in non conducting polymers matrix. These fillers increase sensitivity to resistance changes in the material.

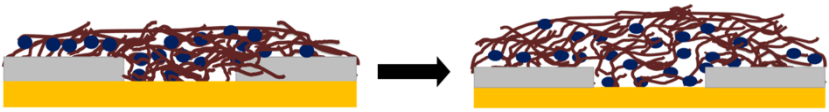

Fig. 6 Schematic of sensing response mechanism of conjugated molecule-carbon black chemiresistor

The response mechanism of the polymer-carbon black composite sensors is explained by percolation theory [70,71]. The resistivity of the polymer – CB composite is related to the content of carbon black in the film. The smaller the concentration of carbon black, the particles will be far apart and the resistance of the composite is high. As the concentration of carbon black is increased, the particles are closer and the resistance of the composite decreases. When the polymer-carbon black film is exposed to atmosphere containing organic vapors, due to affinity, the film absorbs analyte vapor molecules. This results in volumetric change of the film [68]. The process is illustrated in Fig. 6. Due to volumetric change of the film, there would be movement of polymer molecules. The conducting path created by carbon black in the film changes. This triggers a change in the resistance of the device indicating presence of that particular VOC. The connectivity between conductive particles such as carbon black would decrease. There would be movement of carbon black also that will contribute to the change in conductivity. This is why carbon black addition increases the response of the sensor. The change in resistance is sharp at the percolation threshold of carbon black in polymer matrix.

The conductivity of conjugated molecules is not very high. These organic compounds exhibit electronic conductivities between about 10^{-9} and 10^{3} S cm−1. The table shows dc conductivity of commonly used conjugated molecules. In conjugated molecule-carbon black composites, the carbon black particles increase the conductivity of the composite film. In addition to increasing the conductivity, addition of carbon black increases the response of the sensor.

Table 2 Conductivity of conjugated molecules

Material	Conductivity (S/cm)	Reference
Doped polyaniline	0.144×10^{-2}	[72]
Polypyrrole	0.59	[73]
Poly(3-hexylthiophene)	6.77×10^{-9}	[74]

The chemiresistor response is shown in the Fig.7. The base line resistance is measured in air. Then the sensor is exposed to analyte vapor. The resistance of the sensor raises sharp and reaches a maximum value. When the vapors are turn off the resistance decreases back to its original value. The resistance can also decrease depending on the nature of sensing layer-analyte interaction.

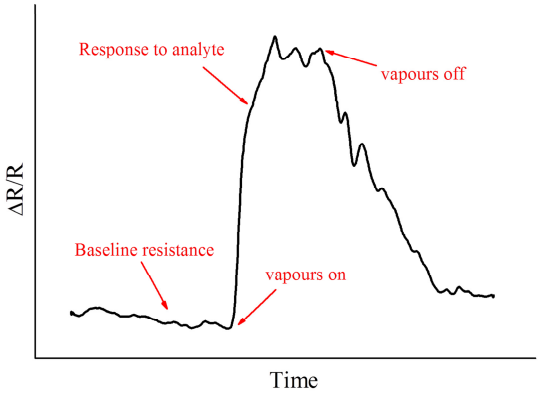

Fig. 7 Chemiresistor sensor response to analyte

OPD is a conjugated molecule. Carbon black is added to make a low resistance and enhance the response to the vapors. The response of a sensor to an analyte is a time dependent signal. The various methods to analyse output of the sensor signal are differential, relative, fractional baseline manipulated response. The

fractional baseline manipulation method or also called relative resistance change (in case of resistance) or percent change is common method used to analyze sensor response from conducting polymer sensors [75,76]. The percent change of sensor response is given by equation (4).

$$[(R_v\text{-}R_o)/R_o] \times 100 \text{ or } \Delta R/R_o \times .100 \quad (4)$$

Where $\Delta R = (R_v\text{-}R_o)$, R_o is the value of the sensor signal in the absence of vapor, and R_v is the sensor signal observed during each vapor exposure i.e., R_v is the sensor response. The response of the OPD-CB sensor was analysed by plotting the relative resistance change with time (Fig. 7).

6 Testing OPD-CB Sensor for Aldehyde Detection

OPD-CB sensor was tested for acetaldehyde, benzaldehyde, formaldehyde, acetone, methanol, and ethanol. Twelve OPD-CB sensors were fabricated and tested for each measurement. A number of VOCs co-exist with aldehydes in contaminated air [5]. Hence here the sensor was also tested for acetone, methanol and ethanol for cross sensitivity. Fig. 8 shows the OPD-CB chemiresistor response obtained. The relative change in resistance of the sensor is plotted.

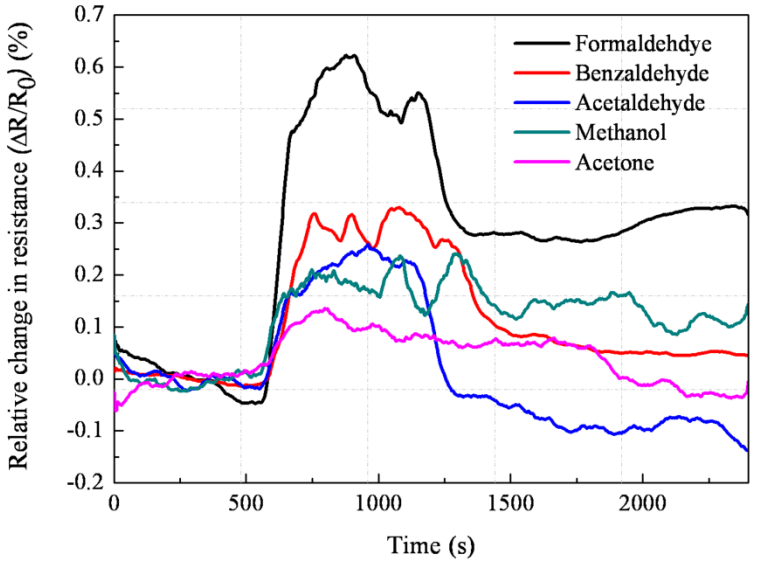

Fig. 8 Relative change in resistance of the OPD-CB sensor for various VOCs tested

The relative change of resistance for formaldehyde is observed to be ~ 0.6% and is higher than for benzaldehyde and acetaldehyde. Among the three aldehydes evaluated, it is observed that OPD-CB sensor shows maximum

response for formaldehyde vapors. It can also be observed that the sensor recovers completely to its initial position on removal of vapors only for acetaldehyde. On exposure to acetaldehyde vapors the resistance of the sensor increased to about 0.25 %, of its initial value as shown in Fig. 8. When the vapors were withdrawn from the sensor it was observed that the resistance decreases beyond its initial resistance value. The rearrangement of carbon black particles is attributed for this behaviour. The sensor response is observed to be 1 to 2 min for 12 sensors (for acetaldehyde). The recovery time was observed to be around 4 to 10 min. The other VOCs tested were acetone, methanol, and ethanol. The sensor also responds to acetone and methanol. The OPD-CB sensor does not respond to the vapors of ethanol. That is there is no change in resistance of OPD-CB sensor on introducing the vapors of ethanol. Furthermore, it is observed that the response of methanol and acetone overlap with that of aldehydes. The sensor shows stable resistance for aldehydes than for acetone and methanol.

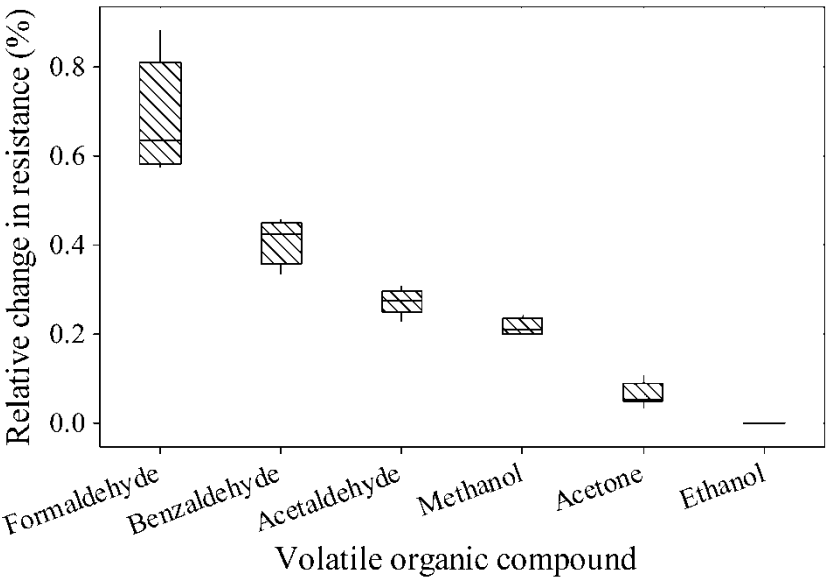

Fig. 9 Cross sensitivity towards various VOCs of OPD-CB sensor

Fig. 9 shows the cross sensitivity towards various VOCs of sensor OPD-CB sensor. Twelve OPD-CB sensors were tested for each VOC. The sensor response is higher to formaldehyde than other VOC vapors and the response of OPD-CB sensor to interfering vapors is small. Hence this indicates the selective behavior of the OPD-CB sensor towards aldehydes.

7 Molecular Modelling to Validate Sensing Mechanism

Molecular modelling is used to understand the mechanism of sensing. The selectivity of the material to a particular vapor can be understood by simulation. Shevade et al [77] have used model of polymer-CB composite was in such a way that would describe making the composite in experiment. In experiment sensing films are made by dissolving polymer in a solvent, mixing with carbon black and drop casting into thin film and then evaporation of the solvent. The model for polymer-CB composite was developed. The simulations were first carried out under no solvent condition and then under solvent condition. The interaction energy of the solvent molecule with the polymer-CB system was calculated. This would show the selective interaction of polymers with the vapors. Belmares et al [78] had used cohesive energy density method to estimate the Hildebrand and Hansen solubility parameter and have used it to analyse the obtained sensor response. Molecular dynamics method was used to generate structure and packing of molecules so that correct densities of the structures are achieved to obtain uniform stress distribution in the molecules were presented. Similarly, for OPD-CB sensors, molecular modelling was performed to simulate the response of OPD-CB composite to VOCs. A procedure for construction of the organic molecule-composite is developed and used to investigate the selective sensing property of OPD-CB system. In this work, three works [77-79] that have simulation studies on polymer-carbon black composite for sensors have been referred in developing the new procedure. Molecular simulations were carried out using Materials Studio v6.0.0 (Accelyrs Software Inc.) [80].

The approach to model OPD-CB composite sensor is similar to the one used by Shevade et al [77]. That is the model of OPD-CB composite is developed such that experimental conditions are tried to include in the procedure developed. The OPD and CB composition of 80 wt% and 20 wt% respectively was used. The experimental density of OPD-CB was determined. The density of OPD-CB was obtained as 1.114 g/cm^3. Carbon black is modelled as naphthalene ring with no hydrogen atoms [77]. OPD is unstable in solutions and when exposed to ambient it oxidizes to form brown color 2, 3 Diaminophenazine (DAP) product (Fig. 10(a)). Therefore DAP was also considered to be present in the composite. An amorphous unit cell was built using AMORPHOUS CELL module of Materials Studio package with starting density as 50 % of the target density. 40 wt% of OPD and DAP each and 20 wt % of carbon black was loaded into amorphous cell. The amorphous cell was minimized and subjected to molecular dynamics (MD) simulation - NVT and NPT to achieve experimental value of density -1.114 g/cm^3. Fig. 10(b) shows the packing of OPD-DAP-CB molecules in the amorphous unit cell.

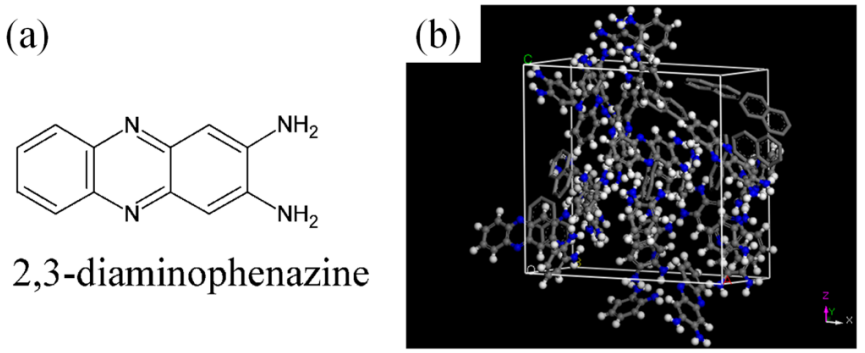

Fig. 10 (a) Structure of 2,3 diaminophenazine (DAP) (b) OPD-DAP-CB packing in amorphous unit cell

To model the solution of OPD-CB composite, the composite was then packed with solvent dimethyl propylene urea (DMPU). The close contacts were monitored. The experimental density of OPD-CB solution is 0.977 g/cm^3. The density of the packed cell here also was set to 50 % of the target density. 64 DMPU molecules were loaded in to the cell. The cell was minimized and equilibrated by molecular dynamics – using NVT and NPT ensembles as previously done for OPD-CB system so that target density is reached. Snapshots were taken at every 5ps. The final density achieved is shown in the Fig. 11. Fig. 12 shows the packing of the molecules in the cell after the cell is relaxed to room temperature.

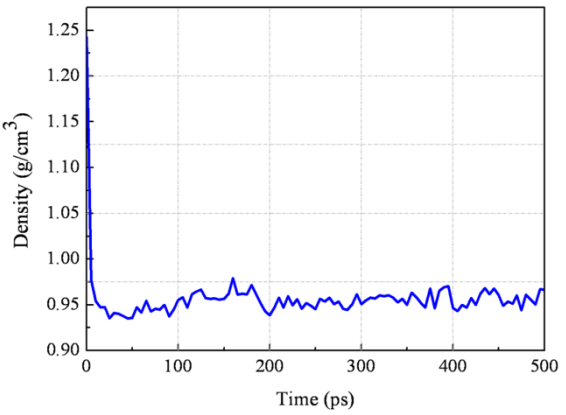

Fig. 11 Final density of OPD-CB composite in DMPU solution

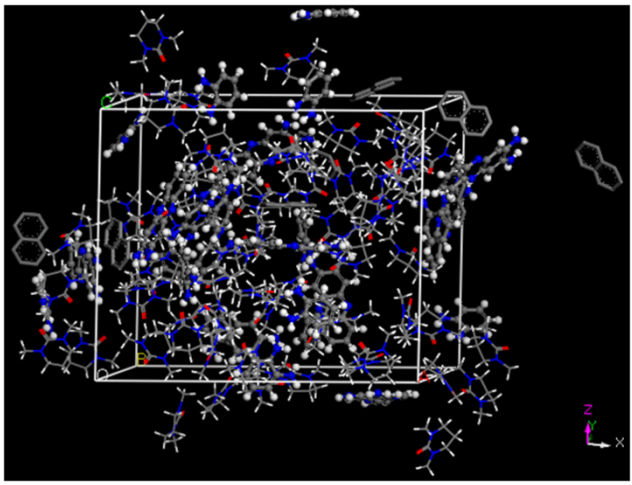

Fig. 12 OPD-DAP-CB composite with DMPU solvent molecules packed in the cell

Misra et al [79] have used molecular modelling to construct a thin film of polymers to study their property. After mixing the OPB-CB in DMPU solvent, the composite is drop casted over the senor substrate to form thin film. Therefore to model the thin film, OPD-DAP-CB cell was then confined to two dimensional boundary conditions to from a thin film. This was done so that the OPD-DAP-CB system sees the neighbouring molecules only in x and y directions and not in z-direction. The geometry optimization of the film was done at a pressure of 2.133×10^{-5} GPa (60 mmHg). The same pressure was maintained during the drying of the film in actual experiment. The film was annealed for 5 cycles using anneal task in Forcite module. The temperature of the system was increased from room temperature of 300 K to 343 K with heating ramp/cycle=3. Then the film was minimized by molecular dynamics NVT and NPT. The trajectory file obtained from the dynamics resulted in 3 frames. The 3rd frame was used for further analysis. The solvent molecules would be evaporated after heating. Therefore DMPU molecules were deleted from the 3rd frame structure taken. The structure was further minimized by geometry optimization. The structure was brought to equilibrium at room temperature and atmospheric pressure using molecular dynamics ensemble NVT and NPT. One of the frames was taken for the composite–analyte interaction studies. The final packing of molecules in the thin film is as shown in Fig. 13.

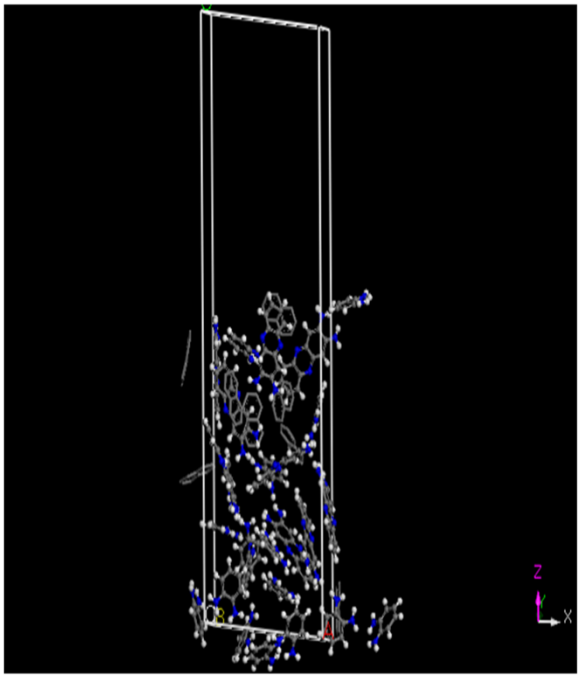

Fig. 13 OPD-DAP-CB composite thin film

7.1 Aldehyde Interaction with OPD-CB Composite

Sorption module in materials studio allows to simulate the sorption of analyte molecule into sorbent. The NPT-MD 3rd structure minimized at room temperature and pressure in the previous step is the sorbent (called as OPD-DAP-CB thin film). The OPD-DAP-CB film is fixed in Cartesian co-ordinate space. The analyte molecules are inserted in the OPD-DAP-CB thin film by Sorption module. The "Fixed loading" of analyte molecule is used in Sorption module. Only one analyte molecule is loaded to represent the low concentration of analyte vapors [77]. 300000 insertion steps were used to insert analyte molecule in to the matrix. Metropolis Monte Carlo simulation method is used for the analysis. The 10th frame of the lowest energy structure is used.

The interaction energy of the analyte with the OPD-DAP-CB is calculated as

$$E_{interaction} = E_{total} - (E_{opd\text{-}dap\text{-}cb\ only} + E_{analyte\ only}) \quad (5)$$

The interaction energy is shown in the Fig. 14. It can be seen that the interaction energy for aldehydes is higher than that for other VOCs. During the sorption studies, water is also taken because formaldehyde solution and acetaldehyde solution contain water. It is observed that the interaction energy for water is very less compared to the formaldehyde and acetaldehyde.

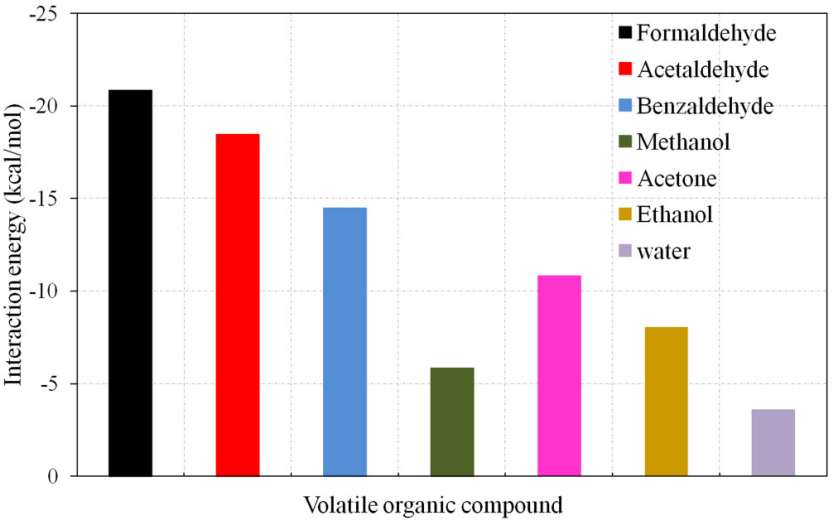

Fig. 14 OPD-DAP-CB composite –analyte interaction energy

7.2 Radial Distribution Function Calculation to Investigate Interaction of OPD with Vapors

The radial distribution function g(r) also known as pair distribution function is a measure of the probability of finding atom/molecule between a distance r and (r+dr) from another atom/molecule. The radial distribution function (RDF) calculations are performed by simulations for polymer blends, composites, polymer solutions to investigate the interaction between the two types of molecules in the system [77, 81-83]. For OPD-CB composite sensor, radial distribution function calculation was performed to investigate the selectivity interaction between the OPD molecule and analyte molecule. The OPD is in solid phase (thin film) and the analyte is in vapor phase.

The reason for selecting OPD molecule for sensing aldehydes is that, OPD molecule has two amine groups and it is known that aldehyes react with amine groups. In OPD there are 8 hydrogen atoms as can be seen from the inset of the figure. Four hydrogen atoms are with the amine groups. Four hydrogen atoms on the phenyl ring of OPD molecule. The function group of aldehyde is carbonyl group C=O. Oxygen atom can interact with any hydrogen atom on the OPD molecule. So RDF calculation of O-H pair at various positions was carried out. The H in amine is named as O-HN and H on phenyl ring as O-H. The position of H atoms on the molecule is labelled as shown in Fig. 15. The RDF calculation g(r) shows that HN at 2nd and 3rd positon is more likely to interact with oxygen atom on carbonyl group of formaldehyde molecule. The distance at which this interaction takes place is 2.14 Å. The O-HN(1) and O-HN(4) is at 3.54 Å. The RDF of O-H(1), O-H(2), O-H(3), O-H(4) is farther distances. Thus the functional group on aldehye interacts with the -NH group on OPD molecule.

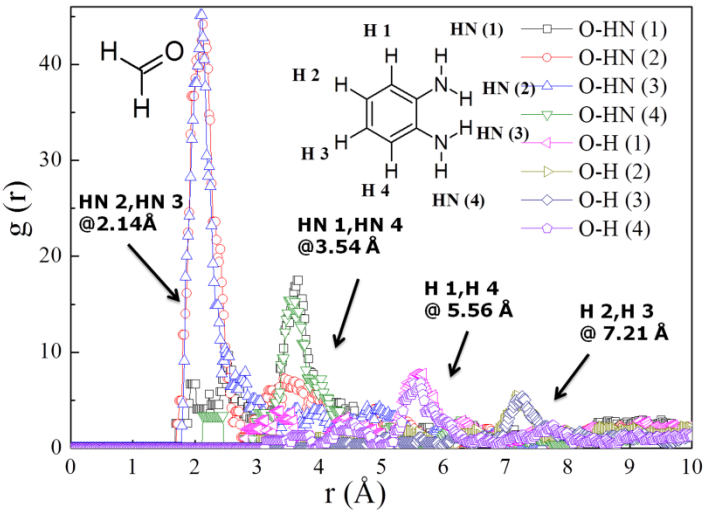

Fig. 15 Radial distribution function g(r) of O-HN for Formaldehyde-OPD

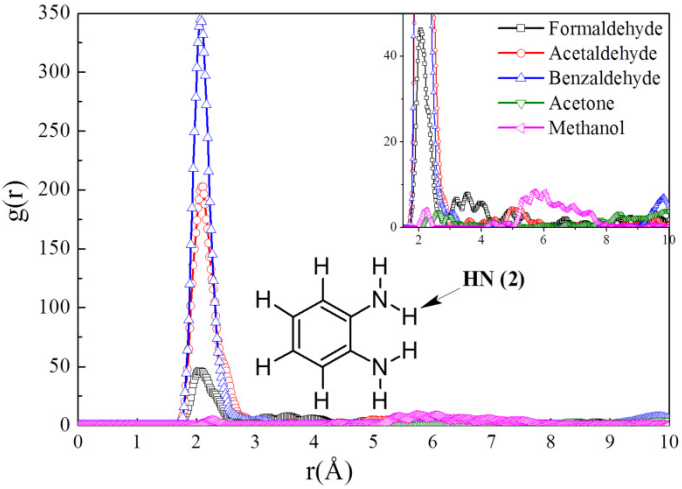

Fig. 16 Radial distribution function g(r) of O-HN for VOC-OPD

Simulated RDF calculation for OPD interaction with other analyte molecules was also carried out. The interaction between oxygen atom in the functional group of VOC and H of amine group (HN (2)) in OPD was monitored. That is g(r) for O-NH (2) is performed. Here O is in functional group of VOC and HN (2) is in amine group on OPD at 2nd position (inset of Fig. 16). A pronounced peak at around 2 Å is observed. The g(r) value is highest for benzaldehyde indicated that interaction is stronger with OPD than with acetaldehyde and formaldehyde (Fig. 16). It can be observed that g(r) for O-NH is not pronounced peak for

acetone or methanol. This indicates that there is least interaction of oxygen of atom of acetone and methanol with NH group of OPD. Thus OPD shows selective interaction for aldehydes. This was observed in the sensors testing experiment also. Thus the experiment and simulation are in good agreement.

8 Mechanism of OPD Interaction with Aldehyde

To understand why the carbonyl group of aldehyde only interacts with amine group of OPD, we have to consider the chemical structure of the functional group. Chemical vapor can interact with the organic molecules. The interaction n can be hydrogen bonding, dispersion interaction, dipole-dipole or dipole-induced dipole interaction. The strength of interaction depends on the affinity of the vapor towards the conjugated molecule and distance of the vapour from the conjugated molecule [49]. Volatile organic compounds are not reactive at room temperature. They are detected because of their weak interaction with the organic molecule that results in adsorption and change in electrical property of the sensing film [52]. This is observed as a response to VOC in a chemiresistor. In OPD-CB sensor, the interaction of VOC resulted in increase in resistance of the sensor. The interaction of OPD-CB with VOCs is because the functional group of VOC interacts with amine group on OPD. This was observed form RDF calculation for o-HN pair. It was also observed for RDF calculations that g(r) for O-HN pair is higher for aldehyde. Therefore the structure of carbonyl group and hydroxyl group is examined (Fig. 17).

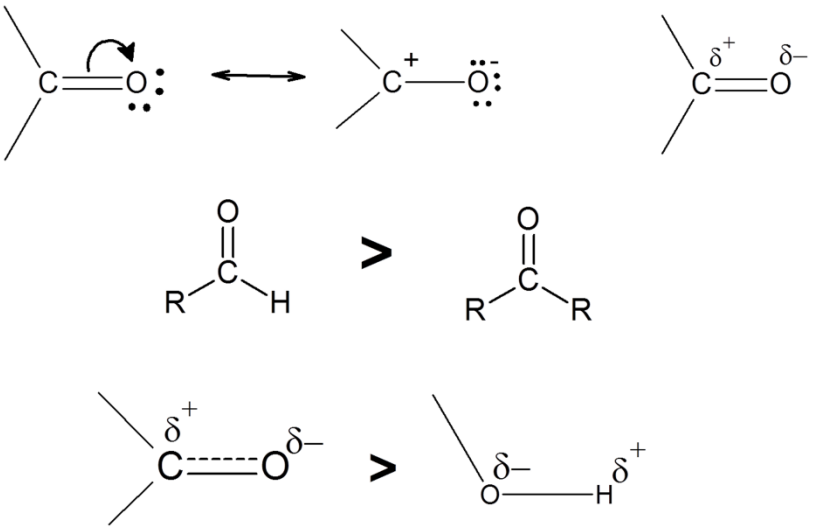

Fig. 17 Structure of carbonyl and hydroxyl group and comparison of their reactivity

The oxygen atom is more electronegative than carbon in carbonyl group. The carbonyl group is present on ketone also. The carbonyl group on aldehyde is susceptible to react since ketone is more stable than aldehydes. This may be the reason for observed higher response to aldehyde than ketone. In case of alcohol, the hydroxyl group is more stable than the carbonyl group because of the unsaturated bond in carbonyl group. Hence it is proposed that aldehyde can interact with OPD more than ketone and alcohol.

9 Conclusion

In summary, an organic nanocomposite, O-phenylene diamine (OPD)-carbon black (CB) sensor was fabricated. The sensor shows selectivity to aldehyde vapors. There are various sensors for aldehyde detection. Their working mechanism, method for improving selectivity and detection limit are presented. The sensing materials were either organic or inorganic materials. Some of them are metal oxide semiconductors, organic compounds, polymers and organic-inorganic hybrid composites. Conjugated materials are blended with inorganic materials to reduce the operating temperature. These materials when used alone also exhibit good sensing properties. The organic sensor with conductivity change as detection method can be fabricated as chemiresistor, CHEMFET or by electrochemical sensor. The chemiresistor is a simple device. Therefore chemiresistor with OPD-CB as sensing element was fabricated for testing aldehyde. The mechanism of chemiresistor response to vapors is explained. The reason for choosing OPD as the conjugated molecule was it is conjugated and has amine group. The amine group is known to interact with carbonyl group and carbonyl group is present in aldehydes. The OPD-CB sensor was tested for VOCs of acetone and alcohol also to check the cross sensitivity. The sensors shows higher response towards aldehyde vapors and the response of interfering vapors is weak. It is proposed that weak interaction of carbonyl group of aldehyde with amine of OPD is the reason for higher response of OPD-CB sensor to aldehydes. Molecular modelling procedure was developed to simulate the OPD-CB sensing film. The interaction energy calculated from molecular simulation method also suggests that the interaction energy of the aldehydes with the composite is higher than that for other VOCs. The simulated radial distribution function calculation was carried out. The results indicate that the amine group in OPD interacts with the carbonyl group of aldehyde. When the RDF calculation for other functional group of other VOC and amine group of OPD was carried out, it was observed that the functional group of acetone and alcohol showed small or negligible interaction with amine group of OPD. To further understand the interaction, the chemical structure of carbonyl and hydroxyl group was examined and the mechanism for the interaction is proposed. Thus OPD-CB sensor shows selectivity to aldehydes and hence can be used for detection of aldehyde vapors.

References

[1] Pesis, E.: The role of the anaerobic metabolites, acetaldehyde and ethanol, in fruit ripening, enhancement of fruit quality and fruit deterioration. Postharvest Biol. Technol. 37, 1–19 (2005)

[2] Di Pietra, A.M., Cavrini, V., Raggi, M.A.: Determination of benzaldehyde traces in benzyl alcohol by liquid chromatography (HPLC) and derivative UV spectrophotometry. Int. J. Pharm. 35, 13–20 (1987)

[3] Report on Environmental Health Criteria 167 - Acetaldehyde, International programme on chemical safety, World health organisation, Geneva (1995), http://www.inchem.org/documents/ehc/ehc/ehc167.htm

[4] Kaseleht, K., Paalme, T., Nisamedtinov, I.: Quantitative Analysis of Acetaldehyde in Foods Consumed by Children using SPME/GC-MS(Tof), On-fiber Derivatization and Deuterated Acetaldehyde as an Internal Standard. Agronomy Research 9 (Special Issue II), 341–395 (2011)

[5] Cao, X., Zhang, Z., Zhang, X.: A novel gaseous acetaldehyde sensor utilizing cataluminescence on nanosized BaCO3. Sens. Actuators. B 99, 30–35 (2004)

[6] Wu, Y., Zhang, S., Wang, X., Na, N., Zhang, Z.: Development of a benzaldehyde sensor utilizing chemiluminescence on nanosized Y2O3. Luminescence 23, 376–380 (2008)

[7] Mohr, G.J.: New chromogenic and fluorogenic reagents and sensors for neutral and ionic analytes based on covalent bond formation–a review of recent developments. Anal. Bioanal. Chem. 386, 1201–1214 (2006)

[8] Kawamura, K., Kerman, K., Fujihara, M., Nagatani, N., Hashiba, T., Tamiya, E.: Development of a novel hand-held formaldehyde gas sensor for the rapid detection of sick building syndrome. Sens. Actuators B 105, 495–501 (2005)

[9] Toda, K., Yoshioka, K.I., Mori, K., Hirata, S.: Portable system for near-real time measurement of gaseous formaldehyde by means of parallel scrubber stopped-flow absorptiometry. Anal. Chim. Acta 531, 41–49 (2005)

[10] Feng, L., Musto, C.J., Suslick, K.S.: A Simple and Highly Sensitive Colorimetric Detection Method for Gaseous Formaldehyde. J. Am. Chem. Soc. 132, 4046–4047 (2010)

[11] Chen, T., Liu, Q.J., Zhou, Z.L., Wang, Y.D.: A high sensitivity gas sensor for formaldehyde based on CdO and In2O3 doped nanocrystalline SnO2. Nanotechnology 19, 095506 (5pp) (2008)

[12] Fang, C., Wang, S., Wang, Q., Liu, J., Geng, B.: Coralloid SnO2 with hierarchical structure and their application as recoverable gas sensors for the detection of benzaldehyde/acetone. Mater. Chem. Phys. 122, 30–34 (2010)

[13] Calestani, D., Mosca, R., Zanichelli, M., Villani, M., Zappettini, A.: Aldehyde detection by ZnO tetrapod-based gas sensors. J. Mater. Chem. 21, 15532–15536 (2011)

[14] Castro-Hurtado, I., Mandayo, G.G., Castaño, E.: Conductometric formaldehyde gas sensors. A review: From conventional films to nanostructured materials. Thin Solid Films 548, 665–676 (2013)

[15] Shimizu, Y., Yamaguchi, K., Fukunaga, K., Takao, Y., Hyodo, T., Egashira, M.: Acetaldehyde Gas-Sensing Properties and Surface Chemistry of SnO2-Based Sensor Materials. J. Electrochem. Soc. 146, 1222–1226 (1999)

[16] Knake, R., Jacquinot, P., Hauser, P.C.: Amperometric Detection of Gaseous Formaldehyde in the ppb Range. Electroanal 13, 631–634 (2001)
[17] Han, N., Tian, Y., Wu, X., Chen, Y.: Improving humidity selectivity in formaldehyde gas sensing by a two-sensor array made of Ga-doped ZnO. Sens. Actuators B 138, 228–235 (2009)
[18] Wang, X.F., Ding, B., Sun, M., Yu, J.Y., Sun, G.: Nanofibrous polyethyleneimine membranes as sensitive coatings for quartz crystal microbalance-based formaldehyde sensors. Sens. Actuators B 144, 11–17 (2010)
[19] Ding, B., Wang, X., Yu, J., Wang, M.: Polyamide 6 composite nano-fiber/net functionalized by polyethyleneimine on quartz crystal microbalance for highly sensitive formaldehyde sensors. J. Mater. Chem. 21, 12784 (2011)
[20] Hirayamaa, K., Sakaib, Y., Kameokaa, K., Nodac, K., Naganawa, R.: Preparation of a sensor device with specific recognition sites for acetaldehyde by molecular imprinting technique. Sens. Actuators B 86, 20–25 (2002)
[21] Zhu, Y., Li, H., Zheng, Q., Xu, J., Li, X.: Amine-Functionalized SBA-15 with Uniform Morphology and Well- Defined Mesostructure for Highly Sensitive Chemosensors To Detect Formaldehyde Vapor. Langmuir 28, 7843–7850 (2012)
[22] Zheng, J., Li, G., Ma, X., Wang, Y., Wu, G., Cheng, Y.: Polyaniline–TiO2 nanocomposite- based trimethylamine QCM sensor and its thermal behavior studies. Sens. Actuators B 133, 374–380 (2008)
[23] Sigawi, S., Smutok, O., Demkiv, O., Gayda, G., Vus, B., Nitzan, Y., Gonchar, M., Nisnevitch, M.: Detection of Waterborne and Airborne Formaldehyde: From Amperometric Chemosensing to a Visual Biosensor Based on Alcohol Oxidase. Materials 7, 1055–1068 (2014)
[24] Zhao, X.J., Yang, J.H., Liu, Y., Gao, P.F., Li, Y.F.: Metal–organic coordination polymers of Tb2-xEux(BDC)3(H2O)n with tunable fluorescence and smart response toward aldehydes (0 £ x £ 2, BDC =1,4-benzenedicarboxylate). RSC Adv. 4, 2573–2576 (2014)
[25] Xing, Y., Wang, S., Mao, X., Zhao, X., Wei, D.: An Easy and Efficient Fluorescent Method for Detecting Aldehydes and Its Application in Biotransformation. J. Fluorescence 21, 587–594 (2011)
[26] Li, Z., Xue, Z., Wu, Z., Han, J., Han, S.: Chromo-fluorogenic detection of aldehydes with a rhodamine based sensor featuring an intramolecular deoxylactam. Org. Biomol. Chem. 9, 7652–7654 (2011)
[27] Salahuddin, S., Renaudet, O., Reymond, J.-L.: Aldehyde detection by chromogenic/fluorogenic oxime bond Fragmentation. Org. Biomol. Chem. 2, 1471–1475 (2004)
[28] Jana, N.R., Hsiao-hua, E., Ali, M., Zheng, Y., Ying, J.Y.: Controlled photostability of luminescence of nanocrytalline ZnO solution for selective detection of aldehydes. Chem. Commun. 14, 1406–1408 (2007)
[29] Mohr, G.J., Spichiger, U.E., Jona, W., Langhals, H.: Using N-Aminoperylene-3,4:9,10-tetracarboxylbisimide as a Fluorogenic Reactand in the Optical Sensing of Aqueous Propionaldehyde. Anal. Chem. 72, 1084–1087 (2000)
[30] Srinives, S., Sarkar, T., Mulchandani, A.: Primary amine-functionalized polyaniline nanothin film sensor for detecting formaldehyde. Sens. Actuators B 194, 255–259 (2014)
[31] Alizadeh, T., Soltani, L.H.: Graphene/poly(methyl methacrylate) chemiresistor sensor for formaldehyde odor sensing. J. Hazard Mater 248–249, 401–406 (2013)

[32] Mashayekhi, H.A., Rezaee, M., Garmaroudi, S.S., Montazeri, N., Ahmadi, S.J.: Rapid and Sensitive Determination of Benzaldehyde Arising from Benzyl Alcohol Used as Preservative in an Injectable Formulation Solution Using Dispersive Liquid–Liquid Microextraction Followed by Gas Chromatography. Anal. Sci. 27, 865–868 (2011)

[33] Kazemifard, A.G., Moore, D.E., Mohammadi, A., Kebriyaeezadeh, A.: Capillary gas chromatography determination of benzaldehyde arising from benzyl alcohol used as preservative in injectable formulations. Journal of Pharmaceut Biomed, 31, 685–691 (2003)

[34] Rizk, M., Ibrahim, F., Hefnawy, M., Jeehan Nasr, J.: Micellar liquid chromatographic analysis of benzyl alcohol and benzaldehyde in injectable formulations. Acta. Pharm. 57, 231–239 (2007)

[35] La Course, W.R., Krull, I.S.: Photoelectrochemical Detection of Benzaldehyde in Foodstuffs. Anal. Chem. 59, 49–53 (1987)

[36] Sensitive and Selective Formaldehyde Sensor technology profile, Advanced solid state metal oxide sensor that uses nanostructured materials for formaldehyde detection, Synkera Technologies, Inc. (April 2010), http://www.synkerainc.com

[37] Formaldehyde Gas Detector - FP-30, portable gas detectors use photoelectric photometry method with colorimetric detection tab, RKI instruments (2003), http://www.rkiinstruments.com/pages/fp30.htm

[38] Technical Note TN-128, RAE Systems Formaldehyde (HCHO) Sensor, RAE Systems, Inc., http://www.raesystems.com

[39] ab112113 Aldehyde Quantitation Kit (Colorimetric), uses a proprietary dye that generates a chromogenic product upon reacting with an aldehyde, Abcam (2012), http://www.abcam.com

[40] AppliedSensor iAQ-2000 Indoor air quality module, MEMS metal oxide semiconductor sensing technology, Applied sensors, http://www.appliedsensor.com

[41] Hosono, I., Matsubara, N., Murayama, S., Woosuck, N., Izu, N.: Synthesis of Polypyrrole/MoO3 Hybrid Thin Films and Their Volatile Organic Compound Gas-Sensing Properties. Chem. Mater. 17, 349–354 (2005)

[42] Coppedè, N., Villani, M., Mosca, R., Iannotta, S., Zappettini, A., Calestani, D.: Low Temperature Sensing Properties of a Nano Hybrid Material Based on ZnO Nanotetrapods and Titanyl Phthalocyanine. Sensors 13, 3445–3453 (2013)

[43] de Lacy Costello, B.P.J., Evans, P., Ewen, R.J., Honeybourne, C.L., Ratcliffe, N.M.: Novel composite organic-inorganic semiconductor sensors for the quantitative detection of target organic vapor. J. Mater. Chem. 6, 289–294 (1996)

[44] Carquigny, S., Redon, N., Plaisance, H., Reynaudp, S.: Development of a Polyaniline/Fluoral-P Chemical Sensor for Gaseous Formaldehyde Detection. IEEE Sensors J. 12, 1300–1306 (2012)

[45] Itoh, T., Matsubara, I., Shin, W., Izu, N.: Preparation and characterization of a layered molybdenum trioxide with poly (o-anisidine) hybrid thin film and its aldehydic gases sensing properties. Bull. Chem. Soc. Jpn. 80, 1011–1016 (2007)

[46] Itoh, T., Matsubara, I., Ck Shin, W., Izu, N., Nishibori, M.: Preparation of layered organic-inorganic nanohybrid thin films of molybdenum trioxide with polyaniline derivatives for aldehyde gas sensors of several tens ppb level. Sens. and Actuators B 128, 512–520 (2008)

[47] Lieber, C.S.: Metabolic effects of acetaldehyde. Biochem. Soc. Trans. 16, 241–247 (1998)

[48] Chen, H., Josowicz, M., Janata, J.: Chemical Effects in Organic Electronics. Chem. Mater. 16, 4728–4735 (2004)
[49] Janata, J.: Principles of Chemical Sensors, 2nd edn. Springer, New York (2009)
[50] Freund, M.S., Lewis, N.S.: A chemically diverse conducting polymer-based "electronic nose". Proc. Natl. Acad. Sci. USA 92, 2652–2656 (1995)
[51] Patel, S.V., Jenkins, M.W., Hughes, R.C., Yelton, W.G., Ricco, A.J.: Differentiation of Chemical Components in a Binary Solvent Vapor Mixture Using Carbon/ Polymer Composite-Based Chemiresistors. Anal. Chem. 72, 1532–1542 (2000)
[52] Bai, H., Shi, G.: Gas sensors based on conducting polymers. Sensors 7, 267–307 (2007)
[53] Huang, J., Virji, S., Weiller, B.H., Kaner, R.B.: Nanostructured Polyaniline Sensors. Chem. Eur. J. 10, 1314–1319 (2004)
[54] Dong, X.M., Fu, R.W., Zhang, M.Q., Zhang, B., Rong, M.Z.: Electrical resistance response of carbon black filled amorphous polymer composite sensors to organic vapors at low vapor concentrations. Carbon 42, 2551–2559 (2004)
[55] Eastman, M.P., Hughes, R.C., Yelton, G., Ricco, A.J., Patel, S.V., Jenkins, M.W.: Application of the Solubility Parameter Concept to the Design of Chemiresistor Arrays. J. Electrochem. Soc. 146, 3907–3913 (1999)
[56] Bouvree, A., Feller, J.F., Castroa, M., Grohens, Y., Rinaudo, M.: Conductive Polymer nano-bioComposites (CPC): Chitosan-carbon nanoparticles a good candidate to design polar vapor sensors. Sens. Actuators B 138, 138–147 (2009)
[57] Zilberman, Y., Tisch, U., Shuster, G., Pisula, W., Feng, X., Mullen, K., Haick, H.: Carbon nanotube/hexa-peri-hexabenzocoronene bilayers for discrimination between nonpolar volatile organic compounds of cancer and humid atmospheres. Adv. Mater. 22, 4317–4320 (2010)
[58] Grate, J.W., Abraham, M.H.: Solubility interactions and the design of chemically selective sorbent coatings for chemical sensors and arrays. Sens. Actuators B 3, 85–111 (1991)
[59] Albert, K.J., Lewis, N.S., Schauer, C.L., Sotzing, G.A., Stitzel, S.E., Vaid, T.P., Walt, D.R.: Cross-Reactive Chemical Sensor Arrays. Chem. Rev. 100, 2595–2626 (2000)
[60] Ogura, K., Fujii, A., Shiigi, H., Nakayama, M., Tonosaki, T.: Effect of Hygroscopicity of Insulating Unit of Polymer Composites on Their Response to Relative Humidity. J. Electrochem Society 147, 1105–1109 (2000)
[61] Pfeifer, K.B., Hughes, R.C., Jenkins, M.W., Schneider, T.W.: Viologen Polymer-Coated Impedance Sensors for Midrange Humidity Levels and Other Volatile Organic Compounds. J. Electrochem. Soc. 146, 794–799 (1999)
[62] Venedam, R., Eastman, M.P., Wheeler, B.L., McClellan, C., Coulliette, C., Eastman, N.L.: The Effect of Water Vapor on the AC Impedance of Thin Films of Hectorite. J. Electrochem. Soc. 138, 1709–1712 (1991)
[63] Ramamurthy, P.C., Amadio, B.S.: Robust low resistance vapor sensor materials, U. S. Patent 8,012,420 (2011)
[64] West, J.A., Ramamurthy, P.C: U.S. Patent Methods of Minimizing Temperature Cross-Sensitivity In Vapor Sensors and Compositions Thereof" US patent # US 2007/0095678 (A1) (2007)
[65] Hwang, B.J., Yang, J.Y., Lin, C.W.: Recognition of alcohol vapor molecules by simultaneous measurements of resistance changes on polypyrrole-based composite thin films and mass changes on a piezoelectric crystal. Sens. Actuators B 75, 67–75 (2001)
[66] Khadkikar, P., Ramamurthy, P. C., Zimmermann, B.: Capacitive Vapor Sensor, US patent # US7421883, US 2007/0131021 (A1) (2007)

[67] Blok, E., Ramamurthy, P.C, Starling, J., Amadio, B.: U.S. Patent "Vapor Sensor and Materials Thereof" US patent # US20060292033 (A1) {US7645422 (B2)} 2006, European patent # EP1895293 (A2) 2008 and (A3) 2009, Japanese patent # JP2008051795, Mexican patent # MX2007004752 (A), Chinese patent # CN101135660 (A), Canadian patent # CA2583632 (A1), Australian patent # AU2007201456 (A1)
[68] Ramamurthy, P.C: U.S. Patent, Vapor Sensor Materials Having Polymer-Grafted Conductive Particles US patent # US2008025876 (A1) (2008)
[69] Ramamurthy, P.C.: Single use flammable vapor sensor films, U. S. 2009/0130421 A1 (2009)
[70] Lei, H., Pitt, W.G., McGrath, L.K., Ho, C.K.: Modeling carbon black/polymer composite sensors. Sens. Actuators B 125, 396–407 (2007)
[71] Lonergan, M.C., Severin, E.J., Doleman, B.J., Beaber, S.A., Grubb, R.H., Lewis, N.S.: Array-based vapor sensing using chemically sensitive, carbon black–polymer resistors. Chem. Mater. 8, 2298–2312 (1996)
[72] Lodha, A., Kilbey II, S.M., Ramamurthy, P.C., Gregory, R.V.: Effect of Annealing on Electrical Conductivity and Morphology of Polyaniline Films. J. Appl. Polym. Sci. 82, 3602–3610 (2001)
[73] Geckeler, K.E., Arsalani, N., Rivas, B.L.: Synthesis and properties of hydrophilic polymers, 6. Water-soluble poly(pyrrole) graft copolymers with electrical conductivity. Macromol. Rapid Commun. 18, 503–508 (1997)
[74] Obrzut, J., Page, K.A.: Electrical conductivity and relaxation in poly(3-hexylthiophene). Physical Review B 80, 195211(1-7) (2009)
[75] Arshak, K., Moore, E., Lyons, G.M., Harris, J., Clifford, S.: A review of gas sensors employed in electronic nose applications. Sensor Review 24, 181–198 (2004)
[76] Gardner, J.W., Bartlett, P.N.: A brief history of electronic noses. Sens. Actuators B 18-19, 211–220 (1994)
[77] Shevade, A.V., Ryan, M.A., Homer, M.L., Manfreda, A.M., Zhou, H., Manatt, K.S.: Molecular modeling of polymer composite–analyte interactions in electronic nose sensors. Sens. Actuators B 93, 84–91 (2003)
[78] Belmares, M., Blanco, M., Goddard III, W.A., Ross, R.B., Caldwell, G., Chou, S.H., Pham, J., Olofson, P.M., Thomas, C.: Hildebrand and Hansen Solubility Parameters from Molecular Dynamics with Applications to Electronic Nose Polymer Sensors. J. Comput. Chemistry 25, 1814–1826 (2004)
[79] Misra, S., Fleming III, P.D., Mattice, W.L.: Structure and energy of the thin films of poly (1,4 cis butadiene): A new atomistic approach. J. Comput.-Aided Mater. Des. 2, 101–112 (1995)
[80] Materials Studio v6.0.0, San Diego: Accelrys Software Inc., http://accelrys.com/products/materials-studio/index.html
[81] Suknuntha, K., Tantishaiyakul, V., Soongnern, V.V., Espidel, Y., Cosgrove, T.: Molecular Modeling simulation and experimental Measurements to characterize chitosan and poly (vinyl pyrrolidone) blend interactions. Journal of Polymer Science, Part B, Polymer Physic 46, 1258–1264 (2008)
[82] Tunga, K., Lua, K., Ruaanb, R., Laia, J.: Molecular dynamics study of the effect of solvent types on the dynamic properties of polymer chains in solution. Desalination 192, 380–390 (2006)
[83] Gestoso, P., Brisson, J.: Investigation of the effect of chain rigidity on orientation of polymer blends: The case of poly (vinyl phenol)/poly (ethylene terephthalate) blends. Polymer 44, 7765–7776 (2003)

Noncontact Temperature Profiling of Rotating Cylinder by Laser-Ultrasound

I. Ihara*, Y. Ono, A. Kosugi, and I. Matsuya

Department of Mechanical Engineering, Nagaoka University of Technology,
Nagaoka, Niigata 940-2188, Japan
ihara@mech.nagaokaut.ac.jp

Abstract. In the fields of engineering and manufacturing industries, it is often required to know quantitative information about surface and internal temperatures of rotating objects. In this work, a new ultrasonic method for measuring such temperatures of a heated rotating cylinder is presented. A laser-ultrasonic technique which provides noncontact ultrasonic measurements is employed in the present method. To make a quantitative evaluation of the internal temperature distribution in the radial direction of a heated rotating cylinder having axisymmetric temperature distribution, an effective method consisting of surface temperature measurements with a laser-ultrasonic technique and one-dimensional unsteady heat conduction analyses with a finite difference calculation is developed. To demonstrate the feasibility of the method, experiments with heated steel cylinders of 100 mm and 30 mm in diameter rotating at 300 min^{-1} are conducted. A pulsed laser generator and a laser Doppler vibrometer are used for generating and detecting surface acoustic waves (SAWs) on the steel cylinder, respectively. Measured SAWs are used for determining both surface and internal temperatures of the cylinder. The estimated temperature distributions during heating almost agree with those measured by an infrared radiation camera. Thus, it has been shown that the noncontact temperature measurement technique with laser ultrasound is a promising tool for on-line monitoring of heated rotating cylinders.

Keywords: Laser ultrasound, Ultrasonic thermometry, Temperature distribution, Noncontact measurement, Rotating cylinder, *In situ* measurement, Finite different calculation.

1 Introduction

It has been known that material properties such as mechanical, electrical, and chemical characteristics are closely related to temperature and often show a strong temperature dependence of the properties. Therefore, measuring temperature and understanding its deviation comprehensively are important issues in a basic

* Corresponding author.

A. Mason et al. (eds.), *Sensing Technology: Current Status and Future Trends III*,
Smart Sensors, Measurement and Instrumentation 11, DOI: 10.1007/978-3-319-10948-0_16

research, development and fabrication of advanced materials and related products. In particular, for manufacturing processes such as machining or welding in industries, it is strongly required to monitor the temperature distribution and its transient variation of the work piece or working tool during the processing at high temperatures because the temperature state in material crucially influences the quality and productivity of final products. Thus, real-time or in-process monitoring technique for temperature distributions could be quite beneficial not only for a basic research of materials processing but also for realizing an effective quality control of manufacturing systems.

Ultrasound, because of its high sensitivity to temperature, is expected to be a potential candidate for temperature measurements. Since there are some advantages in ultrasonic measurements, such as non-invasive and faster time response, several studies on the temperature estimations by ultrasound have been made [1-7]. In our previous works [8-11], ultrasonic methods for measuring internal temperature distributions of heated materials were developed and applied to internal temperature profiling of heated materials. Furthermore, it is successfully demonstrated that the use of surface acoustic waves (SAWs) propagating on a material surface provides effective surface temperature measurements [12-13]. It is also noted that noncontact methods with a laser-ultrasonic technique [12-14] can be useful for measuring not only SAWs but also bulk waves such as longitudinal or shear waves for heated materials. Thus, it is quite attractive and highly expected to apply the laser-ultrasonic technique to some practical uses such as temperature profiling of materials under processing or machining.

In several fields of engineering and manufacturing industries, it is often required to make condition and/or health monitoring of rotating objects such as rotors of motors or turbines, and rotating machining tools. In such rotating cylinders, quantitative information about surface and internal temperatures of the cylinders are very important and indispensable to know because they are closely related to the strength or structural integrity of the cylinders. It is therefore required to realize “online monitoring” of such temperatures of the rotating cylinders. The laser-ultrasonic technique mentioned above may be a potential candidate for the temperature monitoring. Fig. 1 shows a schematic of the application of a laser-ultrasonic technique to noncontact temperature monitoring of a friction stir welding (FSW) which is well known as a solid-state joining process. In this welding a rotating FSW tool is plunged between two clamped plates and the frictional heat causes a plasticized zone to form around the tool. The rotating tool moves along the joint line so that a consolidated solid-phase joint can be formed [15]. In order to improve the quality of the joint, temperature distributions of the rotating tool as well as the plasticized zone during joining process is necessary to know because the temperature distributions around friction zone which is a superheated region play an important role to dominate weld quality. However, it is very difficult to measure such temperatures of the rotating tool using any conventional measurement techniques such as thermocouples or infrared radiation methods. Although infrared radiation method enables

noncontact measurements of the surface temperatures of the tool, it does not allow internal temperature measurements. In addition, accurate measurements with infrared radiation are often hindered by the different emissivity and reflection of infrared radiation from other heat sources. It is noted that similar problems in temperature measurements are also found in not only FSW process but also other machining processes such as tuning and milling. Therefore, it is quite beneficial to develop an effective temperature monitoring technique for such rotating objects. It is proposed in Fig. 1 that a laser ultrasound is employed to measure ultrasonic waves in the rotating tool so that temperature distributions inside the tool and its transient variation could be monitored during processing. In this work, we have applied a laser-ultrasonic technique to a heated rotating cylinder to demonstrate the feasibility of non-contact temperature monitoring of rotating objects.

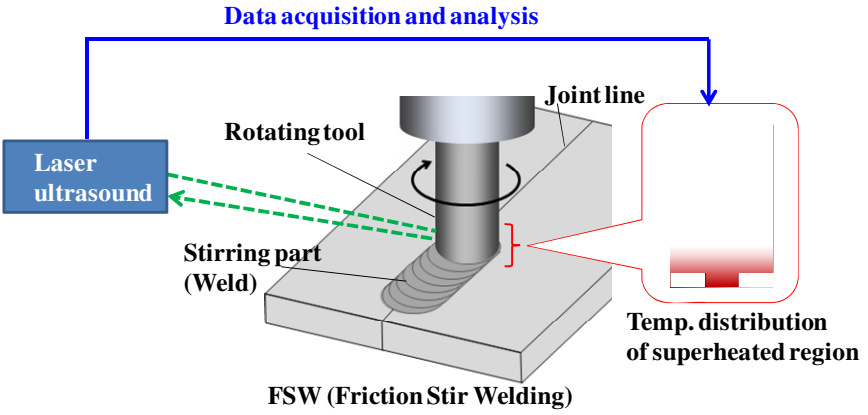

Fig. 1 A schematic showing an application of laser-ultrasonic technique to online non-contact temperature measurements inside the rotating tool during friction stir welding (FSW) process

2 Determination of Temperature Distribution of Cylinder by Ultrasound

The principle of temperature determination by ultrasound is based on the temperature dependence of ultrasonic wave velocity, in which the velocity of an ultrasonic wave propagating through a material changes with the temperature of the material [9-14]. To determine the temperature distributions inside a cylinder quantitatively, an effective method consisting of surface acoustic wave (SAW) measurements by laser-ultrasonic technique and unsteady heat conduction analyses has been developed.

Fig. 2 shows a schematic of the cross section of a cylinder that is uniformly heated at the whole circumference. Assuming that (i) there is no heat source inside the cylinder, (ii) the cylinder has an axisymmetric temperature distribution which

means no temperature distribution in the circumferential direction, and (iii) there is no temperature distribution in the axial direction of the cylinder, one-dimensional unsteady heat conduction equation in the radial direction of the cylinder is given by [16]

$$\frac{\partial T}{\partial t} = \alpha\left(\frac{\partial^2 T}{\partial r^2} + \frac{1}{r}\frac{\partial T}{\partial r}\right), \tag{1}$$

where cylindrical coordinate system is employed, α is thermal diffusivity coefficient, T is temperature, t is elapsed time after heating starts, and r is the radius at an arbitrary position in the cross section. The temperature distribution in the radial direction can be estimated by solving (1) under a certain boundary condition. In actual heating process, however, the thermal boundary condition at the outer surface is often unstable and unknown. Therefore, it is difficult to determine the temperature distribution from (1) without the boundary condition at the outer surface. To overcome such problem, ultrasonic measurements are utilized for obtaining the boundary condition, i.e., the SAW velocity on the cylinder is measured and the surface temperature of the outer surface is then determined based on the temperature dependence of the SAW velocity. Since this surface temperature can be utilized as the boundary condition, the internal temperature distribution in the radial direction is then determined from heat conduction analysis. In this work, a one-dimensional finite difference model composed of large numbers of small elements and grids as shown in Fig. 2 is used for analyzing the temperature distribution in the radial direction of the cylinder. In the analysis, the temperature distribution before heating starts is given as an initial condition. Considering that the heating at the outer surface is started at a time step n=0, the temperature of each grid point inside the cylinder at time step n+1 (that is a very short elapsed time after heating starts) can be given by [16]

$$T_i^{n+1} = T_i^n + R\left\{\left(1+\frac{1}{2i}\right)T_{i+1}^n + \left(1-\frac{1}{2i}\right)T_{i-1}^n - 2T_i^n\right\} \quad (i = 1 \sim N-1) \tag{2}$$

$$T_0^{n+1} = T_0^n + 4R(T_1^n - T_0^n), \tag{3}$$

$$R = \frac{\alpha\tau}{h^2}, \tag{4}$$

where N is the number of the grid point, i and n are indices corresponding to spatial coordinate and consecutive time, respectively. T_i^n is the temperature of each grid point i at time step n. The coefficient R is called "the Von Neumann stability criterion" and should be taken to be less than 0.5 to be able to obtain appropriate and stable solutions in the finite difference analysis. τ is the time step and h is the spatial interval between the grid points. We define i=0 as the center of the cylinder and i=N as the outer surface. Since we can calculate the temperatures T_i^{n+1} (i=0, ···, N-1) from (2), (3) and (4), it is now required to know the

temperatures at the outer surface, T_N^{n+1}, so that the temperature distribution in the radial direction of the cylinder could be fully determined. When the SAW propagating on the cylinder is precisely measured, the T_N^{n+1} can be determined by

$$T_N^{n+1} = \frac{L - b\, t_{SAW}}{a\, t_{SAW}}, \tag{5}$$

where L is the propagation distance of the SAW, t_{SAW} is the transit time of the SAW propagating through the distance L, and a and b are coefficients of the temperature dependence of the SAW velocity of the cylinder shown in the following equation,

$$v_{SAW}(T) = aT + b \ . \tag{6}$$

It should be noted that the temperature dependence can be expressed as a linear equation when the temperature variation is limited in a certain range [10-13]. The two constants a and b are determined experimentally in the range from 20 °C to 100 °C. Thus, the temperature distribution in the radial direction of the heated

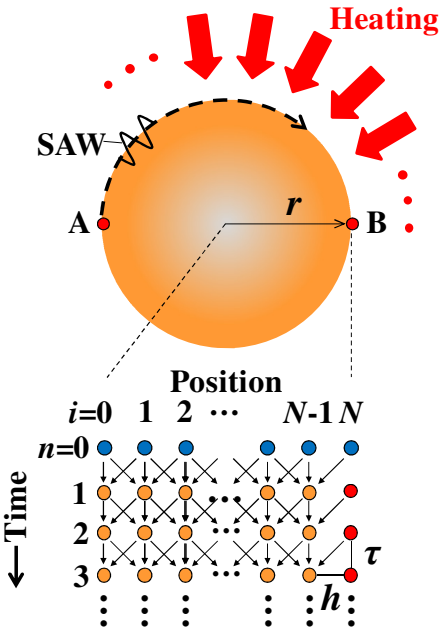

Fig. 2 A model used for estimating the temperature distribution in radial direction of a cylinder: a heated cylinder with an axisymmetric temperature distribution (upper) and a schematic of staggered grids for a one-dimensional finite difference calculation for determining the internal temperature distribution in radial direction of the cylinder and its time progress (lower)

cylinder can be determined at a certain time step just after heating starts. Once we obtain the temperature distribution at the initial stage, the temporal variation of the temperature distribution with time step can be obtained in the same way, as long as the SAW measurements on the cylinder surface are continuously being performed. Fig. 3 shows the flaw chart of determining the temperature distribution.

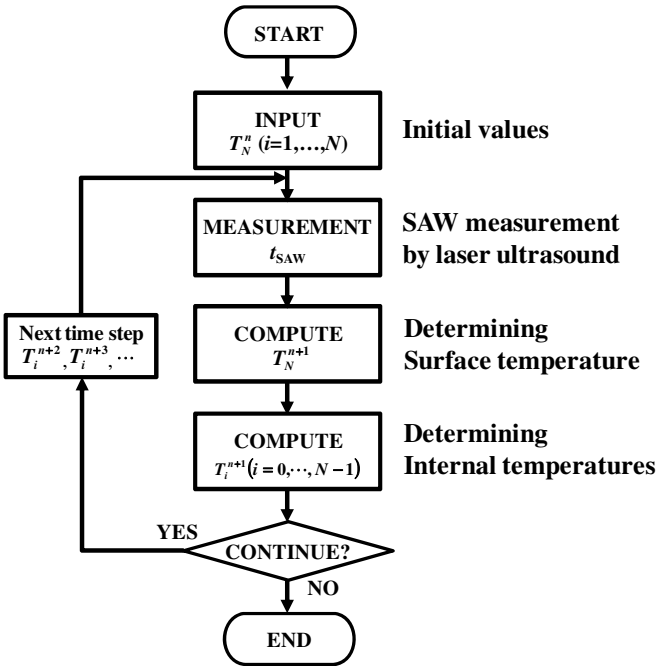

Fig. 3 Flaw chart of determining temperature distribution

3 Experimental Setup

Fig. 4 shows a schematic of noncontact ultrasonic measurements using a laser-ultrasonic technique. When a pulsed laser is irradiated onto a cylinder surface, surface acoustic wave (SAW) is generated by ablation and/or thermo-elastic effect due to the laser irradiation. The SAW propagates along the circumference of the cylinder and is then measured by a laser Doppler vibrometer. Thus, SAWs on the cylinder can be measured non-contactly.

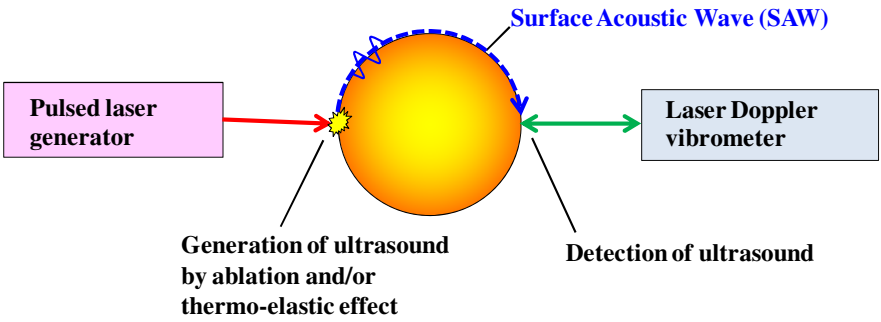

Fig. 4 A schematic showing non-contact ultrasonic measurements using a laser-ultrasonic technique

To demonstrate the feasibility of the proposed method, surface and internal temperatures in a rotating steel cylinder (diameter: 100 mm, rotating speed: 300 min^{-1}) heated up to around 100 ^{o}C on the surface are evaluated during heating. Fig. 5 shows a schematic of the experimental setup. The surface of the rotating cylinder is heated using a gas burner and SAWs propagating along the circumference of the cylinder are measured using a laser ultrasonic system consisting of a pulsed laser generator (Nd:YAG, Q-switch pulse, wavelength 1064 nm, energy 180 mJ/pulse, pulse width 3 ns, from Vossa Nova Technology Co.) and a laser Doppler vibrometer (He-Ne, CW, wavelength 633 nm, power <1 mW, from Polytec Inc.), where the laser generator and Doppler vibrometer are used for generating and detecting SAWs, respectively. The distance between the pulsed laser generator and the cylinder is approximately 300 mm and the distance between the Doppler vibrometer and the cylinder is approximately 500 mm. The center frequency of the SAWs is about 2 MHz. The SAWs are continuously acquired every 0.2 s with a PC based real-time acquisition system with sampling rate of 100 MHz. The transit time of each SAW is precisely determined by taking the cross correlation of the detected signal of SAW during heating, and then used for the analysis to determine both the surface and internal temperature distribution of the cylinder. The temperature distributions of the side surface of the cylinder during the heating are also measured using an infrared radiation camera to make a comparison with those estimated by the ultrasonic method. Fig. 6 shows the photos of a pulsed laser generator and laser Doppler vibrometer used.

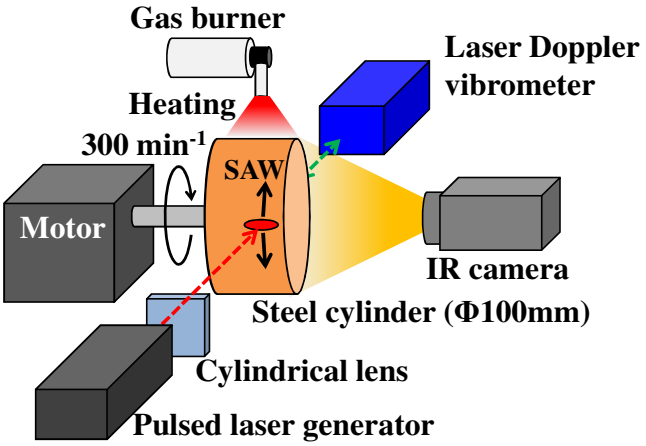

Fig. 5 A schematic of the experimental setup for measuring SAWs on a rotating cylinder by a laser-ultrasonic technique

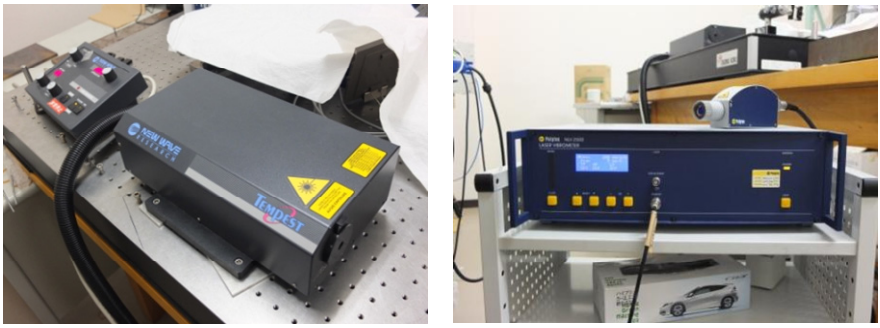

Fig. 6 External views of the pulsed laser generator (left) and laser Doppler vibrometer used (right)

4 Results

Fig. 7 shows a schematic layout of SAW generation and detection on the cylinder by lasers (left) and measured SAW signals on the cylinder during rotating (right). Two SAWs, SAW A and SAW B are simultaneously generated by the pulsed laser irradiation and propagate along the cylinder surface as shown in the left side of Fig. 7. We can see two distinct echoes, SAW A and SAW B in Fig. 7 (right). The detection of SAW A is earlier than that of SAW B because of the SAW generation-detection configuration of the laser ultrasound measurements as shown in Fig. 7 (left). It is obvious that the sum of the transit times t_A for SAW A and t_B for SAW B is exactly the transit time of SAW around the cylinder in the

circumferential direction. The transit time of each SAW is precisely determined by taking the cross correlation of the detected signal and the sum of each transit time is used for the analysis to determine both the surface and internal temperature distribution of the cylinder.

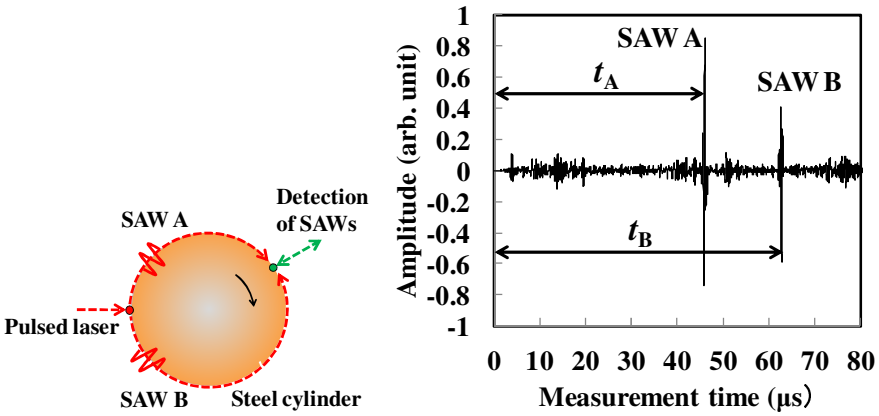

Fig. 7 Schematic layout of SAW generation and detection on the cylinder by lasers (left) and measured SAW signals on the cylinder during rotating (right)

Fig. 8 shows variations in the transit time of the SAW and estimated surface temperature with elapsed time after heating starts. As expected, the transit time of SAW rapidly increases with the elapsed measurement immediately after the heating starts. Surface temperature of the cylinder is then determined from (5) and used for estimating internal temperature distribution of the cylinder from (2), (3) and (4).

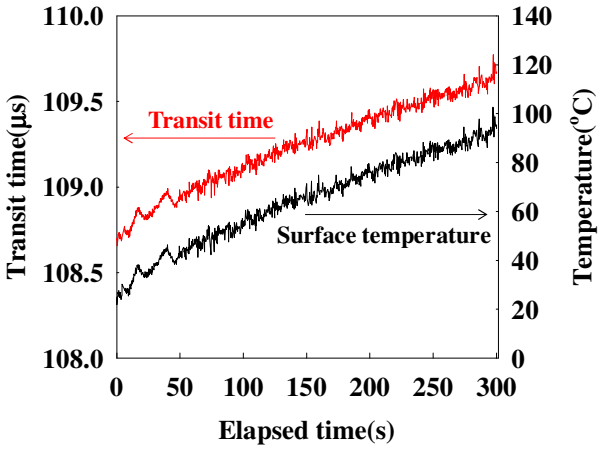

Fig. 8 Variations in the transit time of the SAW and estimated surface temperature with elapsed time after heating starts

As mentioned in Section 2, the temperature dependence of the SAW plays an important role in determining surface temperature and therefore, it is necessary to obtain quantitative information of the temperature dependence of the cylinder. Fig. 9 shows the measured result of the relationship between the SAW velocity and temperature of the steel cylinder used. It is seen that the relationship between them is almost linear. The temperature dependence is found approximately to be v_{SAW} = - 0.3883T + 3092.1 (m/s) and is used for estimating surface temperature.

Fig. 10 shows the estimated temperature distribution of the steel cylinder and its variation with the elapsed time after heating starts, where the ultrasonically estimated results (solid circles) by the present method are compared with those measured using the infrared radiation camera (lines). Because the outer surface of the cylinder is uniformly being heated during rotating, the temperature is highest at the outer surface and gradually decreases from the surface towards the center. It can be seen that both temperature distributions determined by the ultrasound and the infrared radiation agree well with each other. Thus, it has been found that the ultrasonic method does work properly to monitor the temperature distribution of a rotating cylinder. Fig. 11 shows the internal temperature distribution images estimated from the experimental results shown in Fig. 10.

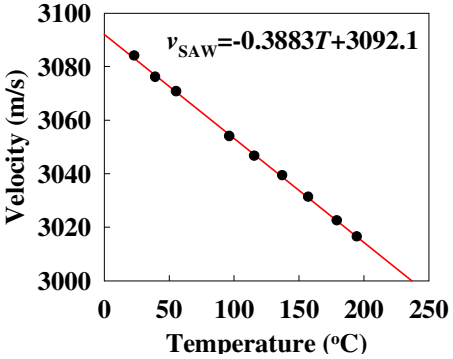

Fig. 9 Temperature dependence of SAW velocity for the steel cylinder

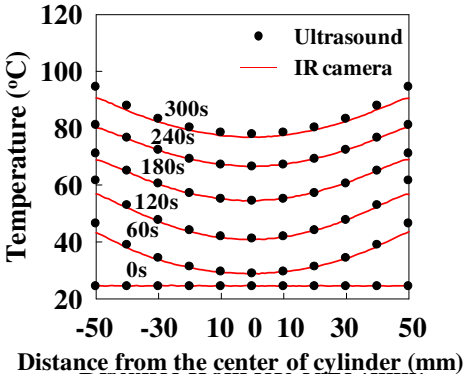

Fig. 10 Variations in the internal temperature distributions of the rotating steel cylinder with the elapsed time after heating starts

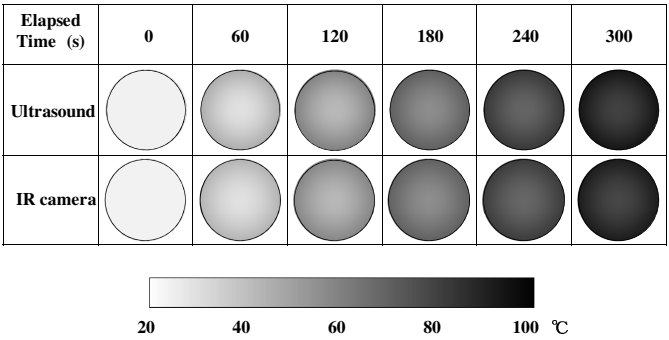

Fig. 11 Comparison of internal temperature distribution images estimated by the proposed ultrasonic method (upper) and a conventional infrared radiation camera (lower)

In the ultrasonic method, it is also important to understand the influence of the circumferential speed of the rotating cylinder on the error in the estimated temperature. Fig. 12 shows the relationship between the systematic error in the ultrasonically estimated surface temperatures and the circumference speed of the cylinder. The systematic error is estimated based on geometrical consideration of the rotating cylinder. As expected intuitively, the systematic error almost linearly increases with the rotating speed. It is noted from the Fig. 12 that the systematic error due to the rotation in the present experiment is found to be approximately 0.9 ^{o}C while the circumferential speed is approximately 1.7 m/s. It is also noted that another factor influencing the error in the estimated temperature in the method is thermal expansion of the cylinder during heating. It is numerically estimated considering temperature rise during heating that the systematic error due to the thermal expansion in the present experiment is to be approximately a few degrees Celsius.

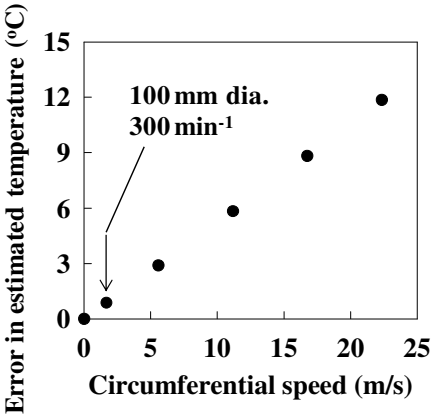

Fig. 12 Relationship between the error in the ultrasonically estimated surface temperatures and the circumference speed of the cylinder

A similar experiment with a steel cylinder of 30 mm in diameter has been performed. The same laser-ultrasonic technique has been applied to the heated cylinder rotating at 300 min^{-1}. Fig. 13 shows the estimated temperature distribution of the steel cylinder and its variation with the elapsed time after heating starts, where solid circles denote the ultrasonically estimated results and solid lines are interpolation. The temperature distribution and its variation for the 30 mm cylinder are similar to those for 100 mm cylinder shown in Fig. 10. It is interesting that the present ultrasonic method can successfully monitor rapid change in temperature distribution within 1 s just after heating started. The obtained result reveals that the present thermometry with the laser ultrasonic technique is a promising method for monitoring transient variations in temperature during material processes.

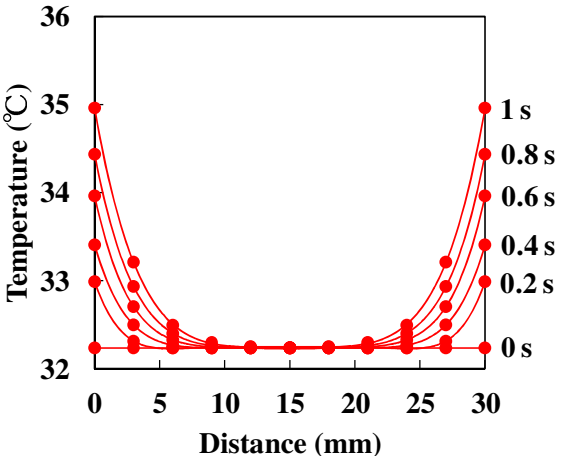

Fig. 13 Variation in the internal temperature distribution of the rotating steel cylinder of 30 mm in diameter within 1 s just after heating starts

5 Conclusions

A new ultrasonic method for noncontact monitoring of temperature distributions of a heated rotating cylinder is presented and its feasibility is successfully demonstrated through an experiment with rotating steel cylinders. One of the advantages of the present method, so-called ultrasonic thermometry, is that not only surface temperatures but also internal temperatures can noninvasively be profiled. It should be noted that internal temperature profiles are easily monitored if bulk waves such as longitudinal waves instead of SAWs are effectively employed. Although further study is necessary to improve the practicability and robustness in the method, it is highly expected that the ultrasonic method could be a useful means for online temperature monitoring of machining processes at high temperatures such as FSW, tuning, milling and drilling processes. There are

ongoing attempts by the authors to make noncontact temperature profiling of other types of a moving or rotating objectives at elevated temperatures. The demonstrative results will be reported soon.

Acknowledgements. This work is supported by JSPS KAKENHI Grants (B25289238) and Toyota Motor Co.

References

[1] Chen, T.-F., Nguyen, K.-T., Wen, S.-S., Jen, C.-K.: Temperature measurement of polymer extrusion by ultrasonic techniques. Meas. Sci. Technol. 10, 139–145 (1999)
[2] Balasubramainiam, K., Shah, V.V., Costley, R.D., Boudreaux, G., Singh, J.P.: High temperature ultrasonic sensor for the simultaneous measurement of viscosity and temperature of melts. Rev. Sci. Instrum. 70-12, 4618–4623 (1999)
[3] Tsai, W.-Y., Chen, H.-C., Liao, T.-L.: An ultrasonic air temperature measurement system with self-correction function for humidity. Meas. Sci. Technol. 16, 548–555 (2005)
[4] Mizutani, K., Kawabe, S., Saito, I., Masuyama, H.: Measurement of temperature distribution using acoustic reflector. Jpn. J. Appl. Phys. 45-5B, 4516–4520 (2006)
[5] Degertekin, F.L., Pei, J., Khuri-Yakub, B.T., Saraswat, K.C.: In-situ acoustic temperature tomography of semiconductor wafers. Appl. Phys. Lett. 64, 1040–1338 (1994)
[6] Huang, K.N., Huang, C.F., Li, Y.C., Young, M.S.: High precision fast ultrasonic thermometer based on measurement of the speed of sound in air. Rev. Sci. Instrum. 11, 4022–4027 (2002)
[7] Simon, C., Van Baren, P., Ebbini, E.: Two-dimensional temperature estimation using diagnostic ultrasound. IEEE Trans. on Ultrason. Ferroelectr. Freq. Control 45(4), 1088–1099 (1998)
[8] Takahashi, M., Ihara, I.: Ultrasonic Monitoring of Internal Temperature Distribution in a Heated Material. Jpn. J. App. Phys. 47, 3894–3898 (2008)
[9] Takahashi, M., Ihara, I.: Ultrasonic determination of temperature distribution in thick plates during single sided heating. Modern Physics Letters B 22-11, 971–976 (2008)
[10] Ihara, I., Takahashi, M.: Non-invasive Monitoring of Temperature Distribution inside Materials with Ultrasound Inversion Method. Int. J. Intelligent Systems Technologies and Applications 7-1, 80–91 (2009)
[11] Ihara, I., Tomomatsu, T.: In-Situ Measurement of Internal Temperature Distribution of Sintered Materials Using Ultrasonic Technique. IOP Conf. Series: Materials Science and Engineering 18, 22008 (2011)
[12] Takahashi, M., Ihara, I.: Quantitative evaluation of one-dimensional temperature distribution on material surface using surface acoustic wave. Jpn. J. App. Phys. 48, GB04-1-5 (2009)
[13] Yamada, H., Kosugi, A., Ihara, I.: Non-contact monitoring of surface temperature distribution by laser ultrasound scanning. Jpn. J. App. Phys. 50, 07HC06-1-5 (2011)
[14] Kosugi, A., Ihara, I., Matsuya, I.: Accuracy Evaluation of Surface Temperature Profiling by a Laser Ultrasonic Method. Jpn. J. App. Phys. 51, 07GB01-1-8 (2012)
[15] Dawes, C., et al.: An introduction of friction stir welding and its development, pp. 13–16. Welding & Metal Fabrication (January 1995)
[16] Ozisik, M.N.: Boundary Value Problems of Heat Conduction, p. 412. Dover Publications, New York (1989)

Modelling of Sensing Performance of Electrostrictive Capacitive Sensors

O.P. Thakur and Nidhi Agrawal*

School of Applied Sciences,
Netaji Subhas Institute of Technology, Sector 3, Dwarka,
New Delhi-110078, India
opthakur@yahoo.com, itznidhi@gmail.com

Abstract. Electrostriction is the quadratic coupling between the strain developed in a material and the electric field applied, while piezoelectricity is a linear coupling mechanism existing in a material without center of symmetry. Electrostrictive capacitive sensors have many advantages over vacuum or air gap capacitive sensors. Electrostrictive materials show reproducible, non-hysteric and tunable strain response. Electrostrictive dielectric material sandwiched between two electrodes in a capacitive sensor plays a very important role in performance of the sensor. The dielectric material to be selected is required to possess good electromechanical properties like high strain, high permittivity, good breakdown strength etc.

Standard equations are available for calculation of electrically induced strain in dielectric material and researchers have simplified the standard equation for calculation of electrically induced strain in dielectric material of the sensor. Simplification of equations for six different materials has been analyzed. In case of one simplified equation, error has been found in the range of underestimation from 96% to 3273% and in case of other equation, range of error is from underestimation of 36% to overestimation of 1842%. These errors occur because researchers have neglected many parameters like edge effect, contribution from lateral stress etc., while simplifying these equations.

Electrostrictive dielectric materials have good electromechanical properties for various applications including sensors, but to further enhance properties like permittivity, tensile strength etc. of the dielectric material used in the sensor, nano fillers are incorporated into the dielectric material. In this work, study has been done on two filler materials, TiO_2 and ZnO and it is found that the increase in permittivity is more in the materials filled with TiO_2 in comparison to ZnO filled materials for same level of filler concentration.

Keywords: electrostrictive capacitive sensor, dielectric material, strain, permittivity.

* Corresponding author.

A. Mason et al. (eds.), *Sensing Technology: Current Status and Future Trends III*,
Smart Sensors, Measurement and Instrumentation 11, DOI: 10.1007/978-3-319-10948-0_17

1 Introduction

When electrostatic field is applied to an isotropic dielectric, stresses and strains are induced in the dielectric. Stresses are induced by the Maxwell Stress effect and strains are induced due to electrostriction phenomenon [1].

Electrostriction is the process of variation of dielectric constant of the material with electrically induced strain on the application of external electric field. It is commonly treated as a fourth-rank tensor of electrostrictive coefficients which links the strain tensor to the electric field E. Electrostrictive dielectric materials have many advantages over other dielectric materials like their dielectric constant also changes with strain making them ideal for sensors and hence, are preferred while designing capacitive sensors.

For designing an efficient capacitive sensor, correct mathematical modelling of sensing equation is very important. Two different models of these equations are well known, but errors have been found in these models and reasons for these errors have also been highlighted in present study.

The dielectric material selected for sensors should have good electrical, mechanical, optical etc. properties depending on the application where it has to be used. In our study, we have studied six different materials and found the best electrostrictive material out of them.

Electrostrictive dielectric materials are incorporated with filler materials for getting desired properties. Nano fillers enhance the properties of the dielectric material and thus, improve sensor's response. Interfacial zones formed around nano fillers are responsible for getting desired properties of the material.

2 Electrostrictive Materials – Background

Primary electromechanical coupling mechanism present in centric crystals and amorphous solids is called electrostriction since early 20th century [2]. It is defined as the quadratic coupling between electrically induced strain (x) and electric field (E). It is a fourth-rank tensor represented by the following relationship:

$X_{ij} = M_{ijmn} E_m E_n$, where, X_{ij} is the strain tensor, E_m and E_n components of the electric field vector, and M_{ijmn} the fourth-rank field related electrostriction tensor. The M coefficients are defined in units of m^2 / V^2.

Piezoelectricity is a linear coupling mechanism which is found only in materials without a center of symmetry. The non-centro symmetric point groups generally exhibit piezoelectric effects which are larger in magnitude than the electrostrictive effects.

Electric and elastic properties of the material are assumed to be isotropic in unstrained state. On application of electric field, the variation in permittivity is dependent on components of strain and as a result, the material becomes

anisotropic electrically. In static equilibrium, the elastic forces induced during deformation will balance the mechanical forces induced by the static field. Relation between the mechanical stress (T_{ij}) and strain (S_{ij}) is governed by Hooke's law.

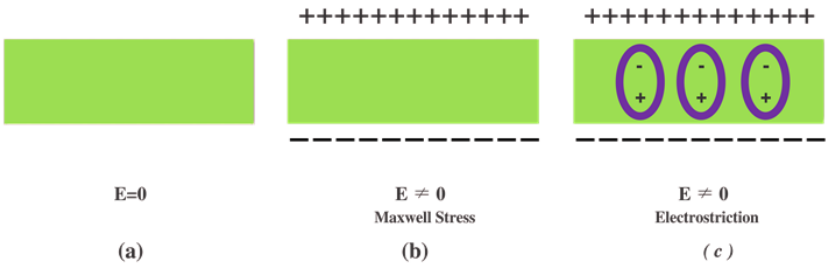

Fig. 1 Schematic diagram showing (a) pure linear elastic film (b) Maxwell stress produced by surface charge (c) electrostriction stress developed due to alignment of dipoles [3]

After application of external field, material gets deformed under Maxwell stress and electrostriction; and deformed body becomes anisotropic resulting into tensor form of dielectric constant as given below

$$\varepsilon_{ij} = \varepsilon^0 \delta_{ij} + a_1 S_{ij} + a_2 S_{kk} \delta_{ij}, \tag{1}$$

where,

ε^0 is the permittivity of undeformed body and

a_1 and a_2 are two parameters describing the variation in dielectric properties of the material in shear and bulk deformation respectively,

S_{ij} is the strain tensor,

δ_{ij} is the kronecker delta function.

For linear and anisotropic dielectric with small deformation, the variation in dielectric tensor ε_{ij} is given as

$$\delta\varepsilon_{ij} = \sum_{k=1}^{3}\sum_{l=1}^{3} a_{ijkl}\delta S_{kl}, \tag{2}$$

and the coefficients,

$$a_{ijkl} = \frac{\partial \varepsilon_{ij}}{\partial S_{kl}}$$

Eq. (2) represents a tensor of rank four and the characteristic of dielectrics, and also has different values at different points in an inhomogeneous dielectric medium. However, all but two classes of coefficients are approximated to zero, namely the body strains coefficients a_{iiii} and a_{iijj} and the shearing strain coefficients a_{ijij}.

If the elastic polymer is not electrostrictive, a_1 and a_2 vanish, indicating that dielectric constant is independent of deformation and only Maxwell stress exists. In eq. (1), Maxwell stress effect along with electrostriction is considered by introducing a_1 and a_2 [4].

Electromechanical phenomena have been observed in several macroscopic systems like polycrystalline ceramics, ceramic polymer composites, several organic polymers, biopolymers, single crystal, system with liquid component etc.

Dielectric elastomers are long chain soft polymers. They convert electrical energy into mechanical energy when subjected to high voltage. They find application in robotics, prosthetic devices, medical implants, pumps and valves, sensors and actuators etc. A linear electromechanical effect does not exist in case of elastomers and the Hooke's law based on thermodynamics consideration (Helmholtz free energy and Gibbs free energy concept) should not be applied for elastomers up to a large extent due to their nonlinear elastic behavior.

When external voltage is applied, dielectric elastomer membrane becomes thinner and expands in area due to electro-stress. A dielectric can be polar or non-polar. Non polar dielectric in absence of electric field show electro-stress due to Maxwell stress and electrostriction where electrostriction is change of dielectric constant and this change can vary from 2 to 6. Maxwell stress occurs when charges accumulate on both sides of electrode surfaces. Opposite charges attract each other and form a stress in vertical direction of film. In electrostriction, elongation of the material in the vertical direction is accompanied by displacement of charged particles inside the dielectric in the presence of voltage.

Reduction in thickness and expansion in area on application of voltage result in higher electric field in the elastomer and the film breaks down at a particular value of field which is called critical electrical field [5]. Such a failure of DE film is known as instability of the material. This failure of the film can affect usefulness of DE in sensor applications, but it can be improved a lot by pre-stretching. It is also important that mechanical strength of dielectric material should be good, otherwise on stretching cracks might develop on the surface of the material.

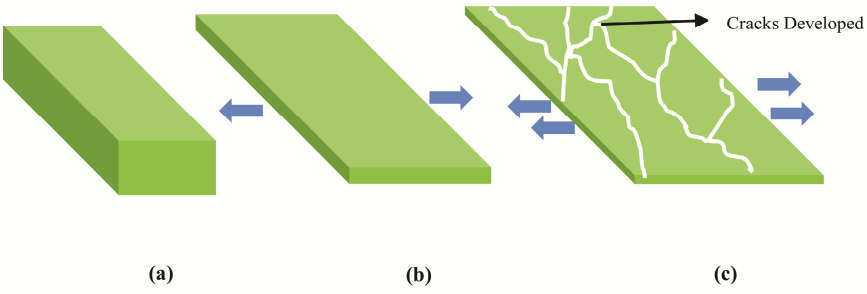

Fig. 2 Schematic diagram showing (a) a film before stretching (b) a pre-stretched film (c) cracks developed on surface of film on further stretching

Dielectrostriction represents strain dielectric response of a material and it provides an avenue to study electrostriction effect and it is challenging to control the boundary conditions of a thin film specimen [6]. However, a planar capacitor sensor does not require any physical contact with the specimen and thus, overcomes this problem.

3 Electrostrictive Material for Sensing Applications

Sensor response depends on relative change in permittivity ($\Delta\varepsilon/\varepsilon$) of the electrostrictive dielectric material used in it. Sensing response of electrostriction based elastic dielectric materials to deformation is better due to transmission of stress to the capacitor's electrodes. Therefore, electrostrictive material is a preferred dielectric for use in a capacitive sensor in comparison to conventional dielectric materials.

The variation in principal component of dielectric tensor, which contributes to the deformation response of the sensor, is given [7] as

$$\Delta\varepsilon = (a_1 + k_\varepsilon a_2)(\Delta h/h), \quad 0 \leq k_\varepsilon \leq 1, \tag{3}$$

where,

the coefficient $k_\varepsilon = 0$ for unconstrained incompressible dielectric, and
$k_\varepsilon = 1$ for constrained material,
a_1 and a_2 are electrostrictive parameters and
$\Delta h/h$ represents relative deformation.

In this study, it is observed that the deformation response is enhanced due to electrostriction effects. Values of electrostrictive coefficients are dependent on different testing conditions. In electrostriction, the field induced stresses are considered for a more appropriate approach. The field induced stresses depend on the extent of polarization inside the dielectric and the effect of strain is described by electrostriction parameters. Strain derivatives of dielectric coefficients are identified by general thermodynamic considerations of dielectric solids [6].

Many dielectric elastomer materials are used for various sensor applications. Silicon is an excellent dielectric elastomer material, having good reliability and durability, high responsive speed, high efficiency, high energy densities, large strains etc. These properties make it an ideal material for use in sensors and actuators [8].

Electro-active materials having properties of elongation and bending under electric fields are being studied in detail [9-15]. While there are various materials available, dielectric elastomer (DE) is a preferred material due to its excellent properties of large recoverable deformation and fast response. Remarkable

mechanical properties of DE make it very suitable in industrial areas where flexibility, small size and high precision are essential. Factors which effect electro-active behaviour of DE are its microstructure and mechanical properties along with the voltage applied across the electrodes. Compliant electrodes are made by spreading carbon grease on both sides of the DE film and the film expands in one direction and contracts in perpendicular direction on application of voltage across electrodes.

Many industrial applications need study of humidity levels. Humidity sensors using nano-scale sensing elements, like nanocomposites, nanotubes, porous materials etc. have been developed due to the advantage of their large surface-to-volume ratio. Porous materials are selected in sensing applications due to their large surface area. Porous silicon (PS) possesses excellent mechanical and thermal properties and is also compatible with silicon-based microelectronics technology. But PS based sensors have some disadvantages like they need extra heating equipment, long response time etc. and hence, it is a challenge to make a porous silicon-based humidity sensor. Thus, PS based sensors with new nanostructure need to be developed.

Researchers [16] have developed and studied nickel/silicon micro channel plate (Ni/Si-MCP) composites used in the fabrication of novel humidity sensor. Sensing response of this material has been thoroughly investigated by observing the variation in capacitance using Ni/Si-MCP composite under the influence of water vapour. It has been observed that Ni/Si-MCP composite exhibits micro porous and channel ordered characteristics resulting in better humidity response than other porous materials. It is pertinent to note that the materials can absorb water vapour resulting in changes in dielectric constant of MCP. Material particles of this structure have large surface to volume ratio and as a result of this, there is a tendency to absorb more water vapour from the ambience. The relative merits and demerits along with its performance have been thoroughly examined for uncoated Si-MCP, un-annealed Ni/Si-MCP, and annealed Ni/Si-MCP. It is found that annealed Ni/Si-MCP array exhibits faster response with higher sensitivity to vapour humidity in the environment. Ni/Si-MCP based humidity sensors have improved performance

In many industrial applications particularly in designing electronic circuits, good mechanical strain is required apart from the electrical conductivity [17]. For example, retina-shaped photo sensor arrays must undergo one-time large deformation from flat to spherical.

Elastomer film thickness reduces due to Maxwell stress but increases because of electrostriction [4]. This change in dimensions of the film will be useful for actuation purposes and need to be investigated carefully. Free energy model is used for studying transformation between electric and mechanical energy in DE actuation [18-21].

4 Electrostrictive Capacitive Sensors

Capacitive sensors can directly sense a variety of things—motion, chemical composition, electric field and indirectly sense many other variables which can be converted into motion or dielectric constant, such as pressure, acceleration, fluid level etc. Many materials can be used as dielectric in the capacitor and even vacuum can be one of the options. With a vacuum dielectric, the relative dielectric constant ε_r or K is 1. An air dielectric increases K to 1.0006, but it changes slightly with pressure, temperature and humidity. Typical dielectric materials such as plastic or oil have dielectric constants of 3 to 10, and some polar fluids such as water have dielectric constants of value 50 or more.

For accurate measurement, the electric field from a capacitive sensor needs to be contained within the space between the probe's sensing area and the specimen. If the electric field is allowed to spread to other items or other areas, change in position of other item will be measured resulting in error. To avoid it, a technique called guarding is used. To create a guarded probe, the back and sides of the sensing area are surrounded by another conductor which is at the same voltage as the sensing area itself. When excitation voltage is applied to the sensing area, a separate circuit applies the same voltage to the guard. As there is no difference in voltage between the sensing area and the guard, there is no electric field between them to cause current flow. Only the unguarded front of the sensing area is allowed to form an electric field to the specimen.

Electrostrictive capacitive sensors have electrostrictive dielectric material between electrodes. Solid state capacitive sensors particularly electrostrictive capacitive sensors have many advantages over other type of sensors. In most of the traditional capacitor designs, the dielectric constant does not change with the applied field and the change in capacitance due to variation in geometry can be measured by various methods [22, 23]. However, the variation in geometry is restricted to micro machining of the capacitive sensor arrays with a large area and small gap for increasing capacitance. The electrostrictive capacitive sensor with enhanced capacitance overcomes this limitation. The electrostriction properties of the material improve the sensor's response [24].

The capacitance, C of a capacitor with an area, A and gap, d between the plates is [7]:

$$C = \frac{\varepsilon\varepsilon_o A}{d}\left[1 + O\left\{\frac{\log\left(\frac{\sqrt{A}}{d}\right)}{\frac{2\sqrt{A}}{d}}\right\}\right], \tag{4}$$

where,

ε is the dielectric constant of the material between the plates,
ε_o is the dielectric permittivity of free space,
A is the area of plates of sensor and
d is the separation between the plates.

The contribution of fringing effect is estimated in many cases for various geometrical configurations of capacitive sensor and it is found that the value is high and should be taken into consideration [25].

Electrode of a capacitive sensor can either be elastic or rigid. If volume force is applied to a perfectly rigid body, the motion in it can be considered as translation of the whole body and rotation about its center of mass. On the other hand, if electrode is deformable it will also undergo motion or displacement after application of force. Extent of this displacement will be determined by the internal forces developed due to external force applied. These internal forces are termed as stresses and they oppose any motion and when equilibrium is reached, displacement ceases and any change in dimension of the body under stress is called strain. In an un-stressed, continuous medium a point O is marked with respect to a fixed origin (chosen arbitrary) by the radius R. Now when external force is applied, medium undergoes deformation resulting in displacement of matter located at O to O' at R' = R + d. The displacement d depends on co-ordinates of point O assuming d to be continuous function of R.

A typical electrostrictive capacitive sensor consists of elastic membrane between compliant electrodes. Compliant electrodes are the electrodes which follow deformation of the dielectric material i.e. these are mechanically compliant to avoid any gap between the electrode and the dielectric, so that edge effect doesn't creep in (Fig.3). Compliant electrodes should also be able to pass the entire electrical signal effectively to the dielectric. Therefore, while choosing material for compliant electrodes two requirements have to be kept in mind: first the material should have good mechanical stability and its flexibility should be comparable with that of dielectric material and secondly, it should be a good conductor. In order to fulfill these two most important requirements, the material of electrodes must exhibit low modulus of elasticity and high electrical conductivity.

While designing capacitive sensors it is important to check that compliant electrodes don't impede the functionality of the sensor. Many materials are being studied to be used as compliant electrodes, for example: graphite powder, conducting carbon grease, very finely grounded carbon powder, VHB 4910 etc. VHB 4910 is capable of stretching up to 36 times in area without breaking and is also sticky and translucent. These properties make it suitable for compliant electrodes [26]. Graphite electrodes which have high Young's modulus are not suitable for applications like pressure sensors as under the influence of high stress they may exhibit cracks on their surface [27].

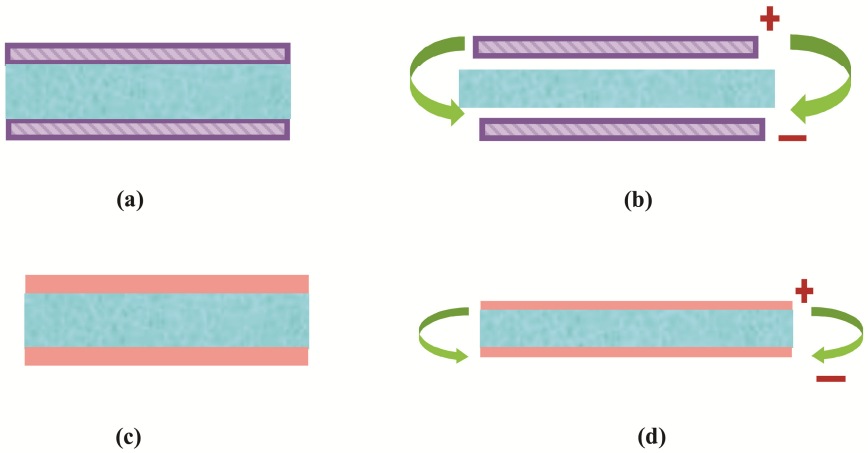

Fig. 3 Schematic diagram showing (a) electroelastic material between rigid electrodes at zero electric field (E) (b) contraction in one direction and expansion in other direction of electroelastic material on application of E resulting in edge effect due to gap created between the rigid electrode and dielectric (c) electroelastic material between compliant electrodes at zero E (d) compliant electrodes deform along with electroelastic material reducing edge effect

5 Conventional Sensing Models

In equilibrium, total forces i.e. total internal body forces F_{int} and total external forces F_{ext}, like forces due to gravitational field etc., in every volume element of elastic dielectric must be balanced i.e.

$$F_{\text{int}} + F_{ext} = 0, \tag{5}$$

$$\sum_{j=1}^{3} \frac{\partial T_{ij}}{\partial x_j} + \rho g_i = 0, \tag{6}$$

where, $F_{ext} = \rho g_i$ is an external force due to gravitational field g_i in vertically downward direction. If there is a different external force instead of gravitational force, the vector ρg_i on right hand side of above eq. (5) must be replaced accordingly. But in absence of any external field, we have

$$\sum_{j=1}^{3} \frac{\partial T_{ij}}{\partial x_j} = 0 \tag{7}$$

The strain tensor, S_{ij}, describes the state of an elastic dielectric material with small deformation and is given as

$$S_{ij} = S_{ji} = \frac{1}{2}\left(\frac{\partial s_i}{\partial x_j} + \frac{\partial s_j}{\partial x_i} \right) \quad i \neq j, \tag{8}$$

where, s is a displacement vector. The Maxwell stress tensor is a result of the force produced by the electric field and is given as

$$T_{ij} = T_{ij}^0 + \frac{\varepsilon_0}{2}\left(2\varepsilon^0 - a_1\right)E_i E_j - \frac{\varepsilon_0}{2}\left(\varepsilon^0 + a_2\right)E^2\delta_{ij}, \tag{9}$$

where, T_{ij}^0 is the stress tensor in the absence of electric field and is generally neglected in isotropic dielectrics.

If the direction of electric field is assumed to be along X_3-axis (k direction) in Cartesian coordinate system, the principal stresses, which are induced electrically, are

$$T_{33} = T_{33}^0 - \frac{1}{2}\varepsilon_0\varepsilon^0 E^2\left(1 - \frac{a_1 + a_2}{\varepsilon^0}\right) \tag{10}$$

$$T_{11} = T_{22} = T_{11}^0 + \frac{1}{2}\varepsilon_0\varepsilon^0 E^2\left(1 + \frac{a_2}{\varepsilon^0}\right), \tag{11}$$

where, $a_1 = \partial\varepsilon/\partial S_1 = \partial\varepsilon/\partial S_2$, due to strain in X_1-X_2 plane, and $a_2 = \partial\varepsilon/\partial S_3$, express the increment in the field direction i.e. along X_3 axis. T_{11}^0 and T_{33}^0 are the stresses even in absence of external field.

For a linear elastic dielectric material (described by Hooke's law), the electrically induced stresses will also generate elastic stress and strain in equilibrium condition and the elastic stress tensor, T_{ij}, is given in terms of the elastic strain tensor, S_{ij}, Young modulus Y and Poisson's ratio, σ, by

$$T_{ij} = \frac{Y}{1+\sigma}\left(S_{ij} + \frac{\sigma}{1-2\sigma} S_{kk}\delta_{ij} \right) \tag{12}$$

Conversely,

$$S_{ij} = \frac{1}{Y}\left[(1+\sigma)T_{ij} - \sigma T_{kk}\delta_{ij}\right] \tag{13}$$

If the force is acting only along X_3 direction i.e. along the direction of electric field E, then we have $S_{11} = S_{22} = 0$ and if the sides of dielectric material are also fixed

then we have $S_{32} = S_{31} = 0$. For such a unilateral deformation, the principal elastic stresses and strains are

$$T_{11} = T_{22} = \frac{Y}{(1+\sigma)(1-2\sigma)} S_{33} \tag{14}$$

$$T_{33} = \frac{Y(1-\sigma)}{(1+\sigma)(1-2\sigma)} S_{33} \tag{15}$$

$$S_{33} = \frac{p(1+\sigma)(1-2\sigma)}{Y(1-\sigma)}, \tag{16}$$

where, $T_{33} = p$ is a compressive force i.e. pressure. On putting the principal value of Maxwell stress tensor (assuming, $T_{11}^0 = T_{33}^0 = 0$) from eq. (10 and 11) into eq. (13), we get principal elastic strains as

$$S_{11} = S_{22} = \frac{1}{2}\varepsilon_0 \varepsilon^0 E^2 \left[1 - \frac{a_1}{\varepsilon^0} + \frac{(1-2\sigma)a_2}{\varepsilon^0}\right] Y^{-1} \tag{17}$$

Deformation of elastic dielectric material is due to (i) Maxwell stress effect with strain due to variation in electric field distribution and (ii) Electrostriction.

Standard equation to calculate electrically induced strain in dielectric material is given by:

$$S_{33} = -\frac{1}{2}\varepsilon_0 \varepsilon^0 E^2 \left[(1+2\sigma) - \frac{a_1 + (1-2\sigma)a_2}{\varepsilon^0}\right] Y^{-1}, \tag{18}$$

where,

ε^0 is permittivity of the undeformed body,

a_1 and a_2 are two parameters describing the variation in dielectric properties of the material in shear and bulk deformation respectively,

ε_0 is permittivity of free space,

σ is Poisson's ratio,

Y is Young's modulus,

E is the applied electric field.

Some researchers [28, 29] have simplified the standard equation of calculation of induced strain. In this chapter, strain of six dielectric materials has been analyzed to understand the effect of these simplifications. The study reveals that this simplification leads to substantial error in the results, when compared to results obtained from the standard equation of strain.

Researcher [28] has used Maxwell's principal stress eq. (10) and calculated eq. (19) for determination of electromechanical response of dielectric material without considering lateral stress etc.

$$\frac{\Delta x_3}{x_3} = -\frac{1}{2Y}\varepsilon_0 \varepsilon^0 E^2 \left(1 - \frac{a_1 + a_2}{\varepsilon^0}\right) \tag{19}$$

Similarly, researcher [29] has determined the electromechanical response of polyurethane elastomer (Dow 2103-80AE) based on eq. (20) without considering lateral stress, edge effect, boundary conditions and tensor form of permittivity.

$$\frac{\Delta x_3}{x_3} = \frac{1}{2Y}\varepsilon_0 \varepsilon^0 E^2 = S_{33} \tag{20}$$

6 Error in Conventional Sensing Models

Materials having high Poisson's ratio like polyurethane, show high lateral strain on application of field and therefore, lateral stress should not be ignored for correct estimation of electrically induced strain, particularly for such materials. Theoretically, Poisson's ratio varies from -1 to +0.5, but in practice, no material is available with $\sigma < 0$. Poisson's ratio for polymers has been found to be $0.499 \approx 0.5$. On putting $\sigma = 0.5$ in eq. (18), we get,

$$S_{33} = -\frac{1}{2}\varepsilon_0 \varepsilon^0 E^2 \left[2 - \frac{a_1}{\varepsilon_0}\right] Y^{-1} \tag{21}$$

This equation is quite different from eq. (19) as the contribution from the term a_2 has been cancelled due to presence of $(1\text{-}2\sigma)$ term in eq. (18). Actually, the longitudinal principal strain S_{33} calculated from eq. (21) is twice the value of strain calculated [29] from eq. (20) for a material with $\sigma = 0.5$ and $a_1 = 0$.

Edge effect is also an important parameter that needs to be taken into consideration [30] as it can lead to high error especially when nanometric sensors are considered [25].

Due to electrostrictive deformation, the permittivity of two regions is different and hence, solution to the field or potential must also be different. The appropriate electrical boundary conditions must be satisfied at the interface between two regions [30].

Dielectric material gets deformed on application of applied electric field and therefore, it doesn't remain isotropic. Scalar permittivity becomes dielectric tensor for anisotropic body. Hence, use of eq. (19) and eq. (20) is limited to the linear and isotropic elastic dielectric materials with small deformation.

In this study six dielectric materials namely polypropylene homo-polymer, polyurethane, polyketone, polyphthalamide (PPA), epoxy cure resin, and nylon 6 have been studied, as these are the commonly used electroelastic materials. Parameters a_1 and a_2 are calculated from the formulae used by the researcher [31]. Electrically induced strain for these materials has been calculated using eq. (18) and tabulated in Table 1.

Table 1 Electrically induced strain of dielectric materials

Dielectric Material	Dielec. Const.	σ	a_1	a_2	Proportionate Strain
Polypropylene homo-polymer	2.2	0.45	0.58	1.49	1.5705
Polyurethane	3.33	0.5	2.18	3.42	1.3479
Polyketone	3.68	0.4	2.87	4.12	0.795
Polyphthalamide (PPA)	4.17	0.38	4.02	5.18	0.498
Epoxy cure resin	4.45	0.39	4.76	5.83	0.4219
Nylon 6	4.86	0.35	5.96	6.84	0.0515

As observed from Table 1, polypropylene homopolymer has maximum strain, which means that, this material when used in a capacitive sensor can increase its sensitivity while nylon 6, having minimum strain, should not be preferred as a dielectric material. Selection of dielectric material depends on the application of the sensor. For mechanical sensors like pressure sensor, tactile sensing, pressure gauge, proximity sensors etc. dielectric material should have high strain, so that even for small inputs large strain is produced, enhancing sensor response. For electrical sensors like galvanometer, MEMS magnetic sensors etc. material should have high electrical properties.

Now strain calculated from standard eq. (18) that has been tabulated in Table 1 is compared with strain calculated from simplified eq. (19) and (20). Results are tabulated in Table 2.

Table 2 Percentage error in eq. (19) and (20)

Dielectric Material	% Error in Eq. (19)	% Error in Eq.(20)
Polypropylene homo-polymer	-96	-36
Polyurethane	-150	-25.8
Polyketone	-213	25.7
Polyphthalamide (PPA)	-342.2	100.8
Epoxy cure resin	-427	137
Nylon 6	-3273	1842

After comparing values of strain calculated using standard eq. (18) with those calculated using simplified eq. (19), error has been found in the range of underestimation from 96% to 3273%. Similarly, after comparing values of strain obtained from eq. (18) with those obtained using eq. (20), overestimation from 1842% to 25.7% is found in four materials and underestimation of 25.8% and 36% has been found for two materials. Thus, it can be concluded from the above table, that simplification of the equation for calculation of strain has resulted in very large errors.

7 Role of Fillers in Enhancement of Sensing Performance

Researchers [32, 33] are incorporating filler particles into the base material for enhancement of its electromechanical properties. Use of filler particles, particularly of nanometric size, enhances properties like dielectric breakdown strength, relative dielectric permittivity. By incorporating nano fillers tan delta of the composite also get reduced but addition of fillers beyond a certain concentration; reduce flexibility of the composite which is not desirable in many applications. When flexibility of the material reduces, its strain reduces and the material becomes rigid. Therefore, quantity of the filler to be incorporated in the base material depends on application of the sensor. Pressure gauge sensors require dielectric material to be flexible and thus, very low amount of filler needs to be incorporated in it, whereas for electrical sensors, high electrical properties are required and good amount of filler can be incorporated into it to increase permittivity of the material.

But preparation of nanocomposite which is free of all defects and agglomeration is a challenging task. Formation of clusters of nanofillers hinders the performance of the composite and therefore, process of annealing is commonly used for proper dispersion of fillers into the matrix.

Change in properties of nanocomposite depends on many factors like size, shape, type, and concentration etc. of filler particle. In this study change in real permittivity of material with filler concentration and the type of filler material has been studied.

Graphs showing variation of relative real permittivity with filler concentration for epoxy cure resin on incorporating nano filler particles of ZnO and TiO_2 have been plotted using the data from [34].

From Fig. 5, it is observed that permittivity of the nanocomposite drops initially for loading of TiO_2 fillers in comparison to pure material but after 0.1% loading rise in permittivity is observed up to 10% filler concentration. Similar behavior is observed in Fig. 6, where ZnO fillers have been used. However, in this case permittivity remains lower in comparison to unfilled epoxy up to 3% loading.

Comparing both the graphs at 5% filler concentration, permittivity of the ZnO nanocomposite is lower than TiO_2 composite which could be due to higher permittivity of TiO_2 as compared to ZnO.

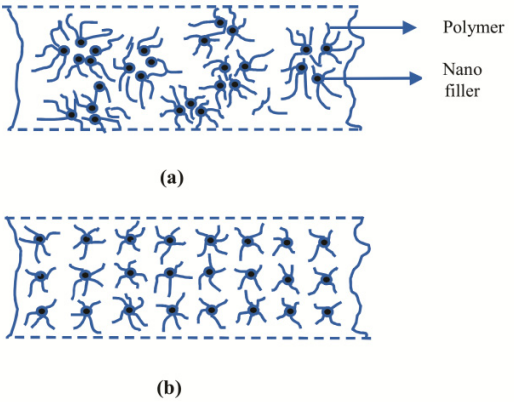

Fig. 4 Schematic diagram showing: (a) formation of clusters – non-uniform dispersion of nanofillers (b) uniform dispersion of nanofillers

Reduction in permittivity for lower values of filler concentration could be attributed to hindrance in mobility of polymer chains and dipoles. From this it appears that on increasing filler concentration permittivity should continue decreasing, but it does not happen so. After a certain filler concentration permittivity starts increasing, which may be due to the reason that permittivity of filler material now starts playing important role and increases the permittivity of nanocomposite [34].

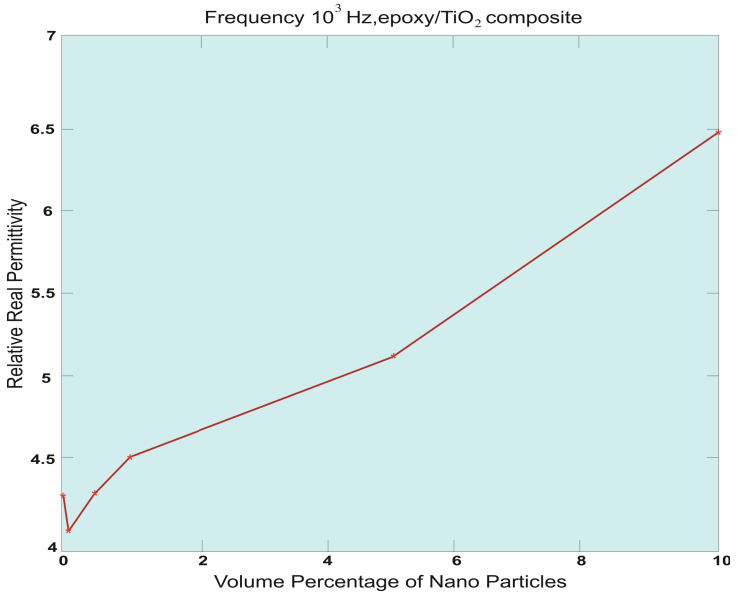

Fig. 5 Graph showing variation of relative permittivity (real part) with filler loading at 10^3 Hz for epoxy-TiO_2 nanocomposite

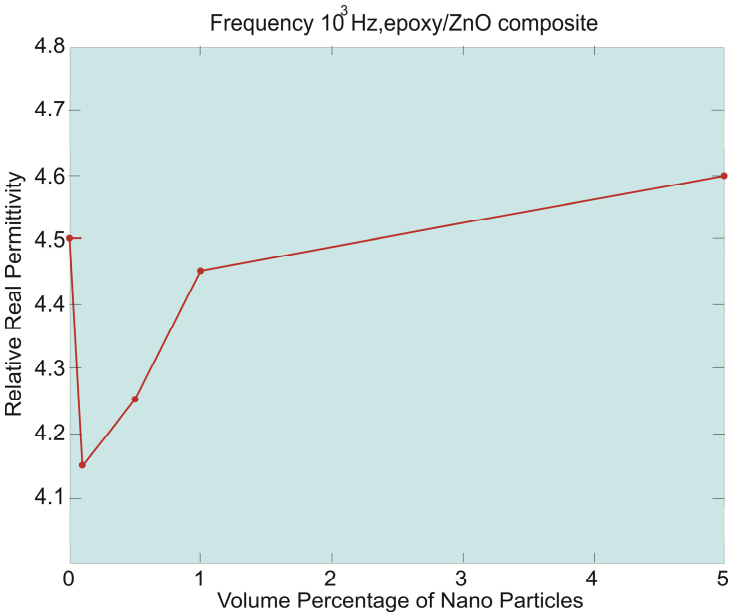

Fig. 6 Graph showing variation of relative permittivity (real part) with filler loading at 10^3 Hz for epoxy-ZnO nanocomposite

Interfacial contribution is responsible for change in properties of the composite after adding nano fillers. On reducing the filler particle size interfacial volume fraction increases tremendously. The interfacial volume fraction is 0.006 for 1% volume filler loading at 5nm radius of filler particle, but it increases to 0.06 when radius of particle is reduced to 0.5 nm. Similar increase is observed at 5% volume filler loading also when the interfacial volume fraction increases to 0.3 at 0.5 nm radius from 0.03 at 5nm radius [35]. An interaction zone of altered polymer properties, invariably different from bulk polymer, is created due to tremendous increase in interfacial region. Formation of a double layer is observed around the filler particles at the interface.

8 Conclusion

The electrostrictive dielectric material incorporated between the electrodes has advantages of high mechanical flexibility, low acoustic impedance, low manufacturing cost and ability to be easily moulded into desirable shapes. The electrostriction properties of the material not only improve the sensing response due to perfect transmission of stress to the capacitor's electrodes, but these aspects also make electrostrictive material a better choice for use in capacitive sensor as compared to other conventional dielectric materials. Use of such materials becomes even more important in sensing applications of adverse environments like high pressures, high operating temperatures, high fields, etc.

In past, researchers have used simplified equations for calculation of electrically induced strain, but the results obtained using the standard equations for six materials exhibit large errors from overestimation to underestimation. These errors can be minimized by considering lateral stresses, edge effect, estimation of proper boundary conditions etc. For designing a reliable and efficient sensor it is necessary to have accurate sensing equations. It is observed that interfacial volume fraction increases tremendously on reducing the size of filler particle to nanometric range, particularly for particles of radius less than 5 nm. This tremendous increase in interfacial region creates an interaction zone of altered polymer properties, invariably different from bulk polymer.

References

[1] Krakovsky, I., Romijn, T., Posthuma de Boer, A.: A few remarks on the electrostriction of elastomers. Journal of Applied Physics 85(1), 628–629 (1999)
[2] Cady, W.G.: International Critical Tables, vol. 6, p. 207. McGraw-Hill, New York (1929)
[3] Thakur, O.P., Singh, A.K.: Errors in estimation of electrically induced deformations in elastic dielectrics. Materials Sciences Research Journal 2(3/4) (2008)
[4] Li, B., Liu, L., Wu, J., Zhu, Z., Chen, H.: Electrostriction in dielectric elastomer: Effect on electromechanical actuation. In: Electro Active Polymer Actuators and Devices, EAPAD 2010, Proc. of SPIE, vol. 7642, p. 764212 (2010)
[5] Leng, J., Liu, L., Liu, Y., Yu, K., Sun, S.: Electromechanical stability of dielectric elastomer. Applied Physics Letters 94, 211901 (2009)
[6] Lee, H.Y., Peng, Y., Shkel, Y.M.: Strain-dielectric response of dielectrics as foundation for electrostriction stresses. Journal of Applied Physics 98, 74104 (2005)
[7] Shkel, Y.M., Ferrier, N.J.: Electrostriction Enhancement of Solid-State Capacitance Sensing. IEEE/ASME Transactions on Mechatronics 8(3), 318–325 (2003)
[8] Liu, Y., Liu, L., Zhang, Z., Leng, J.: Dielectric elastomer film actuators: Characterization, experiment and analysis. Smart Materials and Structures 18, 95024 (2009)
[9] Pelrine, R., Kornbluh, R., Pei, Q., Joseph, J.: High-Speed Electrically Actuated Elastomers with Strain Greater than 100%. Science 287(5454), 836–839 (2000)
[10] Smela, E., Inganäs, O., Lundström, I.: Controlled folding of micrometer-size structures. Science 268, 1735–1738 (1995)
[11] Pelrine, R.E., Kornbluh, R.D., Joseph, J.P.: Electrostriction of polymer dielectrics with compliant electrodes as a means of actuation. Sensors and Actuators A: Physical 64(1), 77–85 (1998)
[12] Plante, J.S., Dubowsky, S.: On the Properties of Dielectric Elastomer Actuators and Their Design Implications. Smart Materials and Structures 16(20), S227-S236 (2007)
[13] Wissler, M., Mazza, E.: Electromechanical coupling in dielectric elastomer actuators. Sensors and Actuators A: Physical 138(2), 384–393 (2007)
[14] Kofod, G., Paajanen, M., Bauer, S.: Self organized minimum-energy structures for dielectric elastomer actuators. Applied Physics A- Materials Science & Processing 85(2), 141–143 (2006)
[15] Liu, L.W., Fan, J.M., Zhang, Z., Shi, L., Liu, Y.J., Leng, J.S.: Analysis of the Novel Strain Responsive Actuators of Silicone Dielectric Elastomer. Advanced Materials Research 47-50, 298–301 (2008)

[16] Miao, F., Tao, B., Sun, L., Liu, T., You, J., Wang, L., Chu, P.K.: Capacitive humidity sensing behavior of ordered Ni/Si microchannel plate nanocomposites. Sensors and Actuators A: Physical 160, 48–53 (2010)
[17] Lacour, S.P., Wagner, S., Huang, Z., Suo, Z.: Stretchable gold conductors on elastomeric substrates. Applied Physics Letters 82(15), 2404–2406 (2003)
[18] Zhao, X., Suo, Z.: Method to analyze electromechanical stability of dielectric elastomers. Applied Physics Letters 91, 61921 (2007)
[19] Díaz-Calleja, R., Riande, E., Sanchis, M.J.: On electromechanical stability of dielectric elastomers. Applied Physics Letters 93, 101902 (2008)
[20] Zhao, X., Hong, W., Suo, Z.: Electromechanical hysteresis and coexistent states in dielectric elastomers. Physical Review B 76, 134113 (2007)
[21] Liu, Y., Liu, L., Sun, S., Leng, J.: An investigation on electromechanical stability of dielectric elastomer undergoing large deformation. Smart Materials and Structures 18, 95040 (2009)
[22] Doebelin, E.O.: Measurement systems: Application and design, 4th edn. Mcgraw-Hill, Inc. (1990)
[23] Holman, J.P.: Experimental methods for engineers, 6th edn. Mcgraw-Hill, Inc. (1994)
[24] Thakur, O.P., Singh, A.K.: Modelling of capacitive censor filled with elastic dielectrics and its advantages. In: 3rd International Conference on Sensing Technology ICST 2008, Taiwan, pp. 467–471 (2008)
[25] Thakur, O.P., Agrawal, N.: Mathematical modelling of error contribution for various dimensions of capacitive sensors from centimetric to nanometric Range. Advanced Studies in Theoretical Physics 7(1), 1–9 (2013)
[26] Kofod, G., Sommer-Larsen, P., Kornbluh, R., Pelrine, R.: Actuation Response of Polyacrylate Dielectric Elastomers. Journal of Intelligent Material Systems and Structures 14(12), 787–793 (2003)
[27] Khodaparast, P., Ghaffarian, S.R., Khosroshahi, M.R., Yousefimehr, N., Zamani, D.: Electrode structures in high strain actuator technology. Journal of Optoelectronics and Advanced Materials 9(11), 3585–3591 (2007)
[28] Shkel, Y.M., Klingenberg, D.J.: Material parameters for electrostriction. Journal of Applied Physics 80(8), 4566–4572 (1996)
[29] Zhang, Q.M., Su, J., Kim, C.H., Ting, R., Capps, R.: An experimental investigation of electromechanical responses in a polyurethane elastomer. Journal of Applied Physics 81(6), 2770–2776 (1997)
[30] Thakur, O.P., Singh, A.K.: Electrostriction and electromechanical coupling in elastic dielectrics at nanometric interfaces. Materials Science - Poland 27(3), 839–850 (2009)
[31] Shkel, Y.M.: Electrostriction: Material parameters and stress/strain constitutive relations. Philosophical Magazine 87(11), 1743–1767 (2007)
[32] Elansezhian, R., Saravanan, L.: Effect of nano silica fillers on mechanical and abrasive wear behaviour of vinyl ester resin. International Journal of Applied Research in Mechanical Engineering 1(1), 105–108 (2011)
[33] Rocha, J.G., Paleo, A.J., Van Hattum, F.W.J., Lanceros-Mendez, S.: Polypropylene-Carbon nanofiber composites as strain-gauge sensor. IEEE Sensors Journal 13(7), 2603–2609 (2013)
[34] Singha, S., Thomas, M.J.: Dielectric properties of epoxy nanocomposites. IEEE Transactions on Dielectrics and Electrical Insulation 15(1), 12–23 (2008)
[35] Thakur, O.P., Agrawal, N.: Effect of Fillers on Electromechanical Properties of Composites for Potential Sensing Applications. IEEE Sensors Journal (April 2014), doi:10.1109/JSEN.2014.2314775.

Measurements for the Thermodynamic Model of a Pneumatic Muscle Actuator

L. Kopecny[1,*] and L. Zalud[2]

[1] CEITEC (Central European Institute of Technology), Brno University of Technology, Brno, Czech Republic
[2] Department of Control and Instrumentation, Faculty of Electrical Engineering and Communication, BUT Brno, Czech Republic
lukas.kopecny@ceitec.vutbr.cz

Abstract. The paper presents the selection of sensors and especially their placement for evaluating the thermodynamical model of a pneumatic muscle actuator.

Pneumatic Muscles are undoubtedly one of the most promising actuators among the currently applicable modern muscle-like actuators. This actuator is, on the one hand, characterized by exceptional utility properties, the second highly non-linear and complex internal friction. Complicated and still not enough precise models currently do not allow this promising drive to expand behind the walls of experimental laboratories.

This paper also provides a description of McKibben pneumatic muscle and represents the current state of its mathematical model. The main objective of this work is to extend the mathematical model of the pneumatic muscle, especially in the field of thermodynamics. The authors apply a method originally designed for pneumatic linear drives on pneumatic muscles, create a new thermodynamic model and discuss the results obtained. Subsequently, the method is significantly extended by another independent thermodynamic variable, and the newly proposed mathematical model includes the heat generated by friction, which exerts major influence on the behavior of the actuator.

Importance of the extended thermodynamic model is demonstrated by simulations of ideal thermodynamic processes and, in particular, by comparing the present model with a realistic position servo drive system with pneumatic muscle. Sensor choice and placement on the muscle test bed is evaluated, and the obtained results are discussed.

Keywords: pneumatic muscle actuator, temperature sensor, temperature measurement, thermodynamic, modeling.

* Corresponding author.

A. Mason et al. (eds.), *Sensing Technology: Current Status and Future Trends III*,
Smart Sensors, Measurement and Instrumentation 11, DOI: 10.1007/978-3-319-10948-0_18

1 Introduction

Modern haptic interfaces and other applications in robotics require high-performance force actuators with high force output per weight unit. Traditional geared electrical motors cannot provide these characteristics [1], [9].

Many concepts of “uncommon” actuators are employed in latest robotics. Undoubtedly one of the most promising actuators is pMA – the Pneumatic Muscle Actuator [2], [15]. It has a number of exceptional properties:

- Actuators exhibit exceptionally high power and force to weight volume ratios.
- The pMA can be made in any diameter and length.
- Pneumatic muscles are naturally compliant, and therefore they are ideal for interaction - even with humans [10].
- Direct drive actuator with linear motion output.
- The structure of the pMA makes it comparable in shape, properties and performance to human muscles - it is easy to implement a pMA in a human/computer interface.
- The actual achievable displacement (contraction) is typically 30% of the dilated length.
- The muscles are highly flexible, soft in contact and offer excellent safety potential (by limited contraction).
- Controllers developed for the muscle systems have proved them to be controllable to an accuracy of 1% of displacement. The bandwidth of the muscles reaching up to 5 Hz can be achieved.
- The contractile force of the actuator can be over 300 N/cm2 for a pMA (compared to 20-40 N/cm2 for natural muscles).
- Accurate smooth motion from start to stop.
- Low cost, powerful actuation, lightweight compact device.
- High safety – applicable in a wet or explosive environment.

Fig. 1 The pneumatic muscle actuator built at CEITEC

Although this actuator was invented already in the 1950s, it has not found wide application to date. The difficulty of control, mainly due to the highly nonlinear structure, still keeps the pneumatic muscle actuator at the edge of interest of industrial manufacturers. However, there are a lot of phenomena influencing the tricky behavior of pneumatic muscles; one of the most important features is the natural damping of the pMA caused by very complex inner friction [3]. The friction is highly temperature dependent, and this is also the main reason why the described thermodynamical model was developed.

Other problems which have hitherto not been satisfactorily solved include:

- Compensation of the muscle end deformations (the mathematical model assumes an exact cylinder shape).
- Compensation of the rubber wall elasticity.
- Compensation of the thread elasticity [7].
- Thermodynamical modeling.
- Air transport delay compensation.
- Braided sleeving to the rubber wall movements.
- Complex inner friction.

Because pneumatic muscles can develop an active force only in one direction of motion - contraction – they must be arranged in the antagonist, either as a pair of opposite acting muscles (Fig. 2(a)) or a muscle coupled with a spring (Fig. 2(b)) [17].

The linear movement of the muscle can be easily converted to rotational motion by a system of rods and rollers (Fig. 2). The same arrangement is common in animal muscles.

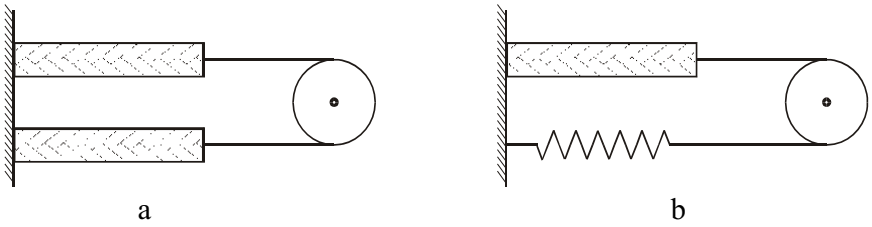

Fig. 2 The antagonist arrangement: muscle x muscle (a), muscle x spring (b)

2 Basic Static Model of a Pneumatic Muscle Actuator

A pneumatic muscle actuator comprises an inner rubber tube placed into a braided sleeving and clamped to the sealing caps on both muscle ends (Fig. 1).

A pneumatic muscle converts pneumatic energy into mechanical. Applying a pressure to the inner layer leads to the muscle contraction and exerting traction. The following section describes the basic dependence of the contractile force of a pneumatic muscle actuator on the instantaneous length of the actuator.

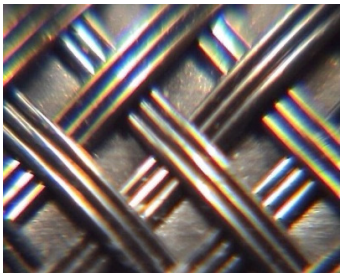

Fig. 3 A macro photo of the braided muscle wall

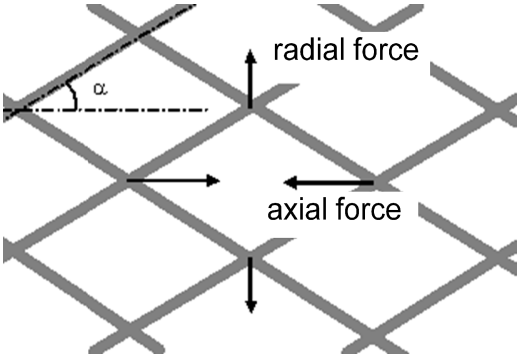

Fig. 4 The basic principle of contractile force generation: the muscle wall pantograph cells.

The input work of gas acting force on the muscle wall can be calculated from the equation

$$dW_{in} = \int_{S_i} \left(P - P_0\right) dl_i \cdot ds_i = pdV \ , \tag{1}$$

where P is the absolute pressure of the gas in the muscle [Pa], P_0 the absolute pressure of the surrounding gas [Pa], P the differential pressure (P - P_0) [Pa], S_i the entire inner surface of the muscle [m^2], ds_i the differential of the inner muscle surface [m^2], dl_i the displacement of the inner surface [m], dV the change in the muscle volume [m^3].

The output work W_{out} executed by the shortening of the muscle is

$$dW_{out} = -FdL \ , \tag{2}$$

where F [N] is the axial contractile force of the muscle, and dL is the axial displacement [m]. From the perspective of the law of conservation of energy, neglecting the losses, the output work equals the input. Thus, we have:

$$dW_{out} = dW_{in} \ . \tag{3}$$

Substituting from (1) and (2), we obtain

$$-FdL = pdV \quad , \quad F = -p\frac{dV}{dL} \quad . \tag{4}$$

To estimate dV / dL, let us consider the active part of the muscle in the shape of an ideal cylinder, where L is the height [m], D the diameter of the cylinder [m], n the number of fibers wrapped around the cylinder [-], and b the fiber length [m] (see Fig. 6). L and D can be expressed as a function of θ with constant parameters n and b.

Now we can derive from (4) the final expression for the tensile strength of the muscle as a function of p and θ. We then have

$$F = -p\frac{dV}{dL} = -p\frac{dV/d\theta}{dV/d\theta} = \frac{pb^2\left(3\cos^2\theta - 1\right)}{4\pi n^2}, \tag{5}$$

or as a function of p and L:

$$F = \frac{p\left(3L^2 - b^2\right)}{4\pi n^2} \quad . \tag{6}$$

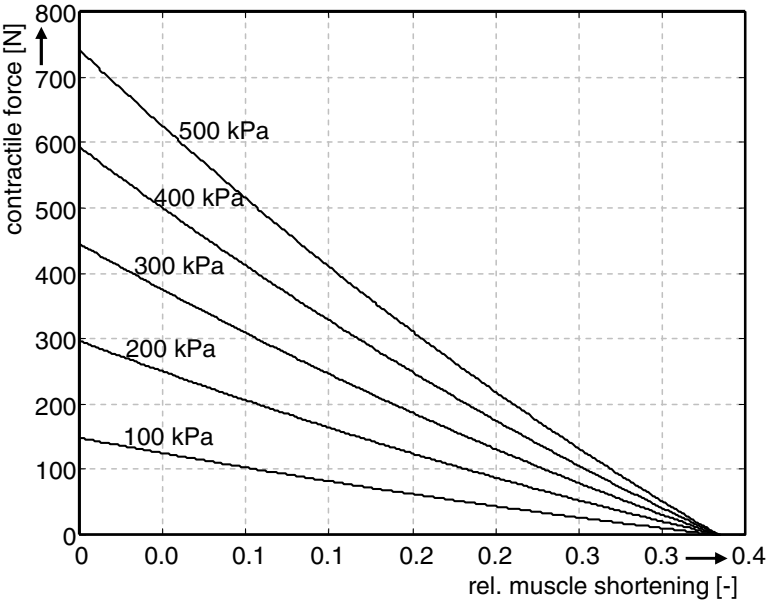

Fig. 5 The dependence of the contraction force on the relative shortening of the pneumatic muscle

Fig. 5 shows the dependence of the contraction force on the relative shortening of the muscle ($\varepsilon = (L_{max} - L) / L_{max}$) for the following values: L_{max} = 30 cm, n = 3, b = 32 cm. The maximum length L_{max} of the muscle is determined by the braid type and depends on the smallest possible angle of the fibers. In this case, there holds θ_{min} = 20 °. The diameter D of this muscle is 28 mm at the maximum contraction.

3 Thermodynamic Model of the pMA

In this section, a differential equation is developed that links the muscle pressure to the mass flow through the system, muscle contraction, and contraction speed.

In similar papers describing mathematical models of the pneumatic cylinder, the authors derive these equations using the assumption that both the charging and the discharging processes were adiabatic. In reference [4], the authors found experimentally that the temperature inside the cylinder lies between the theoretical adiabatic and isothermal curves. The temperature was close to the adiabatic curve only for the charging process.

There is an assumption that a similar principle should be valid also for the pneumatic Muscle Actuator.

The most general model for the volume of gas consists of three equations:

1. Equation of state (ideal gas law).
2. Conservation of mass (continuity) equation.
3. Energy equation.

Let us assume that:

- the gas is perfect;
- the pressure and temperature inside the muscle are homogeneous;
- the kinetic and potential energies are negligible (the pMA is a pneustatic device).

$$P = \rho R T \,. \tag{7}$$

$$\dot{m} = \dot{m}_{in} - \dot{m}_{out} = \frac{d}{dt}(\rho V) = \dot{\rho} V + \rho \dot{V} \,. \tag{8}$$

$$q_{in} - q_{out} + k C_v (\dot{m}_{in} T_{in} - \dot{m}_{out} T) - \dot{W} = \dot{U} \,. \tag{9}$$

Here, P is the pressure, V the volume with density ρ, R the ideal gas constant, T the thermodynamic temperature, m the mass, $\dot{m}_{in,out}$ the mass flows entering (or leaving) the muscle, $q_{in,out}$ are the heat transfer terms (heat flows), k is the specific heat ratio, C_v the specific heat at a constant volume, T_{in} tthe emperature of the incoming gas flow, $\dot{W}$ the rate of change in the work, $\dot{U}$ the change of internal energy.

The total change in internal energy is:

$$\dot{U} = \frac{d}{dt}\left(C_v mT\right) = \frac{1}{k-1}\frac{d}{dt}\left(PV\right) = \frac{1}{k-1}\left(V\dot{P} + P\dot{V}\right) \quad (10)$$

Substituting $\dot{W} = PV$ and Eq. (10) into Eq. (9) and assuming that the incoming flow is already at the temperature of the gas in the muscle, the energy equation becomes:

$$\frac{k-1}{kP}\left(q_{in} - q_{out}\right) + \frac{1}{\rho}\left(m_{in} - m_{out}\right) - \dot{V} = \frac{V}{kP}\dot{P} \quad (11)$$

If the process is considered to be adiabatic ($q_{in} - q_{out} = 0$), the time derivative of the muscle pressure is:

$$\dot{P} = k\frac{P}{\rho V}\left(\dot{m}_{in} - \dot{m}_{out}\right) - k\frac{P}{V}\dot{V} = k\frac{RT}{V}\left(\dot{m}_{in} - \dot{m}_{out}\right) - k\frac{P}{V}\dot{V} \quad (12)$$

If the process is considered to be isothermal, then Eq. 11 can be written as:

$$q_{in} - q_{out} = P\dot{V} - \frac{P}{\rho}\left(m_{in} - m_{out}\right) \quad (13)$$

The rate of change in the pressure is:

$$\dot{P} = \frac{RT}{V}\left(\dot{m}_{in} - \dot{m}_{out}\right) - \frac{P}{V}\dot{V} \quad (14)$$

The only difference between Eq. 12 and Eq. 14 is in the specific heat ratio term *k*. Thus, both these equations can be rewritten as:

$$\dot{P} = \frac{RT}{V}\left(\alpha_{in}\dot{m}_{in} - \alpha_{out}\dot{m}_{out}\right) - \alpha\frac{P}{V}\dot{V} \quad (15)$$

with $\alpha, \alpha_{in}, \alpha_{out}$ taking values between 1 and *k*.

The volume *V* of the pMA can be expressed [5] as

$$V = \frac{L\left(b^2 - L^2\right)}{4\pi\, n^2} \quad (16)$$

and its time derivative $\dot{V}$ as

$$\dot{V} = \frac{\dot{L}\left(b^2 - 3L^2\right)}{4\pi\, n^2} \quad (17)$$

where L is the current muscle length, b the muscle thread length, and n the number of thread turns.

Substituing Eq. (16) and (17) into (15), the time derivative for the muscle pressure becomes:

$$\dot{P} = \frac{4\pi n^2 RT}{L\left(b^2 - L^2\right)}\left(\alpha_{in}\dot{m}_{in} - \alpha_{out}\dot{m}_{out}\right) - \alpha\frac{P\left(b^2 - 3L^2\right)}{L(b^2 - L^2)}\dot{L} \tag{18}$$

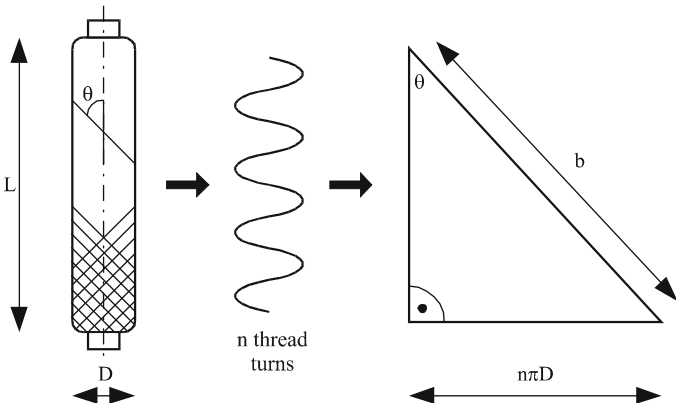

Fig. 6 The determining of the coefficients n and b

In this form, the pressure equation accounts different heat transfer characteristics of the charging and discharging processes and air compression and expansion due to muscle contraction or extension.

4 Temperature Sensors

In this chapter, we will explain the following aspects:

- Muscle temperature measurement.
- Temperature sensor selection.
- Essential structural changes in muscle design.

Let us start with the basic assumption from Chapter 3, namely that the temperature inside the muscle is homogeneous. As can be seen on the thermal image of the standard pneumatic muscle actuator in Fig. 7, the temperature distribution along the horizontal axis of the muscle is far away from a homogeneous course.

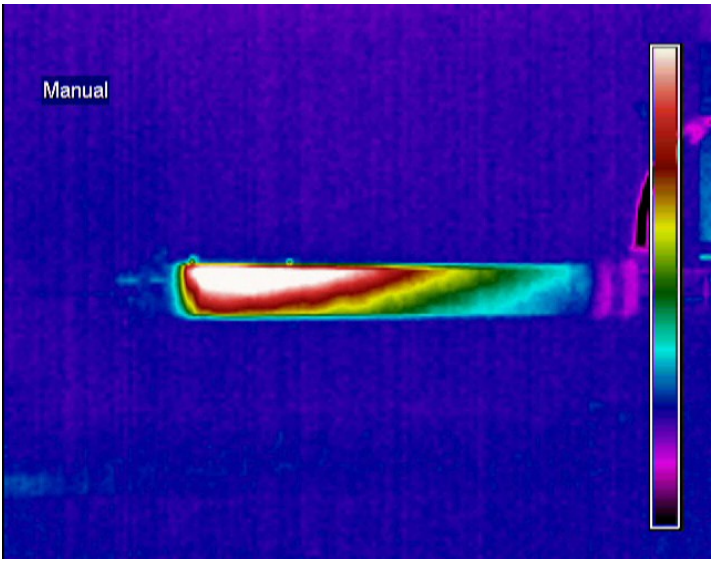

Fig. 7 A thermal image of the pMA after 20 working strokes (scale 20 to 40 °C)

The above-indicated condition is caused mostly by the manner of gas exchange in the pneumatic muscle; the exchange is significantly better on the muscle air port side.

This looks like a serious problem for temperature measuring of filling gas, even if we are interested in changes in temperature rather than in its absolute value.

The second critical parameter is the time response of the temperature sensor. We have to choose a pneumatic muscle actuator working cycle fast enough to provide sufficient thermodynamic temperature response. To obtain measurable temperature changes, we have to go to the isotonic working cycle at a frequency of at least 0.5 Hz. The temperature sensor time constant should be at least one order better [14], which means the maximum time constant of 200 ms for the whole temperature sensing system.

For an appropriate measurement of the muscle internal temperature, we look for a temperature sensor with:

1. Fast time response.
2. Ability of spatial temperature averaging to suppress the temperature non-homogenity.

We tried to solve the temperature measuring problem in four different ways:

1. A far-infrared thermal camera was used to sense the surface temperature of the pneumatic muscle actuator.
2. A small bead platinum temperature sensor was integrated into the braided sleeving of the muscle wall.
3. A fast-response, low-mass foil platinum sensor was placed inside the pneumatic muscle actuator.
4. We used an array of fast response sensors to suppress the temperature non-homogenity inside the pneumatic muscle.

4.1 Thermal Imager Measurement

A thermal imaging camera with the far-infrared (FIR – wavelength > 15 μm) technology image sensing is a very fast sensing device with a time constant value of around 20 ms.

The problem is that the infrared electromagnetic radiation is radiated mostly by the pneumatic muscle wall instead by muscle filling gas.

There are two options to place the sensing thermal imager:

1. Inside the pneumatic muscle actuator.
2. Outside the pneumatic muscle actuator.

The first solution necessitates an extremely small thermal imager device and/or an exceptionally large pneumatic muscle actuator. Furthermore, we have to face the problem with the view angle to cover the whole inner area of the pneumatic muscle wall. A high flow rate of pressurized gas is necessary to supply a large-volume pneumatic muscle.

The second solution senses the pneumatic muscle from the outside. There is no problem related with the room to accommodate the thermal imager, but it measures outside braided sleeving instead of the inner gas temperature. This measurement method brings about a significant time delay and makes its result highly distorted.

4.2 Wall-Integrated Sensor

We tried to integrate the temperature sensor into the braided sleeving of the muscle wall (Fig. 8). This placement proved to be an unfavorable solution. The sensor provides data more about the rubber muscle wall temperature (heated by material friction) instead of the inside gas temperature changes.

Also, the mechanical properties of this design are very poor. The movements between the muscle braided sleeving and the muscle rubber wall brake off the terminals of the temperature sensor and cause its malfunctioning.

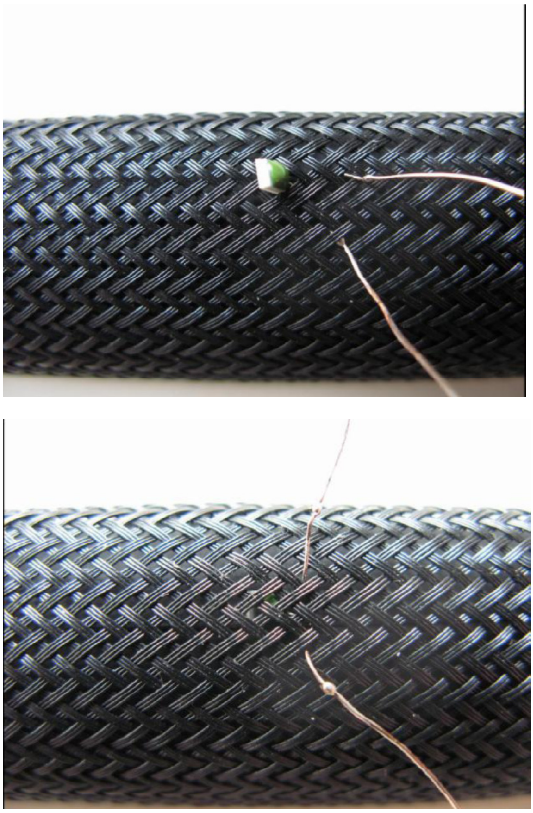

Fig. 8 The temperature sensor integrated into the muscle wall

4.3 Fast Inner Sensor

We had to place a temperature sensor inside the pneumatic muscle. A fast-response, low-mass foil platinum sensor with the resistance of 100 Ohms for 20°C was used. The sensor was placed into a light carbon housing, which protected it against damage. The housed sensor was placed approximately in the centre of the pneumatic muscle's inside (see Fig. 9).

With this arrangement, we obtained the best results, namely fast response and high-amplitude measurement. But such results are still not credible enough because of the uncertainty caused by non-homogeneous temperature distribution inside the pneumatic muscle.

It is obvious that the right solution is to combine a fast inner sensor with changes in the pneumatic muscle design (chapter 5). Thus, we can obtain the result indicated in Fig. 16.

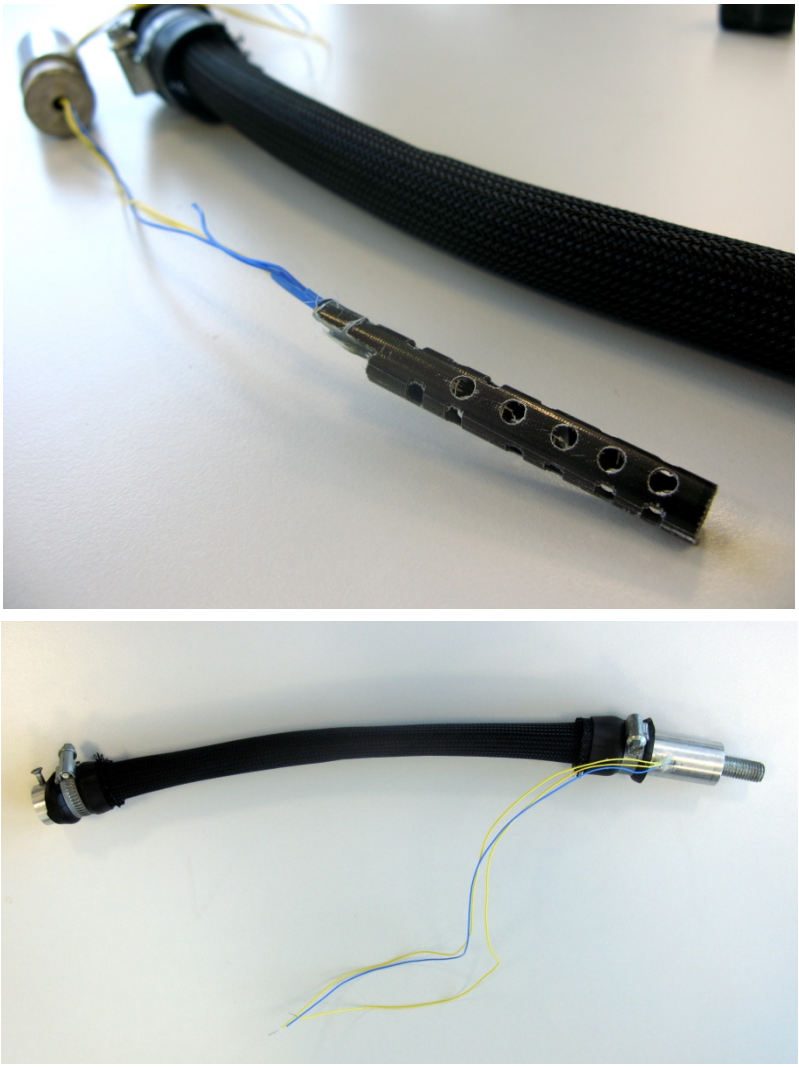

Fig. 9 The temperature sensor placed inside the pneumatic muscle

4.4 Array of Temperature Sensors

The use of an array of fast-response sensors should suppress the temperature non-homogeneity inside the pneumatic muscle (Fig. 10).

We proposed several designs of temperature sensor arrays, but all of them shared the problem of low reliability due to mechanical deformations. As no fixed mounting point is available inside the pneumatic muscle actuator and all the surfaces in the muscle are moving respectively, there is very limited opportunity to reliably place the temperature sensor array covering the muscle volume in a sufficient manner.

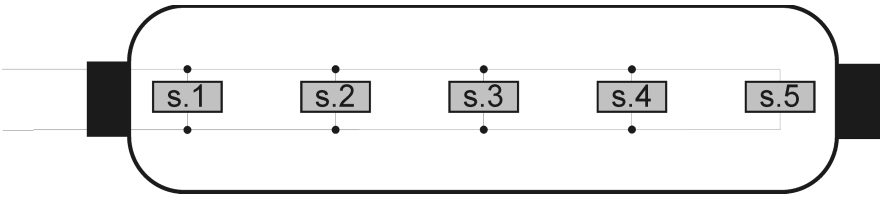

Fig. 10 The array of temperature sensors inside a pneumatic muscle

5 Muscle Design Changes

It is obvious from chapter 4 that non-homogeneous temperature distribution constitutes a serious problem. The pneumatic muscle actuator is much warmer at the end opposite to the gas intake/outlet manifold. On the other hand, the muscle part where the gas intake/outlet manifold is connected remains at the ambient temperature due to good gas exchange (see Fig. 12). All the thermal images show the pneumatic muscle actuators after approx. 20 semi-isotonic 0,5 Hz working cycles (Fig. 11).

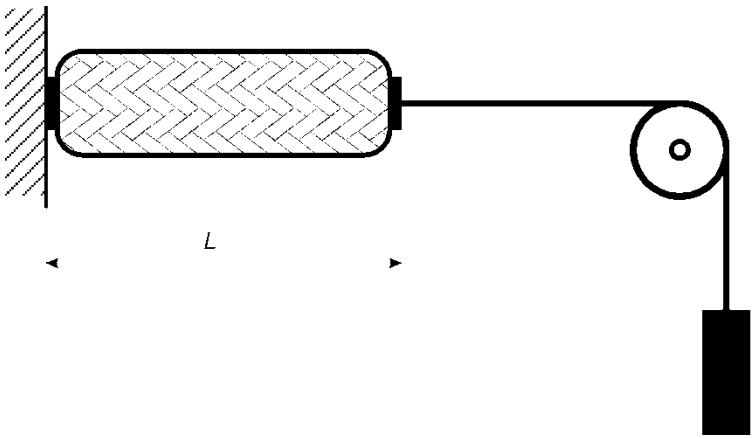

Fig. 11 The semi-isotonic working cycle arrangement

The way to improve the temperature distribution is to ensure uniform air change inside the pneumatic muscle during the muscle working cycle. The only feasible procedure, to achieve this objective is to carry out some muscle filling/venting design changes.

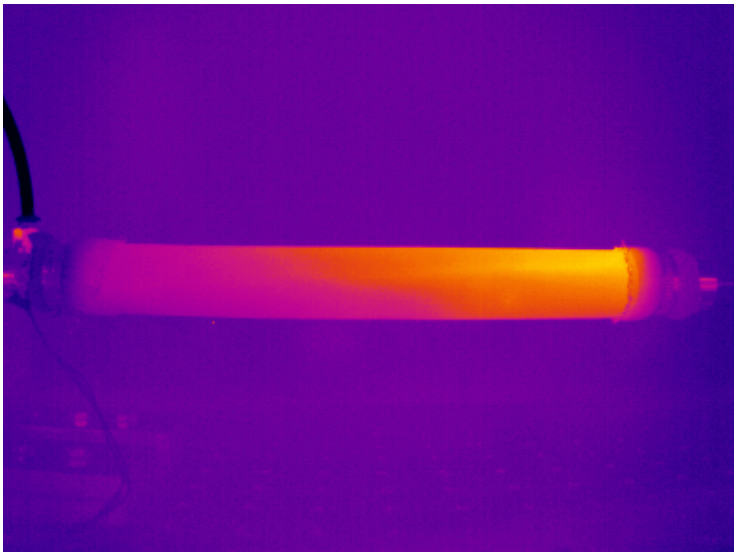

Fig. 12 The thermal image of a common pneumatic muscle

The easiest design change method is to conduct the intake medium to the center of the pneumatic muscle instead of leading it only to the end cup. A similar solution consists in a perforated tube bringing the cold working gas to the entire muscle volume (Fig. 13). The results of this design change can be seen in Fig. 14.

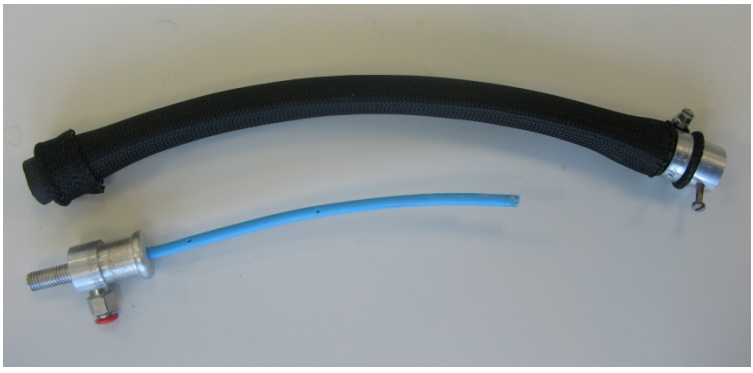

Fig. 13 A pneumatic muscle with gas-leading perforation

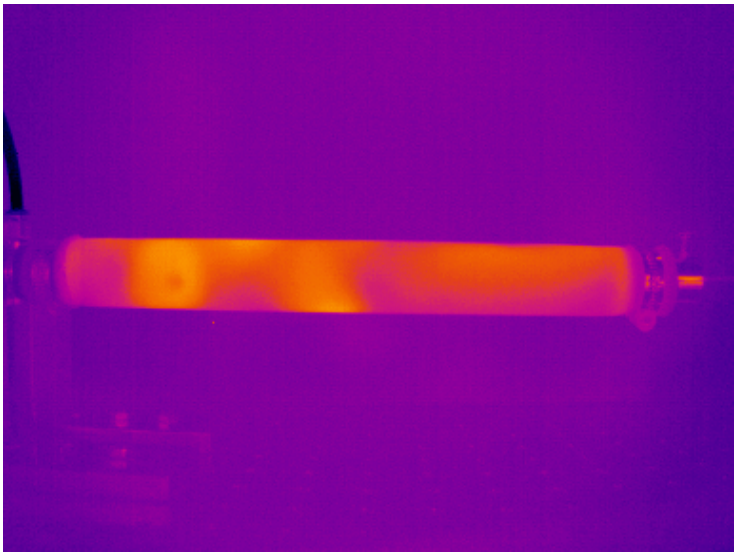

Fig. 14 The thermal image of a pneumatic muscle with a gas-leading perforating tube

A substantially better solution ensuring continuous gas mass flow through the whole volume of a pneumatic muscle is to divide the tubing into intake and outlet lines and to double the filling/venting manifold. The new design has the intake line and manifold at one muscle end cup, while the outlet line and manifold are placed at the opposite muscle end cup. The results of this design change can be seen in Fig. 15.

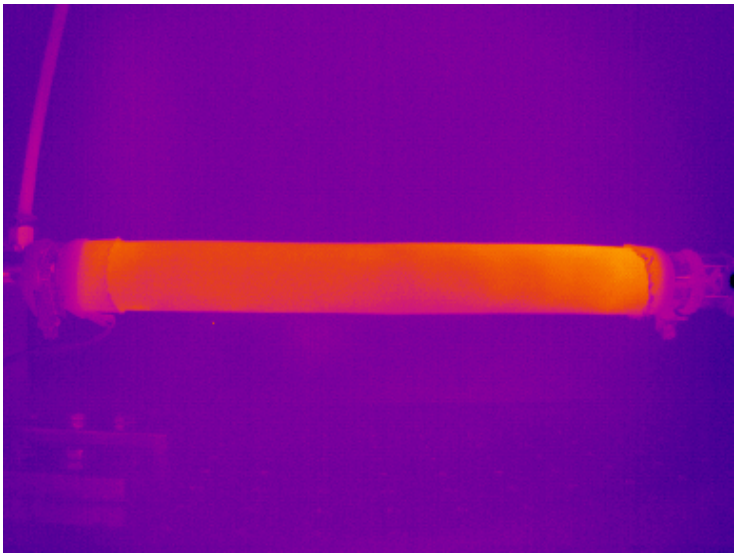

Fig. 15 The thermal image of the flow through the pneumatic muscle design

Now we can obtain homogenous temperature distribution enabling us to use a single, fast temperature sensor placed in the centre inside the pneumatic muscle actuator (chapter 4).

6 Verification of the Mathematical Model

The mathematical model of the system based on the equations from the previous chapter was created for the numerical simulation in Matlab Simulink. First, the model is verified with a simulated working cycle, and then comparison with the waveforms of the real system is carried out.

The isotonic working cycle is simulated; the pneumatic muscle is inflated during the half- period by a constant mass flow of gas, and subsequently deflated with the same mass flow during the other half of the period.

The progress of the temperature measured in the actual muscle and the temperature derived from the model is shown in the graph presented in Fig. 16.

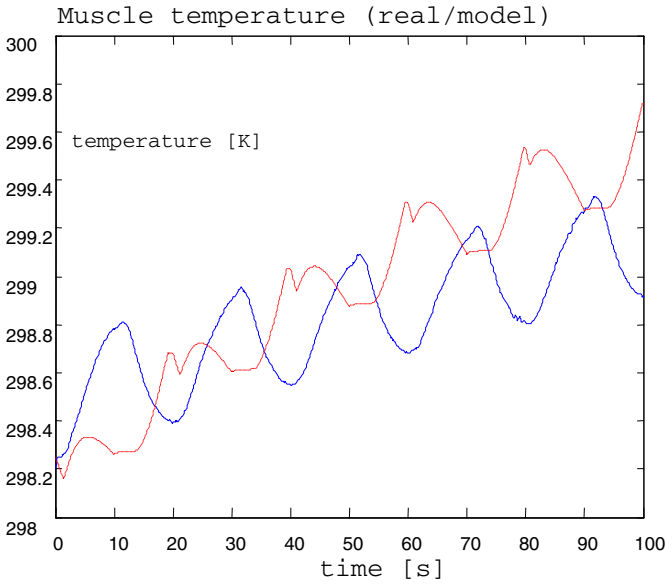

Fig. 16 The instantaneous temperature in a pneumatic muscle – the real system (blue) and model (red)

Let us consider the inertia of the temperature sensor and the time shift caused by the rapid filling and venting of the muscle in the real system against the system model. We can thus see a rough shape match between the signal obtained from a mathematical simulation model and that measured on the real system. The reason for the slower growth of the real muscle temperature is the cooling by the ambient air flowing under the thermal insulation when the muscle is moving.

7 Conclusion

The main objective of this work is to extend the mathematical model of a pneumatic muscle, especially in the field of thermodynamics. The paper applies the method originally designed for pneumatic linear drives [4] on pneumatic muscles, creating a new thermodynamic model; the newly proposed mathematical model includes the heat generated by friction, which has significant influence on the behavior of the actuator.

If the principal task consists in the description of the physical (mainly thermomechanical) phenomena taking place during the working cycle of the muscle rather than in the precise identification of a specific muscle, we obtained a good degree of consistency in the behavior of the model and the real system. The aim of the verification of the model is based on qualitative comparison with the actual behavior of the real system; the related quantitative assessment of accuracy constitutes only a secondary problem.

The paper is focused also on temperature sensor selection and placement. The placement possibilities were described and verified, and the design changes were performed and proved. Thermal imaging camera pictures show the progress of the design of an appropriate temperature measuring system.

The measurements are compared with the simulations, and the obtained results are discussed.

Acknowledgements. This work was supported by the project CZ.1.07/2.3.00/30.0005 of Brno University of Technology.

References

[1] Richer, E., Hurmuzlu, Y.: A High Performance Pneumatic Force Actuator System: Part I-Nonlinear Mathematical Model. ASME J. Dyn. Syst., Meas. Control 122, 416–425 (1999)

[2] Tondu, B., Lopez, P.: Modeling and Control of McKibben Artificial Muscle Robot Actuators. IEEE Control Systems Magazine, 15 – 38 (April 2000)

[3] Doumit, M., Fahim, A., Munro, M.: Analytical Modeling and Experimental Validation of the Braided Pneumatic Muscle. IEEE Transactions on Robotics 25(6), 1282–1291 (2009)

[4] AI-Ibrahim, A.M., Otis, D.R.: Transient Air Temperature and Pressure Measurements During the Charging and Discharging Processes of an Actuating Pneumatic Cylinder. In: Proceedings of the 45th National Conference on Fluid Power (1992)

[5] Chou, C.P., Hannaford, B.: Static and Dynamic Characteristic of McKibben Pneumatic Artificial Muscles. In: IEEE International Conference on Robotics and Automation, vol. 1, pp. 281–286 (1994)

[6] Caldwell, G.D., Medrano-Cerda, G.A., Goodwin, M.: Control of Pneumatic Muscle Actuators. IEEE Control Systems Journal 15(1), 40–48 (1995)

[7] Davis, S.: Enhanced Modelling and Performance in Integrated, Redundant and Self Healing Actuators. University of Salford, 182 p. Ph.D Thesis (2005)

[8] Daerden, F.: Conception and Realization of Pleated Pneumatic Artificial Muscles and their Use as Compliant Actuation Elements. Vrije Universitrit Brusel, 176 p. Ph.D. Thesis (1999)
[9] Davis, S., Canderle, J., Artrit, P., Tsagarakis, N., Caldwell, D.G.: Enhanced dynamic performance in pneumatic muscle actuators. In: Proceedings 2002 IEEE International Conference on Robotics and Automation, USA, vol. 3, pp. 41–2836 (2002)
[10] Burdea, G.: Force and Touch Feedback for Virtual Reality, 339 p. John Wiley (1996) ISBN 0-471-02141-5
[11] Richer, E., Hurmuzlu, Y.: A High Performance Pneumatic Force Actuator System: Part I-Nonlinear Mathematical Model. ASME Journal of Dynamic Systems, Measurement, and Control 122, 416–425 (2000)
[12] Tsagarakis, N., Caldwell, G.D., Medrano-Cerda, G.A.: 7 DOF pneumatic muscle actuator (pMA) powered exoskeleton. In: 8th IEEE International Workshop on Robot and Human Interaction RO-MAN 1999, Rome, pp. 327–333 (1999)
[13] Varga, Z., Moucka, M.: Mechanic of Pneumatic Artifical Muscle. Journal of Applied Science in the Thermodynamics and Fluid Mechanics 3(2/2009), 1–6 (2009)
[14] Caldwell, G.D., Medrano-Cerda, G.A., Goodwin, M.: Characteristics and Adaptive Control of Pneumatic Muscle Actuators for a Robotic Elbow. In: Proceedings of 1994 IEEE International Conference on Robotics and Automation, San Diego, California, pp. 3558–3563 (1994)
[15] Tsagarakis, N., Caldwell, G.D.: Improved Modelling and Assessment of pneumatic Muscle Actuators. In: Proceedings of International Conference on Robotics & Automation, pp. 3641–3646. Dept. of Electronic Engineering University of Salford Manchester M5 4WT, San Francisco (2000)
[16] Davis, S., Caldwell, G.D.: Braid Effects on Contractile Range and Friction Modeling in Pneumatic Muscle Actuators. The International Journal of Robotics Research 25(4), 359–369 (2006)
[17] Bharadwaj, K., Hollander, K.W., Mathis, C.A., Sugar, T.G.: Spring over muscle (SOM) actuator for rehabilitation devices. In: Proceedings of the 26th Annual International Conference of the IEEE EMBS, San Francisco, CA, USA, pp. 2726–2729 (September 2004)

Coordinate Measurement on Wafer Level – From Single Sensors to Sensor Arrays

T. Krah[1,2,*], N. Ferreira[1,2], S. Büttgenbach[2], A. Wedmann[1], F. Härtig[1], and K. Kniel[1]

[1] Physikalisch-Technische Bundesanstalt, Braunschweig und Berlin, Braunschweig, Bundesallee 100, D-38116, Germany
[2] Institute for Microtechnology, Technische Universität Braunschweig, Braunschweig, Alte Salzdahlumer Str. 203, D-38124, Germany
thomas.krah@ptb.de

Abstract. Systems fabricated in microtechnological processes are increasingly employed in industrial products. For that purpose, it is necessary to have a method at hand to measure them, just as macroscopic components and systems too, for reasons of quality assurance. Whereas there already exist a multitude of different systems based on diverse measurement principles for the measurement of single microsystems, a cost-effective measurement of a large number of microsystems on wafer level is currently realizable with optical measurement systems only, a fact that owes less to a technical advantage than to a faster measurement rate. This article portrays arrays fit for a parallelized tactile measurement of geometric dimensions and mechanical qualities of microsystems on a wafer. Moreover, it introduces innovative tactile elements for various measuring tasks and structures to be measured.

Keywords: 3D microprobing, tactile coordinate measurement, sensor array, probe tips.

1 Introduction

Systems fabricated in microtechnological processes are increasingly employed in industrial products, as a consequence of which a method is needed to be able to measure them, just like macroscopic components and systems too, for reasons of quality assurance. Yet, due to the production of microsystems as well as to their qualities, those measurement systems used for measurements in macroscopic dimensions are of a limited suitability only for the measurement of microsystems.

The production of microsystems differs decisively from the production of components and systems of macroscopic range. Whereas macroscopic components are generated either in serial or in partly parallel production, microsystems are

* Corresponding author.

A. Mason et al. (eds.), *Sensing Technology: Current Status and Future Trends III*,
Smart Sensors, Measurement and Instrumentation 11, DOI: 10.1007/978-3-319-10948-0_19

fabricated entirely in parallel. Customarily, as exemplified in Fig. 1, microsystems are arranged in lines and columns in a fixed periodical array on a shared substrate. All microsystems on a shared substrate are produced in parallel, i.e. simultaneously. It is often the case that several substrates are produced at the same time, resulting in an effective output, which in return means a reduction of the costs for the single system. The measurement of all wafers already in the very process of their production is indispensable since flawed specimens can be sorted out instantly, and thus unnecessary costs can be avoided. The most diverse measuring devices with varying measurement principles are available to fulfill the respective measuring tasks. In order to avoid a delay in the fabrication process and thus an increase in cost for the single system, it is beneficial for the measuring devices with which the separate microsystems are measured to allow for the same performance rate as the production facility. However, the expenditure of time depends on the respective measuring device in use. As a basic principle, you can divide measuring devices into tactile measurement systems on the one hand, and non-contact ones on the other hand. While tactile measurement systems have the advantage that they can be used for the measurement of numerous dimensions, it is a disadvantage that they work mostly serially, i.e. every single system must be measured separately one after the other. The measurement process is particularly time-consuming when the shape of all systems found on a wafer has to be determined. Optical measurement systems may have the capacity to measure bigger ranges in one go, but face their limits in structures with high steep edges and narrow gaps. Furthermore, measuring surfaces that reflect strongly and transparent material holds is difficulties. Undercuts cannot be measured by means of optical measurement processes.

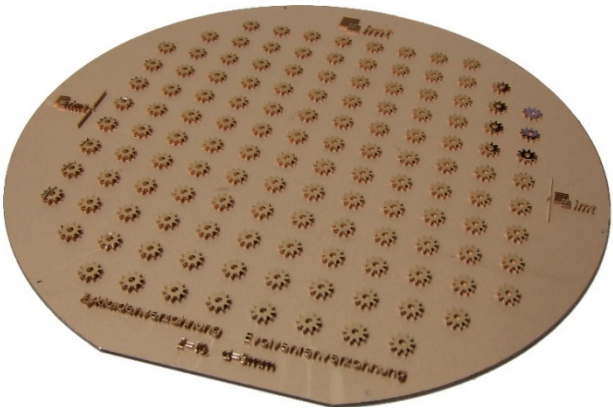

Fig. 1 Typical arrangement of microsystems on a wafer

Microsystems are becoming ever smaller as well as more complex. Yet, the transmitters presently at hand are too big, and the measurement systems do not offer the required resolutions. A multitude of tactile probing systems adjusted especially to microtechnological requirements have been introduced in recent

years. Surveys can be found e.g. in [1] and [2]. These probing systems are partially available in commercial coordinate measuring machines (CMM) and have the advantage of working with extremely small touch forces with the effect that the workpieces are not damaged and offer a high resolution.

The employment of a parallelized tactile metrology comes in handy to realize a cost-effective measurement of a large number of different geometries and thus systems from a batch production, with the possibility to use all advantages of adjusted tactile systems without having to deal with the disadvantage of extensive measuring periods. This article specifies arrays consisting of probes whose lateral distance to the respective neighboring probe corresponds with the distance of the microsystems on the substrate, with the effect that the microsystems are no longer measured one after the other, but all at once in a single measuring process (Fig. 2). The arrays portrayed facilitate not only the measurement of structural dimensions of single systems, but also of shape deviations of a substrate in the process of its generation as well as of forces and displacements in all three spatial directions.

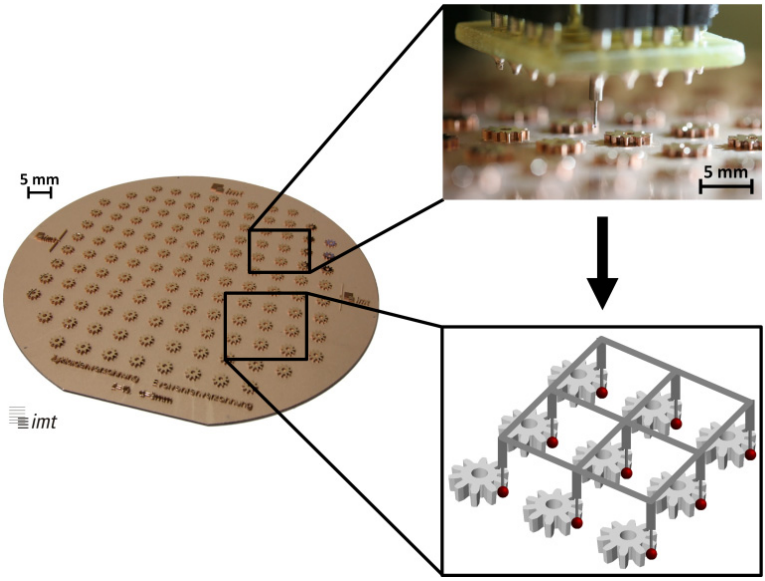

Fig. 2 Transition from measuring microsystems with a single probe to the employment of a probe array

2 Sensor Elements for Tactile Probing of Microstructures

Prior to an in-depth presentation of different models of the probe array, an explanation of the array's operation mode seems reasonable. Looking at the sensor array on a simplified level, it is an arrangement of single sensor elements in a predetermined grid. Based upon this contemplation, it is sufficient to understand

the functions of a single sensor element to be able to comprehend the function of the entire array.

A single sensor element of the sensor array consists of a silicon substrate into which a membrane with center stiffening, the so-called boss, has been etched by means of anisotropic wet-chemical etching. In order to be able to use the component as sensor for force or distance measurement, the tactile elements adjusted to the respective task are deposited onto the boss. They permit a selective force discharge into the membranes. Once the forces take effect upon the tactile elements, the membrane is deformed as shown in Fig. 3. Piezoresistive resistors have been brought into the range of the biggest mechanical tensions, with which the deformation of the membrane can be measured. They are connected to four separate Wheatstone bridges each. Fig. 4 exemplifies a possible lateral arrangement and connection of the resistors.

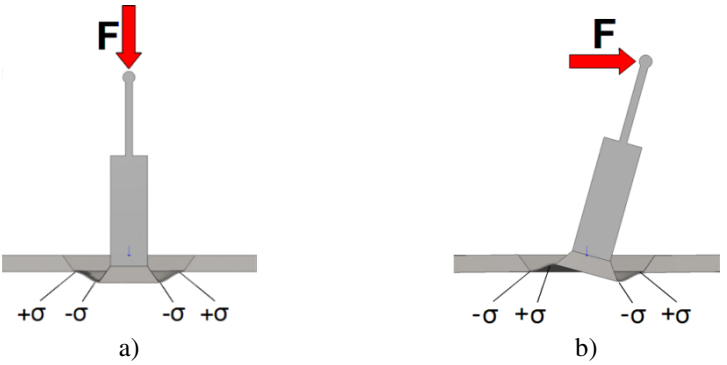

Fig. 3 Deformation state of the membrane of a single sensor with a) vertical, b) horizontal force effect

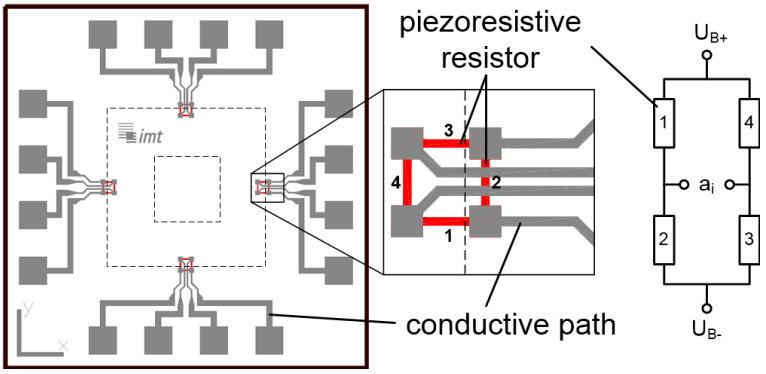

Fig. 4 Single sensor with four Wheatstone bridges

Single sensors for force or distance measurements working on the basis of the same principle have already been introduced in [3] and [4]. In [5], for the first time, the integration of such a probe as depicted above into a commercially available gear measuring instrument is presented (Fig. 5). With the help of an innovative change system (Fig. 6) microstructures of single components can be measured with high precision with already existing measuring devices without the necessity to use microcoordinate measuring machines particularly adjusted to the task, with the effect that a larger measuring range can be used with almost the same precision.

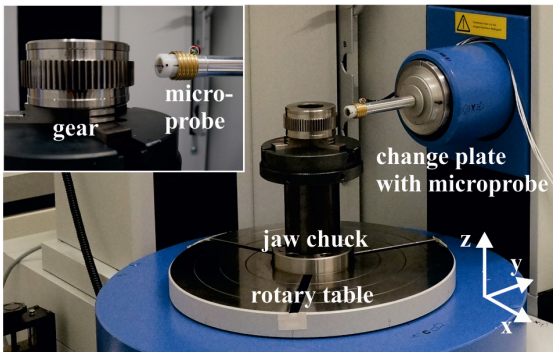

Fig. 5 Set-up for the measurement of a spur gear with the new microprobe system

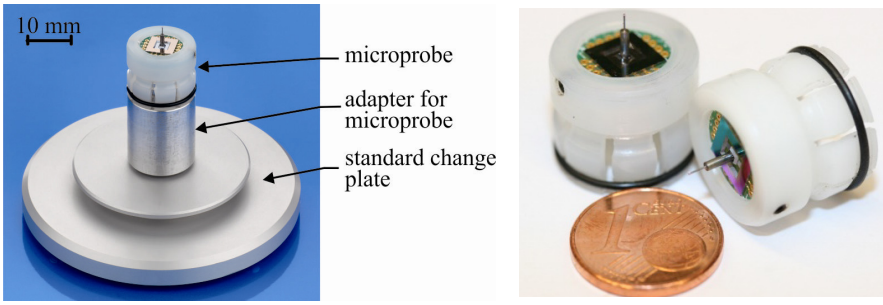

a) b)

Fig. 6 a) Microprobe mounted on a standard change plate, b) assembled 3D microprobing system

To demonstrate and verify the capabilities of the microprobe system shown in Fig. 6 a calibrated spur gear with involute profile was measured on the commercially available gear measuring instrument P40 fabricated by Klingelnberg. The parameters of the gear are listed in Table 1. Before performing measurements with the microprobe, a standard calibration procedure has been carried out on the GMI, during which mechanical and geometrical properties of the stylus are characterized. After this calibration procedure, the microprobe can be used for highly accurate measurements of microgears. The gear measuring

program can be started and the microprobe is selected as probing system. Repeated measurements have been carried out on a calibrated spur gear in a measuring room at a constant temperature of 20°C ± 0.2°C.

Table 1 Parameters for the calibrated involute spur gear

Gear parameter	Value
Normal module m_n	1 mm
Number of teeth z	67
Base circle diameter d_b	62.9594 mm
Pressure angle α	20°
Helix angle β	0°
Tooth width b	15 mm

The slope deviation ($f_{H\alpha}$, $f_{H\beta}$), the form deviation ($f_{f\alpha}$, $f_{f\beta}$) and the total deviation (F_α, F_β) have been measured for the profile and the helix, respectively, and also for the left and right flank of a calibrated tooth. The measurements have been repeated to analyze the repeatability of the microprobe compared to the calibration values obtained with customarily CMMs. According to Table 2 the standard deviations of the measurements with the microprobe are in the range of some 10 nm. The extremely small standard deviations demonstrate the high repeatability of measurements performed with the microprobe. The deviations of the results of the microprobe from the calibration values are mostly in the range of some 100 nm. Even if the microprobe is in a development phase, the results are very accurate and comply with standard calibration measurements to be performed by means of industrial GMIs and standard probing systems.

Table 2 Comparison of the calibration values of the involute spur gear and measured values yielded with the microprobe

Type	Measurand		Calibration		Microprobe		Dev.
			Value in µm	σ in µm	Value in µm	σ in µm	in µm
Profile	Left	$f_{H\alpha}$	-1.66	0.05	-1.80	0.04	0.14
		$f_{f\alpha}$	0.59	0.12	0.42	0.05	0.17
		F_α	1.80	0.09	2.03	0.09	0.23
	Right	$f_{H\alpha}$	-1.64	0.15	-1.56	0.01	0.08
		$f_{f\alpha}$	0.80	0.18	0.58	0.04	0.22
		F_α	1.75	0.19	1.73	0.06	0.02
Helix	Left	$f_{H\beta}$	0.76	0.09	0.53	0.05	0.23
		$f_{f\beta}$	0.46	0.12	0.20	0.02	0.26
		F_β	0.93	0.17	0.50	0.00	0.43
	Right	$f_{H\beta}$	0.74	0.16	0.68	0.04	0.06
		$f_{f\beta}$	0.49	0.15	0.34	0.02	0.15
		F_β	0.98	0.12	0.67	0.06	0.31

In order to be able to measure even smaller gears and microstructures it is necessary to further reduce the diameter of the probe spheres. At the moment the smallest probe sphere diameters commercially available amount to a minimum of 70 µm. There are two main problems accompanying decreasing sphere diameters, one being an easy detachment of the probe spheres from the shaft as the surface at the end of the shaft is too small for connecting the sphere to it. The other problem lies in the fact that standards lead to a big length at a small shaft diameter in the tactile elements. As a consequence, the tactile elements are scarcely bending resistant, a phenomenon already present in tactile elements with a 125 µm-size probe sphere. Therefore, there is the need for further tactile elements that are adjusted to the respective measuring task. In chapter 4 "Tactile elements adjusted for the measurement of Microsystems" different tactile elements will be described in detail. At this point only single probes are presented, onto which straight styli with probe sphere diameters of 100 µm and 50 µm are attached (Fig. 7). A detailed description of these probes can be found in [6].

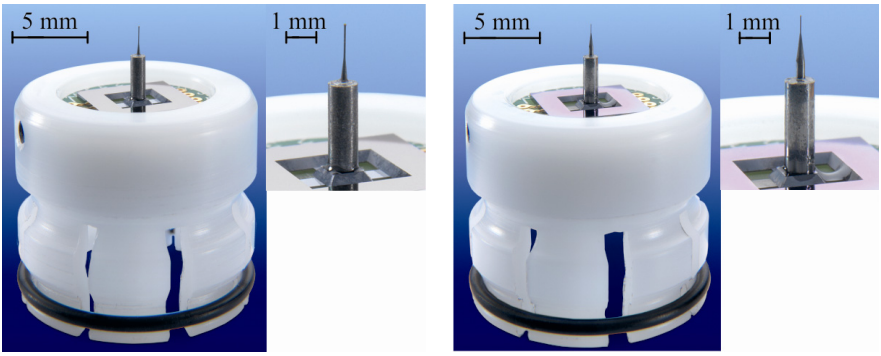

Fig. 7 Photographs of mounted 3D microprobing systems with different probe sphere diameters, a) probe sphere diameter 100 µm, b) probe sphere diameter 50 µm

3 Tactile Sensor Array

For the measurement of structures of microcomponents left on a shared substrate as common during their fabrication, a single probe as described above is no longer eligible for a cost-effective employment. Measuring all systems on a substrate would take up too much time. The solution is a parallelized probing of microsystems.

3.1 Requirements for Parallel Probing

In general, requirements posed to a tactile sensor array for the employment in coordinate metrology and those posed to a tactile sensor with e single tactile

element are basically the same, among them touch forces as little as possible to avoid the risk of damaging or even destroying the structures to be measured with the penetrating sphere. A prerequisite for little touch forces is not only an obligatory insignificant stiffness, but, considering the fact that the touch force is also proportional to a low moving mass [7]. Apart from that the sensor ought to have a high eigenfrequency to permit the selection of a respectively high measurement speed. These demands can be met by using a stiff deformation element, which would, however, result in a considerable increase of the touch force, and by allowing the sensor to have a low weight only. A low weight would shorten des CMM's stopping distance or rather the sensor's stopping distance when in the process of touching a workpiece and thus bring along the consequence that the probe sphere penetrates the workpiece less deeply, which means in return that the achievable measurement insecurity is reduced. Another required quality is a preferably low crosstalk, with regard to the sensor among the separate signals, and with regard to the array additionally among neighboring single probes as conspicuous crosstalk could prevent a clear distinction of the touch direction. If it is intended to apply the sensor not only as a switching, but also as a scanning sensor, it is desirable to have a preferably linear relationship of the sensor output signal and the deflection of the tactile element for the benefit of a particularly easy conversion of the different dimensions.

A tactile sensor array for the use in coordinate metrology faces several further demands, an obvious one being the equipment with the same grid dimensions as the microsystems on the wafer that are to be measured. If the grid dimension of the microsystems is smaller than the smallest possible distance between two neighboring probes of the sensor array, it is either necessary to re-create a distance of the microsystems on the wafer that corresponds with the distance of the sensor array, or the grid dimensions of the microsystems and the sensor arrays need to be adjusted in such a way that the distance of the probes is an integer multiple of the distance between the microsystems on the wafer. Further requirements can be deduced from the fact that the sensor array portrayed in this paper is a statically over-determined system. It is vital for the tactile elements to be both all of the same length and to be assembled in the identical grid dimension as the single sensor elements. In order to measure the same measuring point with the single microsystems, all tactile elements must be brought in contact with the systems to be measured, which is achieved by moving the sensor array until that is the case. Unlike possible with w sensor with a single tactile element the sensor element cannot be turned arbitrarily to reach places with difficult access. Therefore, it is exclusively the shape of the tactile elements that warrants the fact that a broad range of different structures can be measured. The housing of the sensor array also requires more attention than with a single sensor. Unfavorable housing might deform the sensor element decisively to such an extent that, just as the case with strongly deviating lengths of the tactile elements, some of the elements may fail to have contact with the structures to be measured before the measuring range of individual sensor elements of the array has been exceeded. Moreover, crosstalk may increase from one sensor element to the other.

The special requirements of the sensor array have to be taken into account not only with regard to the mechanical set-up. Wiring and signal evaluation as customary with a single sensor are no longer practical with a sensor array due to the large number of signals to be processed. In spite of relatively large dimensions of a sensor array distinct problems of space can occur during the wiring, both on the sensor element and in the housing, depending on the respective design. As a consequence, it has to be an important objective under the designing of the sensor to reduce the number of contacts and use the surface available as efficient as possible.

For reasons of completeness it should be mentioned that the touching and evaluation strategy, too, poses special requirements, factors which, however, are not meant to be eluminated here as they form the focus of other papers. The touching and evaluation strategies play a tangential role only in that respect that the sensor array and the CMM in use have to be calibrated. The relevant calibration structures are presented in chapter 3.4.

3.2 Mechanical Set-Up

The probe arrays portrayed in this paper are composed of a shared substrate of monocrystalline silicon. Just as performed with the single probes, boss membranes have been etched into the substrate in regular intervals by means of anisotropic wet-chemical etching. The distance of the sensor's boss membranes correlates with the distance of the systems on the wafer to be measured, or an integer multiple of that distance. Both for the probe arrays presented here as well as for the test specimens in use a homogeneous grid dimension of 6.5 mm was chosen, aiming at providing enough space to try out the diverse types of connection alternatives. Likewise, the membranes' deflections are determined with brought-in piezoresistive resistors. Compared to single probes, in case of probe arrays the application of the tactile elements requires particular attention. Whereas the orientation of the tactile elements plays a lesser significant role with single probes, it is an essential issue for the function of a probe array. Applying every stylus onto the sensor array one by one results in statistically allocated deviations in x-, y- and z-direction as well as from the right angle opposite the sensor surface. If these deviations grow too big, the probe spheres no longer touch the workpieces to be measured simultaneously. If additionally too extreme dimensional variations occur in the structures to be measured, it may be the case that some single probes on the probe array have not yet touched the respective workpiece, while others have already exceeded the limits of the permitted measuring range. A special assembly jig was designed to secure that all tactile elements have the same orientation. With it, all tactile elements are applied to the sensor element in a parallel procedure. This assembly jig is described in detail in [8]. Fig. 8 a shows a probe array in a 3 x 3 arrangement.

The probe array is connected to a coordinate measuring machine (CMM), both mechanically and electrically, by means of a printed circuit board (PCB), onto

which the array is applied by using flip-chip technology (Fig. 8 b). Flip-chip technology is a technology which proves beneficial as it facilitates an even distribution of contact pads over the complete sensor element and thus the creation of a steady connection of sensor element to PCB. Moreover, it is possible to set up a defined gap whereby a mechanical stop vertical to the sensor element's surface is implemented.

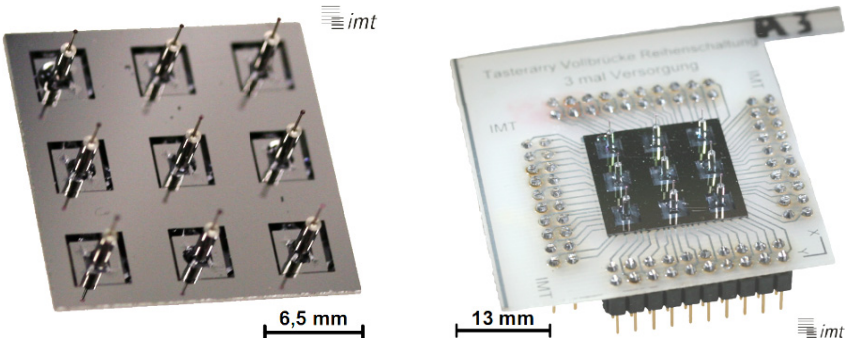

a) b)

Fig. 8 Probe array in 3 x 3 arrangement; a) front view of the sensor element with tactile elements, b) probe array applied to the printed circuit board by means of flip-chip

Sensor elements with a plastic deformation element can be used to reduce touch forces. However, compared to sensor elements entirely made of monocrystalline silicon, sensor elements with a plastic membrane show a smaller linearity on the one hand, and considerably more significant hysteresis effects on the other, with the arrays' structure and operational mode remaining unaltered. It is solely the process steps and the geometries connected and reached that undergo a change. Fig. 9 a presents a probe array whose frame and deformation elements are made entirely of plastic. A description of the fabrication process of this array can be found in [9]. Depending on the required sensitivity, the membrane consists alternatively of a layer of PerMX 3020 or PerMX 3050 provided by DuPont in either 20 µm or 50 µm thickness, the frame having a layer of EP SUEX D TDFS by DJ DevCorp in a varying thickness between 500 µm – 1000 µm. The membranes' deformations are measured with piezoresistive resistors. Fig. 9 b shows the example of a further design variety as a single probe. [10] offers an elaborate characterization of the probe. It consists of a frame of monocrystalline silicon with all four internal sides each holding a cantilever with piezoresistive resistors to measure the deformation. A membrane made up of a layer of PerMX 3050 is laminated onto the frame and the cantilevers. Finally, the tactile element is fixed to the membrane's very center. By contrast with probes with a silicon membrane, probes with plastic membrane offer decisive advantages – not only the smaller touch forces due to the clearly smaller E-module, but also the fact that owing to their tough behavior the membranes are less prone to break. Apart from that, it is possible to observe the workpieces to be measured optically through the sensor element under the touch process.

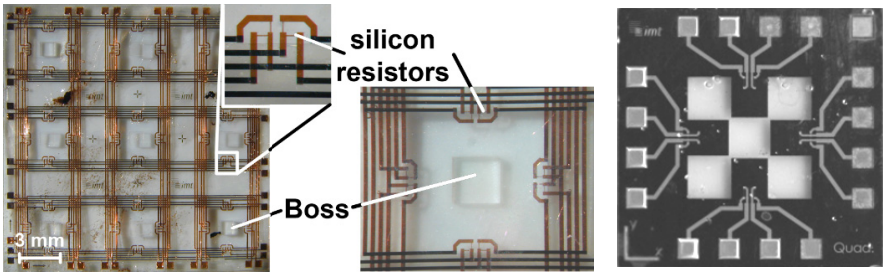

Fig. 9 Sensor elements with plastic membrane; a) probe array fabricated entirely of plastic, with piezoresistive resistors made of silicon, b) single silicon probe with four cantilevers with piezoresistive resistors and plastic membrane

3.3 Electric Connection

The simple arrangement of single probes as e.g. in Fig. 8 b in a shared substrate bears its disadvantages for the electric connection of a probe array. The expenditure for the wiring would quickly rise high, inevitably leading to problems of space both on the adapter board and in the feed lines. A probe array in a 3 x 3 arrangement calls for 144 contact pads. This means that the number of needed pads for a square array would grow with every line and column by the factor $16 \cdot x^2$, x representing the number of lines or columns. Along with this large number of contact pads the probability of deficient contacts and thus, of the entire array, would increase. Therefore, the minimization of contact pads is the paramount objective for the electric connection of a sensor array.

Diverse arrangements of the piezoresistive resistors and the electric connection have been established for a 3 x 3 probe as shown in Fig. 10 a. In a first design adjustment, the resistors in a square arrangement were sorted along the four exterior sides of the membrane according to Fig.4. All bridges of the probe arrays were connected in series. Fig. 10 presents the layout of the sensor element that facilitates a reduction of the number of contact pads can by nearly half down to 74. The additional pads that can be seen in Fig. 10 a, serve solely the purpose of being able to bridge single probes damaged under probing in order to prevent the array as a whole from becoming useless. However, the number of pads needed continues to amount to $8 \cdot x^2+2$ for a square probe array. This connection has the advantage that for the connection of the resistors, it necessitates one metallization layer only, a circumstance that downsizes error rate, production time and costs of the sensor element substantially. Furthermore, the ever-presence of all output voltages of the bridges renders possible different layouts and variations of the amplifier circuit, the analog-digital-converters and multiplexers as well as of the signal analysis.

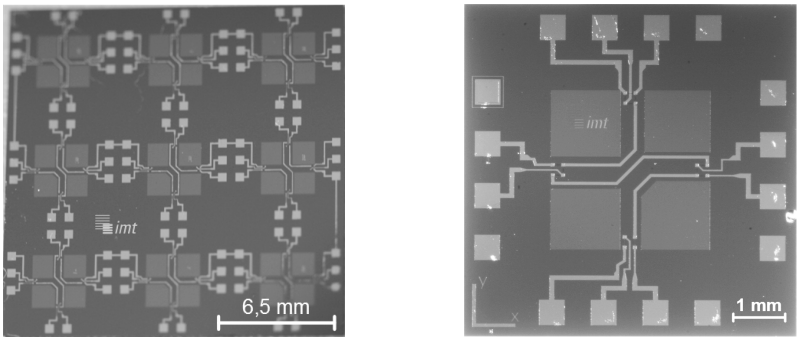

Fig. 10 First adjustment of design, a) connecting all bridges of the probe array in series, b) connection for a single probe

The wiring expenditure for the design presented in Fig. 10 a continues to be notably high. Various designs with an arrangement of the resistors along the four sides of the membranes in lines and columns were implemented with the aim to minimize the expenditure for the primary electronics and to further reduce the number of contact pads. Fig. 11 a demonstrates a design in which, while selecting the appropriate line and column, the four bridges of a single sensor were energized and the diagonal voltages of the bridges were picked off via the associated signal lines. The signal lines were also arranged in lines and columns. With this design, the number of pads could be reduced down to 30, which equals a reduction by 79 % compared to an array of single probes, and by 60 % compared to the first design adjustment. A further advantage of this design is the position of all pads on the sensor edge, which means that the sensor can also be contacted by means of wire bonding. The resistors of the design shown in Fig. 11 b were connected to Wheatstone bridges, too. The difference to the design in Fig. 11 a lies in the fact that the resistors are not connected to Wheatstone bridges while on the sensor

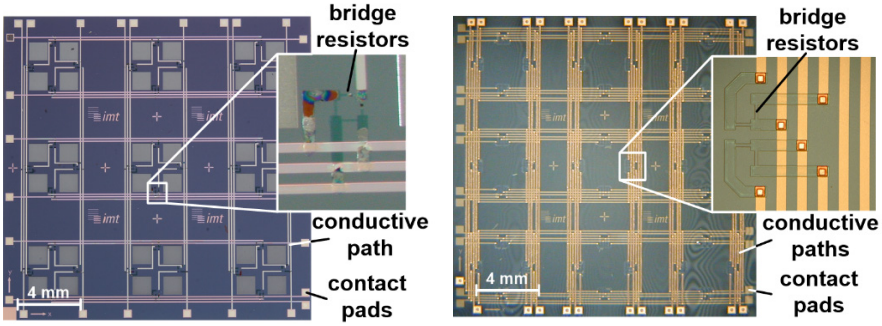

Fig. 11 Probe array with the signal and supply lines arranged in lines and columns, a) serial connection of the four bridges of a single sensor, b) external connection of the resistors to Wheatstone bridges

element, but via an external circuitry, the intention behind this being the effort to avoid an influence of other bridges upon the diagonal voltage of a single bridge or rather a single sensor's bridges. But then, this alternative craves a significantly larger number of contact pads (48 pads).

Fig. 12 displays yet another design. With this example, the deflection of the stylus is determined exclusively by the employment of a single resistor on every side of the membrane. The application of this design has brought forth a further successful reduction of the number of pads down to 14, i.e. a cutback of pads by 81 % in comparison with the design shown in Fig. 10 and by over 90 % in contrast with the connection as in a single probe. The resistance values for the design presented in Fig. 12 a can be measured with several different measurement procedures, the simplest being a simultaneous measurement of current and voltage. Fig. 12 b exemplifies a design whose resistance values are defined by measuring the length of time in which a capacitor is charged via the resistor to be determined, a process which holds the advantage of displaying the resistance value directly as a digital numerical value without necessitating a prior conversion into other intermediate quantities. Capacitors have already been integrated on the sensor element to keep a measurement deviation caused by different capacity values as insignificant as possible. For the purpose of compensating changes in resistance emerging from varying temperatures, resistors for the measurement of temperatures in the probe array have been brought in outside the range of mechanical tensions with both designs.

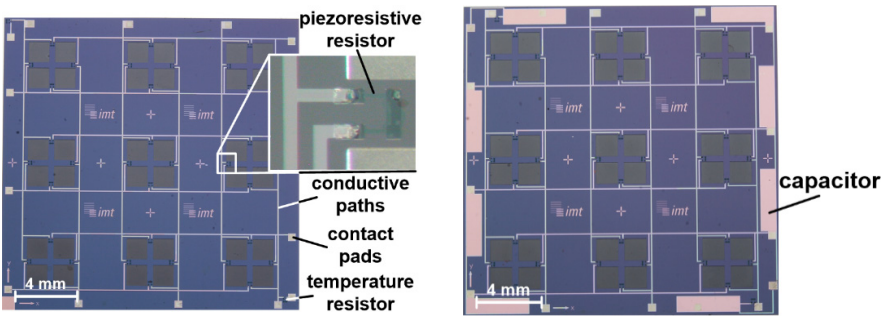

Fig. 12 Sensor array with a) a single resistor per membrane side, b) with additional capacitors

3.4 Characterizing the Probe Array

The characterization of a probe array according to the design shown in Fig. 10 (thickness of membrane 25 µm, arrangement of resistors as in Fig. 4) serves as an example at this point, with the objective to present rather the special features and

effects of a probe array during a parallelized touching process than to display a range of absolute numerical values of single parameters in the different probe designs.

A sphere plate is used as calibration phantom, with sapphire spheres with a diameter of 3 mm fixed on a silicon base body (Fig. 13), the grid dimension of the spheres amounting to 6.5 mm ± 2 µm. Every single sphere was measured in 5 rings at altogether 47 locations. To define the correlation between the deflection of the probe sphere and the sensor signal the array was manually placed parallel to the specimen in the 3 possible angular positions. After touching the first probe sphere the array or rather the calibration phantom has been moved by 50 µm in x- and y-direction, by 15 µm in z-direction. Sensor 7 was excluded from consideration in the measurements documented here as the signal of one of the four bridges failed and would thus not have delivered representative results.

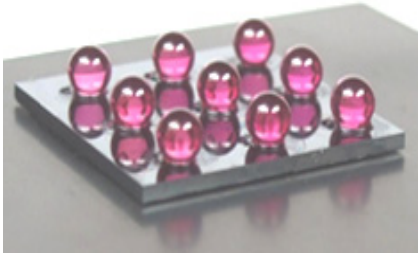

Fig. 13 Sphere plate with ruby spheres in a 3 x 3 arrangement to calibrate probe arrays

Fig. 14 exemplifies the signals of a probe array for a touch performance in x-direction. Strikingly, the characteristic curve of the single sensors start at different positions on the feed direction. The reason for it is the fact that the single probe spheres are not arranged precisely in the prescribed grid. Due to angular deviations of the tactile elements and probe spheres positioned on the shaft not exactly in center, the probe spheres come in contact with the spheres of the calibration phantom at different points in time or, to phrase it differently, at different positions of the array. The deviations of the calibration sphere diameters and centers amount to 0.25 µm and less than 0.3 µm respectively and are therefore negligible. We learn from Fig. 14 that there is a maximum deviation from the prescribed grid dimension of approximately 43 µm. The sensitivities of the separate sensors range between 0.118 ± 0.007 V/µm, which corresponds with the values found in comparable single sensors. Accordingly, the variation of approximately 12 % is comparable to that of single probes. The linearity fault of max. 0.08 %, though, is decisively smaller. Generalized conclusions with regard to all sensor arrays must not be drawn too readily as so far not a sufficient number of measurements with different probe arrays has been carried out upon which could

be claimed to be statistically valid. However, with a value of max. 0.1 %, other probe arrays show similarly small linearity faults, so that it seems safe to assume that the arrangement of the single probe in a probe array as well as the selected mounting and connection technology have a positive influence on linearity.

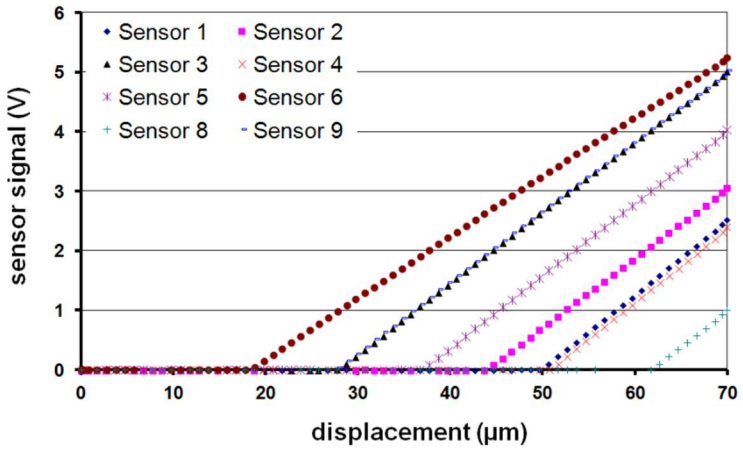

Fig. 14 Lateral touch performance

Fig. 15 depicts the signals of a probe array for a touch performance in z-direction. From the diagram it can be gathered that the majority of the probe spheres do not have any contact with the calibration phantom. The curves for the respective single probes do not show any deflection, a problem that should however not be blamed entirely on a defective assembly of the tactile elements. On the one hand, touch performances in z-direction have a considerably smaller measuring range than those in x- or y-direction, which results in a greater effect of the deviations of the probe sphere's position. On the other hand, measurements of the shaft lengths have shown that the length deviations of the thinner part of the commercial tactile elements are already too significant to be eligible for the use in the assembly jig presented in [8]. For those single probes which have had contact with the corresponding calibration spheres, a maximum linearity fault of 0.5 % could be determined, the sensitivities amounting to 0.294 ± 0.021 V/µm, which is a 2.5 to 3 fold higher sensitivity than in horizontal direction. While single probes show an increased sensitivity in z-direction, too, for full-membranes it is about 8-9 times higher in vertical than in horizontal direction. Further tests, amongst others with structured membranes such as cross-membranes, will have to reveal whether the obvious difference between the behavior of a single probe and that of the array is caused by a potential compression of the air enclosed beneath the sensor element, whether the flip-chip connection in use is influenced, or whether the influence on the value owes solely to process variations occurring under the fabrication.

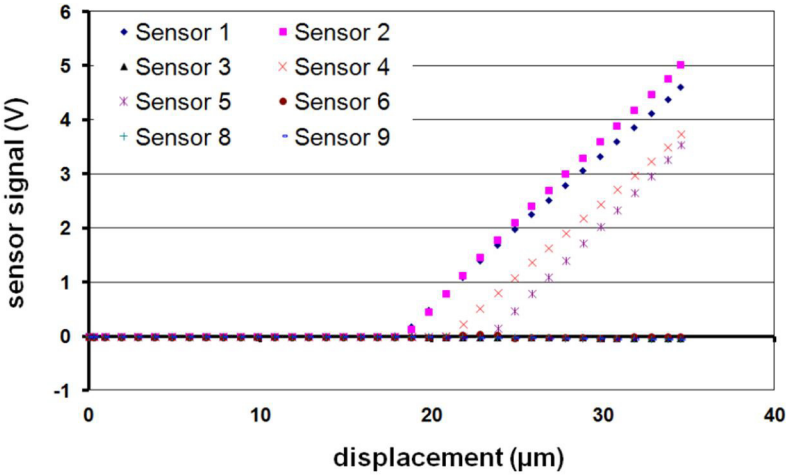

Fig. 15 Vertical touch performance

4 Tactile Elements Adjusted for the Measurement of Microsystems

In contrast to single probes, as a consequence of the necessary orientation towards the microsystems on the wafer, probe arrays cannot be turned arbitrarily in any direction in order to be able to collect measuring points anywhere on the workpiece. Therefore, it is indispensable to have tactile elements at hand, by means of which as many measuring points as possible can be measured at one setting. Currently, the only tactile elements commercially available for the measurement of microstructures, as e.g. used for the probe array in Fig. 8, are straight and made of hard metal with ruby probe spheres. For the time being, the smallest probe sphere diameters amount to 70 µm. The production tolerance that exceeds the acceptable limit poses the greatest disadvantage for the employment of these tactile elements in probe arrays. As a consequence, there is the need for further tactile elements that are adjusted to the respective measuring task.

Laterally protruding probes are necessary for the measurement of inner microstructures or microundercuts. The measurement of inner microthreads is commercially most significant for the measurement of inner microstructures. For the measurement of inner threads, generally tactile elements with two laterally protruding probe spheres, so-called T-shaped probes, are employed. At present, the T-shaped probes available for the measurement of threads do not have probe sphere diameters smaller than 300 µm, which means in return that with them only inner threads larger than M3 x 0,5 can be measured. Robust innovative micro T-shaped probes have been developed for the measurement of smaller threads

(Fig. 16) [11, 12]. They feature the method of clamping the probe spheres, and not, as hitherto customary, brazing or gluing them, which facilitates an easy replacement of the spheres in case of wearout or irremovable staining. Furthermore, the new design provides a secure frame of the probe spheres and a high stability of the probe. The base body of the micro T-shaped stylus consists of hard metal and is fabricated by means of micro electrical discharge machining (EDM). The probe spheres in use can consist of any material adjusted to the qualities of the workpiece. The smallest probe spheres relevant for the tests described in this article are made of ruby and have a diameter of currently 110 µm. For probes with this probe sphere diameter the length of the shaft is set to 1.82 mm, its cross-section to 200 µm x 250 µm and the stylus constant (length between the spheres' outside) to 490 µm. Measurements of thread gauge rings in a size M10, M0.9 and M0.7, each with a pitch of 0.175 µm, carried out with a T-shaped stylus as shown in Fig. 16, have turned out successfully.

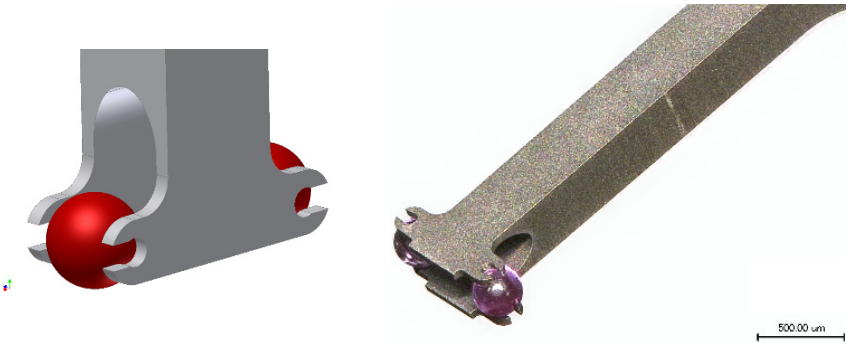

a) b)

Fig. 16 T-shaped microprobe for the measurement of inner microstructures, a) sketch, b) photograph

In order to demonstrate the performance of the new T-shaped styli comparative measurements were performed. For this purpose, a thread ring gauge of a size M3 x 0.5 was calibrated with the smallest T-shaped microprobe with standard design commercially available (carbide probe spheres soldered up obtusely with the laterally projecting shaft). For comparison, two new T-shaped microprobes with ruby probing spheres were applied, one of them being glued in addition to the clampering. The probe sphere diameter of all three styli in use amounted to 290 µm respectively. The styli were applied in a commercial 3D coordinate measuring machine. System parameters of the CMM as probing force, dynamics and velocity were adapted to the needs of the stylus within the possibilities of the CMM. Measuring the inner microthreads was performed as measurements of macroscopic inner threads. In accordance with [13] two measuring points were

recorded on one side of the thread, another one on the opposite (Fig. 17). By calculating the average of point P_1 and P_2 and a subsequent subtraction of the x- or y-values with regard to point P_3, the diameters are calculated. The measurement results obtained fort he thread ring gauge M3 x 0.5 (Table 3) with the T-shaped microprobes correspond excellently with the calibrated values – within the scope of measurement inaccuracy (pitch diameter: U = 1.5 µm, k=2). Looking critically at the measurements of the pitch diameter, it can even be stated that in case of the T-shaped microprobe with the glued probe spheres the average values of the measurements match completely. The average pitch diameter of the measurements performed with the T-shaped microprobe with the clampered probe spheres lies 0.6 µm below the one obtained with the probe in standard design. The divergences of the pitch diameter with ten measurements carried out each amount to 0.4 µm for the probe in standard design, to 0.2 µm for the T-shaped microprobe with glued probe spheres, and to 0.3 µm for the T-shaped microprobe with clampered probe spheres. With regard to the T-shaped microprobe with clamped probe spheres the results show that the probe spheres do not move in the shaft when touched. With an insufficient clamping force an unacceptably large pitch diameter would have been measured. Apart from that, no run-in or settlement processes could be observed. The results for the core diameter are similarly good. In a comparison of the average values of the core diameters measured for the T-shaped microprobe with the ones measured for the T-shaped probe in standard design, the average diameter for the T-shaped microprobe with glued probe spheres amounts to 0.6 µm and for the T-shaped microprobe with clampered probe spheres 1 µm below the one measured for the T-shaped probe in standard design. The divergences amount to 0.1 µm respectively for the T-shaped probe in standard design and for the T-shaped microprobe with glued probe spheres, and to 0.5 µm for the T-shaped microprobe with clampered probe spheres. The slope of the thread ring gauge amounted to 0.5 mm for all three T-shaped probes. The divergences amounted to 0.1 µm in all three cases.

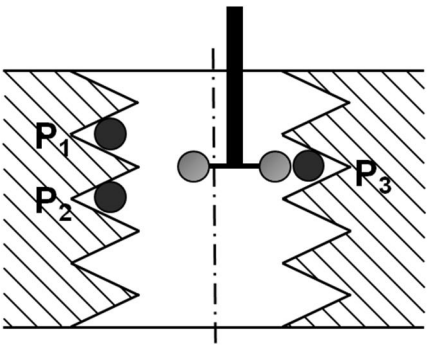

Fig. 17 Measurement of an inner thread according to [13]

Table 3 Comparison of the calibration values of the involute spur gear and the measured values yielded with the microprobe

			µ probe sphere glued		**µ probe sphere clamped**	
		standard construction (calibration)	**measurement value**	**deviation from standard construction**	**measurement value**	**deviation from standard construction**
pitch diameter	mean value in mm	2.6554	2.6554	0	2.6548	-0.0006
inner diameter	mean value in mm	2.4325	2.4319	-0.0006	2.4315	-0.001
pitch	mean value in mm	0.5	0.5001	+0.0001	0.5001	+0.0001

More reliable results could be obtained with the microthread ring gauges M10 x 0.175, M0.9 x 0.175 and M0.7 x 0.175. To measure them, the probe shown in Fig. 16 with a probe sphere diameter of 120 µm were used. Likewise according to [13], the thread ring gauges were measured concerning the parameters pitch diameter, core diameter, and slope. At this point, a display of the calibration values for these thread ring gauges is done without, as they are prototypes with which in part innovative manufacturing processes were tested, and the calibration of such threads is not yet feasible as the necessary prerequisites are not yet fulfilled. However, first measurements have shown that the divergences have the same dimensions as with the thread ring gauge of a size M3 x 0.5, which means that the portrayed design of a T-shaped probe is also suitable for the measurement of threads significantly smaller than M1.

The styli presented in Fig. 18 were also developed for the measurement of microundercut structures, but for structures with a better accessibility. The styli shown stand out due to the fact that the probe spheres are not attached in any way, but have been fabricated in one piece with the shaft, an innovation which eliminates the risk that the probe sphere might be detached from the shaft under the probing of a workpiece. The styli are produced by using micro wire-electro discharge machining (WEDG), with the smallest probe sphere diameters amounting to 40 µm. Fig. 19 elucidates the process. A tungsten carbide electrode with a diameter of 300 µm poses as source material for the process. First of all, the electrode is shortened at the processing wire (diameter 200 µm) in order to receive

a defined face surface. Once the electrode is centered and positioned on top of the processing wire, the outline contour of the tactile elements is traced, starting with the probe sphere. The electrode rotates during the entire process. Depending on the respective measurement task, diameters of spheres and shafts as well as the required stiffness, it may become necessary to produce a taper in the transition section from the thicker to the thinner part to reduce the bending length. In a last step, the tactile element is separated from the electrode at the desired length. Tungsten carbide rods with a diameter of 1 mm serve as source material for the production of the carriers. At first, single pieces were separated from the rods with a precision diamond disc saw. Afterwards, the required number of holes was drilled by means of EDM with a 300 µm electrode. After machining, the styli are assembled into the various required probe shapes. A connection of shaft and carrier is established by means of adhesion. Continuative information on the styli shown in Fig. 18 can be found in [14].

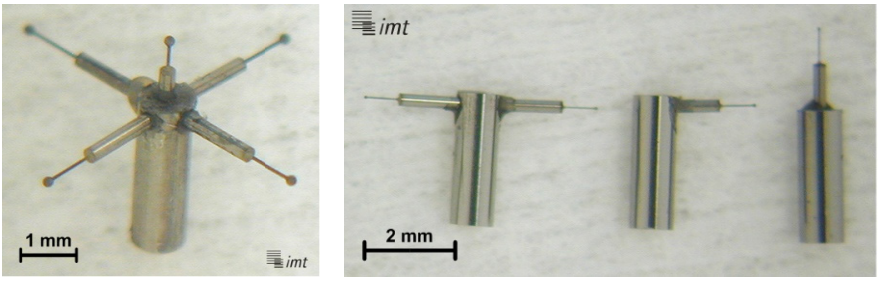

a) b)

Fig. 18 Survey of the different shapes of the tactile elements fabricated

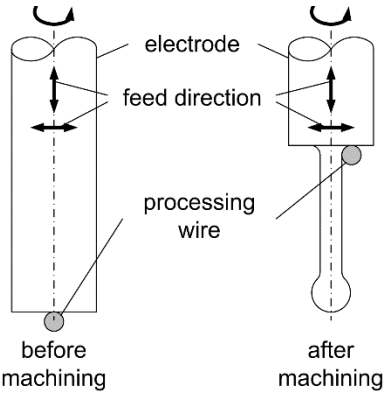

Fig. 19 Producing the shafts by means of wire-electro discharge machining

5 Summary and Prospect

The probe arrays presented in this paper pose an innovative additional tactile measurement procedure to the hitherto existing tactile and optical ones customarily employed in the measurement of microsystems on wafer level. The application of the probe arrays succeeds in overcoming the biggest disadvantage of tactile measurement systems, namely the slow measurement rate when measuring all microsystems on a wafer. As a result, for the first time ever, a cost-effective performance of tactile measurements on wafer level is feasible. Another positive aspect about the probe array is its suitability for the performance of traceable measurements.

The biggest difference of carrying out measurements with a probe array compared to using a single probe is the fact that it is not possible to turn the array arbitrarily in any direction to collect measuring points, which makes an exact orientation of the probe array towards the microsystems on the wafer prior to the performance of measurements indispensable. Therefore, an adjustment of the touch strategy to this constraint is vital. A compensation of the missing rotatory degrees of freedom can be obtained by adjusting the tactile elements to the respective measuring task.

There is a need for further investigations both in the field of membrane shapes, in particular membranes with openings, and with regard to the mounting and connection technology in order to better grasp their effect on the probe array's qualities. Equally important is an extended statistical research. Also, more styli adjusted to different measuring tasks will have to be developed, the adjustment taking either place in terms of trying new materials to optimize the probe qualities or to lower the costs, or the geometries such as the orientation of the shafts or the probe sphere diameter will have to be conformed.

Acknowledgements. This paper is funded by the Deutsche Forschungsgemeinschaft – German society of scientific research (DFG) in the framework of priority program SPP 1159 "New strategies in metrology and testing technique for the production of microsystems and nanostructures" and the Federal Ministry of Economics and Technology within the funding program MNPQ Transfer. The Physikalisch-Technische Bundesanstalt (PTB) would like to thank Emuge Franken and Lehren- und Messgerätewerk Schmalkalden for kindly providing the thread gauge rings. One of the authors (S.B.) gratefully acknowledges financial support by the Volkswagen Foundation.

References

[1] Weckenmann, A., Peggs, G., Hoffmann, J.: Probing systems for dimensional micro- and nano-metrology. Measurement Science and Technology 17, 504–509 (2006)

[2] Cao, S., et al.: Recent developments in dimensional metrology for microsystem components. Microsystem Technologies 8, 3–6 (2002)

[3] Bütefisch, S., Dauer, S., Büttgenbach, S.: Silicon three-axial tactile sensor for the investigation of micromechanical structures. In: 9th International Trade Faire and Conference for Sensors, Transducers & Systems (Sensor 1999), vol. 2, pp. 321–326 (1999)
[4] Phataralaoha, A., Büttgenbach, S.: A novel design and characterization of micro probe based on a silicon membrane for dimensional metrology. In: Proc. XIX Eurosensors, vol. 2, p. WPb31, Barcelona, Spain (2005)
[5] Ferreira, N., et al.: Integration of a silicon based microprobe into a gear measuring instrument for accurate measurement of micro gears. In: Proc. 11th International Symposium of Measurement Technology and Intelligent Instruments, Aachen, Germany (2013)
[6] Ferreira, N., et al.: Reducing the Probe Ball Diameters of 3D Silicon-Based Microprobes for Dimensional Metrology. In: Proc. 7th International Conference on Sensing Technology, Wellington, New Zealand, pp. 301–306 (2013)
[7] Claverley, J.D., Leach, R.K.: A vibrating micro-scale CMM probe for measuring high aspect ratio structures. Microsystem Technologies 16(8 – 9), 1507–1512 (2010)
[8] Krah, T., Büttgenbach, S.: Vorrichtung zur parallelen Montage von Mikro-Kraftsensorarrays und taktilen Elementen. In: Proc. Mikrosystemtechnik Kongress, Dresden, Germany, pp. 651–654 (2007)
[9] Krah, T.: Mikrotasterarrays zur parallelisierten Messung von Mikrostrukturen, Dissertation. Shaker Verlag (2011)
[10] Ferreira, N., Krah, T., Büttgenbach, S.: Micro sensors with structurable polymer membrane for accurate 3D force and displacement measurements. In: Proc. IEEE Sensors 2013, Baltimore, Maryland, USA, pp. 1074–1077 (2013), doi:10.1109/ICSENS.2013.6688397, ISBN: 978-1-4673-4642-9
[11] Krah, T., Wedmann, A., Kniel, K., Härtig, F.: Measurement and evaluation processes for inner micro structures. In: Proc. 13th International Conference of the EUSPEN, vol. 1, pp. 120–123 (2013)
[12] Krah, T., Wedmann, A., Kniel, K., Härtig, F.: Mess- und Auswerteverfahren für Mikroinnenstrukturen. In: 6th Kolloquium Mikroproduktion 2013. Schriftenreihe des Institus für Produktionsmesstechnik, Shaker Verlag, vol. 10, p. B22 (2013)
[13] EURAMET cg-10, Version 2.0, Determination of Pitch Diameter of Parallel Thread Gauges by Mechanical Probing (2011)
[14] Krah, T., Lesche, C., Schrader, C., Büttgenbach, S.: Star probes machined by micro-EDM for the use in micro-coordinate metrology. In: Proc. 7th International Workshop on Microfactories, Daejeon, Korea (2010)

Tailoring of Magnetic Properties and GMI Effect of Amorphous Microwires by Annealing

A. Zhukov[1,2,*], M. Ipatov[1], A. Talaat[1], J.M. Blanco[3], and V. Zhukova[1]

[1] Department of Material Physics, Basque Country University, UPV/EHU, 20018 San Sebastian, Spain
[2] IKERBASQUE, Basque Foundation for Science, 48011 Bilbao, Spain
[3] Department of Applied Physics, EUPDS, Basque Country University, UPV/EHU, 20018, San Sebastian, Spain
arkadi.joukov@ehu.es

Abstract. We studied Giant magnetoimpedance (GMI) effect and magnetic properties of amorphous Fe-Co rich as-prepared and annealed microwires. We measured the GMI magnetic field and frequency dependences, hysteresis loops and domain walls (DWs) dynamics of composite microwires produced by the Taylor-Ulitovski technique. We observed that these properties can be tailored either controlling magnetoelastic anisotropy of as-prepared CoFeBSiC microwires or controlling their magnetic anisotropy by heat treatment. High GMI effect has been observed in as-prepared Co-rich microwires. High DW velocity and rectangular hysteresis loops we observed in heat treated Co-rich microwires. We observe increasing of the DW velocity under stress in some annealed samples. At certain annealing conditions we observed coexistence of GMI effect and fast DW propagation in the same annealed sample.

Keywords: Glass-coated microwires, GMI effect, Magnetic softness, Domain wall dynamics, magnetoelastic anisotropy.

1 Introduction

Amorphous magnetic materials have been intensively studied along last decades owing to excellent soft magnetic properties suitable for applications in magnetic devices requiring magnetically soft materials such as transformers, inductive devices, magnetic sensors [1, 2]. Extremely soft magnetic properties achieved in amorphous materials are related to lack of long-range atomic order (and consequently magnetocrystalline anisotropy), of microstructural inhomogeneities and defects typical for crystalline materials and elevated electrical resistance. Consequently amorphous materials can present very low coercivity, high magnetic permeability and low magnetic losses. The most convenient method of preparation

* Corresponding author.

A. Mason et al. (eds.), *Sensing Technology: Current Status and Future Trends III*,
Smart Sensors, Measurement and Instrumentation 11, DOI: 10.1007/978-3-319-10948-0_20

of amorphous materials involves rapid quenching from the melt allowing fabrication of amorphous ribbons and wires [1, 3]. In the absence of magnetocrystalline anisotropy and defects typical for crystalline magnets shape magnetic anisotropy of amorphous materials with high magnetic permeability becomes relevant. Consequently magnetic properties of amorphous ribbons and wires are rather different.

Amorphous wires introduced at the end of 80^{th} present several magnetic properties quite interesting for applications in magnetic sensors, such as magnetic bistability and giant magnetoimpedance, GMI, effect [4-7]. These features are closely related to specific magnetic domain structure of amorphous wires presenting cylindrical symmetry, i.e. with core-shell domain structure and high circular magnetic permeability of Co-rich amorphous wires with circular magnetization easy direction.

In fact both magnetic bistability and GMI effect can be also realized in amorphous ribbons [8, 9], but magnetic shape and magnetoelastic anisotropies of amorphous wires are more favorable for realization of both effects.

The origin of magnetoelastic anisotropy of amorphous wire is related to quenching stresses distribution arising during rapid solidification from the melt [10]. The solidification process during rapid quenching starts from the surface. Consequently the outer shell that first solidified induces strong and complex residual stresses inside the wire. The interplay between the shape and magnetoelastic anisotropies give rise to axial easy magnetization direction in the inner core and either radial or circular (depending on the magnetostriction constant sign) easy magnetization direction in the outer shell of wires [10, 11].

Conventional technique for amorphous wires preparation is the "in-rotating-water" quenching technique allowing fabrication of amorphous wires with diameter between 70 and 200 μm [4-11]. Aforementioned magnetic bistability of amorphous wire observed in magnetostrictive compositions (either Fe-rich or Co-rich) is related to the presence of a single Large Barkhausen Jump interpreted as the magnetization reversal in a large single domain [10, 11]. This peculiar phenomenon is quite interesting for various applications, but large Barkhausen jump is observed above some critical length [12]. This critical length correlates well with the demagnetizing factor [12]. The origin of the critical length has been explained considering that the closure end domains penetrate from the wire ends inside the internal axially magnetized core destroying the single domain structure [12]. For the case of Fe-rich amorphous wires (with diameter about 120 μm) this critical length is about 7 cm, which is quite inconvenient for applications in magnetic micro-sensors and microelectronics. For Co-rich amorphous wires (with diameter about 120 μm) the critical length is about 4 cm [13]. Below such critical length the hysteresis loop of amorphous wires loses its squared shape.

Consequently additional efforts on modification or existing technology and/or development of alternative technology have been performed. Proposed modification of the "in-rotating-water" quenching technique consists in posterior cold drawing of cast wires [10, 14]. Moreover alternative technologies such as

melt extraction or glass-coating techniques have been proposed for fabrication of thinner amorphous microwires [15-17].

It is demonstrated that the Taylor-Ulitovsky technique for fabrication of glass-coated microwires allows preparation of thinnest microwires (with metallic nucleus diameters from about 100 μm down to 0.05 μm) [17, 18]. Consequently considerable reduction of the critical length has been achieved for the case of glass-coated microwires: in microwires with diameter about 10 μm the critical length is about 2 mm, which is quite suitable for applications in microsensors [17, 18]. Additionally existence of glass-coating in many occasions is beneficial for properties of glass-coating microwires allowing improvement of mechanical and corrosive properties [18, 19].

Similarly the demagnetizing factor affects the GMI effect and therefore drastic metallic nucleus diameters reduction achieved in the case of glass-coated microwire is essentially relevant for the GMI related applications as well [20].

It is worth mentioning that all aforementioned technologies for preparation of amorphous wires with reduced dimensionality present certain disadvantages. For the case of cold drawn microwires the drawing technique can damage the surface layer that affects the GMI inducing the GMI hysteresis [21]. Melt extraction usually allowing fabrication of microwires with diameter above 30 μm similarly with ribbons involves different quenching regimes in contact and free surfaces [15]. Consequently the morphology, internal stresses strength and spatial distribution and even the structure might be different in these two regions. Finally Taylor-Ulitovsky technique involving simultaneous solidification of metallic nucleus inside the glass coating results in elevated internal stresses arising from different thermal expansion coefficients of the metallic alloy and glass [5]. These internal stresses give rise to the additional magnetoelastic anisotropy. Therefore special efforts are needed for minimization of elevated magnetoelastic anisotropy and optimization of magnetic properties of glass-coated microwires. At the same time the magnetoelastic energy of glass-coated microwires is determined by the ratio, ρ, of metallic nucleus diameter, d, to total microwire diameter, D. Therefore controlling the geometry of glass coated microwires through the thickness of glass-coating and metallic nucleus diameter we can tailor the strength on internal stresses and hence the magnetoelastic anisotropy and various magnetic properties like switching field which depends on internal stresses [5, 18, 21-23].

In glass-coated microwires with diameter about 10 μm this critical length is much shorter (about 2 mm) which is quite suitable for applications in microsensors.

Magnetic bistability of amorphous wires was interpreted in terms of nucleation or depinning of the reversed domains inside the internal single domain and the consequent domain wall, DW, propagation [24-27]. Perfectly rectangular hysteresis loop shape in this case is related with a very high velocity of such DW propagation. It is demonstrated by few methods that the remagnetization process of such magnetic microwire starts from the sample ends as a consequence of the depinning of the domain walls and subsequent DW propagation from the closure domains [12, 27].

As mentioned above the method of fast solidification of thin metallic nucleus in the presence of glass coating induces additional complex internal stresses. Therefore recently considerable attention has been paid to the optimization of magnetic properties using different kinds of processing such as annealing or glass coating removal [18, 28-30].

Aforementioned magnetoelastic energy, K_{me}, plays the determining role in the formation of magnetic properties of amorphous microwires. As described elsewhere [18], the magnetoelastic energy is given by

$$K_{me} \approx 3/2\ \lambda_s \sigma_i, \tag{1}$$

where λ_s is the magnetostriction constant, and total stresses $\sigma = \sigma_{appl} + \sigma_i$, where σ_{appl} and σ_i are applied and internal stresses respectively.

The magnetostriction constant, λ_s, depends mostly on the chemical composition of amorphous metallic alloy. Vanishing λ_s values can be achieved in amorphous Fe-Co based alloys with Co/Fe ≈70/5 [18, 31, 32].

On the other hand, the value of internal stresses inside the metallic nucleus, σ_i is determined by the ρ-ratio between the metallic nucleus diameter, d, and total microwire diameter, D ($\rho = d/D$).The strength of internal stresses increase with decreasing of the ρ-ratio [22,23].

The conventional way to relax internal stresses and stabilize magnetic properties is a heat treatment.

Additionally in low magnetostrictive compositions stress (either applied or internal) dependence of the magnetostriction can be relevant. The dependence of the magnetostriction on stress can be expressed as [33]:

$$\lambda_{s,\,\sigma} = \lambda_{s,0} - B\sigma \tag{2}$$

where $\lambda_{s,\sigma}$ is the magnetostriction constant under stress, $\lambda_{s,0}$ is the zero-stress magnetostriction constant and B is a positive coefficient of order 10^{-10} MPa and σ– stresses. This change of the magnetostriction can be associated with both applied, σ_{appl}, and internal, σ_i, stresses ($\sigma = \sigma_{appl} + \sigma_i$). Therefore for the low-magnetostrictive compositions (with $\lambda_{s,0} \approx 10^{-7}$) and internal stresses of the order of 1000 MPa the second term of eq. (2) is almost of the same order as the first one. Consequently, one can expect drastic changes of magnetic properties for the same compositions with ρ-ratio.

Aforementioned GMI effect is considered as one of most promising for applications in low magnetic field detection [5, 14, 16, 18, 34]. Magnetic sensors developed using amorphous wires with GMI effect allow achieving pT magnetic field sensitivity with low noise [14, 35]. The origin of the GMI effect is related to the skin effect of magnetically soft conductor [6, 7]. High circumferential permeability usually exhibited by amorphous wires with vanishing magnetostriction constant is essential for observation of high GMI effect [5-7, 34-36]. On the other hand GMI effect in amorphous microwires with positive magnetostriction constant exhibiting rectangular hysteresis loop is usually quite small because of low initial permeability [37]. Therefore special efforts for

improving of GMI effect in amorphous microwires with non-zero magnetostriction constant are needed. Successful attempts of improvement of the GMI effect either by nanocrystallization of amorphous precursor or by induction of transverse easy magnetization direction under special heat treatment (under stress and/or magnetic field) have been reported [37-40].

On the other hand quite fast magnetization switching in magnetically bistable microwires and related fast DW propagation along the wire are intensively studied [41-43]. The DW velocity is affected by the magnetoelastic energy, K_{me} in the way that the highest DW velocity is reported for amorphous microwires with the lowest magnetoelastic energy, K_{me} [43].

The understanding of the origin of high DW velocity in magnetic microwires can be important for technological applications for data storage and magnetic logics using DW dynamics [44-46].

Consequently presently most promising applications of glass-coated magnetic microwires are related with optimization of the GMI effect and DW dynamics.

The necessary condition for observation of fast DW propagation is the magnetic bistability typically observed in Fe-rich microwires with rectangular hysteresis loops [5,43]. On the other hand the condition for achievement of considerable GMI effect is high circular magnetic permeability usually observed in Co-rich microwires with low and negative magnetostriction constant [1,2, 21]. Consequently it is believed that GMI effect related to high circular magnetic permeability and fast DW propagation related to magnetic bistability cannot be simultaneously observed in the same microwire. But from the point of view of applications creation of the samples exhibiting both aforementioned properties is very attractive.

On the other hand when the even small changes of the composition or even stress relaxation can drastically affect the magnetic properties of glass-coated microwires in the case of metallic nucleus with nearly-zero magnetostriction constant [18, 47].

Therefore, the purpose of this chapter is to study the effect of magnetoelastic anisotropy on magnetic properties, GMI effect and DW propagation in amorphous magnetically soft microwires paying attention to find the conditions for observation of these two effects simultaneously.

This chapter provides a critical review of the state-of-the-art of aforementioned properties suitable for magnetic wires application and of recent studies and state-of-the-art real-time methods of tailoring of magnetic properties and GMI effect of magnetically soft glass-coated microwires in order to fit requirements in magnetic microsensor applications.

2 Fabrication of Microwires and Experimental Technique for Studies of Magnetic Properties and GMI Effect

Studied glass-coated microwires produced by modified Taylor-Ulitovsky method described elsewhere [5,18]. Schematic picture of the process is shown in Fig.1.

Essentially the laboratory process consists of the molten metal that fills the glass capillary and a microwire is thus formed where the metal core is completely coated by a glass. We concentrated on studies of $Co_{69.2}Fe_{4.1}B_{11.8}Si_{13.8}C_{1.1}$ (D=30.2; d=25.6 μm) glass-coated microwires with magnetic properties typical for most demanded microwires with nearly-zero negative magnetostriction constant.

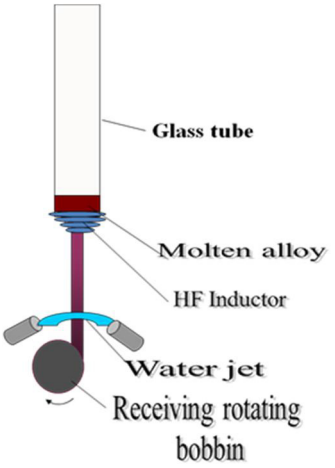

Fig. 1 Schematic picture of the fabrication process allowing preparation of glass-coated microwires

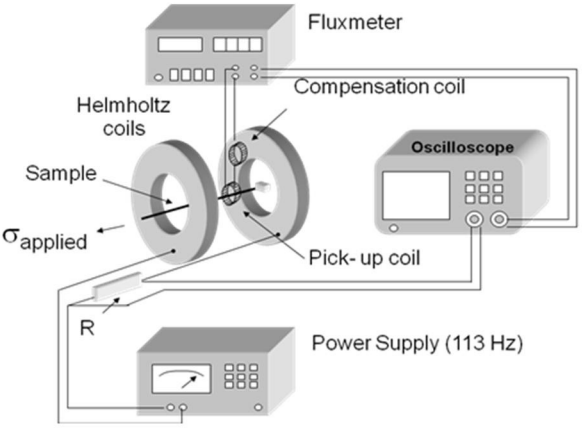

Fig. 2 Schematic picture of the experimental set-up for measurements of hysteresis loops

Hysteresis loops have been determined by flux-metric method (see schematic picture in Fig.2), as described elsewhere [26].

We measured magnetic field dependences of impedance, *Z*, and GMI ratio, $\Delta Z/Z$, for as-prepared samples and after heat treatments.

The magneto impedance ratio, $\Delta Z/Z$, has been defined as:

$$\Delta Z/Z = [Z(H) - Z(H_{max})]\ 100 / Z(H_{max}), \quad (3)$$

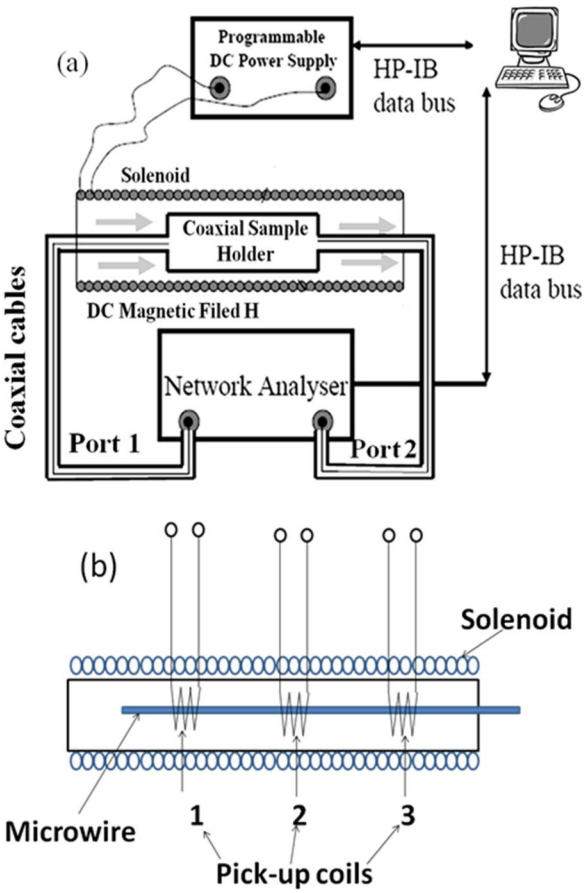

Fig. 3 Schematic picture showing principles for revealing of the diagonal, ς_{zz}, and off-diagonal, $\varsigma_{z\varphi}$, impedance matrix elements (a) and experimental set-up for DW velocity measurements (b)

An axial *DC*-field with maximum value, H_{max}, up to 8 kA/m was supplied by a magnetization coils.

We used specially designed micro-strip sample holder. The sample holder was placed inside a sufficiently long solenoid that creates a homogeneous magnetic field, *H*. The sample longitudinal impedance Zw = Zz*l*, where l is the wire length, was measured using vector network analyzer from reflection coefficient S_{11}. The static bias field H_B was created by the DC bias current I_B applied to the sample through a bias-tee element (see Fig.3a). The off-diagonal impedance $Z_{\phi z}$ was measured as transmission coefficient S_{21} as a voltage induced in a 2-mm long

pick-up coil wound over the wire. All experimental graphs show both ascending and descending branches of the field dependencies of the real part of impedance Z so that the magnetic hysteresis can be evaluated. More details on experimental technique can be found in our previous publications (see for example [48]).

The technique allowing measuring the DW velocity in thin wires is well described elsewhere [26,49]. In order to activate DW propagation always from the other wire end in our experiment we placed one end of the sample outside the magnetization solenoid. We used 3 pick-up coils, mounted along the length of the wire and propagating DW induces electromotive force (*emf*) in the coils, as described in ref. [49] (see Fig.3b). These *emf* sharp peaks are picked up at an oscilloscope upon passing the propagating wall.

Then, DW velocity, v, is estimated as:

$$v = \frac{l}{\Delta t} \tag{4}$$

where l is the distance between pick-up coils and Δt is the time difference between the maximum in the induced *emf*.

The microwire is placed coaxially inside of the primary and pick-up coils so, that one end is inside of the primary coil. Magnetic field, H, is generated by solenoid applying rectangular shaped voltage.

Samples annealing under stress or without has been performed in conventional furnace as described elsewhere [28].

3 Giant Magneto-Impedance Effect

As already mentioned in the introduction, the GMI effect usually observed in soft magnetic materials phenomenologically consists of the change of the AC impedance, $Z = R + iX$ (where R is the real part, or resistance, and X is the imaginary part, or reactance), when submitted to an external magnetic field, H (see Fig.4a). The GMI effect was well interpreted in terms of the classical skin effect in a magnetic conductor assuming the dependence of the penetration depth of the *ac* current flowing through the magnetically soft conductor on the *dc* applied magnetic field [5,6]. Extremely high sensitivity of the GMI effect to even low magnetic field attracted great interest in the field of applied magnetism basically for applications for low magnetic field detection.

Generally, the GMI effect was interpreted assuming scalar character for the magnetic permeability, as a consequence of the change in the penetration depth of the *ac* current caused by the *dc* applied magnetic field. The electrical impedance, Z, of a magnetic conductor in this case is given by [6,7]:

$$Z = R_{dc}\, krJ_0(kr)/2J_1(kr) \tag{5}$$

with $k = (1 + j)/\delta$, where J_0 and J_1 are the Bessel functions, r –wire's radius and δ the penetration depth given by:

$$\delta = \sqrt{\pi\sigma\mu_\phi f} \tag{6}$$

where σ is the electrical conductivity, f the frequency of the current along the sample, and $\mu\phi$ the circular magnetic permeability assumed to be scalar. The *dc* applied magnetic field introduces significant changes in the circular permeability, $\mu\phi$. Therefore, the penetration depth also changes through and finally results in a change of Z [6,7].

Usually for quantification of the GMI effect the magneto impedance ratio, $\Delta Z/Z$, defined above by eq. (3) is used.

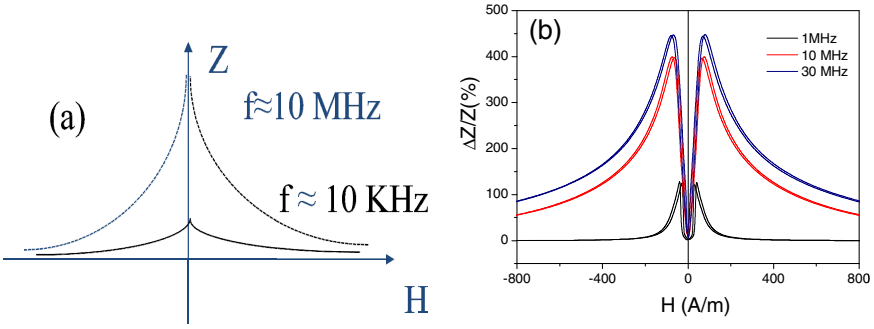

Fig. 4 Schematic representation of GMI effect (a) and magnetic dependence of GMI ratio (b) measured in $Co_{67}Fe_{3.85}Ni_{1.45}B_{11.5}Si_{14.5}Mo_{1.7}$ microwire

The main features of the GMI effect are the following:

i). Large change in the total impedance usually above 100%. Usually for the case of amorphous wires with high circumferential permeability the highest GMI effect is reported [6,7]. Thus, tailoring the magnetic anisotropy through the geometry of amorphous microwires few researchers reported on achievement of up to 600% GMI ratio observation in Co-rich microwires (see example in Fig.4b for $Co_{67}Fe_{3.85}Ni_{1.45}B_{11.5}Si_{14.5}Mo_{1.7}$ microwire) with vanishing magnetostriction constant [18,36]. In this case, it is quite promising for the application of magnetic sensors.

ii). The GMI materials, whether wires, ribbons or films, are usually extremely soft magnetic materials. It was pointed out [18] that the good magnetic softness is directly related to the GMI effect: the magnetic field dependence of the GMI spectra is mainly determined by the type of magnetic anisotropy [18,20]. Thus the circumferential anisotropy leads to the observation of the maximum of the real component of wire impedance (and consequently of the GMI ratio) as a function

of the external magnetic field. On the other hand, in the case of axial magnetic anisotropy the maximum value of the GMI ratio corresponds to zero magnetic fields [20], i.e. results in a monotonic decay of the GMI ratio with the axial magnetic field.

iii). The alternating current plays an important part in the GMI effect. The main reason is that like magnetic permeability, GMI effect presents tensor character [18]. Therefore AC current flowing through the sample creates circumferential magnetic field.

There are many publications related with the origin of the GMI effect [6,7,20]. It must be underlined, that the GMI effect origin has been explained based on the theory of classical electrodynamics [6,7].

iiii). Cylindrical shape and high circumferential permeability observed in amorphous wires are quite favorable for achievement of high GMI effect [6,7,10,20]. As a rule, better soft magnetic properties are observed for nearly-zero magnetostrictive compositions. It is worth mentioning, that the magnetostriction constant, λ_s, in system $(Co_xFe_{1-x})_{75}Si_{15}B_{10}$ changes with x from $-5x10^{-6}$ at x= 1, to $\lambda s \approx 35\ x10^{-6}$ at x≈0.2, achieving nearly-zero values at Co/Fe about 70/5 [31,32].

In ferromagnetic materials with high circumferential anisotropy (the case of magnetic wires) the magnetic permeability possesses the tensor nature and the classic form of impedance definition is not valid.

Consequently the "scalar" model of GMI effect was significantly modified taking into account the tensor origin of the magnetic permeability and magneto impedance [20,36]. Non-diagonal components of the magnetic permeability tensor and impedance tensor were introduced [20,36] in order to describe the circumferential magnetic anisotropy in amorphous wires. It was established that to achieve high GMI effect, the magnetic anisotropy should be as small as possible [20].

From the point of view of industrial applications low hysteretic GMI effect with linear magnetic field dependence of the output signal are desirable [14]. Anti-symmetrical magnetic field dependence of the output voltage with linear region has been obtained for pulsed GMI effect based on detection of the off-diagonal GMI component of amorphous wires [18,36].

As mentioned above, the shape of magnetic field dependence of the GMI effect (including off-diagonal components) is intrinsically related with the magnetic anisotropy and peculiar surface domain structure of amorphous wires [18,20,36]. Magnetic anisotropy of amorphous microwires in the absence of magnetocrystalline anisotropy is determined mostly by the magnetoelastic term [18, 36]. Therefore the magnetic anisotropy can be tailored by thermal treatment [18, 36]. On the other hand recently considerable GMI hysteresis has been observed and analyzed in microwires [48]. This GMI hysteresis has been explained through the helical magnetic anisotropy [48].

Below we overview a few recent results on GMI effect in microwires paying attention on it suitability for magnetic sensors applications.

4 Fast Domain Wall Dynamics in Thin Wires and Magnetic Bistability

One of the main technological interests for utilization of amorphous microwires is related with Large and single Barkhausen Jump (LBJ) observed above some value of applied magnetic field, called switching field between two stable remanent states[5,17,18] Such particular magnetization process has been observed previously also in conventional amorphous wires [5,11,12]. Abrupt magnetization jump and sharp electrical pulses related with the magnetization switching during LBJ have been proposed in different kinds of magnetic sensors, such as magnetic markers and magnetoelastic sensors [18].

It is worth mentioning that appearance of Large and single Barkhausen jump takes place under magnetic field above some critical value (denominated as switching field) and also if the sample length is above some critical value denominated also as critical length. As described above, switching field depends on magnetoelastic energy determined by the strength of the internal stresses, applied stresses and magnetostriction constant determined by the chemical composition of ferromagnetic metallic nucleus [18,36].

Regarding the critical length, detailed studies of the ferromagnetic wire diameter on magnetization profile and size of the edge closure domains have been performed in [17]. Particularly, critical length, l_c, for magnetic bistability in conventional Fe-rich samples (120 μm in diameter) is about 7 cm. This critical length depends on saturation magnetization, magnetoelastic energy, domain structure and magnetostatic energy [17,18]. Thus, in Co-rich conventional amorphous wires (120 μm in diameter) such critical length is about 4 cm [18]. Below such critical length hysteresis loop loses its squared shape.

The magnetostatic energy depends on the demagnetizing field, H_d, expressed as:

$$H_d=NM_s \tag{7}$$

where N is the demagnetizing factor given for the case of long cylinder with length, l, and diameter, D, as:

$$N=4\pi(\ln(2l/D)-1](D/l)^2) \tag{8}$$

Phenomenon of magnetic bistability observed in different families of amorphous wires is certainly quite interesting for the magnetic sensors applications. But, quite large critical length, l_c, (of the order of few cm) observed in conventional amorphous wires limited these applications. On the other hand, reduction of the metallic nucleus diameter in the case of glass-coated microwires (almost one order lower) results in drastic reduction of the critical length, making them quite attractive for micro-sensor applications. Thus, magnetic bistability for the sample length L= 2 mm has been observed for Fe-rich microwire with metallic nucleus diameter, d, about 10 μm [17,18].

The rectangular hysteresis loop could be interpreted in terms of nucleation or depinning of the reversed domains inside the internal single domain and the consequent domain wall propagation [17,18, 25-27]. Perfectly rectangular shape of the hysteresis loop has been related with a very high velocity of such domain wall propagation.

As mentioned in the introduction recent growing interest on DW propagation is related with proposals for prospective logic and memory devices [41,42]. In these devices, information is encoded in the magnetic states of domains in lithographically patterned nanowires. DW motion along the wires allows for the access and manipulation of the stored information. The speed at which a DW can travel in a wire has an impact on the viability of many proposed technological applications in sensing, storage, and logic operation [25-27].

Quite high DW velocities achieving up to 18 km/s have been reported in glass-coated microwires with few μm diameter [26, 27]. The magnetization process in axial direction runs through the propagation of the single head-to head DW. Consequently glass-coated microwires with reduced diameters presenting magnetic bistability and high DW velocity are quite interesting for sensors applications.

5 Tailoring of Magnetic Properties and GMI of Nearly-Zero Magnetostrictive Microwires by Annealing

As-prepared $Co_{69.2}Fe_{4.1}B_{11.8}Si_{13.8}C_{1.1}$ amorphous microwires present soft magnetic behavior with very low coercivity (about 8 A/m, see Fig.5a). Similar magnetic properties have been previously reported in Co-rich amorphous microwires with nearly-zero negative magnetostriction constant of similar composition [50]. Annealing even for very short time (5 min) at different temperatures induced considerable changes of the hysteresis loops. Effect of annealing temperature, T_{ann}, on character of hysteresis loops is shown in Figs.5b,c. Even 5 minutes annealing at T_{ann}=200^o C considerably affects the hysteresis loops.

Annealing time, t_{ann}, is the other important parameter affecting magnetic properties of studied microwires. Influence of on t_{ann} hysteresis loops of $Co_{69.2}Fe_{4.1}B_{11.8}Si_{13.8}C_{1.1}$ microwires is depicted in Fig.6.

Similarly after annealing at T_{ann} =200^{o}C we were able to observe transformation of initially inclined hysteresis loop to perfectly rectangular when t_{ann} =60 min (fig.7).

As we can appreciate from Figs 5-7 the coercivity, H_c, of studied $Co_{69.2}Fe_{4.1}B_{11.8}Si_{13.8}C_{1.1}$ microwires increases with increasing of the annealing time and annealing temperature. For illustration we presented $H_c(t_{ann})$ dependence measured in $Co_{69.2}Fe_{4.1}B_{11.8}Si_{13.8}C_{1.1}$ microwires at annealing temperature 250 ^{o}C and 300^o C (Fig.8).

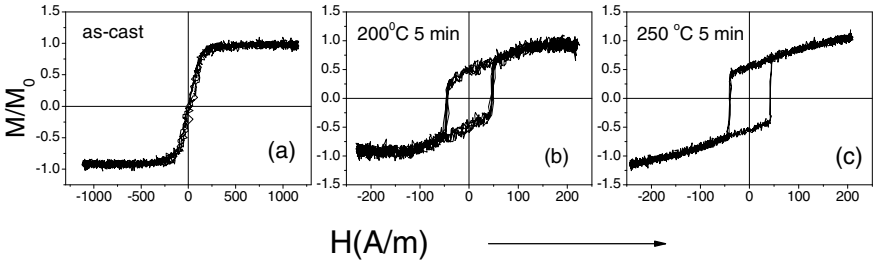

Fig. 5 Hysteresis loops of as-prepared and annealed for 5 min at different temperatures $Co_{69.2}Fe_{4.1}B_{11.8}Si_{13.8}C_{1.1}$ microwires

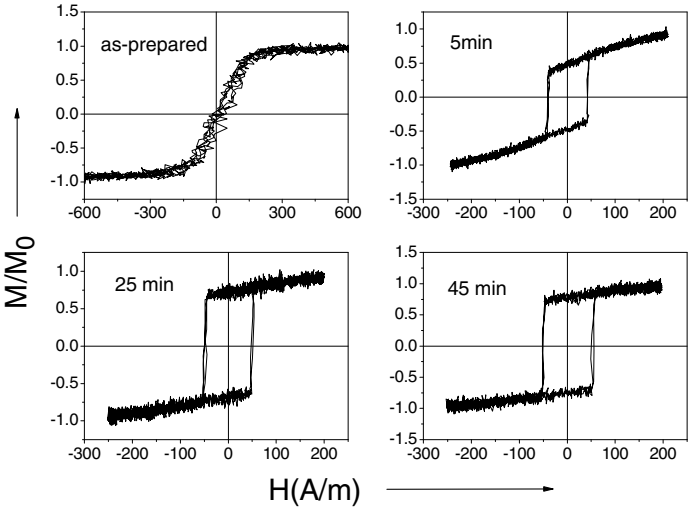

Fig. 6 Effect of annealing time on hysteresis loops of $Co_{69.2}Fe_{4.1}B_{11.8}Si_{13.8}C_{1.1}$ microwires annealed at T_{ann} =250° C

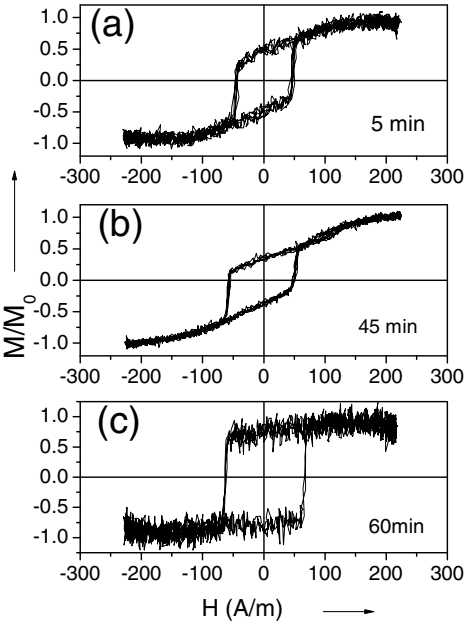

Fig. 7 Effect of annealing time on hysteresis loops of $Co_{69.2}Fe_{4.1}B_{11.8}Si_{13.8}C_{1.1}$ microwires annealed at 200° C

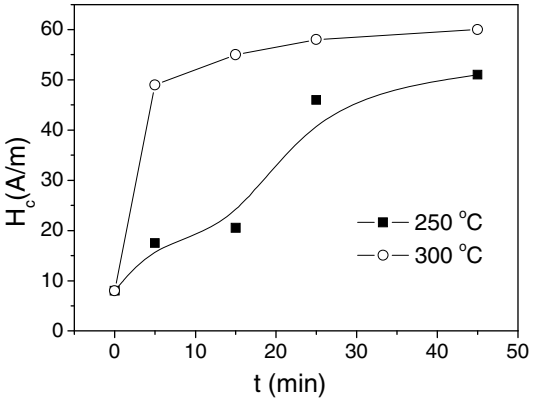

Fig. 8 Dependence of coercivity on annealing time measured in amorphous $Co_{69.2}Fe_{4.1}B_{11.8}Si_{13.8}C_{1.1}$ microwires at two different annealing temperatures: T_{ann}=250 °C and T_{ann}=300 °C

We can observe considerable increasing of coercivity with increasing of both annealing time and annealing temperature.

Usually the inverse tendency: decreasing of coercivity after annealing at temperature below the crystallization temperature is observed in amorphous alloys. One of the conventional mechanisms responsible for the decreasing of the coercivity is the stress relaxation.

For interpretation of observed unusual increasing of coercivity after annealing we must consider not only the stress relaxation but also change of the character of the remagnetization process induced by heat treatment.

Considering the effect of stress relaxation on magnetostriction constant and different character of hysteresis loop in microwires with negative and positive magnetostriction constant we can assume that the second term of the eq. (2) decreases after annealing. This decreasing must be related to the internal stress relaxation (decreasing of σ_i).

Considering comparable values of both terms of eq. (1) one can expect decreasing of magnetostriction constant under applied stresses.

On the other hand there are various factors affecting soft magnetic behavior of amorphous materials.

At least five pinning effects have been identified and discussed by H. Kronmüller [51] as contributing to the total coercivity:

1. Intrinsic fluctuations of exchange energies and local anisotropies, $H_c(i)$
2. Clusters and chemical short ordered regions, $H_c(SO)$
3. Surface irregularities, $H_c(surf)$
4. Relaxation effects due to local structural rearrangements, $H_c(rel)$
5. Volume pinning of domain walls by defect structures in magnetostrictive alloys, $H_c(\sigma)$

Within the framework of the statistical potential theory, the resultant total coercivity was expressed as following [51]:

$$H_c(total)=[\ H_c(\sigma)^2 + H_c(surf)^2 + H_c(SO)^2 + H_c(i)^2\ ]^{1/2} + H_c(rel) \qquad (9)$$

In the case when the surface irregularities give largest contribution, the various terms add linearly [51,52], i.e.:

$$H_c(total)= H_c(\sigma) + H_c(surf) + H_c(SO) + H_c(i) + H_c(rel) \qquad (10)$$

Thermal treatments affect the magnetoelastic anisotropy: after annealing the magnetoelastic anisotropy drastically decreases. On the other hand, after annealing (especially in the presence of magnetic field or/and applied stress) induced magnetic anisotropy can play an important role in amorphous materials.

Thus filed annealing at elevated temperature but below the Curie temperature induces a macroscopic magnetic anisotropy with the preferred axis determined by the direction of the magnetization during the annealing [53]. Moreover, field induced anisotropy increases as the annealing temperature increases, similarly as

the magnetization with the temperature, vanishing at Curie temperature. This behavior has been experimentally observed in metallic glasses with different composition [54-57]. The microscopic origin of this field-induced anisotropy has been successfully explained considering the directional ordering of atomic pairs mechanism developed by Néel [54, 55, 58]. This model predicts a dependence of the field-induced anisotropy with the annealing temperature as:

$$K_{ind}(T) = k\, M_s^n(T) \tag{11}$$

Where n is a constant, the value of which can be assumed to be equal 2 if the microscopic origin is the directional ordering of atomic pairs. Theoretical predicted value of the index n was experimental found in FeNi-based metallic glasses [58]. Nevertheless, deviations of such theoretical value have been obtained in Co-Fe based metallic glasses [59, 60]. In this case, an additional contribution coming from the single-ion (initially n = 3) is considered. Moreover depending of the annealing temperature each contribution could be different according to the content of magnetic elements.

Therefore macroscopically isotropic amorphous alloys can exhibit macroscopic magnetic anisotropy in the case if they are subjected to suitable annealing treatments at the presence of either a magnetic field (field annealing, FA) or a mechanical stress (stress annealing, SA).

The case of glass-coated microwires is even more complex, because the presence of glass-coating induces strong internal stresses. Consequently these internal stresses must be considered as the factor that can affect magnetic anisotropy after annealing of glass-coated microwires even without applied stresses. Particularly unusually strong effect of applied magnetic on overall shape of hysteresis loops and hysteretic magnetic properties (coercivity, magnetic permeability etc) has been explained considering effect of stress+field annealing [28, 61].

Previously stress+field annealing has been performed in several amorphous alloys and it has been shown that the stress+field induced magnetic anisotropy cannot be supposed as a simple sum of the stress-induced anisotropy and the field induced anisotropy. The stress+field induced magnetic anisotropy is much stronger that just superposition of the stress-induced anisotropy and the field induced anisotropy [43]. The evolution of these two kinds of anisotropy as a function of the annealing temperature is quite different with respect to field induced anisotropy. The origin of stress+field induced magnetic anisotropy has been ascribed to the magnetic ordering of pair atoms at high annealing temperatures the development of a longitudinal plastic component and change of the local short range order which is introduced by the stress during the thermal treatment at lower annealing temperature [56, 62].

Considering aforementioned we can predict that application of tensile stress during annealing must reinforce above reported tendency on increasing of coercivity after annealing.

Therefore we performed stress annealing of $Co_{69.2}Fe_{4.1}B_{11.8}Si_{13.8}C_{1.1}$ microwire without stress and under applied stress. As can be appreciated from Fig.9

hysteresis loops changed drastically after annealing at T_{ann} =300 C. Coercivity of annealed sample increased few times. But stress annealed sample exhibit lower coercivity (Fig.9c).

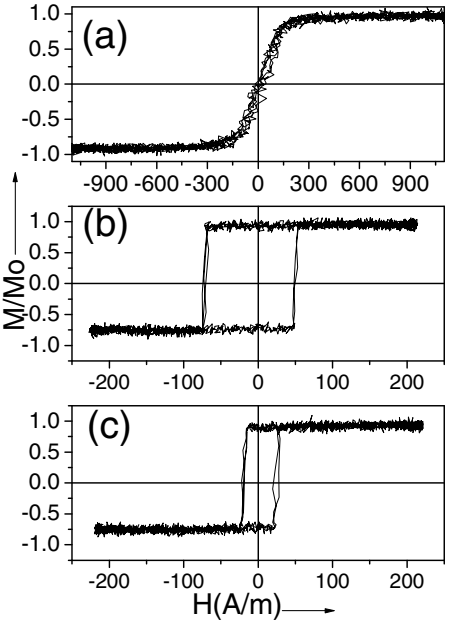

Fig. 9 Hysteresis loops of as-prepared (a) and annealed at T_{ann} = 300 °C for 45 min $Co_{69.2}Fe_{4.1}B_{11.8}Si_{13.8}C_{1.1}$ microwires without applied stress (b) and under stress (c)

Previously we performed stress annealing of Fe-rich glass-coated microwires and we observed drastic changes of hysteresis loops, increasing of magnetic permeability, GMI effect and decreasing of coercivity [40, 63,64]. These changes in amorphous microwires containing only one magnetic element (Fe) have been explained considering so called "back" stresses arising from glass-coating and compensating internal stresses induced during fabrication process with the axial component predominant in most of the metallic nucleus volume.

For interpretation of observed coercivity decreasing after stress annealing we must consider aforementioned knowledge of mechanism of stress induced anisotropy in different families of amorphous materials.

If similarly to the case of Fe-rich microwires we consider "back stresses" arising during the stress annealing, we must take into account the influence of bask stresses on magnetostriction constant (see eq.2).

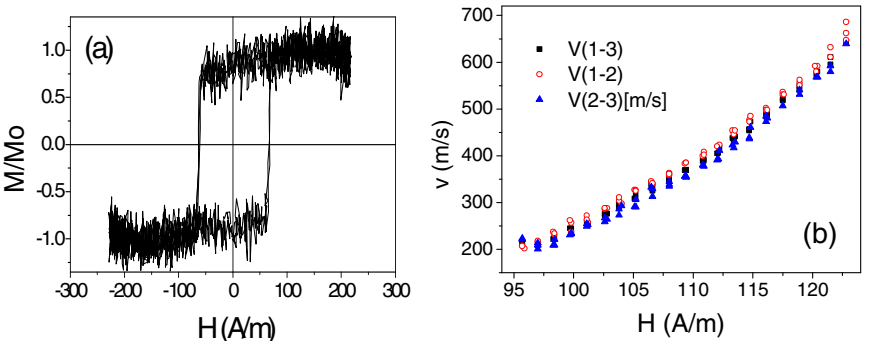

Fig. 10 Hysteresis loop (a) and dependence of DW velocity on magnetic field (b) measured in $Co_{69.2}Fe_{4.1}B_{11.8}Si_{13.8}C_{1.1}$ microwires annealed at T_{ann} =200 ^{0}C for 60 min

Then indeed considering that stress relaxation after annealing without stress induce stress relaxation and change of the magnetostriction sign from low negative to low positive back stresses must produce decreasing of the magnetostriction constant in according to eq.(2).

In according to this explanation increasing of coercivity and rectangular character of hysteresis loops (Figs. 6,7) after annealing must be attributed to the stress relaxation and corresponding magnetostriction change.

Considering two contributions in the magnetoelastic energy given by eq. (1) we can assume that if the magnetostriction constant is low and positive we must consider two opposite effects of applied stresses. The first contribution is increasing of the total magnetoelastic energy (as usually described elsewhere, see [26,43]). The second one must be related to the effect of applied stress on the magnetostriction constant and in according to eq. (2) must be relevant only for the case of the low magnetostriction constant. In according to the eq. (2) the magnetostriction constant under stress, $\lambda_{s,\sigma,}$ must decrease and can be considerable if the zero-stress magnetostriction constant, $\lambda_{s,0}$, is low.

We performed measurements of the DW dynamics considering the rectangular character of hysteresis loops in annealed $Co_{69.2}Fe_{4.1}B_{11.8}Si_{13.8}C_{1.1}$ microwire. Indeed, although in as-prepared state studied sample had inclined hysteresis loop indicating that the remagnetization of this sample is running through the DW propagation within the inner single-domain core (Fig.10).

The DW velocity achieved in this sample was not very high. Higher DW velocities, v, have been observed in the $Co_{69.2}Fe_{4.1}B_{11.8}Si_{13.8}C_{1.1}$ microwire annealed at 300 ^{0}C for 45 min which also presents rectangular hysteresis loop (Fig.11 a). As can be appreciated, $v(H)$ dependences present typical nearly-linear growth of DW velocity with magnetic field, H. Observed DW velocity are high enough, similarly to other v values reported for low magnetostrictive microwires with magnetic bistability presenting fast DW propagation [26,43]. The most unusual behavior is that instead of usually observed DW decreasing under effect of applied stresses we observed considerable enhancement of DW velocity at given H-values (Fig.11b).

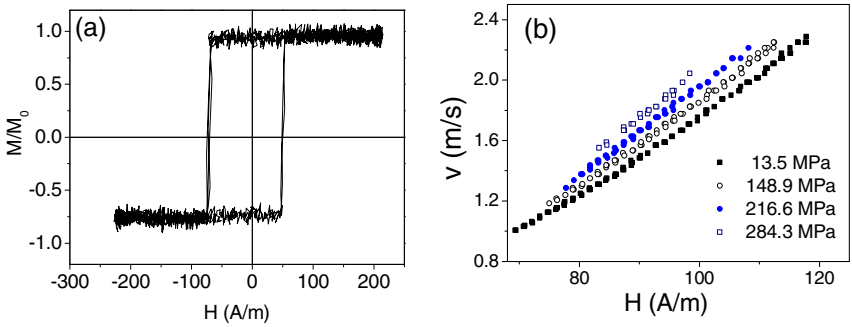

Fig. 11 Hysteresis loop (a), dependence of DW velocity on magnetic field measured in $Co_{69.2}Fe_{4.1}B_{11.8}Si_{13.8}C_{1.1}$ microwires annealed at T_{ann} =300 ^{0}C for 45 min under different stresses (b)

This DW velocity increasing must be attributed to the decreasing of the magnetostriction constant under effect of applied stress.

As-prepared $Co_{69.2}Fe_{4.1}B_{11.8}Si_{13.8}C_{1.1}$ microwire present rather high GMI effect (GMI ratio, ΔZ/Z, up to 300%, see Fig.12a). We studied also GMI effect in annealed samples. As can be appreciated from Fig.12 the GMI ratio of annealed at 300 C for 5 minutes microwire is lower than in as-prepared microwire (ΔZ/Z≈160%). Additionally we observed a change of the magnetic field dependence of *ΔZ/Z*: the field of maximum is lower in annealed microwire for all measured frequencies. As discussed elsewhere the field of maximum corresponds to the magnetic anisotropy field [6]. Moreover magnetic field dependence of GMI ratio is strongly affected by magnetic anisotropy [65,66].

It is worth mentioned that annealed sample also present considerable off-diagonal GMI effect represented by S_{21} (Fig.12c). Like reported for other Co-rich microwires bias field, H_B, produced by bias current, I_B, strongly affects the off-diagonal impedance (Fig.12c). But even under I_B=70 mA considerable hysteresis is observed reflecting considerable helical magnetic anisotropy of the sample [48]. Even more unusual is that annealed sample exhibiting considerable GMI effect (ΔZ/Z, up to 150% at 100 MHz) has roughly rectangular hysteresis loop (Fig.13a). But it is worth mentioning, that the flat regions of the hysteresis loop present considerable slope, i.e. considerably high magnetic permeability than microwires annealed longer time (compare Fig.13a and Fig.11a). We can therefore assume that the outer domain shell presents high magnetic permeability. On the other hand the same sample presents also quite fast domain wall dynamics: we observed typical single DW propagation with nearly-linear growth of DW velocity v with magnetic field, H. Maximum DW velocity observed in this sample was about 2.5 km/s.

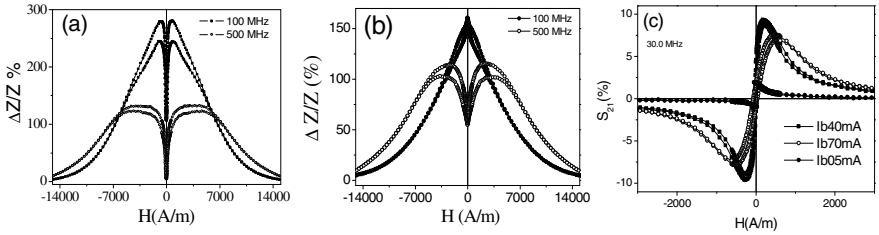

Fig. 12 Diagonal GMI effect of as-prepared (a) and diagonal (b) and off diagonal (c) GMI effect measured in annealed at 300ºC for 5 minutes $Co_{69.2}Fe_{4.1}B_{11.8}Si_{13.8}C_{1.1}$ microwires measured at different frequencies

Observed dependences allow deducing that annealing induces axial magnetic anisotropy.

Indeed, samples annealed at higher temperature for longer time present perfectly rectangular hysteresis loops typical for microwires with positive magnetostriction constant presenting axial easy magnetization axis (see Fig.6).

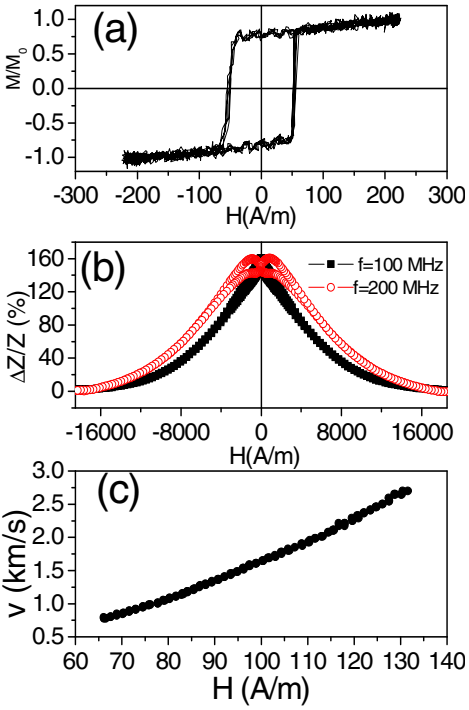

Fig. 13 Hysteresis loop (a) magnetic field dependence of the GMI ratio (b) and v(H) dependence measure in of annealed at 300ºC for 5 minutes $Co_{69.2}Fe_{4.1}B_{11.8}Si_{13.8}C_{1.1}$ microwires

As mentioned above to explain observed dependences we must consider two parallel phenomena:

i) Stress relaxation induced by the annealing affects the magnetostriction constant. Moreover after annealing of $Co_{69.2}Fe_{4.1}B_{11.8}Si_{13.8}C_{1.1}$ microwire even change the magnetostriction sign from negative to positive takes place.

ii) Applying tensile stresses affects the magnetostriction constant allowing reduction of magnetoelastic energy and achievement faster DW propagation.

Tensile stress applied during annealing creates "back" stresses reducing the magnetostriction constant.

Understanding of the processes affecting formation of magnetic anisotropy and determining the remagnetization process of Co-Fe rich microwires with low magnetostriction constant allows us to tailor magnetic properties and to find the annealing conditions at which we can observe simultaneously fast DW propagation and considerable GMI effect.

6 Conclusions

This chapter reviewed the most promising properties for industrial applications of magnetically soft thin wires in magnetic sensors: GMI effect and fast domain wall propagation.

It is demonstrated that magnetic properties of amorphous Co-rich microwires can be tailored by annealing. Conventional and stress annealing considerably affect hysteresis loop, GMI effect and DW dynamics of studied samples. Observed dependences discussed considering stress relaxation and change of the magnetostriction after samples annealing. At certain annealing conditions we observed coexistence of GMI effect and fast DW propagation in the same annealed sample. Moreover after annealing at certain conditions we observed increasing of DW velocity under applied tensile stress. Understanding of the processes affecting formation of magnetic anisotropy and determining the remagnetization process of Co-Fe rich microwires with low magnetostriction constant allows us to tailor magnetic properties and to find the annealing conditions at which we can observe simultaneously fast DW propagation and considerable GMI effect.

Acknowledgements. This work was supported by EU ERA-NET program under project "SoMaMicSens" (MANUNET-2010-Basque-3), by EU under FP7 "EM-safety" project, by Spanish Ministry of Science and Innovation, MICINN under Project MAT2010-18914, by the Basque Government under SAIOTEK-2012 MEMFOMAG (S-PE12UN139) and SAIOTEK 13 PROMAGMI (SA-2013/00035) and DURADMAG (SA-2013/00018) projects.

References

[1] McHenry, M.E., Willard, M.A., Laughlin, D.E.: Amophous and nanocrystalline materials for application as soft magnet. Progress in Materials Science 44, 291–433 (1999)

[2] Durand, J.: Magnetic Properties of Metallic Glasses. In: Beck, H., Giintherodt, H.-J. (eds.) Topics in Applied Physics. Glassy Metals II, vol. 53, Springer, New York (1983)

[3] Herzer, G.: Amorphous and Nanocrystalline Materials. In: Encyclopedia of Materials: Science and Technology, pp. 149–157. Elsevier Science Ltd. (2001) ISBN: 0-08-0431526

[4] Kanno, T., Mohri, K., Yagi, T., Uchiyama, T., Shen, L.P.: Amorphous wire range ordered proton transport through cyclotron resonance. IEEE Trans. Magn. Mag-33, 3358–3360 (1997)

[5] Vazquez, M., Chiriac, H., Zhukov, A., Panina, L., Uchiyama, T.: On the state-of-the-art in magnetic microwires and expected trends for scientific and technological studies. Phys. Status Solidi A 208, 493–501 (2011)

[6] Panina, L.V., Mohri, K.: Magneto- Impedance Effect in Amorphous Wires. Appl. Phys. Lett. 65, 1189–1191 (1994)

[7] Beach, R., Berkowitz, A.: Giant magnetic field dependent impedance of amorphous. FeCoSiB wire. Appl. Phys. Lett. 64, 3652–3654 (1994)

[8] Ponomrev, B.K., Zhukov, A.: Start field fluctuations in amorphous Co70Fe5Si10B15 alloy. Fizika Tverdogo Tela 26(10), 2974–2979 (1984)

[9] Guo, H.Q., Kronmüller, H., Dragon, T., Cheng, Z.H., Shen, B.G.: Influence of nanocrystallization on the evolution of domain patterns and the magnetoimpedance effect in amorphous Fe73.5Cu1Nb3Si13.5B9 ribbons. J. Appl. Phys. 89, 514–520 (2001)

[10] Mohri, K., Humphrey, F.B., Kawashima, K., Kimura, K., Muzutani, M.: Large Barkhausen and Matteucci effects in FeCoSiB, FeCrSiB and FeNiSiB amorphous wires. IEEE Trans. Magn. Mag-26, 1789–1793 (1990)

[11] Vazquez, M., Hernando, A.: A soft magnetic wire for sensor application. J. Phys. D: Appl. Phys. 29, 939–949 (1996)

[12] Vazquez, M., Gomez-Polo, C., Chen, D.-X.: Switching mechanism and domain structure of bistable amorphous wires. IEEE Trans. Magn. 28(5), 3147–3149 (1992)

[13] Zhukova, V., Zhukov, A., Blanco, J.M., Usov, N., Gonzalez, J.: Effect of applied stress on remagnetizationand magnetization profile of CoSiB amorphous wires. J. Magn. Magn. Mater. 258-259, 189–191 (2003)

[14] Mohri, K., Honkura, Y.: Amorphous Wire and CMOS IC Based Magneto-Impedance Sensors– Origin, Topics, and Future. Sensor Lett. 5(2), 267–270 (2007)

[15] Zhukova, V., Zhukov, A., Garcia, K.L., Kraposhin, V., Prokoshin, A., Gonzalez, J., Vazquez, M.: Magnetic properties and GMI of soft melt-extracted magnetic amorphous fibers. Sensors and Actuators (A) 106, 225–229 (2003)

[16] Menard, D., Britel, M., Ciureanu, P., Yelon, A.: Giant magneto impedance in a cylindrical magnetic conductor. J. Appl. Phys. 84(5), 2805–2814 (1998)

[17] Zhukov, A.P., Vazquez, M., Velazquez, J., Chiriac, H., Larin, V.: The remagnetization process in thin and ultra thin Fe-rich amorphous wires. J. Magn. Magn. Mat. 151, 132–138 (1995)

[18] Zhukov, A., Zhukova, V.: Magnetic properties and applications of ferromagnetic microwires with amorphous and nanocrystalline structure. Nova Science Publishers, New York (2009) ISBN: 978-1-60741-770-5

[19] Zhukova, V., Cobeño, A.F., Zhukov, A., de Arellano Lopez, A.R., Lopez-Pombero, S., Blanco, J.M., Larin, V., Gonzalez, J.: Correlation between magnetic and mechanical properties of devitrified glass-coated Fe71.8Cu1Nb3.1Si15B9.1 microwires. J. Magn. Magn. Mat. 249, 79–84 (2002)

[20] Usov, N.A., Antonov, N.A.A.S., Lagar'kov, A.N.: Theory of giant magneto-impedance effect in amorphous wires with different types of magnetic anisotropy. J. Magn. Magn. Mat. 185, 159–173 (1998)

[21] Vázquez, M., García-Beneytez, J.M., García, J.M., Sinnecker, J.P., Zhukov, A.: Giant magneto-impedance in heterogeneous microwires. J. Appl. Phys. 88, 6501–6505 (2000)

[22] Chiriac, H., Ovari, T.-A., Zhukov, A.: Magnetoelastic anisotropy of amorphous microwires. Magn. Magn. Mater. 254–255, 469–471 (2003)

[23] Antonov, A.S., Borisov, V.T., Borisov, O.V., Prokoshin, A.F., Usov, N.A.: Residual quenching stresses in glass coated amorphous ferromagnetic microwires. J. Phys. D: Appl. Phys. 33, 1161–1168 (2000)

[24] Panina, L.V., Mizutani, M., Mohri, K., Humphrey, F.B., Ogasawara, I.: Dynamics and relaxation of large Barkhausen discontinuity in amorphous wires. IEEE Trans. Magn. 27(6), 5331–5333 (1991)

[25] del Real, R.P., Prados, C., Chen, D.-X., Hernando, A., Vazquez, M.: Eddy current damping of planar domain wall in bistable amorphous wires. Appl. Phys. Lett. 63, 3518–3520 (1993)

[26] Zhukov, A., Blanco, J.M., Ipatov, M., Zhukova, V.: Fast magnetization switching in thin wires: Magnetoelastic and defects contributions. Sensor Letters 11(1), 170–176 (2013)

[27] Varga, R., Richter, K., Zhukov, A., Larin, V.: Domain wall propagation in thin magnetic wires. IEEE Trans. Magn. 44(11), 3925–3930 (2008)

[28] Garcia Prieto, M.J., Pina, E., Zhukov, A.P., Larin, V., Marin, P., Vázquez, M., Hernando, A.: Glass coated Co-rich Amorphous Microwires with Improved Permeability. Sensors & Actuators A 81(1-3), 227–231 (2000)

[29] Catalan, C.F., Prida, V.M., Alonso, J., Vázquez, M., Zhukov, A., Hernando, B., Velázquez, J.: Effect of glass coating on magnetic properties of amorphous microwires. Rapidly Quenched & Metastable Materials, Materials Science & Engineering A, Supplement, 438–441 (1997)

[30] Zhukova, V., Cobeño, A.F., Zhukov, A., Blanco, J.M., Puerta, S., Gonzalez, J., Vázquez, M.: Tailoring of magnetic properties of glass coated microwires by current annealing. Non-crystalline Solids 287, 31–36 (2001)

[31] Zhukov, A., Zhukova, V., Blanco, J.M., Cobeño, A.F., Vazquez, M., Gonzalez, J.: Magnetostriction in glass-coated magnetic microwires. J. Magn. Magn. Mater. 258-259, 151–157 (2003)

[32] Konno, Y., Mohri, K.: Magnetostriction measurements for amorphous wires. IEEE Trans. Magn. 25(5), 3623–3625 (1989)

[33] Barandiaran, M., Hernando, A., Madurga, V., Nielsen, O.V., Vazquez, M., Vazquez-Lopez, M.: Temprature, stress, and structural relaxtion dependece of the magnetostriction in metallic glasses. Phys. Rev. B 35, 5066–5071 (1987)

[34] Qin, F., Peng, H.-X.: Ferromagnetic microwires enabled multifunctional composite materials. Progress in Materials Science 58, 183–259 (2013)

[35] Uchiyama, T., Mohri, K., Nakayama, S.: Measurement of spontaneous oscillatory magnetic field of guinea-pig stomach muscle preparation using pico-Tesla resolution amorphous wire magneto-impedance sensor. IEEE Trans. Magn. 47(10), 3070–3073 (2011)

[36] Zhukova, V., Ipatov, M.: Thin magnetically soft wires for magnetic microsensors. Sensors 9, 9216–9240 (2009)

[37] Churyukanova, M., Zhukova, V., Talaat, A., del Val, J.J., Kaloshkin, S., Kostitcyna, E., Shuvaeva, E., Sudarchikova, V., Zhukov, A.: Studies of thermal and magnetic properties of Fe- based amorphous and nanocrystalline glass coated microwires. J. Alloys Comp. (2013), http://dx.doi.org/10.1016/j.jallcom.2013.12.030

[38] Talaat, A., Zhukova, V., Ipatov, M., Blanco, J.M., Churyukanova, M., Kaloshkin, S., Kostitcyna, E., Shuvaeva, E., Sudarchikova, V., Gonzalez-Legarreta, L., Hernando, B., Zhukov, A.: Giant Magnetoimpedance Effect in Nanocrystalline Microwires. In: PIERS Proceedings, Stockholm, Sweden, August 12-15, pp. 12–46 (2013)

[39] Zhukov, A., Zhukova, V., Larin, V., Blanco, J.M., Gonzalez, J.: Tailoring of magnetic anisotropy of Fe-rich microwires by stress induced anisotropy. Physica B 384, 1–4 (2006)

[40] Zhukova, V., Larin, V.S., Zhukov, A.: Stress induced magnetic anisotropy and giant magnetoimpedance in Fe-rich glass/coated magnetic microwires. J. Appl. Phys. 94(2), 1115–1118 (2003)

[41] Hayashi, M., Thomas, L., Rettner, C., Moriya, R., Jiang, X., Parkin, S.: Dependence of Current and Field Driven Depinning of Domain Walls on Their Structure and Chirality in Permalloy Nanowires. Phys. Rev. Lett. 97, 207205 (2006)

[42] Allwood, D.A., Xiong, G., Faulkner, C.C., Atkinson, D., Petit, D., Cowburn, R.P.: Magnetic Domain-Wall Logic. Science 309, 1688–1692 (2005)

[43] Zhukov, A., Blanco, J.M., Ipatov, M., Chizhik, A., Zhukova, V.: Manipulation of domain wall dynamics in amorphous microwires through the magnetoelastic anisotropy. Nanoscale Research Letters 7, 223 (1-8) (2012)

[44] Varga, R., Zhukov, A., Blanco, J.M., et al.: Fast magnetic domain wall in magnetic microwires. Phys. Rev. B 74, 212405 (2006)

[45] Parkin, S.S.P., Hayashi, M., Thomas, L.: Magnetic domain wall racetrack memory. Science 320, 190–194 (2008)

[46] Yang, J., Nistor, C., Beach, G.S.D., Erskine, J.L.: Magnetic domain-wall velocity oscillations in permalloy nanowires. Phys. Rev. B 77, 14413 (2008)

[47] Cobeño, A.F., Zhukov, A., de Arellano-Lopez, A.R., Elías, F., Blanco, J.M., Larin, V., González, J.: Stress Dependence of switching field in ultra-thin amorphous wires. J. Mater. Res. 14, 3775–3783 (1999)

[48] Ipatov, M., Zhukova, V., Zhukov, A., Gonzalez, J., Zvezdin, A.: Low-field hysteresis in the magnetoimpedance of amorphous microwires. Phys. Rev. B 81, 134421 (2010)

[49] Zhukov, A., Blanco, J.M., Chizhik, A., Ipatov, M., Rodionova, V., Zhukova, V.: Manipulation of domain wall dynamics in amorphous microwires through domain wall collision. J. Appl. Phys. 114, 43910 (2013)

[50] Zhukov, A., Ipatov, M., Churyukanova, M., Kaloshkin, S., Zhukova, V.: Giant magnetoimpedance in thin amorphous wires: From manipulation of magnetic field dependence to industrial applications. J. Alloys Comp. 586(suppl. 1), S279–S286 (2014)

[51] Kronmüller, H., Fähnle, M., Domann, M., Grimm, H., Grimm, R., Groger, B.: Magnetic properties of amorphous ferromagnetic alloys. J. Magn. Magn. Mat. 13, 53–70 (1979)
[52] Kronmüller, H.: Micromagnetism and microstructure of amorphous alloy. J. Appl. Phys. 52, 1859–1864 (1981)
[53] Vázquez, M., Ascasibar, E., Hernando, A., Nielsen, O.V.: Co-Si-B and Fe-Co-B amorphous alloys: Induced anisotropy and various magnetic properties. J. Magn. Magn. Mat. 66, 37–44 (1987)
[54] Luborsky, F.E., Walker, J.L.: Magnetic Anneal Anisotropy in Amorphous Alloys. IEEE Trans. Magn. Mag-13, 953–956 (1977)
[55] Miyazaki, T., Takahashi, M.: Magnetic Annealing Effect of Amorphous (Fe1-xCox)77Si10B13 Alloys. Jap. J. Appl. Phys. 17, 1755–1763 (1978)
[56] Nielsen, O.V., Nielsen, H.J.V.: Strain- and field-induced magnetic anisotropy in metallic glasses with positive or negative γs. Solid State Communications 35, 281–284 (1980)
[57] González, J., Vázquez, M., Barandiarán, J.M., Madurga, V., Hernando, A.: Different Kinds of Anisotropies Induced by Current Annealing in Metallic Glasses. J. Magn. Magn. Mat. 68, 151–156 (1987)
[58] Néel, M.L.: Anisotropie magnétique superficielle et surstructures d'orientation. J. Phys. Radium 15, 225–239 (1954)
[59] Chen, D.X., Tai, L.C.: Temprature dependence of induced magnetic anisotropies in metallic glasses (Fe1 – xCox)78Si10B12. J. Magn. Magn. Mat. 50, 329–334 (1985)
[60] Chen, D.X.: Induced anisotropy and magnetostriction in metallic glasses. J. Appl. Phys. 61, 3781–3783 (1987)
[61] Zhukov, A., Gonzalez, J., Blanco, J.M., Prieto, M.J., Pina, E., Vazquez, M.: Induced Magnetic Anisotropy in Co-Mn-Si-B Amorphous Microwires. J. Appl. Phys. 87, 1402–1408 (2000)
[62] González, J., Barandiarán, J.M., Vázquez, M., Hernando, A.: Effects of Current Annealing on the Hysteresis Loop of Amorphous Alloys. Anales de Física (B) 86, 184–186 (1990)
[63] Zhukov, A., Ipatov, M., Garcia, C., Churyukanova, M., Kaloshkin, S., Zhukova, V.: 'From Manipulation of Giant Magnetoimpedance in Thin Wires to Industrial Applications. J. Supercond. Nov. Magn. 26(4), 1045–1054 (2013)
[64] Zhukov, A.: Design of magnetic properties of Fe-rich glass – coated magnetic microwires for technical applications. Adv. Func. Mat. 16(5), 675–680 (2006)
[65] Blanco, J.M., Zhukov, A., Gonzalez, J.: Asymmetric torsion stress giant magnetoimpedance in nearly-zero magnetostrictive amorphous wires. J. Appl. Phys. 87(9), 4813–4815 (2000)

Author Index